Complexity

Theoretical and Applied Contributions to Robust Stability Analysis of Complex Systems

Lead Guest Editor: Baltazar Aguirre-Hernandez
Guest Editors: Raúl Villafuerte-Segura, Alberto Luviano Juárez, and John Cortés-Romero

Theoretical and Applied Contributions to Robust Stability Analysis of Complex Systems

Complexity

Theoretical and Applied Contributions to Robust Stability Analysis of Complex Systems

Lead Guest Editor: Baltazar Aguirre-Hernandez
Guest Editors: Raúl Villafuerte-Segura, Alberto Luviano Juárez, and John Cortés-Romero

Contents

Hindawi
Complexity
Volume 2020, Article ID 7083781, 2 pages
https://doi.org/10.1155/2020/7083781

Editorial

Theoretical and Applied Contributions to Robust Stability Analysis of Complex Systems

Baltazar Aguirre-Hernández,[1] **Raúl Villafuerte-Segura**,[2] **Alberto Luviano-Juárez**,[3] **and John Cortés-Romero**[4]

[1]*Departamento de Matemáticas, Universidad Autónoma Metropolitana—Iztapalapa, San Rafael Atlixco 186, CDMX, México 09340, Mexico*
[2]*Centro de Investigación en Tecnologías de Información y Sistemas, Universidad Autónoma Del Estado de Hidalgo, Pachuca, Hidalgo, Mexico*
[3]*Instituto Politécnico Nacional, UPIITA, Mexico City, Mexico*
[4]*Universidad Nacional de Colombia, Bogotá, Colombia*

Correspondence should be addressed to Baltazar Aguirre-Hernández; bahe@xanum.uam.mx

Received 25 February 2020; Accepted 25 February 2020; Published 10 June 2020

In the study of the dynamics of a complex system, stability is one of the more interesting aspects since a stability analysis provides the principles and methods useful for engineers, mathematicians, and others to obtain a better understanding of the system. This allows us to understand the nature of the dynamics of the system and propose a new controller or improve control designs, optimizing or increasing performance.

On the other hand, it is common that the mathematical models of dynamic complex systems are, in practice, imprecise due to uncertainties, parametric variations, nonmodeled dynamics, neglected terms in simplifications, etc., among others. Hence, a robust stability analysis for complex systems is essential to achieve results that more closely resemble real-world platforms.

Without a doubt, the robustness of stability is one of the most active research areas in the framework of the analysis and control of dynamic systems.

In the paper "A PI-Type Sliding Mode Controller Design for PMSG-Based Wind Turbine," J. Liu et al. improve the stabilization of a permanent magnet synchronous generator-(PMSG-) based wind energy conversion systems (WECS) by means of a PI-Type sliding mode controller. The results are supported by the application of the Lyapunov stability theory and numerical simulations.

The paper "Robust Finite-Time Tracking for Uncertain Linear Systems with Actuator Faults" by X. Peng et al. presents a robust finite-time fault-tolerant control (FTC) scheme for a class of uncertain linear systems in the presence of multiple actuator faults. The adaptive laws were used to compensate the effects of faults and uncertainties. It is shown that the proposed state-feedback model reference adaptive finite-time FTC scheme can guarantee that the tracking error converges to a small neighborhood of the origin in finite time. Simulations are presented for illustrating the proposed design.

In the paper "Research on Optimization of Production Decision Based on Payment Time and Price Coordination," Y. Yan et al. construct a mathematical model of the optimal quote and delivery time of orders between a manufacturer and several retailers, which also includes penalties for late delivery to the manufacturer, in a supply chain. The authors apply the shorter processing time rule (SPT) to solve the problem of production scheduling and use the fact that the gain function (objective function) is a convex function to find the delivery time and the optimal price.

The paper "Ground Attack Strategy of Cooperative UAVs for Multitargets" by Q. Zhang and R. Wei proposes a strategy of a parallel multiview splicing on clouds (PMVSC) unmanned aerial vehicles using precise target recognition and attack and task assignment. Simulations and experiments are performed on an experimental cooperative UAVs platform in order to implement the proposed algorithm.

In the paper "Risk Analysis of Emergency Based on Fuzzy Evidential Reasoning" by X. Qiao and D. Shi, the proposed analytical reference framework allows the authors to provide an approach based on fuzzy evidential reasoning to analyze, model, and process emergency risks.

The paper "LMI-Based Robust Stabilization of a Class of Input-Constrained Uncertain Nonlinear Systems with Application to a Helicopter Model" by H. Gritli considers the robust stabilization of the pitch dynamics of a helicopter model with uncertainties and disturbances via a theoretical framework based on a LMI approach in order to design a state-feedback control law.

The reachable set bounding for homogeneous nonlinear time-delay systems with bounded disturbance is studied in the paper "Reachable Set Bounding for Homogeneous Nonlinear Systems with Delay and Disturbance" by X. Zhu and Y. Sun. Here, the authors establish a necessary and sufficient condition such that all the system solutions converge asymptotically within a specific ball. Finally, a numerical example is presented to illustrate the proposed theoretical results.

A saturation control with a feedforward term to the trajectory tracking task of a magnetic levitation system connected to a beam mechanism is proposed in the paper "Nested Saturation Function Control of a Magnetic Levitation System" by O. Gutíerrez-Frías et al. The proposal consists in using the flatness of the system to transform the system in an integrator chain, while a controller based on a nested saturated function and a feedforward term are used to force the output trajectories to converge towards the reference trajectory. The closed-loop solution is proven to be locally exponentially stable by means of the second method of Lyapunov. Lastly, numerical simulations prove the effectiveness of the proposal.

The event-triggered strategy for multiple neural networks with parameter uncertainty and time delay is presented in the paper "Global Robust Exponential Synchronization of Multiple Uncertain Neural Networks Subject to Event-Triggered Strategy" by J.-E. Zhang and H. Liu. Here, several sufficient criteria to ensure global robust exponential synchronization of coupling neural networks using matrix inequality techniques are given. Eventually, three numerical examples are offered to illustrate the obtained results.

A fuzzy robust control to mitigate the bullwhip effect in the uncertain closed-loop supply chain with lead times is proposed in the paper "Mitigation of Bullwhip Effect in Closed-Loop Supply Chain Based on Fuzzy Robust Control Approach" by S. Zhang and M. Zhang. For this, the lead times are included in the closed-loop supply chain models, an additional Takagi-Sugeno fuzzy controller for lead times is designed, and a new fuzzy robust control approach is put forward to effectively mitigate the bullwhip effect caused by uncertainties and lead times, and the stability of the closed-loop supply chain system using LMIs is ensured.

A trajectory tracking control algorithm based on a fractional-order PD controller for a wheeled mobile robot is presented in the paper "Design, Implementation, and Validation of Robust Fractional-Order PD Controller for Wheeled Mobile Robot Trajectory Tracking" by L. Zhang et al. For robust fractional-order controller regulation, an improved flat phase property as a robust controller tuning specification is put forward to guarantee the robust flat phase frequency interval width instead of only one flat phase frequency.

The problem of establishing tuning rules to a proportional retarded controller for LTI systems is addressed in the paper "σ-Stabilization of a Flexible Joint Robotic Arm via Delayed Controllers" by G. Ochoa-Ortega et al. The proposal consists in giving analytic conditions to σ-stabilize this system class and guarantee a maximal decay rate in the system response. The conditions presented in this paper are tested experimentally in tracking tasks on a underactuated mechanical nonlinear system known as flexible joint robotic arm using a feedback linearization approach.

Concerning the robust stabilization of systems subject to oscillations and possible impacts, a robust LMI-based control approach is proposed in the paper "Robust Position Control of a Two-Sided 1-DoF Impacting Mechanical Oscillator Subject to an External Persistent Disturbance by Means of a State-Feedback Controller," by F. Turkia et al. The authors provide the stabilization conditions of the controlled hybrid dynamics by means of the S-procedure in terms of bilinear matrix inequalities, which are converted into linear matrix inequalities. Numerical simulations for different conditions are provided to show the effectiveness of the proposal.

Considering again fractional-order systems but with an adaptive backstepping control scheme, the paper "Adaptive Neural Network Control of a Class of Fractional Order Uncertain Nonlinear MIMO Systems with Input Constraints" by C. Wang et al. ensures the convergence of tracking errors even with dead-zone and saturation nonlinearities in the controller input. In this work, unknown nonlinear uncertainties are approximated by a radial basis function neural network and the parameters update laws with incommensurate fractional order are used in the controller to compensate those unknown nonlinearities. Two simulation results are presented to validate the efficacy of the proposed scheme.

Conflicts of Interest

The guest editors declare that they have no conflicts of interest regarding the publication of this Special Issue.

Acknowledgments

The guest editors would like to thank the authors of all the papers submitted to their interest in this Special Issue and express their enormous thankfulness to the reviewers for their valuable time and effort as well as for providing constructive comments to the authors, making this Special Issue viable.

Baltazar Aguirre-Hernández
Raúl Villafuerte-Segura
Alberto Luviano-Juárez
John Cortés-Romero

Hindawi
Complexity
Volume 2020, Article ID 3545374, 9 pages
https://doi.org/10.1155/2020/3545374

Research Article

Nested Saturation Function Control of a Magnetic Levitation System

Octavio Gutiérrez-Frías, Norma Lozada-Castillo, J. Alejandro Aguirre-Anaya, and Diego A. Flores-Hernández

Instituto Politécnico Nacional-UPIITA, Av. IPN 2580 Col. Barrio La Laguna Ticomán, Ciudad de México, Mexico CP. 07320

Correspondence should be addressed to Octavio Gutiérrez-Frías; ogutierrezf@ipn.mx

Received 28 June 2019; Revised 22 January 2020; Accepted 5 February 2020; Published 29 April 2020

Guest Editor: Raúl Villafuerte Segura

The trajectory tracking task of a magnetic levitation system connected to a beam mechanism is solved by means of a nested saturation control with a feedforward term. The flatness property of the system allows to use the nested saturation control technique and the feedforward control to stabilize the output tracking error around the equilibrium. The closed-loop error dynamics is proven to be locally exponentially stable. Numerical simulations prove the effectiveness of the proposal.

1. Introduction

Underactuated systems are currently an active research area in automatic control design. On the one hand, their amount of advantages such as lighter structures, economic designs, the possibility of compensating a failure on a fully actuated system, among others, has allowed their use in many applications such as mobile robotics, marine systems, aerospace robotic systems, cranes, flexible robots, and fault compensation systems [1–4]. On the other hand, the control problems of regulation and trajectory tracking of underactuated systems lead to complex solutions which cannot be solved by classical schemes [5]; some of the complexities are due to the difficulties to find general properties concerning their capacity of being linearizable, relations between degrees of freedom and independent control actuators [6], passivity [7, 8], ill-defined relative degrees [9], and so on. Most of the solutions for this class of systems deal with the regulation problem, where energy-based schemes are the most popular. The trajectory planning tasks and their tracking demand more complex strategies. This is due to the fact that not all joint trajectories are attainable for this class of systems [10]. To overcome this problem, the capacity of finding a set of variables that can parameterize the system trajectories (differentially flatness [11–13]) allows to establish a trajectory planning and a subsequent controller synthesis.

In particular, magnetic levitation systems have been extensively analysed and used in the design of frictionless bearings [14], vibration isolation [15], manipulation and micromanipulation systems [16, 17], drug and people transporting [18, 19], energy harvesting [20–22], etc., where noncontact motion control or avoiding the use of lubrication systems is desirable [23–25]. The control of this class of systems has been tackled from a wide variety of nonlinear approaches [26, 27]. The magnetic levitation in a beam balance configuration has been approached by feedback linearization [28]. In [29], the regulation problem of a beam balance system is solved though a Lyapunov-based control considering restrictions in states and input. Hu et al. [30] developed a saturated linear feedback to solve the same problem achieving a larger attraction region with respect to linear techniques. Passivity-based control is also implemented though the interconnection and damping assignment [31]. In [32], a sliding mode controller is used for the regulation problem using two magnetic actuators in an agonist-antagonist configuration. The problem of trajectory tracking for a ball levitation system controlled by magnetic

bearings has been solved by a flatness-based control [33–35], where path planning is used to avoid the input constraints in the control design although the natural saturations are not part of the control design in contrast with other schemes. The idea of using the saturations as a part of the control design in combination with the advantages of a flatness-based control seems to be a good alternative to solve the problem of trajectory tracking enhancing the control response in case the control saturation may arise. The nested saturation function approach was introduced by A. Teel in [36] to solve the stabilization of a chain of integrator of arbitrary order, and it can also be used for trajectory tracking for a class of trajectories restricted. Other works that solve this problem are presented in [37–39]. Besides, this technique has been used for stabilization of a class of underactuated systems [40–43].

In this sense, this article deals with the problem of trajectory tracking of a beam balance levitation system by means of a nested saturation function approach in combination with the flatness property of the system. The proposal consists in using the flatness of the system to transform the system in an integrator chain, and then, a controller based on a nested saturated function and a feedforward term is used to force the output trajectories to converge towards the reference trajectory. The closed-loop solution is proven to be locally exponentially stable by means of the second method of Lyapunov.

The remainder of the article is given as follows: the dynamical model of the magnetic levitation system, the flatness property, and the problem formulation are given in Section 2. The control proposal and its stability proof are provided in Section 3. Some numerical simulations which show the behaviour of the proposal are presented in Section 4, and finally, some concluding remarks are stated.

2. System Model

Consider the magnetic levitation system, shown in Figure 1, where a beam can rotate freely, and its movement is affected by the gravity effects and the control input derived from a magnetic force generated on a controlled electromagnet coil. The dynamical model is given as follows:

$$\begin{aligned}
\dot{x}_1(t) &= x_2(t),\\
\dot{x}_2(t) &= \frac{Ce}{J}\left[\frac{x_3(t)}{l\sin(x_1(t))}\right]^2 - \frac{mgr\cos(x_1(t))}{J},\\
\dot{x}_3(t) &= \frac{u(t)}{L} - \frac{Rx_3(t)}{L},
\end{aligned} \tag{1}$$

where $x_1(t)$ is the angular position of the pendulum, $x_2(t)$ is its corresponding angular velocity, and $x_3(t)$ is the current of the inductor. Ce represents the electromagnetic force proportionality constant. J is the inertia moment of the beam, l is the distance between the pivot and the center of the permanent magnet, m denotes the mass of the beam, g is the gravity constant, and r is the radial distance of the center of mass of the beam to the rotational center. L and R are the inductance and resistance parameters of the electromagnetic subsystem. Finally, $u(t)$ is the control input, applied on the electromagnetic system. It is assumed that the output variable is the position of the beam $x_1(t)$.

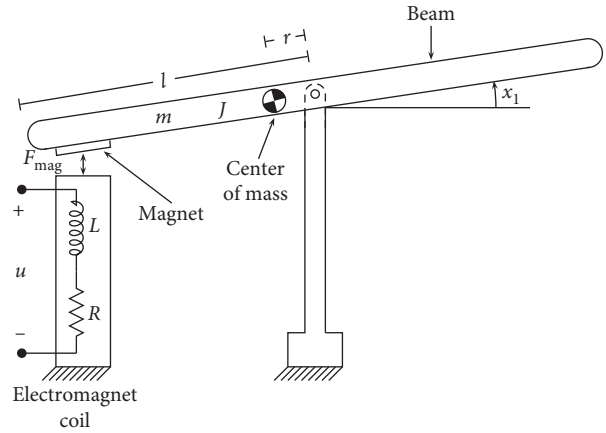

Figure 1: Magnetic levitation system.

Last system admits a canonical controllable form by means of the following change of coordinates [44]:

$$\begin{aligned}
F_1(t) &= x_1(t),\\
F_2(t) &= x_2(t),\\
F_3(t) &= \alpha_1\left(\frac{x_3(t)}{\sin(x_1(t))}\right)^2 - \alpha_2\cos(x_1(t)),
\end{aligned} \tag{2}$$

where $\alpha_1 = (Ce/Jl^2)$ and $\alpha_2 = (mgr/J)$.

We have the following inverse transform:

$$\begin{aligned}
x_1(t) &= F_1(t)\\
x_2(t) &= F_2(t)\\
x_3(t) &= \sqrt{\frac{1}{\alpha_1}\left(F_3(t) + \alpha_2\cos(F_1(t))\right)\sin^2(F_1(t))}.
\end{aligned} \tag{3}$$

The dynamics of (1) in terms of coordinate transformation (2) is given as follows:

$$\begin{aligned}
\dot{F}_1(t) &= F_2(t),\\
\dot{F}_2(t) &= F_3(t),\\
\dot{F}_3(t) &= -2\left(F_3(t) + \alpha_2\cos(F_1(t))\right)r\left(F_1(t), F_2(t)\right)\\
&\quad + \alpha_2\sin(F_1(t))F_2(t)\\
&\quad + \frac{2\sqrt{\alpha_1}}{L}\sqrt{\frac{F_3(t) + \alpha_1\cos(F_1(t))}{\sin^2(F_1(t))}}u(t),
\end{aligned} \tag{4}$$

where

$$r\left(F_1(t), F_2(t)\right) = \left(\frac{R}{L} + F_2(t)\cot(F_1(t))\right). \tag{5}$$

This system can be controllable except when $F_1(t) = 0$ or in the set $F_3(t) + \alpha_1 \cos(F_1(t)) = 0$.

2.1. Problem Formulation. The following problem formulation is established: given a smooth admissible reference trajectory of the beam angle, denoted as $x_1^*(t)$, devise an output feedback control law $u(t)$ such that the trajectory tracking error remains after a settling time on a vicinity of the origin of the phase variable plane, as small as allowed by the system nonlinearities and the control gains to be designed.

3. Nested Function Control Design

From (4), it can be shown that the system is differentially flat [11, 12] with flat output $F_1(t) = x_1(t)$. That is, system (4) has the form

$$F_{(1)}^{(3)}(t) = h\left(F_1(t), \dot{F}_1(t), \ddot{F}_1(t)\right) + p\left(F_1(t), \ddot{F}_1(t)\right)u(t), \tag{6}$$

with

$$h\left(F_1(t), \dot{F}_1(t), \ddot{F}_1(t)\right) = -2\left(\ddot{F}_1(t) + \alpha_2 \cos\left(F_1(t)\right)\right) \times \left(\frac{R}{L} + \dot{F}_1(t)\cot\left(F_1(t)\right)\right) + \alpha_2 \sin\left(F_1(t)\right)\dot{F}_1(t)$$

$$p\left(F_1(t), \ddot{F}_1(t)\right) = \frac{2\sqrt{\alpha_1}}{L}\sqrt{\frac{\ddot{F}_1(t) + \alpha_1 \cos\left(F_1(t)\right)}{\sin^2\left(F_1(t)\right)}}. \tag{7}$$

The following linearizing control input

$$u(t) = \frac{1}{p\left(F_1(t), \ddot{F}_1(t)\right)}\left(-h\left(F_1(t), \dot{F}_1(t), \ddot{F}_1(t)\right) + \overline{v}(t)\right), \tag{8}$$

yields the following linear controllable in the Brunovsky canonical form

$$F_{(1)}^{(3)}(t) = \overline{v}(t). \tag{9}$$

Let us define the flat output error as $e_{F1}(t) := F_1(t) - F_1^*(t)$, where $F_1^*(t) = x_1^*(t)$. In order to express the dynamics in terms of the tracking error coordinates, the following feedforward input term is introduced in the last expression:

$$\overline{v}(t) = F_1^{*(3)}(t) + v(t). \tag{10}$$

Thus, using (8) and (10) in (4), the following expression is obtained:

$$e_{F1}^{(3)}(t) = v(t). \tag{11}$$

Last system admits the following canonical representation:

$$\begin{aligned} \dot{e}_{F1}(t) &= e_{F2}(t), \\ \dot{e}_{F2}(t) &= e_{F3}(t), \\ \dot{e}_{F3}(t) &= v(t). \end{aligned} \tag{12}$$

Let us introduce the following linear transformation [36, 45]:

$$\begin{bmatrix} q_1(t) \\ q_2(t) \\ q_3(t) \end{bmatrix} = \begin{bmatrix} 1 & 2 & 1 \\ 0 & 1 & 1 \\ 0 & 0 & 1 \end{bmatrix}\begin{bmatrix} e_{F1}(t) \\ e_{F2}(t) \\ e_{F3}(t) \end{bmatrix}. \tag{13}$$

Last transformation leads system (12) to

$$\begin{aligned} \dot{q}_1(t) &= q_2(t) + q_3(t) + v(t), \\ \dot{q}_2(t) &= q_3(t) + v(t), \\ \dot{q}_3(t) &= v(t). \end{aligned} \tag{14}$$

Therefore, as system (12) is expressed with a chain of integrator, we suggested a controller based on nested saturation function. This technique, proposed in [36], has been used for controlling a wide class of the underactuated system [40–42, 46]. Thus, our stability problem will be solved as follows. First, a linear transformation is used to directly propose a trajectory tracking controller; then, it is shown that the proposed controller guarantees the boundedness of all states, and after a finite time, it is possible to ensure that all states converge to zero [43].

Let us define the following saturation function:

Definition 1. The linear saturation function $\sigma_m(s)$: $\mathbb{R} \longrightarrow \mathbb{R}$ is defined as

$$\sigma_m(s) = \begin{cases} s, & \text{if} \quad |s| \le m, \\ m \cdot \text{sign}(s), & \text{if} \quad |s| > m. \end{cases} \tag{15}$$

Finally, the trajectory tracking controller can be proposed as

$$v(t) = -q_3(t) - K\sigma_\alpha\left(\frac{q_2(t) + \sigma_\beta\left(q_1(t)\right)}{K}\right), \tag{16}$$

where K is a positive constant, $\alpha > 0$ and $\beta > 0$ are fixed parameters, and σ_m is a linear saturation function.

3.1. Boundedness of All States. We show in three simple steps that the closed-loop solution of the proposed closed-loop systems (14) and (16) ensures that all the states are bounded. Moreover, the bound of each state directly depends on the designed parameters of the controller.

Step 1. We define a positive definite function

$$V_3(q_3, t) = \frac{q_3^2(t)}{2}. \tag{17}$$

Then, differentiating (17) and using the third differential equation of (14), we have the time derivative of $V_3(q_3, t)$ given by

$$\dot{V}_3(q_3,t) = -q_3^2(t) - q_3(t)K\sigma_\alpha\left(\frac{q_2(t)+\sigma_\beta(q_1(t))}{K}\right). \tag{18}$$

It is clear that $\dot{V}_3(q_3,t) < 0$ when $|q_3(t)| \geq \alpha K$; therefore, there is a finite time $T_1 > 0$ such that

$$|q_3(t)| < \alpha K, \quad \forall t > T_1, \tag{19}$$

where $K > 0$.

Step 2. Now, we proceed to analyze the behaviour of the state $q_2(t)$. Hence, we introduce a positive definite function $V_2(q_2,t) = q_2^2(t)/2$. Differentiating $V_2(q_2,t)$, we obtain after substituting (16) into second differential equation of (14)

$$\dot{V}_2(q_2,t) = -q_2(t)K\sigma_\alpha\left(\frac{q_2(t)+\sigma_\beta(q_1(t))}{K}\right), \tag{20}$$

where α and β are selected such that $\alpha > 2\beta$. Evidently, if $|q_2(t)| > \beta$, then $\dot{V}_2(q_2,t) < 0$, and there is finite $T_2 > T_1$ after which

$$|q_2(t)| < \beta, \quad \forall t > T_2, \tag{21}$$

when this condition is satisfied, and the control $v(t)$ turns out to be

$$v(t) = -q_3(t) - q_2(t) - \sigma_\beta(q_1(t)). \tag{22}$$

Step 3. Substituting (22) into first differential equation of (14), we obtain

$$\dot{q}_1(t) = -\sigma_\beta(q_1(t)). \tag{23}$$

Now, we define an auxiliary positive definite function $V_1(q_1,t) = q_1^2(t)/2$. By differentiating $V_1(q_1,t)$ along the trajectories of (23), we obtain

$$\dot{V}_1(q_1,t) = -q_1(t)\sigma_\beta(q_1(t)), \tag{24}$$

where β must be chosen such that $\beta > 0$. If $|q_1(t)| > 0$, then $\dot{V}_1(q_1,t) < 0$, and hence, there is finite $T_3 > T_2$ after which

$$|q_1(t)| < 0, \quad \forall t > T_3. \tag{25}$$

Consequently, q_1 is also bounded. So, all previous constraints on parameters α and β can be summarized as

$$\begin{aligned} \alpha &> 2\beta, \\ \beta &> 0. \end{aligned} \tag{26}$$

Manipulating the last inequalities, we can select the control parameters as follows:

$$\begin{aligned} \alpha &= 2\lambda, \\ \beta &= \lambda, \end{aligned} \tag{27}$$

where $\lambda > 0$.

3.2. Convergence of All States to Zero. We shall prove that the closed-loop system given by (14) and (16) is asymptotically stable and locally exponentially stable, provided that the controller parameters satisfy (26).

We must note that, after $t > T_3$, the control law is no longer saturated, that is,

$$v(t) = -q_3(t) - q_2(t) - q_1(t), \tag{28}$$

and the closed-loop system can be expressed as

$$\begin{aligned} \dot{q}_1(t) &= -q_1(t), \\ \dot{q}_2(t) &= -q_2(t) - q_3(t), \\ \dot{q}_3(t) &= -q_3(t) - q_2(t) - q_1(t). \end{aligned} \tag{29}$$

Let us define the following Lyapunov function:

$$V(q,t) = \frac{1}{2}q(t)^\intercal q(t), \tag{30}$$

with $q(t) := \begin{bmatrix} q_1(t) & q_2(t) & q_3(t) \end{bmatrix}^\intercal$. Now, differentiating $V(q,t)$ along the trajectories of (29), we obtain

$$\dot{V}(q,t) = -q(t)^\intercal M q(t), \tag{31}$$

where

$$M = \begin{bmatrix} 1 & 1/2 & 1/2 \\ 1/2 & 1 & 1/2 \\ 1/2 & 1/2 & 1 \end{bmatrix}. \tag{32}$$

Note that $\lambda_{\min}\{M\} = 1/2$, and therefore, M is positive definite Therefore, $\dot{V}(q,t)$ is negative definite, and the vector state q locally exponentially converges to zero after $t > T_3$.

From the above discussion, we have the following.

Proposition 1. *Consider the magnetic levitation system as described (1) in a closed loop with controller (8). Then, the closed-loop system is asymptotically stable and locally exponentially stable provided that the control parameters α and β satisfy the inequalities.*

4. Numerical Simulations

To test the performance of the controller, we carried out some numerical simulations using MATLAB program, and the results were obtained based on the numerical method of Runge–Kutta of fourth order with the fixed step of 0.001 s. The physical parameters of the system are $C_e = 9.9081\times^{-6}\,(\mathrm{Nm^2/A^2})$, $J = 0.01\,(\mathrm{kg\,m^2})$, $l = 0.2\,(\mathrm{m})$, $m = 0.6\,(\mathrm{kg})$, $g = 9.81\,(\mathrm{m/s^2})$, $r = 0.009\,(\mathrm{m})$, $L = 0.2703\,(\mathrm{H})$, and $R = 4.5\,(\Omega)$, and the controller parameter values were set as $\alpha = 3$, $\beta = 1.5$, and $K = 1$.

The first experiment shows the behaviour of the system, for a rest-to-rest trajectory, and in this case, we use a reference trajectory-type Bezier polynomial $(x_1^*(t))$. The initial conditions were set as $x_1(0) = -0.1\,(\mathrm{rad})$, $x_2(0) = 0\,(\mathrm{rad/s})$, and $x_3(0) = 0.5\,(\mathrm{A})$. In Figure 2, the output tracking response is shown, and we can see that the controller effectively brings the system from initial position $(x_1(0) = -0.1\,(\mathrm{rad}))$ to the final rest position $(x_1^*(t_f) = 0.4)$ after 7 seconds. The behaviour for the states $x_2(t)$ and $x_3(t)$ is shown in Figure 3. Finally, Figure 4 depicts the control input.

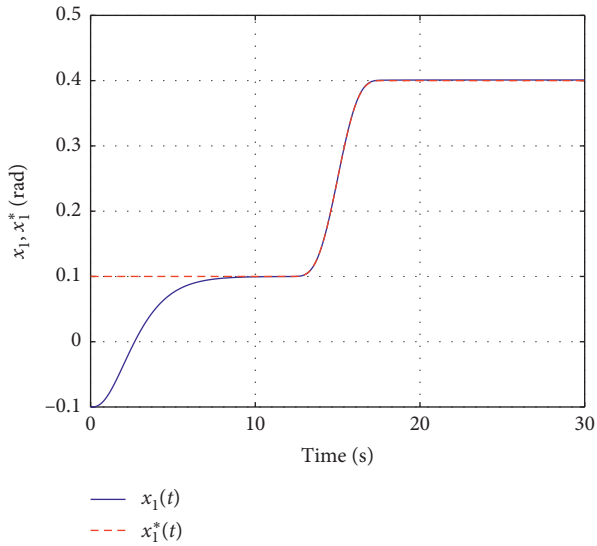

Figure 2: Output tracking response for a rest-to-rest trajectory.

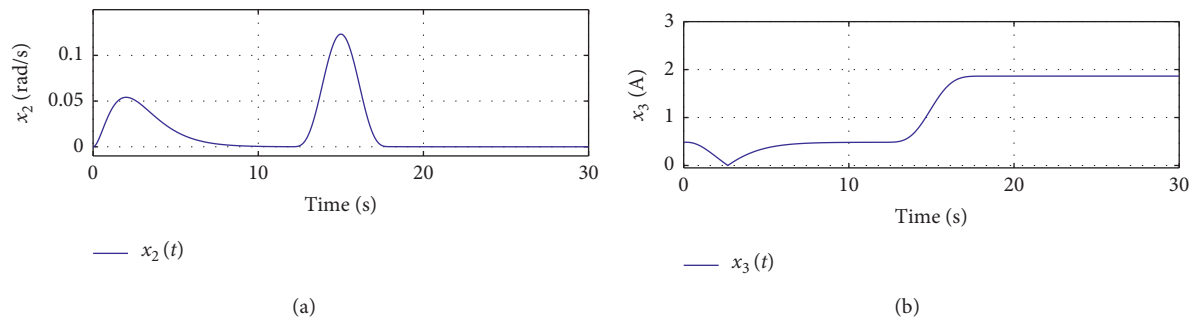

Figure 3: State behaviour in a rest-to-rest trajectory.

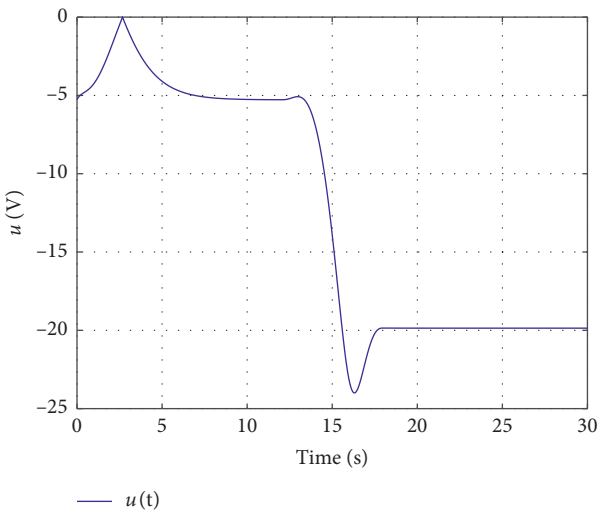

Figure 4: Control input.

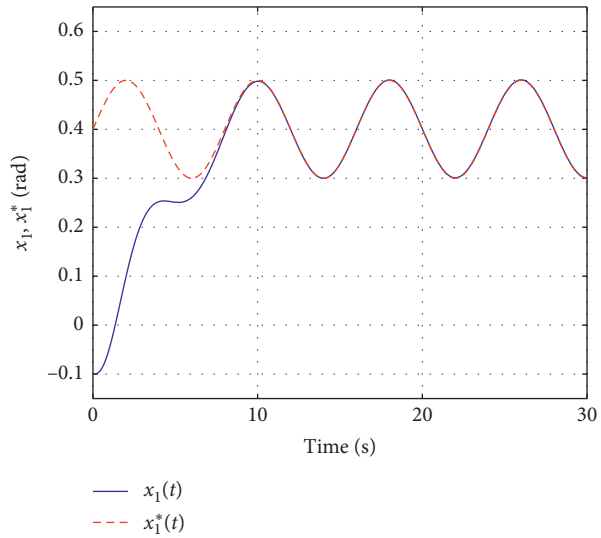

Figure 5: Output tracking response for a sinusoidal trajectory.

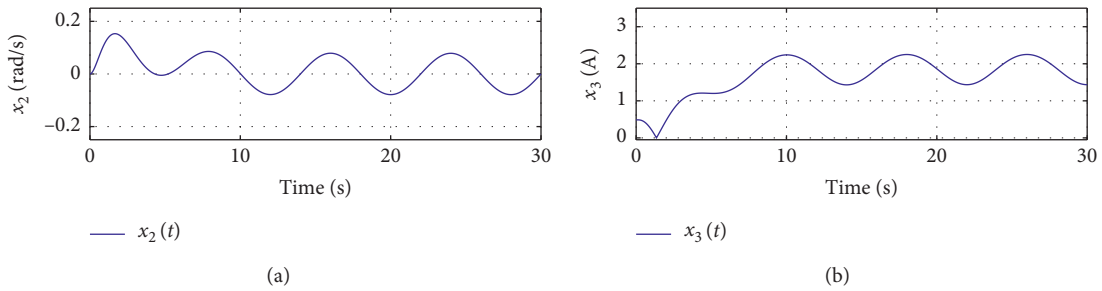

Figure 6: State behaviour in a sinusoidal trajectory.

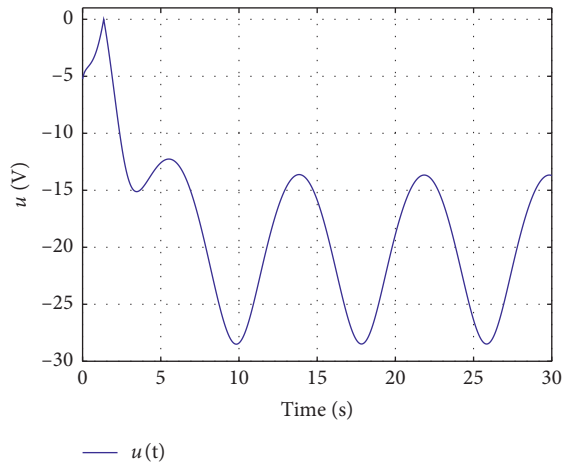

Figure 7: Control input (sinusoidal reference).

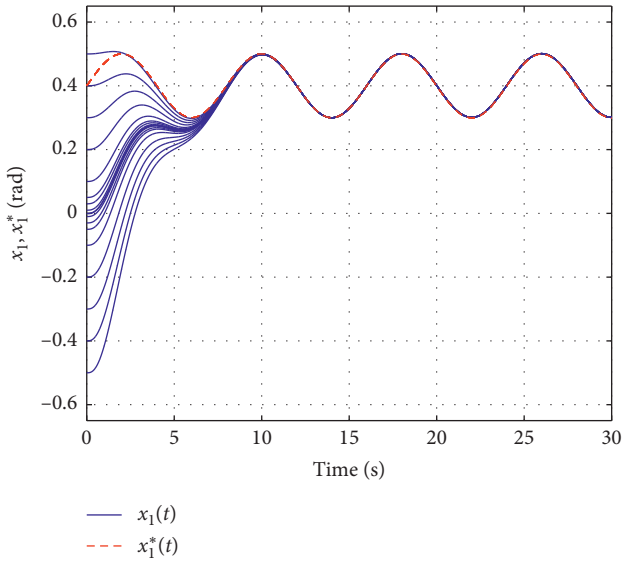

Figure 8: Output tracking response for a sinusoidal trajectory under different initial conditions.

The second experiment was designed under the same setup, but in this case, we use a reference sinusoidal trajectory $(x_1^*(t) = 0.4 + 0.1\sin(\pi t/4))$. The result of the experiment is presented in Figure 5. From this figure, we can see that the controller was capable of performing the task of tracking a sinusoidal trajectory. In Figure 6, the behaviour for the states $x_2(t)$ and $x_3(t)$ is shown. Finally, Figure 7 presents the control input.

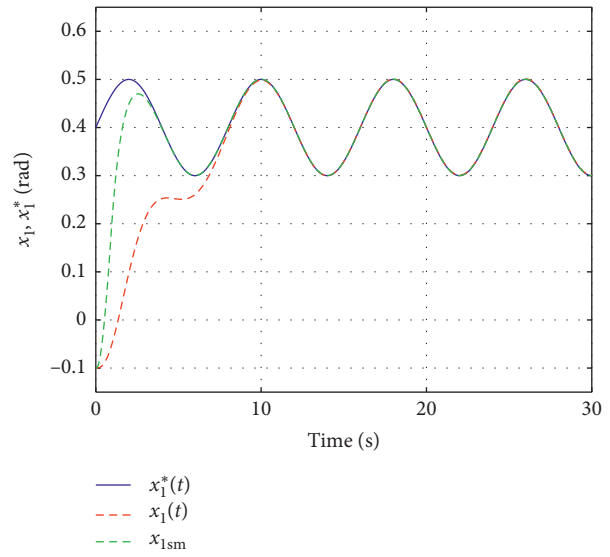

Figure 9: Comparison results for sinusoidal trajectory tracking.

In Figure 8, the output tracking response for a sinusoidal trajectory with different initial conditions is shown. In this case, $x_1(0) = [-0.5, 0.5]$ (rad), and we can see that the controller was capable of performing the task of tracking a sinusoidal trajectory adequately. Some tests were carried out in order to verify the sensitivity of the control scheme with respect to the initial conditions, in which a set of different initial conditions in an admissible operation range was used. The results indicate that the response is not affected by the initial conditions, and there is a lack of overshooting effects which are typical in high-gain schemes.

4.1. A Comparison Test. In order to assess the behaviour of the control proposal, a comparison test was made against a robust control strategy, consisting in a sliding mode controller (see [47]). The sliding mode controller was set to be

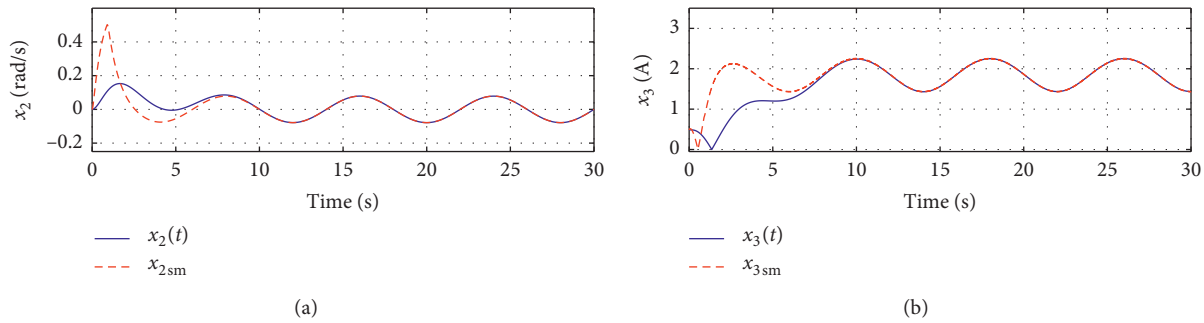

Figure 10: State behaviour (comparison test).

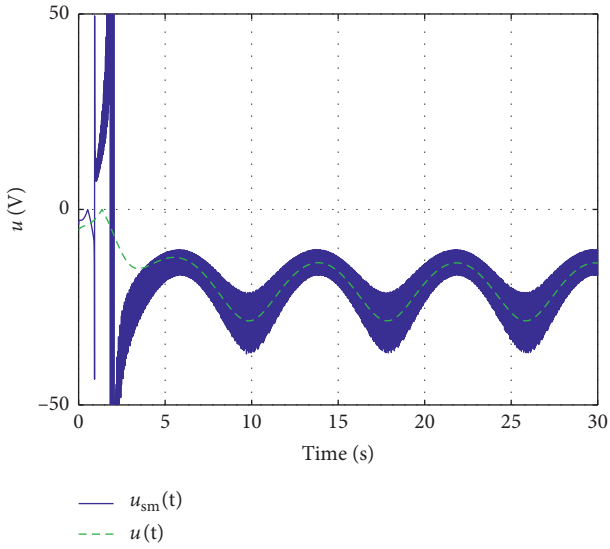

Figure 11: Control input (comparison test).

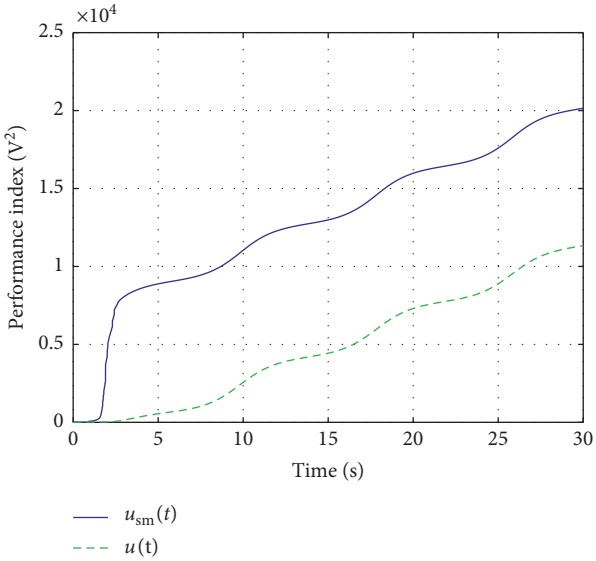

Figure 12: Performance index of the input control.

$$u(t) = \frac{1}{p\left(F_1(t), \ddot{F}_1(t)\right)}\left(-h\left(F_1(t), \dot{F}_1(t), \ddot{F}_1(t)\right) + \overline{v}_{sm}(t)\right),$$

$$\overline{v}_{sm}(t) = F_1^{*(3)} - \lambda_2 e_{F3} - \lambda_1 e_{F2} - W\,\text{sign}(\sigma),$$

$$\sigma = e_{F3} + \lambda_2 e_{F2} + \lambda_1 e_{F1},$$

$$\text{with} : \lambda_2, \lambda_1 \in \mathbb{R}^+. \tag{33}$$

The control parameters used in the test were $W = 20$, $\lambda_2 = 24$, and $\lambda_1 = 36$. Figure 9 shows the tracking results, where the sliding mode results (denoted by the subindex sm) converged faster without any overshooting effects. Figure 10 depicts the states x_2 and x_3, in which both schemes had similar values (reachable for experimental implementations). Figure 11 shows the advantages of the proposal since the voltage input of the sliding mode showed the high-frequency behaviour, which is a classic problem in sliding mode control implementations which may demand high control efforts. Notice that the proposal has a better energy management, leading to similar results with a smoother control input. This can be noticed with the obtained performance index $\int u^2$ which is shown in Figure 12.

5. Conclusion

A nested saturation-based controller for the trajectory tracking task on a beam levitation system was introduced and proven to be effective. The flatness property of the magnetic levitation system permits to express the system as a third-order integrator chain, allowing the use of nested saturation functions to design a trajectory tracking controller.

The proposed scheme forces the system output to track the reference trajectory even in the presence of the input constraints and ensures that all states converge exponentially to the desired trajectory. The stability analysis is based on the second method of Lyapunov using a simple candidate function. Some computer simulations showed the effectiveness of the proposal in the tracking of a rest-to-rest and sinusoidal trajectories.

On the contrary, as a future research, some other nonlinearities such as hysteresis in the magnetic actuator [48] can be addressed. This effect is important for the design of maglev systems in superconductor-based transportation system applications.

Data Availability

No data were used to support this study.

Conflicts of Interest

The authors declare that there are no conflicts of interest regarding the publication of this article.

Acknowledgments

This article was supported by the Secretaría de Investigación y Posgrado of the Instituto Politécnico Nacional (SIP-IPN) under the research grants 20195901, 20196059, 20196079, 20196855 ,20201768, 20201829 and 20201830. J. Alejandro Aguirre-Anaya is a scholarship holder of the CONACYT.

References

[1] J. Moreno-Valenzuela and C. Aguilar-Avelar, *Motion Control of Underactuated Mechanical Systems*, Springer, Berlin, Germany, 2018.

[2] S. Rudra, R. K. Barai, and M. Maitra, *Block Backstepping Design of Nonlinear State Feedback Control Law for Underactuated Mechanical Systems*, Springer, Berlin, Germany, 2017.

[3] R. Olfati-Saber, *Nonlinear control of underactuated mechanical systems with application to robotics and aerospace vehicles*, Massachusetts Institute of Technology, Cambridge, MA, USA, Ph.D. dissertation, 2001.

[4] M. Spong, "Underactuated mechanical systems," in *Control Problems in Robotics and Automation*, pp. 135–150, Springer, Berlin, Germany, 1998.

[5] A. Choukchou-Braham, B. Cherki, M. Djemai, and K. Busawon, *Analysis and Control of Underactuated Mechanical Systems*, Springer Science & Business Media, Berlin, Germany, 2013.

[6] G. Oriolo and Y. Nakamura, "Control of mechanical systems with second-order nonholonomic constraints: underactuated manipulators," in *Proceedings of the 30th IEEE Conference on Decision and Control*, pp. 2398–2403, IEEE, Brighton, UK, December 1991.

[7] R. Ortega, A. Loría, P. Nicklasson, and H. Sira-Ramirez, *Passivity-based Control of Euler-Lagrange Systems: Mechanical, Electrical and Electromechanical Applications*, Springer Science & Business Media, Berlin, Germany, 1998.

[8] R. Ortega, M. W. Spong, F. Gomez-Estern, and G. Blankenstein, "Stabilization of a class of underactuated mechanical systems via interconnection and damping assignment," *IEEE Transactions on Automatic Control*, vol. 47, no. 8, pp. 1218–1233, 2002.

[9] J. Hauser, S. Sastry, and P. Kokotovic, "Nonlinear control via approximate input-output linearization: the ball and beam example," *IEEE Transactions on Automatic Control*, vol. 37, no. 3, pp. 392–398, 1992.

[10] S. K. Agrawal and V. Sangwan, "Differentially flat designs of underactuated open-chain planar robots," *IEEE Transactions on Robotics*, vol. 24, no. 6, pp. 1445–1451, 2008.

[11] M. Fliess, J. Lévine, P. Martin, and P. Rouchon, "Flatness and defect of non-linear systems: introductory theory and examples," *International Journal of Control*, vol. 61, no. 6, pp. 1327–1361, 1995.

[12] H. Sira-Ramirez and S. Agrawal, *Differentially Flat Systems*, CRC Press, Boca Raton, FL, USA, 2004.

[13] J. Levine, *Analysis and Control of Nonlinear Systems: A Flatness-Based Approach*, Springer Science & Business Media, Berlin, Germany, 2009.

[14] W. Amrhein, W. Gruber, W. Bauer, and M. Reisinger, "Magnetic levitation systems for cost-sensitive applications-some design aspects," *IEEE Transactions on Industry Applications*, vol. 52, no. 5, pp. 3739–3752, 2016.

[15] I. Abed, N. Kacem, N. Bouhaddi, and M. Bouazizi, "Multimodal vibration energy harvesting approach based on nonlinear oscillator arrays under magnetic levitation," *Smart Materials and Structures*, vol. 25, no. 2, Article ID 025018, 2016.

[16] E. Shameli, M. B. Khamesee, and J. P. Huissoon, "Real-time control of a magnetic levitation device based on instantaneous modeling of magnetic field," *Mechatronics*, vol. 18, no. 10, pp. 536–544, 2008.

[17] E. Diller, J. Giltinan, G. Z. Lum, Z. Ye, and M. Sitti, "Six-degree-of-freedom magnetic actuation for wireless microrobotics," *The International Journal of Robotics Research*, vol. 35, no. 1–3, pp. 114–128, 2016.

[18] S. Kim and K. Ishiyama, "Magnetic robot and manipulation for active-locomotion with targeted drug release," *IEEE/ASME Transactions on Mechatronics*, vol. 19, no. 5, pp. 1651–1659, 2014.

[19] H. Lee, K. Kim, and J. Lee, "Review of maglev train technologies," *IEEE Transactions on Magnetics*, vol. 42, no. 7, pp. 1917–1925, 2006.

[20] C. Drezet, N. Kacem, and N. Bouhaddi, "Design of a nonlinear energy harvester based on high static low dynamic stiffness for low frequency random vibrations," *Sensors and Actuators A: Physical*, vol. 283, pp. 54–64, 2018.

[21] S. Mahmoudi, N. Kacem, and N. Bouhaddi, "Enhancement of the performance of a hybrid nonlinear vibration energy harvester based on piezoelectric and electromagnetic transductions," *Smart Materials and Structures*, vol. 23, no. 7, Article ID 075024, 2014.

[22] Z. Zergoune, N. Kacem, and N. Bouhaddi, "On the energy localization in weakly coupled oscillators for electromagnetic vibration energy harvesting," *Smart Materials and Structures*, vol. 28, no. 7, Article ID 07LT02, 2019.

[23] B. Mann and N. Sims, "Energy harvesting from the nonlinear oscillations of magnetic levitation," *Journal of Sound and Vibration*, vol. 319, no. 1-2, pp. 515–530, 2009.

[24] Z.-J. Yang and M. Tateishi, "Adaptive robust nonlinear control of a magnetic levitation system," *Automatica*, vol. 37, no. 7, pp. 1125–1131, 2001.

[25] C. Knospe and E. Collins, "Special issue on magnetic bearing control," *IEEE Transactions on Control Systems Technology*, vol. 4, no. 5, p. 481, 1996.

[26] J.-H. Lee, P. E. Allaire, G. Tao, and X. Zhang, "Integral sliding-mode control of a magnetically suspended balance beam: analysis, simulation, and experiment," *IEEE/ASME Transactions on Mechatronics*, vol. 6, no. 3, pp. 338–346, 2001.

[27] R. T. Rocha, J. M. Balthazar, A. M. Tusset, S. L. T. de Souza, F. C. Janzen, and H. C. Arbex, "On a non-ideal magnetic levitation system: nonlinear dynamical behavior and energy

harvesting analyses," *Nonlinear Dynamics*, vol. 95, no. 4, pp. 3423–3438, 2019.

[28] J. D. Lindlau and C. R. Knospe, "Feedback linearization of an active magnetic bearing with voltage control," *IEEE Transactions on Control Systems Technology*, vol. 10, no. 1, pp. 21–31, 2002.

[29] A. D. Mahindrakar and V. Sankaranarayanan, "State-constrained stabilization of beam-balance systems," *International Journal of Robust and Nonlinear Control*, vol. 18, no. 3, pp. 333–350, 2008.

[30] T. Hu, Z. Lin, W. Jiang, and P. E. Allaire, "Constrained control design for magnetic bearing systems," *Journal of Dynamic Systems, Measurement, and Control*, vol. 127, no. 4, pp. 601–616, 2005.

[31] H. Rodriguez, R. Ortega, and I. Mareels, "A novel passivity-based controller for an active magnetic bearing benchmark experiment," in *Proceedings of the 2000 American Control Conference. ACC (IEEE Cat. No.00CH36334)*, vol. 3, pp. 2144–2148, IEEE, Chicago, IL, USA, June 2000.

[32] J. Lee, P. Allaire, G. Tao, J. Decker, and X. Zhang, "Experimental study of sliding mode control for a benchmark magnetic bearing system and artificial heart pump suspension," *IEEE Transactions on Control Systems Technology*, vol. 11, no. 1, pp. 128–138, 2003.

[33] J. Levine, J. Lottin, and J.-C. Ponsart, "A nonlinear approach to the control of magnetic bearings," *IEEE Transactions on Control Systems Technology*, vol. 4, no. 5, pp. 524–544, 1996.

[34] R. Morales and H. Sira-Ramírez, "Trajectory tracking for the magnetic ball levitation system via exact feedforward linearisation and gpi control," *International Journal of Control*, vol. 83, no. 6, pp. 1155–1166, 2010.

[35] R. Morales, V. Feliu, and H. Sira-Ramirez, "Nonlinear control for magnetic levitation systems based on fast online algebraic identification of the input gain," *IEEE Transactions on Control Systems Technology*, vol. 19, no. 4, pp. 757–771, 2011.

[36] A. R. Teel, "Global stabilization and restricted tracking for multiple integrators with bounded controls," *Systems & Control Letters*, vol. 18, no. 3, pp. 165–171, 1992.

[37] S. Gayaka, L. Lu, and B. Yao, "Global stabilization of a chain of integrators with input saturation and disturbances: a new approach," *Automatica*, vol. 48, no. 7, pp. 1389–1396, 2012.

[38] S. K. Kannan and E. N. Johnson, "Adaptive control with a nested saturation reference model," in *Proceedings of the AIAA Guidance, Navigation and Control Conference*, pp. 1–11, Austin, TX, USA, August 2003.

[39] N. Marchand and A. Hably, "Global stabilization of multiple integrators with bounded controls," *Automatica*, vol. 41, no. 12, pp. 2147–2152, 2005.

[40] R. Lozano and D. D. Dimogianopoulos, "Stabilization of a chain of integrators with nonlinear perturbations: application to the inverted pendulum," *in Proceedings. 42nd IEEE Conference on Decision and Control*, IEEE, vol. 5, pp. 5191–5196, 2003.

[41] C. Barbu, R. Sepulchre, W. Lin, and P. V. Kokotovic, "Global asymptotic stabilization of the ball-and-beam system," in *Proceedings of the 36th IEEE Conference on Decision and Control*, vol. 3, pp. 2351–2355, IEEE, San Diego, CA, USA, December 1997.

[42] P. Castillo, R. Lozano, and A. Dzul, "Stabilization of a mini rotorcraft with four rotors," *IEEE Control Systems*, vol. 25, no. 6, pp. 45–55, 2005.

[43] C. Aguilar-Ibañez, O. O. Gutiérrez-Frías, and M. S. Suárez-Castañón, "Controlling the strongly damping inertia wheel pendulum via nested saturation functions," *Computación y Sistemas*, vol. 12, no. 4, 2009.

[44] A. Isidori, *Nonlinear Control Systems*, Springer, Berlin, Germany, 1995.

[45] C. A. Ibañez and O. G. Frias, "Controlling the inverted pendulum by means of a nested saturation function," *Nonlinear Dynamics*, vol. 53, no. 4, pp. 273–280, 2008.

[46] C. Aguilar Ibanez, J. C. Martinez Garcia, A. Soria Lopez, J. d. J. Rubio, and M. S. Suarez Castanon, "Stabilization of the inverted cart-pendulum system with linear friction," *IEEE Latin America Transactions*, vol. 16, no. 6, pp. 1650–1657, 2018.

[47] N. F. Al-Muthairi and M. Zribi, "Sliding mode control of a magnetic levitation system," *Mathematical Problems in Engineering*, vol. 2004, Article ID 657503, 15 pages, 2004.

[48] Z. Deng, J. Wang, J. Zheng et al., "Performance advances of hts maglev vehicle system in three essential aspects," *IEEE Transactions on Applied Superconductivity*, vol. 19, no. 3, pp. 2137–2141, 2009.

Hindawi
Complexity
Volume 2020, Article ID 9523549, 12 pages
https://doi.org/10.1155/2020/9523549

Research Article

Design, Implementation, and Validation of Robust Fractional-Order PD Controller for Wheeled Mobile Robot Trajectory Tracking

Lichuan Zhang,[1] **Lu Liu**,[1] **and Shuo Zhang**[2]

[1]*School of Marine Science and Technology, Northwestern Polytechnical University, Xi'an 710072, China*
[2]*Department of Applied Mathematics, Northwestern Polytechnical University, Xi'an 710072, China*

Correspondence should be addressed to Lu Liu; liulu12201220@nwpu.edu.cn

Received 28 August 2019; Accepted 26 November 2019; Published 1 February 2020

Guest Editor: Raúl Villafuerte-Segura

In this paper, a trajectory tracking control algorithm is proposed based on the fractional-order PD (FOPD) controller for a Wheeled Mobile Robot (WMR). Firstly, an improved flat phase property is put forward as a robust controller tuning specification. This specification is capable of guaranteeing the flatness of the phase curve in a frequency interval, so the controlled system robustness can be improved. Then, the stabilization process is discussed with respect to the parameters of the FOPD controller through a visualized 3-dimensional surface, so both the stability and robustness of the controlled system can be guaranteed under the proposed controller. Furthermore, the implementation of the proposed robust FOPD controller is presented, which makes the control algorithm easy to be realized. At last, the effectiveness of the proposed trajectory tracking control algorithm is verified by the simulation and experiment results.

1. Introduction

Wheeled Mobile Robots (WMRs) are capable of working in different situations, including the inclement, dangerous, or even harmful ones. In the past few decades, WMRs have been widely applied in a great variety of civilian and military tasks, for example, space exploration, materials transportation, supplies delivery, mine clearance, and search and rescue [1–6]. Currently, trajectory tracking and regulation is one of the most concerned problems in WMRs related studies [7]. Without an effective control strategy, a predefined tracking strategy is hard to follow, especially in long distance or complicated environment tasks. The nonholomic properties, internal dynamics, feedback sensors of WMRs, and external load disturbance may bring in different kinds of immeasurable uncertainties [8]. Therefore, more precise and robust trajectory tracking strategy will certainly help in improving the operation efficiency of WMRs.

Typically, Proportional-Integral-Derivative (PID) controller is always used in the control process of industrial robotics including WMRs. But its control effect has been suspicious at times when better robustness and transient performance are required. However, the combination of fractional calculus and traditional PID controller, namely, fractional-order PID (FOPID) controller, provides novel potential and opportunity of solving this kind of problem. Many studies have investigated the design and application of FOPID type controllers [9–11]. One of the most representative works is the $PI^{\lambda}D^{\mu}$ controller proposed by Podlubny, which is an extension of the traditional PID controller with two extra order parameters [10]. Another kind of FOPID controller designed based on phase and magnitude margin frequency specifications is presented by Vinagre et al. [12]. Except for phase and magnitude margin specifications, Monje et.al. added the extrasensitivity and complementary sensitivity functions in the design specifications of the FOPID controller [13]. A similar FOPI controller whose parameters were tuned by symmetrical optimization function was studied by Maione and Lino [14]. In [15, 16], the original and modified Ziegler–Nichols methods were used in

the design process of FOPID controllers. The Newton–Raphson recursive algorithm was applied by Feliu et al. in the parameter optimization process of an FOPI controller [17]. Moreover, some intelligent control algorithm-based FOPID tuning methods have also been studied [18–22]. An autotuning variable-order fuzzy FOPID controller is investigated in [18] by Liu et al. in which all the parameters can be tuned online to deal with random time delay or system parameter uncertainties. The detailed advantages of the FOPID type controller can be concluded as following. Firstly, the FOPID type controller inherits the characteristics of the traditional PID controller, such as simple structure, clear physical, and meaning. Secondly, through the extra-differential and integral order parameters, the design flexibility of the controller is increased so better dynamic performance and robustness may be achieved with this type of controller. Subsequently, the FOPID type controller has the memory property and can adjust the output of the controller properly following the error history information in order to obtain better performance. At last, the added fractional-order terms can help adjust the high-frequency and low-frequency characteristics of the closed-loop easily [23].

In addition, the practical applicability of the FO controller has been verified in some practical applications. Several FO control examples, including industrial plants and electromechanic actuator, are presented in [24]. A brief summary and introduction of FOPID controllers applied in various kinds of industrial situations is given in [25]. The CRONE controller which can compensate the disturbance caused by parameter uncertainties and load changes has been successfully used in vehicle suspension [26] and path tracking [27]. A series of robust FOPID controllers tuned based on the flat phase property have been used in motion control [28, 29]. Moreover, in [30], an FO controller is used in the trajectory tracking task of a differential drive WMR. The experimental results show that the control performance of the FO controller is more satisfactory compared with the traditional PD controller. Another speed and direction control task accomplished by the FOPI controller for skid-steered WMR is presented in [31], which also achieves superior control performance. Nevertheless, the related studies are still quite limited at present. The stability of the controlled systems and the advantages of FO controllers applied in speed regulation, trajectory tracking, and other practical applications of WMRs need more exploration.

The main contribution of this paper includes the design, implementation, and validation of an FOPD controller for precise trajectory tracking of WMRs. For robust FO controller regulation, the flat phase property has been widely used as a design specification [29, 32]. This is because it can guarantee the flatness of the phase curve around the interested crossover frequency ω_c, so the system phase margin can remain constant and the system is robust to load variations. However, there are mainly two drawbacks of the original flat phase property. The first one is that it can only guarantee the flatness of the phase curve at one frequency, namely, ω_c. The other one is there are several nonlinear equations to be solved in the controller design process, so it is hard to find a solution. The improved flat phase property proposed in this paper can guarantee the robust flat phase frequency interval width instead of only one flat phase frequency and at least one parameter set which satisfies all the specifications can be found. In addition, the system stabilization and implementation problems are also discussed. The simulation and experiments results are shown to verify the effectiveness of the proposed trajectory tracking control algorithm.

The rest of this paper is organized as follows: In Section 2, the modelling of XQ WMR is given; then, the fractional calculus and FOPD controller are presented in Section 3; Section 4 shows the proposed controller design specifications; Section 5 discusses the stabilizing process for FO delay systems with the FOPD controller; furthermore, the experiment results and discussion are illustrated in Section 6 to verify the effectiveness and flexibility of the proposed controller; finally, the conclusion is drawn in Section 7.

2. Modelling of WMR

The XQ WMR studied in this paper is a three-wheeled differential drive robot, as shown in Figure 1.

2.1. Kinematic Model of XQ WMR. There are two front drive wheels and a universal follower wheel on the chassis of XQ WMR. The two front wheels driven by DC motors provide the forward power, so the movement and orientation of XQ WMR can be accomplished by the velocity difference between the two drive wheels; the universal follower wheel is mounted on the rear of the chassis. The kinematic model of XQ WMR is illustrated in Figure 2. As it is shown in Figure 2, denote v_c, v_r, and v_l as the chassis linear, right wheel, and left wheel velocities, respectively, θ as the angular displacement and ω as the angular velocity, where $\dot{\theta} = \omega$, and $2R$ as the distance between the two drive wheels. Denote the state vector S of XQ WMR as follows:

$$S = \begin{bmatrix} x \\ y \\ \theta \end{bmatrix}, \tag{1}$$

where x and y are coordinates of the center mass of XQ WMR. Therefore, the forward kinematic model of XQ WMR can be obtained as follows:

$$\dot{S} = \begin{bmatrix} \dot{x} \\ \dot{y} \\ \dot{\theta} \end{bmatrix} = \begin{bmatrix} v_c \cos(\theta) \\ v_c \sin(\theta) \\ \omega \end{bmatrix} = \begin{bmatrix} \frac{1}{2}(v_r + v_l)\cos(\theta) \\ \frac{1}{2}(v_r + v_l)\sin(\theta) \\ \omega \end{bmatrix}. \tag{2}$$

Then, in order to achieve the input desirable right and left wheel velocities, the inverse kinematic model of XQ WMR is achieved as

Figure 1: XQ WMR.

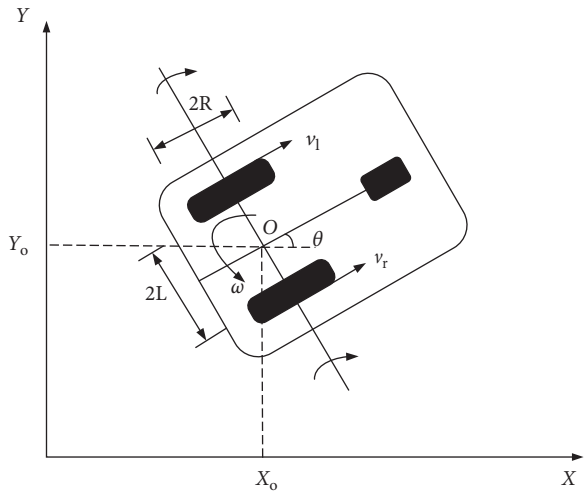

Figure 2: XQ WMR kinematic model.

$$\begin{bmatrix} v_r \\ v_l \end{bmatrix} = \begin{bmatrix} 1 & R \\ 1 & -R \end{bmatrix} \begin{bmatrix} v_c \\ \omega \end{bmatrix}. \tag{3}$$

The control scheme proposed in this paper is shown in Figure 3. Note that the centre of the two drive wheels O is assumed to be the mass centre of XQ WMR.

2.2. Motor Dynamic Model of XQ WMR. Before controller design procedure, the motor dynamic model should be achieved first. Figure 4 is the schematic diagram of the DC motor, where R_m and L_m are the total resistance and total inductance of the armature winding; V_m is the armature voltage; $T(s)$ is the electromagnetic torque; ω_m is the rotational angular velocity of the motor; and J_m is the rotational inertia on the deceleration shaft.

The transfer function of XQ WMR DC motor can be achieved as follows:

$$G(s) = \frac{\theta(s)}{V_m(s)} = \frac{k_m}{s\left[\left(L_m s + R_m\right)\left(J_m s + k_f\right) + k_b k_m\right]}, \tag{4}$$

where k_f and k_m are constants related to the magnetic flux. Ignoring some of the negligible values and the parameters which have less impact on the overall mathematical model, a simplified DC mathematical model can be obtained as a second-order transfer function as follows:

$$G(s) = \frac{\theta(s)}{V_m(s)} = \frac{k_m}{s\left[\left(L_m s + R_m\right)\left(J_m s + k_f\right) + k_b k_m\right]} = \frac{K}{s(\tau s + 1)}, \tag{5}$$

where the time constant is $\tau = R_m J_m / (R_m k_f + k_b k_m)$ and $K = k_m / (R_m k_f + k_b k_m)$.

From the experimental identification, the parameters of the DC motor are achieved as $\tau = 0.325$ and $K = 7.74/20$.

3. Fractional Calculus and FOPD Controller

3.1. Fractional-Order Derivative. Fractional calculus, which is an extension of traditional calculus, has not got a unified definition so far. There are three definitions which have been extensively used [10, 33], namely, Grunwald–Letnikov definition, Riemann–Liouville definition, and Caputo definition. Each of the definitions has its own properties. The definitions should be applied appropriately in different research fields, such as engineering, applied mathematics, and computer science. The initial values of Caputo definition are the same with that of the integer-order system and own practical physical meaning [34, 35]. Therefore, the Caputo definition is used in this paper.

An FO integral-differential operator ${}_{t_0}D_t^{\delta}$ can be depicted as follows:

$${}_{t_0}D_t^{\delta} = \begin{cases} \int_{t_0}^{t} f(\tau) \mathrm{d}\tau^{-\delta}, & \delta < 0, \\ f(t), & \delta = 0, \\ \dfrac{\mathrm{d}^{\delta}}{\mathrm{d}t^{\delta}} f(t), & \delta > 0, \end{cases} \tag{6}$$

where $\delta \in R$ is the integral or differential order and t_0 and t are lower and upper limits of the FO operator, respectively.

The Caputo derivative of order δ for a function $f(t) \in C^{m+1}([t_0, +\infty], R)$ is defined as follows[33]:

$${}_{t_0}D_t^{\delta} f(t) = \frac{1}{\Gamma(m-\delta)} \int_{t_0}^{t} \frac{f^{(m)}(\tau)}{(t-\tau)^{\delta+1-m}} \mathrm{d}\tau, \tag{7}$$

where $m - 1 < \delta \le m$, and m is a positive integer.

The Laplace transformation corresponding to Caputo definition can be obtained as follows:

$$\mathscr{L}\{{}_{t_0}D_t^{\delta} f(t)\} = s^{\delta} F(s) - \sum_{k=0}^{m-1} s^{\delta-k-1} f^{(k)}(t_0), \tag{8}$$

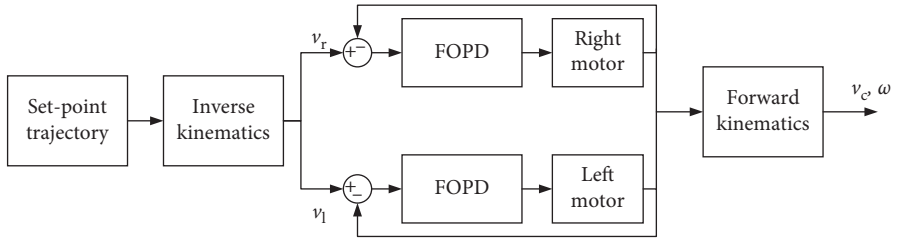

Figure 3: XQ WMR control strategy.

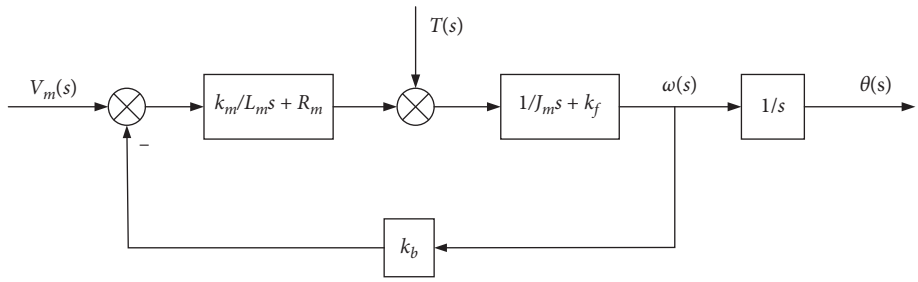

Figure 4: XQ WMR DC motor control structure diagram.

where s is the Laplace transformation operator and $\mathscr{L}\{\cdot\}$ represents the transformation.

3.2. The Considered Fractional-Order PD Controller. Different from the traditional PD controller, there are three parameters in the proposed FOPD controller which are formulated as follows:

$$C(s) = K_p + K_d s^{\gamma}, \tag{9}$$

where $0 < \gamma < 2$. This is a specific form of the FOPID controller which involves an integrator order λ ($\lambda = 0$ in this paper) and a differentiator order γ [36, 37].

4. FOPD Controller Design Specifications with Guaranteed Flat Phase Interval

The open-loop transfer function of WMR can be achieved from the above sections as follows:

$$G(s) = P(s)C(s) = \frac{k_p + k_d s^{\gamma}}{s(Ts + 1)}. \tag{10}$$

Based on the definitions of gain and phase margins, the following design specifications are introduced:

4.1. Gain Crossover Frequency Specification. The amplitude of the open-loop system should be zero at its gain crossover frequency in logarithmic frequency domain. In other words, the amplitude should equal to 1 at its gain crossover frequency, which can be expressed as follows:

$$|G(j\omega)||_{\omega=\omega_c} = |P(j\omega)C(j\omega)||_{\omega=\omega_c} = 1, \tag{11}$$

where ω_c is the interested crossover frequency.

4.2. Phase Margin Specification. Denote φ_m as the required phase margin, and this specification can be depicted as follows:

$$\text{Arg}[G(j\omega)]|_{\omega=\omega_c} = \text{Arg}[P(j\omega)C(j\omega)]|_{\omega=\omega_c} = -\pi + \varphi_m. \tag{12}$$

4.3. Flat Phase Interval Guaranteed Robustness Specification. To realize the robustness for the controlled system, the flat phase robust tuning specification can be described by the following condition at crossover frequency ω_c:

$$\left.\frac{\mathrm{d}(\text{Arg}[G(j\omega)])}{\mathrm{d}\omega}\right|_{\omega=\omega_c} = 0. \tag{13}$$

However, there are a few drawbacks of the flat phase specification in equation (13), which have already been discussed in Section 1. Here, we give the following condition to improve the existing flat phase specification:

$$\left|\frac{\mathrm{d}(Arg[G(j\omega)])}{\mathrm{d}\omega}\right|_{\omega\in[\omega_{\min},\omega_{\max}]}\Bigg| \le \varepsilon, \tag{14}$$

where $0 < \varepsilon \ll 1$ is a small enough scalar and smaller ε means better flatness of the phase curve; given ε, $\omega_{\min}$, and $\omega_{\max}$ are the minimum and maximum frequency near ω_c ($\omega_c \in [\omega_{\min}, \omega_{\max}]$) between which the flat phase interval can be guaranteed. Define $l = \omega_{\max} - \omega_{\min}$ as the width of the flat phase with regards to ε. Longer l means better robust performance under the same ε. Next, we present the steps to obtain l.

Step 1: given ε, compute whether the following inequality holds or not:

$$\left|\frac{\mathrm{d}(\text{Arg}[G(j\omega)])}{\mathrm{d}\omega}\right|_{\omega=\omega_c}\Bigg| < \varepsilon. \tag{15}$$

If yes, go to Step 2. If not, it obtains $l = 0$.

Step 2: if inequality (3) holds, solve the next equation and gain its solutions:

$$\left|\frac{\mathrm{d}(\mathrm{Arg}[\mathrm{G}(j\omega)])}{\mathrm{d}\omega}\right| = \varepsilon. \tag{16}$$

Let $\omega_{\min}$ and $\omega_{\max}$ be the solutions which are the nearest to ω_c in negative and positive directions, respectively.

Step 3: give the width $l = \omega_{\max} - \omega_{\min}$.

Remark 1. All the above steps need to be processed under a given $\varepsilon > 0$. When $\varepsilon > 0$ is fixed, longer l could offer better robustness for the controlled system. However, an excessively small $\varepsilon > 0$ may lead to $l = 0$. Thus, ε should be well chosen according to the practical requirements.

5. Design Procedure

Stability is the primary concern in control systems. So, the proposed controller design procedure is finding out the complete parameter sets which can stabilize the controlled system first, and then pick up the parameters which satisfy the proposed design specifications from the complete sets.

5.1. Control Process Stabilizing. The stabilizing process is investigated with respect to parameters of the proposed FOPD controller, namely, k_p, k_d, and γ.

One single closed-loop transfer function depicted in Figure 3 can be yielded according to equation (10) as follows:

$$F(s) = \frac{G(s)}{1 + G(s)} = \frac{K\left(k_p + k_d s^{\gamma}\right)}{s(Ts+1) + K\left(k_p + k_d s^{\gamma}\right)}. \tag{17}$$

So, the characteristic equation of the XQ WMR motor system is

$$D\left(k_p, k_d, \gamma; s\right) = s(Ts+1) + K\left(k_p + k_d s^{\gamma}\right). \tag{18}$$

The controlled system stability is determined by the root locations of its characteristic equation in (11). If all the roots locate in the left half of s-domain, the system is supposed to be bounded-input bounded-output stable. Therefore, the stability region of the XQ WMR motor system can be obtained by seeking for the parameter sets which can ensure the roots of equation (11) lie in the left half of s-domain in $D(k_p, k_d, \gamma; s)$. The boundaries of the stability region derived from $D(k_p, k_d, \gamma; s)$ can be achieved by finding the corresponding IRB (infinite root boundary), CRB (complex root boundary), and RRB (real root boundary) [38]. Note that if a system is strictly proper, it will not have IRB [39]. So, only RRB and CRB are taken into consideration in this paper.

(i) RRB is defined by

$$D\left(k_p, k_d, \gamma; s = 0\right) = Kk_p = 0. \tag{19}$$

So that $k_p = 0$.

(ii) CRB can be expressed as follows:

$$\begin{aligned} &D\left(k_p, k_d, \gamma; s = j\omega\right) \\ &= T\omega\cos\left(\frac{\pi}{2}\right) + jT\omega\sin\left(\frac{\pi}{2}\right) + j\omega + Kk_p\cos(\omega L) \\ &\quad - Kk_p j\sin(\omega L) + Kk_p\omega^{\gamma}\left[\cos\left(\frac{\pi\gamma}{2}\right) + j\sin\left(\frac{\pi\gamma}{2}\right)\right] = 0, \end{aligned} \tag{20}$$

where $j^{\gamma} = e^{\gamma\pi j/2} = \cos(\gamma\pi/2) + j\sin(\gamma\pi/2)$.

Here, both the real part and imaginary part of equation (20) should be equal to 0:

$$\begin{aligned} A_1 + k_p K + k_d K\omega^{\mu} B_1 = 0, \\ A_2 - k_p K + k_d K\omega^{\mu} C_1 = 0, \end{aligned} \tag{21}$$

where

$$\begin{aligned} A_1 &= T\omega\cos\left(\frac{\pi}{2}\right), \\ A_2 &= T\omega\sin\left(\frac{\pi}{2}\right) + \omega, \\ B_1 &= \cos\left(\frac{\gamma\pi}{2}\right), \\ C_1 &= \sin\left(\frac{\gamma\pi}{2}\right). \end{aligned} \tag{22}$$

Then, one can get from equation (21) that

$$\begin{aligned} k_p &= \frac{A_1 - A_2}{K(B_1 + C_1)}, \\ k_d &= -\frac{A_1 C_1 + A_2 B_1}{K\omega^{\gamma}(C_1 + B_1)}. \end{aligned} \tag{23}$$

Therefore, with $\omega \longrightarrow +\infty$ from 0, the stability region of a fixed fractional order γ composed by the corresponding RRB and CRB can be achieved. All parameter sets (k_p, k_d) in the region can guarantee the stability of the controlled XQ WMR motor system. Then, a three-dimensional surface of (k_p, k_d, γ) can be determined by sweeping the differential order $\gamma \in (0, \gamma_{\max})$. $\gamma_{\max}$ is the biggest γ which can ensure that the control system is strictly proper. The achieved surface is the *maximum stability surface* of the XQ WMR system under the FOPD controller because the phase margin φ_m is assumed to be 0 at this moment. Parameter sets (k_p, k_d, γ) on this surface can ensure the stability of the controlled system; however, no design specification is satisfied at this stage.

Substitute s in equations (10) and (11) by $j\omega$ as follows:

$$\begin{aligned} G(j\omega) &= \frac{K\left(k_p + k_d\omega^{\gamma} j^{\gamma}\right)}{j\omega(T\omega j + 1)}, \\ |G(j\omega)| &= \frac{K\left[D^2 + E^2\right]^{1/2}}{\left[B_2^2 + C_2^2\right]^{1/2}} = 1, \end{aligned} \tag{24}$$

where

$$
\begin{aligned}
D &= k_p + k_d\omega^{\gamma}\cos\left(\frac{\gamma\pi}{2}\right),\\
E &= k_d\omega^{\gamma}\sin\left(\frac{\gamma\pi}{2}\right),\\
B_2 &= T\omega\cos\left(\frac{\pi}{2}\right) + \omega,\\
C_2 &= T\omega\sin\left(\frac{\pi}{2}\right).
\end{aligned}
\tag{25}
$$

Then, one can get

$$
D^2 + E^2 = \frac{\left(B_2^2 + C_2^2\right)}{K^2}. \tag{26}
$$

Multiply both sides of equation (16) with $e^{\pi j/2}$ and yields,

$$
\begin{aligned}
e^{j(\pi/2)}G(j\omega) &= \frac{K\left(k_p + k_d\omega^{\gamma}j^{\gamma}\right)}{T\omega j + \omega}\\
&= K\frac{DB_2 + EC_2 + j\left(EB_2 - DC_2\right)}{B_2^2 + C_2^2}.
\end{aligned}
\tag{27}
$$

Hence, equation (13) is obtained as follows:

$$
\mathrm{Arg}[G(j\omega)] = \arctan\left(\frac{EB_2 - DC_2}{DB_2 + EC_2}\right) - \frac{\pi}{2} + n\pi = -\pi + \varphi_m. \tag{28}
$$

Denote

$$
N = \frac{EB_2 - DC_2}{DB_2 + EC_2} = \tan\left(-\pi + \varphi_m + \frac{\pi}{2} - n\pi\right). \tag{29}
$$

From equation (28), one can obtain

$$
D = \frac{B_2 - NC_2}{NB_2 - C_2}E. \tag{30}
$$

From equations (26) and (30), E can be obtained as follows:

$$
E = \left\{\frac{B_2^2 + C_2^2/K^2}{\left[1 + \left(B_2 - NC_2/NB_2 - C_2\right)^2\right]}\right\}^{1/2}. \tag{31}
$$

Substituting E in equation (26) by equation (30), k_p and k_i are achieved as follows:

$$
\begin{aligned}
k_d &= \frac{E}{\omega^{\gamma}\sin(\pi\gamma/2)},\\
k_p &= \frac{B_2 - NC_2}{NB_2 - C_2}E - k_d\omega^{\gamma}\cos\left(\frac{\pi\gamma}{2}\right).
\end{aligned}
\tag{32}
$$

When φ_m is predefined, with $\omega \longrightarrow +\infty$ from 0 and $\gamma \longrightarrow \gamma_{\max}$ from 0, an *available stability surface* can be obtained from equation (32). Then, if an interested ω_c is chosen, an *available stability curve* can be achieved. At this stage, the design specifications in equations (11) and (12) are fulfilled by parameters (k_p, k_d, γ) on the *available stability curve*. Remark that ω_c cannot be bigger than ω_m, where ω_m is determined by the intersection points of RRB and CRB. It is the maximum ω value which can ensure the stability of the control system.

From equations (14) and (28), one can obtain

$$
\begin{aligned}
&\frac{\mathrm{dArg}[G(j\omega)]}{\mathrm{d}\omega},\\
&= \frac{\left[\left(D\mathrm{d}E/\mathrm{d}\omega - E\mathrm{d}D/\mathrm{d}\omega\right)\left(C_2^2 + B_2^2\right) + \left(C_2\mathrm{d}B_2/\mathrm{d}\omega - B_2\mathrm{d}C_2/\mathrm{d}\omega\right)\left(D^2 + E^2\right)\right]}{\left[\left(DB_2 + EC_2\right)^2 + \left(EB_2 - DC_2\right)^2\right]},
\end{aligned}
\tag{33}
$$

where

$$
\begin{aligned}
\mathrm{d}D/\mathrm{d}\omega &= \gamma\omega^{\gamma-1}k_d\cos\left(\frac{\pi\gamma}{2}\right),\\
\mathrm{d}E/\mathrm{d}\omega &= \gamma\omega^{\gamma-1}k_d\sin\left(\frac{\pi\gamma}{2}\right),\\
\mathrm{d}B_2/\mathrm{d}\omega &= \omega T\cos\left(\frac{\pi}{2}\right) + 1,\\
\mathrm{d}C_2/\mathrm{d}\omega &= \omega T\sin\left(\frac{\pi}{2}\right).
\end{aligned}
\tag{34}
$$

At last, the proposed FOPD parameters (k_p, k_d, γ) are determined by checking all the parameter sets on the obtained *available stability curve* and finding out the one which satisfy the robust design specification in equation (14). So, the obtained FOPD controller satisfies all the three design specifications in Section 3 and can also ensure the stability of the closed-loop system.

On a whole, the design procedure can be summarized as follows:

Step 1: find the *maximum stability surface* of XQ WMR under the FOPD controller with $\omega \longrightarrow +\infty$ from 0 by sweeping $\gamma \in (0, \gamma_{\max})$. The parameter sets on *maximum stability surface* can only guarantee the stability of the controlled system.

Step 2: define phase margin φ_m and find the *available stability surface*. Then, choose the interested crossover frequency ω_c, so the *available stability curve* can be obtained on the *available stability surface*. The parameter sets on *available stability curve* satisfy both the gain crossover frequency and phase margin specifications.

Step 3: check all the parameter sets on the achieved *available stability curve* and find the one fulfill the robust design specification mostly.

6. Experiment and Discussion

6.1. Implementation of FOPD Controller. The implementation of the FOPD controller is one of the critical problems to achieve desirable trajectory tracking performance. The key point of the FOPD controller implementation concentrates on the approximation of the fractional operator in equation (9). In this section, the widely used Oustaloup et al. approximation method is applied without loss of generality [40].

A fractional operator can be expressed as follows:

$$F_o(s) = \left(\frac{s}{w_j}\right)^{\beta}, \quad \beta \in R^+. \tag{35}$$

Consider the interested approximation frequency interval as (w_1, w_2), so the operator s/w_j can be substituted by

$$k_0 \frac{1 + s/w_s}{1 + s/w_b}, \tag{36}$$

where $k_0 = w_s/w_j = w_j/w_b, w_s < w_1, w_b > w_2$.

Then, equation (35) can be updated as follows:

$$F_o(s) = k\left(\frac{1 + s/w_s}{1 + s/w_b}\right)^{\beta}, \tag{37}$$

where $k = k_0^{\beta}$.

The transfer function above can be transformed into a zero-pole form as follows:

$$F_o(s) = \lim_{m \longrightarrow \infty} \widehat{F}_o(s), \tag{38}$$

where

$$\begin{aligned} \widehat{F}_o(s) &= \left(\frac{w_j}{w_l}\right)^{\beta} \prod_{n=-m}^{m} \frac{1 + s/w_n}{1 + s/w_n'}, \\ w_n &= w_s\left(\frac{w_b}{w_s}\right)^{((1-\beta)+n+m)/(2m+1)}, \\ w_n' &= w_s\left(\frac{w_b}{w_s}\right)^{(1/2(1+\beta)+n+m)/(2m+1)}. \end{aligned} \tag{39}$$

The 7th Oustaloup approximation with expected frequency range $(10^{-3}, 10^{3})$ is used in this section.

6.2. Controller Parameters Regulation. According to the controller design procedures in Section 4, the *maximum stability surface* is obtained for XQ WMR in Figure 5. So, all the parameter sets on the surface can guarantee the stability of the control system.

Set the phase margin as $\varphi = 45^{\circ}$, the *available stability surface* can be obtained, as shown in Figure 6. It can be seen that the area of the *available stability surface* is inversely proportional to the chosen phase margin. Then, $\omega_c = 1$ is set as the interested crossover frequency, so the *available stability curve* can be obtained on the *available stability surface*. The parameters on the achieved curve satisfy the gain crossover frequency and phase margin specifications.

Finally, the parameter sets on the *available stability curve* are checked according to the robustness specification and the proposed FOPD controller parameters are obtained as $k_p = 19.5332, k_d = 6.4041$, and $\gamma = 0.9581$. Correspondingly, for fair comparison, a PID controller which is tuned by the optimal tuning method in [41] with similar specifications is also designed here.

Figure 7 illustrates the speed regulation comparison under the FOPD controller and PID controller with step input. It is shown that the speed regulation process under the FOPD controller has smaller rising time, accommodation time, steady state error, and almost no overshoot, which outperforms the control performance under the PID controller.

The robustness and precision comparisons are demonstrated in Figure 8 with different gain variations and external disturbance at $t = 5$ s. Note that the gain variations here can be regarded as load disturbance of XQ WMR. It is shown that the speed regulation process under the FOPD controller changes little with respect to different kinds of disturbance. However, there are obvious changes in the overshoot and accommodation time of the speed regulation process under the PID controller, which means the XQ WMR system controlled by the PID controller may not achieve precise and robust control performance in practice.

6.3. Experiment. In this section, the trajectory tracking experiment results of XQ WMR are shown to verify the effectiveness of the proposed FOPD controller. For fair comparison, a traditional PD controller, whose proportional and derivative parameters are the same with that of the proposed FOPD controller, is also implemented. The reference signal is depicted as follows:

$$\begin{cases} x_r(t) = 3\sin\left(\dfrac{\pi}{45t}\right), \\ \\ y_r(t) = 2\sin\left(\dfrac{2\pi}{45t}\right), \end{cases} \tag{40}$$

where $x_r(t)$ and $y_r(t)$ are the x-axis and y-axis reference trajectories. The sampling time is $T = 1$ ms.

The comparison of XQ WMR trajectory tracking performance is shown in Figure 9. It can be seen that the tracking performances under both controllers are acceptable. However, from the zoomed in areas of Figure 9, it is observed that the tracking performance under the proposed FOPD controller is more precise and the settling time is much shorter, which is also verified by the absolute error and x-axis error shown in Figures 10 and 11 illustrates the left and right speed comparisons of XQ WMR, and the control signal comparisons are demonstrated in Figure 12. These comparisons show that there is smaller oscillation in the speed control process of the proposed controller compared with the traditional PD controller, though the two controllers have the same proportional and derivative parameters.

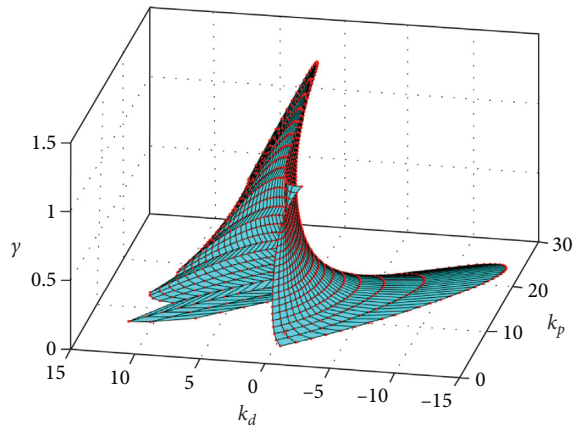

Figure 5: Maximum stability surface.

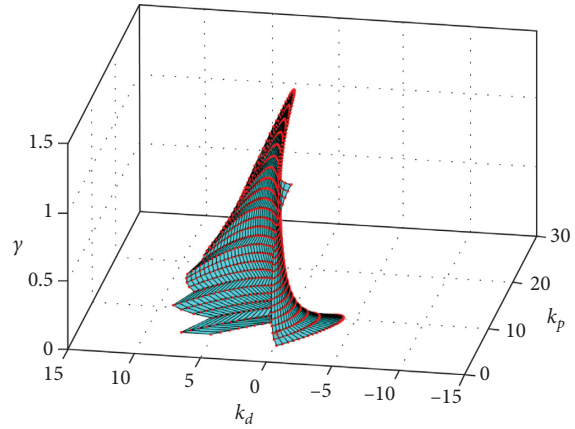

Figure 6: Available stability surface with $\varphi = 45°$.

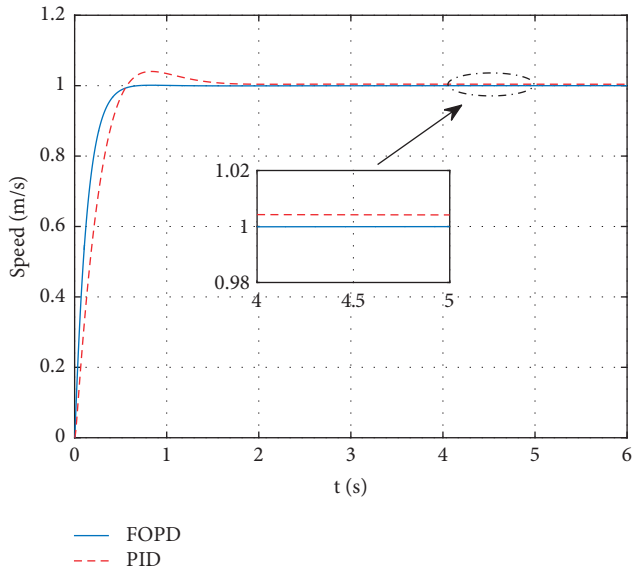

Figure 7: Speed regulation comparison.

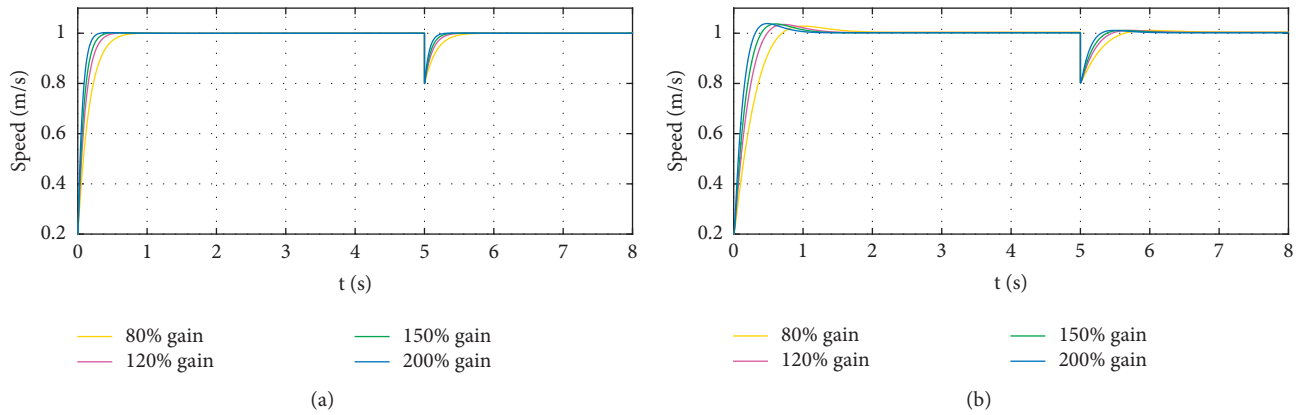

Figure 8: Speed regulation comparison with disturbance and gain variations: (a) FOPID and (b) PID.

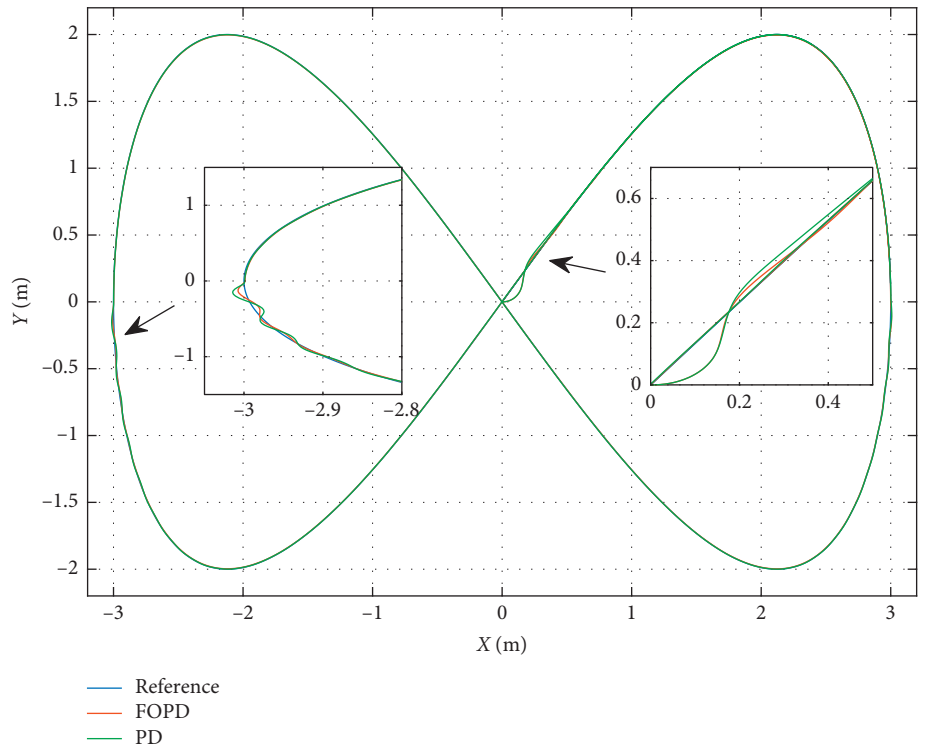

Figure 9: Trajectory tracking performance comparison.

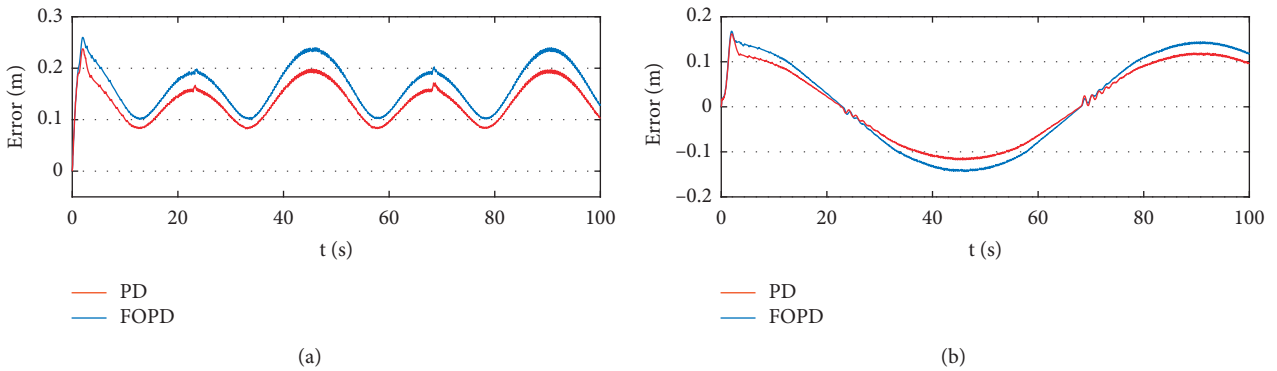

Figure 10: Errors comparison. (a) Absolute error. (b) X axis error.

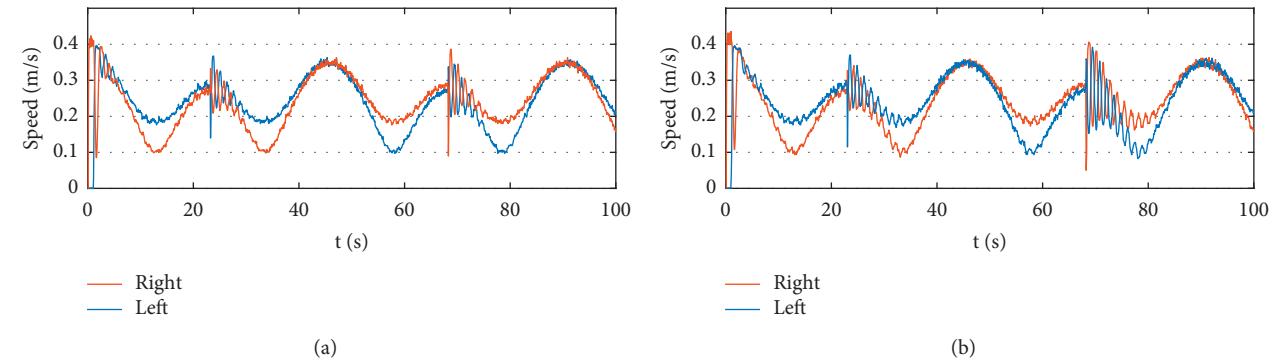

Figure 11: Speeds comparison. (a) FOPID and (b) PID.

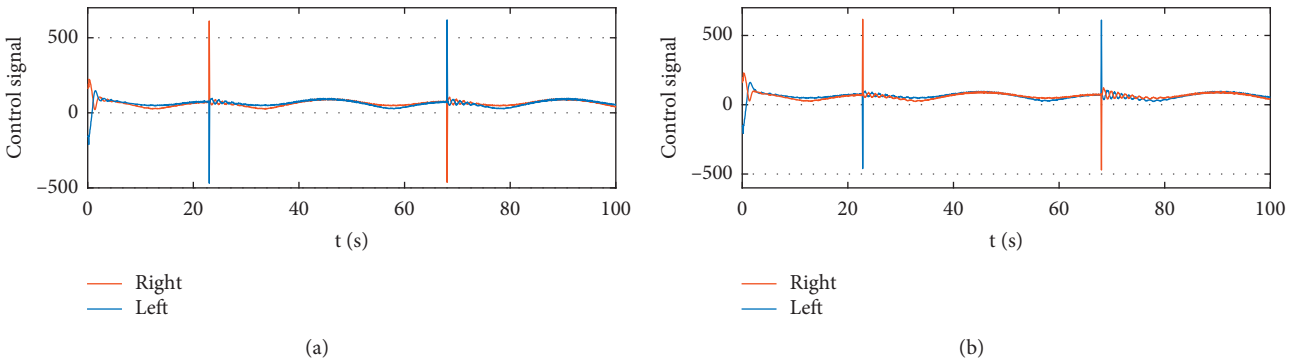

Figure 12: Control signals comparison. (a) FOPID and (b) PID.

7. Conclusion

In this paper, a synthesis of the FOPD controller for XQ WMR trajectory tracking control is proposed. Different from other robust FO controller tuning methods, the flat phase property can be guaranteed in a frequency interval instead of one frequency point, so the robustness of the control system is enhanced. The stabilizing process is also studied, so that the proposed FOPD controller can guarantee both the robustness and stability of the controlled system In addition, there is no complicated nonlinear equations which should be solved in this paper, so at least one parameter set which satisfies all the specifications can be found. The implementation and experiment results are presented to show the advantages of the proposed trajectory tracking algorithm. The proposed control algorithm is also capable of fulfilling different control requirements.

Data Availability

The data used to support the findings of this study are currently under embargo while the research findings are commercialized. Requests for data, 6 months after publication of this article, will be considered by the corresponding author.

Conflicts of Interest

The authors declare that they have no conflicts of interest.

Acknowledgments

This work was supported by the National Natural Science Foundation of China (Nos. 11902252 and 51979229), the Fundamental Research Funds for the Central Universities of China (Nos. G2018KY0305 and G2018KY0302), China Postdoctoral Science Foundation (No. 2019M663811), the Natural Science Foundation of Shaanxi Province (No. 2019JQ-164), and the Opening Foundation of Key Laboratory of Ocean Engineering, Shanghai Jiao Tong University (No. 1817).

References

[1] M. Chen, "Disturbance attenuation tracking control for wheeled mobile robots with skidding and slipping," *IEEE Transactions on Industrial Electronics*, vol. 64, no. 4, pp. 3359–3368, 2017.

[2] I. Rañó and R. Iglesias, "Application of systems identification to the implementation of motion camouflage in mobile robots," *Autonomous Robots*, vol. 40, no. 2, pp. 229–244, 2016.

[3] H. Peng, B. Shi, X. Wang, and C. Li, "Interval estimation and optimization for motion trajectory of overhead crane under uncertainty," *Nonlinear Dynamics*, vol. 96, no. 2, pp. 1693–1715, 2019.

[4] W. He, Y. Dong, and C. Sun, "Adaptive neural impedance control of a robotic manipulator with input saturation," *IEEE Transactions on Systems, Man, and Cybernetics: Systems*, vol. 46, no. 3, pp. 334–344, 2016.

[5] H. Peng, F. Li, J. Liu et al., "A symplectic instantaneous optimal control for robot trajectory tracking with differential-algebraic equation models," *IEEE Transactions on Industrial Electronics*, p. 1, 2019.

[6] X. Wang, J. Liu, Y. Zhang et al., "A unified symplectic pseudospectral method for motion planning and tracking control of 3D underactuated overhead cranes," *International Journal of Robust and Nonlinear Control*, vol. 29, no. 2, pp. 2236–2253, 2019.

[7] B. Li, Y. Fang, G. Hu, and X. Zhang, "Model-free unified tracking and regulation visual servoing of wheeled mobile robots," *IEEE Transactions on Control Systems Technology*, vol. 24, no. 4, pp. 1328–1339, 2016.

[8] C. S. Shijin and K. Udayakumar, "Speed control of wheeled mobile robots using PID with dynamic and kinematic modelling," in *Proceedings of the International Conference On Innovations in Information, Embedded and Communication Systems*, pp. 1–7, Coimbatore, India, March 2017.

[9] S. Zhang and L. Liu, "Normalized robust FOPID controller regulation based on small gain theorem," *Complexity*, vol. 2018, Article ID 5690630, 10 pages, 2018.

[10] I. Podlubny, "Fractional-order systems and PI/sup/spl lambda//D/sup/spl mu//-controllers," *IEEE Transactions on Automatic Control*, vol. 44, no. 1, pp. 208–214, 1999.

[11] L. Liu and S. Zhang, "Robust fractional-order PID controller tuning based on Bode's optimal loop shaping," *Complexity*, vol. 2018, Article ID 6570560, 14 pages, 2018.

[12] B. M. Vinagre, I. Podlubny, L. Dorcak, and V. Feliu, "On fractional PID controllers: a frequency domain approach," in *Proceedings of IFAC Workshop on Digital Control Past*, Terrassa, Spain, April 2000.

[13] C. A. Monje, B. M. Vinagre, V. Feliu, and Y. Chen, "Tuning and auto-tuning of fractional order controllers for industry applications," *Control Engineering Practice*, vol. 16, no. 7, pp. 798–812, 2008.

[14] G. Maione and P. Lino, "New tuning rules for fractional PI^{λ} controllers," *Nonlinear Dynamics*, vol. 49, no. 1-2, pp. 251–257, 2006.

[15] D. Valrio and C. J. Sda, "Tuning of fractional PID controllers with Ziegler-Nichols-type rules," *Signal Processing*, vol. 86, no. 10, pp. 2771–2784, 2006.

[16] J. J. Gude and E. Kahoraho, "Modified Ziegler-Nichols method for fractional PI controllers," in *Proceedings Of IEEE International Conference On Emerging Technologies and Factory Automation*, pp. 1–5, Bilbao, Spain, September 2010.

[17] V. Feliu, R. R. Prez, and L. S. Rodrguez, "Fractional robust control of main irrigation canals with variable dynamic parameters," *Control Engineering Practice*, vol. 15, no. 6, pp. 673–686, 2007.

[18] L. Liu, F. Pan, and D. Xue, "Variable-order fuzzy fractional PID controller," *ISA Transactions*, vol. 55, pp. 227–233, 2015.

[19] T. Vinopraba, N. Sivakumaran, and S. Narayanan, "IMC based fractional order PID controller," in *Proceedings of IEEE International Conference on Industrial Technology*, pp. 71–76, Auburn, AL, USA, March 2011.

[20] N. Sadati, A. Ghaffarkhah, and S. Ostadabbas, "A new neural network based FOPID controller," in *Proceedings of IEEE International Conference on Networking, Sensing and Control*, pp. 762–767, Sanya, China, April 2008.

[21] C. Yin, Y. Chen, and S.-m. Zhong, "Fractional-order sliding mode based extremum seeking control of a class of nonlinear systems," *Automatica*, vol. 50, no. 12, pp. 3173–3181, 2014.

[22] B. Jakovljevic, A. Pisano, M. R. Rapaic, and E. Usai, "On the slidingmode control of fractional order nonlinear uncertain dynamics," *International Journal of Robust & Nonlinear Control*, vol. 26, no. 4, pp. 782–798, 2016.

[23] D. Xue, *Fractional-order Control Systems Fundamentals and Numerical Implementations*, Northeastern University, Shenyang, China, 2017.

[24] A. Tepljakov and A. Tepljakov, *Applications of Fractional-Order Control*, Springer International Publishing, Berlin, Germany, 2017.

[25] M. Ö. Efe, "Fractional order systems in industrial automation-a survey," *IEEE Transactions on Industrial Informatics*, vol. 7, no. 4, pp. 582–591, 2011.

[26] O. Altet, X. Moreau, M. Moze, P. Lanusse, and A. Oustaloup, "Principles and synthesis of hydractive CRONE suspension," *Nonlinear Dynamics*, vol. 38, no. 1–4, pp. 435–459, 2004.

[27] N. Yousfi, P. Melchior, P. Lanusse, N. Derbel, and A. Oustaloup, "Decentralized CRONE control of nonsquare multivariable systems in path-tracking design," *Nonlinear Dynamics*, vol. 76, no. 1, pp. 447–457, 2014.

[28] S. Zhang, L. Liu, and X. Cui, "Robust FOPID controller design for fractional-order delay systems using positive stability region analysis," *International Journal of Robust and Nonlinear Control*, vol. 29, no. 15, pp. 5195–5212, 2019.

[29] L. Liu, S. Zhang, D. Xue, and Y. Q. Chen, "General robustness analysis and robust fractional-order PD controller design for fractional-order plants," *IET Control Theory & Applications*, vol. 12, no. 12, pp. 1730–1736, 2018.

[30] A. Rojas-Moreno and G. Perez-Valenzuela, "Fractional order tracking control of a wheeled mobile robot," in *Proceedings of the 2017 IEEE XXIV International Conference on Electronics, Electrical Engineering and Computing (INTERCON)*, pp. 1–4, Cusco, Peru, August 2017.

[31] A. Derdiyok, K. Orman, and A. Basci, "Speed and direction angle control of four wheel drive skid-steered mobile robot by using fractional order PI controller," *Elektronika IR Elektrotechnika*, vol. 22, no. 5, 2016.

[32] Y. Jin, Y.-Q. Chen, and D. Xue, "Time-constant robust analysis of a fractional order [proportional derivative] controller," *IET Control Theory & Applications*, vol. 5, no. 1, pp. 164–172, 2011.

[33] S. Zhang, Y. Yu, and Q. Wang, "Stability analysis of fractional-order Hopfield neural networks with discontinuous activation functions," *Neurocomputing*, vol. 171, pp. 1075–1084, 2016.

[34] S. Zhang, Y. Yu, and H. Wang, "Mittag-Leffler stability of fractional-order Hopfield neural networks," *Nonlinear Analysis: Hybrid Systems*, vol. 16, pp. 104–121, 2015.

[35] L. Liu, S. Tian, D. Xue, T. Zhang, and Y. Chen, "Continuous fractional-order zero phase error tracking control," *ISA Transactions*, vol. 75, pp. 226–235, 2018.

[36] H. Li, Y. Luo, and Y. Chen, "A fractional order proportional and derivative (FOPD) motion controller: tuning rule and experiments," *IEEE Transactions on Control Systems Technology*, vol. 18, no. 2, pp. 516–520, 2010.

[37] L. Liu, S. Zhang, D. Xue, and Y. Chen, "Robust stability analysis for fractional-order systems with time delay based on finite spectrum assignment," *International Journal of Robust and Nonlinear Control*, vol. 29, no. 8, pp. 2283–2295, 2019.

[38] K. Chen, R. Tang, and C. Li, "Phase-constrained fractional order PI controller for second-order-plus dead time systems," *Transactions of the Institute of Measurement & Control*, vol. 39, no. 8, 2016.

[39] S. E. Hamamci, "Stabilization using fractional-order PI and PID controllers," *Nonlinear Dynamics*, vol. 51, no. 1-2, pp. 329–343, 2008.

[40] A. Oustaloup, P. Melchior, P. Lanusse, O. Cois, and F. Dancla, "The CRONE toolbox for MATLAB," in *An Introduction to Reservoir Simulation Using MATLAB/GNU Octave*, Cambridge University Press, Cambridge, UK, 2000.

[41] L. Liu, D. Xue, and S. Zhang, "Closed-loop time response analysis of irrational fractional-order systems with numerical Laplace transform technique," *Applied Mathematics and Computation*, vol. 350, pp. 133–152, 2018.

Hindawi
Complexity
Volume 2020, Article ID 7025761, 22 pages
https://doi.org/10.1155/2020/7025761

Research Article

LMI-Based Robust Stabilization of a Class of Input-Constrained Uncertain Nonlinear Systems with Application to a Helicopter Model

Hassène Gritli [1,2]

[1]*Institut Supérieur des Technologies de l'Information et de la Communication, Université de Carthage, 1164 Borj Cedria, Tunis, Tunisia*
[2]*Laboratoire Robotique, Informatique et Systèmes Complexes (RISC-LR16ES07), Ecole Nationale d'Ingénieurs de Tunis, Université de Tunis El Manar, BP. 37, Le Belvédère, 1002 Tunis, Tunisia*

Correspondence should be addressed to Hassène Gritli; grhass@yahoo.fr

Received 22 August 2019; Revised 21 November 2019; Accepted 10 December 2019; Published 25 January 2020

Guest Editor: Baltazar Aguirre-Hernandez

This paper is concerned with the robust stabilization of a class of continuous-time nonlinear systems, with an application to the pitch dynamics of a simple helicopter model, via an affine state-feedback control law using the linear matrix inequality (LMI) approach. The nonlinear dynamics is subject to norm-bounded parametric uncertainties and disturbances. In addition, the problem of actuator nonlinearity is addressed by considering the saturation effect of the control law. We demonstrate first that the synthesis problem of the saturated controller is expressed in terms of bilinear matrix inequalities (BMIs). Thanks to the Schur complement lemma and the matrix inversion lemma, we convert these BMIs into LMIs allowing the simultaneous computation of the two gains of the affine controller. Furthermore, we address in this work the estimation problem of the domain of attraction using the invariant set concept. This is solved by computing the largest attractive invariant ellipsoid. Compared with previous works, the research procedure of such ellipsoidal set is achieved in a single step with a reduced number of LMI constraints and then with less conservative conditions. A portfolio of numerical results is presented. The effectiveness and robustness of the proposed saturated controller in the stabilization of the adopted helicopter pitch model toward parametric uncertainties and disturbances are illustrated through simulation results.

1. Introduction

1.1. Background and Literature Review. Mechatronics, such as aircraft, spacecrafts, launch vehicles, unmanned autonomous vehicles, missiles, walking robots, robot manipulators, electronic vehicles, and unmanned aerial vehicles, has played a very important role in modern industry-related applications. Nowadays, there is an ever-increasing demand of advanced control strategies for mechatronic systems with enhanced performances.

It is known, on the one hand, that almost all existing physical and mechatronic systems unavoidably include uncertainties and disturbances due to inaccurate modeling, measurement errors, exterior conditions, or parameter variations. The presence of uncertainties may cause instability and bad performances on a controlled system. Thus, considerable efforts have been assigned to the robust stability and stabilization of linear and nonlinear systems with parametric uncertainties. For a recent literature, we refer the readers to [1–8]. Two types of parametric uncertainties are very often considered in systems: norm-bounded uncertainty and polytopic uncertainty. In recent years, the linear matrix inequality (LMI) technique [9] has been widely used to solve the robust control for uncertain linear and nonlinear systems with polytopic uncertain parameters and norm-bounded uncertain parameters. However, most control synthesis problems cannot be written in a LMI form. However, they are written in terms of a more general form known as a bilinear matrix inequality (BMI), which is usually not exploitable numerically to solve. For some BMI

problems with simple bilinearities, the YALMIP toolbox [10] was used to solve such problems. There are several approaches and different relaxed synthesis conditions proposed for conducting the BMIs into LMIs, such as in [5–7, 9, 11–16], just to mention a few.

On the other hand, the actuator saturation nonlinearity exists commonly in practical control systems. Indeed, the signal amplitude that an actuator can deliver is usually limited by physical or safety constraints. Thus, the neglect of the actuator constraints in the controller design may cause instability of the closed-loop system [17–19]. The design of controllers for continuous-time and discrete-time systems by taking into consideration the actuator saturation has been extensively studied in the past few decades [17–36]. Some works have investigated the problem of uncertainties and actuator saturation in mechatronic systems such as the vehicle lateral dynamics [37], the vehicle active suspension systems [38–41], the rigid spacecraft [42, 43], the inertia wheel inverted pendulum [12], the supercavitating vehicle [44], the flexible robotic manipulator [45], and the marine surface vessel [46], among others.

The concept of attractive invariant sets has been generally proposed for linear systems involving actuator saturation [5, 20, 28, 29, 36, 44, 47–51]. Moreover, through such concept, numerous studies have focused on the characterization of the maximum attraction set for linear systems subject to saturated linear feedback. Thus, some research works focused on writing the saturation function of the control input as a linear convex combination of some constrained variables [18, 20, 27, 36, 47, 48, 50–53]. This approach leads to sufficient conditions in terms of a very large number of LMIs that are difficult to solve numerically [27–29]. The common goal of almost all of these previous research works is to find the largest attractive invariant ellipsoidal set in order to provide an estimation of the domain of attraction for initial conditions.

In addition, it is well recognized that most practical control systems are inherently nonlinear. The number of available results by taking the actuator saturation nonlinearity into account in the design and analysis of nonlinear control systems is still limited. Because of the difficulty of the problem itself, most research works have been focused on particular classes of nonlinear systems to design saturated controllers [5, 25, 26]. Furthermore, the simultaneous presence of parametric uncertainties and actuator saturation nonlinearity in physical systems has led many authors to combine the techniques of the robust control theory and those of constrained control [5, 54].

1.2. Objective of the Paper. In this paper, we are interested in the design of a robust controller to stabilize a class of nonlinear systems, for which the zero state is not the equilibrium point. As a motivation application, we consider the pitch dynamics of a simple helicopter model [55–57]. In fact, such helicopter pitch model has been considered as a testbed used in order to develop new advanced control strategies. Authors in [56] approximated the pitch dynamics of the helicopter with a set of piecewise affine stochastic systems. The proposed stochastic affine feedback controller is designed for the approximated model and implemented on the main nonlinear system. Authors in [57] designed an observer-based minimum variance control for the same objective by taking into consideration norm-bounded uncertainties. Such uncertainties arise in the form of the difference between the actual nonlinear dynamics and its piecewise-affine approximation. Furthermore, authors in [55] approximated also the simplified pitch model of the helicopter via a piecewise affine system. In these works [55–57], the saturation effect in the actuators was not taken into consideration in the control design.

In the present work, we propose an affine state-feedback control law for the adopted class of nonlinear systems, with a particular interest to the pitch dynamics of the helicopter model, where all the states are assumed to be available for direct measurement. Our main objective is to control, via such affine feedback control law, the adopted nonlinear systems to the zero state. Moreover, we consider the problem of norm-bounded parametric uncertainties and also the problem of external disturbances. Furthermore, we take into consideration the problem of actuator saturation in the design of the robust affine state-feedback control law. Thus, the main role of such control law is to asymptotically bring the trajectory of the nonlinear system to the zero state even if it is subject to the parametric uncertainties, the disturbances, and the actuator saturation. In addition, in this work, the problem of searching for appropriate feedback gain matrices of the affine state-feedback control law is realized also by solving the problem of estimating the largest attractive invariant set. Our design methodology of the saturated stabilizing affine state-feedback control law is based on the framework of LMIs. We show at first that the affine state-feedback controller is designed by solving an optimization problem subject to three BMI constraints. Then, by using some judicious congruence transformations and some technical lemmas, we convert these BMIs into three LMI constraints. In the end of this work, we demonstrate through simulations the effectiveness of the proposed affine state-feedback control law in the robust stabilization of the pitch dynamics of the helicopter model while the largest attractive invariant set is guaranteed.

1.3. Contributions and Innovations. The main contributions and innovations of the work in this paper can be summarized as follows:

(1) The problem of robust stabilization of a class of nonlinear systems, with an application to the pitch dynamics of a simple helicopter model, under norm-bounded parametric uncertainties, external disturbance, and input saturation nonlinearity, is considered using the concept of the invariant set. The main objective is to control the disturbed uncertain nonlinear system to the zero state, which is not the equilibrium point in the open loop.

(2) A saturated affine state-feedback controller is designed based on the LMI approach. To the best of

the authors' knowledge, such problem was not developed in the literature. Only the linear state/output feedback controllers have been considered.

(3) A transformation of the BMI stability condition, related to the input saturation problem, into an LMI condition is achieved using the matrix inversion lemma and the Schur complement lemma.

(4) An estimation of the ellipsoidal region of attraction for the nonlinear system under study is also realized. Compared with previous works [20, 47–50, 52, 58], our research procedure of the largest invariant attractive ellipsoid is achieved in only one step with a reduced number of LMI constraints.

1.4. Structure of the Paper. The rest of this paper is organized as follows. In Section 2, we present first some technical lemmas that will be used in this work, the adopted class of the nonlinear systems, and the problem formulation. The simple helicopter model, as a motivation application, and its pitch dynamics are also described in this section. The design of the robust affine state-feedback controller under saturation, based on the LMI approach, is discussed in Section 3. Transformation of the BMIs into LMIs is also realized in this section. The problem of computation/estimation of the domain of attraction (the largest attractive ellipsoid) is addressed in Section 4. Simulation results and some comparisons are presented in Section 5. Finally, concluding remarks and future works are drawn in Section 6.

1.5. Notations. Throughout this paper, $\mathbf{A}^{\mathrm{T}}$ represents the transpose of $\mathbf{A}$, the symbol $(\star)$ in matrix inequality denotes the symmetric term of the matrix, for example, $\begin{bmatrix} \mathbf{X} & \mathbf{Y} \\ (\star) & \mathbf{Z} \end{bmatrix} = \begin{bmatrix} \mathbf{X} & \mathbf{Y} \\ \mathbf{Y}^{\mathrm{T}} & \mathbf{Z} \end{bmatrix}$ and $\mathbf{X} + (\star) = \mathbf{X} + \mathbf{X}^{\mathrm{T}}$, $\mathbf{X} > 0$ (< 0) means $\mathbf{X}$ is a symmetric positive (negative) definite matrix, and $\mathrm{diag}(A, B, \ldots, Z)$ represents a diagonal matrix. Moreover, $\mathcal{O}$ and $\mathcal{I}$ denote the zero matrix and the identity matrix, respectively, with appropriate dimensions.

2. Preliminaries and Problem Statement

In this section, we define the class of continuous-time nonlinear systems that will be investigated in this paper. The pitch dynamics of a simple helicopter model is given as an illustrative example. First of all, we present some technical lemmas that will be used subsequently.

2.1. Some Technical Lemmas

Lemma 1 (see [41]). *The Lyapunov candidate function $V(t)$ is bounded given that the initial condition $V(0)$ is bounded, $V(t) \geq 0$ is continuous, and if the following equation is true:*

$$\dot{V}(t) \leq -\mu V(t) + \eta, \tag{1}$$

where $\mu > 0$ and $\eta > 0$.

Lemma 2 (the Young relation [12]). *Given constant matrices $\mathbf{X}$ and $\mathbf{Y}$ with appropriate dimensions, the following inequality holds:*

$$\mathbf{X}^{\mathrm{T}}\mathbf{Y} + \mathbf{Y}^{\mathrm{T}}\mathbf{X} \leq \varepsilon \mathbf{X}^{\mathrm{T}}\mathbf{X} + \varepsilon^{-1}\mathbf{Y}^{\mathrm{T}}\mathbf{Y}, \tag{2}$$

for all positive scalar ε.

Lemma 3 (the matrix inversion lemma [9, 12]). *Given invertible matrices $\mathbf{A}$ and $\mathbf{B}$ such that $\mathbf{A} \in \mathbb{R}^{n\times n}$ and $\mathbf{B} \in \mathbb{R}^{m\times m}$. Moreover, given matrices $\mathbf{C}$ and $\mathbf{D}$ with appropriate dimensions: $\mathbf{C} \in \mathbb{R}^{n\times m}$ and $\mathbf{D} \in \mathbb{R}^{m\times n}$. Then,*

$$(\mathbf{A} + \mathbf{CBD})^{-1} = \mathbf{A}^{-1} - \mathbf{A}^{-1}\mathbf{C}\left(\mathbf{B}^{-1} + \mathbf{D}\mathbf{A}^{-1}\mathbf{C}\right)^{-1}\mathbf{D}\mathbf{A}^{-1}. \tag{3}$$

Lemma 4 (the Schur complement lemma [9, 12]). *Given matrices $\mathcal{Q} = \mathcal{Q}^{T}$, $\mathcal{R} = \mathcal{R}^{T}$, and $\mathcal{S}$ with appropriate dimensions, the following propositions are equivalent:*

$$\begin{bmatrix} \mathcal{Q} & \mathcal{S} \\ (\star) & \mathcal{R} \end{bmatrix} > 0,$$
$$\begin{cases} \mathcal{R} > 0, \\ \mathcal{Q} - \mathcal{S}\mathcal{R}^{-1}\mathcal{S}^{\mathrm{T}} > 0. \end{cases} \tag{4}$$

Lemma 5 (the S-procedure lemma [9, 12]). *Let $\mathcal{F}_0, \ldots, \mathcal{F}_p \in \mathbb{R}^{n\times n}$ be symmetric matrices. We consider the following conditions on $\mathcal{F}_0, \ldots, \mathcal{F}_p$:*

$$\begin{aligned} &\zeta^{\mathrm{T}}\mathcal{F}_0\zeta > 0, && \forall \zeta \neq 0, \\ \text{s.t.}\quad &\zeta^{\mathrm{T}}\mathcal{F}_i\zeta \geq 0, && \forall i = 1, \ldots, p. \end{aligned} \tag{5}$$

If there exist scalar variables $\tau_1 \geq 0, \ldots, \tau_p \geq 0$, such that

$$\mathcal{F}_0 - \sum_{i=1}^{p} \tau_i \mathcal{F}_i > 0, \tag{6}$$

then (5) holds.

2.2. Class of Nonlinear Systems. A general class of continuous-time nonlinear systems with a control input $\mathbf{u}$ and under disturbance signal $\mathbf{w}$ is defined by the following form:

$$\dot{\mathbf{x}} = \mathbf{F}(\mathbf{x}, \mathbf{u}, \mathbf{w}), \tag{7}$$

where $\mathbf{x} \in \mathbb{R}^{n_a}$, $\mathbf{u} \in \mathbb{R}^{n_u}$, and $\mathbf{w} \in \mathbb{R}^{n_w}$.

In this work, we will consider a particular class of these nonlinear systems, for which the mathematical model is given by the following differential equation:

$$\dot{\mathbf{x}} = \mathbf{A}\mathbf{x} + \mathbf{B}\mathbf{u} + \sum_{i=1}^{n_f} \mathbf{C}_i f_i(\mathbf{x}) + \mathbf{E}\mathbf{w}, \tag{8}$$

where $\mathbf{A} \in \mathbb{R}^{n_x\times n_x}$, $\mathbf{B} \in \mathbb{R}^{n_x\times n_u}$, $\mathbf{C}_i \in \mathbb{R}^{n_x\times 1}$, $\mathbf{E} \in \mathbb{R}^{n_x\times n_w}$, and the nonlinear functions $f_i(\mathbf{x})$ are scalars, i.e., $f_i(\mathbf{x}) \in \mathbb{R}$ for all $i = 1, \ldots, n_f$. Moreover, we will consider that, in the nonlinear system (7), we have $\mathbf{F}(0, 0, 0) \neq 0$. This means that the state $\mathbf{x} = 0$ is not the equilibrium point. Hence, in the dynamics (8), we have

$$\sum_{i=1}^{n_f} \mathbf{C}_i f_i(0) \neq 0. \tag{9}$$

In addition, we will consider, without loss of generality, that

$$\left|f_i(\mathbf{x})\right| \leq 1, \quad \forall i = 1, \ldots, n_f. \tag{10}$$

Remark 1. In this work, we consider a class of nonlinear systems (8), in which the nonlinear terms $\mathbf{f}_i(\mathbf{x})$, for all $i = 1, \ldots, n_f$, satisfy the constraints in (10). Our LMI-based approach for the design of a stabilizing control law $\mathbf{u}$, which will be designed in the sequel, can be applied for a general class of fully nonlinear systems such as (hyper) chaotic systems as in [59, 60], robotic/mechatronic systems as in [43, 46], and underactuated mechanical systems [61, 62], just to mention a few. Thus, the nonlinearity term, saying $\mathbf{h}(\mathbf{x}) = \sum_{i=1}^{n_f} \mathbf{C}_i f_i(\mathbf{x})$, can be assumed to satisfy the following quadratic inequality [12]:

$$\mathbf{h}^{\mathrm{T}}(\mathbf{x})\mathbf{h}(\mathbf{x}) \leq \lambda^2 \mathbf{x}^{\mathrm{T}} \mathbf{H}^T \mathbf{H} \mathbf{x}, \tag{11}$$

where λ is a positive scalar and $\mathbf{H}$ is a constant matrix having appropriate dimension.

Some other research papers have considered ellipsoidal condition or one-sided Lipschitz condition on the nonlinearity $\mathbf{h}(\mathbf{x})$. For this subject, we refer the readers to, for example, [3, 8, 60, 63–65] and references therein.

2.3. Motivation Application: The Simplified Pitch Dynamics of the Helicopter Model. As an illustrative motivation application, we will consider in this work a simplified helicopter pitch dynamics model. The schematic model of the helicopter is shown in Figure 1. We refer our readers to [55–57] for further details on this simplified model. The pitch dynamics of the simplified helicopter model has two degrees of freedom with only one actuator. Such model was employed to develop new control strategies for mechatronic systems [55–57].

The nonlinear model of the pitch dynamics of the simplified helicopter is described by the following differential equations [55–57]:

$$\begin{aligned} \dot{x}_1 &= x_2, \\ \dot{x}_2 &= \frac{1}{I_{yy}}\left(-m_{\mathrm{heli}} l_{cgx} \cos(x_1) - m_{\mathrm{heli}} l_{cgz} g \sin(x_1) - F_{vM} x_2 + u\right) \\ &\quad + \frac{s}{I_{yy}} w, \end{aligned} \tag{12}$$

where x_1 and x_2 represent the pitch angle (θ in Figure 1) and pitch rate, respectively; I_{yy} is the second moment around the y-axis; m_{heli} is the mass of the helicopter; l_{cgx} and l_{cgz} are displacements from the center of mass (GC in Figure 1) relative to the rotation joint B shown in Figure 1; F_{vM} is the pitch damping; s is the variance of the moment disturbance; u is the control torque exerted by the main blade of the helicopter around the y-axis; and w is the external disturbance, which is modeled as an additive white noise representing the turbulent moments on the helicopter [55–57].

For simplicity, let us introduce the following change of variables: $a = -(F_{vM}/I_{yy})$, $b = 1/I_{yy}$, $c = -(m_{\mathrm{heli}} l_{cgx}/I_{yy})$, $d = -(m_{\mathrm{heli}} l_{cgz} g/I_{yy})$, and $e = s/I_{yy}$. Then, the nonlinear differential equations in (12) can be rewritten under the particular class (8), where $\mathbf{x} = \begin{bmatrix} x_1 \\ x_2 \end{bmatrix}$, $\mathbf{A} = \begin{bmatrix} 0 & 1 \\ 0 & a \end{bmatrix}$, $\mathbf{B} = \begin{bmatrix} 0 \\ b \end{bmatrix}$, $\mathbf{C}_1 = \begin{bmatrix} 0 \\ c \end{bmatrix}$, $\mathbf{C}_2 = \begin{bmatrix} 0 \\ d \end{bmatrix}$, $\mathbf{E} = \begin{bmatrix} 0 \\ e \end{bmatrix}$, $f_1(\mathbf{x}) = f_1(x_1) = \cos(x_1)$, and $f_2(\mathbf{x}) = f_2(x_1) = \sin(x_1)$.

Notice that the two nonlinear terms $f_1(\mathbf{x})$ and $f_2(\mathbf{x})$ satisfy condition (10) and also constraint (9). Hence, the zero state, $\mathbf{x} = 0$, is not the equilibrium (singular) point of the pitch dynamics of the helicopter model and then of the undisturbed uncontrolled nonlinear system (8), i.e., for $w = 0$ and $u = 0$.

Remark 2. It is worth to note that the model of the simple pitch dynamics (8) of the helicopter in Figure 1 was adopted from [55–57]. It is a simple model where the propeller dynamics (including motor, propeller interaction, air stream interaction, gyroscopic moments, and propeller flexing), the perturbation modelling (including wind gust modelling and payload modelling), and the cyclic/collective mechanism modelling are not considered in this study. Only the turbulent moments are taken into account as an external disturbance input, w. We emphasize that all these previous unmodelled dynamics can be lumped into a single term, saying that $\boldsymbol{\delta}(\mathbf{x})$ can be majored according to condition (11).

For more general and basic pitch models for helicopters that reproduce basic dynamic properties of these vehicles, we can refer to [66] for typical helicopter models or [67] for more modern applications.

2.4. Problem Statement. In the sequel, and for simplicity in developing and designing LMI stability conditions, we will consider that, in (8), $n_f = 2$, and then the class of nonlinear systems to consider is as follows:

$$\dot{\mathbf{x}} = \mathbf{A}\mathbf{x} + \mathbf{B}\mathbf{u} + \mathbf{C} f(\mathbf{x}) + \mathbf{D} g(\mathbf{x}) + \mathbf{E}\mathbf{w}, \tag{13}$$

where $f(\mathbf{x}) = f_1(\mathbf{x})$ and $g(\mathbf{x}) = f_2(\mathbf{x})$ are the two scalar nonlinearities satisfying conditions (9) and (10).

As noted before, the zero state $\mathbf{x} = 0$ is not the equilibrium point of the undisturbed uncontrolled nonlinear system (8) and then the simplified nonlinear system (13). Thus, we obtain $\mathbf{C} f(0) + \mathbf{D} g(0) \neq 0$.

Our objective in this work is to control dynamics (13) to the zero state by designing a feedback controller, even if the dynamics is under parametric uncertainties or subject to the disturbance vector $\mathbf{w}$. Thus, we assume that the disturbance signal $\mathbf{w}$ is bounded such that

$$\mathbf{w}^{\mathrm{T}} \mathbf{w} \leq \rho, \tag{14}$$

for some positive scalar ρ.

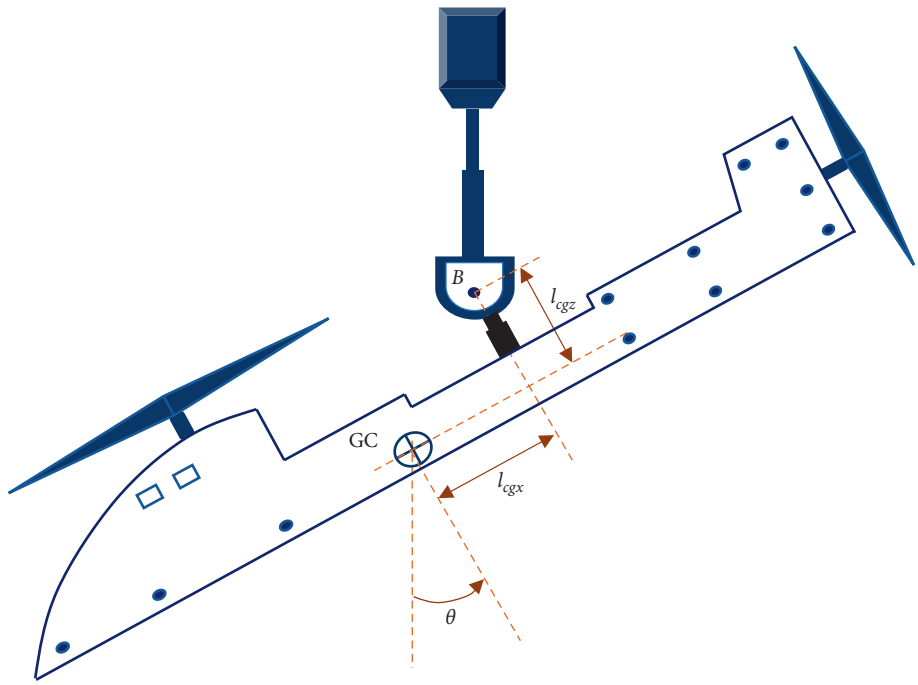

Figure 1: Simplified pitch model of the helicopter, from [55–57].

Furthermore, we assume that all parameters in the nonlinear system (13) are uncertain and are with a bounded norm. The values of these parameters presented in the nonlinear dynamics (13) are considered to be the nominal ones. Thus, the nonlinear system (13) will be considered as the nominal system, for which $(\mathbf{A}, \mathbf{B})$ is controllable.

Hence, under parametric uncertainties, the nominal system (13) will be rewritten as follows:

$$\begin{aligned}\dot{\mathbf{x}} = {} & (\mathbf{A} + \Delta\mathbf{A})\mathbf{x} + (\mathbf{B} + \Delta\mathbf{B})\mathbf{u} + (\mathbf{C} + \Delta\mathbf{C})\mathbf{f}(\mathbf{x}) \\ & + (\mathbf{D} + \Delta\,\mathbf{D})\mathbf{g}(\mathbf{x}) + (\mathbf{E} + \Delta\mathbf{E})\mathbf{w},\end{aligned} \tag{15}$$

where $\Delta\mathbf{A}$, $\Delta\mathbf{B}$, $\Delta\mathbf{C}$, $\Delta\,\mathbf{D}$, and $\Delta\mathbf{E}$ are matrices containing parametric uncertainties and satisfying the following expressions:

$$\Delta\mathbf{A} = \sum_{i_1=1}^{q_1} \delta_a^{i_1} \mathbf{A}_1^{i_1} \mathbf{A}_2^{i_1}, \tag{16a}$$

$$\Delta\mathbf{B} = \sum_{i_2=1}^{q_2} \delta_b^{i_2} \mathbf{B}_1^{i_2} \mathbf{B}_2^{i_2}, \tag{16b}$$

$$\Delta\mathbf{C} = \sum_{i_3=1}^{q_3} \delta_c^{i_3} \mathbf{C}_1^{i_3} \mathbf{C}_2^{i_3}, \tag{16c}$$

$$\Delta\,\mathbf{D} = \sum_{i_4=1}^{q_4} \delta_d^{i_4} \mathbf{D}_1^{i_4} \mathbf{D}_2^{i_4}, \tag{16d}$$

$$\Delta\mathbf{E} = \sum_{i_5=1}^{q_5} \delta_e^{i_5} \mathbf{E}_1^{i_5} \mathbf{E}_2^{i_5}, \tag{16e}$$

where the matrices $\mathbf{A}_1^{i_1}, \mathbf{A}_2^{i_1}, \mathbf{B}_1^{i_2}, \mathbf{B}_2^{i_2}, \mathbf{C}_1^{i_3}, \mathbf{C}_2^{i_3}, \mathbf{D}_1^{i_4}, \mathbf{D}_2^{i_4}, \mathbf{E}_1^{i_5}$, and $\mathbf{E}_2^{i_5}$ are with appropriate dimensions. Moreover, all the uncertainties $\delta_a^{i_1}$, $\delta_b^{i_2}$, $\delta_c^{i_3}$, $\delta_d^{i_4}$, and $\delta_e^{i_5}$, for all $i_1 = 1, \ldots, q_1$, $i_2 = 1, \ldots, q_2$, $i_3 = 1, \ldots, q_3$, $i_4 = 1, \ldots, q_4$, and $i_5 = 1, \ldots, q_5$, are with a bounded norm, i.e.,

$$\left|\delta_i^j\right| \leq \overline{\delta}_i^j, \tag{17}$$

for all $i \in \{a, b, c, d, e\}$ and for all $j \in \{i_1, i_2, i_3, i_4, i_5\}$.

In addition, we will consider that the uncertain nonlinear dynamics (15) is subject to an input saturation of the controller $\mathbf{u}$:

$$-u_{\max}^i \leq u^i \leq u_{\max}^i, \quad \forall i = 1, \ldots, n_u, \tag{18}$$

where $u_{\max}^i$, for all $i = 1, \ldots, n_u$, are prescribed positive scalars and u^i is the ith element of the control vector $\mathbf{u}$.

The problem we are addressing in this work is to find, for the uncertain disturbed nonlinear system (15), an affine state-feedback control law

$$\mathbf{u} = \mathbf{K}\mathbf{x} + \mathbf{m}, \tag{19}$$

where $\mathbf{K} \in \mathbb{R}^{n_u \times n_x}$ and $\mathbf{m} \in \mathbb{R}^{n_u}$ are the feedback gains to design, for which the control law $\mathbf{u}$ is constrained according to condition (18). The proposed control law (19) is actually a linear state-feedback law augmented with the constant term, $\mathbf{m}$, to keep the system state around an operating point, that is, the zero-equilibrium point $\mathbf{x} = 0$.

Let us define the following set:

$$\mathscr{L}(\mathbf{K}, \mathbf{m}, \mathbf{u}_{\max}) = \{\mathbf{x} \in \mathbb{R}^{n_x} : |\mathbf{K}\mathbf{x} + \mathbf{m}| \leq \mathbf{u}_{\max}\}, \tag{20}$$

as the region in the state space where the feedback control law $\mathbf{m}$ in (19) is linear (affine) in terms of the state vector $\mathbf{x}$.

In addition, let $\mathbf{P} \in \mathbb{R}^{n_x \times n_x}$ be a positive-definite symmetric matrix and denote the Lyapunov level set as

$$\varepsilon(\mathbf{P}, \gamma) = \left\{ \mathbf{x} \in \mathbb{R}^{n_x} : x^{\mathrm{T}} \mathbf{P} \mathbf{x} \leq \gamma \right\}, \tag{21}$$

where γ is a prescribed positive scalar.

The level set $\varepsilon(\mathbf{P}, \gamma)$ defined by (21) is an invariant set [5, 52]. Moreover, it is associated with the Lyapunov function $V(\mathbf{x}) = \mathbf{x}^{\mathrm{T}} \mathbf{P} \mathbf{x}$ for the closed-loop system. Consequently, $\varepsilon(\mathbf{P}, \gamma)$ is an invariant set of the nonlinear system (15) with the control law (19) in the sense of the following definition.

Definition 1. A set $\mathcal{S} \subset \mathbb{R}^{n_x}$ is said to be invariant with respect to motion of system (14), if for all initial conditions $\mathbf{x}(0) \in \mathcal{S}$, the motion of the system $\mathbf{x}(t)$ remains in $\mathcal{S}$ for all $t > 0$.

Accordingly, the ellipsoid $\varepsilon(\mathbf{P}, \gamma)$ is said to be contractively invariant if $\dot{V}(\mathbf{x}) < 0$ for all $\mathbf{x} \in \varepsilon(\mathbf{P}, \gamma) \backslash \{0\}$. Clearly, if $\varepsilon(\mathbf{P}, \gamma)$ is contractively invariant, then it is inside the domain of attraction [5, 52].

According to Lemma 1 and by posing $\eta = \mu\gamma$, we will have

$$\dot{V}(\mathbf{x}) \leq -\mu (V(\mathbf{x}) - \gamma). \tag{22}$$

Thus, on the boundary of the set $\varepsilon(\mathbf{P}, \gamma)$, we have $\mathbf{x}^{\mathrm{T}} \mathbf{P} \mathbf{x} = \gamma$. Hence, $\dot{V}(\mathbf{x}) < 0$. It follows that $\varepsilon(\mathbf{P}, \gamma)$ is a strictly ellipsoidal invariant set [5, 47].

Condition (22) will be used in the sequel in order to design the robust stabilization conditions of the closed-loop nonlinear system (15) with the norm-bounded parametric uncertainties (17) under the bounded external disturbance (14) and subject to the saturation (18) of the affine state-feedback control law (19) under condition (35).

As we look for stability conditions for the uncertain disturbed nonlinear system (15) under the saturated feedback control law u inside the invariant ellipsoid (21), we should have the following constraint:

$$\varepsilon(\mathbf{P}, \gamma) \subset \mathscr{L}(\mathbf{K}, \mathbf{m}, \mathbf{u}_{\max}). \tag{23}$$

Therefore, if for a certain Lyapunov matrix $\mathbf{P} = \mathbf{P}^{\mathrm{T}} > 0$ satisfying conditions (22) and (23), then taking any initial condition in the invariant ellipsoid $\varepsilon(\mathbf{P}, \gamma)$, we will have $u = \mathbf{K}\mathbf{x} + \mathbf{m}$ belongs to the set $\mathscr{L}(\mathbf{K}, \mathbf{m}, \mathbf{u}_{\max})$.

In the sequel, we will develop conditions under which the ellipsoid $\varepsilon(\mathbf{P}, \gamma)$ is contractively invariant and the disturbed uncertain nonlinear system (15) is robustly stable by means of the saturated affine state-feedback control law (19). Moreover, we will show how to compute the gains $\mathbf{K}$ and $\mathbf{m}$ and the Lyapunov matrix $\mathbf{P}$, which determine the largest ellipsoid $\varepsilon(\mathbf{P}, \gamma)$ and hence obtain an estimate of the domain of attraction.

It is worth noting that, for the case of the pitch dynamics of the helicopter model, the uncertainty matrices are $\Delta\mathbf{A} = \begin{bmatrix} 0 & 0 \\ 0 & \delta_a \end{bmatrix}$, $\Delta\mathbf{B} = \begin{bmatrix} 0 \\ \delta_b \end{bmatrix}$, $\Delta\mathbf{C} = \begin{bmatrix} 0 \\ \delta_c \end{bmatrix}$, $\Delta\mathbf{D} = \begin{bmatrix} 0 \\ \delta_d \end{bmatrix}$, and $\Delta\mathbf{E} = \begin{bmatrix} 0 \\ \delta_e \end{bmatrix}$.

Moreover, it is easy to show that these uncertainty matrices $\Delta\mathbf{A}$, $\Delta\mathbf{B}$, $\Delta\mathbf{C}$, $\Delta\mathbf{D}$, and $\Delta\mathbf{E}$ can be rewritten like so:

$$\begin{aligned} \Delta\mathbf{A} &= \delta_a \mathbf{F}\mathbf{F}^{\mathrm{T}}, \\ \Delta\mathbf{B} &= \delta_b \mathbf{F}, \\ \Delta\mathbf{C} &= \delta_c \mathbf{F}, \\ \Delta\mathbf{D} &= \delta_d \mathbf{F}, \\ \Delta\mathbf{E} &= \delta_e \mathbf{F}, \end{aligned} \tag{24}$$

where $\mathbf{F} = \begin{bmatrix} 0 & 1 \end{bmatrix}^{\mathrm{T}}$.

Thus, in (16a)–(16e), we have $q_1 = 1$, $q_2 = 1$, $q_3 = 1$, $q_4 = 1$, and $q_5 = 1$ and then $\mathbf{A}_1^1 = \mathbf{F}$, $\mathbf{A}_2^1 = \mathbf{F}^{\mathrm{T}}$, $\mathbf{B}_1^1 = \mathbf{F}$, $\mathbf{B}_2^1 = 1$, $\mathbf{C}_1^1 = \mathbf{F}$, $\mathbf{C}_2^1 = 1$, $\mathbf{D}_1^1 = \mathbf{F}$, $\mathbf{D}_2^1 = 1$, $\mathbf{E}_1^1 = \mathbf{F}$, and $\mathbf{E}_2^1 = 1$.

Furthermore, the uncertainties δ_a, δ_b, δ_c, δ_d, and δ_e should satisfy condition (17) and then $|\delta_i| \leq \overline{\delta}_i$, for all $i \in \{a, b, c, d, e\}$.

In the sequel of this work, without loss of generality, we will take in (16a)–(16e), $q_1 = 1$, $q_2 = 1$, $q_3 = 1$, $q_4 = 1$, and $q_5 = 1$. Moreover, we will consider a single control input $\mathbf{u}$ and also a single disturbance signal $\mathbf{w}$, i.e., $n_u = 1$ and $n_w = 1$. We will also consider the expression of the uncertainty matrices in (24).

3. Design of the Robust Saturated Affine State-Feedback Controller

In this section, we develop conditions satisfying robust stabilization of the uncertain disturbed nonlinear dynamics (15) under the affine state-feedback control law (19) subject to the saturation constraint (18). Thus, these stability conditions must verify constraints (22) and (23). We show first that the stability conditions are expressed in terms of BMIs. Next, by means of previously provided technical lemmas, we transform these BMIs into LMIs. Finally, we present an optimization problem providing the allowable maximum values of the parametric uncertainties δ_a, δ_b, δ_c, δ_d, and δ_e.

3.1. BMI-Based Stability Conditions. These stability conditions of the disturbed uncertain nonlinear system (15) under the saturated affine state-feedback control law defined by expression (19), constraint (18), and condition (35) are presented in the following theorem.

Theorem 1. *The nonlinear system (15) with norm-bounded parametric uncertainties (17), under the bounded external disturbance (14), is robustly stabilizable by implementing the affine state-feedback control law (19) subject to the saturation constraint (18), if for some fixed positive parameters γ, ε_m, $\overline{\delta}_a$, $\overline{\delta}_b$, $\overline{\delta}_c$, $\overline{\delta}_d$, and $\overline{\delta}_e$, there exist a symmetric matrix $\mathbf{P} > 0$, a feedback matrix $\mathbf{K}$, a feedback constant m, and some positive scalars ε_1, ε_2, ε_3, ε_4, ε_5, ε_6, ε_7, ε_8, ε_9, μ, and η such that the following set of matrix inequalities is feasible:*

$$\begin{bmatrix} (\mathbf{PA}+\mathbf{PBK})+(\star)+\mu\mathbf{P}+\mathbb{A}_1 & \mathbf{PB}m \\ (\star) & -\mu\gamma+\xi \end{bmatrix}<0, \quad (25)$$

$$\begin{bmatrix} \mathbf{K}^{\mathrm{T}}\mathbf{K}-\eta\mathbf{P} & \mathbf{K}^{T}m \\ (\star) & \eta\gamma+m^{T}m-u_{\max}^{2} \end{bmatrix}<0, \quad (26)$$

$$(\mathbf{B}m+\widehat{\mathbf{C}})^{\mathrm{T}}(\mathbf{B}m+\widehat{\mathbf{C}})<\varepsilon_m, \quad (27)$$

where

$$\begin{aligned}\mathbb{A}_1 &= \varepsilon_1\mathbf{PCC}^{T}\mathbf{P}+\varepsilon_2\mathbf{P}\,\mathbf{DD}^{T}\mathbf{P}+\varepsilon_3\mathbf{PEE}^{T}\mathbf{P}\\ &\quad+(\varepsilon_4+\varepsilon_5+\varepsilon_6+\varepsilon_7+\varepsilon_8+\varepsilon_9)\mathbf{PFF}^{\mathrm{T}}\mathbf{P}+\varepsilon_4^{-1}\overline{\delta}_a^{2}\mathbf{FF}^{\mathrm{T}}\\ &\quad+\varepsilon_5^{-1}\overline{\delta}_b^{2}\mathbf{K}^{\mathrm{T}}\mathbf{K},\\ \xi &= \varepsilon_1^{-1}+\varepsilon_2^{-1}+\varepsilon_3^{-1}+\varepsilon_6^{-1}\overline{\delta}_b^{2}m^{\mathrm{T}}m+\varepsilon_7^{-1}\overline{\delta}_c^{2}+\varepsilon_8^{-1}\overline{\delta}_d^{2}+\varepsilon_9^{-1}\overline{\delta}_e^{2}\rho^{2}.\end{aligned} \quad (28)$$

Proof. By using system (15) and control law (19), the derivative of the Lyapunov function, $V(\mathbf{x})=\mathbf{x}^{\mathrm{T}}\mathbf{P}\mathbf{x}$, is given by

$$\begin{aligned}\dot{V}(\mathbf{x}) &= 2\mathbf{x}^{\mathrm{T}}\mathbf{P}\overline{\mathbf{A}}\mathbf{x}+2\mathbf{x}^{\mathrm{T}}\mathbf{PB}m+2\mathbf{x}^{\mathrm{T}}\mathbf{PCf}(\mathbf{x})+2\mathbf{x}^{\mathrm{T}}\mathbf{PDg}(\mathbf{x})\\ &\quad+2\mathbf{x}^{\mathrm{T}}\mathbf{PE}w+2\mathbf{x}^{\mathrm{T}}\mathbf{P}\Delta\mathbf{Ax}+2\mathbf{x}^{\mathrm{T}}\mathbf{P}\Delta\mathbf{BKx}+2\mathbf{x}^{\mathrm{T}}\mathbf{P}\Delta\mathbf{B}m\\ &\quad+2\mathbf{x}^{\mathrm{T}}\mathbf{P}\Delta\mathbf{Cf}(\mathbf{x})+2\mathbf{x}^{\mathrm{T}}\mathbf{P}\Delta\mathbf{Dg}(x)+2\mathbf{x}^{\mathrm{T}}\mathbf{P}\Delta\mathbf{E}w,\end{aligned} \quad (29)$$

with $\overline{\mathbf{A}}=\mathbf{A}+\mathbf{BK}$.

We now consider condition (22) on the Lyapunov function $V(\mathbf{x})$ and also conditions (10), (14), and (17). Then, using expressions of the uncertainties matrices in (24) and relying on the Young relation (Lemma 2), we obtain the following condition:

$$\begin{aligned}\dot{V}(\mathbf{x})+\mu(V(\mathbf{x})-\gamma) &\le \mu\mathbf{x}^{\mathrm{T}}\mathbf{P}\mathbf{x}-\mu\gamma+2\mathbf{x}^{\mathrm{T}}\mathbf{P}\overline{\mathbf{A}}\mathbf{x}+2\mathbf{x}^{\mathrm{T}}\mathbf{PB}m\\ &\quad+\varepsilon_1x^{\mathrm{T}}\mathbf{PCC}^{\mathrm{T}}\mathbf{P}\mathbf{x}+\varepsilon_1^{-1}+\varepsilon_2^{-1}+\varepsilon_3^{-1}\\ &\quad+\varepsilon_2\mathbf{x}^{\mathrm{T}}\mathbf{PDD}^{\mathrm{T}}\mathbf{P}\mathbf{x}\\ &\quad+\varepsilon_3\mathbf{x}^{\mathrm{T}}\mathbf{PEE}^{\mathrm{T}}\mathbf{P}\mathbf{x}+(\varepsilon_4+\varepsilon_5+\varepsilon_6+\varepsilon_7\\ &\quad+\varepsilon_8+\varepsilon_9)\mathbf{x}^{\mathrm{T}}\mathbf{PFF}^{\mathrm{T}}\mathbf{P}\mathbf{x}\\ &\quad+\varepsilon_4^{-1}\overline{\delta}_a^{2}x^{\mathrm{T}}\mathbf{FF}^{\mathrm{T}}\mathbf{x}+\varepsilon_5^{-1}\overline{\delta}_b^{2}\mathbf{x}^{\mathrm{T}}\mathbf{K}^{\mathrm{T}}\mathbf{K}\mathbf{x}\\ &\quad+\varepsilon_6^{-1}\overline{\delta}_b^{2}m^{T}m+\varepsilon_7^{-1}\overline{\delta}_c^{2}\\ &\quad+\varepsilon_8^{-1}\overline{\delta}_d^{2}+\varepsilon_9^{-1}\overline{\delta}_e^{2}\rho^{2}<0.\end{aligned} \quad (30)$$

This last inequality constraint can be rewritten as follows:

$$\begin{bmatrix}\mathbf{x}\\1\end{bmatrix}^{\mathrm{T}}\begin{bmatrix}\mathbb{A}_2+\mu\mathbf{P} & \mathbf{PB}m\\ (\star) & -\mu\gamma+\xi\end{bmatrix}\begin{bmatrix}\mathbf{x}\\1\end{bmatrix}<0, \quad (31)$$

where $\mathbb{A}_2=\mathbf{P}\overline{\mathbf{A}}+(\star)+\varepsilon_1\mathbf{PCC}^{\mathrm{T}}\mathbf{P}+\varepsilon_2\mathbf{P}\,\mathbf{DD}^{\mathrm{T}}\mathbf{P}+\varepsilon_3\mathbf{PEE}^{\mathrm{T}}\mathbf{P}+(\varepsilon_4+\varepsilon_5+\varepsilon_6+\varepsilon_7+\varepsilon_8+\varepsilon_9)\mathbf{PFF}^{\mathrm{T}}\mathbf{P}+\varepsilon_4^{-1}\overline{\delta}_a^{2}\mathbf{FF}^{\mathrm{T}}+\varepsilon_5^{-1}\overline{\delta}_b^{2}\mathbf{K}^{\mathrm{T}}\mathbf{K}$ and $\xi=\varepsilon_1^{-1}+\varepsilon_2^{-1}+\varepsilon_3^{-1}+\varepsilon_6^{-1}\overline{\delta}_b^{2}m^{T}m+\varepsilon_7^{-1}\overline{\delta}_c^{2}+\varepsilon_8^{-1}\overline{\delta}_d^{2}+\varepsilon_9^{-1}\overline{\delta}_e^{2}\rho^{2}$.

Hence, we obtain the matrix inequality (25).

Furthermore, from expressions (20) and (21), rewrite $\mathbf{x}\in\varepsilon(\mathbf{P},\gamma)$ as

$$\begin{bmatrix}\mathbf{x}\\1\end{bmatrix}^{\mathrm{T}}\begin{bmatrix}\mathbf{P} & \mathcal{O}\\ (\star) & -\gamma\end{bmatrix}\begin{bmatrix}\mathbf{x}\\1\end{bmatrix}\le 0, \quad (32)$$

and $\mathbf{x}\in\mathscr{L}(\mathbf{K},\mathbf{m},\mathbf{u}_{\max})$ as

$$\begin{bmatrix}\mathbf{x}\\1\end{bmatrix}^{\mathrm{T}}\begin{bmatrix}\mathbf{K}^{\mathrm{T}}\mathbf{K} & \mathbf{K}^{\mathrm{T}}m\\ (\star) & m^{T}m-u_{\max}^{2}\end{bmatrix}\begin{bmatrix}\mathbf{x}\\1\end{bmatrix}\le 0. \quad (33)$$

It is worth to note that the condition $\varepsilon(\mathbf{P},\gamma)\subset\mathscr{L}(\mathbf{K},\mathbf{m},\mathbf{u}_{\max})$ (constraint (23)) is nothing than the implication (32) $\Longrightarrow$ (33). Therefore, by using the S-procedure lemma, this implication condition is equivalent to the existence of a positive scalar η such that the matrix inequality (26) holds.

As noted in the beginning of the previous section, the zero state $\mathbf{x}=0$ is not the equilibrium point. Then, under the affine state-feedback control law (19) and for a certain and undisturbed dynamics (that is, for the nominal dynamics (13)), the zero-equilibrium point should verify the following condition:

$$\mathbf{B}m+\mathbf{C}f(0)+\mathbf{D}g(0)=0. \quad (34)$$

Posing $\widehat{\mathbf{C}}=\mathbf{C}f(0)+\mathbf{D}g(0)$, then relation (34) is recast as follows:

$$\mathbf{B}m+\widehat{\mathbf{C}}=0. \quad (35)$$

It is worth to note that, in condition (35), the term $\mathbf{B}m+\widehat{\mathbf{C}}$ is a column vector. Then, such relation in (35) can be written in a (scalar) matrix form like so:

$$(\mathbf{B}m+\widehat{\mathbf{C}})^{\mathrm{T}}(\mathbf{B}m+\widehat{\mathbf{C}})=0. \quad (36)$$

For a small enough positive scalar ε_m, equality (36) can be transformed into condition (27). This completes the proof of Theorem 1.

It is worth mentioning that the three matrix inequalities (25)–(27) in Theorem 1 are BMIs, which are hardly tractable numerically. Thus, our objective is to convert these BMIs (25)–(27) into LMIs, which is the objective of the next section. □

Remark 3. Recall that, in the previous development of the BMI stability conditions, we have considered a single control input u and then $n_u=1$. Hence, we used one row matrix gain $\mathbf{K}$ and one scalar gain m. This choice has led to the design of only one condition (26) satisfying the saturation condition of the controller u. For a general case and then for $n_u>1$, $\mathbf{K}\in\mathbb{R}^{n_u\times n_x}$, $\mathbf{m}\in\mathbb{R}^{n_u}$, and $\mathbf{u}_{\max}\in\mathbb{R}^{n_u}$, the stability condition (26) becomes

$$\begin{bmatrix}\mathbf{K}^{\mathrm{T}}\mathbf{e}_i^{\mathrm{T}}\mathbf{e}_i\mathbf{K}-\eta_i\mathbf{P} & \mathbf{K}^{\mathrm{T}}\mathbf{e}_i^{\mathrm{T}}\mathbf{e}_i\mathbf{m}\\ (\star) & \eta_i\gamma+\mathbf{m}^{\mathrm{T}}\mathbf{e}_i^{\mathrm{T}}\mathbf{e}_i\mathbf{m}-\mathbf{u}_{\max}^{\mathrm{T}}\mathbf{e}_i^{\mathrm{T}}\mathbf{e}_i\mathbf{u}_{\max}\end{bmatrix}<0,\quad \forall i=1,\ldots,n_u, \quad (37)$$

where $\mathbf{e}_i=\underbrace{(0,\ldots,0,\overbrace{1}^{i^{\mathrm{th}}},0,\ldots,0)}_{n_u\text{ components}}\in\mathbb{R}^{1\times n_u}$ and $\eta_i>0$ for all $i=1,\ldots,n_u$.

3.2. LMI-Based Stability Conditions. In this part, we aim at linearizing the three BMIs (25)–(27) in Theorem 1. Thus, we first linearize the BMI (25). After that, we linearize the BMI (26) and the BMI (27).

3.2.1. Linearization of the BMI (25). Let us put first $\mathbf{S} = \mathbf{P}^{-1}$. We premultiply and postmultiply the BMI (25) by the matrix $\mathrm{diag}(\mathbf{S}, 1)$. Then, we obtain

$$\begin{bmatrix} (\mathbf{AS} + \mathbf{BR}) + (\star) + \mu\mathbf{S} + \mathbb{A}_3 & \mathbf{B}m \\ (\star) & -\mu\gamma + \xi \end{bmatrix} < 0, \tag{38}$$

where $\mathbf{R} = \mathbf{KS}$ and $\mathbb{A}_3 = \varepsilon_1\mathbf{CC}^{\mathrm{T}} + \varepsilon_2\mathbf{DD}^{\mathrm{T}} + \varepsilon_3\ \mathbf{EE}^{\mathrm{T}} + (\varepsilon_4 + \varepsilon_5 + \varepsilon_6 + \varepsilon_7 + \varepsilon_8 + \varepsilon_9)\mathbf{FF}^{\mathrm{T}} + \varepsilon_4^{-1}\overline{\delta}_a^2\mathbf{SFF}^{\mathrm{T}}\mathbf{S} + \varepsilon_5^{-1}\overline{\delta}_b^2\mathbf{R}^{\mathrm{T}}\mathbf{R}$.

Based on the Schur complement lemma, matrix inequality (38) is equivalent to

$$\begin{bmatrix} \mathbb{A}_4 + \mu\mathbf{S} & \mathbf{B}m & \mathbb{A}_5 & \mathcal{O} \\ (\star) & -\mu\gamma & \mathcal{O} & \mathbb{A}_7 \\ (\star) & (\star) & -\mathbb{A}_6 & \mathcal{O} \\ (\star) & (\star) & (\star) & -\mathbb{A}_8 \end{bmatrix} < 0, \tag{39}$$

where $\mathbb{A}_4 = (\mathbf{AS} + \mathbf{BR}) + (\star) + \varepsilon_1\mathbf{CC}^{\mathrm{T}} + \varepsilon_2\mathbf{DD}^{\mathrm{T}} + \varepsilon_3\mathbf{EE}^{\mathrm{T}} + (\varepsilon_4 + \varepsilon_5 + \varepsilon_6 + \varepsilon_7 + \varepsilon_8 + \varepsilon_9)\mathbf{FF}^{\mathrm{T}}$, $\mathbb{A}_5 = \begin{bmatrix} \overline{\delta}_a\mathbf{SF} & \overline{\delta}_b\mathbf{R}^T \end{bmatrix}$, $\mathbb{A}_6 = \mathrm{diag}(\varepsilon_4, \varepsilon_5)$, $\mathbb{A}_7 = \begin{bmatrix} 1 & 1 & 1 & \overline{\delta}_b m^{\mathrm{T}} & \overline{\delta}_c & \overline{\delta}_d & \overline{\delta}_e\rho \end{bmatrix}$, and $\mathbb{A}_8 = \mathrm{diag}(\varepsilon_1, \varepsilon_2, \varepsilon_3, \varepsilon_6, \varepsilon_7, \varepsilon_8, \varepsilon_9)$.

3.2.2. Linearization of the BMI (26). We premultiply and postmultiply the BMI (26) by the matrix $\mathrm{diag}(\mathbf{S}, 1)$. As a result, we obtain

$$\begin{bmatrix} \mathbf{R}^{\mathrm{T}}\mathbf{R} - \eta\mathbf{S} & \mathbf{R}^T m \\ (\star) & -u_{\max}^2 + m^T m + \eta\gamma \end{bmatrix} < 0. \tag{40}$$

Let us introduce a new change of variables by posing $\mathbf{G} = \begin{bmatrix} \mathbf{R}^T & \mathcal{O} \end{bmatrix}$, $\mathbf{L} = \begin{bmatrix} m \\ 1 \end{bmatrix}$, $\mathbf{M} = \begin{bmatrix} 1 & 0 \\ 0 & 1/\eta\gamma \end{bmatrix}$, and $\alpha = -u_{\max}^2$. Then, we have $\mathbf{R}^{\mathrm{T}}\mathbf{R} = \mathbf{GG}^{\mathrm{T}} = \mathbf{GMG}^{\mathrm{T}}$, $\mathbf{R}^{\mathrm{T}}m = \mathbf{GL}$, and $-u_{\max}^2 + m^{\mathrm{T}}m + \eta\gamma = \alpha + \mathbf{L}^{\mathrm{T}}\mathbf{M}^{-1}\mathbf{L}$.

Then, by applying the Schur lemma to inequality (40), we obtain

$$-\eta\mathbf{S} + \mathbf{GMG}^{\mathrm{T}} - \mathbf{GL}\psi^{-1}\mathbf{L}^{\mathrm{T}}\mathbf{G}^{\mathrm{T}} < 0, \tag{41}$$

$$\psi = \alpha + \mathbf{L}^{\mathrm{T}}\mathbf{M}^{-1}\mathbf{L} < 0. \tag{42}$$

Relying on the matrix inversion lemma (see Lemma 3), its follows that

$$\psi^{-1} = \alpha^{-1} - \alpha^{-2}\mathbf{L}^T\mathbf{H}^{-1}\mathbf{L}, \tag{43}$$

with

$$\mathbf{H} = \mathbf{M} + \alpha^{-1}\mathbf{LL}^{\mathrm{T}}. \tag{44}$$

Then, by substituting expression (43) in inequality (41), this last inequality (41) can be rewritten like so:

$$-\eta\mathbf{S} + \mathbf{GMG}^{\mathrm{T}} - \alpha^{-1}\mathbf{GLL}^{\mathrm{T}}\mathbf{G}^{\mathrm{T}} + \alpha^{-2}\mathbf{GLL}^{\mathrm{T}}\mathbf{H}^{-1}\mathbf{LL}^{\mathrm{T}}\mathbf{G}^T < 0. \tag{45}$$

Through expression (44), it is straightforward to show that

$$\alpha^{-1}\mathbf{GLL}^{\mathrm{T}} = \mathbf{GH} - \mathbf{GM}. \tag{46}$$

Therefore, based on this relation, we can note the following:

$$\alpha^{-1}\mathbf{GLL}^{\mathrm{T}}\mathbf{G}^{\mathrm{T}} = \mathbf{GHG}^{\mathrm{T}} - \mathbf{GMG}^{\mathrm{T}}, \tag{47}$$

$$\alpha^{-2}\mathbf{GLL}^{\mathrm{T}}\mathbf{H}^{-1}\mathbf{LL}^{\mathrm{T}}\mathbf{G}^{\mathrm{T}} = \mathbf{GHG}^{\mathrm{T}} - 2\mathbf{GMG}^{\mathrm{T}} + \mathbf{GMH}^{-1}\mathbf{MG}^{\mathrm{T}}. \tag{48}$$

Thus, as $\mathbf{GM} = \mathbf{G}$, substituting relations (47) and (48) in inequality (45) yields

$$\eta\mathbf{S} - \mathbf{GH}^{-1}\mathbf{G}^{\mathrm{T}} > 0. \tag{49}$$

Accordingly, inequality (41) is transformed into inequality (49).

Our concern now is the auxiliary condition (42). As $\mathbf{M} > 0$, then through the Schur lemma, inequality (42) is equivalent to

$$\begin{bmatrix} \alpha & \mathbf{L}^{\mathrm{T}} \\ (\star) & -\mathbf{M} \end{bmatrix} < 0. \tag{50}$$

By applying again the Schur lemma on inequality (50), we obtain

$$-\mathbf{M} - \alpha^{-1}\mathbf{LL}^{\mathrm{T}} < 0. \tag{51}$$

Hence, it follows that $\mathbf{H} > 0$. Thus, by multiplying inequality (49) by (η^{-1}) and relying on the Schur lemma, we obtain the following matrix inequality:

$$\begin{bmatrix} \mathbf{S} & \mathbf{G} \\ (\star) & \eta\mathbf{H} \end{bmatrix} > 0. \tag{52}$$

Since $\alpha = -u_{\max}^2$, then we can write the following:

$$\eta\mathbf{H} = \eta\mathbf{M} - \frac{\eta}{u_{\max}^2}\mathbf{LL}^{\mathrm{T}}, \tag{53}$$

with $\eta\mathbf{M} = \begin{bmatrix} \eta & 0 \\ 0 & 1/\gamma \end{bmatrix}$.

Therefore, by taking into account relation (53), the Schur complement lemma states that inequality (52) is equivalent to

$$\begin{bmatrix} \mathbf{S} & \mathbf{G} & \mathcal{O} \\ (\star) & \eta\mathbf{M} & \mathbf{L} \\ (\star) & (\star) & \dfrac{u_{\max}^2}{\eta} \end{bmatrix} > 0. \tag{54}$$

Hence, the BMI (26) is converted into the LMI (54), where the two parameters γ and η should be fixed a priori.

3.2.3. Linearization of the BMI (27). We now consider the BMI (27). It can be rewritten like so:

$$m^{\mathrm{T}}\mathbf{B}^{\mathrm{T}}\mathbf{B}m + 2\mathbf{C}^{\mathrm{T}}\mathbf{B}m + \widehat{\mathbf{C}}^{\mathrm{T}}\widehat{\mathbf{C}} < \varepsilon_m. \tag{55}$$

By applying the Schur lemma, this matrix inequality (55) is equivalent to the following LMI:

$$\begin{bmatrix} \widehat{\mathbf{C}}^{\mathrm{T}}\widehat{\mathbf{C}} + 2\widehat{\mathbf{C}}^{\mathrm{T}}\mathbf{B}m - \varepsilon_m & m^{T}\mathbf{B}^{T} \\ (\star) & -\mathscr{I} \end{bmatrix} < 0. \tag{56}$$

3.2.4. LMI Conditions. According to the previous linearization results, we state the following new theorem.

Theorem 2. *Assume that, for some positive parameters γ, μ, η, ε_m, ρ, $\overline{\delta}_a$, $\overline{\delta}_b$, $\overline{\delta}_c$, $\overline{\delta}_d$, and $\overline{\delta}_e$ fixed a priori, there exist a symmetric matrix $\mathbf{S}$, a matrix $\mathbf{R}$, a scalar m, and some scalars ε_1, ε_2, ε_3, ε_4, ε_5, ε_6, ε_7, ε_8, and ε_9 so that the following set of LMIs is feasible:*

$$\begin{bmatrix} \mathbb{A}_4 + \mu\mathbf{S} & \mathbf{B}m & \mathbb{A}_5 & \mathscr{O} \\ (\star) & -\mu\gamma & \mathscr{O} & \mathbb{A}_7 \\ (\star) & (\star) & -\mathbb{A}_6 & \mathscr{O} \\ (\star) & (\star) & (\star) & -\mathbb{A}_8 \end{bmatrix} < 0, \tag{57}$$

$$\begin{bmatrix} \mathbf{S} & \mathbf{R}^{\mathrm{T}} & \mathscr{O} & \mathscr{O} \\ (\star) & \eta & \mathscr{O} & m \\ (\star) & (\star) & \dfrac{1}{\gamma} & 1 \\ (\star) & (\star) & (\star) & \dfrac{u_{\max}^2}{\eta} \end{bmatrix} > 0, \tag{58}$$

$$\begin{bmatrix} \widehat{\mathbf{C}}^{\mathrm{T}}\widehat{\mathbf{C}} + 2\widehat{\mathbf{C}}^{\mathrm{T}}\mathbf{B}m - \varepsilon_m & m^{T}\mathbf{B}^{T} \\ (\star) & -\mathscr{I} \end{bmatrix} < 0, \tag{59}$$

where

$$\begin{aligned} \mathbb{A}_4 &= (\mathbf{AS} + \mathbf{BR}) + (\star) + \varepsilon_1\mathbf{C}\mathbf{C}^{\mathrm{T}} + \varepsilon_2\mathbf{D}\mathbf{D}^{\mathrm{T}} + \varepsilon_3\mathbf{E}\mathbf{E}^{\mathrm{T}} \\ &\quad + (\varepsilon_4 + \varepsilon_5 + \varepsilon_6 + \varepsilon_7 + \varepsilon_8 + \varepsilon_9)\mathbf{F}\mathbf{F}^{\mathrm{T}}, \\ \mathbb{A}_5 &= \begin{bmatrix} \overline{\delta}_a\mathbf{S}\mathbf{F} & \overline{\delta}_b\mathbf{R}^{\mathrm{T}} \end{bmatrix}, \\ \mathbb{A}_6 &= \mathrm{diag}(\varepsilon_4, \varepsilon_5), \\ \mathbb{A}_7 &= \begin{bmatrix} 1 & 1 & 1 & \overline{\delta}_b m^{\mathrm{T}} & \overline{\delta}_c & \overline{\delta}_d & \overline{\delta}_e\rho \end{bmatrix}, \\ \mathbb{A}_8 &= \mathrm{diag}(\varepsilon_1, \varepsilon_2, \varepsilon_3, \varepsilon_6, \varepsilon_7, \varepsilon_8, \varepsilon_9). \end{aligned} \tag{60}$$

Then, the nonlinear system (15) with norm-bounded parametric uncertainties (17) and bounded disturbance (14) is robustly stabilizable by means of the saturated affine state-feedback control law (19) subject to constraint (18). Moreover, the matrix gain $\mathbf{K}$ of the control law (19) is

$$\mathbf{K} = \mathbf{R}\mathbf{S}^{-1}. \tag{61}$$

Proof. The proof of this theorem was already achieved in the previous sections.

As noted in Theorem 2, the parameters γ, μ, η, ε_m, ρ, $\overline{\delta}_a$, $\overline{\delta}_b$, $\overline{\delta}_c$, $\overline{\delta}_d$, and $\overline{\delta}_e$ should be fixed a priori to obtain a solution of LMIs (57)–(59). Thus, the computation complexity for solving these three LMIs is reduced. However, in this way, the design conservatism will increase and obtaining a solution becomes more difficult. Indeed, we should test several times the feasibility of these LMIs (57)–(59) with different values of all these fixed parameters. Therefore, in order to reduce the conservatism of the designed LMIs, we should consider these parameters as decision variables, which should be optimized numerically. To this end, we next present improved LMI conditions. We note that the parameter ε_m can be selected as a decision variable to be minimized. Nevertheless, we will consider it as a predefined constant scalar, which will be fixed to be very small. □

Remark 4. As noted in Remark 3, for a general case where $n_u > 1$, we obtain the BMI (37) instead of the BMI (26). The linearization of the BMI stability condition (37) leads to the following LMI:

$$\begin{bmatrix} \mathbf{S} & (\star) & \mathscr{O} & \mathscr{O} \\ \mathbf{e}_i\mathbf{R} & \eta_i & \mathscr{O} & \mathbf{e}_i m \\ (\star) & (\star) & \dfrac{1}{\gamma} & 1 \\ (\star) & (\star) & (\star) & \dfrac{1}{\eta_i}\mathbf{u}_{\max}^{\mathrm{T}}\mathbf{e}_i^{\mathrm{T}}\mathbf{e}_i\mathbf{u}_{\max} \end{bmatrix} > 0, \quad \forall i = 1, 2, \ldots, n_u. \tag{62}$$

3.3. Enhanced LMI Stability Conditions. Our immediate concern is to convert the constant parameters γ, μ, η, ρ, $\overline{\delta}_a$, $\overline{\delta}_b$, $\overline{\delta}_c$, $\overline{\delta}_d$, and $\overline{\delta}_e$ into decision variables. First of all, it is evident that the two parameters $\overline{\delta}_c$ and $\overline{\delta}_d$ presented in the LMI (57) are independent of other unknown variables. Then, they can be considered as decision variables. However, the two main difficulties lie on the one hand in the parameters γ, μ, and η and on the other hand in the three parameters $\overline{\delta}_a$, $\overline{\delta}_b$, $\overline{\delta}_e$, and ρ. Transformation of $\overline{\delta}_a$, $\overline{\delta}_e$, and ρ is simple [12]. Furthermore, transformation of the parameters γ and $\overline{\delta}_b$ requires a certain judicious mathematical manipulation. Note that the parameter γ appears in both LMI (57) and LMI (58). However, transformation of the two remaining parameters μ and η is quite difficult and perhaps impossible. To simplify computation, we can pose $\mu = \eta$. Hence, we state the following enhanced version of Theorem 2.

Theorem 3. *Assume that, for some positive parameters λ and ϵ_m fixed a priori such that $\epsilon_m \ll 1$, there exist a symmetric matrix $\mathbf{S}$, a matrix $\mathbf{R}$, a gain m, and some scalars γ, $\alpha > 0$, $\beta > 0$, $\varphi > 0$, ϵ_1, ϵ_2, ϵ_3, ϵ_4, ϵ_5, ϵ_6, ϵ_7, ϵ_8, ϵ_9, $\overline{\delta}_c$, and $\overline{\delta}_d$ so that the*

following optimization problem with LMI constraints is feasible:

$$\text{minimize} \quad \left(\varepsilon_4+\varepsilon_5+\varepsilon_6+\varepsilon_9\right)-\left(\alpha+\beta+\varphi+\overline{\delta}_c+\overline{\delta}_d+\rho\right)$$

$$\text{subject to} \begin{bmatrix} \widehat{\mathbb{A}}_4+\lambda\mathbf{S} & \mathbf{B}m & \widehat{\mathbb{A}}_5 & \mathcal{O} \\ (\star) & -\lambda\gamma & \mathcal{O} & \widehat{\mathbb{A}}_7 \\ (\star) & (\star) & -\mathbb{A}_6 & \mathcal{O} \\ (\star) & (\star) & (\star) & -\mathbb{A}_8 \end{bmatrix} < 0, \tag{63}$$

$$\begin{bmatrix} \mathbf{S} & \mathbf{R}^{\mathrm{T}} & \mathcal{O} \\ (\star) & \lambda & m \\ (\star) & (\star) & \dfrac{u_{\max}^2}{\lambda}-\gamma \end{bmatrix} > 0, \tag{64}$$

$$\begin{bmatrix} \widehat{\mathbf{C}}^{\mathrm{T}}\widehat{\mathbf{C}}+2\widehat{\mathbf{C}}^{\mathrm{T}}\mathbf{B}m-\varepsilon_m & m^{\mathrm{T}}\mathbf{B}^{\mathrm{T}} \\ (\star) & -\mathcal{J} \end{bmatrix} < 0, \tag{65}$$

where

$$\begin{aligned} \widehat{\mathbb{A}}_4 &= (\mathbf{AS}+\mathbf{BR})+(\star)+\varepsilon_1\mathbf{C}\mathbf{C}^{\mathrm{T}}+\varepsilon_2\mathbf{D}\mathbf{D}^{\mathrm{T}}+\varepsilon_3\mathbf{E}\mathbf{E}^{\mathrm{T}} \\ &\quad +\left(\alpha+\beta+\varphi+\varepsilon_7+\varepsilon_8\right)\mathbf{F}\mathbf{F}^{\mathrm{T}}, \\ \widehat{\mathbb{A}}_5 &= \begin{bmatrix} \mathbf{SF} & \mathbf{R}^{\mathrm{T}} \end{bmatrix}, \\ \mathbb{A}_6 &= \operatorname{diag}\left(\varepsilon_4,\varepsilon_5\right), \\ \widehat{\mathbb{A}}_7 &= \begin{bmatrix} 1 & 1 & 1 & m^T & \overline{\delta}_c & \overline{\delta}_d & \rho \end{bmatrix}, \\ \mathbb{A}_8 &= \operatorname{diag}\left(\varepsilon_1,\varepsilon_2,\varepsilon_3,\varepsilon_6,\varepsilon_7,\varepsilon_8,\varepsilon_9\right). \end{aligned} \tag{66}$$

Then, the uncertain disturbed nonlinear system (14) is robustly stabilizable via the saturated affine state-feedback control law (18), with $\mathbf{K}=\mathbf{R}\mathbf{S}^{-1}$, and

$$\begin{aligned} \overline{\delta}_a &= \sqrt{\frac{\alpha}{\varepsilon_4}}, \\ \overline{\delta}_b &= \sqrt{\frac{\beta}{\varepsilon_5+\varepsilon_6}}, \\ \overline{\delta}_e &= \sqrt{\frac{\varphi}{\varepsilon_9}}. \end{aligned} \tag{67}$$

Proof. We first consider expression (29). Thus, by applying the Young relation, we can obtain another related condition instead of inequality (30):

$$\begin{aligned} \dot{V}(\mathbf{x})+\mu\left(V(\mathbf{x})-\gamma\right) &\le \mu\mathbf{x}^{\mathrm{T}}\mathbf{P}\mathbf{x}-\mu\gamma+2\mathbf{x}^{\mathrm{T}}\mathbf{P}\overline{\mathbf{A}}\mathbf{x}+2\mathbf{x}^{\mathrm{T}}\mathbf{P}\mathbf{B}m \\ &\quad +\varepsilon_1\mathbf{x}^{\mathrm{T}}\mathbf{P}\mathbf{C}\mathbf{C}^{\mathrm{T}}\mathbf{P}\mathbf{x}+\varepsilon_1^{-1}+\varepsilon_2^{-1}+\varepsilon_3^{-1}+\varepsilon_2\mathbf{x}^{\mathrm{T}}\mathbf{P}\,\mathbf{D}\mathbf{D}^{\mathrm{T}}\mathbf{P}\mathbf{x} \\ &\quad +\varepsilon_3\mathbf{x}^{\mathrm{T}}\mathbf{P}\mathbf{E}\mathbf{E}^{\mathrm{T}}\mathbf{P}\mathbf{x}+\left(\varepsilon_4\overline{\delta}_a^2+\left(\varepsilon_5+\varepsilon_6\right)\overline{\delta}_b^2+\varepsilon_7+\varepsilon_8+\varepsilon_9\overline{\delta}_e^2\right) \\ &\quad \cdot\mathbf{x}^{\mathrm{T}}\mathbf{P}\mathbf{F}\mathbf{F}^{\mathrm{T}}\mathbf{P}\mathbf{x}+\varepsilon_4^{-1}\mathbf{x}^{\mathrm{T}}\mathbf{F}\mathbf{F}^{\mathrm{T}}\mathbf{x}+\varepsilon_5^{-1}\mathbf{x}^{\mathrm{T}}\mathbf{K}^{\mathrm{T}}\mathbf{K}\mathbf{x}+\varepsilon_6^{-1}m^Tm \\ &\quad +\varepsilon_7^{-1}\overline{\delta}_c^2+\varepsilon_8^{-1}\overline{\delta}_d^2+\varepsilon_9^{-1}\rho^2<0. \end{aligned} \tag{68}$$

Let us introduce a new change of variables by posing $\alpha=\varepsilon_4\overline{\delta}_a^2$, $\beta=(\varepsilon_5+\varepsilon_6)\overline{\delta}_b^2$, and $\varphi=\varepsilon_9\overline{\delta}_e^2$. Then, according to the previous section, we obtain the LMI (64), in which α, β, and φ are three decision variables. Hence, once the values of α, β, φ, ε_4, ε_5, ε_6, and ε_9 are obtained, we calculate $\overline{\delta}_a$, $\overline{\delta}_b$, and $\overline{\delta}_e$ according to the following relations: $\overline{\delta}_a=\sqrt{\alpha/\varepsilon_4}$, $\overline{\delta}_b=\sqrt{\beta/(\varepsilon_5+\varepsilon_6)}$, and $\overline{\delta}_e=\sqrt{\varphi/\varepsilon_9}$.

The remaining problem is the parameter γ, which appears in both LMI (57) and LMI (58). We premultiply and postmultiply LMI (58) by the matrix $\begin{bmatrix} \mathcal{J} & \mathcal{O} & \mathcal{O} & \mathcal{O} \\ (\star) & \mathcal{J} & \mathcal{O} & \mathcal{O} \\ (\star) & (\star) & \mathcal{O} & \mathcal{J} \\ (\star) & (\star) & (\star) & \mathcal{O} \end{bmatrix}$ and then we obtain

$$\begin{bmatrix} \mathbf{S} & \mathbf{R}^{\mathrm{T}} & \mathcal{O} & \mathcal{O} \\ (\star) & \eta & m & \mathcal{O} \\ (\star) & (\star) & \dfrac{u_{\max}^2}{\eta} & 1 \\ (\star) & (\star) & (\star) & \dfrac{1}{\gamma} \end{bmatrix} > 0. \tag{69}$$

By applying the Schur lemma, inequality (69) is equivalent to the LMI (64). Now, the parameter γ is linear in the two LMIs (63) and (64).

In addition, the parameter μ appears in the LMI (57), whereas the parameter η appears in the LMI (58). As noted before, it is difficult to transform μ and η into two decision variables. Then, to simplify the computation procedure, we can pose $\mu=\eta=\lambda$.

The objective is to look for maximum values of the uncertainty bounds $\overline{\delta}_a$, $\overline{\delta}_b$, $\overline{\delta}_c$, $\overline{\delta}_d$, and $\overline{\delta}_e$ and the disturbance bound ρ. The three parameters $\overline{\delta}_c$, $\overline{\delta}_d$, and ρ appear directly in the LMI (63) (matrix $\widehat{\mathbb{A}}_7$). Then, these parameters should be maximized. However, the variables $\overline{\delta}_a$, $\overline{\delta}_b$, and $\overline{\delta}_e$ are incorporated, respectively, in the parameters α, β, and φ: $\alpha=\varepsilon_4\overline{\delta}_a^2$, $\beta=(\varepsilon_5+\varepsilon_6)\overline{\delta}_b^2$, and $\varphi=\varepsilon_9\overline{\delta}_e^2$. Then, to maximize $\overline{\delta}_a$, $\overline{\delta}_b$, and $\overline{\delta}_e$, we should maximize α, β, and φ. Moreover, as α (resp. β, φ) depends on ε_4 (resp. ε_5 and ε_6, ε_9), we should minimize ε_4, ε_5, ε_6, and ε_9 in order to ensure maximized values of $\overline{\delta}_a$, $\overline{\delta}_b$, and $\overline{\delta}_e$. We emphasize that, in order to obtain a minimization objective function that can be handled with the LMI toolbox, we should transform the maximization problem of the variables α, β, φ, $\overline{\delta}_c$, $\overline{\delta}_d$, and ρ into a minimization problem of the quantity $-(\alpha+\beta+\varphi+\overline{\delta}_c+\overline{\delta}_d+\rho)$. This completes the proof of Theorem 3.

It is worth to mention that Theorem 3 offers a wider choice of invariant ellipsoids $\varepsilon(\mathbf{P},\gamma)$ (as γ varies) for optimization and will lead to less conservative estimation of the domain of attraction.

In addition, we stress that, in Theorem 3, we imposed the two free parameters μ and η in Theorem 2 to be equal, i.e., $\mu=\eta=\lambda$, in order to obtain an LMI with a single parameter λ. Nevertheless, this choice, which is the only solution to simplify computation, injects some degree of conservatism in the LMI conditions (63)–(65). Furthermore, the parameter λ is the only one that should be fixed a priori to obtain a solution of the optimization problem in Theorem 3. □

4. Estimation of the Domain of Attraction

With all the ellipsoids satisfying the set invariance condition (21), we would like to choose from among them the largest one to get at least an estimation of the domain of attraction. Certain criteria are used in the literature to maximize the size of the attractive invariant ellipsoid $\varepsilon(\mathbf{P}, \gamma)$, such as maximization of its volume and maximization of the sum of its semiaxis [5, 9, 18, 21, 27, 47, 48, 52]. Actually, maximization of the volume of an ellipsoid is equivalent to minimization of the determinant of the Lyapunov matrix $\mathbf{P}$, and maximization of the sum of its semiaxis is equivalent to minimization of the trace of the matrix $\mathbf{P}$ [9].

In this part, our main goal is to find a robust saturated affine state-feedback control law (18) associated to the largest invariant ellipsoid $\varepsilon_\star(\mathbf{P}_\star, \gamma_\star)$. Such largest invariant ellipsoid will be found for desired values of the maximum bounds of the parametric uncertainties $\overline{\delta}_a$, $\overline{\delta}_b$, $\overline{\delta}_c$, $\overline{\delta}_d$, and $\overline{\delta}_e$ and also the maximum bound of the disturbance ρ. Thus, we will use LMI (63) (or systematically LMI (57)) for predefined values of these maximum bounds. However, we should also use the two LMIs (64) and (65) to look for a maximum value of the parameter γ and hence the associated gains $\mathbf{K}$ and m.

Next, the size of the attractive invariant ellipsoid $\varepsilon(\mathbf{P}, \gamma)$ is measured through the sum of its semiaxis. For this subject, we introduce the following theorem.

Theorem 4. *The largest attractive invariant ellipsoid of the nonlinear system (15) with bounded disturbance (14) and norm-bounded parametric uncertainties (17), subject to the saturated affine state-feedback control law defined by expression (19) and constraint (18), is the ellipsoid $\varepsilon(\mathbf{P}, \gamma)$, for a fixed positive scalar $\varepsilon_m \ll 1$ and some positive parameter λ known a priori, where $\mathbf{P} = \mathbf{S}^{-1}$ and γ, together with ε_1, ε_2, ε_3, ε_4, ε_5, ε_6, ε_7, ε_8, and ε_9, are a solution of the following LMI-based optimization problem:*

$$\text{minimize}\,(-\text{trace}\,(\mathbf{S}) - \gamma),$$

$$\begin{bmatrix} \mathbb{A}_4 + \lambda\mathbf{S} & \mathbf{B}m & \mathbb{A}_5 & \mathcal{O} \\ (\star) & -\lambda\gamma & \mathcal{O} & \mathbb{A}_7 \\ (\star) & (\star) & -\mathbb{A}_6 & \mathcal{O} \\ (\star) & (\star) & (\star) & -\mathbb{A}_8 \end{bmatrix} < 0,$$

$$\begin{bmatrix} \mathbf{S} & \mathbf{R}^{\mathrm{T}} & \mathcal{O} \\ (\star) & \lambda & m \\ (\star) & (\star) & \dfrac{u_{\max}^2}{\lambda} - \gamma \end{bmatrix} > 0, \tag{70}$$

$$\begin{bmatrix} \widehat{\mathbf{C}}^{\mathrm{T}}\widehat{\mathbf{C}} + 2\widehat{\mathbf{C}}^{\mathrm{T}}\mathbf{B}m - \varepsilon_m & m^{\mathrm{T}}\mathbf{B}^{\mathrm{T}} \\ (\star) & -\mathcal{I} \end{bmatrix} < 0.$$

Proof. In expression (21), the attractive invariant ellipsoid $\mathcal{E}(\mathbf{P}, \gamma)$ can be recast as

$$\varepsilon\left(\frac{\mathbf{P}}{\gamma}, 1\right) = \left\{\mathbf{x} \in \mathbb{R}^2 \colon \mathbf{x}^{\mathrm{T}}\frac{\mathbf{P}}{\gamma}\mathbf{x} \le 1\right\}. \tag{71}$$

We emphasize that the trace of the matrix $\mathbf{P}/\gamma$ is equal to the sum of the semiaxis of the invariant ellipsoid $\varepsilon(\mathbf{P}/\gamma, 1)$ for some fixed γ. Hence, the size (the length of the semiaxis) of $\varepsilon(\mathbf{P}/\gamma, 1)$ increases as the trace of the matrix $\mathbf{P}/\gamma$ decreases. As $\mathbf{P} = \mathbf{S}^{-1}$, $\mathbf{P}/\gamma = (\gamma\mathbf{S})^{-1}$. Therefore, maximization of the size of $\varepsilon((\gamma\mathbf{S})^{-1}, 1)$ is equivalent to the maximization of the trace of the matrix $\gamma\mathbf{S}$. As a result, to guarantee the largest attractive invariant ellipsoid $\varepsilon((\gamma\mathbf{S})^{-1}, 1)$, we should maximize the parameter γ and also the trace of the matrix $\mathbf{S}$. Notice that maximizing γ and $\text{trace}\,(\mathbf{S})$ is equivalent to minimizing $(-\text{trace}\,(\mathbf{S}) - \gamma)$. This completes the proof of Theorem 4.

It is worth to note that, for each fixed value of the parameter λ, the optimization problem in Theorem 4 provides a solution associated to an attractive invariant ellipsoid $\varepsilon(\mathbf{P}, \gamma)$ with a (local) largest size, which is obtained for such λ. Therefore, in order to obtain the global maximum, we should vary the parameter λ, $0 < \lambda < \infty$. To this end, the best manner is the use of the gridding method [68]. This method consists in making a new change of variable by defining $\kappa = \lambda/(1 + \lambda)$ and then $\lambda = \kappa/(1 - \kappa)$. We know that $\lambda > 0$ if and only if $\kappa \in]0, 1[$. Then, we assign a uniform subdivision of the interval $]0, 1[$ and we solve the optimization problem in Theorem 4 for each value of this subdivision. Once this interval is covered, we look for the maximum value between all the obtained results. This maximum value corresponds to the largest invariant ellipsoid, which was obtained for some $\kappa_\star$ and then for some optimal values of the parameter λ, saying $\lambda_\star$.

In fact, finding the optimal value $\lambda_\star$ and then the largest invariant attractive ellipsoid $\varepsilon_\star$ takes a lot of time. Indeed, suppose that we uniformly subdivide the interval $]0, 1[$, in which the parameter κ varies, and then we take N_κ values. Thus, for each value of κ, we run the optimization algorithm in Theorem 4. Let us assume that a single run takes t_κ. Hence, the total simulation time in order to obtain the largest ellipsoid $\varepsilon_\star$ is about $t_c \approx N_\kappa \times t_\kappa$. □

Remark 5. In several research works presented in the literature, the computation of the largest attractive invariant ellipsoid $\varepsilon_\star(\mathbf{P}_\star, \gamma_\star)$ is achieved mainly in two steps:

(1) Hunt for an invariant ellipsoid $\varepsilon(\mathbf{P}, 1)$ by obtaining the matrix $\mathbf{P}$

(2) With such $\mathbf{P}$, maximize the value of the parameter γ

Actually, these two steps are realized via two optimization algorithms. Compared with this hunting procedure, our proposed design of the saturated feedback control law guarantees the determination of the largest invariant ellipsoid $\varepsilon_\star(\mathbf{P}_\star, \gamma_\star)$ in only one step and then with only one optimization algorithm.

5. Simulation Results

In this section, we provide some simulation results to demonstrate the effectiveness of our developed method for the synthesis of the saturated affine state-feedback control law (19) for the robust stabilization of the disturbed uncertain nonlinear dynamics (15) of the pitch model of the helicopter. Moreover, we aim at identifying and analyzing the largest attractive invariant ellipsoid $\varepsilon_\star(\mathbf{P}_\star, \gamma_\star)$ in order to obtain an estimation of the domain of attraction. Thus, in the sequel, we take two values of the saturation level in (18) of the control law u: $u_{\max} = 1$ and $u_{\max} = 10$. Moreover, we fix the parameter $\varepsilon_m = 10^{-5}$.

The values of the parameters figured in the nonlinear dynamics (12) or of the pitch model of the helicopter are as follows [55–57]: $I_{yy} = 0.0283\,(\mathrm{kg/m^2})$, $m_{\mathrm{heli}} = 0.9941\,(\mathrm{Kg})$, $l_{cgx} = 0.0134\,(\mathrm{m})$, $l_{cgz} = 0.0289\,(\mathrm{m})$, $F_{vM} = 0.0041$ (Nm/rad/s), $g = 9.81\,(\mathrm{m/s^2})$, and $s = 0.0057\,(\mathrm{m/s^2})$.

Remark 6. The choice of the parameters of the maximum value of the control input u, $u_{\max}$, is based on two facts: (1) in the literature, the common choice of the saturation limit is $u_{\max} = 1$ according to the invariance sets' concept and (2) in the present work, we have considered a general case of the actuator saturation limit in the development of LMI constraints and hence in the design of the state-feedback controller in order to show the effect of the saturation limit $u_{\max}$ on the largeness of the invariant attractive ellipsoid.

Thus, in our investigation, we selected two values of the saturation limit: $u_{\max} = 1$ (which is the classical choice) and $u_{\max} = 10$. We can also choose another value of such saturation limit such as $u_{\max} = 24$, and we will obtain similar results.

Actually, the saturation limits are the intrinsic requirement of the physical actuators. Thus, the adopted different values of the $u_{\max}$ will be used in the sequel just to show the feasibility and the conservativeness of the proposed design method of the two gains of the affine state-feedback controller and also for the computation of the largest domain of attraction in different situations.

Remark 7. It is worth to mention that for the computation of the solutions of the LMIs in Theorem 2 and the LMI-based optimization problem in Theorems 3 and 4, we use the LMI toolbox of MATLAB. We can also use the toolbox YALMIP [10] in order to solve these LMI problems. Moreover, we can use it to (locally) solve some BMI problems using the bisection method.

5.1. Numerical Results. The optimization problem subject to LMI constraints in Theorem 3 provides numerical results illustrated in Table 1 for the saturation level $u_{\max} = 1$ and for different values of the fixed parameter λ. In this table, we provide the two gains, $\mathbf{K}$ and m, of the saturated affine state-feedback control law u, the maximum bounds of the parametric uncertainties, i.e., $\overline{\delta}_a$, $\overline{\delta}_b$, $\overline{\delta}_c$, $\overline{\delta}_d$, and $\overline{\delta}_e$, the maximum bound of the disturbance w, i.e., ρ, and the parameter γ. It is obvious that the three uncertainty bounds, $\overline{\delta}_a$, $\overline{\delta}_b$, and $\overline{\delta}_e$, are very small, around 10^{-4}. The two parameters, $\overline{\delta}_c$ and $\overline{\delta}_d$, are found to be equal and decrease slightly as λ increases. However, the value of the allowable disturbance bound ρ is found to be very high, about 6×10^3.

We emphasize that the obtained results for the allowable maximum bounds of the parametric uncertainties, $\overline{\delta}_a$, $\overline{\delta}_b$, and $\overline{\delta}_e$, are dissatisfying (they are found to be very small). Moreover, the maximum disturbance bound is found to be very high. It is worth noting that the optimization algorithm in Theorem 3 is characterized by an objective function that depends on 10 parameters ε_4, ε_5, ε_6, ε_9, α, β, φ, $\overline{\delta}_c$, $\overline{\delta}_d$, and ρ, which are optimized together. Then, in order to improve the obtained results, we will fix in the next the parameter ρ and the remaining ones will be optimized. As discussed in the beginning of this paper, in the second section, the external disturbance w can represent the turbulent moments on the helicopter. Without loss of generality, we will fix $\rho = 10$.

Thus, for $\rho = 10$, the optimization algorithm subject to LMI constraints in Theorem 3 gives numerical results illustrated in Table 2 for the case $u_{\max} = 1$ and in Table 3 for $u_{\max} = 10$. As in Table 1, we provide, for different values of the parameter λ, the gain matrix $\mathbf{K}$, the gain constant m, the maximum bounds of the parametric uncertainties $\overline{\delta}_a$, $\overline{\delta}_b$, $\overline{\delta}_c$, $\overline{\delta}_d$, and $\overline{\delta}_e$, and the parameter γ.

We note from Tables 2 and 3 that the optimization problem provides identical values for the two uncertainty bounds $\overline{\delta}_c$ and $\overline{\delta}_d$. Moreover, for all values of λ, the value of the gain m is about 0.0133 as in Table 1. In addition, it is evident that, for the same value of parameter λ, we have almost the same gain matrix $\mathbf{K}$. Furthermore, as λ increases, the size of the gain matrix $\mathbf{K}$ and the uncertainty bounds, $\overline{\delta}_a$, $\overline{\delta}_b$, and $\overline{\delta}_e$, increase. For $u_{\max} = 1$, $\overline{\delta}_c$ is found to be around 10^{-3}, whereas for $u_{\max} = 10$, $\overline{\delta}_c$ is about 14. In addition, it is evident that the values of the maximum bounds of the parametric uncertainties $\overline{\delta}_a$, $\overline{\delta}_b$, and $\overline{\delta}_e$ are bigger than those obtained in Table 1 since the parameter ρ is fixed here.

We can also observe from Tables 2 and 3 that, as the parameter λ increases, the value of the parameter γ decreases. Actually, we can note that $\gamma \approx u_{\max}^2/\lambda$. This shows that the size of the attractive invariant ellipsoid, which depends on γ, varies with respect to the value of the saturation level $u_{\max}$.

5.2. Computation of the Largest Attractive Invariant Ellipsoid. To obtain the largest attractive invariant ellipsoid $\varepsilon_\star(\mathbf{P}_\star, \gamma_\star)$, we solve the optimization problem in Theorem 4. Thus, in order to obtain the global largest ellipsoid $\varepsilon_\star(\mathbf{P}_\star, \gamma_\star)$, we should vary the free parameter λ according to the gridding method as noted before. Moreover, in this optimization problem, we fix the bounds of the parametric uncertainties and we take a common value, $\overline{\delta}$, for all these bounds like so: for $u_{\max} = 1$, we take $\overline{\delta}_a = \cdots = \overline{\delta}_e = \overline{\delta} = 1$, whereas for $u_{\max} = 10$, we fix $\overline{\delta}_a = \cdots = \overline{\delta}_e = \overline{\delta} = 10$. Actually, with $\overline{\delta} = 10$ and $u_{\max} = 1$, the optimization problem in Theorem 4 is unfeasible. It was found unfeasible also for all $\overline{\delta} \geq 2$ and $u_{\max} = 1$. Then, we minimized the uncertainty bound to

Table 1: Numerical simulation results obtained using the optimization algorithm in Theorem 3 for different values of the parameter λ and for $u_{\max} = 1$.

	$\lambda = 0.01$	$\lambda = 0.1$	$\lambda = 1$	$\lambda = 10$	$\lambda = 100$
$\mathbf{K}^{\mathrm{T}}$	$10^{-3} \times \begin{bmatrix} -0.0372 \\ -0.2566 \end{bmatrix}$	$10^{-3} \times \begin{bmatrix} -0.3786 \\ -2.6152 \end{bmatrix}$	$\begin{bmatrix} -0.0204 \\ -0.0437 \end{bmatrix}$	$\begin{bmatrix} -2.3360 \\ -0.5053 \end{bmatrix}$	$\begin{bmatrix} -236.7854 \\ -5.1249 \end{bmatrix}$
m	0.013321	0.013321	0.013321	0.013321	0.013321
$\overline{\delta}_a$	$10^{-4} \times 4.5975$	$10^{-4} \times 4.6197$	$10^{-4} \times 3.0634$	$10^{-4} \times 2.7950$	$10^{-4} \times 2.7613$
$\overline{\delta}_b$	$10^{-4} \times 3.2525$	$10^{-4} \times 3.2666$	$10^{-4} \times 2.1641$	$10^{-4} \times 1.9764$	$10^{-4} \times 1.9526$
$\overline{\delta}_c = \overline{\delta}_d$	3.6314	3.6515	2.2531	1.9868	1.9407
$\overline{\delta}_e$	$10^{-4} \times 4.5944$	$10^{-4} \times 4.6215$	$10^{-4} \times 3.0796$	$10^{-4} \times 2.7990$	$10^{-4} \times 2.7613$
ρ	$10^3 \times 6.4069$	$10^3 \times 6.4673$	$10^3 \times 6.0719$	$10^3 \times 5.4419$	$10^3 \times 5.7484$
γ	81.4039	8.1419	0.8527	0.0863	0.0087

Table 2: Numerical simulation results using Theorem 3 for different values of the parameter λ and for $\rho = 10$ and $u_{\max} = 1$.

	$\lambda = 0.01$	$\lambda = 0.1$	$\lambda = 1$	$\lambda = 10$	$\lambda = 100$	$\lambda = 200$
$\mathbf{K}^{\mathrm{T}}$	$\begin{bmatrix} -0.00089 \\ -0.00503 \end{bmatrix}$	$\begin{bmatrix} -0.00298 \\ -0.02858 \end{bmatrix}$	$\begin{bmatrix} -0.09235 \\ -0.11705 \end{bmatrix}$	$\begin{bmatrix} -3.6488 \\ -0.6523 \end{bmatrix}$	$\begin{bmatrix} -298.7673 \\ -5.8965 \end{bmatrix}$	$10^3 \times \begin{bmatrix} -1.1796 \\ -0.0117 \end{bmatrix}$
m	0.013275	0.013283	0.013268	0.013243	0.013251	0.013262
$\overline{\delta}_a$	0.0067	0.0181	0.7729	1.9138	5.4867	7.7133
$\overline{\delta}_b$	0.0800	0.1020	2.2687	2.6586	2.6496	2.6447
$\overline{\delta}_c = \overline{\delta}_d$	0.0048	0.0029	0.0043	0.0011	0.0022	0.0038
$\overline{\delta}_e$	0.0112	0.0155	0.4577	0.7132	0.7459	0.7475
γ	99.1571	9.9099	0.9893	0.0986	0.0099	0.0049

Table 3: Numerical simulation results using Theorem 3 for different values of the parameter λ and for $\rho = 10$ and $u_{\max} = 10$.

	$\lambda = 0.01$	$\lambda = 0.1$	$\lambda = 1$	$\lambda = 10$	$\lambda = 100$	$\lambda = 200$
$\mathbf{K}^{\mathrm{T}}$	$\begin{bmatrix} -0.00048 \\ -0.04438 \end{bmatrix}$	$\begin{bmatrix} -0.00581 \\ -0.05694 \end{bmatrix}$	$\begin{bmatrix} -0.0917 \\ -0.1166 \end{bmatrix}$	$\begin{bmatrix} -3.6420 \\ -0.6515 \end{bmatrix}$	$\begin{bmatrix} -297.9499 \\ -5.8866 \end{bmatrix}$	$10^3 \times \begin{bmatrix} -1.1761 \\ -0.0117 \end{bmatrix}$
m	0.01327	0.013319	0.013316	0.013320	0.013321	0.013321
$\overline{\delta}_a$	0.0321	0.8835	1.2411	2.4613	6.8305	9.3191
$\overline{\delta}_b$	0.1500	3.6262	3.6585	3.4313	3.3309	3.3217
$\overline{\delta}_c = \overline{\delta}_d$	9.9995	14.5636	14.3332	14.3665	14.4657	14.7111
$\overline{\delta}_e$	0.0360	2.1881	4.8950	6.0531	6.2291	6.1668
γ	9990.7	997.292	99.0173	9.8937	0.9851	0.4922

obtain a feasible solution. This will be demonstrated and discussed next.

Figure 2 reveals evolution of the trace of the matrix $\gamma\mathbf{S}$, or systematically the sum of the semiaxis of the invariant ellipsoid $\varepsilon(\mathbf{S}^{-1}, \gamma)$, as the parameter λ varies. It is obvious from Figure 2 that, by sweeping through λ, we obtain the maximum trace of the matrix $\gamma\mathbf{S}$ for the two cases $u_{\max} = 1$ and $u_{\max} = 10$. Such maximum trace corresponds to the largest invariant ellipsoid $\varepsilon_\star(\mathbf{P}_\star, \gamma_\star)$. Obtained results are summarized in Table 4. In this table, we provide the parameters, $\mathbf{P}_\star$ and $\gamma_\star$, of the largest attractive invariant ellipsoid $\varepsilon_\star(\mathbf{P}_\star, \gamma_\star)$, the associated feedback gains, $\mathbf{K}_\star$ and $m_\star$, of the saturated affine state-feedback control law u, the nominal value, $\lambda_\star$, of the free parameter λ, and the size of the attractive invariant ellipsoid $\varepsilon_\star(\mathbf{P}_\star, \gamma_\star)$. According to Figure 2 and Table 4, in the first case $u_{\max} = 1$, the size of the largest invariant ellipsoid is about 1.7906. However, in the second case $u_{\max} = 10$, such ellipsoid has a size about 46.5870. We recall that, for $u_{\max} = 1$, we have chosen $\overline{\delta} = 1$ and for $u_{\max} = 10$, we have adopted $\overline{\delta} = 10$.

Our objective now is to see the effect of the maximum bound of the different parametric uncertainties $\overline{\delta}_a$, $\overline{\delta}_b$, $\overline{\delta}_c$, $\overline{\delta}_d$, and $\overline{\delta}_e$ and also the saturation limit $u_{\max}$ on the size of the attractive invariant ellipsoid $\varepsilon(\mathbf{P}, \gamma)$. To do this, we used the optimization algorithm in Theorem 4 and we varied the parameter λ as mentioned previously. This task was achieved for a single value of the maximum uncertainty bound, saying $\delta_{\max} = \overline{\delta}_a = \cdots = \overline{\delta}_e$. Thus, we obtained the largest ellipsoid $\varepsilon_\star(\mathbf{P}_\star, \gamma_\star)$. Now, we will repeat the same procedure by also varying the parameter $\delta_{\max}$ and fixing the saturation level $u_{\max}$. Figure 3 reveals obtained results for $u_{\max} = 1$ and $u_{\max} = 10$. We stress first that, for $u_{\max} = 1$, the allowable maximum bound of the parametric uncertainty allowing to obtain an invariant ellipsoid $\varepsilon_\star(\mathbf{P}_\star, \gamma_\star)$ is $\delta_{\max} = 1.06$. However, for $u_{\max} = 10$, this value of $\delta_{\max}$ increases considerably and reaches the limit 12.05.

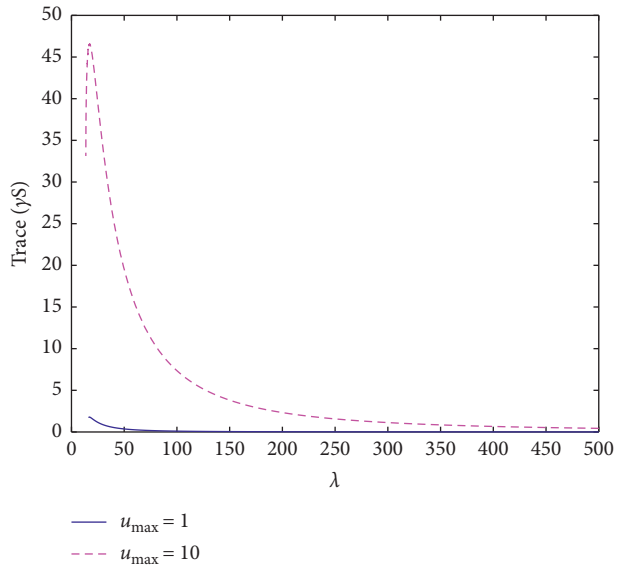

Figure 2: Variation of the trace of the matrix $\gamma \mathbf{S}$ with respect to the parameter λ and for two different values of the saturation level: $u_{max} = 1$ and $u_{max} = 10$. Here, for $u_{max} = 1$ (resp. $u_{max} = 10$), we have adopted $\overline{\delta} = 1$ (resp. $\overline{\delta} = 10$). Moreover, in the two cases, we have fixed $\rho = 10$.

Moreover, it is obvious that, for each value of u_{max}, the size of the largest ellipsoid increases rapidly as δ_{max} decreases. A tiny decrease of the uncertainty bound δ_{max} leads to a very important increase in the size of the ellipsoid $\varepsilon_\star(\mathbf{P}_\star, \gamma_\star)$. For example, for $u_{max} = 1$ and for $\delta_{max} = 0.5$, the size is about 10^3 and for $\delta_{max} = 0.1$, the size is around 10^9. Similarly, for the saturation limit $u_{max} = 10$ and for $\delta_{max} = 0.5$, the size is around 10^8 and for $\delta_{max} = 1.5$, the size is around 10^5.

Furthermore, it is clear that the size of the largest invariant ellipsoid decreases as δ_{max} increases. The ellipsoid becomes smaller as the uncertainty bound δ_{max} approaches its feasible limit (i.e., the value 1.06 for $u_{max} = 1$ and 12.05 for $u_{max} = 10$).

In addition, we remark that, for the same value of uncertainty bound δ_{max}, the size of the largest ellipsoid $\varepsilon_\star(\mathbf{P}_\star, \gamma_\star)$ increases as the saturation limit u_{max} increases (as noted previously for $\delta_{max} = 0.5$).

Using numerical results illustrated in Table 4, we plotted in Figure 4 the corresponding largest attractive invariant ellipsoids $\varepsilon_\star(\mathbf{P}_\star, \gamma_\star)$ for the two cases $u_{max} = 1$ and $u_{max} = 10$. In Figure 4, the two inclined lines (colored in pink and green) correspond to the bounds of the actuator saturation (20), which are defined as $\mathbf{K}\mathbf{x} + m = \pm u_{max}$. The lower line (colored in pink) is depicted for $\mathbf{K}\mathbf{x} + m = u_{max}$.

It is obvious from Figure 4 that, in the two cases, the largest invariant ellipsoid $\varepsilon_\star(\mathbf{P}_\star, \gamma_\star)$ is contained in the region $\mathscr{L}(\mathbf{K}, \mathbf{m}, \mathbf{u}_{max})$, where $|\mathbf{K}\mathbf{x} + m| \le u_{max}$. Therefore, the constraints on the affine state-feedback control law given in (18) are well respected.

In the end of this part, we can note the two following statements:

Table 4: Numerical results using Theorem 4 corresponding to the largest attractive invariant ellipsoid $\varepsilon_\star(\mathbf{P}_\star, \gamma_\star)$ for $u_{max} = 1$ and $u_{max} = 10$.

	$u_{max} = 1$ and $\overline{\delta} = 1$	$u_{max} = 10$ and $\overline{\delta} = 10$
$\mathbf{P}_\star$	$\begin{bmatrix} 10.1505 & 0.5523 \\ 0.5523 & 0.0628 \end{bmatrix}$	$\begin{bmatrix} 64.4531 & 2.1626 \\ 2.1626 & 0.1963 \end{bmatrix}$
$\mathbf{K}_\star$	$\begin{bmatrix} -9.0604 \\ -1.0242 \end{bmatrix}$	$\begin{bmatrix} -20.3362 \\ -1.8458 \end{bmatrix}$
$m_\star$	0.013235	0.013303
$\lambda_\star$	16.9211	17.3824
$\gamma_\star$	0.0583	5.7446
$\text{trace}(\gamma_\star \mathbf{S}_\star)$	1.7906	46.5870

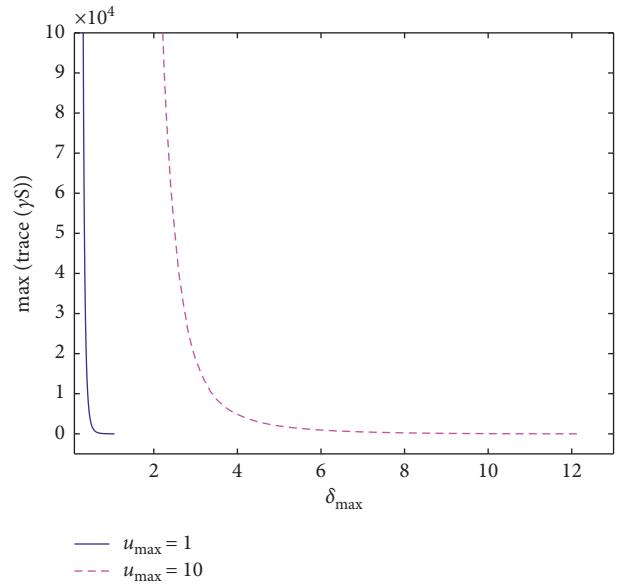

Figure 3: Variation of the size of the largest attractive invariant ellipsoid $\varepsilon_\star(\mathbf{P}_\star, \gamma_\star)$ with respect to the variation of the allowable maximum bound of the parametric uncertainties for the two cases: $u_{max} = 1$ and $u_{max} = 10$. Here, we have fixed $\overline{\delta}_a = \cdots = \overline{\delta}_e = \delta_{max}$, with always $\rho = 10$.

(1) For a constant saturation limit u_{max}, an increase of the maximum bound of the parametric uncertainties leads to the decrease of the largeness of the attractive invariant ellipsoid.

(2) For a constant maximum bound of the uncertainty, an increase of the saturation limit u_{max} causes the attractive invariant ellipsoid to become larger.

Remark 8. In some research papers, the definition of the attractive invariant ellipsoid was chosen to be as follows:

$$\acute{\varepsilon}(\mathbf{P}) = \left\{\mathbf{x} \in \mathbb{R}^{n_x} : \mathbf{x}^{\mathrm{T}}\mathbf{P}\mathbf{x} \le 1\right\}. \tag{72}$$

This set $\acute{\varepsilon}(\mathbf{P})$ is equivalent to that adopted in the present work in (21), that is, $\varepsilon(\mathbf{P}, 1)$. Hence, we have $\gamma = 1$. Our immediate concern is to show that the adopted ellipsoid (21) with a free parameter γ gives less conservative results

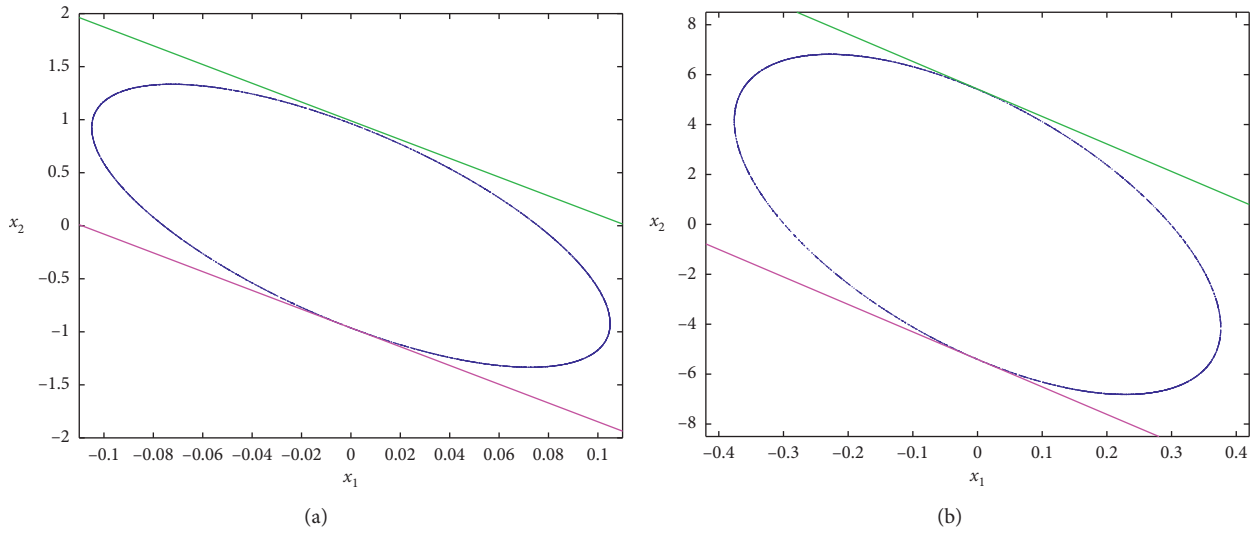

Figure 4: Largest attractive invariant ellipsoids $\varepsilon_\star(\mathbf{P}_\star, \gamma_\star)$ computed for two different values of $u_{\max}$.

compared with the ellipsoid (72). We use the same optimization algorithm in Theorem 4 where in the present case, we fix the parameter γ as a constant one and then we take $\gamma = 1$. Table 5 shows the numerical results obtained for a fixed parameter $\gamma = 1$. Notice that the symbol (!) in Table 5 means that the LMI-based optimization problem in Theorem 4 is unfeasible. To realize a comparison from conservatism point of view, we adopt the same parameters in Table 4. As noted previously, the maximum bound of the disturbance is fixed to $\rho = 10$. It is clear from Table 5 that, for the first case $u_{\max} = 1$ and $\overline{\delta} = 1$, the optimization problem in Theorem 4 was found to be unfeasible, with $\gamma = 1$. It was found to be feasible for all $\overline{\delta} \leq 0.648$. Recall that, for a free parameter γ, the optimization problem was found to be feasible for all $\overline{\delta} < 2$. This fact shows that, using a free parameter γ in the definition of the attractive invariant ellipsoid $\varepsilon(\mathbf{P}, \gamma)$, that is, the set (21), instead of fixing $\gamma = 1$, gives less conservative stability conditions. Moreover, from Table 5 and for the case $u_{\max} = 10$ and $\overline{\delta} = 10$, the optimization problem with $\gamma = 1$ is found to be feasible, as in Table 4. Nevertheless, the largest ellipsoid $\varepsilon'_\star(\mathbf{P}_\star)$ obtained for $\gamma = 1$, is too small compared with that obtained using a free parameter γ, that is, the ellipsoid $\varepsilon_\star(\mathbf{P}_\star, \gamma_\star)$. Recall that the largeness of the attractive invariant ellipsoid is measured by the "trace" function as noted in Tables 4 and 5. As noted in Table 4, for a free parameter γ, the volume of the largest ellipsoid was found to be about 46.5870. However, for a fixed parameter $\gamma = 1$, the volume of the largest ellipsoid $\varepsilon'_\star(\mathbf{P}_\star)$ is about 7.3840. The difference between the two sizes of the ellipsoid is evident. Another attractive result that can be observed from Table 5 is that the obtained matrix gain $\mathbf{K}_\star$ is too large compared with that obtained in Table 4.

Accordingly, we emphasize that the parameter γ in the definition of the attractive ellipsoid (21) leads to less conservative results and then less restrictive LMI stability conditions. In addition, it contributes in obtaining a largest ellipsoid with a controller gain having a small size. Hence, the choice of $\gamma \neq 0$ reduces the conservatism of the LMI-based optimization problem in Theorem 4.

Remark 9. We noted in the end of Section 4, just before Remark 5, that the computation time for solving the LMI-based optimization problem in Theorem 4 and then for the identification of the largest invariant attractive ellipsoid $\varepsilon_\star(\mathbf{P}_\star, \gamma_\star)$ depends on the number N_κ of uniformly distributed points κ in the interval $]0, 1[$ and the simulation time t_κ for each value of the parameter κ. The total simulation time t_c can be computed to be about $t_c \approx N_\kappa \times t_\kappa$. Tables 6 and 7 present the simulation results for different values of the parameters N_κ for $u_{\max} = 1$ (Table 6) and for $u_{\max} = 10$ (Table 7). Recall that, for $u_{\max} = 1$, we have $\overline{\delta} = 1$, whereas for $u_{\max} = 10$, we fixed $\overline{\delta} = 10$. Moreover, the maximum bound ρ of the disturbance is fixed to be $\rho = 10$ in the two cases. Actually, in order to obtain these results in Tables 6 and 7, we have fixed the interval in which the parameter κ varies as follows: [0.01: δ_κ: 0.99], where we have selected four cases: $\delta_\kappa = 0.01$, $\delta_\kappa = 0.001$, $\delta_\kappa = 0.0005$, and $\delta_\kappa = 0.0002$. For these values of δ_κ, it corresponds, respectively, the number $N_\kappa = 99$, $N_\kappa = 981$, $N_\kappa = 1961$, and $N_\kappa = 4901$. Thus, using these intervals and these values of the parameters N_κ, we simulated the optimization problem under LMI constraints in Theorem 4 and then we obtained the results in Tables 6 and 7. In these Tables, we give the two optimal gains, $\mathbf{K}_\star$ and $m_\star$, of the controller, $\lambda_\star$ (notice that $\lambda = \kappa/(1-\kappa)$), $\gamma_\star$, the size of the ellipsoid (trace $(\gamma_\star \mathbf{S}_\star)$), the simulation/computation time t_c, and the number of feasible solutions N_{fs}. It is important to note that not all the N_κ-cases are feasible. From the results in Tables 6 and 7, it reveals that the number of feasible solutions is only about 4.8% for $u_{\max} = 1$ and about 6% for $u_{\max} = 10$. The computation time t_c for finding the largest ellipsoid increases significantly as N_κ increases too. We also stress that as N_κ increases, the optimal solution converges to that already obtained in Table 4. We found the same values for $N_\kappa = 4901$. Nevertheless, in this case, the computation time

Table 5: Numerical results using Theorem 4 with a fixed parameter $\gamma = 1$ and for $u_{\max} = 1$ and $u_{\max} = 10$.

	$u_{\max} = 1$ and $\overline{\delta} = 1$	$u_{\max} = 10$ and $\overline{\delta} = 10$
$\mathbf{P}_\star$	(!)	$10^3 \times \begin{bmatrix} 2.1069 & 0.0255 \\ 0.0255 & 0.0004 \end{bmatrix}$
$\mathbf{K}_\star$	(!)	$10^2 \times \begin{bmatrix} -2.8612 \\ -0.0633 \end{bmatrix}$
$m_\star$	(!)	0.013317
$\lambda_\star$	(!)	99.6036
$\text{trace}(\mathbf{S}_\star)$	(!)	7.3840

Table 6: Computation time for solving the LMI-based optimization algorithm in Theorem 4 for the case $u_{\max} = 1$.

N_κ	99	981	1961	4901
$\mathbf{K}_\star^T$	$\begin{bmatrix} -10.5679 \\ -1.1050 \end{bmatrix}$	$\begin{bmatrix} -9.2061 \\ -1.0321 \end{bmatrix}$	$\begin{bmatrix} -9.1147 \\ -1.0271 \end{bmatrix}$	$\begin{bmatrix} -9.0604 \\ -1.0242 \end{bmatrix}$
$m_\star$	0.013238	0.013237	0.013239	0.013235
$\lambda_\star$	19.0000	17.1818	17.0180	16.9211
$\gamma_\star$	0.0519	0.0574	0.0580	0.0583
$\text{trace}(\gamma_\star \mathbf{S}_\star)$	1.6557	1.7874	1.7894	1.7906
$t_c[s]$	6.1988	54.9516	106.1182	264.1296
N_{fs}	5	48	95	238

Table 7: Computation time for solving the LMI-based optimization algorithm in Theorem 4 for the case $u_{\max} = 10$.

N_κ	99	981	1961	4901
$\mathbf{K}_\star^T$	$\begin{bmatrix} -18.6484 \\ -1.8069 \end{bmatrix}$	$\begin{bmatrix} -19.7871 \\ -1.8309 \end{bmatrix}$	$\begin{bmatrix} -20.3059 \\ -1.8453 \end{bmatrix}$	$\begin{bmatrix} -20.3362 \\ -1.8458 \end{bmatrix}$
$m_\star$	0.013306	0.013311	0.013306	0.013303
$\lambda_\star$	15.6667	16.8571	17.3486	17.3824
$\gamma_\star$	6.3740	5.9236	5.7557	5.7446
$\text{trace}(\gamma_\star \mathbf{S}_\star)$	45.7911	46.5153	46.5625	46.5870
$t_c[s]$	3.1946	27.3301	53.4916	132.4823
N_{fs}	6	59	117	293

is very high, it is computed to be about 4.5 minutes for $u_{\max} = 1$ and it is about 2.2 minutes for the second case $u_{\max} = 10$.

5.3. Simulations for the Robust Stabilization of the Pitch Dynamics. In this part, we would show the robustness and effectiveness of the designed saturated affine state-feedback control law (19) in the robust stabilization of the uncertain disturbed nonlinear dynamics (15) of the pitch model of the helicopter. The control gains $\mathbf{K}$ and m are provided in Table 4. We recall that, for $u_{\max} = 1$, we have $\overline{\delta}_a = \overline{\delta}_b = \overline{\delta}_c = \overline{\delta}_d = \overline{\delta}_e = 1$, whereas for $u_{\max} = 10$, we take $\overline{\delta}_a = \overline{\delta}_b = \overline{\delta}_c = \overline{\delta}_d = \overline{\delta}_e = 10$. Moreover, we recall that the external disturbance w in the nonlinear dynamics (15) is bounded according to condition (14) with $\rho = 10$. In addition, the uncertain parameters δ_a, δ_b, δ_c, δ_d, and δ_e in (15) vary randomly over time so that the boundedness condition (17) is satisfied. Furthermore, for the simulation of the controlled nonlinear system (15), we will take first an initial condition, $\mathbf{x}_0$, located outside the largest attractive ellipsoid $\varepsilon_\star(\mathbf{P}_\star, \gamma_\star)$: for the case $u_{\max} = 1$, we take $\mathbf{x}_0 = \begin{bmatrix} 0.1 & -1 \end{bmatrix}^{\text{T}}$, whereas for the case $u_{\max} = 10$, we take $\mathbf{x}_0 = \begin{bmatrix} 0.3 & -6 \end{bmatrix}^{\text{T}}$. Each initial condition is located near the boundary of the corresponding ellipsoid (see Figure 4). Furthermore, we will take an initial condition located outside the invariant attractive ellipsoid: $\mathbf{x}_0 = \begin{bmatrix} 5 & -10 \end{bmatrix}^{\text{T}}$, for the two saturation limits.

First of all, we will study the dynamics of the helicopter model under the saturated control law u in the nominal case, that is, without parametric uncertainties and disturbance. Figure 5(a) shows temporal evolution of the states x_1 and x_2 of the certain undisturbed controlled nonlinear system (15), and Figure 5(b) reveals the saturated affine state-feedback control law u for the saturation limit $u_{\max} = 1$. It is obvious that the state of the pitch dynamics converges to zero, which is our main objective in this paper. Moreover, the control law u converges to a constant value, which is found to be equal to the gain m. Actually, such constant value of the control input will ensure that the pitch dynamics of the helicopter stays at the zero state. In addition, we note that the reached maximum value of the control law u is about 0.23, which is less than the desired saturation limit $u_{\max} = 1$.

We have also analyzed the nominal pitch dynamics of the helicopter model for the case $u_{\max} = 10$. We have observed almost the same behavior in Figure 5. The reached

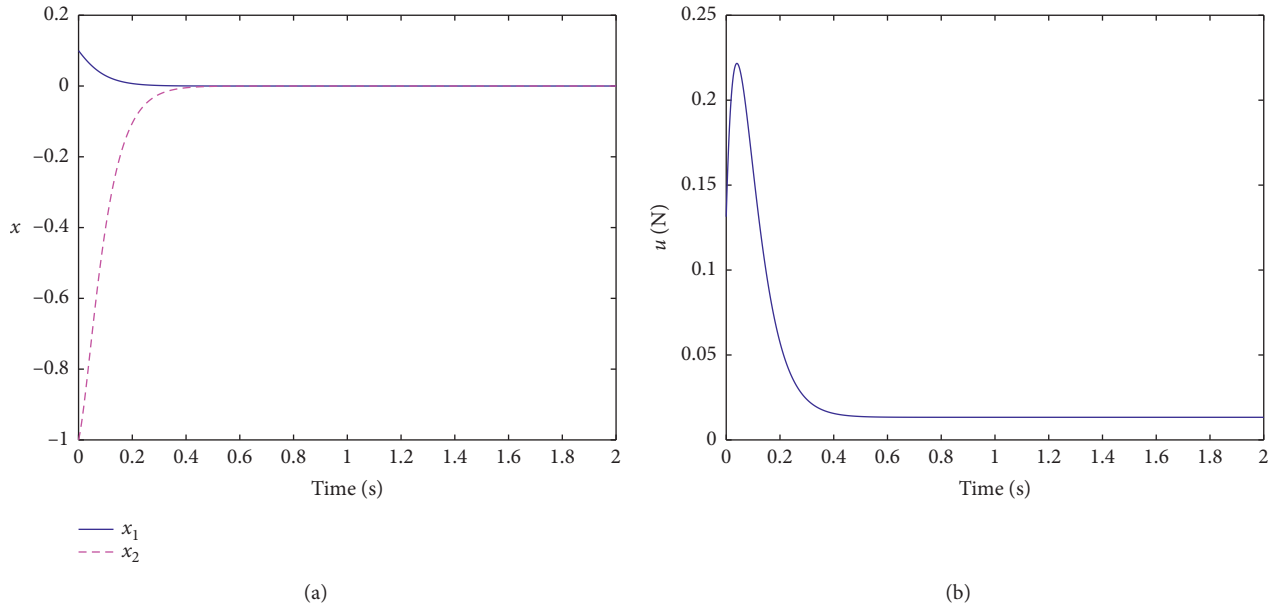

FIGURE 5: Evolution of the two states, x_1 and x_2, of the nonlinear system (15) and the saturated affine state-feedback control law u for $u_{\max} = 1$ in the nominal case. Here, the system is without uncertainties ($\delta_{a,b,c,d,e} = 0$) and disturbance ($w = 0$).

maximum value of the controller u is around 5. The controller converges to the constant value $m \approx 0.01336$.

Now, we will show simulation results for the controlled nonlinear system subject to both parametric uncertainties and external disturbance. Simulation results are shown in Figure 6 for $u_{\max} = 1$ and Figure 7 for $u_{\max} = 10$. Figure 6(a) (resp. Figure 7(a)) presents temporal evolution of the two states, x_1 and x_2, of the nonlinear system (15) under uncertainties and disturbance. Figure 6(b) (resp. Figure 7(b)) reveals evolution of the saturated control law u for $u_{\max} = 1$ (resp. $u_{\max} = 10$). As noted previously, the initial condition is located inside the largest attractive invariant ellipsoid. Moreover, the disturbance w is injected into the system at $t = 2[s]$ and during $3[s]$. We recall that the external disturbance w satisfies condition (14) with $\rho = 10$.

It is obvious from Figure 6(a) that the motion of the pitch dynamics of the helicopter model experiences some fluctuations around the desired zero state when the disturbance is applied. Once the effect of the external disturbing torque w vanishes, the controlled system stabilizes again around its desired position with some very weak perturbations provoked by the injected parametric uncertainties. Moreover, in Figure 6(b), the control signal u varies around the value $m = 0.0133$. The control signal varies between two very small values: ± 0.1. We stress that the effects of the parametric uncertainties and the external disturbance are compensated. This shows the robustness of the control law u towards the parametric uncertainties and the external disturbance with high amplitude.

However, for $u_{\max} = 10$, the effect of the parametric uncertainties and the external disturbance w is clear in Figure 7. Figure 7(a) is almost identical to Figure 6(a). Moreover, when the disturbance is injected, the control signal u undergoes some fluctuations, which vary between ± 1.5. This happens because the maximum bound of the uncertainties is very large ($\overline{\delta}_{a,\ldots,e} = 10$) in this case compared with the first case, i.e., for $u_{\max} = 1$.

It is worth to note that, in the previous three cases, the saturation level $\pm u_{\max}$ of the controller was well respected.

We have tested another case by taking an initial condition located outside the largest attractive invariant ellipsoid $\varepsilon_\star(\mathbf{P}_\star, \gamma_\star)$. We take here only the case $u_{\max} = 1$, and then the corresponding largest ellipsoid is given by Figure 4(a). As noted previously, the initial condition is chosen to be $\mathbf{x}_0 = \begin{bmatrix} 5 & -10 \end{bmatrix}^{\mathrm{T}}$. Obtained results are illustrated in Figure 8. We observe first from Figure 8(a) that the state x_1 of the helicopter model experiences some smooth oscillations before its convergence and stabilization at the zero position despite the presence of the external disturbance and the parametric uncertainties. In fact, only weak fluctuations are observed as in Figure 7(a). However, the interesting phenomenon observed here is the saturation of the control law u depicted in Figure 8(b).

Remark 10. It is worth to note that, for a predefined set of the system parameters, the previous established optimization problems under LMI constraints are (should be) simulated offline in order to compute the largest attractive ellipsoid and then the associated feedback gains $\mathbf{K}$ and m of the input-saturated affine state-feedback controller u before its application into a real helicopter system in practice. Thus, for a prescribed saturation level $u_{\max}$, the possible maximum allowable bounds of the parametric uncertainties $\overline{\delta}_a$, $\overline{\delta}_b$, $\overline{\delta}_c$, $\overline{\delta}_d$, and $\overline{\delta}_e$ and the possible maximum bound of the external disturbance signal w, i.e., ρ, we look, as described previously, for the largest attractive invariant ellipsoid $\varepsilon_\star(\mathbf{P}_\star, \gamma_\star)$. Thus, once this set is found, the corresponding feedback gains $\mathbf{K}$ and m will be used in order to stabilize the pitch dynamics of the simple helicopter model in a real-world application.

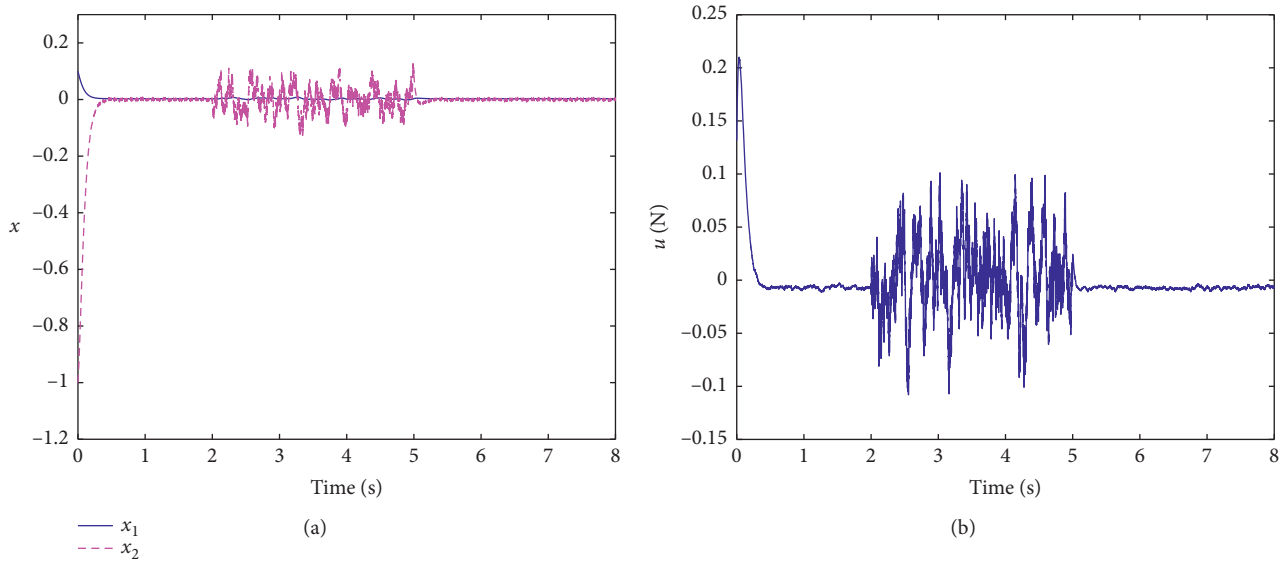

FIGURE 6: Temporal evolution of the states x_1 and x_2 of the nonlinear system (15) and the saturated affine state-feedback control law u for the saturation level $u_{\max} = 1$. Here, the system is subject to randomly time-varying uncertainties and also a randomly time-varying external disturbing torque w. Moreover, $\overline{\delta}_{a,b,c,d,e} = 1$.

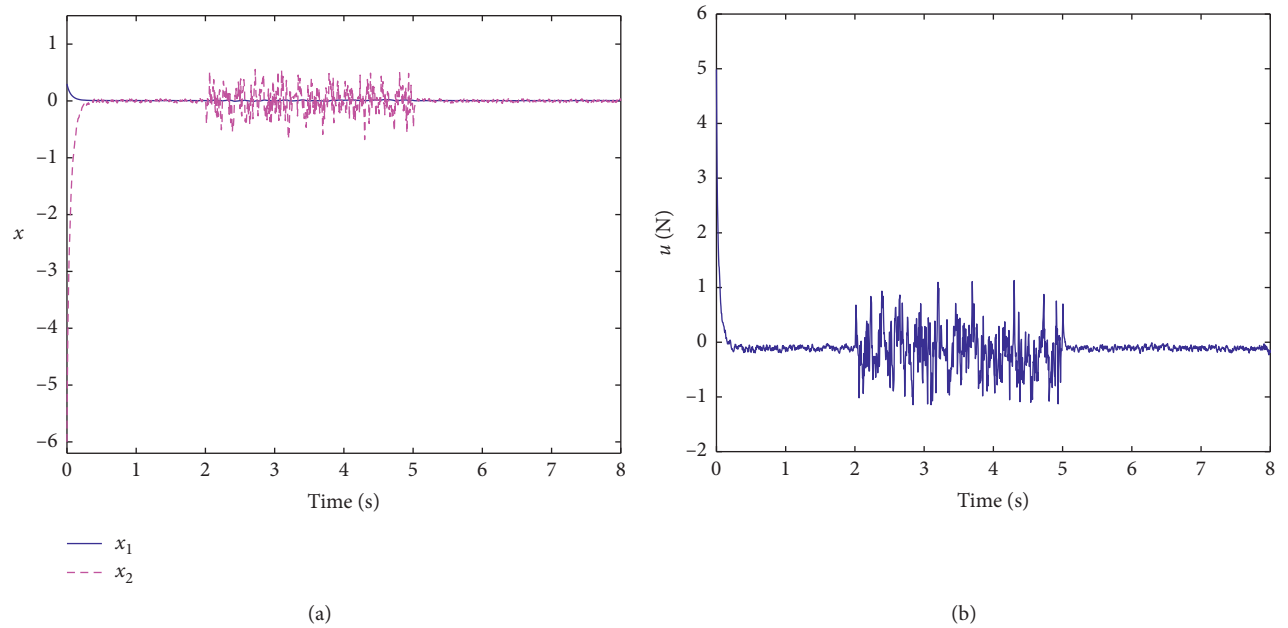

FIGURE 7: Evolution of the two states x_1 and x_2 of the nonlinear system (15) (a) and the saturated affine state-feedback control law u (b) for the saturation level $u_{\max} = 10$. In this case, we have $\overline{\delta}_{a,b,c,d,e} = 10$.

6. Conclusion and Future Works

In this paper, an LMI-based approach for designing a robust affine state-feedback control law to stabilize the pitch dynamics of a helicopter model was proposed. The nonlinear dynamics of the helicopter was subject to an external disturbance and norm-bounded parametric uncertainties. Moreover, the problem of the actuator saturation in the design of the control law was as well addressed. We showed that the stabilization problem is represented as a solving problem of BMI constraints. Furthermore, with a judicious utilization of the Schur lemma and the matrix inversion lemma, these BMIs were transformed into LMIs. We have also developed an optimization problem with enhanced LMI constraints permitting to compute the maximum bounds of the parametric uncertainties.

In addition, we have proposed an LMI-based approach for the maximization of the attractive invariant ellipsoid for the uncertain disturbed nonlinear dynamics of the helicopter model under the saturated affine state-feedback control law.

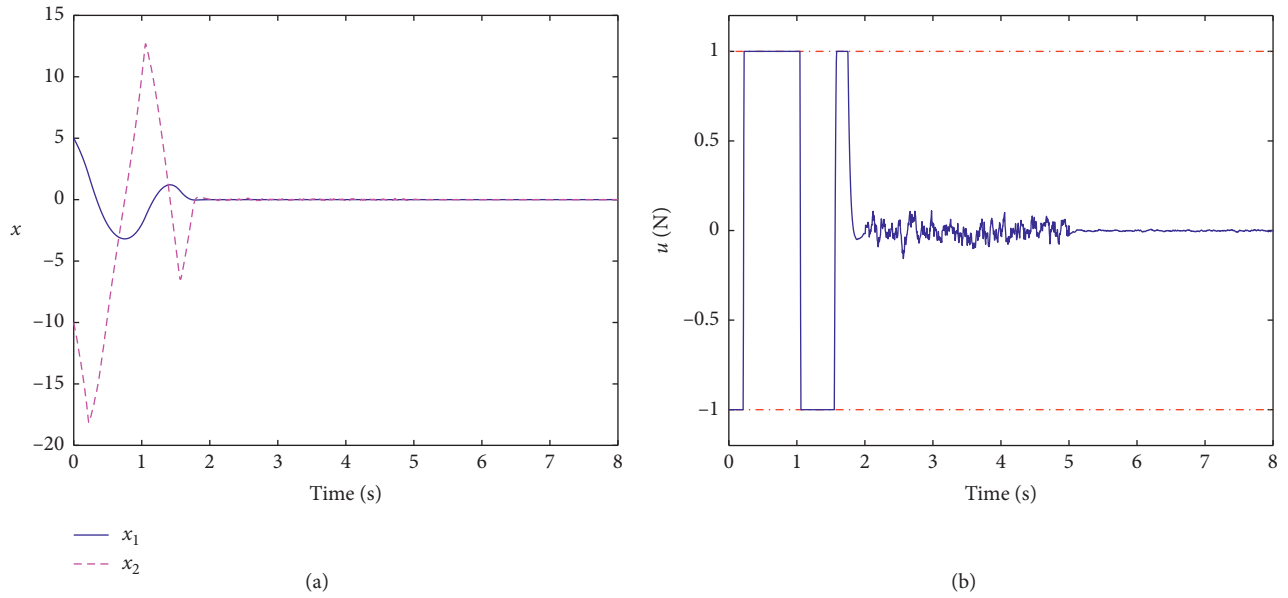

FIGURE 8: Temporal evolution of the two states x_1 and x_2 of the uncertain disturbed nonlinear system (15) and the saturated affine state-feedback control law u for the saturation level $u_{\max} = 1$. Here, the initial condition is selected to be outside the largest attractive invariant ellipsoid $\varepsilon_\star(\mathbf{P}_\star, \gamma_\star)$ in Figure 4(a).

The largeness of the ellipsoid was measured by means of the length of its semiaxis. We have showed that the optimization problem computes efficiently the largest ellipsoid in only one step.

Finally, we have showed through numerical simulations the performance of the synthesized saturated controller in the robust stabilization of the nonlinear dynamics under the norm-bounded parametric uncertainties and the external disturbing torque.

In the literature, the estimation of the domain of attraction of the closed-loop system subject to actuation saturations is one of important issues and several methods have been achieved for both linear and nonlinear systems. The difference between these methods lies in the approach by which the saturation nonlinearity was handled [51]. Its treatment can be classified into three main approaches: (1) the first one is to treat the actuator saturation problem as achieved in the present work, (2) the second approach is to treat it as a locally/generalized sector bounded nonlinearity [17, 69, 70], (3) while the third method is to represent the saturation nonlinearity as a (polytopic or linear) differential inclusion (see [36, 51] and references insides). As noted in Remark 5, the solution presented in this work leads to the computation of the largest attractive invariant ellipsoid in only one step, compared to some related approaches that used a two-step method. Thus, the approach presented in this paper is more simpler and is less restrictive.

In addition, it worth to note that, in this paper, a saturated affine state-feedback controller was designed. To the best of our knowledge, such problem has not been considered in the literature. Generally, a saturated linear feedback controller has been considered to stabilize linear and nonlinear systems. Then, in order to realize a comparison and hence to show the possible efficiency of our design approach, a future work of this paper is the design of a saturated affine feedback controller using the sector-bounded nonlinearity method and the differential inclusion approach.

Furthermore, we aim at extending the present methodology of the saturation affine feedback controller for more complex nonlinear systems with different Lipschitzian conditions [65], and with measurement delays [71, 72] and also for the design of observer-based feedback controllers for Lipschitz nonlinear systems [3, 8, 64]. Moreover, we hope to extend this work for impulsive hybrid nonlinear systems, such as the biped robots [73] and the impact mechanical oscillators subject to multiple rigid constraints [74–76].

In the present work, we considered the simple pitch dynamics of a helicopter model as an application. Moreover, the zero state is not the equilibrium point of such model. Thus, we have designed an affine feedback controller under saturation to achieve the robust stabilization at the zero state. Another important application that has such feature is the robot manipulators [77]. Indeed, because of the gravitational matrix, the dynamics of robot manipulators has an equilibrium point different to the zero state. Thus, several control approaches have been adopted for this subject [77]. Our objective is then to extend the design method of the saturated affine state-feedback controller for the case of manipulator robots.

Data Availability

The data used to support the findings of this study are available from the corresponding author upon request.

Conflicts of Interest

The authors declare that there are no conflicts of interest regarding the publication of this paper.

References

[1] M. G. Safonov, "Origins of robust control: early history and future speculations," *Annual Reviews in Control*, vol. 36, no. 2, pp. 173–181, 2012.

[2] M. S. Sadabadi and D. Peaucelle, "From static output feedback to structured robust static output feedback: a survey," *Annual Reviews in Control*, vol. 42, pp. 11–26, 2016.

[3] S. Ahmad, M. Rehan, and K.-S. Hong, "Observer-based robust control of one-sided Lipschitz nonlinear systems," *ISA Transactions*, vol. 65, pp. 230–240, 2016.

[4] I. R. Petersen and R. Tempo, "Robust control of uncertain systems: classical results and recent developments," *Automatica*, vol. 50, no. 5, pp. 1315–1335, 2014.

[5] A. Poznyak, A. Polyakov, and V. Azhmyakov, *Attractive Ellipsoids in Robust Control, Systems & Control: Foundations & Applications*, Birkhauser Basel, Basel, Switzerland, 1st edition, 2014.

[6] R. K. Yedavalli, *Robust Control of Uncertain Dynamic Systems. A Linear State Space Approach*, Springer, Berlin, Germany, 1st edition, 2014.

[7] B. El Haiek, H. El Aiss, H. Abdelaziz, A. El Hajjaji, and T. El Houssaine, "New approach to robust observer-based control of one-sided Lipschitz non-linear systems," *IET Control Theory & Applications*, vol. 13, no. 9, pp. 333–342, 2019.

[8] M. Rehan, S. Ahmad, and K.-S. Hong, "Novel results on observer-based control of one-sided Lipschitz systems under input saturation," *European Journal of Control*, 2019.

[9] S. Boyd, L. El-Ghaoui, E. Feron, and V. Balakrishnan, *Linear Matrix Inequalities in System and Control Theory*, Vol. 15 of Studies in Applied and Numerical Mathematics, Society for Industrial and Applied Mathematics (SIAM), Philadelphia, PA, USA, 1st edition, 1994.

[10] J. Lofberg, "YALMIP: a toolbox for modeling and optimization in MATLAB," in *Proceedings of the IEEE International Conference on Robotics and Automation*, pp. 284–289, New Orleans, LA, USA, September 2004.

[11] A. Zemouche, R. Rajamani, H. Kheloufi, and F. Bedouhene, "Robust observer-based stabilization of Lipschitz nonlinear uncertain systems via LMIs-discussions and new design procedure," *International Journal of Robust and Nonlinear Control*, vol. 27, no. 11, pp. 1915–1939, 2017.

[12] H. Gritli and S. Belghith, "Robust feedback control of the underactuated inertia wheel inverted pendulum under parametric uncertainties and subject to external disturbances: LMI formulation," *Journal of the Franklin Institute*, vol. 355, no. 18, pp. 9150–9191, 2018.

[13] Y. Wang, R. Rajamani, and A. Zemouche, "Sequential LMI approach for the design of a BMI-based robust observer state feedback controller with nonlinear uncertainties," *International Journal of Robust and Nonlinear Control*, vol. 28, no. 4, pp. 1246–1260, 2018.

[14] A. Aktas, H. Yazici, and M. Sever, "LMI-based design of an I-PD+PD type LPV state feedback controller for a gantry crane," *Transactions of the Institute of Measurement and Control*, vol. 41, no. 6, pp. 1640–1655, 2019.

[15] S. M. Moradi, A. Akbari, and M. Mirzaei, "An offline LMI-based robust model predictive control of vehicle active suspension system with parameter uncertainty," *Transactions of the Institute of Measurement and Control*, vol. 41, no. 6, pp. 1699–1711, 2019.

[16] I. H. Brahim, D. Mehdi, and M. Chaabane, "Sensor fault and state estimation for uncertain fuzzy descriptor systems: an LMI approach," *Transactions of the Institute of Measurement and Control*, vol. 41, no. 1, pp. 135–144, 2019.

[17] S. Tarbouriech, G. Garcia, J. M. Gomes da Silva Jr., and I. Queinnec, *Stability and Stabilization of Linear Systems with Saturating Actuators*, Springer, Berlin, Germany, 1st edition, 2011.

[18] T. Hu and Z. Lin, *Control Systems with Actuator Saturation: Analysis and Design (Control Engineering)*, Birkhauser Basel, Basel, Switzerland, 1st edition, 2011.

[19] M. L. Corradini, A. Cristofaro, F. Giannoni, and G. Orlando, *Control Systems with Saturating Inputs. Analysis Tools and Advanced Design*, Lecture Notes in Control and Information Sciences, Springer, Berlin, Germany, 1st edition, 2012.

[20] T. Hu and Z. Lin, "Exact characterization of invariant ellipsoids for single input linear systems subject to actuator saturation," *IEEE Transactions on Automatic Control*, vol. 47, no. 1, pp. 164–169, 2002.

[21] T. Alamo, A. Cepeda, and D. Limon, "Improved computation of ellipsoidal invariant sets for saturated control systems," in *Proceedings of the 44th IEEE Conference on Decision and Control*, pp. 6216–6221, Seville, Spain, December 2005.

[22] Q. Wang, "Global external stochastic stabilization of linear systems with input saturation: an alternative approach," *Complexity*, vol. 2017, Article ID 3517280, 7 pages, 2017.

[23] B. Zhou and G.-R. Duan, "Global stabilization of linear systems via bounded controls," *Systems & Control Letters*, vol. 58, no. 1, pp. 54–61, 2009.

[24] P. Niamsup and V. N. Phat, "Robust finite-time control for linear time-varying delay systems with bounded control," *Asian Journal of Control*, vol. 18, no. 6, pp. 2317–2324, 2016.

[25] M. Ran, Q. Wang, and C. Dong, "Anti-windup design for uncertain nonlinear systems subject to actuator saturation and external disturbance," *International Journal of Robust and Nonlinear Control*, vol. 26, no. 15, pp. 3421–3438, 2016.

[26] M. Ran, Q. Wang, and C. Dong, "Stabilization of a class of nonlinear systems with actuator saturation via active disturbance rejection control," *Automatica*, vol. 63, pp. 302–310, 2016.

[27] D. W. Kim, "Further refinement on controller design for linear systems with input saturation," *Automatica*, vol. 77, pp. 14–17, 2017.

[28] Y. Li and Z. Lin, "A complete characterization of the maximal contractively invariant ellipsoids of linear systems under saturated linear feedback," *IEEE Transactions on Automatic Control*, vol. 60, no. 1, pp. 179–185, 2015.

[29] Y. Li and Z. Lin, "The maximal contractively invariant ellipsoids for discrete-time linear systems under saturated linear feedback," *Automatica*, vol. 76, pp. 336–344, 2017.

[30] L. Amezquita-Brooks, D. Hernandez, F. Gonzalez-Sanchez, and J. C. Tudón-Martínez, "Linear programming predictive control with actuator saturation: experimental robustness and performance results," *Proceedings of the Institution of Mechanical Engineers, Part I: Journal of Systems and Control Engineering*, vol. 229, no. 8, pp. 700–710, 2015.

[31] T. Binazadeh and M. Bahmani, "Robust time-varying output tracking control in the presence of actuator saturation," *Transactions of the Institute of Measurement and Control*, vol. 40, no. 1, pp. 61–70, 2018.

[32] M. Nasri, D. Saifia, M. Chadli, and S. Labiod, "H∞ static output feedback control for electrical power steering subject to actuator saturation via fuzzy Lyapunov functions," *Transactions of the Institute of Measurement and Control*, vol. 41, no. 12, pp. 3340–3351, 2019.

[33] K. S. T. Alain, A. T. Azar, F. H. Bertrand, and K. Romanic, "Robust observer-based synchronisation of chaotic oscillators with structural perturbations and input nonlinearity," *International Journal of Automation and Control*, vol. 13, no. 4, pp. 387–412, 2019.

[34] R. Mei and C. Yu, "Adaptive neural output feedback control for uncertain robot manipulators with input saturation," *Complexity*, vol. 2017, Article ID 7413642, 12 pages, 2017.

[35] Q. Wang, M. Ran, and C. Dong, "An analysis and design method for a class of nonlinear systems with nested saturations," *International Journal of Control*, vol. 89, no. 8, pp. 1711–1724, 2016.

[36] Y. Li and Z. Lin, "Improvements to the linear differential inclusion approach to stability analysis of linear systems with saturated linear feedback," *Automatica*, vol. 49, no. 3, pp. 821–828, 2013.

[37] H. Du, N. Zhang, and G. Dong, "Stabilizing vehicle lateral dynamics with considerations of parameter uncertainties and control saturation through robust yaw control," *IEEE Transactions on Vehicular Technology*, vol. 59, no. 5, pp. 2593–2597, 2010.

[38] W. Sun, Z. Zhao, and H. Gao, "Saturated adaptive robust control for active suspension systems," *IEEE Transactions on Industrial Electronics*, vol. 60, no. 9, pp. 3889–3896, 2013.

[39] H. Du and N. Zhang, "Fuzzy control for nonlinear uncertain electrohydraulic active suspensions with input constraint," *IEEE Transactions on Fuzzy Systems*, vol. 17, no. 2, pp. 343–356, 2009.

[40] W. Sun, H. Gao, and O. Kaynak, "Vibration isolation for active suspensions with performance constraints and actuator saturation," *IEEE/ASME Transactions on Mechatronics*, vol. 20, no. 2, pp. 675–683, 2015.

[41] F. Zhao, S. S. Ge, M. Dong, F. Tu, and Y. Qin, "Adaptive neural network control for active suspension system with actuator saturation," *IET Control Theory & Applications*, vol. 10, no. 14, pp. 1696–1705, 2016.

[42] K. Lu, Y. Xia, C. Yu, and H. Liu, "Finite-time tracking control of rigid spacecraft under actuator saturations and faults," *IEEE Transactions on Automation Science and Engineering*, vol. 13, no. 1, pp. 368–381, 2016.

[43] L. Sun and Z. Zheng, "Disturbance-observer-based robust backstepping attitude stabilization of spacecraft under input saturation and measurement uncertainty," *IEEE Transactions on Industrial Electronics*, vol. 64, no. 10, pp. 7994–8002, 2017.

[44] B. Qiang and L. Zhang, "Output feedback control design to enlarge the domain of attraction of a supercavitating vehicle subject to actuator saturation," *Transactions of the Institute of Measurement and Control*, vol. 40, no. 10, pp. 3189–3200, 2018.

[45] W. Chang, S. Tong, and Y. Li, "Adaptive fuzzy backstepping output constraint control of flexible manipulator with actuator saturation," *Neural Computing and Applications*, vol. 28, no. 1, pp. 1165–1175, 2017.

[46] Z. Zheng and L. Sun, "Path following control for marine surface vessel with uncertainties and input saturation," *Neurocomputing*, vol. 177, pp. 158–167, 2016.

[47] T. Hu, Z. Lin, and B. M. Chen, "An analysis and design method for linear systems subject to actuator saturation and disturbance," *Automatica*, vol. 38, no. 2, pp. 351–359, 2002.

[48] T. Hu, Z. Lin, and B. M. Chen, "Analysis and design for discrete-time linear systems subject to actuator saturation," *Systems & Control Letters*, vol. 45, no. 2, pp. 97–112, 2002.

[49] Z. Zuo and Y. Wang, "On enlarging the domain of attraction for linear systems subject to actuator saturation," *International Journal of General Systems*, vol. 37, no. 2, pp. 239–248, 2008.

[50] B. Zhou, W. X. Zheng, and G.-R. Duan, "Stability and stabilization of discrete-time periodic linear systems with actuator saturation," *Automatica*, vol. 47, no. 8, pp. 1813–1820, 2011.

[51] B. Zhou, W. X. Zheng, and G.-R. Duan, "An improved treatment of saturation nonlinearity with its application to control of systems subject to nested saturation," *Automatica*, vol. 47, no. 2, pp. 306–315, 2011.

[52] T. Hu and Z. Lin, "On enlarging the basin of attraction for linear systems under saturated linear feedback," *Systems & Control Letters*, vol. 40, no. 1, pp. 59–69, 2000.

[53] Y. Chen, Q. Zhou, and S. Fei, "Robust stabilization and l 2-gain control of uncertain discrete-time constrained piecewise-affine systems," *Nonlinear Dynamics*, vol. 75, no. 1-2, pp. 127–140, 2014.

[54] N. Vafamand, M. H. Asemani, and A. Khayatiyan, "A robust L1 controller design for continuous-time TS systems with persistent bounded disturbance and actuator saturation," *Engineering Applications of Artificial Intelligence*, vol. 56, pp. 212–221, 2016.

[55] B. Samadi and L. Rodrigues, "Stability of sampled-data piecewise affine systems: a time-delay approach," *Automatica*, vol. 45, no. 9, pp. 1995–2001, 2009.

[56] K. Merat, H. Salarieh, A. Alasty, and A. Meghdari, "Stochastic piecewise affine control with application to pitch control of helicopter," *Nonlinear Analysis: Hybrid Systems*, vol. 15, pp. 86–97, 2015.

[57] H. Razavi, K. Merat, H. Salarieh, A. Alasty, and A. Meghdari, "Observer based minimum variance control of uncertain piecewise affine systems subject to additive noise," *Nonlinear Analysis: Hybrid Systems*, vol. 19, pp. 153–167, 2016.

[58] F. Mesquine, H. Ayad, and M. Ait Rami, "Disturbance attenuation for continuous-time linear systems with state and control constraints," *International Journal of Sciences and Techniques of Automatic Control & Computer Engineering Special Issue CSC'07*, pp. 312–324, 2007.

[59] M. Rehan and K.-S. Hong, "Decoupled-architecture-based nonlinear anti-windup design for a class of nonlinear systems," *Nonlinear Dynamics*, vol. 73, no. 3, pp. 1955–1967, 2013.

[60] M. Rehan, M. Tufail, C. K. Ahn, and M. Chadli, "Stabilisation of locally Lipschitz non-linear systems under input saturation and quantisation," *IET Control Theory & Applications*, vol. 11, no. 9, pp. 1459–1466, 2017.

[61] S. Krafes, Z. Chalh, and A. Saka, "A review on the control of second order underactuated mechanical systems," *Complexity*, vol. 2018, Article ID 9573514, 17 pages, 2018.

[62] Y. Liu and H. Yu, "A survey of underactuated mechanical systems," *IET Control Theory & Applications*, vol. 7, no. 7, pp. 921–935, 2013.

[63] W. Zhang, H.-S. Su, Y. Liang, and Z.-Z. Han, "Non-linear observer design for one-sided Lipschitz systems: an linear matrix inequality approach," *IET Control Theory & Applications*, vol. 6, no. 9, pp. 1297–1303, 2012.

[64] S. Ahmad and M. Rehan, "On observer-based control of one-sided Lipschitz systems," *Journal of the Franklin Institute*, vol. 353, no. 4, pp. 903–916, 2016.

[65] H. Gritli and S. Belghith, "LMI-based design of state feedback controller for Lipschitzian nonlinear systems," in *Proceedings of the 15th International Multi-Conference on Systems, Signals & Devices (SSD)*, pp. 306–314, Hammamet, Tunisia, March 2018.

[66] C. Venkatesan, "Fundamentals of helicopter dynamics," in *Engineering & Technology*, CRC Press, Boca Raton, FL, USA, 1st edition, 2014.

[67] I. A. Raptis and K. P. Valavanis, *Linear and Nonlinear Control of Small-Scale Unmanned Helicopters*, Vol. 45 of Intelligent Systems, Control and Automation: Science and Engineering, Springer, Berlin, Germany, 1st edition, 2011.

[68] H. Kheloufi, A. Zemouche, F. Bedouhene, and M. Boutayeb, "On LMI conditions to design observer-based controllers for linear systems with parameter uncertainties," *Automatica*, vol. 49, no. 12, pp. 3700–3704, 2013.

[69] Y. Chen, Y. Li, and S. Fei, "Anti-windup design for time-delay systems via generalised delay-dependent sector conditions," *IET Control Theory & Applications*, vol. 11, no. 10, pp. 1634–1641, 2017.

[70] Y. Chen, Z. Wang, S. Fei, and Q.-L. Han, "Regional stabilization for discrete time-delay systems with actuator saturations via a delay-dependent polytopic approach," *IEEE Transactions on Automatic Control*, vol. 64, no. 3, pp. 1257–1264, 2019.

[71] S. Ahmad, R. Majeed, K.-S. Hong, and M. Rehan, "Observer design for one-sided Lipschitz nonlinear systems subject to measurement delays," *Mathematical Problems in Engineering*, vol. 2015, Article ID 879492, 13 pages, 2015.

[72] S. Ahmad, M. Rehan, and M. Iqbal, "Robust generalized filtering of uncertain Lipschitz nonlinear systems under measurement delays," *Nonlinear Dynamics*, vol. 92, no. 4, pp. 1567–1582, 2018.

[73] H. Gritli and S. Belghith, "Walking dynamics of the passive compass-gait model under OGY-based control: emergence of bifurcations and chaos," *Communications in Nonlinear Science and Numerical Simulation*, vol. 47, pp. 308–327, 2017.

[74] H. Gritli and S. Belghith, "Diversity in the nonlinear dynamic behavior of a one-degree-of-freedom impact mechanical oscillator under OGY-based state-feedback control law: order, chaos and exhibition of the border-collision bifurcation," *Mechanism and Machine Theory*, vol. 124, pp. 1–41, 2018.

[75] H. Gritli, "Robust master-slave synchronization of chaos in a one-sided 1-DoF impact mechanical oscillator subject to parametric uncertainties and disturbances," *Mechanism and Machine Theory*, vol. 142, p. 103610, 2019.

[76] F. Turki, H. Gritli, and S. Belghith, "An LMI-based design of a robust state-feedback control for the master-slave tracking of an impact mechanical oscillator with double-side rigid constraints and subject to bounded-parametric uncertainty," *Communications in Nonlinear Science and Numerical Simulation*, vol. 82, p. 105020, 2020.

[77] R. Kelly, V. Santibáñez Davila, and J. A. Loría Perez, *Control of Robot Manipulators in Joint Space (Advanced Textbooks in Control and Signal Processing)*, Springer, Berlin, Germany, 1st edition, 2005.

Hindawi
Complexity
Volume 2020, Article ID 1085870, 17 pages
https://doi.org/10.1155/2020/1085870

Research Article

Mitigation of Bullwhip Effect in Closed-Loop Supply Chain Based on Fuzzy Robust Control Approach

Songtao Zhang[1] **and Min Zhang**[2]

[1]*School of Logistics, Linyi University, Linyi 276005, China*
[2]*Library, Linyi University, Linyi 276005, China*

Correspondence should be addressed to Min Zhang; zm0205@163.com

Received 25 July 2019; Revised 23 November 2019; Accepted 16 December 2019; Published 21 January 2020

Guest Editor: Raúl Villafuerte-Segura

Uncertainties and lead times make the closed-loop supply chain (CLSC) more complex, less stable, and then the bullwhip effect (BE) will become more intense. This paper will address a fuzzy robust control (FRC) approach to mitigate the BE in the uncertain CLSC with lead times. For the reverse channels for products in the CLSC, the customers' used products are recycled by both the manufacturer and the third party recovery provider, and new products bought by customers within a certain period of time can be returned to the retailer. In the CLSC system, the state transformation equations of the inventories and the total operation cost are set up. A new FRC approach is proposed to mitigate the BE and realize the robust stability of the uncertain CLSC with lead times. A simulation example verifies the mitigation effect of the BE under the proposed FRC approach.

1. Introduction

Whether governments construct green supply chains through governmental interventions [1] or enterprises undertake social responsibility through social work donation [2], the environment can be more friendly. Therefore, both governments and enterprises have been paying more and more attention to the closed-loop supply chain (CLSC) which can achieve sustainable development [3].

The complexity of the business environment results in many uncertainties in the CLSC. Especially in the reverse supply chain, there are uncertainties in quality, quantity, and time of the recycled products, which lead to the uncertainty of remanufacturing profit. For example, ReCellular, one of the largest phone remanufacturers in the United States, divides used phones into six quality levels for remanufacturing. Uncertainty is one of the main reasons for the existence of bullwhip effect (BE), and the other reason is lead time. If BE cannot be effectively mitigated, the operating efficiency of the CLSC will be reduced, and then the operating cost will be increased. In serious cases, the CLSC will collapse. Therefore, for the mitigation issue of the BE in the CLSC with uncertainties and lead times, we will propose a fuzzy robust control (FRC) approach to reduce the BE and realize the robust stability of the CLSC.

The remainder of this paper is formulated as follows: Section 2 offers a review of the related literature. Section 3 puts forward a kind of Takagi–Sugeno fuzzy model for the CLSC with uncertainties and lead times. Section 4 addresses a FRC approach to mitigate the BE in the CLSC system. The simulation studies are carried out in Section 5. The conclusions and future research directions are given in Section 6.

2. Literature Review

In the CLSC, used products can be recycled by various subjects. For example, the used products can be recycled by the manufacturer [4] or by the retailer [5]. Wei and Zhao [6] studied the decision-making issue of the used products recycled by the manufacturer, the retailer, or the third party recovery provider (3PRP). Furthermore, recycling used products can be performed by multiple subjects at the same time to realize more convenient for customers and more efficient for enterprises. This recycling pattern is called hybrid recycling. Therefore, some scholars have

been devoting themselves to the study of the CLSC with hybrid recycling channels; for example, based on hybrid recycling channels, Allah et al. [7] investigated the pricing strategies of the CLSCs with the single-channel forward supply chain and with the dual-channel forward supply chain; Shi and Ma [8] recycled the used medical equipment through hybrid recycling models; under hybrid recycling channels, Ma and Liu [9] analyzed the optimal profit of the CLSC.

For the studies mentioned above, [7–9] did not consider the impacts of uncertainties and lead times on the CLSC system with hybrid recycling channels. However, uncertainties and lead times are two important factors leading to BE. Therefore, many scholars studied the BE caused by uncertainties or lead times; for example, by simulation-based approach, Do et al. [10] quantified the BE with different demands and stochastic lead times; for a two-echelon serial supply chain, Agrawal et al. [11] compared the effects of lead time reduction and information sharing on the mitigation of the BE; using the statistical method, Kim et al. [12] considered the stochastic lead time and provided expressions for quantifying the BE both with information sharing and without information sharing; Modak and Kelle [13] used a hybrid all-unit quantity discount along a franchise fee contract to mitigate the BE in the dual-channel supply chain with the delivery time and stochastic demand; Li and Liu [14] explored the mitigation of the BE in the supply chain with uncertainties and the vendor order placement lead time.

In recent years, approaches based on control theory have been widely applied to mitigate the BE, such as Model Predictive Control (MPC) approach [15], Internal Model Control (IMC) approach [16], Proportional plus Integral Control (PIC) approach [17], and Common Robust Control (CRC) approach [18]. Among these mitigation approaches, the MPC approach, the IMC approach, and the PIC approach cannot implement the switching control, and the CRC approach can only perform the conventional switching control but cannot achieve the flexible switching control of the FRC approach.

Up to now, research on the mitigation of the BE in the CLSC with uncertainties and lead times has not yet been found. But, a fuzzy control approach has been applied to mitigate the BE in uncertain CLSC with hybrid recycling channels by Zhang et al. [19]. Therefore, we will follow the research ideas in [19] to address a control approach for mitigating the BE of the CLSC with uncertainties and lead times. The critical contributions of this paper comparing to [19] are listed as follows.

2.1. Lead Times Are Included in the CLSC Models. There are the manufacturer's production lead time and recycling lead time in the manufacturer' inventory model; the retailer's ordering lead time and the 3PRP's recycling lead time are, respectively, considered in the retailer's inventory model and in the 3PRP's inventory model; all lead times are included in the total operation cost model of the CLSC.

2.2. An Additional Takagi–Sugeno Fuzzy Controller for Lead Times Is Designed. We will design an additional Takagi–Sugeno fuzzy negative feedback controller, which is the product of the inventory feedback gains with lead times and the inventory variables with lead times.

2.3. A New Fuzzy Control Approach Is Put Forward. We will put forward a new FRC approach which can effectively mitigate the BE caused by uncertainties and lead times and ensure the stability of the CLSC system. LMIs (linear matrix inequalities) to be solved in this paper are more complex than those in [19].

3. CLSC Model

3.1. CLSC Model with Uncertainties and Lead Times. As shown in Figure 1, this paper constructs a CLSC model that includes a manufacturer, a retailer, a 3PRP, and customers. Because products recycled by both the manufacturer and the 3PRP are the most effective pattern among hybrid recycling channels [20], for reverse supply chain in our model, the manufacturer and the 3PRP simultaneously recycle customers' used products, and the retailer allows customers to return new products within a certain period of time.

Based on Figure 1, considering the uncertain system parameters and lead times, we set up the inventory equations of the CLSC as follows:

$$\begin{cases} x_1(k+1) = x_1(k) + u_1(k) + u_1(k-\tau_1) + u_3(k) + u_3(k-\tau_3) + (\eta+\Delta\eta)x_4(k) - u_2(k), \\ x_2(k+1) = x_2(k) + u_2(k) + u_2(k-\tau_2) + (\mu+\Delta\mu)x_3(k) - w_1(k), \\ x_3(k+1) = x_3(k) + w_1(k) - u_3(k) - u_4(k) - (\mu+\Delta\mu)x_3(k), \\ x_4(k+1) = x_4(k) + u_4(k) + u_4(k-\tau_4) - (\eta+\Delta\eta)x_4(k) - (\lambda+\Delta\lambda)x_4(k). \end{cases} \tag{1}$$

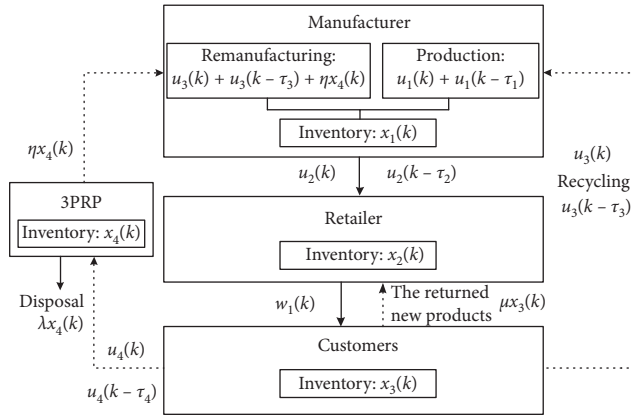

Figure 1: CLSC model.

Accordingly, we set up the total cost equation of the CLSC as follows:

$$\begin{aligned} z(k) = {} & (c_{h1} + \Delta c_{h1})x_1(k) + (c_{h2} + \Delta c_{h2})x_2(k) + (c_{h3} + \Delta c_{h3})x_4(k) \\ & + (c_n + \Delta c_n)[u_1(k) + u_1(k-\tau_1)] \\ & + (c_r + \Delta c_r)[u_3(k) + u_3(k-\tau_3) + (\eta + \Delta\eta)x_4(k)] \\ & + (c_m + \Delta c_m)[u_3(k) + u_3(k-\tau_3)] \\ & + (c_t + \Delta c_t)[u_4(k) + u_4(k-\tau_4)] \\ & + (c_{mt} + \Delta c_{mt})(\eta + \Delta\eta)x_4(k) \\ & + (c_q + \Delta c_q)(\mu + \Delta\mu)x_3(k) \\ & + (c_d + \Delta c_d)(\lambda + \Delta\lambda)x_4(k) \\ & + (c_s + \Delta c_s)[u_2(k) + u_2(k-\tau_2)]. \end{aligned} \tag{2}$$

Equations (1) and (2) are described by the deviation values (deviation value = actual value − nominal value).

In addition, based on different inventory statuses, each node enterprise will design corresponding production patterns or ordering patterns, which leads to some different models in different periods. Then, the ith model of the CLSC can be shown as follows:

$$\begin{cases} \mathbf{x}(k+1) = (\mathbf{A}_i + \Delta\mathbf{A}_i)\mathbf{x}(k) + (\mathbf{B}_i + \Delta\mathbf{B}_i)\mathbf{u}(k) + \sum_{e=1}^{4}(\mathbf{B}_{ie} + \Delta\mathbf{B}_{ie})\mathbf{u}(k-\tau_e) + (\mathbf{B}_{wi} + \Delta\mathbf{B}_{wi})\mathbf{w}(k), \\ z(k) = (\mathbf{C}_i + \Delta\mathbf{C}_i)\mathbf{x}(k) + (\mathbf{D}_i + \Delta\mathbf{D}_i)\mathbf{u}(k) + \sum_{e=1}^{4}(\mathbf{D}_{ie} + \Delta\mathbf{D}_{ie})\mathbf{u}(k-\tau_e), \end{cases} \tag{3}$$

where $\mathbf{x}^{\mathrm{T}}(k) = [x_1(k), x_2(k), x_3(k), x_4(k)]$, $\mathbf{u}^{\mathrm{T}}(k) = [u_1(k), u_2(k), u_3(k), u_4(k)]$, $\mathbf{u}^{\mathrm{T}}(k-\tau_e) = [u_1(k-\tau_1), u_2(k-\tau_2), u_3(k-\tau_3), u_4(k-\tau_4)]$, and $\mathbf{w}^{\mathrm{T}}(k) = [\,w_1(k),\ 0,\ 0,\ 0\,]$; $\mathbf{A}_i$ denotes the inventory status coefficient matrix; $\mathbf{B}_i$ denotes the production, ordering, and recycling coefficient matrix; $\mathbf{B}_{ie}$ denotes the production, ordering, and recycling coefficient matrix with lead times; $\mathbf{B}_{wi}$ denotes the coefficient matrix of the customers' demand; $\mathbf{C}_i$ denotes the coefficient matrix of the inventory cost, the cost of the new products returned, the disposal cost, part of remanufacturing cost, and part of recycling cost; $\mathbf{D}_i$ denotes the coefficient matrix of production cost, ordering cost, part of remanufacturing cost, and part of recycling cost; $\mathbf{D}_{ie}$ denotes the coefficient matrix of production cost, ordering cost, part of remanufacturing cost, and part of recycling cost with lead times; and $\Delta\mathbf{A}_i$, $\Delta\mathbf{B}_i$, $\Delta\mathbf{B}_{ie}$, $\Delta\mathbf{B}_{wi}$, $\Delta\mathbf{C}_i$, $\Delta\mathbf{D}_i$, and $\Delta\mathbf{D}_{ie}$, respectively, denote the corresponding uncertain matrices.

3.2. Takagi–Sugeno Fuzzy Model of CLSC. In the process of wide variation of the inventory level, switching activities will take place among models to maintain a reasonable inventory level in each node enterprise. In order to effectively mitigate the BE of the CLSC, we will utilize Takagi–Sugeno fuzzy systems [21] to implement the flexible switching in the CLSC. Then, Model (3) is transformed into the following discrete Takagi–Sugeno fuzzy model:

R_i: If $x_1(k)$ is M_1^i, ..., $x_j(k)$ is M_j^i, ..., and $x_n(k)$ is M_n^i, then

$$\begin{cases} \mathbf{x}(k+1) = (\mathbf{A}_i + \Delta\mathbf{A}_i)\mathbf{x}(k) + (\mathbf{B}_i + \Delta\mathbf{B}_i)\mathbf{u}(k) + \sum_{e=1}^{g} (\mathbf{B}_{ie} + \Delta\mathbf{B}_{ie})\mathbf{u}(k-\tau_e) + (\mathbf{B}_{wi} + \Delta\mathbf{B}_{wi})\mathbf{w}(k), \\ z(k) = (\mathbf{C}_i + \Delta\mathbf{C}_i)\mathbf{x}(k) + (\mathbf{D}_i + \Delta\mathbf{D}_i)\mathbf{u}(k) + \sum_{e=1}^{g} (\mathbf{D}_{ie} + \Delta\mathbf{D}_{ie})\mathbf{u}(k-\tau_e), \\ \mathbf{x}(k) = \boldsymbol{\varphi}(k), \quad k \in \{0, 1, \ldots, N\}, \end{cases} \tag{4}$$

where $\mathbf{w}(k) \in l_2[\mathbf{0}, \infty)$; $\boldsymbol{\varphi}(k)$ denotes the initial condition of the CLSC; $\mathbf{x}^{\mathrm{T}}(k) = [x_1(k), x_2(k), \ldots, x_n(k)]$; $\mathbf{u}^{\mathrm{T}}(k) = [u_1(k), u_2(k), \ldots, u_n(k)]$; $\mathbf{u}^{\mathrm{T}}(k-\tau_e) = [u_1(k-\tau_1), u_2(k-\tau_2), \ldots, u_n(k-\tau_g)]$; and $\mathbf{w}^{\mathrm{T}}(k) = [w_1(k), w_2(k), \ldots, w_n(k)]$.

By singleton fuzzifier, product inference, and centre-average defuzzifer, Model (4) can be expressed as follows:

$$\begin{cases} \mathbf{x}(k+1) = \sum_{i=1}^{r} h_i(\mathbf{x}(k)) \cdot \left[(\mathbf{A}_i + \Delta\mathbf{A}_i)\mathbf{x}(k) + (\mathbf{B}_i + \Delta\mathbf{B}_i)\mathbf{u}(k) + \sum_{e=1}^{g} (\mathbf{B}_{ie} + \Delta\mathbf{B}_{ie})\mathbf{u}(k-\tau_e) + (\mathbf{B}_{wi} + \Delta\mathbf{B}_{wi})\mathbf{w}(k) \right], \\ z(k) = \sum_{i=1}^{r} h_i(\mathbf{x}(k)) \cdot \left[(\mathbf{C}_i + \Delta\mathbf{C}_i)\mathbf{x}(k) + (\mathbf{D}_i + \Delta\mathbf{D}_i)\mathbf{u}(k) + \sum_{e=1}^{g} (\mathbf{D}_{ie} + \Delta\mathbf{D}_{ie})\mathbf{u}(k-\tau_e) \right], \end{cases} \tag{5}$$

where $h_i(\mathbf{x}(k)) = \mu_i(\mathbf{x}(k)) / \sum_{i=1}^{r} \mu_i(\mathbf{x}(k))$ and $\mu_i(\mathbf{x}(k)) = \prod_{j=1}^{n} M_j^i(x_j(k))$; since $\mu_i(\mathbf{x}(k)) \geq 0$, we have $h_i(\mathbf{x}(k)) \geq 0$ and $\sum_{i=1}^{r} h_i(\mathbf{x}(k)) = 1$. In the following expressions, $\mathbf{x}(k)$ will be elided from $h_i(\mathbf{x}(k))$ for simplicity.

Because of the existence of the membership degree function in Model (5), the flexible switching can be realized among the models of the CLSC.

4. Mitigation of BE

4.1. Measurement of BE. We use the following parameter γ to represent the mitigation degree of BE:

$$\frac{\|\text{total cost of CLSC}\|_2}{\|\text{customers' demand}\|_2} \leq \gamma. \tag{6}$$

From the inequality above, we know that the mitigation degree of BE depends on the size of the total cost of the CLSC and the size of the customers' demand. The lower γ is, the smaller BE is.

4.2. FRC Approach. We introduce known constant matrices $\mathbf{H}_{1i}$, $\mathbf{H}_{2i}$, $\mathbf{E}_{11i}$, $\mathbf{E}_{12i}$, $\mathbf{E}_{13i}$, $\mathbf{E}_{21i}$, $\mathbf{E}_{22i}$, $\mathbf{L}_{\mathrm{ei}}$, and $\mathbf{O}_{\mathrm{ei}}$ and time-varying uncertain matrices $\mathbf{F}_{1i}(k)$ and $\mathbf{F}_{2i}(k)$ to describe the uncertain parameters in the CLSC; $\mathbf{F}_{1i}(k)$, and $\mathbf{F}_{2i}(k)$ are Lebesgue-measurable and satisfy $\mathbf{F}_{1i}^{\mathrm{T}}(k)\mathbf{F}_{1i}(k) \leq \mathbf{I}$ and $\mathbf{F}_{2i}^{\mathrm{T}}(k)\mathbf{F}_{2i}(k) \leq \mathbf{I}$. Then, we represent the uncertain parameter matrices in Model (5) as follows:

$$\begin{aligned} &\left[\Delta\mathbf{A}_i, \Delta\mathbf{B}_i, \Delta\mathbf{B}_{wi}, \Delta\mathbf{B}_{i1}, \ldots, \Delta\mathbf{B}_{ie}, \ldots, \Delta\mathbf{B}_{ig}\right] \\ &\quad = \mathbf{H}_{1i}\mathbf{F}_{1i}(k)\left[\mathbf{E}_{11i}, \mathbf{E}_{12i}, \mathbf{E}_{13i}, \mathbf{L}_{1i}, \ldots, \mathbf{L}_{\mathrm{ei}}, \ldots, \mathbf{L}_{\mathrm{gi}}\right]; \\ &\left[\Delta\mathbf{C}_i, \Delta\mathbf{D}_i, \Delta\mathbf{D}_{i1}, \ldots, \Delta\mathbf{D}_{ie}, \ldots, \Delta\mathbf{D}_{ig}\right] \\ &\quad = \mathbf{H}_{2i}\mathbf{F}_{2i}(k)\left[\mathbf{E}_{21i}, \mathbf{E}_{22i}, \mathbf{O}_{1i}, \ldots, \mathbf{O}_{ei}, \ldots, \mathbf{O}_{gi}\right]. \end{aligned} \tag{7}$$

For the fuzzy CLSC system in Model (5), we design the Takagi–Sugeno fuzzy controller as follows.

Controller rule K^i:

If $x_1(k)$ is M_1^i, ..., $x_j(k)$ is M_j^i, ..., and $x_n(k)$ is M_n^i, then

$$\begin{cases} \mathbf{u}(k) = -\mathbf{K}_i\mathbf{x}(k), & i = 1, 2, \ldots, r, \\ \mathbf{u}(k-\tau_e) = -\mathbf{K}_{ie}\mathbf{x}(k-\tau_e), & e = 1, 2, \ldots, g, \end{cases} \tag{8}$$

where $\mathbf{K}_i$ is the inventory feedback gain matrix and $\mathbf{K}_{ie}$ is the inventory feedback gain matrix with lead times. Furthermore, we can obtain the following overall model of Model (8):

$$\begin{cases} \mathbf{u}(k) = -\sum_{i=1}^{r} h_i\mathbf{K}_i\mathbf{x}(k), \\ \mathbf{u}(k-\tau_e) = -\sum_{i=1}^{r} h_i\mathbf{K}_{ie}\mathbf{x}(k-\tau_e). \end{cases} \tag{9}$$

Therefore, introducing Controller (9) into Model (5), we have

$$\begin{cases} \mathbf{x}(k+1) = \sum_{i=1}^{r}\sum_{j=1}^{r} h_i h_j \left[\left(\overline{\mathbf{A}}_i - \overline{\mathbf{B}}_i \mathbf{K}_j \right) \mathbf{x}(k) - \sum_{e=1}^{g} \overline{\mathbf{B}}_{ie} \mathbf{K}_{je} \mathbf{x}(k-\tau_e) + \overline{\mathbf{B}}_{wi} \mathbf{w}(k) \right], \\ z(k) = \sum_{i=1}^{r}\sum_{j=1}^{r} h_i h_j \left[\left(\overline{\mathbf{C}}_i - \overline{\mathbf{D}}_i \mathbf{K}_j \right) \mathbf{x}(k) - \sum_{e=1}^{g} \overline{\mathbf{D}}_{ie} \mathbf{K}_{je} \mathbf{x}(k-\tau_e) \right]. \end{cases} \tag{10}$$

where $\overline{\mathbf{A}}_i = \mathbf{A}_i + \Delta\mathbf{A}_i$, $\overline{\mathbf{B}}_i = \mathbf{B}_i + \Delta\mathbf{B}_i$, $\overline{\mathbf{B}}_{ie} = \mathbf{B}_{ie} + \Delta\mathbf{B}_{ie}$, $\overline{\mathbf{B}}_{wi} = \mathbf{B}_{wi} + \Delta\mathbf{B}_{wi}$, $\overline{\mathbf{C}}_i = \mathbf{C}_i + \Delta\mathbf{C}_i$, $\overline{\mathbf{D}}_i = \mathbf{D}_i + \Delta\mathbf{D}_i$, and $\overline{\mathbf{D}}_{ie} = \mathbf{D}_{ie} + \Delta\mathbf{D}_{ie}$.

For the further analysis, we introduce the following Definitions, Property, and Lemma.

Definition 1 (see [22]). A cluster of fuzzy sets $\{F_j^m, m = 1, 2, \ldots, q_j\}$ are said to be a standard fuzzy partition in the universe X if each F_j^m is a normal fuzzy set and $F_j^m (m = 1, 2, \ldots, q_j)$ are full-overlapped in the universe X. q_j is said to be the number of fuzzy partitions of the jth input variable on X.

Definition 2 (see [22]). For a given fuzzy system, an overlapped-rule group (ORG) with the largest amount of rules is said to be a maximal overlapped-rule group (MORG).

Definition 3 (see [23]). Given a scalar $\gamma > 0$, discrete switched system (10) is said to be robustly stable with the disturbance attenuation level γ constraint under the H_∞ norm if the following conditions are satisfied:

(1) When $\mathbf{w}(k) \equiv \mathbf{0}$, System (10) is asymptotically stable

(2) When $\mathbf{w}(k) \neq \mathbf{0}$, under the condition of the initial value of zero, any uncertain customers' demand meets $\|z(k)\|_2^2 \leq \gamma \|\mathbf{w}(k)\|_2^2$

Property 1 (see [22]). If the input variables of a fuzzy system adopt standard fuzzy partitions, then all the rules in an ORG must be included in a MORG.

Lemma 1 (see [24]). *For any real matrices $\mathbf{X}_{ij}$ $(1 \leq i, j \leq r)$ and $\mathbf{P} > \mathbf{0}$ with appropriate dimensions, the following inequality holds:*

$$\sum_{i=1}^{r}\sum_{j=1}^{r}\sum_{p=1}^{r}\sum_{q=1}^{r} h_i h_j h_p h_q \mathbf{X}_{ij}^{\mathrm{T}} \mathbf{P} \mathbf{X}_{pq} \leq \sum_{i=1}^{r}\sum_{j=1}^{r} h_i h_j \mathbf{X}_{ij}^{\mathrm{T}} \mathbf{P} \mathbf{X}_{ij}. \tag{11}$$

The FRC approach for the CLSC system will be presented in the following Theorem 1.

Theorem 1. *System (10) with a certain γ and fuzzy sets of inventories satisfying standard fuzzy partitions is robustly asymptotically stable if local common positive definite matrices $\mathbf{P}_c$ and $\mathbf{Q}_{ec}$ can be found in the following inequalities:*

$$\begin{bmatrix} -\overline{\overline{\mathbf{P}}} & * & * \\ \overline{\mathbf{M}}_{ii} & -\mathbf{P}_c^{-1} & * \\ \overline{\mathbf{N}}_{ii} & \mathbf{0} & -\mathbf{I} \end{bmatrix} < \mathbf{0}, \quad i \in I_c, \tag{12}$$

$$\begin{bmatrix} -4\overline{\overline{\mathbf{P}}} & * & * \\ 2\overline{\overline{\mathbf{M}}}_{ij} & -\mathbf{P}_c^{-1} & * \\ 2\overline{\overline{\mathbf{N}}}_{ij} & \mathbf{0} & -\mathbf{I} \end{bmatrix} < \mathbf{0}, \quad i < j, i, j \in I_c, \tag{13}$$

where

$$\begin{aligned} \overline{\overline{\mathbf{P}}} &= \begin{bmatrix} \mathbf{P}_c - \sum_{e=1}^{g} \mathbf{Q}_{ec} & * & * \\ \mathbf{0} & \widehat{\mathbf{Q}} & * \\ \mathbf{0} & \mathbf{0} & \gamma^2 \mathbf{I} \end{bmatrix}, \\ \overline{\overline{\mathbf{M}}}_{\mathbf{ij}} &= \frac{\overline{\mathbf{M}}_{ij} + \overline{\mathbf{M}}_{ji}}{2}, \\ \widehat{\mathbf{Q}} &= \mathrm{diag}\left\{ \mathbf{Q}_{1c} \ \cdots \ \mathbf{Q}_{ec} \ \cdots \ \mathbf{Q}_{gc} \right\}, \\ \overline{\overline{\mathbf{N}}}_{ij} &= \frac{\overline{\mathbf{N}}_{ij} + \overline{\mathbf{N}}_{ji}}{2}. \end{aligned} \tag{14}$$

Proof. Suppose there are f ORGs in System (10), $v_d (d = 1, 2, \ldots, f)$ denotes the operating region of the dth ORG and $L_d = \{$the rule numbers involved in the dth ORG$\}$.

(1) The first part of the proof:

For $\mathbf{x}(k)$ and $\mathbf{x}(k+1)$ in the same ORG, we express the local model of the dth ORG as follows:

$$\begin{cases} \mathbf{x}(k+1) = \sum_{i \in L_d}\sum_{j \in L_d} h_i h_j \left[\mathbf{M}_{ij} \mathbf{x}(k) - \sum_{e=1}^{g} \overline{\mathbf{B}}_{ie} \mathbf{K}_{\mathrm{jec}} \mathbf{x}(k-\tau_e) + \overline{\mathbf{B}}_{wi} \mathbf{w}(k) \right], \\ z(k) = \sum_{i \in L_d}\sum_{j \in L_d} h_i h_j \left[\mathbf{N}_{ij} \mathbf{x}(k) - \sum_{e=1}^{g} \overline{\mathbf{D}}_{ie} \mathbf{K}_{\mathrm{jec}} \mathbf{x}(k-\tau_e) \right], \end{cases} \tag{15}$$

where $\mathbf{M}_{ij} = \overline{\mathbf{A}}_i - \overline{\mathbf{B}}_i\mathbf{K}_{jc}$, $\mathbf{N}_{ij} = \overline{\mathbf{C}}_i - \overline{\mathbf{D}}_i\mathbf{K}_{jc}$, and $\mathbf{K}_{jec}$ denotes the state feedback gain matrix with lead times in the cth MORG.

Furthermore, Model (15) is described further as follows:

$$\begin{cases} \mathbf{x}(k+1) = \sum\limits_{i\in L_d}\sum\limits_{j\in L_d} h_i h_j \overline{\mathbf{M}}_{ij}\overline{\mathbf{x}}(k), \\ z(k) = \sum\limits_{i\in L_d}\sum\limits_{j\in L_d} h_i h_j \overline{\mathbf{N}}_{ij}\overline{\mathbf{x}}(k), \end{cases} \tag{16}$$

where

$$\begin{aligned} \overline{\mathbf{M}}_{ij} &= \left[\mathbf{M}_{ij}, -\overline{\mathbf{B}}_{i1}\mathbf{K}_{j1c}, \ldots, -\overline{\mathbf{B}}_{ie}\mathbf{K}_{jec}, \ldots, -\overline{\mathbf{B}}_{ig}\mathbf{K}_{jgc}, \overline{\mathbf{B}}_{wi}\right], \\ \overline{\mathbf{N}}_{ij} &= \left[\mathbf{N}_{ij}, -\overline{\mathbf{D}}_{i1}\mathbf{K}_{j1c}, \ldots, -\overline{\mathbf{D}}_{ie}\mathbf{K}_{jec}, \ldots, -\overline{\mathbf{D}}_{ig}\mathbf{K}_{jgc}, \mathbf{0}\right], \\ \overline{\mathbf{x}}(k) &= \left[\mathbf{x}(k), \mathbf{x}(k-\tau_1), \ldots, \mathbf{x}(k-\tau_e), \ldots, \mathbf{x}\left(k-\tau_g\right), \mathbf{w}(k)\right]^{\mathrm{T}}. \end{aligned} \tag{17}$$

For System (16), a Lyapunov function is defined as follows:

$$V_d(\mathbf{x}(k)) = \mathbf{x}^{\mathrm{T}}(k)\mathbf{P}_c\mathbf{x}(k) + \sum_{e=1}^{g}\sum_{\xi=k-\tau_e}^{k-1}\mathbf{x}^{\mathrm{T}}(\xi)\mathbf{Q}_{ec}\mathbf{x}(\xi). \tag{18}$$

Then, based on Lemma 1, we obtain the following $\Delta V_d(\mathbf{x}(k))$:

$$\begin{aligned} \Delta V_d(\mathbf{x}(k)) &= V_d(\mathbf{x}(k+1)) - V_d(\mathbf{x}(k)) \\ &= \mathbf{x}^{\mathrm{T}}(k+1)\mathbf{P}_c\mathbf{x}(k+1) - \mathbf{x}^{\mathrm{T}}(k)\mathbf{P}_c\mathbf{x}(k) + \sum_{e=1}^{g}\left[\mathbf{x}^{\mathrm{T}}(k)\mathbf{Q}_{ec}\mathbf{x}(k) - \mathbf{x}^{\mathrm{T}}\left(k-\tau_e\right)\mathbf{Q}_{ec}\mathbf{x}\left(k-\tau_e\right)\right] \\ &= \sum_{i\in L_d}\sum_{j\in L_d} h_i h_j \sum_{p\in L_d}\sum_{q\in L_d} h_p h_q\left[\overline{\mathbf{x}}^{\mathrm{T}}(k)\overline{\mathbf{M}}_{ij}^{\mathrm{T}}\mathbf{P}_c\overline{\mathbf{M}}_{pq}\overline{\mathbf{x}}(k) - \mathbf{x}^{\mathrm{T}}(k)\mathbf{P}_c\mathbf{x}(k)\right] \\ &\quad + \sum_{e=1}^{g}\left[\mathbf{x}^{\mathrm{T}}(k)\mathbf{Q}_{ec}\mathbf{x}(k) - \mathbf{x}^{\mathrm{T}}\left(k-\tau_e\right)\mathbf{Q}_{ec}\mathbf{x}\left(k-\tau_e\right)\right] \\ &= \sum_{i\in L_d}\sum_{j\in L_d} h_i h_j \sum_{p\in L_d}\sum_{q\in L_d} h_p h_q \overline{\mathbf{x}}^{\mathrm{T}}(k)\left(\overline{\mathbf{M}}_{ij}^{\mathrm{T}}\mathbf{P}_c\overline{\mathbf{M}}_{pq} - \overline{\mathbf{P}}\right)\overline{\mathbf{x}}(k) \\ &= \sum_{i\in L_d}\sum_{j\in L_d} h_i h_j \sum_{p\in L_d}\sum_{q\in L_d} h_p h_q \overline{\mathbf{x}}^{\mathrm{T}}(k)\left[\left(\frac{\overline{\mathbf{M}}_{ij} + \overline{\mathbf{M}}_{ji}}{2}\right)^{\mathrm{T}}\mathbf{P}_c\left(\frac{\overline{\mathbf{M}}_{pq} + \overline{\mathbf{M}}_{qp}}{2}\right) - \overline{\mathbf{P}}\right]\overline{\mathbf{x}}(k) \\ &= \sum_{i\in L_d}\sum_{j\in L_d} h_i h_j \sum_{p\in L_d}\sum_{q\in L_d} h_p h_q \overline{\mathbf{x}}^{\mathrm{T}}(k)\left(\overline{\overline{\mathbf{M}}}_{ij}^{\mathrm{T}}\mathbf{P}_c\overline{\overline{\mathbf{M}}}_{pq} - \overline{\mathbf{P}}\right)\overline{\mathbf{x}}(k) \\ &\le \sum_{i\in L_d}\sum_{j\in L_d} h_i h_j \overline{\mathbf{x}}^{\mathrm{T}}(k)\left(\overline{\overline{\mathbf{M}}}_{ij}^{\mathrm{T}}\mathbf{P}_c\overline{\overline{\mathbf{M}}}_{ij} - \overline{\mathbf{P}}\right)\overline{\mathbf{x}}(k), \end{aligned} \tag{19}$$

where

$$\overline{\mathbf{P}} = \begin{bmatrix} \mathbf{P}_c - \sum_{e=1}^{g} \mathbf{Q}_{ec} & * & * \\ \mathbf{0} & \widehat{\mathbf{Q}} & * \\ \mathbf{0} & \mathbf{0} & \mathbf{0} \end{bmatrix},$$
$$\overline{\overline{\mathbf{M}}}_{\mathbf{pq}} = \frac{\overline{\mathbf{M}}_{pq} + \overline{\mathbf{M}}_{qp}}{2}, \tag{20}$$
$$\widehat{\mathbf{Q}} = \mathrm{diag}\{\mathbf{Q}_{1c}, \mathbf{Q}_{2c}, \ldots, \mathbf{Q}_{ec}, \ldots, \mathbf{Q}_{gc}\},$$
$$\overline{\overline{\mathbf{M}}}_{\mathbf{ij}} = \frac{\overline{\mathbf{M}}_{ij} + \overline{\mathbf{M}}_{ji}}{2}.$$

Then, $\Delta V_d(\mathbf{x}(k))$ is described further as

$$\Delta V_d(\mathbf{x}(k)) \le \sum_{i=j, i\in L_d} h_i^2 \overline{\mathbf{x}}^{\mathrm{T}}(k)\left[\overline{\mathbf{M}}_{ii}^{\mathrm{T}}\mathbf{P}_c\overline{\mathbf{M}}_{ii} - \overline{\mathbf{P}}\right]\overline{\mathbf{x}}(k) + 2\sum_{\substack{i<j \\ i\in L_d, j\in L_d}} h_i h_j \overline{\mathbf{x}}^{\mathrm{T}}(k)\left[\overline{\overline{\mathbf{M}}}_{ij}^{\mathrm{T}}\mathbf{P}_c\overline{\overline{\mathbf{M}}}_{ij} - \overline{\mathbf{P}}\right]\overline{\mathbf{x}}(k). \tag{21}$$

For $\mathbf{w}(k) \neq \mathbf{0}$, the H_∞ performance index function is expressed as follows:

$$J_1 = \sum_{k=0}^{N-1}\left[z^{\mathrm{T}}(k)z(k) - \gamma^2\mathbf{w}^{\mathrm{T}}(k)\mathbf{w}(k)\right]. \tag{22}$$

J_1 can be expressed further as

$$J_1 = \sum_{k=0}^{N-1}\left[z^{\mathrm{T}}(k)z(k) - \gamma^2\mathbf{w}^{\mathrm{T}}(k)\mathbf{w}(k) + \Delta V_d(\mathbf{x}(k))\right] - V_d(\mathbf{x}(N)) \le \sum_{k=0}^{N-1}\left[z^{\mathrm{T}}(k)z(k) - \gamma^2\mathbf{w}^{\mathrm{T}}(k)\mathbf{w}(k) + \Delta V_d(\mathbf{x}(k))\right]. \tag{23}$$

After Inequality (21) is introduced into (23), we have

$$J_1 \le \sum_{k=0}^{N-1}\left\{\sum_{i=j, i\in L_d} h_i^2\overline{\mathbf{x}}^{\mathrm{T}}(k)\left[\overline{\mathbf{M}}_{ii}^{\mathrm{T}}\mathbf{P}_c\overline{\mathbf{M}}_{ii} - \overline{\mathbf{P}} + \overline{\mathbf{N}}_{ii}^{\mathrm{T}}\overline{\mathbf{N}}_{ii}\right]\overline{\mathbf{x}}(k)\right\} + 2\sum_{k=0}^{N-1}\left\{\sum_{\substack{i<j, i\in L_d \\ j\in L_d}} h_i h_j \overline{\mathbf{x}}^{\mathrm{T}}(k)\left[\overline{\overline{\mathbf{M}}}_{ij}^{\mathrm{T}}\mathbf{P}_c\overline{\overline{\mathbf{M}}}_{ij} - \overline{\overline{\mathbf{P}}} + \overline{\overline{\mathbf{N}}}_{ij}^{\mathrm{T}}\overline{\overline{\mathbf{N}}}_{ij}\right]\overline{\mathbf{x}}(k)\right\}, \tag{24}$$

where

$$\overline{\overline{\mathbf{P}}} = \begin{bmatrix} \mathbf{P}_c - \sum_{e=1}^{g} \mathbf{Q}_{\mathrm{ec}} & * & * \\ \mathbf{0} & \widehat{\mathbf{Q}} & * \\ \mathbf{0} & \mathbf{0} & \gamma^2\mathbf{I} \end{bmatrix},$$
$$\overline{\overline{\mathbf{N}}}_{\mathbf{ij}} = \frac{\overline{\mathbf{N}}_{ij} + \overline{\mathbf{N}}_{ji}}{2}. \tag{25}$$

By the Schur complement, we have $\overline{\mathbf{M}}_{ii}^{\mathrm{T}}\mathbf{P}_c\overline{\mathbf{M}}_{ii} - \overline{\overline{\mathbf{P}}} + \overline{\mathbf{N}}_{ii}^{\mathrm{T}}\overline{\mathbf{N}}_{ii} < \mathbf{0}$ and $\overline{\overline{\mathbf{M}}}_{ij}^{\mathrm{T}}\mathbf{P}_c\overline{\overline{\mathbf{M}}}_{ij} - \overline{\overline{\mathbf{P}}} + \overline{\overline{\mathbf{N}}}_{ij}^{\mathrm{T}}\overline{\overline{\mathbf{N}}}_{ij} < \mathbf{0}$ which are equivalent to Inequalities (12) and (13), then $J_1 < 0$ holds, i.e., $z^{\mathrm{T}}(k)z(k) < \gamma^2\mathbf{w}^{\mathrm{T}}(k)\mathbf{w}(k)$; furthermore, if let $N \longrightarrow +\infty$, $\|z(k)\|_2^2 < \gamma^2\|\mathbf{w}(k)\|_2^2$ holds. Therefore, CLSC system (16) is asymptotically stable under $\mathbf{w}(k) \neq \mathbf{0}$.

If $\mathbf{w}(k) \equiv \mathbf{0}$, Inequality (21) can be expressed as

$$\Delta V_d(\mathbf{x}(k)) \le \sum_{i=j, i\in L_d} h_i^2\overline{\mathbf{x}}^{\mathrm{T}}(k)\left[\overline{\mathbf{M}}_{ii}^{\mathrm{T}}\mathbf{P}_c\overline{\mathbf{M}}_{ii} - \overline{\overline{\mathbf{P}}}\right]\overline{\mathbf{x}}(k) + 2\sum_{\substack{i<j \\ i\in L_d, j\in L_d}} h_i h_j \overline{\mathbf{x}}^{\mathrm{T}}(k)\left[\overline{\overline{\mathbf{M}}}_{ij}^{\mathrm{T}}\mathbf{P}_c\overline{\overline{\mathbf{M}}}_{ij} - \overline{\overline{\mathbf{P}}}\right]\overline{\mathbf{x}}(k). \tag{26}$$

Based on Inequalities (12) and (13), we have $\overline{\mathbf{M}}_{ii}^{\mathrm{T}}\mathbf{P}_c\overline{\mathbf{M}}_{ii} - \overline{\overline{\mathbf{P}}} < \mathbf{0}$ and $\overline{\overline{\mathbf{M}}}_{ij}^{\mathrm{T}}\mathbf{P}_c\overline{\overline{\mathbf{M}}}_{ij} - \overline{\overline{\mathbf{P}}} < \mathbf{0}$, and then $\Delta V_d(\mathbf{x}(k)) < 0$ can be obtained. Therefore, CLSC system (16) is robustly asymptotically stable under $\mathbf{w}(k) \equiv \mathbf{0}$.

(2) The second part of the proof:

For $\mathbf{x}(k)$ and $\mathbf{x}(k+1)$ in the different ORGs, we first construct the following characteristic function in any ORG:

$$\lambda_d = \begin{cases} 1, & \mathbf{x}(k) \in \nu_d, \\ 0, & \mathbf{x}(k) \notin \nu_d, \end{cases}$$
$$\sum_{d=1}^{f}\lambda_d = 1. \tag{27}$$

Then, the overall system of local system (16) can be expressed as

$$\begin{cases} \mathbf{x}(k+1) = \sum_{d=1}^{f}\lambda_d\left[\sum_{i\in L_d}\sum_{j\in L_d} h_i h_j \overline{\mathbf{M}}_{ij}\overline{\mathbf{x}}(k)\right], \\ z(k) = \sum_{d=1}^{f}\lambda_d\left[\sum_{i\in L_d}\sum_{j\in L_d} h_i h_j \overline{\mathbf{N}}_{ij}\overline{\mathbf{x}}(k)\right]. \end{cases} \tag{28}$$

After $\mathbf{P}_m = \sum_{d=1}^{f}\lambda_d\mathbf{P}_c$ and $\mathbf{Q}_{em} = \sum_{d=1}^{f}\lambda_d\mathbf{Q}_{ec}$ are defined, we present the following Lyapunov function:

$$\begin{aligned} V(\mathbf{x}(k)) &= \mathbf{x}^{\mathrm{T}}(k)\mathbf{P}_m\mathbf{x}(k) + \sum_{e=1}^{g}\sum_{\xi=k-\tau_e}^{k-1}\mathbf{x}^{\mathrm{T}}(\xi)\mathbf{Q}_{em}\mathbf{x}(\xi) \\ &= \mathbf{x}^{\mathrm{T}}(k)\left(\sum_{d=1}^{f}\lambda_d\mathbf{P}_c\right)\mathbf{x}(k) + \sum_{e=1}^{g}\sum_{\xi=k-\tau_e}^{k-1}\mathbf{x}^{\mathrm{T}}(\xi)\left(\sum_{d=1}^{f}\lambda_d\mathbf{Q}_{ec}\right)\mathbf{x}(\xi) \\ &= \sum_{d=1}^{f}\lambda_d\left[\mathbf{x}^{\mathrm{T}}(k)\mathbf{P}_c\mathbf{x}(k) + \sum_{e=1}^{g}\sum_{\xi=k-\tau_e}^{k-1}\mathbf{x}^{\mathrm{T}}(\xi)\mathbf{Q}_{ec}\mathbf{x}(\xi)\right] \\ &= \sum_{d=1}^{f}\lambda_d V_d(\mathbf{x}(k)). \end{aligned} \tag{29}$$

For $\mathbf{w}(k) \neq \mathbf{0}$ in System (28), considering $J_1 = \sum_{k=0}^{N-1}[z^{\mathrm{T}}(k)z(k) - \gamma^2\mathbf{w}^{\mathrm{T}}(k)\mathbf{w}(k)]$, we know $J_2 = \sum_{k=0}^{N-1}\sum_{d=1}^{f}\lambda_d[z^{\mathrm{T}}(k)z(k) - \gamma^2\mathbf{w}^{\mathrm{T}}(k)\mathbf{w}(k)]$. In the same

way, we have $J_2 < 0$, i.e., $z^{\mathrm{T}}(k)z(k) < \gamma^2 \mathbf{w}^{\mathrm{T}}(k)\mathbf{w}(k)$; if let $N \longrightarrow +\infty$, $\|z(k)\|_2^2 < \gamma^2 \|\mathbf{w}(k)\|_2^2$ can be obtained. Therefore, System (28) is asymptotically stable under $\mathbf{w}(k) \neq \mathbf{0}$.

For $\mathbf{w}(k) \equiv \mathbf{0}$ in System (28), we have

$$\begin{aligned}\Delta V(\mathbf{x}(k)) &= V(\mathbf{x}(k+1)) - V(\mathbf{x}(k)) \\ &= \sum_{d=1}^{f} \lambda_d V_d(\mathbf{x}(k+1)) - \sum_{d=1}^{f} \lambda_d V_d(\mathbf{x}(k)) \\ &= \sum_{d=1}^{f} \lambda_d \left[V_d(\mathbf{x}(k+1)) - V_d(\mathbf{x}(k))\right] \\ &= \sum_{d=1}^{f} \lambda_d \Delta V_d(\mathbf{x}(k)) < 0.\end{aligned} \tag{30}$$

Therefore, System (28) under $\mathbf{w}(k) \equiv \mathbf{0}$ is asymptotically stable in any ORG.

From Proposition 1, CLSC system (10) is robustly asymptotically stable if $\mathbf{P}_c$ and $\mathbf{Q}_{ac}$ can be solved in Inequalities (12) and (13) **Q.E.D.**

In order for Inequalities (12) and (13) to be easily solvable LMIs, we transform Theorem 1 into the following Theorem 2. □

Theorem 2. *System (10) with a certain γ and fuzzy sets of inventories satisfying standard fuzzy partitions is robustly asymptotically stable if local common positive definite matrices $\mathbf{P}_c$ and $\mathbf{Q}_{\mathrm{ec}}$, matrices $\mathbf{K}_{ic}$, $\mathbf{K}_{jc}$, $\mathbf{K}_{iec}$, and $\mathbf{K}_{jec}$, and constants $\varepsilon_{ijc} > 0$ and $\varepsilon_{jic} > 0$ can be found in the following Inequalities (31) and (32):*

$$\begin{bmatrix} -\mathbf{P}_c + \sum_{e=1}^{g} \mathbf{Q}_{\mathrm{ec}} & * & * & * & * & * & * \\ \mathbf{0} & -\widehat{\mathbf{Q}} & * & * & * & * & * \\ \mathbf{0} & \mathbf{0} & -\gamma^2\mathbf{I} & * & * & * & * \\ \Omega_1 & -\Omega_3 & \mathbf{B}_{wi} & -\mathbf{I} + \varepsilon_{iic}\mathbf{H}_{1i}\mathbf{H}_{1i}^{\mathrm{T}} & * & * & * \\ \Omega_2 & -\Omega_4 & \mathbf{0} & \mathbf{0} & -\mathbf{I} + \varepsilon_{iic}\mathbf{H}_{2i}\mathbf{H}_{2i}^{\mathrm{T}} & * & * \\ \Delta_1 & -\Delta_3 & \mathbf{E}_{13i} & \mathbf{0} & \mathbf{0} & -\varepsilon_{iic}\mathbf{I} & * \\ \Delta_2 & -\Delta_4 & \mathbf{0} & \mathbf{0} & \mathbf{0} & \mathbf{0} & -\varepsilon_{iic}\mathbf{I} \end{bmatrix} < 0, \quad i \in \mathbf{I}_c, \tag{31}$$

$$\begin{bmatrix} -4\mathbf{P}_c + 4\sum_{e=1}^{g} \mathbf{Q}_{ec} & * & * & * & * & * & * & * & * \\ \mathbf{0} & -4\widehat{\mathbf{Q}} & * & * & * & * & * & * & * \\ \mathbf{0} & \mathbf{0} & -4\gamma^2\mathbf{I} & * & * & * & * & * & * \\ \Omega_5 & -\Omega_7 & \mathbf{B}_{wi} + \mathbf{B}_{wj} & \Delta_{11} & * & * & * & * & * \\ \Omega_6 & -\Omega_8 & \mathbf{0} & \mathbf{0} & \Delta_{12} & * & * & * & * \\ \Delta_5 & -\Delta_3 & \mathrm{E}_{13i} & \mathbf{0} & \mathbf{0} & -\varepsilon_{ijc}\mathbf{I} & * & * & * \\ \Delta_6 & -\Delta_4 & \mathbf{0} & \mathbf{0} & \mathbf{0} & \mathbf{0} & -\varepsilon_{ijc}\mathbf{I} & * & * \\ \Delta_7 & -\Delta_9 & \mathrm{E}_{13j} & \mathbf{0} & \mathbf{0} & \mathbf{0} & \mathbf{0} & -\varepsilon_{jic}\mathbf{I} & * \\ \Delta_8 & -\Delta_{10} & \mathbf{0} & \mathbf{0} & \mathbf{0} & \mathbf{0} & \mathbf{0} & \mathbf{0} & -\varepsilon_{jic}\mathbf{I} \end{bmatrix} < \mathbf{0}, \quad i < j, i, j \in I_c, \tag{32}$$

where

$$
\begin{aligned}
\widehat{\mathbf{Q}} &= \operatorname{diag}\left\{\mathbf{Q}_{1c}, \ldots, \mathbf{Q}_{ec}, \ldots, \mathbf{Q}_{gc}\right\},\\
\Omega_1 &= \mathbf{A}_i - \mathbf{B}_i\mathbf{K}_{ic},\\
\Omega_2 &= \mathbf{C}_i - \mathbf{D}_i\mathbf{K}_{ic},\\
\Omega_3 &= \mathbf{B}_{i1}\mathbf{K}_{i1c}, \ldots, \mathbf{B}_{ie}\mathbf{K}_{iec}, \ldots, \mathbf{B}_{ig}\mathbf{K}_{igc},\\
\Omega_4 &= \left[\mathbf{D}_{i1}\mathbf{K}_{i1c}, \ldots, \mathbf{D}_{ie}\mathbf{K}_{iec}, \ldots, \mathbf{D}_{\mathrm{ig}}\mathbf{K}_{igc}\right],\\
\Omega_5 &= \mathbf{A}_i - \mathbf{B}_i\mathbf{K}_{jc} + \mathbf{A}_j - \mathbf{B}_j\mathbf{K}_{ic},\\
\Omega_6 &= \mathbf{C}_i - \mathbf{D}_i\mathbf{K}_{jc} + \mathbf{C}_j - \mathbf{D}_j\mathbf{K}_{ic},\\
\Omega_7 &= \left[\mathbf{B}_{i1}\mathbf{K}_{j1c} + \mathbf{B}_{j1}\mathbf{K}_{i1c}, \ldots, \mathbf{B}_{ie}\mathbf{K}_{jec} + \mathbf{B}_{je}\mathbf{K}_{iec}, \ldots, \mathbf{B}_{ig}\mathbf{K}_{jgc} + \mathbf{B}_{jg}\mathbf{K}_{igc}\right],\\
\Omega_8 &= \left[\mathbf{D}_{i1}\mathbf{K}_{j1c} + \mathbf{D}_{j1}\mathbf{K}_{i1c}, \ldots, \mathbf{D}_{ie}\mathbf{K}_{jec} + \mathbf{D}_{je}\mathbf{K}_{iec}, \ldots, \mathbf{D}_{ig}\mathbf{K}_{jgc} + \mathbf{D}_{\mathrm{jg}}\mathbf{K}_{igc}\right],\\
\Delta_1 &= \mathbf{E}_{11i} - \mathbf{E}_{12i}\mathbf{K}_{ic},\\
\Delta_2 &= \mathbf{E}_{21i} - \mathbf{E}_{22i}\mathbf{K}_{ic},\\
\Delta_3 &= \left[\mathbf{L}_{1i}\mathbf{K}_{i1c}, \ldots, \mathbf{L}_{ei}\mathbf{K}_{iec}, \ldots, \mathbf{L}_{gi}\mathbf{K}_{igc}\right],\\
\Delta_4 &= \left[\mathbf{O}_{1i}\mathbf{K}_{i1c}, \ldots, \mathbf{O}_{ei}\mathbf{K}_{iec}, \ldots, \mathbf{O}_{gi}\mathbf{K}_{igc}\right],\\
\Delta_5 &= \mathbf{E}_{11i} - \mathbf{E}_{12i}\mathbf{K}_{jc},\\
\Delta_6 &= \mathbf{E}_{21i} - \mathbf{E}_{22i}\mathbf{K}_{jc},\\
\Delta_7 &= \mathbf{E}_{11j} - \mathbf{E}_{12j}\mathbf{K}_{ic},\\
\Delta_8 &= \mathbf{E}_{21j} - \mathbf{E}_{22j}\mathbf{K}_{ic},\\
\Delta_9 &= \left[\mathbf{L}_{1j}\mathbf{K}_{jic}, \ldots, \mathbf{L}_{ej}\mathbf{K}_{jec}, \ldots, \mathbf{L}_{gj}\mathbf{K}_{jgc}\right],\\
\Delta_{10} &= \left[\mathbf{O}_{1j}\mathbf{K}_{j1c}, \ldots, \mathbf{O}_{ej}\mathbf{K}_{jec}, \ldots, \mathbf{O}_{\mathrm{gj}}\mathbf{K}_{jgc}\right],\\
\Delta_{11} &= -\mathbf{I}_c + \varepsilon_{ijc}\mathbf{H}_{1i}\mathbf{H}_{1i}^{\mathrm{T}} + \varepsilon_{jic}\mathbf{H}_{1j}\mathbf{H}_{1j}^{\mathrm{T}},\\
\Delta_{12} &= -\mathbf{I} + \varepsilon_{ijc}\mathbf{H}_{2i}\mathbf{H}_{2i}^{\mathrm{T}} + \varepsilon_{jic}\mathbf{H}_{2j}\mathbf{H}_{2j}^{\mathrm{T}}.
\end{aligned}
\tag{33}
$$

Proof. Theorem 2 can be proved in the same idea as Theorem 1. Therefore, the proof process of Theorem 2 is not shown. **Q.E.D.** □

5. Simulation Analysis

We choose a type of television CLSC composed of a television manufacturer, a television retailer, and a 3PRP as the simulation object to evaluate the mitigation effect of the BE under the FRC approach proposed in Section 4.

The television manufacturer's fuzzy membership functions and the television retailer's fuzzy membership functions are shown in Figure 2. In Figure 2, both $F_1^t(x_1(k))$ and $F_2^s(x_2(k))$ satisfy the conditions of standard fuzzy partition. We set $M_1^1 = M_1^2 = F_1^1$, $M_1^3 = M_1^4 = F_1^2$, $M_2^1 = M_2^4 = F_2^1$, and $M_2^2 = M_2^3 = F_2^2$.

From Figure 2, we know there are 4 fuzzy rules included in one MORG called S. Referring to the product-design strategies in [25], we apply 4 fuzzy rules to describe the manufacturer's production patterns and the retailer's ordering patterns for the different inventory levels as follows:

R_1: the television manufacturer produces new televisions and remanufactures recycled televisions simultaneously. The television retailer allows return of new televisions and orders new televisions simultaneously.

R_2: the television manufacturer produces new televisions and remanufactures recycled televisions simultaneously. The television retailer only allows return of new televisions.

R_3: the television manufacturer only remanufactures recycled televisions. The television retailer only allows return of new televisions.

R_4: the television manufacturer only remanufactures recycled televisions. The television retailer allows return of new televisions and orders new televisions simultaneously.

Therefore, under the different rules, the uncertain CLSC model with hybrid recycling channels and lead times can be expressed as follows:

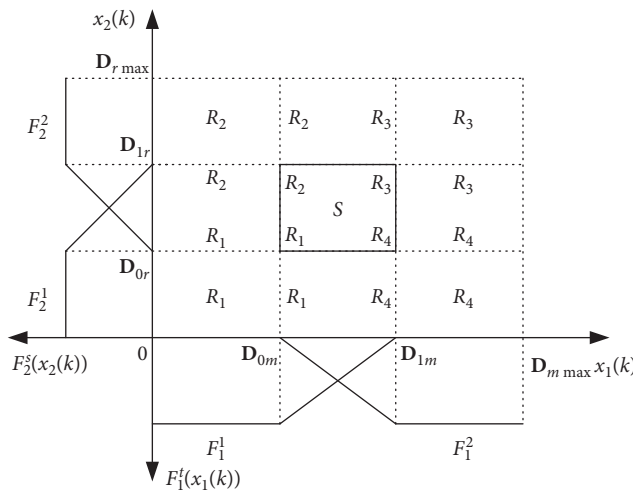

Figure 2: Fuzzy membership functions.

$$R_1:\begin{cases} x_1(k+1) = x_1(k) + u_1(k) + u_1(k-\tau_1) + u_3(k) + u_3(k-\tau_3) + (\eta+\Delta\eta)x_4(k) - u_2(k), \\ x_2(k+1) = x_2(k) + u_2(k) + u_2(k-\tau_2) + (\mu+\Delta\mu)x_3(k) - w_1(k), \\ x_3(k+1) = x_3(k) + w_1(k) - u_3(k) - u_4(k) - (\mu+\Delta\mu)x_3(k), \\ x_4(k+1) = x_4(k) + u_4(k) + u_4(k-\tau_4) - (\eta+\Delta\eta)x_4(k) - (\lambda+\Delta\lambda)x_4(k), \end{cases}$$

$$\begin{aligned} z(k) = {} & (c_{h1}+\Delta c_{h1})x_1(k) + (c_{h2}+\Delta c_{h2})x_2(k) \\ & + (c_{h3}+\Delta c_{h3})x_4(k) + (c_n+\Delta c_n)[u_1(k) + u_1(k-\tau_1)] \\ & + (c_r+\Delta c_r)[u_3(k) + u_3(k-\tau_3) + (\eta+\Delta\eta)x_4(k)] \\ & + (c_m+\Delta c_m)[u_3(k) + u_3(k-\tau_3)] + (c_t+\Delta c_t)[u_4(k) + u_4(k-\tau_4)] \\ & + (c_{mt}+\Delta c_{mt})(\eta+\Delta\eta)x_4(k) + (c_q+\Delta c_q)(\mu+\Delta\mu)x_3(k) \\ & + (c_d+\Delta c_d)(\lambda+\Delta\lambda)x_4(k) + (c_s+\Delta c_s)[u_2(k) + u_2(k-\tau_2)], \end{aligned}$$

$$R_2:\begin{cases} x_1(k+1) = x_1(k) + u_1(k) + u_1(k-\tau_1) + u_3(k) + u_3(k-\tau_3) + (\eta+\Delta\eta)x_4(k), \\ x_2(k+1) = x_2(k) + (\mu+\Delta\mu)x_3(k) - w_1(k), \\ x_3(k+1) = x_3(k) + w_1(k) - u_3(k) - u_4(k) - (\mu+\Delta\mu)x_3(k), \\ x_4(k+1) = x_4(k) + u_4(k) + u_4(k-\tau_4) - (\eta+\Delta\eta)x_4(k) - (\lambda+\Delta\lambda)x_4(k), \end{cases}$$

$$\begin{aligned} z(k) = {} & (c_{h1}+\Delta c_{h1})x_1(k) + (c_{h2}+\Delta c_{h2})x_2(k) + (c_{h3}+\Delta c_{h3})x_4(k) \\ & + (c_n+\Delta c_n)[u_1(k) + u_1(k-\tau_1)] + (c_r+\Delta c_r)[u_3(k) + u_3(k-\tau_3) + (\eta+\Delta\eta)x_4(k)] \\ & + (c_m+\Delta c_m)[u_3(k) + u_3(k-\tau_3)] + (c_t+\Delta c_t)[u_4(k) + u_4(k-\tau_4)] + (c_{mt}+\Delta c_{mt})(\eta+\Delta\eta)x_4(k) \\ & + (c_q+\Delta c_q)(\mu+\Delta\mu)x_3(k) + (c_d+\Delta c_d)(\lambda+\Delta\lambda)x_4(k), \end{aligned}$$

$$R_3:\begin{cases} x_1(k+1) = x_1(k) + u_3(k) + u_3(k-\tau_3) + (\eta+\Delta\eta)x_4(k), \\ x_2(k+1) = x_2(k) + (\mu+\Delta\mu)x_3(k) - w_1(k), \\ x_3(k+1) = x_3(k) + w_1(k) - u_3(k) - u_4(k) - (\mu+\Delta\mu)x_3(k), \\ x_4(k+1) = x_4(k) + u_4(k) + u_4(k-\tau_4) - (\eta+\Delta\eta)x_4(k) - (\lambda+\Delta\lambda)x_4(k), \end{cases}$$

$$\begin{aligned} z(k) = {} & (c_{h1}+\Delta c_{h1})x_1(k) + (c_{h2}+\Delta c_{h2})x_2(k) + (c_{h3}+\Delta c_{h3})x_4(k) \\ & + (c_r+\Delta c_r)[u_3(k) + u_3(k-\tau_3) + (\eta+\Delta\eta)x_4(k)] \\ & + (c_m+\Delta c_m)[u_3(k) + u_3(k-\tau_3)] + (c_t+\Delta c_t)[u_4(k) + u_4(k-\tau_4)] \\ & + (c_{mt}+\Delta c_{mt})(\eta+\Delta\eta)x_4(k) + (c_q+\Delta c_q)(\mu+\Delta\mu)x_3(k) \\ & + (c_d+\Delta c_d)(\lambda+\Delta\lambda)x_4(k), \end{aligned}$$

$$R_4:\begin{cases} x_1(k+1) = x_1(k) + u_3(k) + u_3(k-\tau_3) + (\eta+\Delta\eta)x_4(k) - u_2(k), \\ x_2(k+1) = x_2(k) + u_2(k) + u_2(k-\tau_2) + (\mu+\Delta\mu)x_3(k) - w_1(k), \\ x_3(k+1) = x_3(k) + w_1(k) - u_3(k) - u_4(k) - (\mu+\Delta\mu)x_3(k), \\ x_4(k+1) = x_4(k) + u_4(k) + u_4(k-\tau_4) - (\eta+\Delta\eta)x_4(k) - (\lambda+\Delta\lambda)x_4(k). \end{cases}$$

$$\begin{aligned} z(k) = {} & (c_{h1} + \Delta c_{h1})x_1(k) + (c_{h2} + \Delta c_{h2})x_2(k) + (c_{h3} + \Delta c_{h3})x_4(k) \\ & + (c_r + \Delta c_r)[u_3(k) + u_3(k - \tau_3)] + (\eta + \Delta\eta)x_4(k)] \\ & + (c_m + \Delta c_m)[u_3(k) + u_3(k - \tau_3)] + (c_t + \Delta c_t)[u_4(k) + u_4(k - \tau_4)] \\ & + (c_{mt} + \Delta c_{mt})(\eta + \Delta\eta)x_4(k) \\ & + \left(c_q + \Delta c_q\right)(\mu + \Delta\mu)x_3(k) + (c_d + \Delta c_d)(\lambda + \Delta\lambda)x_4(k) \\ & + (c_s + \Delta c_s)[u_2(k) + u_2(k - \tau_2)] \end{aligned} \tag{34}$$

Furthermore, the fuzzy CLSC model can be obtained as follows:

R_1: If x_1 is M_1^1 and x_2 is M_2^1, then

$$\begin{cases} \mathbf{x}(k+1) = h_1\left[(\mathbf{A}_1 + \Delta\mathbf{A}_1)\mathbf{x}(k) + (\mathbf{B}_1 + \Delta\mathbf{B}_1)\mathbf{u}(k) + \sum_{e=1}^{4}(\mathbf{B}_{1e} + \Delta\mathbf{B}_{1e})\mathbf{u}(k - \tau_e) + (\mathbf{B}_{w1} + \Delta\mathbf{B}_{w1})\mathbf{w}(k)\right], \\ z(k) = h_1\left[(\mathbf{C}_1 + \Delta\mathbf{C}_1)\mathbf{x}(k) + (\mathbf{D}_1 + \Delta\mathbf{D}_1)\mathbf{u}(k) + \sum_{e=1}^{4}(\mathbf{D}_{1e} + \Delta\mathbf{D}_{1e})\mathbf{u}(k - \tau_e)\right]. \end{cases} \tag{35}$$

R_2: If x_1 is M_1^2 and x_2 is M_2^2, then

$$\begin{cases} \mathbf{x}(k+1) = h_2\left[(\mathbf{A}_2 + \Delta\mathbf{A}_2)\mathbf{x}(k) + (\mathbf{B}_2 + \Delta\mathbf{B}_2)\mathbf{u}(k) + \sum_{e=1}^{4}(\mathbf{B}_{2e} + \Delta\mathbf{B}_{2e})\mathbf{u}(k - \tau_e) + (\mathbf{B}_{w2} + \Delta\mathbf{B}_{w2})\mathbf{w}(k)\right], \\ z(k) = h_2\left[(\mathbf{C}_2 + \Delta\mathbf{C}_2)\mathbf{x}(k) + (\mathbf{D}_2 + \Delta\mathbf{D}_2)\mathbf{u}(k) + \sum_{e=1}^{4}(\mathbf{D}_{2e} + \Delta\mathbf{D}_{2e})\mathbf{u}(k - \tau_e)\right]. \end{cases} \tag{36}$$

R_3: If x_1 is M_1^3 and x_2 is M_2^3, then

$$\begin{cases} \mathbf{x}(k+1) = h_3\left[(\mathbf{A}_3 + \Delta\mathbf{A}_3)\mathbf{x}(k) + (\mathbf{B}_3 + \Delta\mathbf{B}_3)\mathbf{u}(k) + \sum_{e=1}^{4}(\mathbf{B}_{3e} + \Delta\mathbf{B}_{3e})\mathbf{u}(k - \tau_e) + (\mathbf{B}_{w3} + \Delta\mathbf{B}_{w3})\mathbf{w}(k)\right], \\ z(k) = h_3\left[(\mathbf{C}_3 + \Delta\mathbf{C}_3)\mathbf{x}(k) + (\mathbf{D}_3 + \Delta\mathbf{D}_3)\mathbf{u}(k) + \sum_{e=1}^{4}(\mathbf{D}_{3e} + \Delta\mathbf{D}_{3e})\mathbf{u}(k - \tau_e)\right]. \end{cases} \tag{37}$$

R_4: If x_1 is M_1^4 and x_2 is M_2^4, then

$$\begin{cases} \mathbf{x}(k+1) = h_4\left[(\mathbf{A}_4 + \Delta\mathbf{A}_4)\mathbf{x}(k) + (\mathbf{B}_4 + \Delta\mathbf{B}_4)\mathbf{u}(k) + \sum_{e=1}^{4}(\mathbf{B}_{4e} + \Delta\mathbf{B}_{4e})\mathbf{u}(k - \tau_e) + (\mathbf{B}_{w4} + \Delta\mathbf{B}_{w4})\mathbf{w}(k)\right], \\ z(k) = h_4\left[(\mathbf{C}_4 + \Delta\mathbf{C}_4)\mathbf{x}(k) + (\mathbf{D}_4 + \Delta\mathbf{D}_4)\mathbf{u}(k) + \sum_{e=1}^{4}(\mathbf{D}_{4e} + \Delta\mathbf{D}_{4e})\mathbf{u}(k - \tau_e)\right]. \end{cases} \tag{38}$$

According to the Takagi–Sugeno fuzzy models mentioned above, we design the following fuzzy feedback controller.

K^i: If $x_1(k)$ is M_1^i and $x_2(k)$ is M_2^i, then

$$\begin{cases} \mathbf{u}(k) = -\sum_{i=1}^{4} h_i\mathbf{K}_{i1}\mathbf{x}(k), \\ \mathbf{u}(k - \tau_1) = -\sum_{i=1}^{4} h_i\mathbf{K}_{i11}\mathbf{x}(k - \tau_1), \\ \mathbf{u}(k - \tau_2) = -\sum_{i=1}^{4} h_i\mathbf{K}_{i21}\mathbf{x}(k - \tau_2), \\ \mathbf{u}(k - \tau_3) = -\sum_{i=1}^{4} h_i\mathbf{K}_{i31}\mathbf{x}(k - \tau_3), \\ \mathbf{u}(k - \tau_4) = -\sum_{i=1}^{4} h_i\mathbf{K}_{i41}\mathbf{x}(k - \tau_4). \end{cases} \tag{39}$$

Considering the actual operation situation of the television CLSC, we set $D_{0m} = 120$, $D_{1m} = 160$, $D_{0r} = 110$, and $D_{1r} = 155$ ($\times 10^3$ sets); $c_{h1} = 0.015$, $c_{h2} = 0.020$, $c_{h3} = 0.015$, $c_n = 0.150$, $c_r = 0.005$, $c_m = 0.100$, $c_{mt} = 0.100$, $c_t = 0.095$, $c_q = 0.020$, $c_d = 0.007$, $c_s = 0.180$ ($\times 10^3$ Yuan); $\eta = 0.98$, $\mu = 0.01$, and $\lambda = 0.02$.

$$\mathbf{A}_1 = \mathbf{A}_2 = \mathbf{A}_3 = \mathbf{A}_4 = \begin{bmatrix} 1 & 0 & 0 & 0.98 \\ 0 & 1 & 0.01 & 0 \\ 0 & 0 & 0.99 & 0 \\ 0 & 0 & 0 & 0 \end{bmatrix},$$

$$\mathbf{B}_1 = \begin{bmatrix} 1 & -1 & 1 & 0 \\ 0 & 1 & 0 & 0 \\ 0 & 0 & -1 & -1 \\ 0 & 0 & 0 & 1 \end{bmatrix},$$

$$\mathbf{B}_2 = \begin{bmatrix} 1 & 0 & 1 & 0 \\ 0 & 0 & 0 & 0 \\ 0 & 0 & -1 & -1 \\ 0 & 0 & 0 & 1 \end{bmatrix},$$

$$\mathbf{B}_3 = \begin{bmatrix} 0 & 0 & 1 & 0 \\ 0 & 0 & 0 & 0 \\ 0 & 0 & -1 & -1 \\ 0 & 0 & 0 & 1 \end{bmatrix},$$

$$\mathbf{B}_4 = \begin{bmatrix} 0 & -1 & 1 & 0 \\ 0 & 1 & 0 & 0 \\ 0 & 0 & -1 & -1 \\ 0 & 0 & 0 & 1 \end{bmatrix},$$

$$\mathbf{B}_{11} = \mathbf{B}_{21} = \begin{bmatrix} 1 & 0 & 0 & 0 \\ 0 & 0 & 0 & 0 \\ 0 & 0 & 0 & 0 \\ 0 & 0 & 0 & 0 \end{bmatrix},$$

$$\mathbf{B}_{31} = \mathbf{B}_{41} = \begin{bmatrix} 0 & 0 & 0 & 0 \\ 0 & 0 & 0 & 0 \\ 0 & 0 & 0 & 0 \\ 0 & 0 & 0 & 0 \end{bmatrix},$$

$$\mathbf{B}_{12} = \mathbf{B}_{42} = \begin{bmatrix} 0 & 0 & 0 & 0 \\ 0 & 1 & 0 & 0 \\ 0 & 0 & 0 & 0 \\ 0 & 0 & 0 & 0 \end{bmatrix},$$

$$\mathbf{B}_{22} = \mathbf{B}_{32} = \begin{bmatrix} 0 & 0 & 0 & 0 \\ 0 & 0 & 0 & 0 \\ 0 & 0 & 0 & 0 \\ 0 & 0 & 0 & 0 \end{bmatrix},$$

$$\mathbf{B}_{13} = \mathbf{B}_{23} = \mathbf{B}_{33} = \mathbf{B}_{43} = \begin{bmatrix} 0 & 0 & 1 & 0 \\ 0 & 0 & 0 & 0 \\ 0 & 0 & 0 & 0 \\ 0 & 0 & 0 & 0 \end{bmatrix},$$

$$\mathbf{B}_{14} = \mathbf{B}_{24} = \mathbf{B}_{34} = \mathbf{B}_{44} = \begin{bmatrix} 0 & 0 & 0 & 0 \\ 0 & 0 & 0 & 0 \\ 0 & 0 & 0 & 0 \\ 0 & 0 & 0 & 1 \end{bmatrix},$$

$$\mathbf{B}_{w1} = \mathbf{B}_{w2} = \mathbf{B}_{w3} = \mathbf{B}_{w4} = \begin{bmatrix} 0 & 0 & 0 & 0 \\ -1 & 0 & 0 & 0 \\ 1 & 0 & 0 & 0 \\ 0 & 0 & 0 & 0 \end{bmatrix}, \tag{40}$$

$$\mathbf{C}_1 = \mathbf{C}_2 = \mathbf{C}_3 = \mathbf{C}_4 = \begin{bmatrix} c_{h1} & c_{h2} & \mu c_q & c_{h3} + \eta c_r + \eta c_{mt} + \lambda c_d \end{bmatrix},$$

$$\mathbf{D}_1 = \begin{bmatrix} c_n & c_s & c_r + c_m & c_t \end{bmatrix},$$

$$\mathbf{D}_2 = \begin{bmatrix} c_n & 0 & c_r + c_m & c_t \end{bmatrix},$$

$$\mathbf{D}_3 = \begin{bmatrix} 0 & 0 & c_r + c_m & c_t \end{bmatrix},$$

$$\mathbf{D}_4 = \begin{bmatrix} 0 & c_s & c_r + c_m & c_t \end{bmatrix},$$

$$\mathbf{D}_{11} = \mathbf{D}_{21} = \begin{bmatrix} c_n & 0 & 0 & 0 \end{bmatrix},$$

$$\mathbf{D}_{31} = \mathbf{D}_{41} = \begin{bmatrix} 0 & 0 & 0 & 0 \end{bmatrix},$$

$$\mathbf{D}_{12} = \mathbf{D}_{42} = \begin{bmatrix} 0 & c_s & 0 & 0 \end{bmatrix},$$

$$\mathbf{D}_{22} = \mathbf{D}_{32} = \begin{bmatrix} 0 & 0 & 0 & 0 \end{bmatrix},$$

$$\mathbf{D}_{13} = \mathbf{D}_{23} = \mathbf{D}_{33} = \mathbf{D}_{43} = \begin{bmatrix} 0 & 0 & c_r + c_m & 0 \end{bmatrix},$$

$$\mathbf{D}_{14} = \mathbf{D}_{24} = \mathbf{D}_{34} = \mathbf{D}_{44} = \begin{bmatrix} 0 & 0 & 0 & c_t \end{bmatrix},$$

$$\mathbf{E}_{11i} = \begin{bmatrix} 0 & 0 & 0 & 0.02 \\ 0 & 0 & 0.02 & 0 \\ 0 & 0 & -0.02 & 0 \\ 0 & 0 & 0 & -0.03 \end{bmatrix},$$

$$\mathbf{E}_{12i} = \mathbf{E}_{13i} = \mathbf{0},$$

$$\mathbf{L}_{1i} = \mathbf{L}_{2i} = \mathbf{L}_{3i} = \mathbf{L}_{4i} = \mathbf{0},$$

$$\mathbf{E}_{21i} = \begin{bmatrix} 0.004 & 0.004 & 0.002 & 0.007 \end{bmatrix},$$

$$\mathbf{E}_{221} = \begin{bmatrix} 0.003 & 0.002 & 0.015 & 0.015 \end{bmatrix},$$

$$\mathbf{E}_{222} = \begin{bmatrix} 0.003 & 0 & 0.015 & 0.015 \end{bmatrix},$$

$$\mathbf{E}_{223} = \begin{bmatrix} 0 & 0 & 0.015 & 0.015 \end{bmatrix},$$

$$\mathbf{E}_{224} = \begin{bmatrix} 0 & 0.002 & 0.015 & 0.015 \end{bmatrix},$$

$$\mathbf{O}_{11} = \mathbf{O}_{21} = \begin{bmatrix} 0.001 & 0 & 0 & 0 \end{bmatrix},$$

$$\mathbf{O}_{31} = \mathbf{O}_{41} = \begin{bmatrix} 0 & 0 & 0 & 0 \end{bmatrix},$$

$$\mathbf{O}_{12} = \mathbf{O}_{42} = \begin{bmatrix} 0 & 0.002 & 0 & 0 \end{bmatrix},$$

$$\mathbf{O}_{22} = \mathbf{O}_{32} = \begin{bmatrix} 0 & 0 & 0 & 0 \end{bmatrix},$$

$$\mathbf{O}_{13} = \mathbf{O}_{23} = \mathbf{O}_{33} = \mathbf{O}_{43} = \begin{bmatrix} 0 & 0 & 0.002 & 0 \end{bmatrix},$$

$$\mathbf{O}_{14} = \mathbf{O}_{24} = \mathbf{O}_{34} = \mathbf{O}_{44} = \begin{bmatrix} 0 & 0 & 0 & 0.001 \end{bmatrix},$$

$$\mathbf{H}_{1i} = 0.1,$$

$$\mathbf{H}_{2i} = 0.2,$$

$$\mathbf{F}_{1i} = \mathbf{F}_{2i} = \sin(k), \quad (i = 1, 2, 3, 4),$$

$$\gamma = 0.5. \tag{41}$$

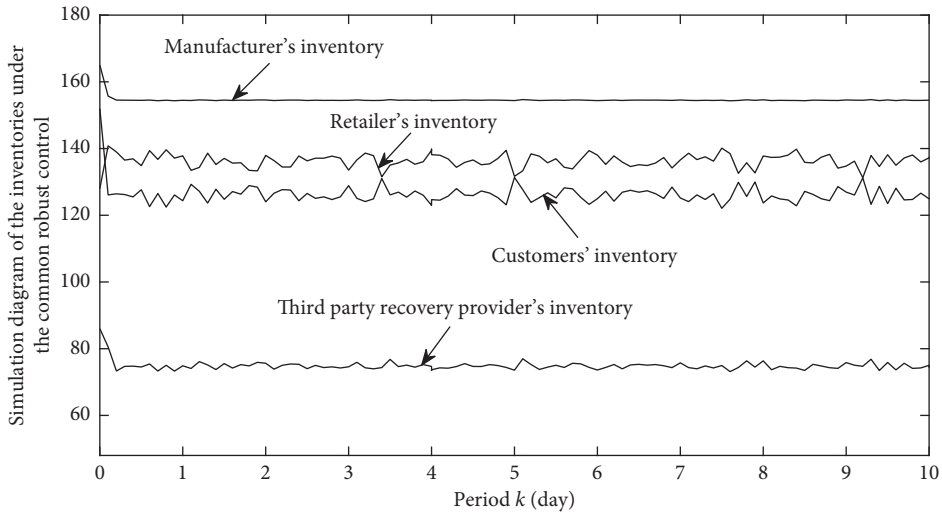

Figure 3: Simulation diagram of the inventories under CRC (unit: $\times 10^3$ sets).

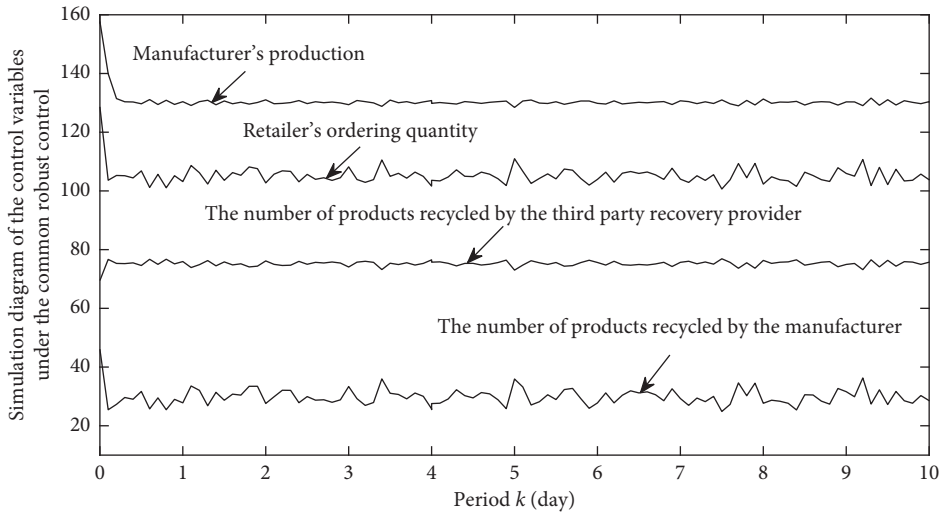

Figure 4: Simulation diagram of the control variables under CRC (unit: $\times 10^3$ sets).

The FRC approach proposed in Section 4 can guarantee the television CLSC system to be robustly stable after the following results, which meet Conditions (31) and (32) in Theorem 2, are obtained.

$$\mathbf{P}_1 = \begin{bmatrix} 121.8898 & 0.0028 & 0.1511 & 0.1485 \\ 0.0028 & 122.7989 & 0.0013 & -0.0113 \\ 0.1511 & 0.0013 & 121.8829 & 0.1509 \\ 0.1485 & -0.0113 & 0.1509 & 121.8811 \end{bmatrix},$$
$$\mathbf{Q}_{11} = \mathbf{Q}_{21} = \mathbf{Q}_{31} = \mathbf{Q}_{41} = \begin{bmatrix} 24.3455 & -0.0000 & -0.0006 & -0.0006 \\ -0.0000 & 24.3419 & -0.0000 & 0.0000 \\ -0.0006 & -0.0000 & 24.3455 & -0.0006 \\ -0.0006 & 0.0000 & -0.0006 & 24.3455 \end{bmatrix}, \tag{42}$$

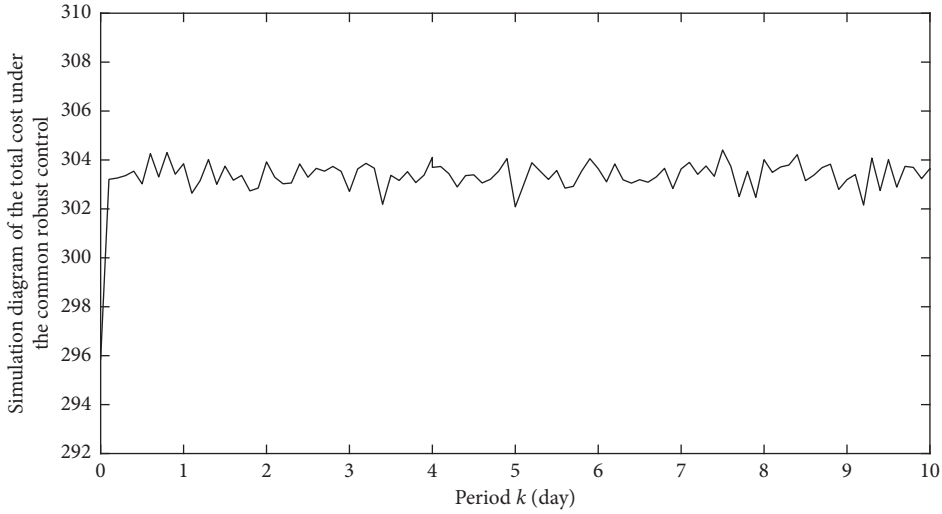

Figure 5: Simulation diagram of the total cost under CRC (unit: $\times 10^5$ Yuan).

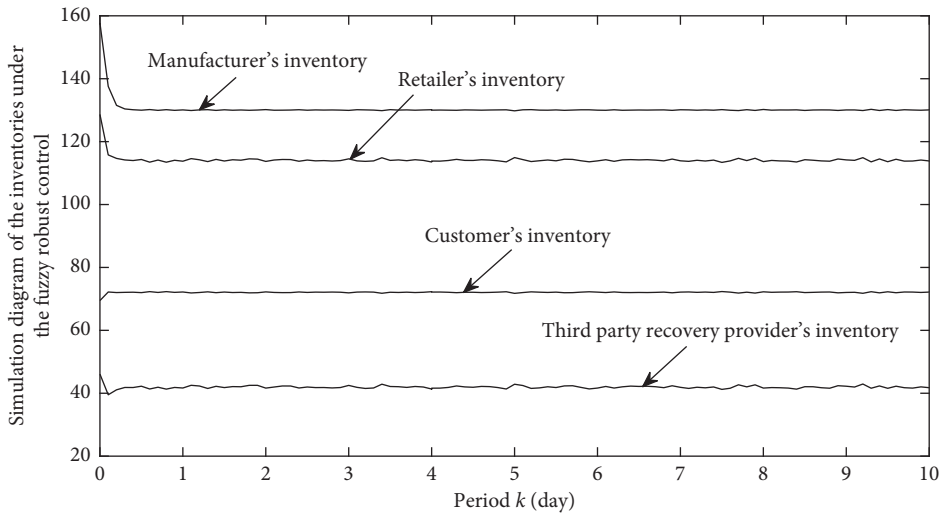

Figure 6: Simulation diagram of the inventories under FRC (unit: $\times 10^3$ sets).

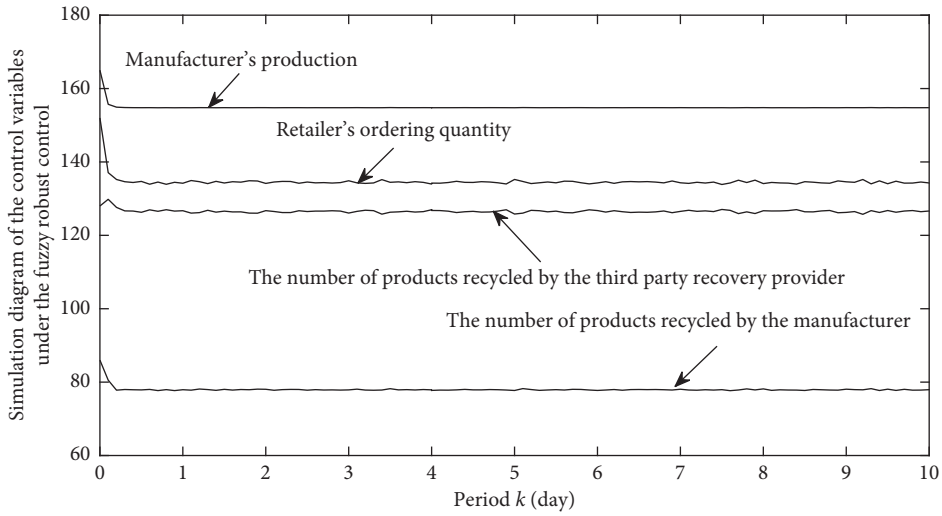

Figure 7: Simulation diagram of the control variables under FRC (unit: $\times 10^3$ sets).

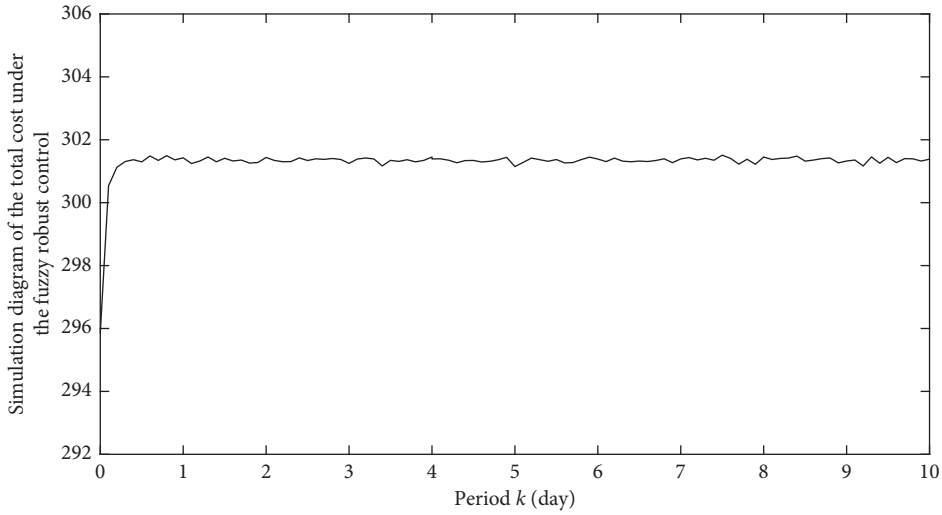

Figure 8: Simulation diagram of the total cost under FRC (unit: $\times 10^5$ Yuan).

Then, we will perform the simulation tests to compare the mitigation effect of the BE between the proposed FRC approach and the CRC approach. Set the initial values as follows: $x_1(0) = 14$, $x_2(0) = 12$, $x_3(0) = 8$, and $x_4(0) = 6$ (unit: $\times 10^3$ sets). Set the nominal values as follows: $\overrightarrow{x}_1 = 155$, $\overrightarrow{x}_2 = 140$, $\overrightarrow{x}_3 = 120$, and $\overrightarrow{x}_4 = 80$ (unit: $\times 10^3$ sets); $\overrightarrow{u}_1 = 130$, $\overrightarrow{u}_2 = 120$, $\overrightarrow{u}_3 = 50$, and $\overrightarrow{u}_4 = 70$ (unit: $\times 10^3$ sets); we let $\tau_1 = \tau_2 = \tau_3 = \tau_4 = 4$ (unit: day), and the customers' demand meets the normal distribution $N(6, 0.3^2)$. Then, the simulation results are shown in Figures 3–8, in which Figures 3–5 are the simulation diagrams under CRC, and Figures 6–8 are the simulation diagrams under FRC.

As shown in Figures 3–5, by utilizing the CRC approach to mitigate the BE of the uncertain CLSC with hybrid recycling channels and lead times, there are larger fluctuations for the variables of the CLSC system, which result in the worse mitigation level of the BE and the higher total cost of the CLSC. On the contrary, it can be seen from Figures 6–8 that the FRC approach proposed in this paper can mitigate the BE more effectively and make the CLSC system to be robustly stable. Also, the fluctuation ranges of all variables under the FRC approach are less that those under the CRC approach. Especially, compared with the CRC approach, the FRC approach realizes the total cost of the CLSC system in the stable and lower levels. Therefore, for the mitigation of the BE caused by uncertainties and lead times, the FRC approach proposed in this paper can more effectively guarantee the interests of enterprises in the supply chain and ensure the long-term and stable development of the CLSC.

6. Conclusions

BE is a universal phenomenon in the operation process of the supply chain system. Therefore, the mitigation of the BE has become one of the most focused and urgent issues for enterprises in the supply chain. In this paper, we have set up an uncertain model of the CLSC with hybrid recycling channels and lead times. To implement the flexible switching in the CLSC system, the aforementioned model is transformed into a CLSC fuzzy model. Then, the manufacturer's production patterns and the retailer's ordering patterns are put forward according to their respective inventory levels. A new FRC approach is proposed to mitigate the BE of the uncertain CLSC with lead times. Simulation results show that this approach can effectively mitigate the impacts of uncertainties and lead times on the BE of the CLSC and guarantee the CLSC system in a robust stable state, which will reduce the loss of the CLSC caused by the BE. It is known from this paper and [19] that the FRC approach is an effective approach to mitigate the BE and can improve the mitigation effect of the CRC approach. For the future research directions, one is how to coordinate the cost sharing among the manufacturer, the retailer, and the 3PRP; another is that the FRC approach is combined with other approaches to more effectively mitigate the BE.

Abbreviations

$x_1(k)$: Manufacturer's inventory at period k
$x_2(k)$: Retailer's inventory at period k
$x_3(k)$: Customers' inventory at period k
$x_4(k)$: 3PRP's inventory at period k
$u_1(k)$: Manufacturer's production variable at period k
$u_2(k)$: Retailer's ordering variable at period k
$u_3(k)$: Manufacturer's used products recycling variable at period k
$u_4(k)$: 3PRP's used products recycling variable at period k
$w_1(k)$: Customers' demand at period k
τ_1: Manufacturer's production lead time
τ_2: Retailer's ordering lead time
τ_3: Lead time of the used products recycled by the manufacturer
τ_4: Lead time of the used products recycled by 3PRP
η: Remanufacturing rate

$\Delta\eta$: Uncertainty of η
μ: Return rate of the new products
$\Delta\mu$: Uncertainty of μ
λ: Disposal rate
$\Delta\lambda$: Uncertainty of λ $0 \le \eta, \mu, \lambda \le 1$, $\eta + \lambda = 1$
$z(k)$: Total cost of the CLSC at period k
c_{h1}: Manufacturer's unit inventory cost
Δc_{h1}: Uncertainty of c_{h1}
c_{h2}: Retailer's unit inventory cost
Δc_{h2}: Uncertainty of c_{h2}
c_{h3}: 3PRP's unit inventory cost
Δc_{h3}: Uncertainty of c_{h3}
c_n: Unit production cost of the new product
Δc_n: Uncertainty of c_n
c_r: Unit remanufacturing cost
Δc_r: Uncertainty of c_r
c_m: Unit recycling cost from customers to the manufacturer
Δc_m: Uncertainty of c_m
c_t: Unit recycling cost from customers to 3PRP
Δc_t: Uncertainty of c_t
c_{mt}: Unit recycling cost from 3PRP to the manufacturer
Δc_{mt}: Uncertainty of c_{mt}
c_q: Unit return cost
Δc_q: Uncertainty of c_q
c_d: Unit disposal cost
Δc_d: Uncertainty of c_d
c_s: Retailer's unit ordering cost
Δc_s: Uncertainty of c_s
R_i: The ith fuzzy rule, $i = 1, 2, \ldots, r$
r: The number of fuzzy rules
M_j^i: The fuzzy set, $j = 1, 2, \ldots, n$
τ_e: The eth lead time, $e = 1, 2, \ldots, g$
g: The number of lead times
n: The number of node enterprises
$M_j^i(x_j(k))$: The grade of membership of $x_j(k)$ in the fuzzy set M_j^i
$\mu_i(\mathbf{x}(k))$: The membership degree of the ith rule
$\|\cdot\|_2$: $\ell_2[0, \infty)$ norm
$\mathbf{G}_c$: The cth MORG, $c = 1, 2, \ldots, \prod_{j=1}^{n}(m_j - 1)$
I_c: The set of the rule numbers in $\mathbf{G}_c$
m_j: The number of the fuzzy partitions of the jth input variable
$F_1^t(x_1(k))$: The fuzzy partitions of $x_1(k)$, $t = 1, 2$
$F_2^s(x_2(k))$: The fuzzy partitions of $x_2(k)$, $s = 1, 2$
D_{0m}: Television manufacturer's safe inventory
D_{1m}: Television manufacturer's expected inventory
$D_{m\max}$: Television manufacturer's maximum inventory
D_{0r}: Television retailer's safe inventory
D_{1r}: Television retailer's expected inventory
$D_{r\max}$: Television retailer's maximum inventory.

Data Availability

The simulation data used to support the findings of this study are included within the manuscript. These data are restricted by the China Video Industry Association in order to protect trade secrets. Data can be available from http://www.cvianet.org.cn for researchers who meet the criteria for access to confidential data.

Conflicts of Interest

The authors declare that they have no conflicts of interest.

Acknowledgments

The authors are grateful for supports from the Shandong Provincial Social Science Plan Foundation, China (no. 19BYSJ13) and the Shandong Provincial Natural Science Foundation, China (no. ZR2018 MG004).

References

[1] D. Yang and T. Xiao, "Pricing and green level decisions of a green supply chain with governmental interventions under fuzzy uncertainties," *Journal of Cleaner Production*, vol. 149, pp. 1174–1187, 2017.

[2] N. M. Modak and P. Kelle, "Using social work donation as a tool of corporate social responsibility in a closed-loop supply chain considering carbon emissions tax and demand uncertainty," *Journal of the Operational Research Society*, pp. 1–17, 2019.

[3] M. Zhalechian, R. Tavakkoli-Moghaddam, B. Zahiri, and M. Mohammadi, "Sustainable design of a closed-loop location-routing-inventory supply chain network under mixed uncertainty," *Transportation Research Part E: Logistics and Transportation Review*, vol. 89, pp. 182–214, 2016.

[4] X.-X. Zheng, Z. Liu, K. W. Li, J. Huang, and J. Chen, "Cooperative game approaches to coordinating a three-echelon closed-loop supply chain with fairness concerns," *International Journal of Production Economics*, vol. 212, pp. 92–110, 2019.

[5] I. H. Hong and J. S. Yeh, "Modeling closed-loop supply chains in the electronics industry: a retailer collection application," *Transportation Research Part E: Logistics and Transportation Review*, vol. 48, no. 4, pp. 817–829, 2012.

[6] J. Wei and J. Zhao, "Reverse channel decisions for a fuzzy closed-loop supply chain," *Applied Mathematical Modelling*, vol. 37, no. 3, pp. 1502–1513, 2013.

[7] A. Allah, M. S. Moshtagh, and I. Moon, "Pricing, product quality, and collection optimization in a decentralized closed-loop supply chain with different channel structures: game theoretical approach," *Journal of Cleaner Production*, vol. 189, pp. 406–431, 2018.

[8] L. Shi and X. Ma, "Strategy analysis of closed loop supply chain for scrapped medical equipment based on hybrid recycling model," *Advanced Materials Research*, vol. 219-220, pp. 722–726, 2011.

[9] X. Ma and R. L. Liu, "Notice of retraction game model of closed loop supply chain under hybrid recycling strategy based on remanufacturing," in *Proceedings of the IEEE International Conference on Computer Science and Information Technology*, vol. 4, pp. 78–81, Chengdu, China, July 2010.

[10] N. A. D. Do, P. Nielsen, Z. Michna, and I. E. Nielsen, "Quantifying the bullwhip effect of multi-echelon system with stochastic dependent lead time," in *Advances in Production Management Systems*, B. Grabot, B. Vallespir, S. Gomes, A. Bouras, and D. Kiritsis, Eds., vol. 438, pp. 419–426, Springer, Berlin, Heidelberg, 2014.

[11] S. Agrawal, R. N. Sengupta, and K. Shanker, "Impact of information sharing and lead time on bullwhip effect and on-hand inventory," *European Journal of Operational Research*, vol. 192, no. 2, pp. 576–593, 2009.

[12] J. G. Kim, D. Chatfield, T. P. Harrison, and J. C. Hayya, "Quantifying the bullwhip effect in a supply chain with stochastic lead time," *European Journal of Operational Research*, vol. 173, no. 2, pp. 617–636, 2006.

[13] N. M. Modak and P. Kelle, "Managing a dual-channel supply chain under price and delivery-time dependent stochastic demand," *European Journal of Operational Research*, vol. 272, no. 1, pp. 147–161, 2019.

[14] C. Li and S. Liu, "A robust optimization approach to reduce the bullwhip effect of supply chains with vendor order placement lead time delays in an uncertain environment," *Applied Mathematical Modelling*, vol. 37, no. 3, pp. 707–718, 2013.

[15] D. Fu, C. Ionescu, E.-H. Aghezzaf, and R. De Keyser, "Quantifying and mitigating the bullwhip effect in a benchmark supply chain system by an extended prediction self-adaptive control ordering policy," *Computers & Industrial Engineering*, vol. 81, pp. 46–57, 2015.

[16] C. A. G. Salcedo, A. I. Hernandez, R. Vilanova, and J. H. Cuartas, "Inventory control of supply chains: mitigating the bullwhip effect by centralized and decentralized internal model control approaches," *European Journal of Operational Research*, vol. 224, no. 2, pp. 261–272, 2013.

[17] C. E. Riddalls and S. Bennett, "Production-inventory system controller design and supply chain dynamics," *International Journal of Systems Science*, vol. 33, no. 3, pp. 181–195, 2002.

[18] X.-Y. Huang, N.-N. Yan, and R.-Z. Qiu, "Dynamic models of closed-loop supply chain and robust H_∞ control strategies," *International Journal of Production Research*, vol. 47, no. 9, pp. 2279–2300, 2009.

[19] S. T. Zhang, X. Li, and C. Y. Zhang, "A fuzzy control model for restraint of bullwhip effect in uncertain closed-loop supply chain with hybrid recycling channels," *IEEE Transactions on Fuzzy Systems*, vol. 25, no. 2, pp. 475–482, 2017.

[20] S. F. Alamdar, M. Rabbani, and J. Heydari, "Pricing, collection, and effort decisions with coordination contracts in a fuzzy, three-level closed-loop supply chain," *Expert Systems with Applications*, vol. 104, pp. 261–276, 2018.

[21] T. Takagi and M. Sugeno, "Fuzzy identification of systems and its applications to modeling and control," *IEEE Transactions on Systems, Man, and Cybernetics*, vol. SMC-15, no. 1, pp. 116–132, 1985.

[22] Z.-H. Xiu and G. Ren, "Stability analysis and systematic design of Takagi-Sugeno fuzzy control systems," *Fuzzy Sets and Systems*, vol. 151, no. 1, pp. 119–138, 2005.

[23] X. D. Liu and Q. L. Zhang, "Approaches to quadratic stability conditions and H_∞ control designs for T-S fuzzy systens," *IEEE Transactions on Fuzzy Systems*, vol. 11, no. 6, pp. 830–839, 2003.

[24] S. T. Zhang, Y. T. Hou, S. Q. Zhang, and M. Zhang, "Fuzzy control model and simulation for nonlinear supply chain system with lead times," *Complexity*, vol. 2017, p. 11, 2017.

[25] Z. Liu, K. W. Li, B.-Y. Li, J. Huang, and J. Tang, "Impact of product-design strategies on the operations of a closed-loop supply chain," *Transportation Research Part E: Logistics and Transportation Review*, vol. 124, pp. 75–91, 2019.

Hindawi
Complexity
Volume 2020, Article ID 2463790, 13 pages
https://doi.org/10.1155/2020/2463790

Research Article

Robust Finite-Time Tracking for Uncertain Linear Systems with Actuator Faults

Xinpeng Fang, Huijin Fan, and Lei Liu

School of Artificial Intelligence and Automation, National Key Laboratory of Science and Technology on Multispectral Information Processing, Huazhong University of Science and Technology, Wuhan 430074, China

Correspondence should be addressed to Huijin Fan; ehjfan@hust.edu.cn

Received 22 July 2019; Revised 25 September 2019; Accepted 25 October 2019; Published 11 January 2020

Guest Editor: Baltazar Aguirre-Hernandez

In this paper, a robust finite-time fault-tolerant control (FTC) scheme is developed for uncertain linear systems in the presence of actuator faults. Since the system uncertainties and actuator faults are unknown, the controller parameters are updated online by the adaptive laws without the need for fault detection and isolation. It is proved that the proposed state-feedback model reference adaptive finite-time FTC scheme can guarantee that the tracking error converges to a small neighborhood of the origin in finite time. An application example for an aircraft lateral-directional dynamic system is presented to show the effectiveness of the proposed control scheme.

1. Introduction

In a practical system, e.g., networked control system and flight control system, the actuator component usually suffers from a partial loss of effectiveness (LOE) or even a total loss of control (LOC) due to the increasing complexity of system itself and operating environment [1–5]. See for example, the rudder of an aircraft may experience a loss of gain in the control channel or be stuck in a fixed position. Such actuator faults may degrade the system performance, cause system instability, and even lead to catastrophic accidents. In order to improve system reliability and security, it is significantly important to consider the fault-tolerant control (FTC) problem. Numerous FTC strategies have been proposed which can be classified into two main types: (1) passive method and (2) active one. Passive FTC is actually a robust scheme by designing a fixed controller which ensures the closed-loop system be insensitive to specific preconsidered faults, see for example [6–9]. Unlike the passive control method, the active FTC method can guarantee the stability of the entire closed-loop system by adjusting the parameters or structure of the controller corresponding to the occurred fault. Therefore, compared with the passive control method, the active method is more flexible and practical. Fault detection and diagnosis (FDD) can provide fault information, for example, a sliding mode observer was developed in [10] for detecting and reconstructing actuator and sensor faults. Several active FTC methods based on FDD have been proposed in literatures, such as switching-based design [11], sliding mode control-based design [12, 13], pseudo-inverse approach [14], and model predictive control-based design [15]. It is noted that the performance of these active methods depends heavily on the accuracy of FDD.

On the contrary, adaptive FTC which is a kind of robust technique and a main class of active FTC has been widely used due to its flexibility and diversity in design and its ability to handle unknown actuator faults without the need for FDD modules [16–28]. By considering that the stuck fault is bounded, a robust adaptive FTC scheme was proposed for uncertain linear systems in [16]. In [17], a direct adaptive control scheme was designed to compensate for spacecraft systems with multiple actuator faults and inertia matrix uncertainties. A robust adaptive control strategy based on the generalized restricted potential function was proposed for linear systems in [18] to achieve the desired tracking error norm bound. By employing the adaptive backstepping technique, an adaptive control strategy was

presented to deal with stochastic LOE faults for half-car active suspension systems in [19]. In [20, 21], two adaptive fault-tolerant controllers were developed with LOC faults only. By designing the auxiliary systems, the fault-tolerant constrained controllers were designed to achieve FTC in the presence of input amplitude saturation in [22, 23]. Moreover, as a promising adaptive control method, model reference adaptive control (MRAC) has been widely applied to guarantee the desired tracking performance and handle unknown actuator faults and system uncertainties. In [29, 30], state-feedback FTC schemes were presented to ensure the plant state asymptotically tracks the reference model state, and in [31, 32], output tracking property was guaranteed by designing state-feedback MRAC schemes.

It is noted that the aforementioned control laws only guarantee the asymptotic stability of the system, that is, they only promise the stability of infinite time. However, in practice, we expect the desired system performance to be achieved in a finite time. For example, the actual attitude of the aircraft must recover the desired attitude within a finite time once fault occurring. Since finite-time control has a faster convergence rate, better robustness against uncertainties and disturbances, it has drawn a lot of attention. Therefore, designing a finite-time FTC scheme is of great significance. In [33–38], the issues of finite-time stability were investigated for fault-free cases. Two finite-time command filtered backstepping-based controllers were proposed in [33, 34], which guarantee the finite-time tracking property. In order to solve the problem of finite-time FTC, a number of control schemes have been developed in [39–41] and applied to spacecraft attitude control. In [39], a finite-time attitude controller was designed based on sliding mode control technology. A finite-time terminal sliding mode controller was proposed in [40] by using the reconstruction information of the adaptive terminal sliding mode observer. It is worth mentioning that the designed controllers in [36, 39, 40] contain the sign functions, which may cause the undesired controller chattering problem. Therefore, it is more valuable to design the chattering-free finite-time FTC scheme. In addition, due to the inevitable existence of uncertainties, it is necessary and a key challenge to develop control strategies for uncertain systems. In [42], a robust adaptive hierarchical insensitive tracking controller was designed for linear systems with uncertainties in the system and input matrices.

Motivated by the above discussion, this paper will study the finite-time tracking control of uncertain linear systems with unknown actuator faults. The main contributions are given as follows:

(1) A robust model reference adaptive fault-tolerant tracking control scheme with finite-time convergence property for linear systems is developed to compensate for time-varying system matrix uncertainty and unknown actuator faults without requiring fault detection and isolation

(2) The unknown parameters caused by system uncertainty and actuator faults can be estimated by the designed tracking error-driven adaptive laws, which promises the adaptivity of the proposed controller

(3) The proposed control law is chattering-free, which is more practical for engineering applications

The rest of this paper is organized as follows. In Section 2, the problem to be addressed is formulated and some preliminaries are introduced. A robust adaptive finite-time FTC scheme is developed in Section 3. In Section 4, an application to an aircraft lateral-directional dynamic system is presented to illustrate the effectiveness of the proposed scheme. Finally, the conclusion is given in Section 5.

Notations. $\mathbb{R}^n$ represents the n-dimensional Euclidean space, while $\mathbb{R}^{n\times m}$ refers to the set of all $n\times m$ real matrices. $x\in\mathbb{R}^n$ denotes that x is an n-dimensional vector, and $x\in\mathbb{R}^{n\times m}$ means that x is an $n\times m$ matrix. $\|\cdot\|$ denotes the Euclidean norm of a vector or matrix. The superscript "T" stands for matrix transposition. diag$\{\ldots\}$ represents a block-diagonal matrix. $\lambda_{\min}(\cdot)$ and $\lambda_{\max}(\cdot)$ denote the minimum and maximum eigenvalues of a matrix, respectively. I_m stands for the m-dimensional identity matrix.

2. Preliminaries and Problem Statement

2.1. Preliminaries.

Definition 1 (see [43]). Consider an autonomous dynamic system:

$$\begin{aligned}\dot{x} &= f(x),\\ f(0) &= 0,\end{aligned} \tag{1}$$

where $f: U_0 \longmapsto \mathbb{R}^n$ is continuous on an open neighborhood U_0 of the origin. The equilibrium $x=0$ of the system is uniformly finite-time stable if it is uniformly Lyapunov stable and for any initial condition $x_0\in U$ where $U\subset U_0$, if there is a settling time function $T: U\longmapsto(0,\infty)$, such that every solution $x(t,x_0)$ of system (1) satisfies $x(t,x_0)\in U\backslash\{0\}$ for $t\in[0,T(x_0))$ with the properties: $\lim_{t\longrightarrow T(x_0)} x(t,x_0)=0$ and $x(t,x_0)=0$, $\forall t\geq T(x_0)$.

If $U=U_0=\mathbb{R}^n$, then the origin is a uniformly globally finite-time stable equilibrium.

Lemma 1 (see [44]). *For $x_j\in\mathbb{R}$, $j=1,2,\ldots,n$, and $0<q<1$, the following relation holds:*

$$\left(\sum_{j=1}^{n}\left|x_j\right|\right)^q \leq \sum_{j=1}^{n}\left|x_j\right|^q. \tag{2}$$

Lemma 2 (see [45]). *For a positive definite matrix $A\in\mathbb{R}^{n\times n}$ and any $x\in\mathbb{R}^n$, the following inequality holds:*

$$\lambda_{\min}(A)\|x\|^2 \leq x^T A x \leq \lambda_{\max}(A)\|x\|^2. \tag{3}$$

Lemma 3 (see [36]). *For any scalar $\delta_0>(1/2)$, matrices K, $\widehat{K}$, $\widetilde{K}\in\mathbb{R}^n$, and $\widetilde{K}=\widehat{K}-K$, the inequality in (4) holds:*

$$-\tilde{K}^T\hat{K} \le -\frac{2\delta_0 - 1}{2\delta_0}\tilde{K}^T\tilde{K} + \frac{\delta_0}{2}K^TK. \tag{4}$$

Lemma 4 (see [46]). *For some constants $a > 0$, $b > 0$, and $\mu > 0$, the following relation holds:*

$$|y|^a|z|^b \le \frac{a}{a+b}\mu|y|^{a+b} + \frac{b}{a+b}\mu^{-a/b}|z|^{a+b}, \tag{5}$$

where y and z are real variables.

Lemma 5 (see [36]). *Consider the system $\dot{x} = f(x,u)$. If there exists a continuous positive definite function $V(x)$, real numbers $\eta > 0$, $0 < \alpha < 1$, and $0 < \overline{\psi} < \infty$, such that*

$$\dot{V}(x) \le -\eta V^{\alpha}(x) + \overline{\psi}, \tag{6}$$

then the system $\dot{x} = f(x,u)$ is practical finite-time stable. The trajectories of the system can reach the set $\{x \mid V^{\alpha}(x) \le (\overline{\psi}/(1-\iota)\eta)\}$ in a finite time T_r, which is defined as

$$T_r \le \frac{V^{1-\alpha}(0)}{\eta\iota(1-\alpha)}, \tag{7}$$

where $0 < \iota < 1$ and $V(0)$ is the initial value of $V(x)$.

2.2. System Model. Consider the linear systems with time-varying system matrix uncertainty described by

$$\dot{x}(t) = (A + \Delta A(t))x(t) + Bu(t), \tag{8}$$

where $x(t) \in \mathbb{R}^n$ is the state vector which can be available at every instant and $u(t) = [u_1(t), u_2(t), \ldots, u_m(t)]^T \in \mathbb{R}^m$ is the control input vector, which means that there are m actuators in the system. $A \in \mathbb{R}^{n\times n}$ and $B \in \mathbb{R}^{n\times m}$ represent the nominal system and input matrices, respectively, where B is full-row rank. $\Delta A(t)$ represents the time-varying system matrix uncertainty which satisfies the following condition:

$$\Delta A(t) = BH(t), \tag{9}$$

where $H(t)$ is an unknown continuous matrix function with $\|H(t)\| \le \overline{h}$ and $\overline{h}$ is an unknown positive constant.

Remark 1. For a practical system, e.g., aircraft system [47] and industrial system [48], it can always be linearized and decoupled into the form of system (8). The full-row rank condition of B is a general requirement for the system, see for example [18, 49], which means that there must be enough control channels in the system, especially for actuator redundancy purpose. Then, the establishment of condition (9) is obvious, since any n-dimensional square matrix can be expressed in the form of (9) by a full-row rank matrix B.

2.3. Actuator Fault Model. The actuator fault model considered in this article is described as

$$\begin{aligned} u_i(t) &= \sigma_i v_i(t) + \rho_i \overline{u}_i(t), \\ \sigma_i\rho_i &= 0, \quad i = 1, 2, \ldots, m, \end{aligned} \tag{10}$$

where $v_i(t)$ denotes the designed control input for the ith actuator, $\overline{u}_i(t)$ represents the ith actuator's uncontrollable time-varying fault, $\sigma_i \in [0,1]$ and $\rho_i \in \{0,1\}$ are unknown fault indicators for the ith actuator, and σ_i and $\overline{u}_i(t)$ are piecewise constant functions of time. More specifically

(1) The ith actuator is fault-free when $\sigma_i = 1$ and $\rho_i = 0$

(2) The ith actuator is partial LOE when $0 < \sigma_i < 1$ and $\rho_i = 0$

(3) The ith actuator corresponds to outage when $\sigma_i = 0$ and $\rho_i = 0$

(4) The ith actuator is stuck at $\overline{u}_i(t)$ when $\sigma_i = 0$ and $\rho_i = 1$

For convenience, the actual input vector $u(t)$ of system (8) can be formulated as

$$u(t) = \sigma v(t) + \rho\overline{u}(t), \tag{11}$$

where

$$\begin{aligned} \sigma &= \mathrm{diag}\{\sigma_1, \sigma_2, \ldots, \sigma_m\}, \\ \rho &= \mathrm{diag}\{\rho_1, \rho_2, \ldots, \rho_m\}, \\ v(t) &= [v_1(t), v_2(t), \ldots, v_m(t)]^T, \\ \overline{u}(t) &= [\overline{u}_1(t), \overline{u}_2(t), \ldots, \overline{u}_m(t)]^T. \end{aligned} \tag{12}$$

Remark 2. The compact fault model (11) includes normal (case 1), partial LOE faults (case 2) and total LOC faults (cases 3 and 4), which can represent most of the possible occurrences of an actuator in a practical system.

2.4. Control Objective. The reference model is given as

$$\dot{x}_m(t) = A_m x_m(t) + B_m r_m(t), \tag{13}$$

where $x_m(t) \in \mathbb{R}^n$ is the reference state vector which can be available at every instant, $r_m(t) \in \mathbb{R}^m$ is the bounded reference input, and $A_m \in \mathbb{R}^{n\times n}$ is a Hurwitz matrix, that is, there exist positive definite matrices $P, Q \in \mathbb{R}^{n\times n}$ such that

$$A_m^TP + PA_m = -Q. \tag{14}$$

Some assumptions are to be introduced.

Assumption 1. $\mathrm{rank}(B\sigma) = \mathrm{rank}(B)$.

Assumption 2. There exist $\overline{K}_x \in \mathbb{R}^{m\times n}$ and $\overline{K}_r \in \mathbb{R}^{m\times m}$ such that

$$\begin{aligned} A + B\overline{K}_x &= A_m, \\ B\overline{K}_r &= B_m. \end{aligned} \tag{15}$$

Remark 3. As discussed in [21], Assumption 1 is an actuator redundancy condition which ensures that the system

remains capable to be stabilized even with actuator faults. In other words, the actuator faults satisfying Assumption 1 can be completely compensated by the proposed algorithm. Assumption 2 is a standard state-feedback state tracking matching condition, i.e., [29, 50]. In our scheme, Assumption 2 ensures that system (8) can match reference model (13) through state-feedback, so as to ensure the performance of state tracking. More specifically, according to Assumptions 1 and 2, it can be concluded that there exist $K_x \in \mathbb{R}^{m\times n}$ and $K_r \in \mathbb{R}^{m\times m}$ such that

$$\begin{aligned} A + B\sigma K_x &= A_m, \\ B\sigma K_r &= B_m. \end{aligned} \tag{16}$$

Lemma 6 (see [51]). *The rank relation in Assumption 1 is a necessary and sufficient condition for the existence of a matrix $k_1 \in \mathbb{R}^m$ such that*

$$B\sigma k_1 = -B\rho\overline{u}. \tag{17}$$

Our control objective is to design a robust adaptive finite-time FTC scheme for system (8) in the presence of unknown actuator faults and system matrix uncertainty, such that the finite-time tracking is ensured for the given reference model (13).

3. Robust Adaptive Finite-Time Fault-Tolerant Control Scheme

In this section, a robust adaptive finite-time FTC scheme is developed to achieve the desired state tracking property in the presence of unknown actuator faults and system matrix uncertainty.

3.1. Controller Structure. Denote the tracking error $e = [e_1, e_2, \ldots, e_n]^T$ as

$$e = x - x_m. \tag{18}$$

Let $\widehat{K}_x = [\widehat{K}_{x1}, \widehat{K}_{x2}, \ldots, \widehat{K}_{xm}]^T \in \mathbb{R}^{m\times n}$, $\widehat{K}_r = [\widehat{K}_{r1}, \widehat{K}_{r2}, \ldots, \widehat{K}_{rm}]^T \in \mathbb{R}^{m\times m}$, and $\widehat{k}_1 = [\widehat{k}_{11}, \widehat{k}_{12}, \ldots, \widehat{k}_{1m}]^T \in \mathbb{R}^m$ be the estimates of K_x, K_r, and k_1, respectively. Then, the finite-time FTC scheme in this article is constructed as

$$v = \widehat{K}_x x + \widehat{K}_r r_m + \widehat{k}_1 + k_2 + k_3 + k_4, \tag{19}$$

where

$$k_2 = \frac{B^T P e e^T Q e}{2\|e^T PB\|^2 + 1}, \tag{20}$$

and k_3 and $k_4 \in \mathbb{R}^m$ will be designed later.

By considering actuator faults (11), substituting (11) and (19) into (8), the closed-loop system can be formulated as

$$\dot{x} = (A + \Delta A)x + B\rho\overline{u} + B\sigma\left(\widehat{K}_x x + \widehat{K}_r r_m + \widehat{k}_1 + k_2 + k_3 + k_4\right). \tag{21}$$

Together with (13), (16), (18), and (21) and using Lemma 6, the tracking error system can be derived as

$$\begin{aligned} \dot{e} = {} & A_m e + BHx + B\sigma\left(\widehat{K}_x - K_x\right)x + B\sigma\left(\widehat{K}_r - K_r\right)r_m \\ & + B\sigma\left(\widehat{k}_1 - k_1\right) + B\sigma\left(k_2 + k_3 + k_4\right). \end{aligned} \tag{22}$$

Lemma 7 (see [16]). *For the diagonal matrix σ in (11), there exists a constant $0 < \chi \le 1$, such that*

$$\chi\left\|e^T PB\right\|^2 \le e^T PB\sigma B^T Pe \le \left\|e^T PB\right\|^2. \tag{23}$$

Now, introducing two unknown positive scalars ξ_1 and ξ_2 as

$$\begin{aligned} \xi_1 &= \frac{1 - l_1\chi}{\chi}, \\ \xi_2 &= \frac{\overline{h}}{\chi}, \end{aligned} \tag{24}$$

where $0 < l_1 < 1$ is a chosen constant and $\overline{h}$ is the upper bound of $H(t)$.

Then, term k_3 in (19) can be designed as

$$k_3 = \begin{cases} -\dfrac{l_2 B^T Pe\left(l_1 + \widehat{\xi}_1\right)\left(e^T Pe\right)^\alpha}{2\left\|e^T PB\right\|^2}, & \text{if } \left\|e^T PB\right\| > 0, \\ 0_{m\times 1}, & \text{if } \left\|e^T PB\right\| = 0, \end{cases} \tag{25}$$

where $\widehat{\xi}_1$ is the estimate of unknown constant ξ_1 and $l_2 > 0$ and $0 < \alpha < 1$ are chosen constants.

Term k_4 in (19) is thus designed as

$$k_4 = -\frac{\widehat{\xi}_2^2 \|x\|^2 B^T Pe}{\widehat{\xi}_2 \|x\| \left\|B^T Pe\right\| + l_3}, \tag{26}$$

where $\widehat{\xi}_2$ is the estimate of ξ_2 and l_3 is a chosen positive constant.

Remark 4. The designed controller (19) consists of six items: $\widehat{K}_x x$, $\widehat{K}_r r_m$, $\widehat{k}_1$, k_2, k_3, and k_4. $\widehat{K}_x x + \widehat{K}_r r_m$ is inherited from the typical state-feedback model reference controller structure. $\widehat{k}_1$ is the estimate of k_1 given in (17), which is to eliminate the effects of the stuck fault $\overline{u}$. k_2 is designed especially for stability analysis purpose. k_3 is actually an exponential term which is related to a finite-time control. k_4 is designed to eliminate the effects of uncertainty.

3.2. Adaptive Laws. To construct v, for $i = 1, 2, \ldots, m$, the adaptive laws to update $\widehat{K}_{xi}$, $\widehat{K}_{ri}$, $\widehat{k}_{1i}$, $\widehat{\xi}_1$, and $\widehat{\xi}_2$ are chosen as

$$\dot{\widehat{K}}_{xi} = -\Gamma_i\left(2xe^T Pb_i + \Lambda_i \widehat{K}_{xi}\right), \tag{27}$$

$$\dot{\widehat{K}}_{ri} = -\Upsilon_i\left(2r_m e^T Pb_i + \Theta_i \widehat{K}_{ri}\right), \tag{28}$$

$$\dot{\widehat{k}}_{1i} = -\mu_i\left(2e^T Pb_i + \tau_i \widehat{k}_{1i}\right), \tag{29}$$

$$\dot{\widehat{\xi}}_1 = c_1\left(l_2\left(e^T Pe\right)^{\alpha} - \varsigma_1\widehat{\xi}_1\right), \tag{30}$$

$$\dot{\widehat{\xi}}_2 = c_2\left(2\left\|e^T PB\right\|\|x\| - \varsigma_2\widehat{\xi}_2\right), \tag{31}$$

where b_i represents the ith column of B, $\Gamma_i, \Lambda_i \in \mathbb{R}^{n\times n}$, and $\Upsilon_i, \Theta_i \in \mathbb{R}^{m\times m}$ are chosen constant diagonal positive definite matrices, and $\mu_i, \tau_i > 0$ and $c_1, c_2, \varsigma_1, \varsigma_2 > 0$ are chosen constants. The initial values of $\widehat{\xi}_1$ and $\widehat{\xi}_2$ are positive, that is, $\widehat{\xi}_1(0) > 0$ and $\widehat{\xi}_2(0) > 0$.

So far we have obtained the state-feedback model reference adaptive finite-time FTC scheme. For clarity, it is summarized in Appendix A.

3.3. Stability Analysis

Theorem 1. *Consider the linear systems described by (8) with unknown actuator faults (11) and system matrix uncertainty, if Assumptions 1 and 2 are satisfied, the control signal in (19) updated by the adaptive laws (27)–(31) can guarantee that the tracking errors converge to a small neighborhood of the origin in finite time.*

Proof. See Appendix B. □

4. Application: Aircraft Attitude Control

In this section, simulation studies on a lateral-directional dynamic model of the F-18 high-angle-of-attack research vehicle (HARV) system [47] are given to illustrate the effectiveness of the proposed robust adaptive finite-time FTC scheme. To present the superiority of the proposed control scheme, the developed controller (19) is compared with the one given in [28].

4.1. F-18 HARV Model. The state variables for the linear lateral-directional dynamic model of the F-18 HARV system are side-slip angle β (deg), roll rate p (deg/s), and yaw rate r (deg/s), that is, $x = [\beta, p, r]^T$. The control input vector $u = [\delta_{DT}, \delta_{AI}, \delta_{RU}, \delta_{RTV}, \delta_{YTV}]^T$, where δ_{DT}, δ_{AI}, δ_{RU}, δ_{RTV}, and δ_{YTV} represent the differential tail deflection (deg), aileron deflection (deg), rudder deflection (deg), roll thrust vector deflection (deg), and yaw thrust vector deflection (deg), respectively.

As in [47], the linear plant is described by (8) with

$$A = \begin{bmatrix} -0.059 & 0.496 & -0.868 \\ -5.513 & -0.939 & 0.665 \\ 0.068 & 0.026 & -0.104 \end{bmatrix},$$
$$B = \begin{bmatrix} 0.006 & 0.006 & 0.004 & 0.000 & 0.090 \\ 1.879 & 1.328 & 0.029 & 0.675 & 0.217 \\ -0.109 & -0.096 & -0.084 & 0.007 & -2.974 \end{bmatrix}. \tag{32}$$

The time-varying matrix $H(t)$ is given as

$$H(t) = \begin{bmatrix} 0.1\sin(0.1t) & 0 & 0 \\ 0 & 0.5 & 0 \\ 0 & 0 & 1.6 \\ 0 & 0 & 0.8 \\ e^{-2t} & -1 & 0 \end{bmatrix}. \tag{33}$$

4.2. Simulation Scenarios. The reference model is chosen as (13) with

$$A_m = \begin{bmatrix} -0.153 & 0.486 & -0.778 \\ -6.310 & -2.971 & 0.331 \\ 3.139 & 0.199 & -3.065 \end{bmatrix}, \qquad B_m = B. \tag{34}$$

To demonstrate the effectiveness of the proposed adaptive finite-time FTC scheme, the following actuator faults are simulated:

$$\begin{cases} u_1(t) = 0.5v_1(t), & \text{for } t \geq 10\text{ s}, \\ u_2(t) = 0, & \text{for } 30\text{ s} \leq t < 50\text{ s}, \\ u_4(t) = -5, & \text{for } 70\text{ s} \leq t < 90\text{ s}, \\ u_i(t) = v_i(t), & i = 1, 2, 3, 4, 5, \text{otherwise}. \end{cases} \tag{35}$$

In (35), $u_1(t) = 0.5v_1(t)$ denotes the differential tail deflection δ_{DT} loses its 50% effectiveness; $u_2(t) = 0$ denotes that the second actuator corresponds to outage, that is, the aileron deflection δ_{AI} stuck at the fixed value 0 deg; and $u_4(t) = -5$ denotes the roll thrust vector deflection δ_{RTV} cannot be influenced by control action $v_4(t)$ and stuck at the fixed value −5 deg. Table 1 shows the fault indication matrices σ and ρ in different time intervals.

The initial conditions of the proposed controller (19) are given as follows:

$$\begin{aligned} x(0) &= [0.1, 0.2, 1.1]^T, \\ x_m(0) &= [-0.1, 0.1, 1]^T, \\ \widehat{K}_{x1}(0) &= [-1, 0, -1]^T, \\ \widehat{K}_{x2}(0) &= [1, -1, 1]^T, \\ \widehat{K}_{x3}(0) &= [-1, -1, 0]^T, \\ \widehat{K}_{x4}(0) &= [0, -1, 0]^T, \\ \widehat{K}_{x5}(0) &= [-1, 0, 1]^T, \\ \widehat{\xi}_1(0) &= 0.5, \\ \widehat{\xi}_2(0) &= 1.8, \\ \widehat{K}_r(0) &= I_5, \\ \widehat{k}_{1i}(0) &= 0, \quad i = 1, 2, 3, 4, 5. \end{aligned} \tag{36}$$

The reference input signal $r_m = [0, 0, 0, 0, 2]^T$. In order to obtain a good FTC effect of the designed controller (19), after

Table 1: Fault indication matrices σ and ρ.

Time interval	σ	ρ
$0 \le t < 10$ s	diag{1, 1, 1, 1, 1}	diag{0, 0, 0, 0, 0}
10 s $\le t < 30$ s		
50 s $\le t < 70$ s	diag{0.5, 1, 1, 1, 1}	diag{0, 0, 0, 0, 0}
and $t \ge 90$ s		
30 s $\le t < 50$ s	diag{0.5, 0, 1, 1, 1}	diag{0, 0, 0, 0, 0}
70 s $\le t < 90$ s	diag{0.5, 1, 1, 0, 1}	diag{0, 0, 0, 1, 0}

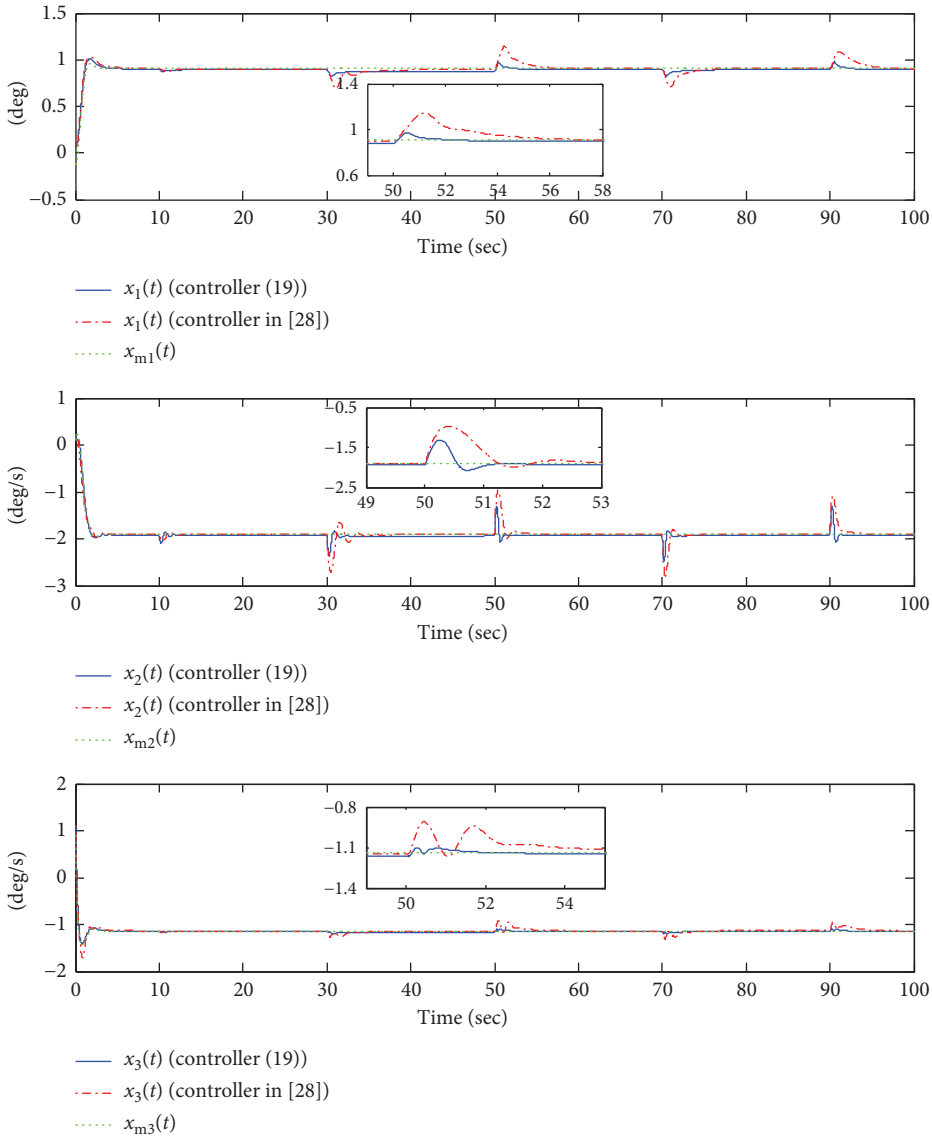

Figure 1: Trajectories of plant state $x(t)$ and reference model state $x_m(t)$.

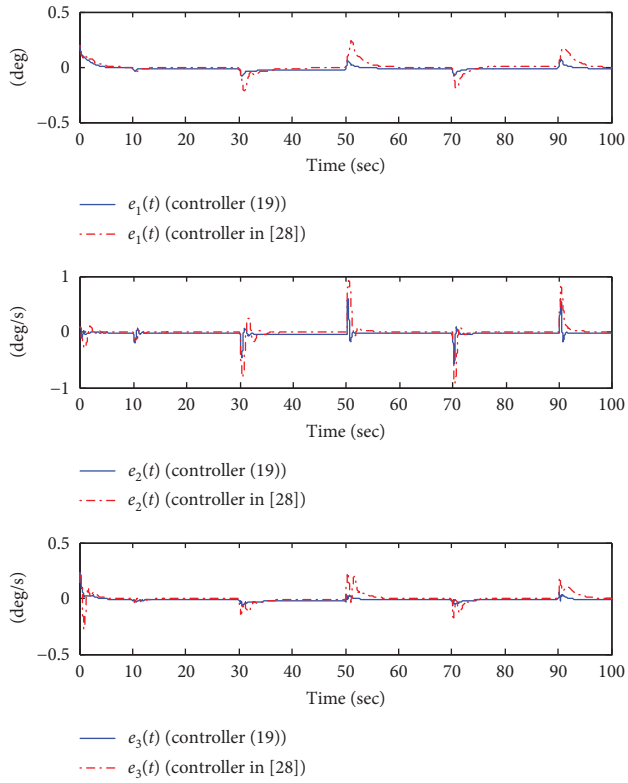

FIGURE 2: Trajectories of state tracking error $e(t)$.

repeatedly debugging, the controller parameters are chosen as

$$\begin{aligned}
\Gamma_i &= I_3, \\
\Lambda_i &= 0.1 I_3, \\
\Upsilon_i &= I_5, \\
\Theta_i &= 0.1 I_5, \\
\mu_i &= 1, \\
\tau_i &= 0.1, \quad i = 1, 2, 3, 4, 5, \\
c_1 &= c_2 = 1, \\
\varsigma_1 &= 0.1, \\
\varsigma_2 &= 0.5, \\
l_1 &= 0.1, \\
l_2 &= 0.5, \\
l_3 &= 1, \\
\alpha &= 0.8.
\end{aligned} \tag{37}$$

Although the parameters are chosen by trial and error, there are still some rules to be referred to. The larger the adaptive gains Γ_i and Λ_i in (27) are, the more drastic the change of K_{xi} is, which leads to stronger control effect.

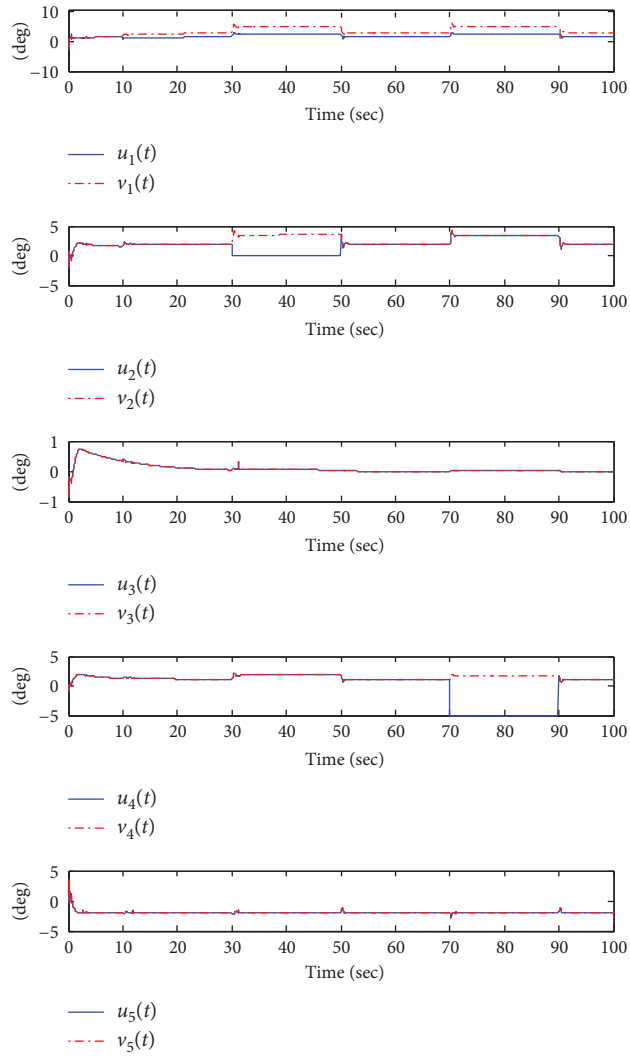

FIGURE 3: Actual control signal $u(t)$ and designed control signal $v(t)$ of controller (19).

Similar phenomenon lies in (28)–(31). However, too-large adaptive gains will affect the smoothness of the controller. l_1 and l_2 have direct impacts on k_3, which means that they will affect the strength of the controller directly. l_3 is a constant relating to the smoothness of the controller, while a large l_3 will lead to a large $\overline{\psi}$ and thus reduce the finite-time convergence accuracy. If α chosen by the designer is too small, then k_3 will exhibit a fast rate of change when the tracking error turns small, which is not expected in a practical system. In sum, to obtain a more practical FTC performance, the designers should choose the parameters with a compromise among the convergence rate, convergence accuracy, and the amplitude and smoothness of the control signals.

Through trial and error, the initial conditions and parameters of the controller given in [28] are chosen as follows to obtain a good FTC effect:

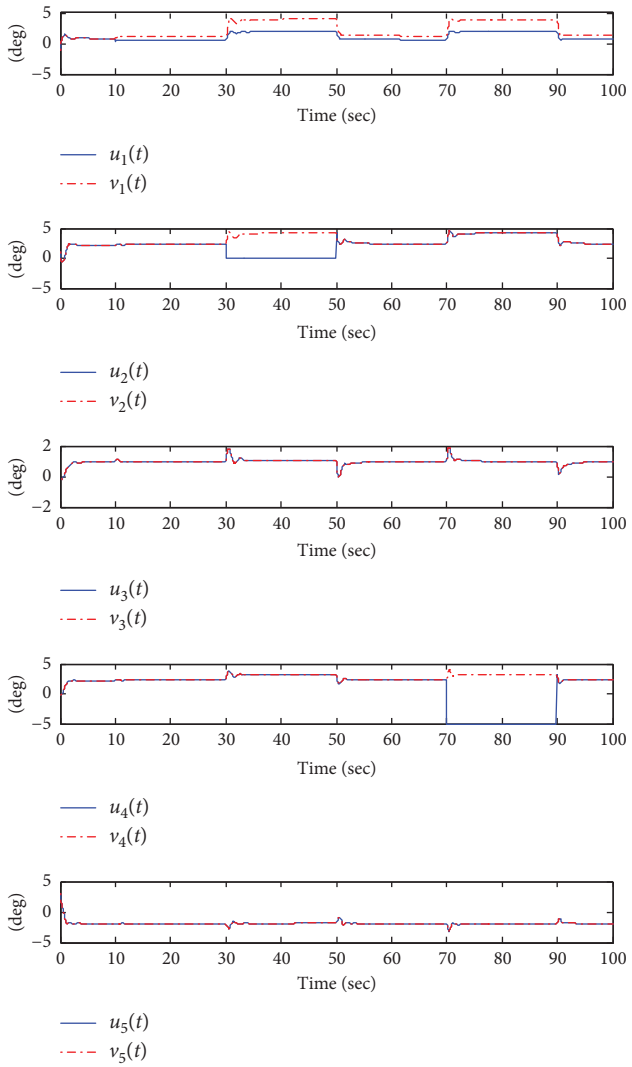

FIGURE 4: Actual control signal $u(t)$ and designed control signal $v(t)$ of the controller given in [28].

$$\begin{aligned}
\widehat{H}_{11}(0) &= [-1,0,-1]^T,\\
\widehat{H}_{12}(0) &= [1,-1,1]^T,\\
\widehat{H}_{13}(0) &= [-1,-1,0]^T,\\
\widehat{H}_{14}(0) &= [0,-1,0]^T,\\
\widehat{H}_{15}(0) &= [-1,0,1]^T,\\
\widehat{k}_1(0) &= \widehat{k}_2(0) = \widehat{k}_3(0) = 0,\\
\widehat{M}_1(0) &= I_5,\\
\eta &= 1,\\
\gamma_1 &= \gamma_2 = \gamma_3 = 0.6,\\
L &= 0,\\
\Gamma_i &= 0.6,\\
\Lambda_i &= 0.6, \quad i = 1,2,3,4,5.
\end{aligned} \tag{38}$$

4.3. Simulation Results. Figure 1 shows the plant state $x(t)$ and reference model state $x_m(t)$ by using the proposed controller (19) and the one given in [28]; Figure 2 shows the state tracking error $e(t)$ by using controller (19) and the one given in [28]; Figure 3 shows the actual control signal $u(t)$ and designed control signal $v(t)$ of controller (19); and Figure 4 shows the actual control signal $u(t)$ and designed control signal $v(t)$ of the controller given in [28].

By using the proposed controller (19), it can be seen that (1) during $0 \le t < 10$ s, there is only system matrix uncertainty and no fault, and the tracking performance can be guaranteed in finite time; (2) whenever a new fault occurs at 10, 30, and 70 s and the fault recovers at 50 and 90 s, after the transient response, the tracking performance recovers. Similar conclusions can be obtained when using the controller given in [28], while it only guarantees the asymptotic tracking property, that is, it only promises the stability of infinite time. It is obvious that the proposed robust finite-time FTC scheme possesses a better transient response and faster convergence rate.

Summarizing all the above results, it is clear that the proposed robust adaptive finite-time FTC scheme can effectively ensure the state practical tracking property in finite time in the presence of unknown actuator faults and system matrix uncertainty.

5. Conclusions

In this article, a state-feedback model reference adaptive finite-time FTC scheme has been developed for linear systems in the presence of unknown actuator faults and system matrix uncertainty. The designed robust controller updated by the adaptive laws ensures that the tracking errors converge to a small neighborhood of the origin in finite time. Finally, the performance of the proposed control scheme is illustrated by simulation results for a lateral-directional dynamic model of the F-18 HARV system.

Our future work will focus on the control problem for the system under practical constrains, such as actuator amplitude saturation, rate limitation, and input matrix uncertainty.

Appendix

A. The Control Algorithm

The proposed control algorithm is summarized as follows:

Step 1. Give the initial state $x(0)$, $x_m(0)$, the reference model input $r_m(t)$, and initial values of parameter estimates $\widehat{K}_x(0)$, $\widehat{K}_r(0)$, $\widehat{k}_1(0)$, $\widehat{\xi}_1(0)$, and $\widehat{\xi}_2(0)$.

Step 2. For $i = 1,2,\ldots,m$, choose the following adaptive gains:

$$\begin{aligned}
&\Gamma_i, \quad \Lambda_i, \quad \Upsilon_i, \quad \Theta_i, \quad \mu_i,\\
&\tau_i, \quad c_1, \quad c_2, \quad \varsigma_1, \quad \varsigma_2,
\end{aligned} \tag{A.1}$$

and constants

$$l_1, \quad l_2, \quad l_3, \quad \alpha. \tag{A.2}$$

Step 3. Estimate the unknown parameters by adaptive laws:

$$\begin{aligned}
\dot{\widehat{K}}_{xi} &= -\Gamma_i\left(2xe^T Pb_i + \Lambda_i \widehat{K}_{xi}\right),\\
\dot{\widehat{K}}_{ri} &= -\Upsilon_i\left(2r_m e^T Pb_i + \Theta_i \widehat{K}_{ri}\right),\\
\dot{\widehat{k}}_{1i} &= -\mu_i\left(2e^T Pb_i + \tau_i \widehat{k}_{1i}\right),\\
\dot{\widehat{\xi}}_1 &= c_1\left(l_2\left(e^T Pe\right)^\alpha - \varsigma_1 \widehat{\xi}_1\right),\\
\dot{\widehat{\xi}}_2 &= c_2\left(2\left\|e^T PB\right\|\|x\| - \varsigma_2 \widehat{\xi}_2\right).
\end{aligned} \tag{A.3}$$

Step 4. Obtain the controller:

$$v = \widehat{K}_x x + \widehat{K}_r r_m + \widehat{k}_1 + k_2 + k_3 + k_4, \tag{A.4}$$

where

$$k_2 = \frac{B^T Pee^T Qe}{2\left\|e^T PB\right\|^2 + 1},$$

$$k_3 = \begin{cases} -\dfrac{l_2 B^T Pe\left(l_1 + \widehat{\xi}_1\right)\left(e^T Pe\right)^\alpha}{2\left\|e^T PB\right\|^2}, & \text{if} \left\|e^T PB\right\| > 0, \\ 0_{m\times 1}, & \text{if} \left\|e^T PB\right\| = 0, \end{cases} \tag{A.5}$$

$$k_4 = -\frac{\widehat{\xi}_2^2 \|x\|^2 B^T Pe}{\widehat{\xi}_2 \|x\| \|B^T Pe\| + l_3}.$$

B. Proof of Theorem 1

Proof. Construct the Lyapunov function as

$$\begin{aligned}
V = e^T Pe &+ \frac{1}{2}\sum_{i=1}^m \sigma_i \widetilde{K}_{xi}^T \Gamma_i^{-1} \widetilde{K}_{xi} + \frac{1}{2}\sum_{i=1}^m \sigma_i \widetilde{K}_{ri}^T \Upsilon_i^{-1} \widetilde{K}_{ri}\\
&+ \frac{1}{2}\sum_{i=1}^m \sigma_i \mu_i^{-1} \widetilde{k}_{1i}^2 + \frac{1}{2} c_1^{-1} \chi \widetilde{\xi}_1^2 + \frac{1}{2} c_2^{-1} \chi \widetilde{\xi}_2^2,
\end{aligned} \tag{B.1}$$

where $\widetilde{K}_{xi} = \widehat{K}_{xi} - K_{xi}$, $\widetilde{K}_{ri} = \widehat{K}_{ri} - K_{ri}$, $\widetilde{k}_{1i} = \widehat{k}_{1i} - k_{1i}$, $\widetilde{\xi}_1 = \widehat{\xi}_1 - \xi_1$, and $\widetilde{\xi}_2 = \widehat{\xi}_2 - \xi_2$.

The time derivative of V can be derived as follows:

$$\begin{aligned}
\dot{V} = 2e^T P\Big[&A_m e + BHx + B\sigma \widetilde{K}_x x + B\sigma \widetilde{K}_r r_m + B\sigma \widetilde{k}_1\\
&+ B\sigma\left(k_2 + k_3 + k_4\right)\Big] + \sum_{i=1}^m \sigma_i \widetilde{K}_{xi}^T \Gamma_i^{-1} \dot{\widehat{K}}_{xi} + \sum_{i=1}^m \sigma_i \widetilde{K}_{ri}^T \Upsilon_i^{-1} \dot{\widehat{K}}_{ri}\\
&+ \sum_{i=1}^m \sigma_i \mu_i^{-1} \widetilde{k}_{1i} \dot{\widehat{k}}_{1i} + c_1^{-1} \chi \widetilde{\xi}_1 \dot{\widehat{\xi}}_1 + c_2^{-1} \chi \widetilde{\xi}_2 \dot{\widehat{\xi}}_2.
\end{aligned} \tag{B.2}$$

Now, discuss the term $2e^T PB\sigma k_3$ in two cases.

Case 1. If $\|e^T PB\| > 0$, by using Lemma 7, it has

$$\begin{aligned}
2e^T PB\sigma k_3 &= -\frac{2l_2 e^T PB\sigma B^T Pe\left(l_1 + \widehat{\xi}_1\right)\left(e^T Pe\right)^\alpha}{2\left\|e^T PB\right\|^2}\\
&\le -\chi l_2\left(l_1 + \widehat{\xi}_1\right)\left(e^T Pe\right)^\alpha.
\end{aligned} \tag{B.3}$$

Case 2. If $\|e^T PB\| = 0$, due to the fact of B being full-row rank, for positive definite matrix P, it follows that PB is full-row rank, that is, in this case $e = 0_{n\times 1}$, hence,

$$2e^T PB\sigma k_3 = -\chi l_2\left(l_1 + \widehat{\xi}_1\right)\left(e^T Pe\right)^\alpha = 0. \tag{B.4}$$

Combining the above discussions, we get

$$\begin{aligned}
2e^T PB\sigma k_3 &\le -\chi l_2\left(l_1 + \widehat{\xi}_1\right)\left(e^T Pe\right)^\alpha\\
&= -l_2\left(e^T Pe\right)^\alpha + l_2\left(1 - l_1\chi\right)\left(e^T Pe\right)^\alpha\\
&\quad - l_2\chi\widehat{\xi}_1\left(e^T Pe\right)^\alpha.
\end{aligned} \tag{B.5}$$

Substituting (20), (26), and (B.5) into (B.2), we obtain

$$\begin{aligned}
\dot{V} \le &-l_2\left(e^T Pe\right)^\alpha + 2e^T PA_m e + 2\left\|e^T PB\right\|\|H\|\|x\|\\
&+ 2e^T PB\sigma \widetilde{K}_x x + 2e^T PB\sigma \widetilde{K}_r r_m + 2e^T PB\sigma \widetilde{k}_1\\
&+ l_2\left(1 - l_1\chi\right)\left(e^T Pe\right)^\alpha - l_2\chi\widehat{\xi}_1\left(e^T Pe\right)^\alpha\\
&- \frac{2\widehat{\xi}_2^2\|x\|^2 e^T PB\sigma B^T Pe}{\widehat{\xi}_2\|x\|\|B^T Pe\| + l_3} + \frac{2e^T PB\sigma B^T Pee^T Qe}{2\left\|e^T PB\right\|^2 + 1}\\
&+ \sum_{i=1}^m \sigma_i \widetilde{K}_{xi}^T \Gamma_i^{-1} \dot{\widehat{K}}_{xi} + \sum_{i=1}^m \sigma_i \widetilde{K}_{ri}^T \Upsilon_i^{-1} \dot{\widehat{K}}_{ri}\\
&+ \sum_{i=1}^m \sigma_i \mu_i^{-1} \widetilde{k}_{1i} \dot{\widehat{k}}_{1i} + c_1^{-1} \chi \widetilde{\xi}_1 \dot{\widehat{\xi}}_1 + c_2^{-1} \chi \widetilde{\xi}_2 \dot{\widehat{\xi}}_2.
\end{aligned} \tag{B.6}$$

According to the definition of ξ_1 and ξ_2 in (24), it has

$$l_2(1-l_1\chi)\left(e^TPe\right)^\alpha = l_2\chi\xi_1\left(e^TPe\right)^\alpha, \tag{B.7}$$

$$\begin{aligned} 2\left\|e^TPB\right\|\|H\|\|x\| &\le 2\overline{h}\left\|e^TPB\right\|\|x\| \\ &= 2\chi\xi_2\left\|e^TPB\right\|\|x\|. \end{aligned} \tag{B.8}$$

Then, using Lemma 7 and substituting (B.7) and (B.8) into (B.6) yields that

$$\begin{aligned} \dot{V} \le & -l_2\left(e^TPe\right)^\alpha + e^T\left(A_m^TP+PA_m\right)e + 2\chi\xi_2\left\|e^TPB\right\|\|x\| \\ & + 2e^TPB\sigma\widetilde{K}_x x + 2e^TPB\sigma\widetilde{K}_r r_m + 2e^TPB\sigma\widetilde{k}_1 \\ & - l_2\chi\widetilde{\xi}_1\left(e^TPe\right)^\alpha - \frac{2\chi\widehat{\xi}_2^2\|x\|^2\left\|e^TPB\right\|^2}{\widehat{\xi}_2\|x\|\|B^TPe\|+l_3} \\ & + \frac{2\left\|e^TPB\right\|^2e^TQe}{2\left\|e^TPB\right\|^2+1} + \sum_{i=1}^m\sigma_i\widetilde{K}_{xi}^T\Gamma_i^{-1}\dot{\widehat{K}}_{xi} \\ & + \sum_{i=1}^m\sigma_i\widetilde{K}_{ri}^T\Upsilon_i^{-1}\dot{\widehat{K}}_{ri} + \sum_{i=1}^m\sigma_i\mu_i^{-1}\widetilde{k}_{1i}\dot{\widehat{k}}_{1i} \\ & + c_1^{-1}\chi\widetilde{\xi}_1\dot{\widehat{\xi}}_1 + c_2^{-1}\chi\widetilde{\xi}_2\dot{\widehat{\xi}}_2. \end{aligned} \tag{B.9}$$

Substituting (14) and adaptive laws in (27)–(31) into (B.9) yields

$$\begin{aligned} \dot{V} \le & -l_2\left(e^TPe\right)^\alpha - e^TQe + 2\chi\xi_2\left\|e^TPB\right\|\|x\| \\ & + 2e^TPB\sigma\widetilde{K}_x x + 2e^TPB\sigma\widetilde{K}_r r_m + 2e^TPB\sigma\widetilde{k}_1 \\ & - l_2\chi\widetilde{\xi}_1\left(e^TPe\right)^\alpha - \frac{2\chi\widehat{\xi}_2^2\|x\|^2\left\|e^TPB\right\|^2}{\widehat{\xi}_2\|x\|\|B^TPe\|+l_3} \\ & + \frac{2\left\|e^TPB\right\|^2e^TQe}{2\left\|e^TPB\right\|^2+1} - 2\sum_{i=1}^m\sigma_i\widetilde{K}_{xi}^T x e^TPb_i \\ & - \sum_{i=1}^m\sigma_i\widetilde{K}_{xi}^T\Lambda_i\widehat{K}_{xi} - 2\sum_{i=1}^m\sigma_i\widetilde{K}_{ri}^T r_m e^TPb_i \\ & - \sum_{i=1}^m\sigma_i\widetilde{K}_{ri}^T\Theta_i\widehat{K}_{ri} - 2\sum_{i=1}^m\sigma_i\widetilde{k}_{1i}e^TPb_i \\ & - \sum_{i=1}^m\sigma_i\widetilde{k}_{1i}\tau_i\widehat{k}_{1i} + l_2\chi\widetilde{\xi}_1\left(e^TPe\right)^\alpha - \varsigma_1\chi\widetilde{\xi}_1\widehat{\xi}_1 \\ & + 2\chi\widetilde{\xi}_2\left\|e^TPB\right\|\|x\| - \varsigma_2\chi\widehat{\xi}_2\widehat{\xi}_2 \\ = & -l_2\left(e^TPe\right)^\alpha - e^TQe - \sum_{i=1}^m\sigma_i\widetilde{K}_{xi}^T\Lambda_i\widehat{K}_{xi} - \varsigma_1\chi\widetilde{\xi}_1\widehat{\xi}_1 \\ & - \sum_{i=1}^m\sigma_i\widetilde{K}_{ri}^T\Theta_i\widehat{K}_{ri} - \sum_{i=1}^m\sigma_i\widetilde{k}_{1i}\tau_i\widehat{k}_{1i} - \varsigma_2\chi\widetilde{\xi}_2\widehat{\xi}_2 \\ & + \frac{2\chi l_3\widehat{\xi}_2\|x\|\left\|e^TPB\right\|}{\widehat{\xi}_2\|x\|\|B^TPe\|+l_3} + \frac{2\left\|e^TPB\right\|^2e^TQe}{2\left\|e^TPB\right\|^2+1}. \end{aligned} \tag{B.10}$$

Then, according to the inequality

$$0 \le \frac{c\ d}{c+d} \le c, \quad \forall c,\ d \ge 0,\ c+d \ne 0, \tag{B.11}$$

it has

$$\frac{2\chi l_3\widehat{\xi}_2\|x\|\left\|e^TPB\right\|}{\widehat{\xi}_2\|x\|\|B^TPe\|+l_3} \le 2\chi l_3, \tag{B.12}$$

$$\frac{2\left\|e^TPB\right\|^2e^TQe}{2\left\|e^TPB\right\|^2+1} \le e^TQe. \tag{B.13}$$

Then, substituting (B.12) and (B.13) into (B.10), we obtain

$$\begin{aligned} \dot{V} \le & -l_2\left(e^TPe\right)^\alpha - \sum_{i=1}^m\sigma_i\widetilde{K}_{xi}^T\Lambda_i\widehat{K}_{xi} - \sum_{i=1}^m\sigma_i\widetilde{K}_{ri}^T\Theta_i\widehat{K}_{ri} \\ & - \sum_{i=1}^m\sigma_i\widetilde{k}_{1i}\tau_i\widehat{k}_{1i} - \varsigma_1\chi\widetilde{\xi}_1\widehat{\xi}_1 - \varsigma_2\chi\widetilde{\xi}_2\widehat{\xi}_2 + 2\chi l_3. \end{aligned} \tag{B.14}$$

From Lemma 3, for any $\vartheta_i, \gamma_i, \omega_i > (1/2)$, $i = 1, 2, \ldots, m$, and $\varrho_1, \varrho_2 > (1/2)$, one has

$$-\widetilde{K}_{xi}^T\widehat{K}_{xi} \le -\frac{2\vartheta_i-1}{2\vartheta_i}\widetilde{K}_{xi}^T\widetilde{K}_{xi} + \frac{\vartheta_i}{2}K_{xi}^TK_{xi}, \tag{B.15}$$

$$-\widetilde{K}_{ri}^T\widehat{K}_{ri} \le -\frac{2\gamma_i-1}{2\gamma_i}\widetilde{K}_{ri}^T\widetilde{K}_{ri} + \frac{\gamma_i}{2}K_{ri}^TK_{ri}, \tag{B.16}$$

$$-\widetilde{k}_{1i}\widehat{k}_{1i} \le -\frac{2\omega_i-1}{2\omega_i}\widetilde{k}_{1i}^2 + \frac{\omega_i}{2}k_{1i}^2, \tag{B.17}$$

$$-\widetilde{\xi}_1\widehat{\xi}_1 \le -\frac{2\varrho_1-1}{2\varrho_1}\widetilde{\xi}_1^2 + \frac{\varrho_1}{2}\xi_1^2, \tag{B.18}$$

$$-\widetilde{\xi}_2\widehat{\xi}_2 \le -\frac{2\varrho_2-1}{2\varrho_2}\widetilde{\xi}_2^2 + \frac{\varrho_2}{2}\xi_2^2. \tag{B.19}$$

Now, substituting (B.15)–(B.19) into (B.14), we have

$$\begin{aligned}\dot{V} \le & -l_2\left(e^T Pe\right)^{\alpha} - \sum_{i=1}^{m}\left(\frac{2\vartheta_i - 1}{2\vartheta_i}\sigma_i \widetilde{K}_{xi}^T \Lambda_i \widetilde{K}_{xi}\right)^{\alpha} \\ & - \sum_{i=1}^{m}\left(\frac{2\gamma_i - 1}{2\gamma_i}\sigma_i \widetilde{K}_{ri}^T \Theta_i \widetilde{K}_{ri}\right)^{\alpha} - \sum_{i=1}^{m}\left(\frac{2\omega_i - 1}{2\omega_i}\sigma_i \tau_i \widetilde{k}_{1i}^2\right)^{\alpha} \\ & - \left(\frac{2\varrho_1 - 1}{2\varrho_1}\varsigma_1 \chi \widetilde{\xi}_1^2\right)^{\alpha} - \left(\frac{2\varrho_2 - 1}{2\varrho_2}\varsigma_2 \chi \widetilde{\xi}_2^2\right)^{\alpha} \\ & + \sum_{i=1}^{m}\left(\frac{2\vartheta_i - 1}{2\vartheta_i}\sigma_i \widetilde{K}_{xi}^T \Lambda_i \widetilde{K}_{xi}\right)^{\alpha} - \sum_{i=1}^{m}\frac{2\vartheta_i - 1}{2\vartheta_i}\sigma_i \widetilde{K}_{xi}^T \Lambda_i \widetilde{K}_{xi} \\ & + \sum_{i=1}^{m}\left(\frac{2\gamma_i - 1}{2\gamma_i}\sigma_i \widetilde{K}_{ri} \Theta_i \widetilde{K}_{ri}\right)^{\alpha} - \sum_{i=1}^{m}\frac{2\gamma_i - 1}{2\gamma_i}\sigma_i \widetilde{K}_{ri}^T \Theta_i \widetilde{K}_{ri} \\ & + \sum_{i=1}^{m}\left(\frac{2\omega_i - 1}{2\omega_i}\sigma_i \tau_i \widetilde{k}_{1i}^2\right)^{\alpha} - \sum_{i=1}^{m}\frac{2\omega_i - 1}{2\omega_i}\sigma_i \tau_i \widetilde{k}_{1i}^2 \\ & + \left(\frac{2\varrho_1 - 1}{2\varrho_1}\varsigma_1 \chi \widetilde{\xi}_1^2\right)^{\alpha} - \frac{2\varrho_1 - 1}{2\varrho_1}\varsigma_1 \chi \widetilde{\xi}_1^2 \\ & + \left(\frac{2\varrho_2 - 1}{2\varrho_2}\varsigma_2 \chi \widetilde{\xi}_2^2\right)^{\alpha} - \frac{2\varrho_2 - 1}{2\varrho_2}\varsigma_2 \chi \widetilde{\xi}_2^2 \\ & + \sum_{i=1}^{m}\frac{\vartheta_i}{2}K_{xi}^T \sigma_i \Lambda_i K_{xi} + \sum_{i=1}^{m}\frac{\gamma_i}{2}K_{ri}^T \sigma_i \Theta_i K_{ri} \\ & + \sum_{i=1}^{m}\frac{\omega_i}{2}\sigma_i \tau_i k_{1i}^2 + \frac{\varrho_1}{2}\varsigma_1 \chi \xi_1^2 + \frac{\varrho_2}{2}\varsigma_2 \chi \xi_2^2 + 2\chi l_3. \end{aligned} \tag{B.20}$$

By applying Lemma 4, let

$$\begin{aligned} y &= \frac{2\vartheta_i - 1}{2\vartheta_i}\sigma_i \widetilde{K}_{xi}^T \Lambda_i \widetilde{K}_{xi}, \\ z &= 1, \\ a &= \alpha, \\ b &= 1 - \alpha, \\ \mu &= \frac{1}{\alpha}, \end{aligned} \tag{B.21}$$

it has

$$\left(\frac{2\vartheta_i - 1}{2\vartheta_i}\sigma_i \widetilde{K}_{xi}^T \Lambda_i \widetilde{K}_{xi}\right)^{\alpha} \le \frac{2\vartheta_i - 1}{2\vartheta_i}\sigma_i \widetilde{K}_{xi}^T \Lambda_i \widetilde{K}_{xi} + \overline{\alpha}, \tag{B.22}$$

where $\overline{\alpha} = (1-\alpha)\alpha^{\alpha/1-\alpha}$.

Similarly, we can conclude that

$$\left(\frac{2\gamma_i - 1}{2\gamma_i}\sigma_i \widetilde{K}_{ri}^T \Theta_i \widetilde{K}_{ri}\right)^{\alpha} \le \frac{2\gamma_i - 1}{2\gamma_i}\sigma_i \widetilde{K}_{ri}^T \Theta_i \widetilde{K}_{ri} + \overline{\alpha}, \tag{B.23}$$

$$\left(\frac{2\omega_i - 1}{2\omega_i}\sigma_i \tau_i \widetilde{k}_{1i}^2\right)^{\alpha} \le \frac{2\omega_i - 1}{2\omega_i}\sigma_i \tau_i \widetilde{k}_{1i}^2 + \overline{\alpha}, \tag{B.24}$$

$$\left(\frac{2\varrho_1 - 1}{2\varrho_1}\varsigma_1 \chi \widetilde{\xi}_1^2\right)^{\alpha} \le \frac{2\varrho_1 - 1}{2\varrho_1}\varsigma_1 \chi \widetilde{\xi}_1^2 + \overline{\alpha}, \tag{B.25}$$

$$\left(\frac{2\varrho_2 - 1}{2\varrho_2}\varsigma_2 \chi \widetilde{\xi}_2^2\right)^{\alpha} \le \frac{2\varrho_2 - 1}{2\varrho_2}\varsigma_2 \chi \widetilde{\xi}_2^2 + \overline{\alpha}. \tag{B.26}$$

Substituting (B.22)–(B.26) into (B.20) and applying Lemma 2, we have

$$\begin{aligned}\dot{V} \le & -\sum_{i=1}^{m}\left(\frac{(2\vartheta_i - 1)\lambda_{\min}(\Lambda_i)}{\vartheta_i \lambda_{\max}(\Gamma_i^{-1})}\right)^{\alpha}\left(\frac{1}{2}\sigma_i \widetilde{K}_{xi}^T \Gamma_i^{-1} \widetilde{K}_{xi}\right)^{\alpha} \\ & - \sum_{i=1}^{m}\left(\frac{(2\gamma_i - 1)\lambda_{\min}(\Theta_i)}{\gamma_i \lambda_{\max}(\Upsilon_i^{-1})}\right)^{\alpha}\left(\frac{1}{2}\sigma_i \widetilde{K}_{ri}^T \Upsilon_i^{-1} \widetilde{K}_{ri}\right)^{\alpha} \\ & - \sum_{i=1}^{m}\left(\frac{(2\omega_i - 1)\mu_i \tau_i}{\omega_i}\right)^{\alpha}\left(\frac{1}{2}\sigma_i \mu_i^{-1} \widetilde{k}_{1i}^2\right)^{\alpha} \\ & - \left(\frac{(2\varrho_1 - 1)c_1 \varsigma_1}{\varrho_1}\right)^{\alpha}\left(\frac{1}{2}c_1^{-1} \chi \widetilde{\xi}_1^2\right)^{\alpha} \\ & - \left(\frac{(2\varrho_2 - 1)c_2 \varsigma_2}{\varrho_2}\right)^{\alpha}\left(\frac{1}{2}c_2^{-1} \chi \widetilde{\xi}_2^2\right)^{\alpha} \\ & - l_2\left(e^T Pe\right)^{\alpha} + \sum_{i=1}^{m}\frac{\vartheta_i}{2}K_{xi}^T \sigma_i \Lambda_i K_{xi} \\ & + \sum_{i=1}^{m}\frac{\gamma_i}{2}K_{ri}^T \sigma_i \Theta_i K_{ri} + \sum_{i=1}^{m}\frac{\omega_i}{2}\sigma_i \tau_i k_{1i}^2 + \frac{\varrho_1}{2}\varsigma_1 \chi \xi_1^2 \\ & + \frac{\varrho_2}{2}\varsigma_2 \chi \xi_2^2 + 2\chi l_3 + (3m + 2)\overline{\alpha} \\ \le & -\eta\left[\left(e^T Pe\right)^{\alpha} + \sum_{i=1}^{m}\left(\frac{1}{2}\sigma_i \widetilde{K}_{xi}^T \Gamma_i^{-1} \widetilde{K}_{xi}\right)^{\alpha} + \sum_{i=1}^{m}\left(\frac{1}{2}\sigma_i \widetilde{K}_{ri}^T \Upsilon_i^{-1} \widetilde{K}_{ri}\right)^{\alpha}\right. \\ & \left. + \sum_{i=1}^{m}\left(\frac{1}{2}\sigma_i \mu_i^{-1} \widetilde{k}_{1i}^2\right)^{\alpha} + \left(\frac{1}{2}c_1^{-1} \chi \widetilde{\xi}_1^2\right)^{\alpha} + \left(\frac{1}{2}c_2^{-1} \chi \widetilde{\xi}_2^2\right)^{\alpha}\right] + \overline{\psi}, \end{aligned} \tag{B.27}$$

where

$$\eta = \min\left\{l_2, \left(\frac{(2\vartheta_i - 1)\lambda_{\min}(\Lambda_i)}{\vartheta_i \lambda_{\max}(\Gamma_i^{-1})}\right)^{\alpha}, \left(\frac{(2\gamma_i - 1)\lambda_{\min}(\Theta_i)}{\gamma_i \lambda_{\max}(\Upsilon_i^{-1})}\right)^{\alpha}, \left(\frac{(2\omega_i - 1)\mu_i \tau_i}{\omega_i}\right)^{\alpha}, \left(\frac{(2\varrho_1 - 1)c_1 \varsigma_1}{\varrho_1}\right)^{\alpha}, \left(\frac{(2\varrho_2 - 1)c_2 \varsigma_2}{\varrho_2}\right)^{\alpha}\right\},$$

$$\overline{\psi} = \sum_{i=1}^{m} \frac{\vartheta_i}{2} K_{xi}^T \sigma_i \Lambda_i K_{xi} + \sum_{i=1}^{m} \frac{\gamma_i}{2} K_{ri}^T \sigma_i \Theta_i K_{ri} + \sum_{i=1}^{m} \frac{\omega_i}{2} \sigma_i \tau_i k_{1i}^2 + \frac{\varrho_1}{2} \varsigma_1 \chi \xi_1^2 + \frac{\varrho_2}{2} \varsigma_2 \chi \xi_2^2 + 2\chi l_3 + (3m + 2)\overline{\alpha}. \tag{B.28}$$

Furthermore, according to Lemma 1, one has

$$\dot{V} \leq -\eta V^{\alpha} + \overline{\psi}. \tag{B.29}$$

Therefore, according to Lemma 5, the decrease of V can drive the trajectories of the closed-loop system into $V^{\alpha} \leq (\overline{\psi}/(1 - \iota)\eta)$ in a finite time T_r with

$$T_r \leq \frac{V^{1-\alpha}(0)}{\eta\iota(1 - \alpha)}, \tag{B.30}$$

where $0 < \iota < 1$.

This completes the proof.

Data Availability

The data used to support the findings of this study are available from the corresponding author upon request.

Conflicts of Interest

The authors declare that there are no conflicts of interest regarding the publication of this paper.

Acknowledgments

This work was supported by the National Natural Science Foundation of China under grant nos. 61573161 and 61873319.

References

[1] Z. Mao and B. Jiang, "Fault identification and fault-tolerant control for a class of networked control systems," *International Journal of Innovative Computing, Information and Control*, vol. 3, no. 5, pp. 1121–1130, 2007.

[2] C. Peng, E. G. Tian, and T. C. Yang, "Robust fault-tolerant control of networked control systems with stochastic actuator failure," *IET Control Theory & Applications*, vol. 4, no. 12, pp. 3003–3011, 2010.

[3] Z. Chen, Q. Chen, X. He, and M. Sun, "Adaptive finite-time command filtered fault-tolerant control for uncertain spacecraft with prescribed performance," *Complexity*, vol. 2018, Article ID 4912483, 12 pages, 2018.

[4] S. Park, J. Bae, Y. Kim, and S. Kim, "Fault tolerant flight control system for the tilt-rotor UAV," *Journal of the Franklin Institute*, vol. 350, no. 9, pp. 2535–2559, 2013.

[5] J. Niu, F. Chen, and G. Tao, "Nonlinear fuzzy fault-tolerant control of hypersonic flight vehicle with parametric uncertainty and actuator fault," *Nonlinear Dynamics*, vol. 92, no. 7, pp. 1299–1315, 2018.

[6] G. Yang, J. L. Wang, and Y. C. Soh, "Reliable H_∞ controller design for linear systems," *Automatica*, vol. 37, no. 5, pp. 717–725, 2001.

[7] S. M. Tabatabaeipour, R. Izadi-Zamanabadi, T. Bak, and A. P. Ravn, "Passive fault-tolerant control of discrete time piecewise affine systems against actuator faults," *International Journal of Systems Science*, vol. 43, no. 11, pp. 1985–1997, 2012.

[8] R. Wang and J. Wang, "Passive actuator fault-tolerant control for a class of overactuated nonlinear systems and applications to electric vehicles," *IEEE Transactions on Vehicular Technology*, vol. 62, no. 3, pp. 972–985, 2013.

[9] A. Nasiri, S. K. Nguang, A. Swain, and D. Almakhles, "Passive actuator fault tolerant control for a class of MIMO nonlinear systems with uncertainties," *International Journal of Control*, vol. 92, no. 3, pp. 693–704, 2019.

[10] C. P. Tan and C. Edwards, "Sliding mode observers for robust detection and reconstruction of actuator and sensor faults," *International Journal of Robust and Nonlinear Control*, vol. 13, no. 5, pp. 443–463, 2003.

[11] L. I. Allerhand and U. Shaked, "Robust switching-based fault tolerant control," *IEEE Transactions on Automatic Control*, vol. 60, no. 8, pp. 2272–2276, 2015.

[12] Z. Gao, P. Cheng, M. Qian, G. Jiang, and J. Lin, "Active fault-tolerant control approach design for rigid spacecraft with multiple actuator faults," *Proceedings of the Institution of Mechanical Engineers, Part I: Journal of Systems and Control Engineering*, vol. 232, no. 10, pp. 1365–1378, 2018.

[13] C.-C. Chen, S. S.-D. Xu, and Y.-W. Liang, "Study of nonlinear integral sliding mode fault-tolerant control," *IEEE/ASME Transactions on Mechatronics*, vol. 21, no. 2, pp. 1160–1168, 2016.

[14] Z. Gao and P. J. Antsaklis, "Stability of the pseudo-inverse method for reconfigurable control systems," *International Journal of Control*, vol. 53, no. 3, pp. 717–729, 1991.

[15] N. Esfahani and K. Khorasani, "A distributed model predictive control (MPC) fault reconfiguration strategy for formation flying satellites," *International Journal of Control*, vol. 89, no. 5, pp. 960–983, 2016.

[16] L.-B. Wu, G.-H. Yang, and D. Ye, "Robust adaptive fault-tolerant control for linear systems with actuator failures and mismatched parameter uncertainties," *IET Control Theory & Applications*, vol. 8, no. 6, pp. 441–449, 2014.

[17] Y. Ma, B. Jiang, G. Tao, and H. Yang, "Adaptive direct compensation control scheme for spacecraft with multiple actuator faults," *Journal of Guidance, Control, and Dynamics*, vol. 42, no. 4, pp. 923–930, 2019.

[18] S. Xiao and J. Dong, "Robust adaptive fault-tolerant tracking control for uncertain linear systems with time-varying performance bounds," *International Journal of Robust and Nonlinear Control*, vol. 29, no. 4, pp. 849–866, 2019.

[19] B. Liu, M. Saif, and H. Fan, "Adaptive fault tolerant control of a half-car active suspension systems subject to random actuator failures," *IEEE/ASME Transactions on Mechatronics*, vol. 21, no. 6, pp. 2847–2857, 2016.

[20] W. Wang, C. Wen, and G. Yang, "Stability analysis of decentralized adaptive backstepping control systems with actuator failures," *Journal of Systems Science and Complexity*, vol. 22, no. 1, pp. 109–121, 2009.

[21] X. Tang, G. Tao, L. Wang, and J. A. Stankovic, "Robust and adaptive actuator failure compensation designs for a rocket

fairing structural-acoustic model," *IEEE Transactions on Aerospace and Electronic Systems*, vol. 40, no. 4, pp. 1359–1366, 2004.

[22] X. Jin, J. Qin, Y. Shi, and W. X. Zheng, "Auxiliary fault tolerant control with actuator amplitude saturation and limited rate," *IEEE Transactions on Systems, Man, and Cybernetics: Systems*, vol. 48, no. 10, pp. 1816–1825, 2017.

[23] X. Jin, S. Lü, J. Qin, and W. X. Zheng, "Auxiliary constrained control of a class of fault-tolerant systems," *IEEE Transactions on Systems, Man, and Cybernetics: Systems*, pp. 1–12, 2019.

[24] C. Wang, C. Wen, and Y. Lin, "Adaptive actuator failure compensation for a class of nonlinear systems with unknown control direction," *IEEE Transactions on Automatic Control*, vol. 62, no. 1, pp. 385–392, 2017.

[25] B. Liu, L. Liu, Y. Wang, and H. Fan, "Stabilization of nonlinear uncertain systems with stochastic actuator failures and time-varying delay," *International Journal of Robust and Nonlinear Control*, vol. 26, no. 9, pp. 1825–1840, 2016.

[26] C.-H. Xie and G.-H. Yang, "Model-free fault-tolerant control approach for uncertain state-constrained linear systems with actuator faults," *International Journal of Adaptive Control and Signal Processing*, vol. 31, no. 2, pp. 223–239, 2017.

[27] A. Ben Brahim, S. Dhahri, F. Ben Hmida, and A. Sellami, "Multiplicative fault estimation-based adaptive sliding mode fault-tolerant control design for nonlinear systems," *Complexity*, vol. 2018, Article ID 1462594, 15 pages, 2018.

[28] S. Xiao and J. Dong, "Robust adaptive fault-tolerant tracking control for uncertain linear systems with actuator failures based on the closed-loop reference model," *IEEE Transactions on Systems, Man, and Cybernetics: Systems*, pp. 1–8, 2018.

[29] S. M. Joshi and P. Patre, "Direct model reference adaptive control with actuator failures and sensor bias," *Journal of Guidance, Control, and Dynamics*, vol. 37, no. 1, pp. 312–317, 2014.

[30] J. Wang, J. Du, F. Chen, B. Jiang, and G. Tao, "Direct adaptive control scheme for a quadrotor helicopter with actuator failures via quantum logic," *Journal of Aerospace Engineering*, vol. 29, no. 5, pp. 1–7, 2016.

[31] L.-B. Wu and G.-H. Yang, "Robust adaptive fault-tolerant tracking control of multiple time-delays systems with mismatched parameter uncertainties and actuator failures," *International Journal of Robust and Nonlinear Control*, vol. 25, no. 16, pp. 2922–2938, 2015.

[32] G. Song and G. Tao, "Adaptive state-feedback control with sensor failure compensation for asymptotic output tracking," *International Journal of Adaptive Control and Signal Processing*, vol. 33, no. 1, pp. 130–156, 2019.

[33] J. Yu, P. Shi, and L. Zhao, "Finite-time command filtered backstepping control for a class of nonlinear systems," *Automatica*, vol. 92, pp. 173–180, 2018.

[34] L. Zhao, J. Yu, and P. Shi, "Command filtered backstepping-based attitude containment control for spacecraft formation," *IEEE Transactions on Systems, Man, and Cybernetics: Systems*, pp. 1–10, 2019.

[35] J. Wang, C. Zhang, S. Li, J. Yang, and Q. Li, "Finite-time output feedback control for PWM-based DC–DC buck power converters of current sensorless mode," *IEEE Transactions on Control Systems Technology*, vol. 25, no. 4, pp. 1359–1371, 2016.

[36] Z. Zhu, Y. Xia, and M. Fu, "Attitude stabilization of rigid spacecraft with finite-time convergence," *International Journal of Robust and Nonlinear Control*, vol. 21, no. 6, pp. 686–702, 2011.

[37] Y. Zhang, Y. Liu, and L. Liu, "Adaptive finite-time NN control for 3-DOF active suspension systems with displacement constraints," *IEEE Access*, vol. 7, pp. 13577–13588, 2019.

[38] F. Wang, X. Zhang, B. Chen, C. Lin, X. Li, and J. Zhang, "Adaptive finite-time tracking control of switched nonlinear systems," *Information Sciences*, vol. 421, pp. 126–135, 2017.

[39] X. Huo, Q. Hu, and B. Xiao, "Finite-time fault tolerant attitude stabilization control for rigid spacecraft," *ISA Transactions*, vol. 53, no. 2, pp. 241–250, 2014.

[40] X.-y. Zhang, Q. Zong, B.-l. Tian, S.-k. Shao, and W.-j. Liu, "Finite-time fault estimation and fault-tolerant control for rigid spacecraft," *Journal of Aerospace Engineering*, vol. 31, no. 6, Article ID 04018091, 2018.

[41] Q. Shen, D. Wang, S. Zhu, and K. Poh, "Finite-time fault-tolerant attitude stabilization for spacecraft with actuator saturation," *IEEE Transactions on Aerospace and Electronic Systems*, vol. 51, no. 3, pp. 2390–2405, 2015.

[42] X.-Z. Jin, S.-F. Wang, G.-H. Yang, and D. Ye, "Robust adaptive hierarchical insensitive tracking control of a class of leader-follower agents," *Information Sciences*, vol. 406-407, pp. 234–247, 2017.

[43] S. P. Bhat and D. S. Bernstein, "Finite-time stability of continuous autonomous systems," *SIAM Journal on Control and Optimization*, vol. 38, no. 3, pp. 751–766, 2000.

[44] H. G. Harold, J. E. Littlewood, and G. Polya, *Inequalities*, Cambridge University Press, Cambridge, UK, 1952.

[45] R. A. Horn and C. R. Johnson, *Matrix Analysis*, Cambridge University Press, Cambridge, UK, 1990.

[46] C. Qian and W. Lin, "Non-lipschitz continuous stabilizers for nonlinear systems with uncontrollable unstable linearization," *Systems & Control Letters*, vol. 42, no. 3, pp. 185–200, 2001.

[47] W. Siwakosit and R. A. Hess, "Multi-input/multi-output reconfigurable flight control design," *Journal of Guidance, Control, and Dynamics*, vol. 24, no. 6, pp. 1079–1088, 2001.

[48] R. Lamouchi, T. Raïssi, M. Amairi, and M. Aoun, "Interval observer framework for fault-tolerant control of linear parameter-varying systems," *International Journal of Control*, vol. 91, no. 3, pp. 524–533, 2018.

[49] X.-Z. Jin, Y.-G. He, and Y.-G. He, "Finite-time robust fault-tolerant control against actuator faults and saturations," *IET Control Theory & Applications*, vol. 11, no. 4, pp. 550–556, 2017.

[50] S. M. Joshi, P. Patre, and G. Tao, "Adaptive control of systems with actuator failures using an adaptive reference model," *Journal of Guidance, Control, and Dynamics*, vol. 35, no. 3, pp. 938–949, 2012.

[51] S. Chen, G. Tao, and S. M. Joshi, "On matching conditions for adaptive state tracking control of systems with actuator failures," *IEEE Transactions on Automatic Control*, vol. 47, no. 3, pp. 473–478, 2002.

Hindawi
Complexity
Volume 2020, Article ID 2107582, 9 pages
https://doi.org/10.1155/2020/2107582

WILEY | Hindawi

Research Article

Research on Optimization of Production Decision Based on Payment Time and Price Coordination

Yanyang Yan,[1] Liang Yuan ,[1] and Yemei Li[2]

[1]*College of Finance and Statistics, Hunan University, Changsha 410006, China*
[2]*The Center for Economic Research, Shandong University, Jinan 250199, China*

Correspondence should be addressed to Liang Yuan; xiabinghuale@163.com

Received 17 April 2019; Accepted 11 July 2019; Published 9 January 2020

Guest Editor: Baltazar Aguirre-Hernandez

This paper focuses on the coordination and optimization between a manufacturer and multiple retailers in a supply chain. The manufacturer makes product quotes and delivery deadlines for all retailers, and each retailer selects product offers and delivery deadlines based on their own needs. Manufacturers maximize their own total profits by setting optimal quotes and delivery deadlines. This paper constructs the mathematical model of the optimal quotation and delivery deadline and proposes a scheduling algorithm that is different from the general M/M/1 and then studies the production scheduling problem and explores the effective implementation of quotation policy in management practice.

1. Introduction

For the order-based production model, delivery time (or order-to-delivery time) guarantees have been applied as an advanced strategic weapon to compete with other companies. In the market, some customers are willing to pay more for faster delivery. In addition, customers have different time sensitivity and price sensitivity in the market. A new strategy is to divide customers into different groups based on their sensitivity to price and time. In a group, customers have the same combination of delivery time guarantees and price quotes. Different quotations and delivery times for different customer groups are evident in the printing and packaging industry. In the literature, this issue is called customer segmentation and aggregation issues [1–3]. In the following example, Printing.com uses this split and merge strategy. Printing.com is a printing service provider. It offers customers a choice of menus with different delivery times and different prices. For short lead times, prices are naturally higher.

With regard to the ability to set up this strategy, there are two situations: the ability of all customers to share and the specific capabilities of each target customer. There are two reasons why dedicated capabilities are supported. First, the use of dedicated capabilities to provide different delivery time guarantees for each customer group is compatible [4]. Second, there is less interference from customers in different fields [1, 5].

In a dedicated capability setting, performing a split and merge strategy can be thought of as multiple single customer group issues, where the only difference is the ability of each group and the sensitivity range of each group customer to price and time. Therefore, the initial work of this strategy is to quote a common optimal price and a common delivery time for each customer group. For this reason, we consider the pricing and production issues of a single customer group in the context of small batch production. In a single group, customers' payment preferences and delay tolerance are different within a known range of price and time sensitivity.

One of our technical contributions is to propose a solution to the problem of joint pricing scheduling faced by manufacturers. We show the property quotes for the best delivery times and have developed an advanced scheduling algorithm to solve the problem optimally. This paper expands Chen and Hall's research on time and scheduling coordination issues by comprehensively considering time and price quotes [6].

2. Literature Review

This article mainly considers the issue of product pricing and production. The relevant literature is mainly elaborated in the following two aspects. On the one hand, the issue of pricing

and production of the delivery deadline is not considered. On the other hand, the issue of price delivery time quotation is considered, which is more relevant to the content of this article.

Regarding pricing and production issues without considering delivery dates, in order to explore this issue, various models are mentioned in related articles [7–9]. These models assume that demand is independent of delivery time and sensitive to time quotes or other factors. In particular, Ata and Olsen reviewed the relevant due date quotes literature in detail and studied dynamic time quotes under different delay costs [10].

Since delivery time and price have a great influence on order acceptance, it is very important to integrate price quotations into delivery deadlines [11, 12]. Several papers consider different delivery times and prices for different customer groups [1, 5, 13–15], and some other literature that considers different customers groups has common price and delivery time quotes [2, 16, 17].

There is a large amount of literature to formulate relevant production policies with a stable queuing model. In these documents, a fixed scheduling rule such as First Come First Service (FCFS) is used. The customer's demand is a deterministic function of price, delivery time, and other attribute variables [17–20]. All these documents regard the production stage as an M/M/1 queue, and therefore, the FCFS rules are used therein. Our model is fundamentally different from those approaches by considering optimal production sequencing.

There are very few literatures that consider the price of production scheduling and the decision-making on the delivery date. Elhafsi studied how to determine the delivery time and price for an order in an order-type manufacturer [21]. Under the premise that the delivery time does not affect the demand, the main purpose is to quote an order of arrival based on FCFS rules for delivery time. Charnsirisakskul et al. also propose a decision model for comprehensive pricing and production decision-making using a single price model or multiple price models [22]. Their decision model is based on the inventory-based production scenario, and our research is based on order-based production. The research provided by Chen and Hall to solve this problem is the closest to our direction. In the context of detailed scheduling, Chen and Hall studied the quoting problem [6]. This article studied joint delivery times and quotations, rather than just studying quotations.

Chen and Hall analyzed the importance of adding detailed scheduling to the study. Compared with uncoordinated pricing decisions, the value of coordinated pricing and production decisions is more accurate. In our study, late fines were also included in the objective function of this article. Charnsirisakskul et al. have previously judged the importance of their participation in the study [22].

Based on the above discussion, what we have studied is the coordination pricing and delivery time quotation taking into account the detailed production scheduling decision mechanism under the order-based production environment. Specifically, the purpose of this study is to formulate a scheduling mechanism that handles delivery quotes, including prices. In the past, the scheduling study mainly solved the problem of the deadline of the quotation that did not take into account the price, so almost no researcher considered both the price and the delivery date quotation. Another major contribution of our research is that we consider the customer's heterogeneity of time and price requirements. In our study, the customer determines the order quantity. Charnsirisakskul et al. and Chen and Hall also made similar assumptions.

Table 1: Variable symbol table.

Variables	Definition
f	Total net profit
i, j	Order
c	Quoting constant for general price and delivery time
m	The number of orders completed on time at a given time t
n	Total order quantity
p	Quotation of all orders in quotation questions at regular prices and delivery times
$[p_c, p_{c+1}]$	The boundary of a particular price zone c
pt_i	The process time of order i in the quotation question of normal price and delivery time
p_i	The quotation of order i
s	The amount of a special price-time zone boundary in the quotation question for normal prices and delivery times
t	All orders in the quotation question of regular price and delivery time report delivery time
$[t_c, t_{c+1}]$	A specific time zone c
t_i	Delivery time for order i
w	General delay weight
C_i	Order i completion time
Q_i	Order quantity of order i
R	Total sales revenue
s_i	Initial process time of order i
T	Total delay penalty
T_i	Delay penalty for order i
Y_i	Process time for order i
α_i	Potential market size of order i
β_i	Price sensitivity of order i
θ_i	Time sensitivity of order i

3. Model Construction

Assuming that there are n retailers, denoted as $i = 1, 2, 3, \ldots, n$, the manufacturer introduces a price and delivery time for all retailers. When a retailer's order is completed, the manufacturer will deliver the order to the retailer. We assume that the scheduling time is not taken into account, and assuming that the production process time of each product is fixed and known, the capacity cost is also fixed and known. The model symbols are summarized in Table 1.

In order to reflect consumer sensitivity to price and delivery time, we assume the following demand function that reflects the number of consumer orders:

$$Q_i(p, t) = \alpha_i - \beta_i \cdot p - \theta_i \cdot t, \tag{1}$$

where $\alpha_i, \beta_i, \theta_i$ is the normal number, α_i indicates the potential market size of order i, β_i indicates the price sensitivity of order i, θ_i indicates the time sensitivity of order i.

We combine (β_i, θ_i) to describe consumer sensitivity to price and delivery time. For the possible zero demand or negative demand quantity, we assume that consumers will not place orders. We assume that a valid order placed by the consumer must be produced and not delivered separately. Assume that the manufacturer is a pure production machine and u denotes the priority given per unit product process time, so the production process time of the order is described as:

$$pt_i = u \cdot Q_i. \tag{2}$$

At the beginning of each planned production cycle, the manufacturer will set product price and delivery time quotation, so the process time of all orders has been determined at the initial moment, so the initial release time standard for all orders is 0.

If the order is completed beyond the delivery time, the manufacturer will bear the delay penalty. Since the consumers we consider come from a consumer group, we have already discussed in the introduction section that it is reasonable to determine a weight penalty for delay for all consumers, that is to say:

$$T_i(p,t) = w \cdot \max(0, C_i - t), \tag{3}$$

where C_i is the completion time of order i and w is the general delay weight for all consumers.

Our goal is to maximize the manufacturer's net profit. Since fixed facility costs do not affect the optimization decision on product prices and delivery time quotes, our profit function will not include fixed facility costs. The specific profit function is expressed as follows:

$$\begin{aligned} &\text{Maximize} f(p,t) = p\sum_{i=1}^{n} \max(Q_i(p,t), 0) - \sum_{i=1}^{n} (g \cdot T_i(p,t)), \\ &\text{Subject to} g = \begin{cases} 0, & Q_i(p,t) \le 0 \\ 1, & Q_i(p,t) < 0 \end{cases}, \quad p, t \ge 0. \end{aligned} \tag{4}$$

Let p^* and t^* denote the optimal solutions for p and t, respectively.

According to the objective function (4), the manufacturer's production plan is introduced into the model, and we will study the optimal production sequence problem for this scheduling problem. The following model will be divided into two types of general models to study. One is fixed quotes, and the other is fixed delivery time.

3.1. Optimal Production Sequence. According to the objective function (4), the optimal net profit is not only related to delivery time and price, but also related to the production sequence of the order. Xia et al. demonstrated that the shortest processing time (SPT) has a gradual optimality [23], and because of the existence of delayed punishment, we have Lemma 1.

Lemma 1. *Shortest processing time (SPT) is the optimal sequence rule for maximizing profit in product production.*

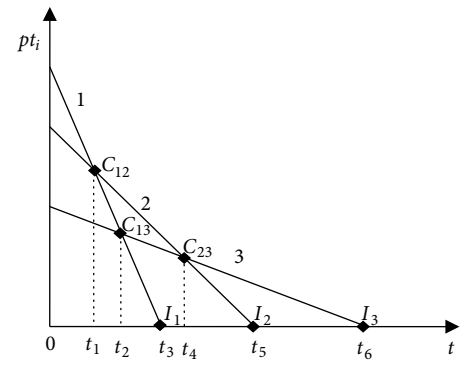

Figure 1: Order processing times with respect to one decision variable.

Table 2: SPT sequences in different time zones.

Time zones	$0-t_1$	t_1-t_2	t_2-t_3	t_3-t_4	t_4-t_5	t_5-t_6
SPT sequences	3–2–1	3–1–2	1–3–2	3–2	2–3	3

This article will apply SPT rules in production scheduling problems. First, we will explain how to combine sequence constraints in the problem of profit maximization.

When the price is assumed to be fixed, the order processing time is a linear function of the delivery time:

$$pt_i = (\alpha_i - \beta_i \cdot p) - \theta_i \cdot t. \tag{5}$$

Figure 1 shows the processing time of three consumer orders. Three lines represent three consumers 1, 2, 3, respectively. The three lines intersect at the intersections of C_{12}, C_{13}, and C_{23}. Each intersection indicates that the processing time of the two orders is equal. As can be seen in Figure 1, the intersection point between the three straight lines and the intersection point of each straight line with the t-axis divide the t-axis into six segments from t_1 to t_6, that is, the SPT sequence of the three orders is uniquely determined in the interval $[0, t_1], [t_1, t_2], \ldots, [t_5, t_6]$. Table 2 shows all SPT production sequences for each time interval or region three orders.

If C_{ij} is the point of intersection of two lines L_i, L_j, then there is an equation $pt_i = pt_j$. Bring Equation (1) into this equation to get the t coordinate of C_{ij} as:

$$t_{ij} = \frac{\alpha_i - \alpha_j + p(\beta_j - \beta_i)}{\theta_i - \theta_j}. \tag{6}$$

According to $pt_i = 0$, the intercept point I_i on the t-axis can be expressed as:

$$t_i = \frac{\alpha_i - p\beta_i}{\theta_i}. \tag{7}$$

With the above formulae (6) and (7), all the time zone boundaries can be calculated and then they are sorted in ascending order. When the price is fixed, the delivery time is variable, and we constrain the time. Use $t_c \le t < t_{c+1}$ to represent the general time zone, where t_c and t_{c+1} represent any two adjacent

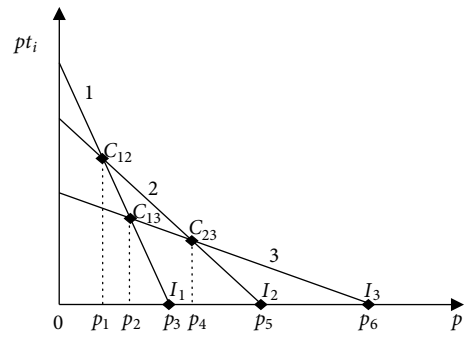

Figure 2: Order price with respect to one decision variable.

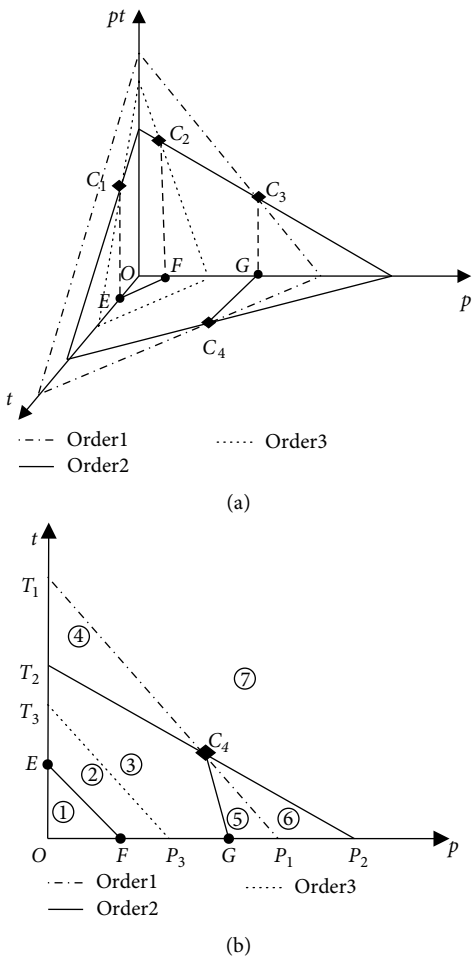

Figure 3: Order processing time function in general problem.

boundaries of a time zone. Under this time limit, the optimal sequence of orders is uniquely determined.

When the delivery time quotation is fixed, similar to the previous analysis, the price range constraint is $p_c \le p < p_{c+1}$, where p_c and p_{c+1} represent any two adjacent boundaries of the price region. As shown in Figure 2, the p coordinate of C_{ij} is expressed as:

$$p_{ij} = \frac{\alpha_j - \alpha_i + t\left(\theta_i - \theta_j\right)}{\beta_j - \beta_i}. \tag{8}$$

The intercept point I_i on the p-axis is expressed as:

$$p_i = \frac{\alpha_i - t\theta_i}{\beta_i}. \tag{9}$$

The boundary values of the price region can be obtained by the above formulas (8) and (9). In this one of the price regions, the unique production sequence can be uniquely determined.

In the general case, the quotation and delivery deadline are two decision variables. For example, the price and time sensitivity of three orders are different. The order processing time is a linear function of t and p; that is:

$$pt_i = \alpha_i - \beta_i \cdot p - \theta_i \cdot t. \tag{10}$$

Figure 3(a) illustrates the processing time for three orders in a three-dimensional Cartesian coordinate system, in which three orders are divided into three planes, (pt, t), (pt, p) and (p, t) plane. Each plane has three orders intersecting at four intersection points C_1, C_2, C_3, and C_4. Each projection point $\left(p_{C_i}, t_{C_i}\right)$ corresponding to C_i can be obtained by solving the following two equations in the (p, t) plane:

$$\alpha_i - \beta_i \cdot p - \theta_i \cdot t = \alpha_i - \beta_j \cdot p - \theta_j \cdot t. \tag{11}$$

$$p = 0, t = 0 \quad \text{or} \quad pt = 0. \tag{12}$$

According to Figure 3(a), it can be seen that the points E, F, and G are projections of the points C_1, C_2, and C_3 on the plane (p, t), respectively. Line C_1C_2 consists of points on $pt_2 = pt_3$. Since EF is a projection of C_1C_2 on the plane (p, t), then a point (p, t) on EF also satisfies $pt_2 = pt_3$.

Figure 3(b) depicts the linear projection in Figure 3(a) projected onto the (p, t) plane, showing its two-dimensional planar graphic region. In Figure 3(b), the straight line is the intersection of the plane i and the plane (p, t) and represents the set of points at the time $pt_i = 0$; that is, the points (p, t) and the straight line satisfy the following equation:

$$\alpha_i - \beta_i \cdot p - \theta_i \cdot t = 0. \tag{13}$$

From the above analysis, we can see that the methods for exploring fixed order price and delivery time are similar. Under normal circumstances, there are only two cases of optimal production sequence change. One is that the two orders' processing time is equal; the other is that it is an order processing time equal to 0. This means that the order of the optimal production of the order is transformed into straight line P_iT_i and lines EF, GC_4 in Figure 3(b).

Therefore, in the first quadrant of Figure 3(b), the optimal production sequence is uniquely determined by the concave regions segmented by the straight lines P_iT_i, EF, GC_4, and t/p axes, and we define these concave regions as price-time regions. In Figure 3(b), each concave area is represented by ① to ⑦. The decision variable is a price-time zone with a unique optimal production order, and each optimal production order zone is shown in Table 3.

In order to obtain the SPT sequences for all price-time regions, all regions in the first quadrant of Figure 3(b) need to be obtained, so we have designed an algorithm to create a detailed price-time region, recorded as a sequence listing algorithm (SLA); the main idea of this algorithm is as follows:

Table 3: All price-time zone SPT ordering for three orders.

Zone index	1	2	3	4	5	6	7
Sequence	2-3-1	3-2-1	2-1	1	1-2	2	None

Step 1. Think of the first quadrant as the entire price-time region, dividing the first quadrant into a series of price-time regions by a single P_iT_i.

Step 2. Check each price-time area to ensure that it is a projection of the intersection of each two order surfaces on the (p, t) plane.

Step 3. Get all price-time zones.

3.2. Optimal Delivery Deadline. In Section 3.1, we studied the optimal SPT sequence for fixing each time zone. This subsection will discuss the change of delivery time when fixing the price of a product. If the special time zone is discussed in Section 3.1, the resulting sequence decision will not be important. Therefore, according to the number of time zones, the problem is decomposed into several simple subproblems. We divide the objective function (4) into two parts. one part is sales revenue; that is:

$$R(t) = p\sum_{i=1}^{n}(\alpha_i - p\cdot\beta_i - t\cdot\theta_i). \tag{14}$$

The other part is the delay penalty:

$$T(t) = w\sum_{i=m+1}^{n}(\alpha_i - p\cdot\beta_i - t\cdot\theta_i) - w(n-m)t, \tag{15}$$

where m is the number of orders completed on time in a given time t.

If m is independent of time t, then the gradient of profit return with respect to time t is:

$$\frac{\partial f}{\partial t} = \frac{\partial R}{\partial t} - \frac{\partial T}{\partial t} = -p\sum_{i=1}^{n}\theta_i - w\sum_{i=m+1}^{n}(-\theta_i) + w(n-m). \tag{16}$$

Theorem 1. *Assume that the profit function (4) is a concave function, then:*

(i) *Small segments between two time nodes are linear functions.*
(ii) *The derivative of each subparagraph with respect to time is decremental.*
(iii) *The first part of the derivative of time is positive, and the latter part of the derivative of time is negative.*
(iv) *The point of maximum return can be obtained between two small segments.*

The conclusion for Theorem 1 can be explained from Figure 4. For a concave profit function with respect to time, a small piecewise linear function is formed between every two time points. Each small fragment is slowly increased before t^*. Its derivative is positive, but the growth rate of its derivative is monotonically decreasing with respect to t. After

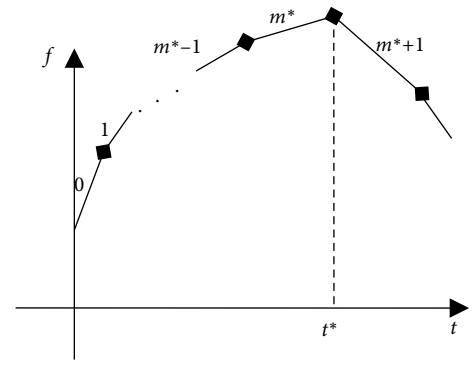

Figure 4: The profit function with respect to delivery time quotation.

t^*, it can be seen that each small segment linear function is declining; that is, the derivative of each small segment linear function is negative and can be seen from the figure. It can be seen that when $t = t^*$, the profit function takes the maximum value.

Corollary 1. *Assume that given a time zone, you can find two possible conditions for obtaining the optimal delivery time*:

(i) *The optimal delivery time is the same as the completion time of an order.*
(ii) *The optimal delivery time is any boundary of the time zone.*

According to Theorem 1 and Figure 4, it can be concluded that the number of small segments represents the number of orders completed on time in that situation. As time t increases, m is also an intermittent increase. The convergence time t of two segments on the t-axis is equal to the completion time of an order. The point of maximum profit is the point of convergence of two small segments. The value of the derivative of the small linear function on the left side of this point with respect to t is positive when $m = m^*$. The derivative of the small linear function on the right side of this point with respect to t is negative when $m = m^* + 1$; that is, it satisfies the following inequality:

$$\frac{\partial f}{\partial t}\Big|(m = m^*) > 0, \tag{17}$$

$$\frac{\partial f}{\partial t}\Big|(m = m^* + 1) \le 0. \tag{18}$$

Based on the above two inequalities, we bring the values of $m = m^*$ and $m = m^* + 1$ into (16), which yields:

$$w(n - m^*) + w\sum_{i=m+1}^{n}\theta_i \le p\sum_{i=1}^{n}\theta_i, \tag{19}$$

$$w(n - m^* + 1) + w\sum_{i=m+1}^{n}\theta_i < p\sum_{i=1}^{n}\theta_i. \tag{20}$$

The value of m^* can be obtained by (19) and (20).

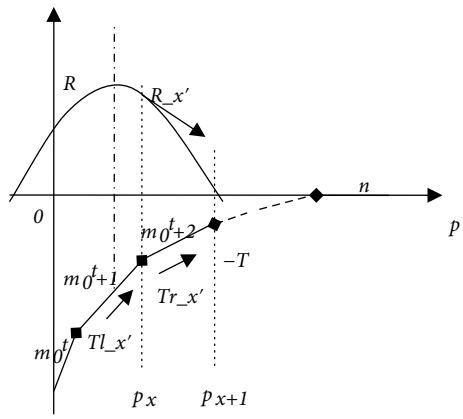

FIGURE 5: The revenue function and the tardiness function.

From Figure 4, we can see that when $t = t^*$, the profit reaches the maximum value. t^* is the completion time of the order in the $(m^*)_{\text{th}}$ sequence, so the optimal delivery time satisfies:

$$t^* = \sum_{i=1}^{m^*} (\alpha_i - p \cdot \beta_i - t^* \cdot \theta_i). \tag{21}$$

Then, t^* is calculated as:

$$t^* = \frac{\sum_{i=1}^{m^*} \alpha_i - p \sum_{i=1}^{m^*} \beta_i}{1 + \sum_{i=1}^{m^*} \theta_i}. \tag{22}$$

Since the obtaining of the optimal production sequence is based on the special time zone $(t_c \le t \le t_{c+1})$, we should verify that t^* is located in each specific time zone. As a result, we need to compare the values of t^* at the boundary of the time zone. If t^* is in the time zone, the optimal delivery time equals t^*. If t^* is outside the time zone $(t^* < t_c)$, the optimal delivery time is t_c or t_{c+1}; that is:

$$t = \begin{cases} t_{c+1}, & t_{c+1} < \dfrac{\sum_{i=1}^{m^*} \alpha_i - p \sum_{i=1}^{m^*} \beta_i}{1 + \sum_{i=1}^{m^*} \theta_i}, \\ \dfrac{\sum_{i=1}^{m^*} \alpha_i - p \sum_{i=1}^{m^*} \beta_i}{1 + \sum_{i=1}^{m^*} \theta_i}, & t_c \le \dfrac{\sum_{i=1}^{m^*} \alpha_i - p \sum_{i=1}^{m^*} \beta_i}{1 + \sum_{i=1}^{m^*} \theta_i} \le t_{c+1}, \\ t_c, & t_c < \dfrac{\sum_{i=1}^{m^*} \alpha_i - p \sum_{i=1}^{m^*} \beta_i}{1 + \sum_{i=1}^{m^*} \theta_i}. \end{cases} \tag{23}$$

The interpretation of Equation (23) is the same as Corollary 1.

3.3. Fixed-Quote Pricing Decision. This section will examine the effect of adjusting the price on optimal profit when the delivery deadline is given. By a method similar to Theorem 1, we can find the corresponding price region $p_c \le p < p_{c+1}$, so that we can get the optimal ordering for each order price area.

Similar to the previous section, we decompose the problem into several subproblems based on the number of price regions, dividing the objective function into two parts: the income function and the delay penalty function. The derivative of the income function is:

$$\frac{\partial R}{\partial p} = -2p \sum_{i=1}^{n} \beta_i + \sum_{i=1}^{n} (\alpha_i - t\theta_i). \tag{24}$$

When the assumption of m does not depend on the price p, the derivative of the price delay penalty function is:

$$\frac{\partial T}{\partial p} = \begin{cases} -w \sum_{i=m+1}^{n} \beta & m = [m_0^t, n-1], \\ 0, & m = n. \end{cases} \tag{25}$$

Theorem 2. *Negative delay penalty $(-T)$ is a piecewise linear function of price p. The function has the following properties:*

(i) *It is a nondecreasing continuous function of the price p.*

(ii) *The absolute gradient of each segment is decreasing relative to the price p.*

(iii) *When the price p is large enough to reach a certain value, the function gradient is 0.*

Corollary 2. *Obtain the optimal price through 3 possible conditions.*

(i) *In the case of optimal prices, the completion time of an order is the same as the delivery time.*

(ii) *The best price is located on the border of the price area.*

(iii) *The optimal price is located in the derivative of the income function and is equal to the gradient of the penalty function.*

In Figure 5, the penalty function $(-T)$ is located below the p-axis, and each small segment on $-T$ indicates that the order was completed on time in the price state at this time. Assuming that when $p = 0$, the number of orders completed in time at a given time t is m_0^t, and then, the connection point between each two-stage function on $-T$ represents the time of completion of an order at a given time t. When the m orders are completed, the time of completion is satisfied:

$$t = \sum_{i=1}^{m} (\alpha_i - p \cdot \beta_i - t \cdot \theta_i). \tag{26}$$

Then,

$$p = \frac{m\alpha_i - (1 + \sum_{i=1}^{m} \theta_i)t}{\sum_{i=1}^{m} \beta_i}. \tag{27}$$

As shown in Figure 5, as the p increases, the order processing time decreases gradually until the delay penalty is reduced to 0 when p increases to p_n^t, i.e., when $p \ge p_n^t$, $T = 0$.

From (24), we can know that the income function is represented by a concave quadratic function. In the function image of the upper half of the p-axis in Figure 5, the maximum point of the profit function is obtained when $\partial R/\partial p = 0$. We can get the maximum point of the income function, which is the highest point in Figure 6:

$$p_0^t = \frac{\sum_{i=1}^{n} \alpha_i - t \sum_{i=1}^{n} \theta_i}{2 \sum_{i=1}^{n} \beta_i}. \tag{28}$$

Now, we discuss the interval. If $p_n^t \le p_0^t$, when $p \ge p_n^t$, since the delay penalty is 0, the maximum profit price is $p^* = p_0^t$.

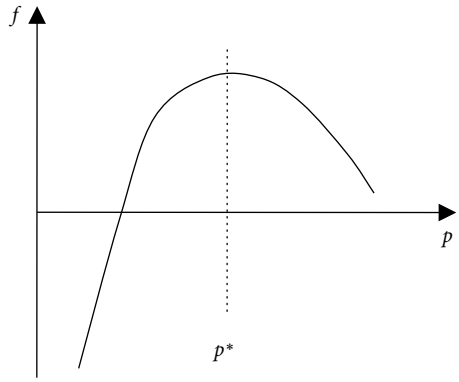

Figure 6: The net profit function.

When $p_n^t > p_0^t$, the situation is more complicated, as discussed in detail below.

In Figure 5, when $p = p_0^t$, the derivative of the income function is 0, while the derivative of $-T$ is positive. When $p > p_0^t$, the derivative of R decreases continuously from 0 to $-\infty$ as p increases. At the same time, $-T$ decreases from a positive value to zero. Therefore, when the derivative of $-T$ is added to the derivative of R, the optimal solution of the objective function is obtained, while $\partial f/\partial p$ reaches the minimum nonnegative value.

If $\partial f/\partial p = 0$, the best quote is:

$$p = \frac{\sum_{i=1}^{n}(\alpha_i - t\theta_i) + w\sum_{i=m+1}^{n}\beta_i}{2\sum_{i=1}^{n}\beta_i}. \tag{29}$$

If $\partial f/\partial p \neq 0$, (29) does not apply to calculate the optimal solution. Based on Figure 5, we have developed a search algorithm to find the best price (optimal price searching algorithm, OPS algorithm). The main idea of this algorithm is to find the value of p when $(\partial R/\partial p - \partial T/\partial p)$ reaches the minimum nonnegative value.

According to the OPS algorithm, since the iteration number of the algorithm only depends on the size range of x, we find that the computational complexity of this algorithm is $O(n)$, so the solution of this problem is established on the entire price axis. However, the entire price axis is divided into price ranges. We assume that the price range is $p_c \le p^* \le p_{c+1}$. Then, we need to compare the size of the boundary between p^* and the price region. The specific section is as follows:

$$p = \begin{cases} p_{c+1}, & p_{c+1} < p^*; \\ p^*, & p_c \le p^* \le p_{c+1}; \\ p_c, & p_c < p^*, \end{cases} \tag{30}$$

where

$$p^* = \begin{cases} \dfrac{\sum_{i=1}^{m}\alpha_i - t\sum_{i=1}^{m}\theta_i}{2\sum_{i=1}^{m}\beta_i}, & \dfrac{\partial R}{\partial p} \neq \dfrac{\partial T}{\partial p}; \\ \dfrac{\sum_{i=1}^{m}\alpha_i - t + w\sum_{i=1}^{m}\beta_i}{\sum_{i=1}^{m}\beta_i}, & \dfrac{\partial R}{\partial p} = \dfrac{\partial T}{\partial p}. \end{cases} \tag{31}$$

3.4. Simultaneous Decision of Quotation and Delivery Time. From Section 3.1, we know that the (p, t) price-time region can be fixed by the SPT production order, and all price-time regions of the corresponding production order can be obtained by the SLA. The solution to the general problem can be solved in each price-time zone, and time series decision-making is not important. Therefore, the entire problem is divided into two simple questions based on the number of price-time regions.

According to the SLA, the price-time region is a concave region consisting of two straight-line boundaries, such as the EF and P_1T_1 lines in Figure 3(b). The mathematical plan for the price-time region has been given in Equation (13). When we study the general time-price region problem, the constraint (13) must be satisfied.

Theorem 3. *The obtaining of the optimal solution requires that any one of the following two conditions be satisfied:*

(i) *The delivery time is consistent with the order completion time.*

(ii) (p^*, t^*) *is the sequence change point, which means that* (p^*, t^*) *allows both the processing time of two orders to equal zero and the processing time of one order equal to zero.*

Next, we will discuss how the two forms in Theorem 3 can get the optimal solution. First, suppose the profit is maximized when the delivery time of one order is the same as the completion time, and the decision variable (p, t) satisfies (27), where m is an integer in $[1, n]$, each possible m value in (27) is computable and replaceable, and a straight line $L_m(p = (\sum_{i=1}^{m}\alpha_i - (1 + \sum_{i=1}^{m}\theta_i)t)/\sum_{i=1}^{m}\beta_i)$is formed in the $p - t$ Cartesian coordinate system. If there are two intersections between the straight line L_m and the price-time zone boundary, then the value of m is valid and stored in an M concentration, $M = m, m + 1, \ldots, m + c$, where c is an integer. Then, in order to find the optimal profit, every element in M is computable.

Bringing formula (27) into formula (13), all price-time zone constraints can be reduced to only constraints on time t; that is, all the inequalities in (13) will become the form of $t_{l1} \le t \le t_{r1}$, where t_{l1} and t_{r1} are integrated by the cluster of inequalities.

Bringing (27) into the objective function (4), the objective function will become a quadratic function only with respect to time t; that is:

$$f(t) = \frac{\sum_{i=1}^{m}\alpha_i - (1 + \sum_{i=1}^{m}\theta_i)t}{\sum_{i=1}^{m}\beta_i}\sum_{i=1}^{n}Q_i(t) - w\sum_{i=m+1}^{n}(C_i(t) - t). \tag{32}$$

By comparing the sizes of $f(t_{l1})$, $f(t_{r1})$, and $f(t|(\partial f/\partial t) = 0)$, the maximum profit is filtered out and the problem is directly solved. We find a solution to each of M's candidates and get the maximum profit at the same time.

Next, we discuss the second condition of Theorem 3 and find the optimal solution for (p^*, t^*) at the point of sequence change. As discussed in Section 3.1, the sequence change point for a time-price region is the boundary point of the $p - t$ Cartesian coordinate system. Each boundary value can be

expressed by Equation (14). In general, the boundary of a special time-price region can be represented by $c_{j1} \cdot p + c_{j2} \cdot t = c_{j3}$, where $j = 1, 2, \ldots, s$, so the decision variable p is a function of the decision variable t; that is:

$$p = \frac{\left(c_{j3} - c_{j2} \cdot t\right)}{c_{j1}}. \tag{33}$$

Bringing (32) to the objective function (4), the objective function becomes a quadratic function with respect to the delivery time t:

$$f(t) = \left(\frac{c_{j3} - c_{j2} \cdot t}{c_{j1}}\right) \sum_{i=1}^{n} \left(\alpha_i - \frac{\left(c_{j3} - c_{j2} \cdot t\right)\beta_i}{c_{j1}} - t\theta_i\right) - w \sum_{i=1}^{n} \max\left(0, C_i - t\right). \tag{34}$$

Bringing (33) to (14), all constraints on the price-time region become constraints only on time t; that is, all inequalities in (13) become $t_{l2} \le t \le t_{r2}$, where t is determined by the family of inequality sets. As a result, this problem can be solved by directly solving $f(t_{l2})$, $f(t_{r2})$, and $f(t\partial f/\partial t = 0)$, and filtering out the maximum profit. We find a solution to the boundary of the price region at each time and filter out one of the largest profits.

The optimal questions about (31) and (33) can be resolved in a clear time-price region. By solving (31) and (33), a detailed price-time region can be filtered out to obtain the maximum profit and optimal solution. For general problems, in order to find the optimal delivery time, we developed a price-time problem algorithm (PTA). The main idea of the PTA is: first, form the SPT sequences for all price-time regions; secondly, based on the formulae (31) and (33), we find the optimal solution for each time-price region; finally, the optimal solution is filtered out of the maximum values in all time-price regions obtained.

Theorem 4. *In the case of $O(n^3)$, for general problems, the algorithm PTA can obtain the optimal solution (p^*, t^*).*

4. Conclusion

In the manufacturer's delivery pricing problem for retailers, the retailer's demand is a determinant function of the commodity price, delivery time, and other attribute variables. In order to maximize production profits, manufacturers publish a common optimal product price and a common delivery time for each customer group. Typically, the manufacturer formulates the relevant production policy through a stable queuing model, which uses a fixed scheduling rule, such as FCFS, which is considered as the M/M/1 queue.

Delivery pricing problems based on the M/M/1 scheduling algorithm apply to quotes for mass production for mass customers. For a single customer group, the pricing, and production problems in the context of small batch production cannot be maximized by the manufacturer's profits through the M/M/1 scheduling algorithm. In a single group of customers, the customer's payment preference and delay tolerance are different within a known range of price and time sensitivity. Based on the optimization of production sequencing, we mainly study the coordination and optimization between a manufacturer and multiple retailers in a supply chain.

Under the scenario of order-based production, we studied the issue of coordination pricing and delivery time quotation taking into account the detailed production scheduling decision mechanism and then formulated a scheduling mechanism that deals with delivery dates, including a price. The mechanism takes into account the customer's heterogeneity of time and price requirements and also includes penalties for late delivery to the manufacturer. In order to maximize the manufacturer's own profit, we constructed a mathematical model of the best quotation and delivery deadline and created a price-time problem algorithm (PTA) to obtain the optimal solution of the model. We proposed a solution to the problem of joint pricing scheduling faced by manufacturers.

Data Availability

The article is about the research of model methods. No data were used to support this study.

Conflicts of Interest

The authors declare that they have no conflicts of interest.

Acknowledgments

This work was supported by the National Social Science Fund of China (16ATJ003) and the National Natural Science Foundation of China (71031004 and 71271047).

References

[1] M. Pangburn and E. Stavrulaki, "Capacity and price setting for dispersed, time-sensitive customer segments," *European Journal of Operational Research*, vol. 184, no. 3, pp. 1100–1121, 2008.

[2] E. L. Plambeck and T. A. Taylor, "Sell the plant? The impact of contract manufacturing on innovation, capacity, and profitability," *Management Science*, vol. 51, no. 1, pp. 133–150, 2005.

[3] J. An, H. Kwak, S. Jung, J. Salminen, and B. J. Jansen, "Customer segmentation using online platforms: isolating behavioral and demographic segments for persona creation via aggregated user data," *Social Network Analysis and Mining*, vol. 8, no. 1, pp. 1–54, 2018.

[4] T. Boyaci and S. Ray, "Product differentiation and capacity cost interaction in time and price sensitive markets," *Manufacturing & Service Operations Management*, vol. 5, no. 1, pp. 18–36, 2003.

[5] B. B. Flynn, B. Huo, and X. Zhao, "The impact of supply chain integration on performance: a contingency and configuration approach," *Journal of Operations Management*, vol. 28, no. 1, pp. 58–71, 2010.

[6] Z. Chen and N. G. Hall, "Supply chain scheduling: conflict and cooperation in assembly systems," *Operations Research*, vol. 55, no. 6, pp. 1072–1089, 2007.

[7] P. Kaminsky and O. Kaya, "Scheduling and due-date quotation in a make-to-order supply chain," *Naval Research Logistics*, vol. 55, no. 5, pp. 444–458, 2008.

[8] L. Zhang, Y. Zhang, D. Du, and Q. Bai, "Improved price of anarchy for machine scheduling games with coordination mechanisms," *Optimization Letters*, vol. 13, no. 4, pp. 949–959, 2018.

[9] H. Mokhtari and A. Hasani, "An energy-efficient multi-objective optimization for flexible job-shop scheduling problem," *Computers & Chemical Engineering*, vol. 104, no. 2, pp. 339–352, 2017.

[10] B. Ata and T. L. Olsen, "Near-optimal dynamic lead-time quotation and scheduling under convex-concave customer delay costs," *Operations Research*, vol. 57, no. 3, pp. 753–768, 2009.

[11] P. Keskinocak and S. Tayur, "Due-date management policies," *Handbook of Quantitative Supply Chain Analysis*, vol. 74, pp. 485–554, 2004.

[12] S. X. Zhu, "Integration of capacity, pricing, and lead-time decisions in a decentralized supply chain," *International Journal of Production Economics*, vol. 164, no. 6, pp. 14–23, 2015.

[13] S. Ray and E. Jewkes, "Customer lead time management when both demand and price are lead time sensitive," *European Journal of Operational Research*, vol. 153, no. 3, pp. 769–781, 2004.

[14] M. Fisher, S. Gallino, and J. Xu, "The value of rapid delivery in online retailing," *Journal of Marketing Research*, vol. 56, no. 5, pp. 732–748, 2019.

[15] D. X. Peng and G. Lu, "Exploring the impact of delivery performance on customer transaction volume and unit price: evidence from an assembly manufacturing supply chain," *Production and Operations Management*, vol. 26, no. 5, pp. 880–902, 2017.

[16] T. Boyaci and S. Ray, "The impact of capacity costs on product differentiation in delivery time, delivery reliability, and price," *Production and Operations Management*, vol. 15, no. 2, pp. 179–197, 2006.

[17] S. Ray and E. Jewkes, "Customer lead time management when both demand and price are lead time sensitive," *European Journal of Operational Research*, vol. 153, no. 3, pp. 769–781, 2007.

[18] K. Palaka, S. Erlebacher, and D. H. Kropp, "Lead-time setting, capacity utilization, and pricing decisions under lead-time dependent demand," *IIE Transactions*, vol. 30, no. 2, pp. 151–163, 1998.

[19] K. C. So and J. S. Song, "Price, delivery time guarantees and capacity selection," *European Journal of Operational Research*, vol. 111, no. 1, pp. 28–49, 1998.

[20] P. Pekgün, P. M. Griffin, and P. Keskinocak, "Coordination of marketing and production for price and leadtime decisions," *IIE Transactions*, vol. 40, no. 1, pp. 12–30, 2008.

[21] M. ElHafsi, "An operational decision model for lead-time and price quotation in congested manufacturing systems," *European Journal of Operational Research*, vol. 126, no. 2, pp. 355–370, 2000.

[22] K. Charnsirisakskul, P. M. Griffin, and P. Keskinocak, "Pricing and scheduling decisions with leadtime flexibility," *European Journal of Operational Research*, vol. 171, no. 1, pp. 153–169, 2006.

[23] C. H. Xia, J. G. Shanthikumar, and P. W. Glynn, "On the asymptotic optimality of the SPT rule for the static flow shop average completion time problem," *Operations Research*, vol. 48, no. 4, pp. 615–622, 2000.

Hindawi
Complexity
Volume 2019, Article ID 7289689, 12 pages
https://doi.org/10.1155/2019/7289689

Research Article

σ-Stabilization of a Flexible Joint Robotic Arm via Delayed Controllers

G. Ochoa-Ortega,[1] **R. Villafuerte-Segura**,[2] **M. Ramírez-Neria**,[1,3] **and L. Vite-Hernández**[2]

[1]*División de Mecatrónica, Universidad Politécnica del Valle de México, Tultitlán 54910, Mexico*
[2]*Centro de Investigación en Tecnologías de Información y Sistemas, Universidad Autónoma del Estado de Hidalgo, Pachuca 42184, Hidalgo, Mexico*
[3]*Departamento de Mecatrónica, Universidad Tecnológica de México-UNITEC MÉXICO-Campus Atizapán, Atizapán de Zaragoza 52999, Mexico*

Correspondence should be addressed to R. Villafuerte-Segura; villafuerte@uaeh.edu.mx

Received 7 September 2019; Revised 6 November 2019; Accepted 28 November 2019; Published 23 December 2019

Academic Editor: Thach Ngoc Dinh

In the present contribution, the problem of establishing tuning rules to proportional retarded controller for LTI systems is addressed. Based on the $\mathcal{D}$-decomposition methodology and σ-stability analysis, analytic conditions are determined on the parameters of a delayed controller that guarantee us that the system response reaches the maximal decay rate. The conditions presented in this paper are tested experimentally in tracking tasks of a flexible joint robotic arm.

1. Introduction

Time delays naturally arise in many mathematical models from engineering, biology, and physics, among other science areas. A common belief is that the appearance of these phenomena can lead to detrimental effects, bad performance of the system, instability, or even damage to the system [1]. Nevertheless, many contributions have shown that the deliberate introduction of a time delay in a feedback control law can provide a stabilizing effect [2–7] and in some cases give or improve the robustness property of the system [8]. The stability analysis of linear time delay systems is studied in the framework of two main approaches: time domain and frequency domain. The former is based on the well-known Lyapunov's criteria and its extensions (Razumikhin and Krasovskii) or by using linear matrix inequalities (LMIs) via convex optimization [9, 10]. However, only sufficient stability conditions are provided, which are generally very conservative or, in some cases, nonexistent, mainly because the feasibility of LMIs (whose parameters are adjusted by a frequency method) is usually nonexistent. The second approach is based on the analysis of the characteristic function of the system, where, unlike the temporal approach, it is possible to provide necessary and sufficient conditions that do not have a conservative nature.

Even when in the recent decades there is a great development in the control theory, where many sophisticated control schemes have been developed, PID controllers remain as one of the most used control strategies in the industrial environment. According to [11, 12], approximately 90–95% of the industrial control loops still use PID-type controllers, many of which do not include the derivative term, mainly because this term induces a noise amplifying effect that can affect the system performance [12–14] or because the derivative of the state is not available for measurement. Some common strategies to avoid the use of the derivative term and, consequently, the noise amplification problem, are the use of filters, and observers or the implementation of estimation schemes.

On the other hand, a common approach consists in replacing the derivative term in PID-type controllers by an approximation of the form

$$\frac{\mathrm{d}x(t)}{\mathrm{d}t} \approx \frac{x(t) - x(t-\tau)}{\tau}, \tag{1}$$

and for an appropriate selection of the delay τ, the closed-loop stability is guaranteed [3, 14–16]. In this framework, in [17], a method for the migration of a double imaginary characteristic root to the left half-plane or the right half-plane under the variation of two parameters of a quasi-polynomial is presented. The idea of deliberately introducing time delays in closed-loop systems and considering it as a control parameter is not a novel approach, but it has been intensively studied in recent years, see [18–20] and the references therein. The analysis of such class of controllers focuses mainly on the following topics: characterization of the stability crossing curves [21], tuning of delayed controllers to stabilize second-order systems [18, 20, 22] (and its noise attenuation analysis [23]), the design of proportional integral controllers for second-order linear systems [19, 24], and design of maximum decay rate using elimination theory [25]. Particularly in [26], a Proportional Integral Retarded (PIR) controller to solve the regulation problem of a general class of stable second-order LTI systems is presented. This result ultimately guarantees a desired exponential decay rate σ. On the other hand, design of nonfragile controllers with a desired exponential decay rate is proposed in [20]. Here, the authors present conditions on the parameters (k_p, k_δ) such that the $p-\delta$ controller of the form $k_p + k_\delta e^{-\tau s}$ ensure the stability of the closed-loop system.

Inspired by the previous contributions, in the present manuscript, following the $\mathscr{D}$-decomposition methodology (see [27–30]), it allows us to delimit and decompose the space of control parameters, determining the stability boundaries by means of a set of parametric equations that depends explicitly on the control parameters, which play a key step to allow us to determine simple analytical expressions for tuning the control parameters of a Proportional Retarded (PR) control law to σ-stabilize a general class of SISO LTI systems. Under these conditions, three dominant real roots are placed in $-\sigma$, which guarantees to reach the maximal exponential decay rate in the system response.

The σ-stabilization of a system can be described as the design and tuning of a controller such that the corresponding characteristic equation of the closed-loop system has dominant roots with real part less than or equal to $-\sigma$, $\sigma \in \mathbb{R}^+$. The σ-stabilization approach can be considered a robust scheme, since when taking parameters within a σ-stable region and by presenting variations on the parameters (that do not leave the σ-stable zone) the system stability is assured.

Delay-based controllers have as their main advantages the simplicity with which control laws are designed and, as a consequence, their practical implementation facility. Common applications of such controllers focus mainly on second-order systems, e.g., regulation problems of DC servomotors [18, 31], haptic virtual systems [20], underactuated mechanical system [32], and numerous academic examples. In the present proposal, a more challenging implementation is addressed: a flexible joint robotic arm (fourth order system), where trajectory tracking tasks are addressed. The main challenges for the design of PR control law are the complexity of its dynamic equations (mainly by the presence of highly nonlinear elements) and the appearance of oscillations at the tip of the link [33, 34]. Thus, a first step in the design of the Proportional Retarded control law is to linearize via an exact linearization approach the dynamic equations of the flexible joint robotic arm [35, 36].

The remainder of this manuscript is organized as follows. In Section 2, the analyzed closed-loop system and the problem formulation are presented and the σ-stability boundaries are determined. In Section 3, analytic conditions to determine the maximal decay rate σ^* are provided. Section 4 is devoted to both the dynamic model of the flexible joint robotic arm under the study and the design of the proportional plus delay controller. Also, a complementary tuning approach is presented. In Section 5, the experimental platform is described and the experimental results are presented. For comparison purposes, a classical feedback state controller law is also designed and implemented. The contributions end with some concluding remarks.

Nomenclature. In the present contribution, $\mathbb{R}$ denotes the real numbers, while $\mathbb{C}$ the complex numbers, and Z^+ stands for the positive integers. Given a vector $x(t) \in \mathbb{R}^n$, then $x(t)^\top$ denotes its transpose. Let $s \in \mathbb{C} \mid s = a + ib$, then $\mathrm{Re}(s) = a$ and $\mathrm{Im}(s) = b$ denote its real and imaginary parts of s, respectively, and i is the imaginary unit. For a function $x(t)$, $\dot{x}(t)$ denotes its time derivative and $\mathrm{d}^k x(t)/\mathrm{d}t^j = x^{(j)}(t)$ and $j \in \mathbb{Z}^+$ defines the jth time derivative.

2. Problem Formulation

Let us consider a LTI-SISO system of the form

$$\dot{x}(t) = Ax(t) + Bu(t), \tag{2}$$

where $A \in \mathbb{R}^{n\times n}$, $B \in \mathbb{R}^n$, $x(t) = [x_1(t), x_2(t), \ldots, x_n(t)]^\top \in \mathbb{R}^n$, and $u(t) \in \mathbb{R}$ is the control input. Let us propose a state feedback a control law of the form

$$u(t) = \widetilde{k}_1 x_1(t) + \widetilde{k}_2 x_2(t) + \cdots + \widetilde{k}_n x_n(t), \tag{3}$$

where $\widetilde{k}_j \in \mathbb{R}$, $j = 1, 2, \ldots, n$, denote the controller gains. This approach demands the knowledge of the complete state vector. Now, let us suppose that at least one of the velocity measurements is not available, and then the implementation of a state observer to estimate the unavailable states would be considered. Instead of this alternative, let us propose a delayed controller as follows:

$$u(t) = k_p x_1(t) - k_r x_1(t-\tau) + \alpha_1 x_3(t) + \cdots + \alpha_{n-2} x_n(t), \tag{4}$$

where k_p, k_r, $\alpha_1 \ldots, \alpha_{n-2} \in \mathbb{R}$ are the controller gains, and $\tau > 0$ is the delay. Here, we assume that the state variable $x_2(t)$ is unable to measure. Then, the closed-loop system is now of form

$$\dot{x}(t) = A_0 x(t) + A_1 x(t-\tau), \tag{5}$$

where $A_0, A_1 \in \mathbb{R}^{n\times n}$. Then, the characteristic function of system (5) is

$$Q\left(s, k_p, k_r, \alpha_1, \ldots, \alpha_{n-2}\right) = p\left(s, k_p, \alpha_1, \ldots, \alpha_{n-2}\right) + k_r q(s) e^{-s\tau}, \tag{6}$$

where $p(\cdot)$ and $q(\cdot)$ are polynomials and $s \in \mathbb{C}$.

In the subsequent sections, analytic conditions will be developed on the control parameters k_r and τ that guarantee a maximal exponential decay rate (denoted by σ^*) on the system response.

3. Decomposition of the Gain Controller Parametric Space

As discussed in the introductory section, a key step to determine the analytic conditions on the parameters to achieve the maximal decay rate is the decomposition of the space of parameters by means of the $\mathscr{D}$-decomposition methodology. To this end, we first study the σ-stability or stability degree $\sigma > 0$ of (6). Then, let us consider $\sigma > 0$ and by proposing the change of variable, $s \longrightarrow (s - \sigma)$, quasi-polynomial (6) takes the form

$$\begin{aligned} Q_\sigma\left(s, k_p, k_r, \alpha_1, \ldots, \alpha_{n-2}\right) &\coloneqq Q\left(s - \sigma, k_p, k_r, \alpha_1, \ldots, \alpha_{n-2}\right) \\ &= p\left(s, k_p, \alpha_1, \ldots, \alpha_{n-2}, \sigma\right) \\ &\quad + k_r e^{\sigma\tau} q(s, \sigma) e^{-s\tau}. \end{aligned} \tag{7}$$

Following the $\mathscr{D}$-decomposition methodology, we first compute $Q_\sigma(\cdot)|_{s=0} = 0$:

$$p\left(0, k_p, \alpha_1, \ldots, \alpha_{n-2}, \sigma\right) + k_r e^{\sigma\tau} q(0, \sigma) = 0, \tag{8}$$

since $p(0, k_p, \alpha_1, \ldots, \alpha_{n-2}, \sigma) \neq 0$ and $q(0, \sigma) \neq 0$, then

$$k_r = -\frac{p\left(0, k_p, \alpha_1, \ldots, \alpha_{n-2}, \sigma\right)}{e^{\sigma\tau} q(0, \sigma)}. \tag{9}$$

Now, evaluating $Q_\sigma(\cdot)$ for $s = i\omega$, $\omega > 0$, results

$$p\left(i\omega, k_p, \alpha_1, \ldots, \alpha_{n-2}, \sigma\right) + k_r e^{\sigma\tau} q(i\omega, \sigma) e^{-i\omega\tau} = 0, \tag{10}$$

or in an equivalent form:

$$-\frac{1}{k_r e^{\sigma\tau}} \left(\frac{p\left(i\omega, k_p, \alpha_1, \ldots, \alpha_{n-2}, \sigma\right)}{q(i\omega, \sigma)} \right) = e^{-i\omega\tau}. \tag{11}$$

Then, from Euler's identity, it follows that

$$\begin{aligned} \cos(\omega\tau) &= -\frac{1}{k_r e^{\sigma\tau}} \operatorname{Re}\left\{ \frac{p\left(i\omega, k_p, \alpha_1, \ldots, \alpha_{n-2}, \sigma\right)}{q(i\omega, \sigma)} \right\}, \\ \sin(\omega\tau) &= \frac{1}{k_r e^{\sigma\tau}} \operatorname{Im}\left\{ \frac{p\left(i\omega, k_p, \alpha_1, \ldots, \alpha_{n-2}, \sigma\right)}{q(i\omega, \sigma)} \right\}, \end{aligned} \tag{12}$$

and from the former equations, an explicit expression for τ can be written as follows:

$$\tau = \frac{1}{\omega} \cot^{-1}\left(-\frac{\operatorname{Re}\left\{ \left(p\left(i\omega, k_p, \alpha_1, \ldots, \alpha_{n-2}, \sigma\right) \right) / \left(q(i\omega, \sigma) \right) \right\}}{\operatorname{Im}\left\{ \left(p\left(i\omega, k_p, \alpha_1, \ldots, \alpha_{n-2}, \sigma\right) \right) / q(i\omega, \sigma) \right\}} \right) + \frac{j\pi}{\omega}, \tag{13}$$

for $j = 0, \pm 1, \pm 2, \ldots$. Finally from equation (12) yields

$$k_r = \frac{1}{e^{\sigma\tau} \sin(\omega\tau)} \operatorname{Im}\left\{ \frac{p\left(i\omega, k_p, \alpha_1, \ldots, \alpha_{n-2}, \sigma\right)}{q(i\omega, \sigma)} \right\}. \tag{14}$$

The above analysis is summarized in the following result.

Proposition 1. *Consider a quasi-polynomial of form (6), and then the σ-stability regions are bounded by the following equations.*

When $s = 0$,

$$k_r = -\frac{p\left(0, k_p, \alpha_1, \ldots, \alpha_{n-2}, \sigma\right)}{e^{\sigma\tau} q(0, \sigma)}, \quad \tau \in \mathbb{R}^+, \tag{15}$$

and for $s = i\omega$

$$\tau = \frac{1}{\omega} \cot^{-1}\left(-\frac{\operatorname{Re}\left\{ \left(p\left(i\omega, k_p, \alpha_1, \ldots, \alpha_{n-2}, \sigma\right) \right) / \left(q(i\omega, \sigma) \right) \right\}}{\operatorname{Im}\left\{ \left(p\left(i\omega, k_p, \alpha_1, \ldots, \alpha_{n-2}, \sigma\right) \right) / \left(q(i\omega, \sigma) \right) \right\}} \right) + \frac{j\pi}{\omega}, \tag{16}$$

$$k_r = \frac{1}{e^{\sigma\tau} \sin(\omega\tau)} \operatorname{Im}\left\{ \frac{p\left(i\omega, k_p, \alpha_1, \ldots, \alpha_{n-2}, \sigma\right)}{q(i\omega, \sigma)} \right\}, \tag{17}$$

where, $j = 0, \pm 1, \pm 2, \ldots$. Expressions (15)–(17) of Proposition 1 define the σ-stability boundaries in the parametric space (τ, k_r). To exemplify these stability boundaries, in Figure 1, a generic parametric map is presented. The outer region denotes the stability boundary of the system, that is, it corresponds to the pair (τ, k_r) for which the eigenvalues of the system lies on the imaginary axis, while each one of the inner contour curves define a region where the system is exponentially stable with a specific decay rate $\sigma > 0$. The red point corresponds to the maximal reachable stability degree, denoted by σ^*, and it occurs when all the σ-stable regions collapse in a single point (τ^*, k_r^*) of the parametric space and it is characterized because the characteristic function present a root of multiplicity at least three at $s = \sigma^*$ (see [22, 26]).

In the next section, analytic expressions to determine the maximal decay rate σ^* and the associated parameters (τ^*, k_r^*) are presented.

4. Tuning of the PR Control Law

In this section, analytic expressions for determining the controller parameters τ^*, k_r^*, and σ^* to reach the maximal decay rate are provided.

Proposition 2. *Let us consider a quasi-polynomial of form (6), then it has a dominant root of multiplicity at least three at the point $s = -\sigma^*$, if σ^* is the smallest positive real root of the polynomial:*

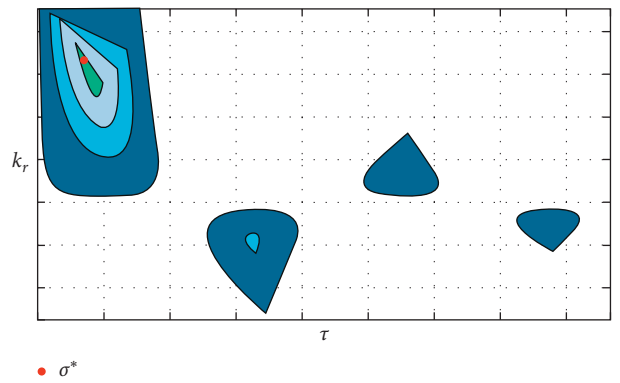

Figure 1: (τ, k_r) parametric space.

$$f(\sigma) = \frac{1}{p\left(0, k_p, \alpha_1, \ldots, \alpha_{n-2}, \sigma\right)}\left[\frac{\partial p\left(s, k_p, \alpha_1, \ldots, \alpha_{n-2}, \sigma\right)}{\partial s} - \frac{p\left(0, k_p, \alpha_1, \ldots, \alpha_{n-2}, \sigma\right)}{q(0,\sigma)}\frac{\partial q(s,\sigma)}{\partial s}\right]^2\Bigg|_{s=0}$$
$$+\frac{2}{q(0,\sigma)}\frac{\partial q(s,\sigma)}{\partial s}\left[\frac{\partial p\left(s, k_p, \alpha_1, \ldots, \alpha_{n-2}, \sigma\right)}{\partial s} - \frac{p\left(0, k_p, \alpha_1, \ldots, \alpha_{n-2}, \sigma\right)}{q(0,\sigma)}\frac{\partial q(s,\sigma)}{\partial s}\right]\Bigg|_{s=0} \tag{18}$$
$$+\left[\frac{p\left(0, k_p, \alpha_1, \ldots, \alpha_{n-2}, \sigma\right)}{q(0,\sigma)}\frac{\partial^2 q(s,\sigma)}{\partial s^2}\right]\Bigg|_{s=0} - \left[\frac{\partial^2 p\left(s, k_p, \alpha_1, \ldots, \alpha_{n-2}, \sigma\right)}{\partial s^2}\right]\Bigg|_{s=0} = 0,$$

and the delay $\tau = \tau(\sigma^*)$ and the controller gain $k_r = k_r(\sigma^*, \tau)$ satisfy the following relations:

$$\tau = -\frac{1}{p\left(0, k_p, \alpha_1, \ldots, \alpha_{n-2}, \sigma\right)}\left[\frac{\partial p\left(s, k_p, \alpha_1, \ldots, \alpha_{n-2}, \sigma\right)}{\partial s} - \frac{p\left(0, k_p, \alpha_1, \ldots, \alpha_{n-2}, \sigma\right)}{q(0,\sigma)}\frac{\partial q(s,\sigma)}{\partial s}\right]\Bigg|_{s=0},$$
$$k_r = -\frac{\left(\partial p\left(s, k_p, \alpha_1, \ldots, \alpha_{n-2}, \sigma\right)\right)/(\partial s)\big|_{s=0}}{e^{\sigma\tau}\left[\left(\partial q(s,\sigma)\right)/(\partial s)\,|_{s=0} - \tau q(0,\sigma)\right]}. \tag{19}$$

Proof 1. If quasi-polynomial (7) has three dominant roots in $s = 0$, it implies that quasi-polynomial (6) has three dominant roots at $s = -\sigma$. Thus, conditions $Q_\sigma(\cdot)|_{s=0} = 0$, $(\partial/\partial s)Q_\sigma(\cdot)|_{s=0} = 0$, and $(\partial^2/\partial s^2)Q_\sigma(\cdot)|_{s=0} = 0$ must hold, i.e.,

$$0 = Q_\sigma(\cdot)_{|s=0} = p\left(0, k_p, \alpha_1, \ldots, \alpha_{n-2}, \sigma\right) + k_r e^{\sigma\tau} q(0,\sigma), \tag{20}$$

$$0 = \frac{\partial}{\partial s}Q_\sigma(\cdot)\Big|_{s=0} = \left[\frac{\partial p\left(s, k_p, \alpha_1, \ldots, \alpha_{n-2}, \sigma\right)}{\partial s} + k_r e^{\sigma\tau}\left[\frac{\partial q(s,\sigma)}{\partial s} - \tau q(s,\sigma)\right]e^{-s\tau}\right]\Bigg|_{s=0}, \tag{21}$$

$$0 = \frac{\partial^2}{\partial s^2}Q_\sigma(\cdot)\Big|_{s=0} = \left[\frac{\partial^2 p\left(s, k_p, \alpha_1, \ldots, \alpha_{n-2}, \sigma\right)}{\partial s^2} + k_r e^{\sigma\tau}\left[\frac{\partial^2 q(s,\sigma)}{\partial s^2} - 2\tau\frac{\partial q(s,\sigma)}{\partial s} + \tau^2 q(s,\sigma)\right]e^{-s\tau}\right]\Bigg|_{s=0}. \tag{22}$$

Condition (19) follows directly from (21). Now, through direct computations, it can be verified that equations (20) and (21) lead us to

$$\tau = -\frac{1}{p\left(0, k_p, \alpha_1, \ldots, \alpha_{n-2}, \sigma\right)}\left[\frac{\partial p\left(s, k_p, \alpha_1, \ldots, \alpha_{n-2}, \sigma\right)}{\partial s} - \frac{p\left(0, k_p, \alpha_1, \ldots, \alpha_{n-2}, \sigma\right)}{q(0,\sigma)}\frac{\partial q(s,\sigma)}{\partial s}\right]\Bigg|_{s=0}. \tag{23}$$

On the other hand, equations (20) and (22), imply that

$$0 = \left[\tau^2 p\left(0, k_p, \alpha_1, \ldots, \alpha_{n-2}, \sigma\right) - 2\tau\frac{p\left(0, k_p, \alpha_1, \ldots, \alpha_{n-2}, \sigma\right)}{q(0,\sigma)}\frac{\partial q(s,\sigma)}{\partial s} - \frac{\partial^2 p\left(s, k_p, \alpha_1, \ldots, \alpha_{n-2}, \sigma\right)}{\partial s^2} + \frac{p\left(0, k_p, \alpha_1, \ldots, \alpha_{n-2}, \sigma\right)}{q(0,\sigma)}\frac{\partial^2 q(s,\sigma)}{\partial s^2}\right]\Bigg|_{s=0}, \tag{24}$$

and finally, by substituting (23) in (24), yields

$$\begin{aligned} f(\sigma) = {} & \frac{1}{p\left(0, k_p, \alpha_1, \ldots, \alpha_{n-2}, \sigma\right)}\left[\frac{\partial p\left(s, k_p, \alpha_1, \ldots, \alpha_{n-2}, \sigma\right)}{\partial s} - \frac{p\left(0, k_p, \alpha_1, \ldots, \alpha_{n-2}, \sigma\right)}{q(0,\sigma)}\frac{\partial q(s,\sigma)}{\partial s}\right]^2\Bigg|_{s=0} \\ & + \frac{2}{q(0,\sigma)}\frac{\partial q(s,\sigma)}{\partial s}\left[\frac{\partial p\left(s, k_p, \alpha_1, \ldots, \alpha_{n-2}, \sigma\right)}{\partial s} - \frac{p\left(0, k_p, \alpha_1, \ldots, \alpha_{n-2}, \sigma\right)}{q(0,\sigma)}\frac{\partial q(s,\sigma)}{\partial s}\right]\Bigg|_{s=0} \\ & + \left[\frac{p\left(0, k_p, \alpha_1, \ldots, \alpha_{n-2}, \sigma\right)}{q(0,\sigma)}\frac{\partial^2 q(s,\sigma)}{\partial s^2}\right]\Bigg|_{s=0} - \left[\frac{\partial^2 p\left(s, k_p, \alpha_1, \ldots, \alpha_{n-2}, \sigma\right)}{\partial s^2}\right]\Bigg|_{s=0} = 0, \end{aligned} \tag{25}$$

that completes the proof. □

5. PR Controller Design for a Flexible Joint Arm

In this section, the conditions proposed to achieve the maximum decay rate σ^* are considered for the design of a Proportional Retarded control law implemented on a flexible joint robotic arm experimental platform.

5.1. Robot Dynamic Model. The schematic representation of the flexible joint robotic arm is given in Figure 2.

The notation used is as follows (for the sake of simplicity of notation, in the following, we will omit the time dependence of the functions). θ_1 and θ_2 are the angular positions of the rotating base and of the arm, respectively. J_1 is the moment of inertia of the rotating base and J_2 is the moment of inertia of the rotating arm. m denotes the mass of the arm, while l represents the arm length. g is the gravity constant, k_s is the spring stiffness, and M is the torque applied to the system. The motor torque M_m and the torque applied to the system M satisfy the relation $M = NM_m$, where N denotes the mechanical advantage of the pulley system.

Following the Euler–Lagrange formulation, the equations of motion of the flexible joint robotic arm can be derived as

$$M = J_1\ddot{\theta}_1 + J_2\left(\ddot{\theta}_1 + \ddot{\theta}_2\right) + \frac{mgl}{2}\sin\left(\theta_1 + \theta_2\right), \tag{26}$$

$$0 = J_2\left(\ddot{\theta}_1 + \ddot{\theta}_2\right) + k_s\theta_2 + \frac{mgl}{2}\sin\left(\theta_1 + \theta_2\right). \tag{27}$$

Besides, the control input voltage applied to the motor V and the torque M_m are related as follows:

$$M_m = \frac{k_m}{R_m}V - \frac{k_m^2 N}{R_m}\dot{\theta}_1, \tag{28}$$

where R_m symbolizes the armature resistance and k_m the torque constant of the motor. Based on the above relations, (26) and (27) are now of the form

$$\begin{aligned} \frac{Nk_m}{R_m}V &= \left(J_1 + J_2\right)\ddot{\theta}_1 + J_2\ddot{\theta}_2 + \frac{k_m^2 N^2}{R_m}\dot{\theta}_1 + \frac{mgl}{2}\sin\left(\theta_1 + \theta_2\right), \\ 0 &= J_2\left(\ddot{\theta}_1 + \ddot{\theta}_2\right) + k_s\theta_2 + \frac{mgl}{2}\sin\left(\theta_1 + \theta_2\right), \end{aligned} \tag{29}$$

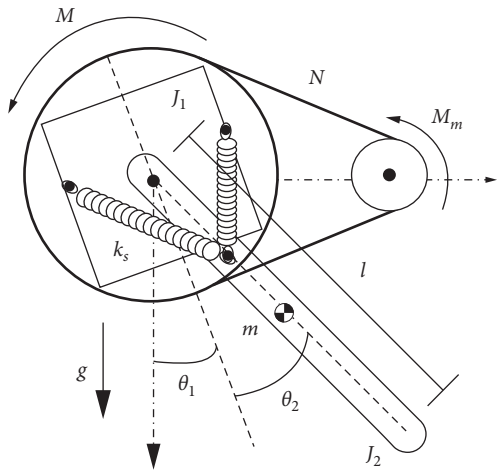

Figure 2: Schematic of a flexible joint robot arm.

or equivalently

$$\ddot{\theta}_1 = \kappa_2\theta_2 - \kappa_1\dot{\theta}_1 + \delta V, \tag{30}$$

$$\ddot{\theta}_2 = -\kappa_3\theta_2 - \kappa_4 \sin(\theta_1 + \theta_2) + \kappa_1\dot{\theta}_1 - \delta V, \tag{31}$$

where

$$\begin{aligned} \kappa_1 &= \frac{k_m^2 N^2}{J_1 R_m}, \\ \kappa_2 &= \frac{k_s}{J_1}, \\ \kappa_3 &= \frac{k_s(J_1 + J_2)}{J_1 J_2}, \\ \kappa_4 &= \frac{mgl}{2J_2}, \\ \delta &= \frac{k_m N}{J_1 R_m}. \end{aligned} \tag{32}$$

5.2. PR Controller Design. By performing the change of variables $x \coloneqq [x_1 x_2 x_3 x_4]^\top = [\theta_1 \dot{\theta}_1 \theta_2 \dot{\theta}_2]^\top$, systems (30) and (31) can be rewritten as

$$\dot{x} = f(x) + g(x)V, \tag{33}$$

where

$$f(x) = \begin{bmatrix} x_2 \\ -\kappa_1 x_2 + \kappa_2 x_3 \\ x_4 \\ \kappa_1 x_2 - \kappa_3 x_3 - \kappa_4 \sin(x_1 + x_3) \end{bmatrix},$$

$$g(x) = \begin{bmatrix} 0 \\ \delta \\ 0 \\ -\delta \end{bmatrix}. \tag{34}$$

The first stage in the design of the delayed controller is to transform nonlinear system (33) into a linear system via feedback linearization approach. Let us define

$$h(x) = x_1 + x_3, \tag{35}$$

as the output function. Denoting $L_f h(x)$ and $L_g h(x)$ as the Lie derivatives of function $h(x)$ with respect of the vector fields f and g, respectively (see [35]). Thus, differentiating the output function $h(x)$,

$$\dot{h}(x) = \frac{\partial h(x)}{\partial x}\dot{x} = L_f h(x) + L_g h(x) = x_2 + x_4, \tag{36}$$

and computing the higher order derivative of $h(x)$,

$$\begin{aligned} \ddot{h}(x) &= L_f^2 h(x), \\ h^{(3)}(x) &= L_f^3 h(x), \\ h^{(4)}(x) &= L_f^4 h(x) + V L_g L_f^3 h(x), \end{aligned} \tag{37}$$

where

$$\begin{aligned} L_f^2 h(x) &= (\kappa_2 - \kappa_3)x_3 - \kappa_4 \sin(x_1 + x_3), \\ L_f^3 h(x) &= -\kappa_4 (x_2 + x_4)\cos(x_1 + x_3) + (\kappa_2 - \kappa_3)x_4, \\ L_f^4 h(x) &= (\kappa_2 - \kappa_3)(\kappa_1 x_2 - \kappa_3 x_3) + \kappa_4 \sin(x_1 + x_3) \\ &\quad \cdot \left[(x_2 + x_4)^2 - (\kappa_2 - \kappa_3) + \kappa_4 \cos(x_1 + x_3)\right] \\ &\quad + \kappa_4 (\kappa_3 - \kappa_2) x_3 \cos(x_1 + x_3), \\ L_g L_f^3 h(x) &= -(\kappa_2 - \kappa_3)\delta. \end{aligned} \tag{38}$$

Hence, the system has relative degree four. Now, let us define the state transformation $z_1 = h(x)$, $z_2 = \dot{h}(x)$, $z_3 = h^{(2)}(x)$, and $z_4 = h^{(3)}(x)$, then it follows that

$$\begin{aligned} \dot{z}_1 &= L_f h(x), \\ \dot{z}_2 &= L_f^2 h(x), \\ \dot{z}_3 &= L_f^3 h(x), \\ \dot{z}_4 &= L_f^4 h(x) + V L_g L_f^3 h(x). \end{aligned} \tag{39}$$

Thus, the linearizing control function is of the form

$$V = \frac{1}{L_g L_f^3 h(x)}\left[u - L_f^4 h(x)\right]. \tag{40}$$

By denoting $h^*(x) = z_1^*$ as the desired trajectory and $h^{(j)*}(x) = z_{(j+1)}^*$, $j = 1, 2, 3, 4$, as its time derivatives, the errors functions are defined as $e_{z_j} = z_j - z_j^*$, then it follows

$$\begin{aligned} \dot{e}_{z_1} &= e_{z_2}, \\ \dot{e}_{z_2} &= e_{z_3}, \\ \dot{e}_{z_3} &= e_{z_4}, \\ \dot{e}_{z_4} &= u. \end{aligned} \tag{41}$$

Now, by proposing the delayed controller,

$$u_{\mathrm{PR}} = -k_p e_{z_1} + k_r e_{z_{1,\tau}} - \alpha_1 e_{z_3} - \alpha_2 e_{z_4}, \tag{42}$$

where the error $e_{z_{1,\tau}}$ is defined as

$$e_{z_1,\tau} = h(x_\tau) - h^*(x_\tau) = [x_1(t-\tau) + x_3(t-\tau)] - [x_1^*(t-\tau) + x_3^*(t-\tau)]. \tag{43}$$

Thus, system (41) in closed-loop, with control law (42), can be expressed as

$$\dot{e}_z = A_0 e_z + A_1 e_{z,\tau}, \tag{44}$$

where $e_z = [e_{z_1} e_{z_2} e_{z_3} e_{z_4}]^\top$ and

$$A_0 = \begin{bmatrix} 0 & 1 & 0 & 0 \\ 0 & 0 & 1 & 0 \\ 0 & 0 & 0 & 1 \\ -k_p & 0 & -\alpha_1 & -\alpha_2 \end{bmatrix}, \quad A_1 = \begin{bmatrix} 0 & 0 & 0 & 0 \\ 0 & 0 & 0 & 0 \\ 0 & 0 & 0 & 0 \\ k_r & 0 & 0 & 0 \end{bmatrix}. \tag{45}$$

The characteristic quasi-polynomial of system (44) is

$$Q(s, k_p, k_r, \alpha_1, \alpha_2) = p(s, k_p, \alpha_1, \alpha_2) + k_r q(s) e^{-s\tau}, \tag{46}$$

where $p(s, k_p, \alpha_1, \alpha_2) = s^4 + \alpha_2 s^3 + \alpha_1 s^2 + k_p$ and $q(s) = -1$. Now, using the change of variable $s = s - \sigma$, (46) takes the form

$$Q_\sigma(s, k_p, k_r, \alpha_1, \alpha_2) = p(s, k_p, \alpha_1, \alpha_2, \sigma) + k_r e^{\sigma\tau} q(s, \sigma) e^{-s\tau}, \tag{47}$$

where

$$\begin{aligned} p(s, k_p, \alpha_1, \alpha_2, \sigma) &= s^4 + (-4\sigma + \alpha_2)s^3 + (6\sigma^2 - 3\alpha_2\sigma + \alpha_1)s^2 \\ &\quad + (-4\sigma^3 + 3\alpha_2\sigma^2 - 2\alpha_1\sigma)s \\ &\quad + (\sigma^4 - \alpha_2\sigma^3 + \alpha_1\sigma^2 + k_p), \\ q(s, \sigma) &= -1. \end{aligned} \tag{48}$$

By Proposition 1, we have that when $s = 0$,

$$k_r = \frac{\sigma^4 - \alpha_2\sigma^3 + \alpha_1\sigma^2 + k_p}{e^{\sigma\tau}}, \tag{49}$$

while for $s = i\omega$

$$\tau = \frac{1}{\omega}\cot^{-1}\left(-\frac{\mathrm{Re}\{(p(i\omega, k_p, \alpha_1, \alpha_2, \sigma))/(q(i\omega, \sigma))\}}{\mathrm{Im}\{(p(i\omega, k_p, \alpha_1, \alpha_2, \sigma))/(q(i\omega, \sigma))\}}\right) + \frac{j\pi}{\omega},$$

$$k_r = \frac{1}{e^{\sigma\tau}\sin(\omega\tau)}\mathrm{Im}\left\{\frac{p(i\omega, k_p, \alpha_1, \alpha_2, \sigma)}{q(i\omega, \sigma)}\right\}, \tag{50}$$

where $j = 0, \pm 1, \pm 2, \ldots$ and

$$\begin{aligned} \mathrm{Re}\left\{\frac{p(i\omega, k_p, \alpha_1, \alpha_2, \sigma)}{q(i\omega, \sigma)}\right\} &= -\sigma^4 + \alpha_2\sigma^3 - (\alpha_1 - 6\omega^2)\sigma^2 \\ &\quad - 3\alpha_2\omega^2\sigma - \omega^4 + \alpha_1\omega^2 - k_p, \\ \mathrm{Im}\left\{\frac{p(i\omega, k_p, \alpha_1, \alpha_2, \sigma)}{q(i\omega, \sigma)}\right\} &= \omega[4\sigma^3 - 3\alpha_2\sigma^2 + (-4\omega^2 + 2\alpha_1)\sigma \\ &\quad + \alpha_2\omega^2]. \end{aligned} \tag{51}$$

According to Proposition 2 we first compute $Q_\sigma(s, k_p, k_r, \alpha_1, \alpha_2)|_{s=0}$, as well as its first and second partial derivatives, that is,

$$Q_\sigma(\cdot)\big|_{s=0} = e^{\sigma\tau}k_r = \sigma^4 - \alpha_2\sigma^3 + \alpha_1\sigma^2 + k_p, \tag{52}$$

$$\frac{\partial}{\partial s}Q_\sigma(\cdot)\bigg|_{s=0} = \tau e^{\sigma\tau}k_r = 4\sigma^3 - 3\alpha_2\sigma^2 + 2\alpha_1\sigma, \tag{53}$$

$$\frac{\partial^2}{\partial s^2}Q_\sigma(\cdot)\bigg|_{s=0} = \tau^2 e^{\sigma\tau}k_r = 12\sigma^2 - 6\alpha_2\sigma + 2\alpha_1. \tag{54}$$

From (52) and (53), we get

$$\tau = \frac{4\sigma^3 - 3\sigma^2\alpha_2 + 2\sigma\alpha_1}{\sigma^4 - \sigma^3\alpha_2 + \sigma^2\alpha_1 + k_p}, \tag{55}$$

and from (52) and (54), it follows that

$$\tau^2 = \frac{12\sigma^2 - 6\sigma\alpha_2 + 2\alpha_1}{\sigma^4 - \sigma^3\alpha_2 + \sigma^2\alpha_1 + k_p}. \tag{56}$$

Substituting (55) into (56), we have

$$\begin{aligned} f(\sigma) &= 4\sigma^6 - 6\sigma^5\alpha_2 + (2\alpha_1 + 3\alpha_2^2)\sigma^4 \\ &\quad - 4\alpha_2\alpha_1\sigma^3 + (2\alpha_1^2 - 12k_p)\sigma^2 + 6\alpha_2 k_p\sigma - 2\alpha_1 k_p. \end{aligned} \tag{57}$$

Summarizing, for given k_p, α_1, and α_2, then if σ^* is the minimum real solution of polynomial (57), then the gains of the controller that determine the σ^* stability of the system with a root of multiplicity at least three are established as

$$\tau^* = \frac{4(\sigma^*)^3 - 3(\sigma^*)^2\alpha_2 + 2\sigma^*\alpha_1}{(\sigma^*)^4 - (\sigma^*)^3\alpha_2 + (\sigma^*)^2\alpha_1 + k_p}, \tag{58}$$

$$k_r^* = \frac{\sigma^*(4(\sigma^*)^2 - 3\sigma^*\alpha_2 + 2\alpha_1)}{\tau^* e^{\sigma^*\tau^*}}. \tag{59}$$

In the previous procedure, analytic expressions to determine the optimal values of parameters k_r^*, τ^*, and σ^* were determined, but there are no words about parameters α_1, α_2, and k_p; thus, in the subsequent paragraphs, a simple methodology for preselection or approximation of these parameters is presented.

First, by computing the Maclaurin series $e^{-s\tau} = 1 - s\tau + ((\tau^2 s^2)/2) - ((\tau^3 s^3)/6)$ and substituting it in (47), we obtain the expression

$$Q_\sigma(s) = s^4 + \left(\alpha_2 + \frac{\tau^3 k_r}{6}\right)s^3 + \left(\alpha_1 - \frac{\tau^2 k_r}{2}\right)s^2 + (\tau k_r)s + \left(k_p - k_r\right). \tag{60}$$

Now, it is desirable to select the controller gains k_p, α_1, and α_2 in such a way that the dynamics of the close-loop system follow those of a proposed Hurwitz polynomial of the form

$$p_a(s) = \left(s^2 + 2\xi\omega_n s + \omega_n^2\right)^2 = s^4 + 4\xi\omega_n s^3 + \left(2\omega_n^2 + 4\xi^2\omega_n^2\right)s^2 + 4\xi\omega_n^3 s + \omega_n^4, \tag{61}$$

where $\xi, \omega_n > 0$. In order to match the dynamics of polynomials (60) and (61), the following parametrized conditions must be fulfilled:

$$k_p > \sqrt{\frac{\left(4\xi\omega_n^3\right)^3}{24\xi\omega_n} + \omega_n^4}, \tag{62}$$

$$\alpha_1 = 2\omega_n^2 + 4\xi^2\omega_n^2 + \frac{\left(4\xi\omega_n^3\right)^2}{2\left(k_p - \omega_n^4\right)}, \tag{63}$$

$$\alpha_2 = 4\xi\omega_n - \frac{\left(4\xi\omega_n^3\right)^3}{6\left(k_p - \omega_n\right)^2}. \tag{64}$$

Remark 1. It is worth mentioning, that expressions (62)–(64) can be considered only as a starting point to set the controller gains k_p, α_1, and α_2 and must be adapted according to the control designer expertise. On the other hand, expressions (57)–(59) guarantee to reach the maximal decay rate for given parameters k_p, α_1, and α_2.

6. Practical Implementation

In this section, the designed PR control law (40) is implemented in a flexible joint arm experimental platform using Matlab-Simulink, through a data acquisition device. The effectiveness of the proposed control law is assessed by means of tracking a rest-to-rest angular position reference trajectory. For comparative purposes, a feedback state control is designed and implemented in the experimental platform.

6.1. Experimental Setup. A block diagram of the experimental prototype is presented in Figure 3. The experimental platform incorporate a DC motor NISCA model NC5475, attached to a rotating base trough a belt pulley system with a 16 : 1 ratio. The flexible joint consists of a main arm attached to the rotating base by springs. The angular positions, of the rotating base and the arm, are measured by incremental encoders. The data acquisition task was performed by a

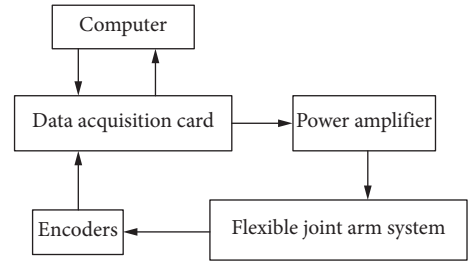

Figure 3: Diagram of the experimental platform architecture.

Sensoray 626 card. The control law was implemented in a Matlab-Simulink real time model, where the sampling period was fixed to be 0.001 s. The values of the flexible joint robotic arm parameters are $l = 0.5\,\text{m}$, $m = 0.1633\,\text{kg}$, $J_1 = 0.0136\,\text{kg}\cdot\text{m}^2$, $J_2 = 0.002405\,\text{kg}\cdot\text{m}^2$, $k_s = 4\,\text{N}\cdot\text{m/rad}$, and $N = 16$, while the motor parameters are $k_m = 0.0724\,\text{N}\cdot\text{m/A}$ and $R_m = 2.983\,\Omega$.

6.2. Feedback State Control. In order to compare PR control law (42) with a classical controller, we propose a feedback state control (FS):

$$u_{\text{FS}} = -\beta_1 e_{z_1} - \beta_2 e_{z_2} - \beta_3 e_{z_3} - \beta_4 e_{z_4}, \tag{65}$$

where the set of gains $[\beta_1, \beta_2, \beta_3, \beta_4]$ are positive constants. Using (40) and (41), we obtain the close-loop dynamic error:

$$e_{z_1}^{(4)} + \beta_4 e_{z_1}^{(3)} + \beta_3 \ddot{e}_{z_1} + \beta_2 \dot{e}_{z_1} + \beta_1 e_{z_1} = 0. \tag{66}$$

The characteristic polynomial is matched with a Hurwitz polynomial of the form

$$p_{\text{FL}}(s) = s^4 + \beta_4 s^3 + \beta_3 s^2 + \beta_2 s + \beta_1 = \left(s^2 + 2\zeta\varpi s + \varpi^2\right)^2. \tag{67}$$

The set of controller gains is chosen as follows:

$$\begin{aligned} \beta_1 &= \varpi^4, \\ \beta_2 &= 4\zeta\varpi^3, \\ \beta_3 &= 4\zeta^2\varpi^2 + 2\varpi^2, \\ \beta_4 &= 4\zeta\varpi. \end{aligned} \tag{68}$$

6.3. Experimental Results. The PR controller gains were selected as follows. We first proposed $\xi = 1.8$ and $\omega_n = 49$, and the gains k_p, α_1, and α_2 were selected from equations (62)–(64); after a slight adjustment, the gains were setted as $k_p = 4.5 \times 10^7$, $\alpha_1 = 5.7 \times 10^4$, and $\alpha_2 = 80$. On the other hand, the minimum real solution of (57) was $\sigma^* = 28.5495$, then using equations (58) and (59) we obtained the values $\tau^* = 0.0349$ and $k_r^* = 3.3 \times 10^7$.

In Figure 4, the σ-stability boundaries are depicted. The red mark represents the maximal achievable decay rate and corresponds to the place where all the σ-stable regions collapsed in a single point. According to (68), the FS controller gains were selected as follows $\zeta = 1.8$ and $\varpi = 52$.

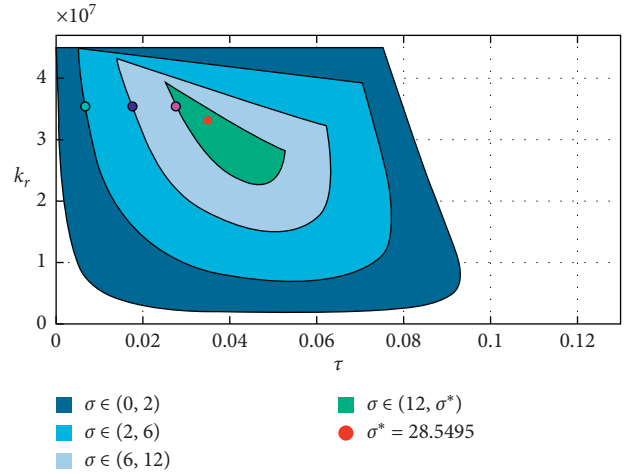

Figure 4: σ^*-stability region.

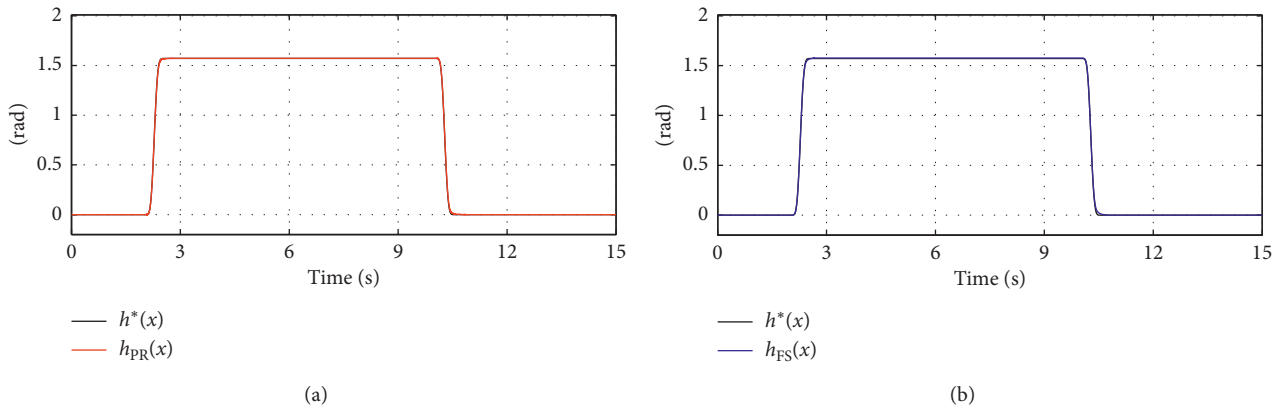

Figure 5: Trajectory tracking performance.

The initial conditions for both experiment PR and FL controllers are setting $\theta_1 = x_1(0) = 0$ and $\theta_2 = x_3(0) = 0$; this implies that output function (35) is $h(x) = 0$. The desired trajectory $h^*(x)$ starts at time $t = 0$ in the position $h^*(x) = 0$, when the time is $t = 1$, and it moves in 0.6 seconds. So, when $t = 1.6$ and $h^*(x) = \pi/2$, it remains in this position for 8 seconds and after this time the reference is moved to the initial location in 0.6 seconds, that is, $h^*(x) = 0$ when $t = 10.6$, and it remains in this position until the test is finished.

Vibrations are a common phenomenon in this class of systems, mainly when rest-to-rest point task is required. Figure 5(a) shows the PR controller performance, the output trajectory tracking $h_{PR}(x)$ depicted in red, and the desired trajectory $h^*(x)$ in black. In the same way, in Figure 5(b), the FL controller output $h_{FS}(x)$ is depicted in blue. We can notice that both outputs $h_{PR}(x)$ and $h_{FS}(x)$ smoothly follows the desired trajectory avoiding overshoot, as well as undesirable oscillations. The tracking trajectory errors e_{PR} (up) and e_{FS} (bottom) are shown in Figure 6. PR error, denoted by e_{PR}, is bounded in a neighborhood of $[-0.02, 0.02]$ rad, while FL error (e_{FS}) is bounded in a neighborhood of $[-0.02, 0.03]$ rad, and it shows some oscillations and a mayor amplitude in comparison with the PR controller.

PR voltage input (V_{PR}) is depicted in Figure 7(a) and the maximum amplitude of the signal is approximately $[-15, 15]$ Volts, and it does not present noise when the system is in the steady state, and FS voltage V_{FS} is shown in Figure 7(b). Here, we can notice similar performance of both V_{PR} and V_{FS} in amplitude and form, but V_{FS} shows a clear increase in noise and frequency: In order to clarify this statement, a Power Density Spectrum (PSD) of each voltage control is depicted in Figure 8. As we can observe, PR_{PSD} exhibits low-frequency components with a small peak at 7.7 Hz. On the other hand, FS_{PSD} shows more high-frequency components. Low-frequency components on the PR controller give us some advantages such as less wear on the actuators, less power consumption, and vibrations, among others. The above can be verified by observing Figures 9 and 10, where the performance of the system is evaluated by means of a quadratic index for both the error and the applied voltage.

Now, it is desirable to evaluate the performance of the flexible joint robotic platform in other points of the parametric space (τ, k_r). Here, we consider points with similar

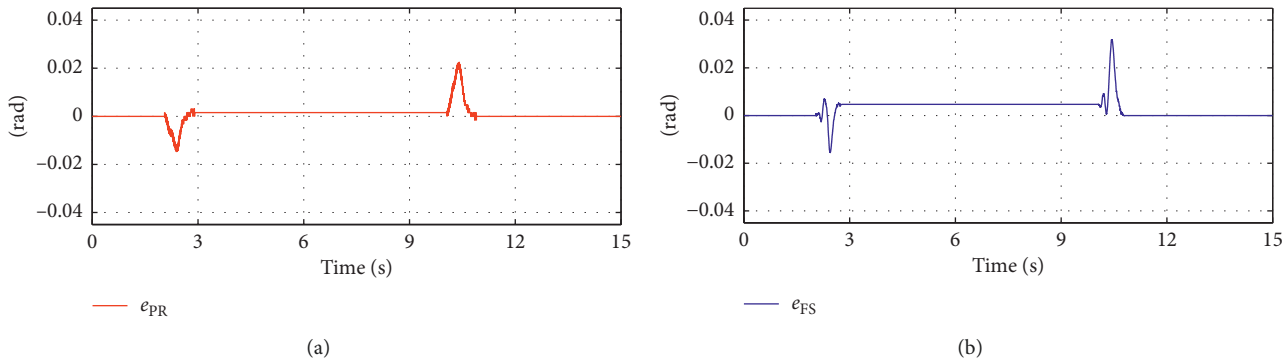

Figure 6: Tracking error.

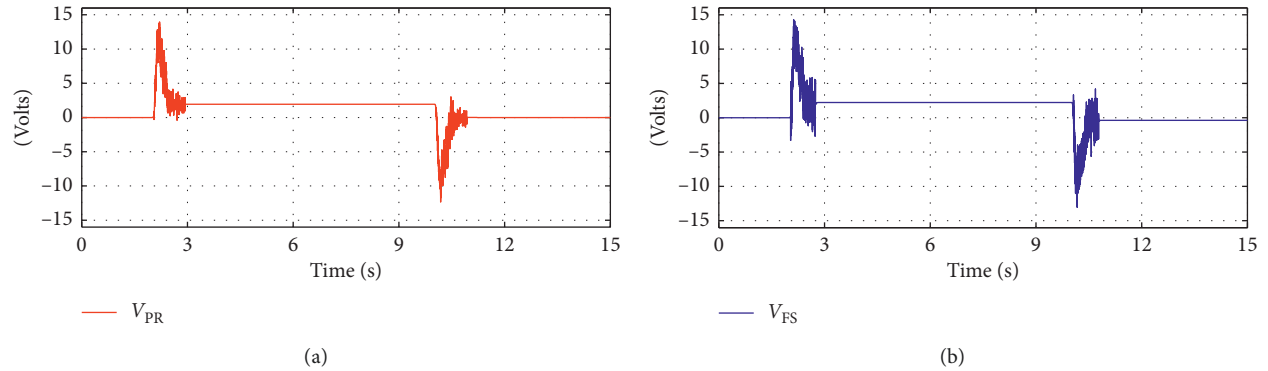

Figure 7: Control input voltage.

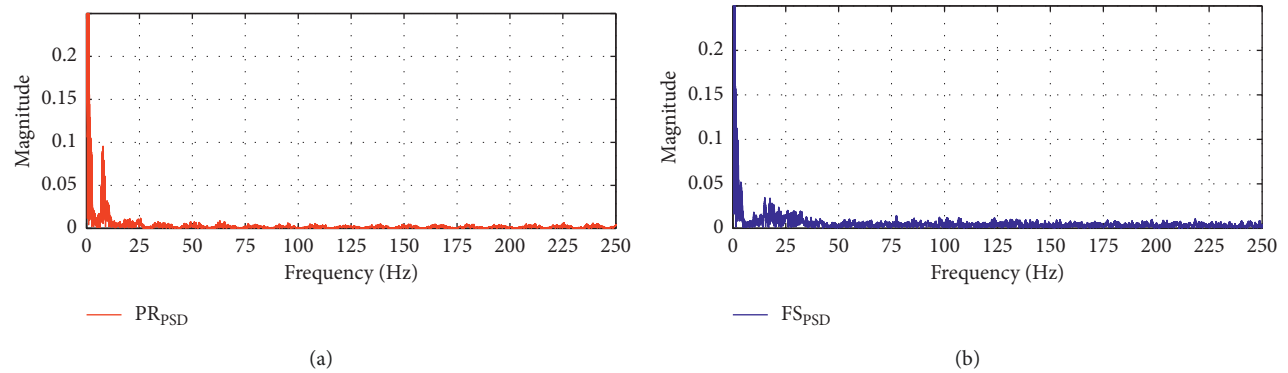

Figure 8: Power spectrum density.

control parameters but with different exponential decay rate σ and consequently a different delay τ. These points are depicted in Figure 4 and its control parameters are given in Table 1.

The system responses, at the selected points, are depicted in Figure 11, where it can be seen that the control tasks were carried out satisfactorily. Since each of the points corresponds to different σ-stable regions with a specific decay rate, the zoom at the bottom of Figure 11 allows us to note that the transient response of the system vanishes according to Table 1, and as expected, the system achieves the maximal decay rate at the point $\sigma^* = 28.5495$. A similar statement can be made, when the error signals are analyzed (see Figure 12).

Remark 2. The σ-stability approach provides us some benefits from the robustness perspective. Since the parameters τ^* and k_r^* are selected deep inside the stability region, the effect of parameter variations only affect the decay rate but not the stability property. This statement can

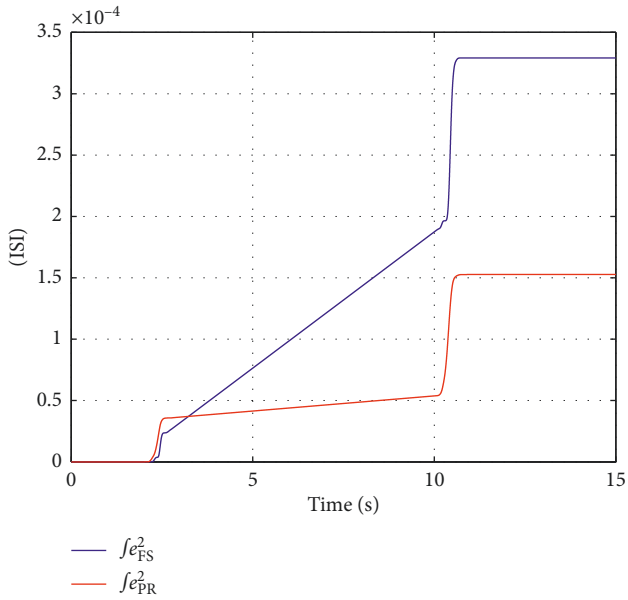

Figure 9: Performance index of the error.

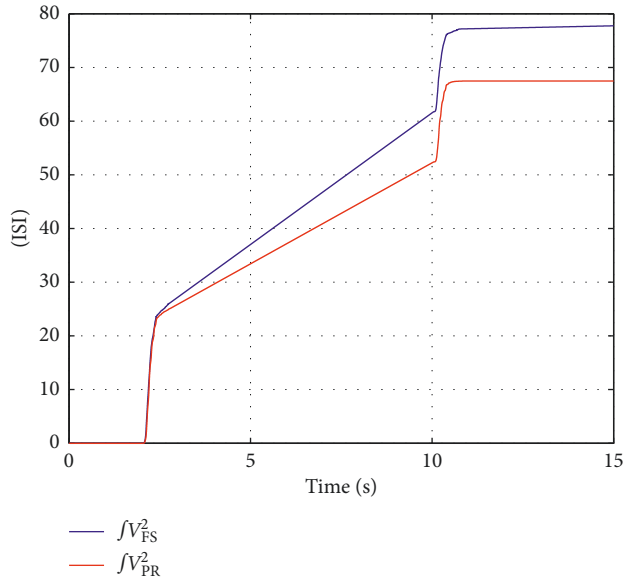

Figure 10: Performance index of the controller.

Table 1: Parameters (k_r, τ) and settling time.

	Parameters			Settling time
Color	σ	k_r	τ (s)	Time (s)
Cyan	2	3.5e7	0.006767	1.128
Blue	6	3.5e7	0.01775	0.947
Magenta	12	3.5e7	0.02784	0.655
Red	28.5495	3.3e7	0.0349	0.321

be verified in Figures 11 and 12, where the performance of the system is evaluated for parameters (τ, k_r) taken far from the point (τ^*, k_r^*). It can be appreciated that the further the control parameters are selected from the point (τ^*, k_r^*), the

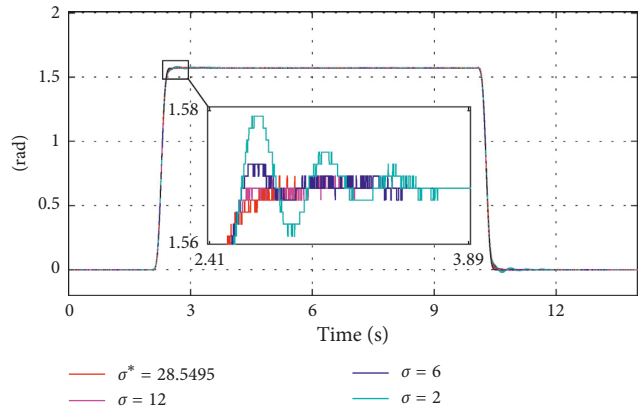

Figure 11: Trajectory tracking results.

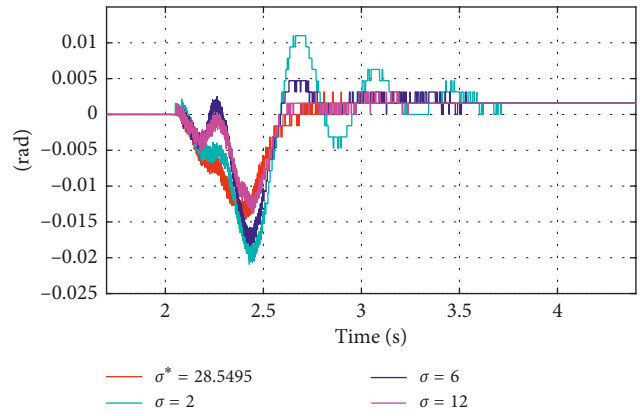

Figure 12: Tracking error signals.

greater the decay rate will be, but the stability of the system remains.

7. Conclusions

Analytic conditions for the design of proportional retarded controllers that guarantee reaching the optimal decay rate for a general class of LTI systems are presented. A detailed design of a proportional retarded controller, which shows the ease with which the proposed conditions can be computed and implemented, is developed for the control of an experimental platform that consists of a flexible joint robotic arm. The experimental results illustrate the effectiveness of the conditions and show remarkable tracking of rest-to-rest trajectories avoiding oscillations, noise, and overshoot.

Data Availability

All the data generated or analyzed during this study are included in this paper.

Conflicts of Interest

The authors declare that there are no conflicts of interest regarding the publication of this paper.

References

[1] R. Sipahi, S.-I. Niculescu, C. T. Abdallah, W. Michiels, and K. Gu, "Stability and stabilization of systems with time delay," *IEEE Control Systems*, vol. 31, no. 1, pp. 38–65, 2011.

[2] C. Abdallah, P. Dorato, J. Benites-Read, and R. Byrne, "Delayed positive feedback can stabilize oscillatory systems," in *Proceedings of the 1993 American Control Conference*, pp. 3106-3107, San Francisco, CA, USA, June 1993.

[3] V. Kharitonov, S.-I. Niculescu, J. Moreno, and W. Michiels, "Static output feedback stabilization: necessary conditions for multiple delay controllers," *IEEE Transactions on Automatic Control*, vol. 50, no. 1, pp. 82–86, 2005.

[4] S.-I. Niculescu and W. Michiels, "Some remarks on stabilizing a chain of integrators using multiple delays," in *Proceedings of the 2003 American Control Conference*, vol. 3, pp. 2664–2669, IEEE, Denver, CO, USA, June 2003.

[5] S.-I. Niculescu and W. Michiels, "Stabilizing a chain of integrators using multiple delays," *IEEE Transactions on Automatic Control*, vol. 49, no. 5, pp. 802–807, 2004.

[6] N. Olgac and M. E. Cavdaroglu, "Full-state feedback controller design with "delay scheduling" for cart-and-pendulum dynamics," *Mechatronics*, vol. 21, no. 1, pp. 38–47, 2011.

[7] K. Pyragas, "Continuous control of chaos by self-controlling feedback," *Physics Letters A*, vol. 170, no. 6, pp. 421–428, 1992.

[8] A. Galip Ulsoy, "Time-delayed control of SISO systems for improved stability margins," *Journal of Dynamic Systems, Measurement, and Control*, vol. 137, no. 4, Article ID 041014, 2015.

[9] K. Gu, V. Kharitonov, and J. Chen, "Stability of time-delay systems," *Addison-Wesley Series in Electrical and Computer Engineering: Control Engineering*, Springer-Verlag, New, York, NY, USA, 2003.

[10] V. L. Kharitonov, *Time Delay Systems: Lyapunov Functionals and Matrices*, Springer Science & Business Media, Berlin, Germany, 2013.

[11] K. J. Aström and T. Hägglund, *Advanced PID Control*, ISA–The Instrumentation, Systems and Automation Society, Research Triangle, CA, USA, 2006.

[12] C. Knospe, "PID control," *IEEE Control Systems Magazine*, vol. 26, no. 1, pp. 30-31, 2006.

[13] M. A. Johnson and M. H. Moradi, *PID Control*, Springer-Verlag, London, UK, 2005.

[14] H. Kokame and T. Mori, "Stability preserving transition from derivative feedback to its difference counterparts," *IFAC Proceedings Volumes*, vol. 35, no. 1, pp. 129–134, 2002.

[15] I. Suh and Z. Bien, "Proportional minus delay controller," *IEEE Transactions on Automatic Control*, vol. 24, no. 2, pp. 370–372, 1979.

[16] H. Suh and Z. Bien, "Use of time-delay actions in the controller design," *IEEE Transactions on Automatic Control*, vol. 25, no. 3, pp. 600–603, 1980.

[17] D. A. Irofti, K. Gu, I. Boussaada, and S.-I. Niculescu, "Some insights into the migration of double imaginary roots under small deviation of two parameters," *Automatica*, vol. 88, pp. 91–97, 2018.

[18] R. Villafuerte and S. Mondié, "Tuning the leading roots of a second order DC servomotor with proportional retarded control," *IFAC Proceedings Volumes*, vol. 43, no. 2, pp. 337–342, 2010.

[19] A. Ramirez, S. Mondie, and R. Garrido, "Proportional integral retarded control of second order linear systems," in *Proceedings of the 52nd IEEE Conference on Decision and Control*, pp. 2239–2244, IEEE, Florence, Italy, December 2013.

[20] J.-E. Hernández-Díez, C.-F. Méndez-Barrios, S. Mondié, S.-I. Niculescu, and E. J. González-Galván, "Proportional-delayed controllers design for LTI-systems: a geometric approach," *International Journal of Control*, vol. 91, no. 4, pp. 907–925, 2017.

[21] C.-I. Morarescu and S.-I. Niculescu, "Stability crossing curves of siso systems controlled by delayed output feedback," *Dynamic of Continous Discrete and Impulsive Systems Series B*, vol. 14, no. 5, p. 659, 2007.

[22] R. Villafuerte, S. Mondie, and R. Garrido, "Tuning of proportional retarded controllers: theory and experiments," *IEEE Transactions on Control Systems Technology*, vol. 21, no. 3, pp. 983–990, 2013.

[23] S. Mondié, R. Villafuerte, and R. Garrido, "Tuning and noise attenuation of a second order system using proportional retarded control," *IFAC Proceedings Volumes*, vol. 44, no. 1, pp. 10337–10342, 2011.

[24] A. Ramírez, R. Garrido, and S. Mondié, "Velocity control of servo systems using an integral retarded algorithm," *ISA Transactions*, vol. 58, pp. 357–366, 2015.

[25] A. Ramírez, R. Sipahi, S. Mondié, and R. Garrido, "Design of maximum decay rate for SISO systems with delayed output feedback using elimination theory," *IFAC-PapersOnLine*, vol. 48, no. 12, pp. 221–226, 2015.

[26] A. Ramirez, S. Mondie, R. Garrido, and R. Sipahi, "Design of proportional-integral-retarded (PIR) controllers for second-order LTI systems," *IEEE Transactions on Automatic Control*, vol. 61, no. 6, pp. 1688–1693, 2016.

[27] E. N. Gryazina, "The D-decomposition theory," *Automation and Remote Control*, vol. 65, no. 12, pp. 1872–1884, 2004.

[28] E. N. Gryazina and B. T. Polyak, "Stability regions in the parameter space: D-decomposition revisited," *Automatica*, vol. 42, no. 1, pp. 13–26, 2006.

[29] E. N. Gryazina, B. T. Polyak, and A. A. Tremba, "D-decomposition technique state-of-the-art," *Automation and Remote Control*, vol. 69, no. 12, pp. 1991–2026, 2008.

[30] J. Neimark, "D-decomposition of the space of quasipolynomials," *Applied Mathematics and Mechanics*, vol. 13, pp. 349–380, 1949.

[31] A. Ramírez, R. Garrido, and S. Mondié, "Integral retarded velocity control of DC servomotors," *IFAC Proceedings Volumes*, vol. 46, no. 3, pp. 558–563, 2013.

[32] R. Villafuerte, F. Medina, L. Vite, and B. Aguirre, "Tuning of a time-delayed controller for a general class of second-order LTI systems with dead-time," *IET Control Theory & Applications*, vol. 13, no. 3, pp. 451–457, 2019.

[33] M. Benosman and G. Le Vey, "Control of flexible manipulators: a survey," *Robotica*, vol. 22, no. 5, pp. 533–545, 2004.

[34] S. Ozgoli and H. Taghirad, "A survey on the control of flexible joint robots," *Asian Journal of Control*, vol. 8, no. 4, pp. 332–344, 2006.

[35] Isidori, *Nonlinear Control Systems*, Springer Science & Business Media, Berlin, Germany, 2013.

[36] H. Sira-Ramirez and S. K. Agrawal, *Differentially Flat Systems*, CRC Press, Boca Raton, FL, USA, 2004.

Hindawi
Complexity
Volume 2019, Article ID 9174284, 14 pages
https://doi.org/10.1155/2019/9174284

Research Article

Robust Position Control of a Two-Sided 1-DoF Impacting Mechanical Oscillator Subject to an External Persistent Disturbance by Means of a State-Feedback Controller

Firas Turki,[1] Hassène Gritli ,[1,2] and Safya Belghith[1]

[1]*Laboratory of Robotics, Informatics and Complex Systems (RISC-Lab, LR16ES07), National Engineering School of Tunis, Université de Tunis El Manar, BP. 37, Le Belvédère, 1002 Tunis, Tunisia*
[2]*Higher Institute of Information and Communication Technologies, Université de Carthage, 1164 Borj-Cedria, Tunis, Tunisia*

Correspondence should be addressed to Hassène Gritli; grhass@yahoo.fr

Received 6 September 2019; Accepted 1 November 2019; Published 7 December 2019

Guest Editor: Alberto Luviano

This paper proposes a state-feedback controller using the linear matrix inequality (LMI) approach for the robust position control of a 1-DoF, periodically forced, impact mechanical oscillator subject to asymmetric two-sided rigid end-stops. The periodic forcing input is considered as a persistent external disturbance. The motion of the impacting oscillator is modeled by an impulsive hybrid dynamics. Thus, the control problem of the impact oscillator is recast as a problem of the robust control of such disturbed impulsive hybrid system. To synthesize stability conditions, we introduce the S-procedure and the Finsler lemmas by only considering the region within which the state evolves. We show that the stability conditions are first expressed in terms of bilinear matrix inequalities (BMIs). Using some technical lemmas, we convert these BMIs into LMIs. Finally, some numerical results and simulations are given. We show the effectiveness of the designed state-feedback controller in the robust stabilization of the position of the impact mechanical oscillator under the disturbance.

1. Introduction

In diverse mechanical systems, there are some working conditions and parameters leading to the exhibition of impacts between the oscillatory elements of certain mechanical systems due to the presence of gaps. Some impacting mechanical systems are the impact dampers, the inertial shakers, the impact print hammers, the pile drivers, the shock absorbers, the forming machines, and much more [1–3]. In one-degree-of-freedom (1-DoF) mechanical oscillators, impacts can occur with rigid/soft end-stops, whereas in multi-DoF oscillators, collisions can also occur amongst moving elements. The wide interest in these impacting systems has spurred researchers and engineers to analyze their motions and hence the implications of impacts, as, for example, in [3–17].

In some working cases, impacts between interacting bodies are considered intrinsic for the operations of many engineering devices. Nevertheless, impacts may provoke some dangerous effects such as impulsive severe forces, rapid transfer of energy, and stresses and provokes a degradation of the performance of the mechanical systems, where we expect to observe a smooth behavior [2, 3, 7, 8, 12, 14]. These effects can lead then to the exhibition of chaotic responses. Thus, the objective is to improve the response and the performances of these impacting mechanical systems through control. The motion of these impacting systems is governed by an impulsive hybrid dynamics, which is composed by a differential equation and an algebraic one associated with its impact conditions. Thus, due to this impulsive hybrid dynamics, which is considered complex enough for analysis and control, the synthesis of controllers for these impacting systems is difficult to realize.

Some control techniques can be found in the literature. The OGY method has been widely adopted and applied to control chaos in vibroimpact systems [13, 18–22]. Some

other authors, e.g., [23–27], used other control techniques such as an external driving force, a delay feedback, a displacement feedback, a discrete-in-time feedback control, and a damping control law, among others. Authors in [28] used a feedback control input to control the position of a 1-DoF impact mechanical oscillator with two asymmetric end-stops. Authors in [29] controlled chaos in a 1-DoF impact oscillator with only one rigid constraint.

In this paper, we consider the control problem of the position of a 1-DoF impact mechanical oscillator with two-sided rigid end-stops [28, 30–32]. Such an impacting oscillator is periodically forced via an external sinusoidal input, which will be considered as a persistent disturbance to compensate its effect via a robust control law. Our main idea lies first in adding a control input to the impact oscillator. The synthesis of the control law will be realized using the LMI approach. In this paper, we will consider the whole impulsive hybrid dynamics of the two-sided 1-DoF impacting oscillator. Both the differential equation and the algebraic equations are considered in the design of the stability condition. In our previous works [30–32], the impact dynamics was not taken into account in the design. Only the differential equation was considered. Moreover, we adopted a state-feedback control law to stabilize the impacting motion around the zero-equilibrium point. As in [28], the forcing input, as a known signal, was canceled via the controller [30]. However, in [31, 32], the forcing input was considered as a disturbance. In this work, we will adopt a state-feedback controller to robustly stabilize the impulsive hybrid dynamics of the two-sided 1-DoF impact oscillator.

In order to synthesize the stability conditions, we use first the S-procedure lemma in order to only take into consideration the working region of the two-sided impacting oscillator, that is, the region between the two end-stops. In addition, we use the Finsler lemma in order to develop stability conditions for the algebraic equation and using the impact conditions. We show then that these stability conditions are expressed in terms of bilinear matrix inequalities (BMIs). In order to obtain numerically traceable LMI conditions, we use mainly the Schur complement and the matrix inversion lemma. Authors in [33, 34] used the LMI approach and these previous lemmas, except the Finsler Lemma, in order to design stabilizing controllers for an underactuated mechanical system, namely, the inertia wheel inverted pendulum, for which its motion is constrained by two symmetric end-stops. Its dynamics is nonlinear and does not present impacts. Our objective in this paper is to extend the design methodology adopted in [33, 34] for the two-sided 1-DoF impact mechanical oscillator, which is characterized by an impulsive hybrid dynamics.

The main contributions of this paper are summarized as follows:

(i) A robust state-feedback control law is designed to stabilize the 1-DoF double-sided mechanical oscillator subject to two asymmetric rigid constraints and an external persistent disturbance.

(ii) Stabilization of the impulsive hybrid dynamics of the impacting oscillator, where the continuous dynamics and the impact dynamics are both considered in the synthesis of the stability conditions.

(iii) Via the S-procedure and Finsler lemmas, the stabilization conditions of the closed-loop impulsive hybrid system are first obtained and expressed in terms of BMIs. The stability conditions are considered to be only satisfied inside the working region.

(iv) By means of the Schur complement lemma and the matrix inversion lemma, the previous BMIs are converted into LMIs.

(v) Several simulations are presented to show that the designed robust control law is able to compensate the effect of the external persistent disturbance and hence stabilize the impact mechanical oscillator at the zero-equilibrium point.

The structure of this paper is as follow. In Section 2, the two-sided 1-DoF impact mechanical oscillator is presented. Its impulsive hybrid dynamics is also presented in this section. The problem formulation and the technical lemmas used through this paper are given in Section 3. Section 4 and Section 5 are devoted to the synthesis of the BMI and the LMI stability conditions, respectively. In Section 6, the numerical results and simulations are demonstrated. Finally, the conclusion is addressed in Section 7.

2. The Double-Sided 1-DoF Impact Mechanical Oscillator

2.1. System Description. Figure 1 shows a 1-DoF impact mechanical oscillator with asymmetric double-sided rigid end-stops. The impacting system is composed of a mass m interconnected to the right end-stop by both a spring of stiffness k and a dashpot of damping coefficient ζ. The gap between the mass m and the rigid stop is d. A second rigid end-step is localized at the left away from the mass of a distance l. The motion impact oscillator is excited via a sinusoidal force input $v = p\cos(wt)$, where the parameters w and p are the excitation frequency and the excitation amplitude, respectively. In Figure 1, u is an additional input, the controller, which will be designed next to control the position of the impact oscillator to the zero-equilibrium point.

From an initial condition, the mechanical oscillator will oscillate horizontally along the axis x and will produce impacts with the two asymmetric rigid constraints with the same coefficient r of restitution inducing hence an instantaneous transition of the velocity.

2.2. Impulsive Hybrid Dynamics of the Impact Oscillator. The dynamics of the two-sided 1-DoF impact mechanical oscillator is governed by the following system:

$$m\ddot{\mathbf{x}} + 2\zeta\dot{\mathbf{x}} + k\mathbf{x} = p\cos(wt), \quad \text{for } l < \mathbf{x} < d, \tag{1a}$$

$$\mathbf{x}^{+} = \mathbf{x}^{-} \text{ and } \dot{\mathbf{x}}^{+} = -r\dot{\mathbf{x}}^{-}, \quad \text{for } \mathbf{x} = d \text{ or } \mathbf{x} = l, \tag{1b}$$

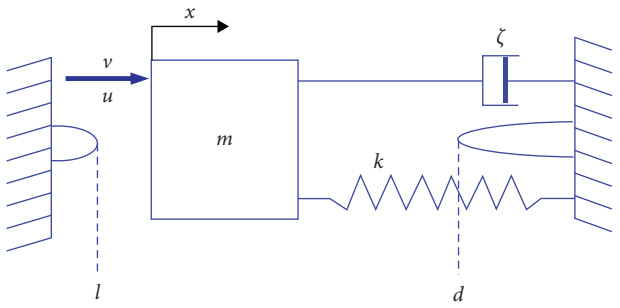

Figure 1: A 1-DoF impact mechanical oscillator under two asymmetric rigid end-stops.

where $\ddot{\mathbf{x}}$, $\dot{\mathbf{x}}$, and $\mathbf{x}$ are the acceleration, velocity, and displacement of the mass of the impacting oscillator, d and l are the right bound and the left bound, respectively, and subscribes $^+$ and $^-$ in (1b) denote, respectively, just after and just before the impact.

2.3. A Brief Look on the Impacting Behavior. It is well known that the double-sided 1-DoF impact mechanical oscillator generates periodic and chaotic behaviors with respect to the parameters p, w, ζ, d, l, and r. We refer our reader to [28] for further details and some bifurcation diagrams. As in [28], the adopted values of different parameters in dynamics (1a) and (1b) are $m = 1\,\text{kg}$, $k = 1\,\text{N/m}$, $\zeta = 0.05\,\text{N/(m/s)}$, $d = 0.3\,\text{m}$, $l = -0.1\,\text{m}$, $p = 0.5\,\text{N}$, and $r = 0.8$. Figure 2 shows the behavior of the impact oscillator for $w = 0.8$. In Figure 2, we plotted the temporal evolution of the position and the velocity of the impacting mechanical system. Figure 3 reveals the corresponding phase portrait simulated for such value of the parameter w. In Figure 4, we presented three Poincaré maps. Figure 4(a) shows the stroboscopic Poincaré map, which reveals the state of the impact oscillator at the period T. Figures 4(b) and 4(c) reveal the impact Poincaré maps. The first one in Figure 4(b) shows the impact time of the oscillator with the right bound with respect to its impact velocity. However, the second impact Poincaré map in Figure 4(c) shows the impact time with the left rigid constraint with respect to the impact velocity. These previous portraits in Figures 2, 3, and 4 demonstrate that the 1-DoF impact mechanical oscillator displays a chaotic behavior.

It is worth to note that it is possible to characterize chaos exhibited in the motion of the 1-DoF impact mechanical oscillator presented in Figure 2 and then in Figures 3 and 4 by means of the spectrum of Lyapunov exponents. Authors in [35] computed numerically the Lyapunov exponents in mechanical systems with impacts using a transcendental map. They applied their computation procedure for the one-sided 1-DoF impact oscillator and also for the impact-pair system. Moreover, authors in [36] computed the Lyapunov exponents of a cantilever beam impacting on a moving base using a discrete modeling. Some other works have also been developed for this subject, as, e.g., in [37, 38]. Author in [39] presented a general method for the calculation of Lyapunov exponents for dynamic systems with discontinuities and then with impacts. Thus, a forced impact oscillator with dry

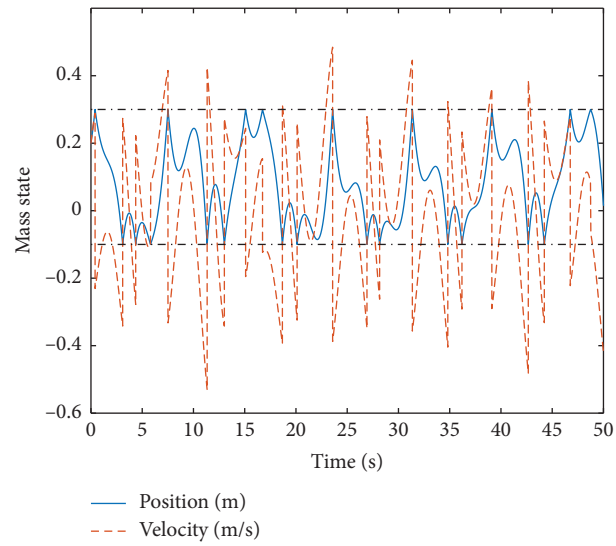

Figure 2: Temporal evolution of the mass position of the double-sided 1-DoF impacting mechanical oscillator for $w = 0.8$.

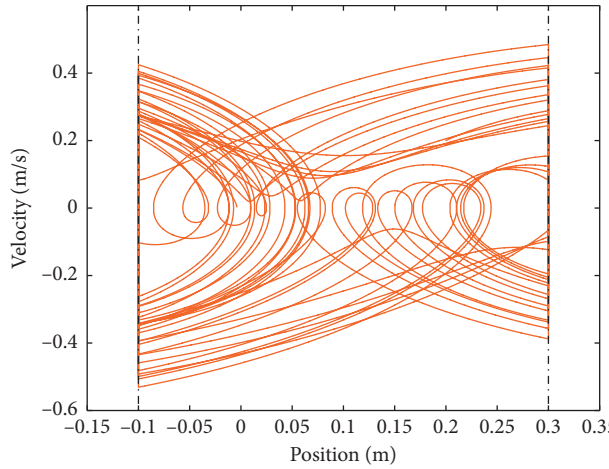

Figure 3: Phase portrait of the double-sided 1-DoF impacting mechanical oscillator for the parameter $w = 0.8$ showing a chaotic attractor.

friction was presented as an illustrative example. In [40, 41], authors computed the spectrum of Lyapunov exponents for more complicated impulsive hybrid systems, namely, the biped robots, using an explicit analytical expression of the (hybrid) Poincaré map.

3. Problem Formulation and Preliminaries

3.1. Problem Statement. Let $\mathbf{z} = [x \;\; \dot{x}]^T$ be the state vector. Then, relying on the equations in (1a) and (1b), the impulsive hybrid dynamics of the 1-DoF impact mechanical oscillator under the double-sided rigid constraints is given as follows:

$$\dot{\mathbf{z}} = \mathscr{A}\mathbf{z} + \mathscr{B}v, \text{ as long as } l < \mathscr{C}^T\mathbf{z} < d, \tag{2a}$$

$$\mathbf{z}^+ = \mathscr{R}\mathbf{z}^-, \text{ whenever } \mathscr{C}^T\mathbf{z} = d \text{ or } \mathscr{C}^T\mathbf{z} = l, \tag{2b}$$

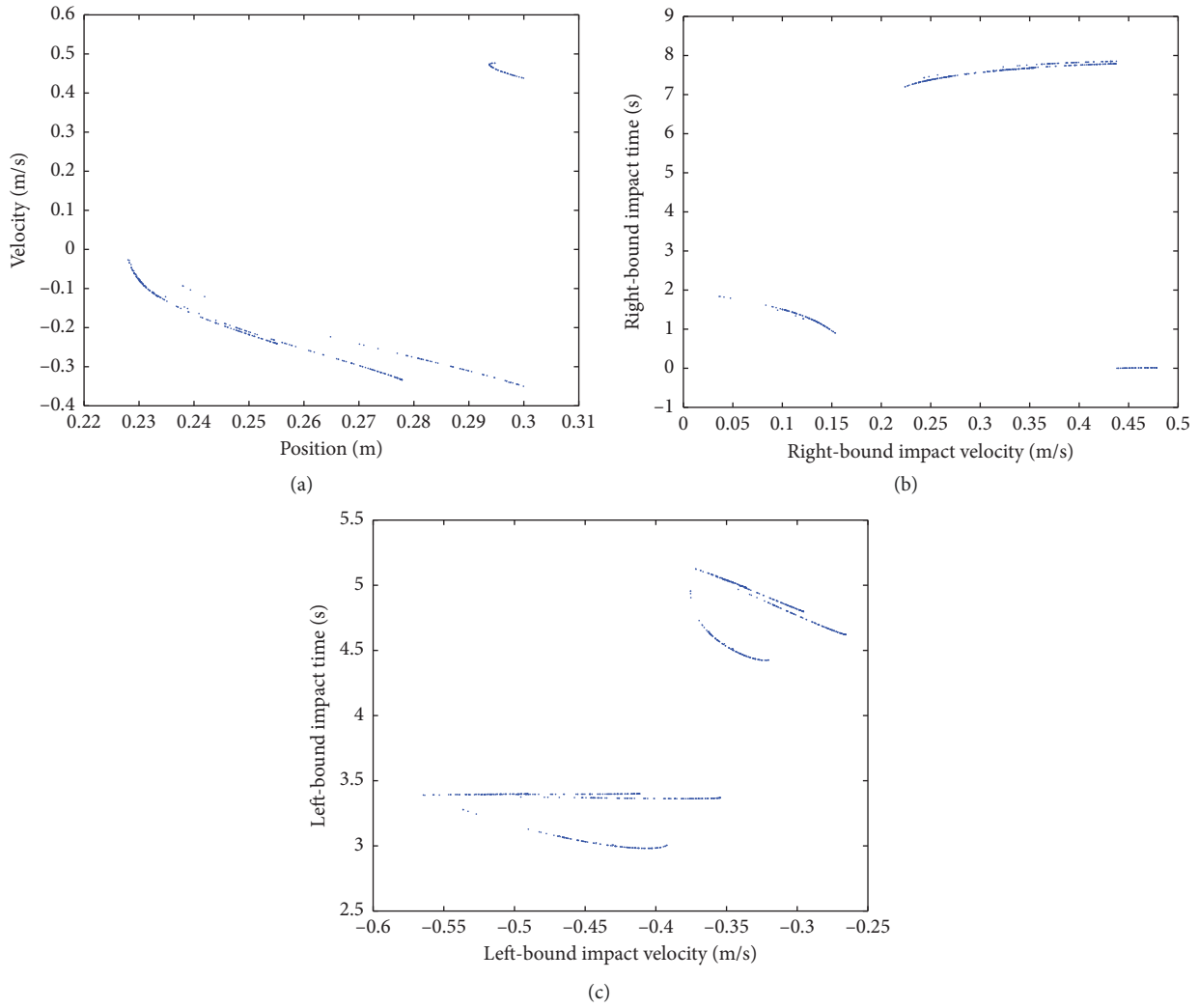

FIGURE 4: Phase portrait of the double-sided 1-DoF impacting mechanical oscillator for the parameter $w = 0.8$ showing a chaotic attractor.

where $\mathscr{A} = \begin{bmatrix} 0 & 1 \\ -(k/m) & -(2\zeta/m) \end{bmatrix}$, $\mathscr{B} = \begin{bmatrix} 0 \\ 1/m \end{bmatrix}$, $\mathscr{R} = \begin{bmatrix} 1 & 0 \\ 0 & -r \end{bmatrix}$, $\mathscr{C} = \begin{bmatrix} 1 \\ 0 \end{bmatrix}$, and $v = p\cos(wt)$. Moreover, we note that $d > 0$ and $l < 0$.

Our main objective in this work is to control the position of the impacting oscillator to the zero-equilibrium point. Then, we need an additional external input, saying u, as the controller, which will be designed next. Moreover, the signal v will be considered next as an external disturbance input applied to the oscillator. Actually, we will consider a general form of the disturbance torque v that can take any expression such that $|v| \leq p$. Accordingly, in (2a), we will have $(u + v)$ instead of v. Thus, the impulsive hybrid dynamics (1a) and (1b) becomes

$$\dot{\mathbf{z}} = \mathscr{A}\mathbf{z} + \mathscr{B}u + \mathscr{B}v, \text{ as long as } \mathbf{z} \in \Omega, \tag{3a}$$

$$\mathbf{z}^{+} = \mathscr{R}\mathbf{z}^{-}, \text{ whenever } \mathbf{z} \in \Gamma. \tag{3b}$$

In (3a) and (3b), Γ represents the impact surface and Ω reveals the oscillation space. They are defined as follows:

$$\begin{aligned} \Omega &= \left\{\mathbf{z} \in \mathbb{R}^{2\times 1}, l < \mathscr{C}^{T}\mathbf{z} < d\right\}, \\ \Gamma &= \left\{\mathbf{z} \in \mathbb{R}^{2\times 1}, \mathscr{C}^{T}\mathbf{z} = d \text{ or } \mathscr{C}^{T}\mathbf{z} = l\right\}. \end{aligned} \tag{4}$$

Our objective in this work is then to design the controller u for the disturbed impulsive hybrid systems (3a) and (3b)–(4) of the 1-DoF impacting mechanical oscillator to robustly stabilize it at (around) the zero-equilibrium point even in the presence of the external disturbance input v. For this subject we assume that all the states, i.e., the position x and the velocity $\dot{x}$ of the mechanical system are available for measurement. Then, under this assumption, we will adopt the following state-feedback controller:

$$u = \begin{cases} \mathscr{K}\mathbf{z}, & \text{whenever } \mathbf{z} \in \Delta, \\ 0, & \text{elsewhere,} \end{cases} \tag{5}$$

with

$$\Delta = \left\{x \in \mathbb{R}, x^2 > \varepsilon\right\}, \tag{6}$$

where $\mathscr{K} \in \mathbb{R}^{1\times 2}$ is a constant gain matrix to design next using the LMI approach and ε is a small enough positive constant. The set Δ in (6) defines the region within which the state-feedback control law is activated. This set Δ can be recast as follows:

$$\Delta = \left\{\mathbf{z} \in \mathbb{R}^{2\times 1}, \mathbf{z}^T \mathscr{C}\mathscr{C}^T \mathbf{z} > \varepsilon\right\}. \tag{7}$$

Remark 1. It is worth to note that the condition $\mathbf{z}^T\mathscr{C}\mathscr{C}^T\mathbf{z} > \varepsilon$ defining the set Δ in expression of the state-feedback control law (5) was added in order to overcome a certain solving problem of the LMI-based stability conditions of the closed-loop impulsive hybrid systems (3a) and (3b) under the state constraints in (4) using the Lyapunov approach [33]. Such a problem will be discussed later (see Remark 4). In [33], authors used the constraint $\|\mathbf{z}\|^2 > \varepsilon$ on the state-feedback control law in (5). This last condition is identical to the constraint $\mathbf{z}^T\mathscr{C}\mathscr{C}^T\mathbf{z} > \varepsilon$ if $\mathscr{C} = \mathscr{I}_2$. We emphasize that the new condition $\mathbf{z}^T\mathscr{C}\mathscr{C}^T\mathbf{z} > \varepsilon$ in (7) will provide less restrictive LMI conditions compared with that obtained via the condition $\mathbf{z}^T\mathbf{z} > \varepsilon$.

By substituting expression of control law (5) in dynamic model (3a), we obtain then the following closed-loop impulsive hybrid dynamics:

$$\dot{\mathbf{z}} = (\mathscr{A} + \mathscr{B}\mathscr{K})\mathbf{z} + \mathscr{B}v, \text{ as long as } \mathbf{z} \in \Omega,\ \mathbf{z} \in \Delta, \tag{8a}$$

$$\mathbf{z}^+ = \mathscr{R}\mathbf{z}^-, \text{ whenever } \mathbf{z} \in \Gamma,\ \mathbf{z} \in \Delta. \tag{8b}$$

Remark 2. It is worth to note that in [28], the position control of the double-sided 1-DoF impacting mechanical oscillator was achieved using the following control law:

$$u = 2\zeta\dot{x} + kx - v(t) - m(ax + b\dot{x}), \tag{9}$$

where the two design parameters a and b are determined such that the eigenvalues of the matrix $\begin{bmatrix} 0 & 1 \\ -a & -b \end{bmatrix}$ are with negative real parts.

In the next part of this work, we will focus on synthesizing stability conditions for the closed-loop impulsive hybrid systems (8a) and (8b).

3.2. Preliminary Lemmas. Before synthesizing the stability conditions for the impulsive hybrid system (8a) and (8b), we need the following technical lemmas. In the sequel, and in large matrix expressions, the symbol $(\star)$ replaces terms that are induced by symmetry. Moreover, $\mathbf{\Omega} + \mathscr{X} + (\star) = \Omega + \mathscr{X} + \mathscr{X}^{\mathrm{T}}$. In addition, $\mathscr{I}$ and $\mathscr{O}$ stand, respectively, for the identity matrix and the null matrix with appropriate dimensions.

Lemma 1 (the Young inequality [42]). *For given constant matrices* $\mathbf{X}$ *and* $\mathbf{Y}$ *with appropriate dimensions and any positive scalar* λ*, the following inequality holds:*

$$\mathbf{X}^T\mathbf{Y} + \mathbf{Y}^T\mathbf{X} \le \lambda\mathbf{X}^T\mathbf{X} + \lambda^{-1}\mathbf{Y}^T\mathbf{Y}. \tag{10}$$

Lemma 2 (the matrix inversion lemma [33, 34]). *For given invertible matrices* $\mathbf{X}$ *and* $\mathbf{Y}$ *such that* $\mathbf{X} \in \mathbb{R}^{n\times n}$ *and* $\mathbf{Y} \in \mathbb{R}^{m\times m}$*. Moreover, given matrices* $\mathbf{U}$ *and* $\mathbf{V}$ *are of appropriate dimensions* $\mathbf{U} \in \mathbb{R}^{n\times m}$ *and* $\mathbf{V} \in \mathbb{R}^{m\times n}$*. Then, the matrix inversion lemma is*

$$(\mathbf{X} + \mathbf{UYV})^{-1} = \mathbf{X}^{-1} - \mathbf{X}^{-1}\mathbf{U}\left(\mathbf{Y}^{-1} + \mathbf{U}\mathbf{X}^{-1}\mathbf{U}\right)^{-1}\mathbf{V}\mathbf{X}^{-1}. \tag{11}$$

Lemma 3 (the Schur complement lemma [42]). *For given matrices* $\mathscr{Q} = \mathscr{Q}^T$*,* $\mathscr{R} = \mathscr{R}^T$*, and* $\mathscr{S}$ *with appropriate dimensions, the following propositions are equivalent:*

$$\begin{bmatrix} \mathscr{Q} & \mathscr{S} \\ \mathscr{S}^T & \mathscr{R} \end{bmatrix} > 0, \tag{12a}$$

$$\begin{cases} \mathscr{R} > 0, \\ \mathscr{Q} - \mathscr{S}\mathscr{R}^{-1}\mathscr{S}^T > 0. \end{cases} \tag{12b}$$

Lemma 4 (the S-procedure lemma [33, 34, 42]). *Let* $\mathscr{F}_0, \ldots, \mathscr{F}_p \in \mathbb{R}^{n\times n}$ *be symmetric matrices. We consider the following condition on* $\mathscr{F}_0, \ldots, \mathscr{F}_p$*:*

$$\zeta^T\mathscr{F}_0\zeta > 0 \text{ for all } \zeta \neq 0, \text{ such that } \zeta^T\mathscr{F}_i\zeta \ge 0, \quad i = 1, \ldots, p. \tag{13}$$

If there exist scalar variables $\tau_1 \ge 0, \ldots, \tau_p \ge 0$*, such that*

$$\mathscr{F}_0 - \sum_{i=1}^{p} \tau_i\mathscr{F}_i > 0, \tag{14}$$

then (13) holds.

Lemma 5 (Finsler's lemma [43]). *Let,* $x \in \mathbb{R}^n, \mathscr{Q} = \mathscr{Q}^T \in \mathbb{R}^{n\times n}$*, and* $\mathscr{B} \in \mathbb{R}^{n\times n}$ *such that* $\mathrm{rank}(B) < n$*. The following statements are equivalent:*

(i) $x^T\mathscr{Q}x < 0$*, for all* $\mathscr{B}x = 0$*,* $x \neq 0$

(ii) $\exists\mu \in \mathbb{R}$*:* $\mathscr{Q} - \mu\mathscr{B}^T\mathscr{B} < 0$

Remark 3. In this paper, we will use the LMI approach to cope with the control problem of the 1-DoF impact mechanical oscillator, which is described by a second-order dynamics. We will design a robust control law in order to stabilize the position of such mechanical systems with impulse effects. Actually, the presence of an impulsive effect can influence the behavior of the solutions and cause dangerous effects in some applications. More than that, the presence of impulsive effects can cause instability of the whole behavior of the impacting mechanical system. These systems are defined by an impulsive hybrid dynamics for which the system undergoes a very instantaneous transition when reaching some state-dependent conditions, as in our case for the two-sided impact mechanical oscillator. Then, in this

paper, we deal with an impulsive hybrid system, which is more complicated than a simple nonlinear system.

In addition, we stress that we deal with homogeneous models (3a) and (3b) allowing the interaction between discrete and continuous parts and the stabilization process was realized for whole models (8a) and (8b). Only the continuous part/model (3a) was found to be under control, whereas the discrete model (3b) or (8b) is without control and also is unstable (the two eigenvalues of the matrix $\mathscr{R}$ are 1 and $-r$). Hence, the main challenge of the present work is to stabilize robustly the whole impulsive hybrid dynamics using a single controller for the continuous part.

Furthermore, to design the stability conditions of the closed-loop systems (8a) and (8b), we will only consider the working region, inside which the state vector is defined and then the impact mechanical oscillator evolved. Actually, we have two working regions: one for the continuous part and another for the discrete part. For the continuous model, the working region is that between the two asymmetric rigid end-stops, that is, the set Ω defined by (4a). However, for the discrete model (8b), the working region is the two end-stops, which are defined by the impact condition and then set Γ defined by (4b). We will use the S-procedure lemma to deal with the working region Ω and the Finsler Lemma to consider the working region Γ for the design of the stability conditions.

4. Synthesis of the Robust State-Feedback Control Law: BMI Conditions

In order to synthesize stability conditions of the disturbed impulsive hybrid systems (8a) and (8b), we adopt the following Lyapunov function:

$$\mathscr{V}(\mathbf{z}) = \mathbf{z}^T \mathscr{P} \mathbf{z}, \tag{15}$$

where $\mathscr{P} = \mathscr{P}^T$.

Thus, the asymptotic stability conditions of systems (8a) and (8b) are given by

$$\mathscr{V}(\mathbf{z}) > 0 \quad \text{s.t. } \mathbf{z} \in \Omega,\ \mathbf{z} \in \Delta, \tag{16a}$$

$$\dot{\mathscr{V}}(\mathbf{z}) < 0, \quad \text{s.t. } \mathbf{z} \in \Omega,\ \mathbf{z} \in \Delta, \tag{16b}$$

$$\mathscr{V}(\mathbf{z}^+) - \mathscr{V}(\mathbf{z}^-) < 0, \quad \text{s.t. } \mathbf{z} \in \Gamma,\ \mathbf{z} \in \Delta. \tag{16c}$$

Theorem 1. *The closed-loop impulsive hybrid systems (8a) and (8b) subject to the external disturbance v, with $\|v\| \le p$, is asymptotically and robustly stable if for some fixed parameter $0 < \varepsilon \ll 1$, there exist a symmetric matrix $\mathscr{P}$, a matrix $\mathscr{K}$, positive scalars $\alpha_1, \alpha_2, \alpha_3, \alpha_4, \beta_1, \beta_2, \beta_3, \beta_4$, and λ, and free two scalars ξ_1 and ξ_2 such that the following matrix inequalities are feasible:*

$$\begin{bmatrix} \mathscr{P} - \beta_3 \mathscr{C}\mathscr{C}^T & (\beta_1 - \beta_2)\mathscr{C} \\ (\star) & \epsilon\beta_3 - 2\beta_1 d + 2\beta_2 l \end{bmatrix} > 0, \tag{17a}$$

$$\begin{bmatrix} \mathscr{P}(\mathscr{A} + \mathscr{B}\mathscr{K}) + (\star) + \lambda \mathscr{P}\mathscr{B}\mathscr{B}^T\mathscr{P} + \alpha_3 \mathscr{C}\mathscr{C}^T & -(\alpha_1 - \alpha_2)\mathscr{C} \\ (\star) & \dfrac{p^2}{\lambda} - \varepsilon\alpha_3 + 2\alpha_1 d - 2\alpha_2 l \end{bmatrix} < 0, \tag{17b}$$

$$\begin{bmatrix} \mathscr{R}\mathscr{P}\mathscr{R} - \mathscr{P} - \xi_1 \mathscr{C}\mathscr{C}^T + \alpha_4 \mathscr{C}\mathscr{C}^T & \xi_1 d\mathscr{C} \\ (\star) & -\alpha_4\varepsilon - \xi_1 d^2 \end{bmatrix} < 0, \tag{17c}$$

$$\begin{bmatrix} \mathscr{R}\mathscr{P}\mathscr{R} - \mathscr{P} - \xi_2 \mathscr{C}\mathscr{C}^T + \beta_4 \mathscr{C}\mathscr{C}^T & \xi_2 l\mathscr{C} \\ (\star) & -\beta_4\varepsilon - \xi_2 l^2 \end{bmatrix} < 0. \tag{17d}$$

Proof. The constraints $\mathbf{z} \in \Omega$, $\mathbf{z} \in \Delta$, and $\mathbf{z} \in \Gamma$ can be rewritten as follows:

$$\mathscr{W}_1(\mathbf{z}) = \begin{bmatrix} \mathbf{z} \\ 1 \end{bmatrix}^T \begin{bmatrix} \mathscr{O} & \mathscr{C} \\ (\star) & -2d \end{bmatrix} \begin{bmatrix} \mathbf{z} \\ 1 \end{bmatrix} < 0, \tag{18a}$$

$$\mathscr{W}_2(\mathbf{z}) = \begin{bmatrix} \mathbf{z} \\ 1 \end{bmatrix}^T \begin{bmatrix} \mathscr{O} & -\mathscr{C} \\ (\star) & 2l \end{bmatrix} \begin{bmatrix} \mathbf{z} \\ 1 \end{bmatrix} < 0, \tag{18b}$$

$$\mathscr{W}_3(\mathbf{z}) = \begin{bmatrix} \mathbf{z} \\ 1 \end{bmatrix}^T \begin{bmatrix} -\mathscr{C}\mathscr{C}^T & \mathscr{O} \\ (\star) & \varepsilon \end{bmatrix} \begin{bmatrix} \mathbf{z} \\ 1 \end{bmatrix} < 0, \tag{18c}$$

$$\mathscr{W}_4(\mathbf{z}) = \begin{bmatrix} \mathscr{C}^T & -d \end{bmatrix} \begin{bmatrix} \mathbf{z} \\ 1 \end{bmatrix} = 0, \tag{18d}$$

$$\mathscr{W}_5(\mathbf{z}) = \begin{bmatrix} \mathscr{C}^T & -l \end{bmatrix} \begin{bmatrix} \mathbf{z} \\ 1 \end{bmatrix} = 0. \tag{18e}$$

The derivative of the Lyapunov function (15) is given as follows:

$$\dot{\mathscr{V}}(\mathbf{z}) = 2\mathbf{z}^T \mathscr{P}(\mathscr{A} + \mathscr{B}\mathscr{K})\mathbf{z} + 2\mathbf{z}^T \mathscr{P}\mathscr{B}v. \tag{19}$$

Relying on the Young relation (Lemma 1) and as $|v| \le p$, we obtain the following condition:

$$2\mathbf{z}^T\mathcal{P}\mathcal{B}v \le \lambda\mathbf{z}^T\mathcal{P}\mathcal{B}\mathcal{B}^T\mathcal{P}\mathbf{z} + \frac{p^2}{\lambda}, \tag{20}$$

with $\lambda > 0$.

By substituting expression (20) in relation (19), then the stability condition becomes

$$\mathcal{U}(\mathbf{z}) = \begin{bmatrix} \mathbf{z} \\ 1 \end{bmatrix}^T \begin{bmatrix} \mathcal{P}(\mathcal{A} + \mathcal{B}\mathcal{K}) + (\star) + \lambda\mathcal{P}\mathcal{B}\mathcal{B}^T\mathcal{P} & \mathcal{O} \\ (\star) & \frac{p^2}{\lambda} \end{bmatrix} \begin{bmatrix} \mathbf{z} \\ 1 \end{bmatrix} < 0. \tag{21}$$

In addition, using the algebraic equation in (8b), then the stability condition in (16c) becomes

$$\mathcal{W}(\mathbf{z}) = \mathbf{z}^T(\mathcal{R}\mathcal{P}\mathcal{R} - \mathcal{P})\mathbf{z} < 0. \tag{22}$$

Accordingly, based on the previous expressions, the stability conditions in (16a)–(16c) are reformulated as follows:

$$\mathcal{V}(\mathbf{z}) > 0, \quad \text{s.t. } \mathcal{W}_1(\mathbf{z}) < 0,\ \mathcal{W}_2(\mathbf{z}) < 0,\ \mathcal{W}_3(\mathbf{z}) < 0, \tag{23a}$$

$$\mathcal{U}(\mathbf{z}) < 0, \quad \text{s.t. } \mathcal{W}_1(\mathbf{z}) < 0,\ \mathcal{W}_2(\mathbf{z}) < 0,\ \mathcal{W}_3(\mathbf{z}) < 0, \tag{23b}$$

$$\mathcal{W}(\mathbf{z}) < 0, \quad \text{s.t. } \mathcal{W}_4(\mathbf{z}) = 0 \text{ or } \mathcal{W}_5(\mathbf{z}) = 0,\ \mathcal{W}_3(\mathbf{z}) < 0. \tag{23c}$$

Relying on the S-procedure lemma (see Lemma 4) and based on the Finsler lemma (see Lemma 5), the conditions in (23a)–(23c) are equivalent, respectively, to the matrix inequalities in (17a)–(17d), for some positive scalars α_i and β_i, $i = 1, 2, 3, 4$, and $\xi_1, \xi_2 \in \mathbb{R}$. This completes the proof of Theorem 1. □

Remark 4. It is worth to note that if we choose $\varepsilon = 0$ in expression of controller (5), then we will have $\mathbf{z} \in \mathbb{R}^n$. As a result, the (2,2) element in BMI (17a) (resp. BMI (17b)) becomes $-2\beta_1 d + 2\beta_2 l$ (resp. $(p^2/\lambda) + 2\alpha_1 d - 2\alpha_2 l$). As $d > 0$ and $l < 0$, then it follows that $-2\beta_1 d + 2\beta_2 l < 0$ and $(p^2/\lambda) + 2\alpha_1 d - 2\alpha_2 l > 0$. Hence, the two BMIs (17a) and (17b) are unfeasible. Therefore, to solve such a feasibility problem, we add the constraint $\mathbf{z}^T\mathcal{C}\mathcal{C}^T\mathbf{z} > \varepsilon$ on the state-feedback controller and with ε as a small enough positive parameter.

5. Synthesis of the Robust State-Feedback Control Law: LMI Conditions

It is worth mentioning that the four inequality conditions in (17a)–(17d) in Theorem 1 are BMIs. Thus, to solve the stability problem of the closed-loop impulsive system by finding the feedback matrix gain $\mathcal{K}$ of the state-feedback control law (5) and the corresponding Lyapunov matrix $\mathcal{P}$, we should transform these BMIs into LMIs.

Theorem 2. *The impulsive hybrid systems (3a) and (3b) subject to the external disturbance $v(t)$, with $\|v(t)\| \le p$, is robustly and asymptotically stabilizable by the state-feedback control law (5) if, for a scalar $0 < \varepsilon \ll 1$ fixed a priori, there exist a symmetric matrix $\mathbf{S}$, a matrix $\widehat{\mathcal{K}}$, and positive scalars μ_1, μ_2, μ_3, μ_4, η_1, η_2, η_3, η_4, $\widehat{\xi}_1$, $\widehat{\xi}_2$, λ, and $\widehat{p}$ such that the following LMI-based optimization problem is feasible:*

maximize $\widehat{p}$

minimize μ_3

s.t.

$$\begin{bmatrix} \mathcal{S} & \mathcal{S}\mathcal{C} & \frac{1}{2d}\mathcal{C} & -\frac{1}{2l}\mathcal{S}\mathcal{C} & \mathcal{O} \\ (\star) & \epsilon\eta_3 & \mathcal{O} & \mathcal{O} & \mathcal{O} \\ (\star) & (\star) & \frac{1}{2d}\eta_1 & \mathcal{O} & \eta_3 \\ (\star) & (\star) & (\star) & -\frac{1}{2l}\eta_2 & \eta_3 \\ (\star) & (\star) & (\star) & (\star) & \eta_3 \end{bmatrix} > 0, \tag{24a}$$

$$\begin{bmatrix} -(\mathcal{A}\mathcal{S} + \mathcal{B}\widehat{\mathcal{K}}) + (\star) - \lambda\mathcal{B}\mathcal{B}^T & \mathcal{S}\mathcal{C} & \frac{1}{2d}\mathcal{S}\mathcal{C} & -\frac{1}{2l}\mathcal{S}\mathcal{C} & \mathcal{O} & \mathcal{O} \\ (\star) & \varepsilon\mu_3 & \mathcal{O} & \mathcal{O} & \mathcal{O} & \mathcal{O} \\ (\star) & (\star) & \frac{1}{2d}\mu_1 & \mathcal{O} & \mathcal{O} & \mu_3 \\ (\star) & (\star) & (\star) & -\frac{1}{2l}\mu_2 & \mathcal{O} & \mu_3 \\ (\star) & (\star) & (\star) & (\star) & \lambda & \widehat{p} \\ (\star) & (\star) & (\star) & (\star) & (\star) & \mu_3 \end{bmatrix} > 0, \tag{24b}$$

$$\begin{bmatrix} \mathcal{S} + \mathcal{S}\mathcal{C}\mathcal{C}^T + (\star) - \left(\widehat{\xi}_1 + \frac{d^2}{\epsilon}\mu_4\right)\mathcal{C}\mathcal{C}^T & \mathcal{S}\mathcal{C} & \mathcal{S}\mathcal{R} \\ (\star) & \mu_4 & \mathcal{O} \\ (\star) & (\star) & \mathcal{S} \end{bmatrix} > 0, \tag{24c}$$

$$\begin{bmatrix} \mathcal{S} + \mathcal{S}\mathcal{C}\mathcal{C}^T + (\star) - \left(\widehat{\xi}_2 + \frac{l^2}{\varepsilon}\eta_4\right)\mathcal{C}\mathcal{C}^T & \mathcal{S}\mathcal{C} & \mathcal{S}\mathcal{R} \\ (\star) & \eta_4 & \mathcal{O} \\ (\star) & (\star) & \mathcal{S} \end{bmatrix} > 0. \tag{24d}$$

Hence, the state-feedback gain is given by

$$\mathcal{K} = \widehat{\mathcal{K}}\mathcal{S}^{-1}, \tag{25}$$

and the maximum bound of the disturbance is defined as follows:

$$p = \frac{\widehat{p}}{\mu_3}. \tag{26}$$

Proof. We begin first by linearizing BMI (17a). Let us pose $\mathcal{S} = \mathcal{P}^{-1}$. We pre- and postmultiplying (17a) by the matrix $\mathrm{diag}(\mathcal{S}, 1)$. Thus, we obtain the following condition:

$$\begin{bmatrix} \mathcal{S} - \beta_3 \mathcal{S}\mathcal{C}\mathcal{C}^T\mathcal{S} & (\beta_1 - \beta_2)\mathcal{S}\mathcal{C} \\ (\star) & \varepsilon\beta_3 - 2\beta_1 d + 2\beta_2 l \end{bmatrix} > 0. \tag{27}$$

For simplicity, posing $\mathcal{N}_1 = \begin{bmatrix} \eta_1 & 0 \\ (\star) & \eta_2 \end{bmatrix}$ with $\eta_1 = \beta_1^{-1}$, $\eta_2 = \beta_2^{-1}$, $\mathcal{Q}^{-1} = \begin{bmatrix} 2d & 0 \\ 0 & -2l \end{bmatrix}$, $\mathcal{G} = \begin{bmatrix} \mathcal{S}\mathcal{C} & -\mathcal{S}\mathcal{C} \end{bmatrix}$, $\mathcal{L} = \begin{bmatrix} 1 \\ 1 \end{bmatrix}$, and $\eta_3^{-1} = \varepsilon\beta_3$. Then, it is easy to show that $\varepsilon\beta_3 - 2\beta_1 d + 2\beta_2 l = \eta_3^{-1} - \mathcal{L}^T(\mathcal{Q}\mathcal{N}_1)^{-1}\mathcal{L}$ and $(\beta_1 - \beta_2)\mathcal{S}\mathcal{C} = \mathcal{G}\mathcal{N}_1^{-1}\mathcal{L}$. Hence, the matrix inequality (27) becomes

$$\begin{bmatrix} \mathcal{S} - (\varepsilon\eta_3)^{-1}\mathcal{S}\mathcal{C}\mathcal{C}^T\mathcal{S} & \mathcal{G}\mathcal{N}_1^{-1}\mathcal{L} \\ (\star) & \eta_3^{-1} - \mathcal{L}^T(\mathcal{Q}\mathcal{N}_1)^{-1}\mathcal{L} \end{bmatrix} > 0. \tag{28}$$

Based on the Schur complement lemma (see Lemma 3), matrix (28) is equivalent to

$$\mathcal{S} - (\varepsilon\eta_3)^{-1}\mathcal{S}\mathcal{C}\mathcal{C}^T\mathcal{S} - \mathcal{G}\mathcal{N}_1^{-1}\mathcal{L}\left(\eta_3^{-1} - \mathcal{L}^T(\mathcal{Q}\mathcal{N}_1)^{-1}\mathcal{L}\right)^{-1} \cdot \mathcal{L}^T\mathcal{N}_1^{-1}\mathcal{G}^T > 0, \tag{29a}$$

$$\eta_3^{-1} - \mathcal{L}^T(\mathcal{Q}\mathcal{N}_1)^{-1}\mathcal{L} > 0. \tag{29b}$$

The matrix inversion lemma (see Lemma 2) states that

$$\left(\eta_3^{-1} - \mathcal{L}^T(\mathcal{Q}\mathcal{N}_1)^{-1}\mathcal{L}\right)^{-1} = \eta_3 - \eta_3^2\mathcal{L}^T\mathcal{H}^{-1}\mathcal{L}, \tag{30}$$

with $\mathcal{H} = \eta_3\mathcal{L}\mathcal{L}^T - \mathcal{Q}\mathcal{N}_1$. If we consider in the next that $\mathcal{H} < 0$, then since $\eta_3 > 0$, we obtain $\eta_3 - \eta_3^2\mathcal{L}^T\mathcal{H}^{-1}\mathcal{L} > 0$. Therefore, condition (29b) is always satisfied. We will only consider in the sequel condition (29a).

Substituting expression (30) in (29a) yields

$$\mathcal{S} - (\varepsilon\eta_3)^{-1}\mathcal{S}\mathcal{C}\mathcal{C}^T\mathcal{S} - \eta_3\mathcal{G}\mathcal{N}_1^{-1}\mathcal{L}\mathcal{L}^T\mathcal{N}_1^{-1}\mathcal{G}^T + \eta_3^2\mathcal{G}\mathcal{N}_1^{-1}\mathcal{L}\mathcal{L}^T\mathcal{H}^{-1}\mathcal{L}\mathcal{L}^T\mathcal{N}_1^{-1}\mathcal{G}^T > 0. \tag{31}$$

Relying on expression of the matrix $\mathcal{H}$, it is straightforward to demonstrate that

$$\eta_3\mathcal{G}\mathcal{N}_1^{-1}\mathcal{L}\mathcal{L}^T = \mathcal{G}\mathcal{N}_1^{-1}(\mathcal{H} + \mathcal{Q}\mathcal{N}_1). \tag{32}$$

Thus, based on this relation (32) and as the matrices $\mathcal{Q}$ and $\mathcal{N}_1$ are diagonal and $\mathcal{H}$ is symmetric, we obtain the following expressions:

$$\eta_3\mathcal{G}\mathcal{N}_1^{-1}\mathcal{L}\mathcal{L}^T\mathcal{N}_1^{-1}\mathcal{G}^T = \mathcal{G}\mathcal{N}_1^{-1}\mathcal{H}\mathcal{N}_1^{-1}\mathcal{G}^T + \mathcal{G}\mathcal{Q}\mathcal{N}_1^{-1}\mathcal{G}^T, \tag{33a}$$

$$\eta_3^2\mathcal{G}\mathcal{N}_1^{-1}\mathcal{L}\mathcal{L}^T\mathcal{H}^{-1}\mathcal{L}\mathcal{L}^T\mathcal{N}_1^{-1}\mathcal{G}^T = \mathcal{G}\mathcal{N}_1^{-1}\mathcal{H}\mathcal{N}_1^{-1}\mathcal{G}^T + 2\mathcal{G}\mathcal{N}_1^{-1}\mathcal{Q}\mathcal{G}^T + \mathcal{G}\mathcal{Q}\mathcal{H}^{-1}\mathcal{Q}\mathcal{G}^T. \tag{33b}$$

By substituting the two expressions (33a) and (33b) in inequality (31), we obtain

$$\mathcal{S} - (\varepsilon\eta_3)^{-1}\mathcal{S}\mathcal{C}\mathcal{C}^T\mathcal{S} + \mathcal{G}\mathcal{N}_1^{-1}\mathcal{Q}\mathcal{G}^T + \mathcal{G}\mathcal{Q}\mathcal{H}^{-1}\mathcal{Q}\mathcal{G}^T > 0. \tag{34}$$

Moreover, as $\mathcal{N}_1^{-1}\mathcal{Q} > 0$, then condition (34) is satisfied if

$$\mathcal{S} - (\varepsilon\eta_3)^{-1}\mathcal{S}\mathcal{C}\mathcal{C}^T\mathcal{S} + \mathcal{G}\mathcal{Q}\mathcal{H}^{-1}\mathcal{Q}\mathcal{G}^T > 0. \tag{35}$$

As $\varepsilon\eta_3 > 0$ and $\mathcal{H} < 0$, then the Schur complement lemma states that the matrix inequality (35) is equivalent to

$$\begin{bmatrix} \mathcal{S} & \mathcal{S}\mathcal{C} & \mathcal{G}\mathcal{Q} \\ (\star) & \varepsilon\eta_3 & \mathcal{O} \\ (\star) & (\star) & \mathcal{N}_1\mathcal{Q} - \eta_3\mathcal{L}\mathcal{L}^T \end{bmatrix} > 0. \tag{36}$$

By applying the Schur complement on elements (33a) and (33b) in (36), we obtain the following matrix inequality:

$$\begin{bmatrix} \mathcal{S} & \mathcal{S}\mathcal{C} & \mathcal{G}\mathcal{Q} & \mathcal{O} \\ (\star) & \varepsilon\eta_3 & \mathcal{O} & \mathcal{O} \\ (\star) & (\star) & \mathcal{N}_1\mathcal{Q} & \eta_3\mathcal{L} \\ (\star) & (\star) & (\star) & \eta_3 \end{bmatrix} > 0. \tag{37}$$

Accordingly, by replacing the different matrices in (37) by their expression, we found the first LMI (24a).

We focus now on BMI (17b). Pre- and postmultiplying the matrix inequality (17b) by the matrix $\mathrm{diag}(\mathcal{S}, 1)$ gives the following condition:

$$\begin{bmatrix} (\mathcal{A}\mathcal{S} + \mathcal{B}\widehat{\mathcal{K}}) + (\star) + \lambda\mathcal{B}\mathcal{B}^T + \alpha_3\mathcal{S}\mathcal{C}\mathcal{C}^T\mathcal{S} & -(\alpha_1 - \alpha_2)\mathcal{S}\mathcal{C} \\ (\star) & -\varepsilon\alpha_3 + \dfrac{p^2}{\lambda} + 2\alpha_1 d - 2\alpha_2 l \end{bmatrix} < 0, \tag{38}$$

where $\widehat{\mathscr{K}} = \mathscr{K}\mathscr{S}$.

For simplicity, posing $\mathscr{G} = [\ \mathscr{S}\mathscr{C}\ \ -\mathscr{S}\mathscr{C}\ \ \mathscr{O}\ ]$, $\mathscr{L} = \begin{bmatrix} 1 \\ 1 \\ 1 \end{bmatrix}$, $\mathscr{Q}^{-1} = \begin{bmatrix} 2d & 0 & 0 \\ 0 & -2l & 0 \\ 0 & 0 & p^2 \end{bmatrix}$, and $\mathscr{N}_2 = \begin{bmatrix} \mu_1 & 0 & 0 \\ 0 & \mu_2 & \\ 0 & 0 & \lambda \end{bmatrix}$ with $\mu_1 = \alpha_1^{-1}$, $\mu_2 = \alpha_2^{-1}$, and $\mu_3^{-1} = \varepsilon\alpha_3$, it is easy to show that $-\varepsilon\alpha_3 + (p^2/\lambda) + 2\alpha_1 d - 2\alpha_2 l = -(\mu_3^{-1} - \mathscr{L}^T(\mathscr{Q}\mathscr{N}_2)^{-1}\mathscr{L})$ and $(\alpha_1 - \alpha_2)\mathscr{S}\mathscr{C} = \mathscr{G}\mathscr{N}_2^{-1}\mathscr{L}$. It is worth to note that $\mathscr{Q} > 0$ and $\mathscr{N}_2 > 0$.

Then, by multiplying the matrix inequality (37) by (-1), we obtain the following result:

$$\begin{bmatrix} -\left((\mathscr{A}\mathscr{S} + \mathscr{B}\widehat{\mathscr{K}}) + (\star) + \lambda\mathscr{B}\mathscr{B}^T\right) - (\varepsilon\mu_3)^{-1}\mathscr{S}\mathscr{C}\mathscr{C}^T\mathscr{S} & \mathscr{G}\mathscr{N}_2^{-1}\mathscr{L} \\ (\star) & \mu_3^{-1} - \mathscr{L}^T(\mathscr{Q}\mathscr{N}_2)^{-1}\mathscr{L} \end{bmatrix} > 0. \tag{39}$$

By following the same linearization methodology adopted previously, we obtain the following simplified equivalent conditions:

$$-(\mathscr{A}\mathscr{S} + \mathscr{B}\widehat{\mathscr{K}}) + (\star) - \lambda\mathscr{B}\mathscr{B}^T - (\varepsilon\mu_3)^{-1}\mathscr{S}\mathscr{C}\mathscr{C}^T\mathscr{S} + \mathscr{G}\mathscr{Q}\mathscr{K}^{-1}\mathscr{Q}\mathscr{G}^T > 0, \tag{40a}$$

$$\mathscr{K} = \mu_3\mathscr{L}\mathscr{L}^T - \mathscr{Q}\mathscr{N}_2 < 0. \tag{40b}$$

Since $\mathscr{K} < 0$ and $(\varepsilon\mu_3) > 0$, the Schur complement states that the matrix inequality (40a) is equivalent to

$$\begin{bmatrix} -(\mathscr{A}\mathscr{S} + \mathscr{B}\widehat{\mathscr{K}}) + (\star) - \lambda\mathscr{B}\mathscr{B}^T & \mathscr{S}\mathscr{C} & \mathscr{G}\mathscr{Q} & \mathscr{O} \\ (\star) & \varepsilon\mu_3 & \mathscr{O} & \mathscr{O} \\ (\star) & (\star) & \mathscr{N}_2\mathscr{Q} & \mu_3\mathscr{L} \\ (\star) & (\star) & (\star) & \mu_3 \end{bmatrix} > 0. \tag{41}$$

By multiplying the matrix inequality (41) from left and right by the matrix diag$(\mathscr{I}, 1, 1, 1, p, 1)$ and by making a new variable change $\widehat{p} = \mu_3 p$, we obtain then LMI (24b).

We focus now in the linearization of BMIs (17c) and (17d). It is clear that these two BMIs are similar. Thus, the linearization of BMI (17d) will be identical to that for BMI (17c). Then, we will only linearize the first BMI (17c).

The Schur complement states that the matrix inequality (17c) is equivalent to

$$\mathscr{R}\mathscr{P}\mathscr{R} - \mathscr{P} - \xi_1\mathscr{C}\mathscr{C}^T + \alpha_4\mathscr{C}\mathscr{C}^T + \xi_1^2 d^2\left(\alpha_4\varepsilon + \xi_1 d^2\right)^{-1}\mathscr{C}\mathscr{C}^T < 0, \tag{42a}$$

$$\alpha_4\varepsilon + \xi_1 d^2 > 0. \tag{42b}$$

The matrix inversion lemma states that

$$\left(\alpha_4\varepsilon + \xi_1 d^2\right)^{-1} = \left(\xi_1 d^2\right)^{-1} - \left(\xi_1 d^2\right)^{-2}\left(\left(\xi_1 d^2\right)^{-1} + (\alpha_4\varepsilon)^{-1}\right)^{-1}. \tag{43}$$

By considering this relation (43) in (42a), this inequality (42a) is simplified as follows:

$$\mathscr{R}\mathscr{P}\mathscr{R} - \mathscr{P} + \alpha_4\mathscr{C}\mathscr{C}^T - \left(\xi_1^{-1} + \frac{d^2}{\alpha_4\varepsilon}\right)^{-1}\mathscr{C}\mathscr{C}^T < 0. \tag{44}$$

We pre- and postmultiply inequality (44) from left and right by $\mathscr{S}$, we obtain

$$\mathscr{S}\mathscr{R}\mathscr{S}^{-1}\mathscr{R}\mathscr{S} - \mathscr{S} + \alpha_4\mathscr{S}\mathscr{C}\mathscr{C}^T\mathscr{S} - \left(\xi_1^{-1} + \frac{d^2}{\alpha_4\varepsilon}\right)^{-1}\mathscr{S}\mathscr{C}\mathscr{C}^T\mathscr{S} < 0. \tag{45}$$

Let $\xi_1 > 0$, $\alpha_4 > 0$, and $\varepsilon > 0$, then condition (42b) is always satisfied, and hence we have $\xi_1^{-1} + (d^2/\alpha_4\varepsilon) > 0$. Then, it is straightforward to demonstrate by means of the Young relation that

$$-\left(\xi_1^{-1} + \frac{d^2}{\alpha_4\varepsilon}\right)^{-1}\mathscr{S}\mathscr{C}\mathscr{C}^T\mathscr{S} \le -\mathscr{S}\mathscr{C}\mathscr{C}^T + (\star) + \left(\xi_1^{-1} + \frac{d^2}{\alpha_4\varepsilon}\right)\mathscr{C}\mathscr{C}^T. \tag{46}$$

Therefore, condition (45) becomes

$$\mathscr{S}\mathscr{R}\mathscr{S}^{-1}\mathscr{R}\mathscr{S} - \mathscr{S} + \alpha_4\mathscr{S}\mathscr{C}\mathscr{C}^T\mathscr{S} - \mathscr{S}\mathscr{C}\mathscr{C}^T + (\star) + \left(\xi_1^{-1} + \frac{d^2}{\alpha_4\varepsilon}\right)\mathscr{C}\mathscr{C}^T < 0. \tag{47}$$

The Schur complement lemma states inequality (47) is equivalent to

$$\begin{bmatrix} -\mathscr{S} - \mathscr{S}\mathscr{C}\mathscr{C}^T + (\star) + \left(\xi_1^{-1} + \frac{d^2}{\alpha_4\varepsilon}\right)\mathscr{C}\mathscr{C}^T & \mathscr{S}\mathscr{C} & \mathscr{S}\mathscr{R} \\ (\star) & -\frac{1}{\alpha_4} & \mathscr{O} \\ (\star) & (\star) & -\mathscr{S} \end{bmatrix} < 0. \tag{48}$$

Posing $\mu_4 = \alpha_4^{-1}$ and $\widehat{\xi}_1 = \xi_1^{-1}$, then the matrix inequality (48) is converted into LMI (24c). Similarly, we will obtain LMI (24d) from BMI (17d). This ends the proof of Theorem 2. □

Table 1: Numerical results for different values of ε.

ε	p	$\mathscr{K}$
10	2.7829	$[-43.2211 \quad -13.4620]$
5	2.7826	$[-41.6121 \quad -12.5971]$
1	2.7834	$[-43.4863 \quad -13.6926]$
0.5	2.7828	$[-41.5044 \quad -12.5713]$
0.1	2.7832	$[-66.3664 \quad -12.3858]$
0.091	2.7826	$[-112.0141 \quad -10.5564]$
0.09	(!)	(!)

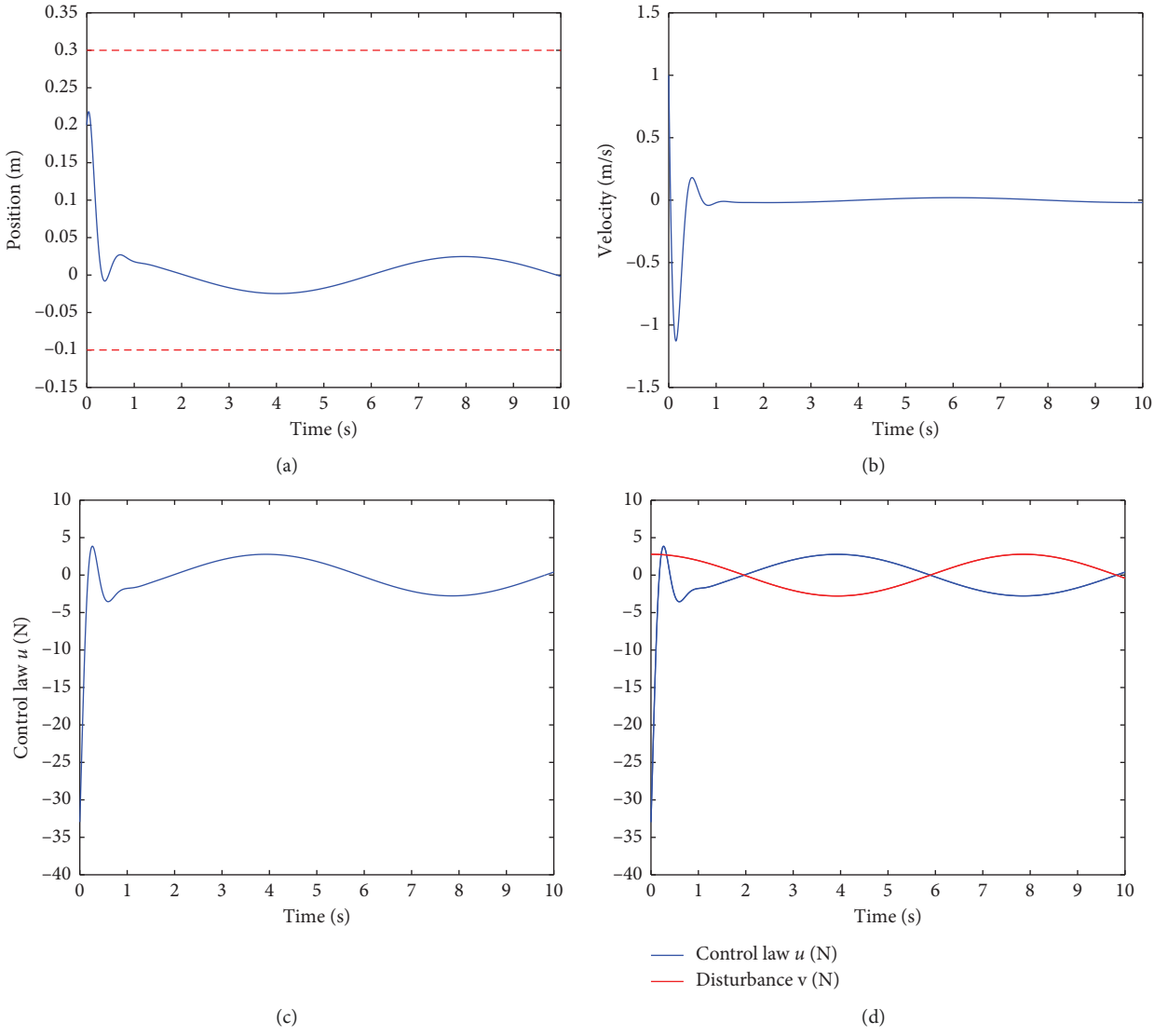

Figure 5: Simulation results of the two-sided asymmetric 1-DoF impact mechanical oscillator. Here, we fixed $d = 0.3$.

6. Simulation Results

In the following simulation section, the parameters of the double-sided 1-DoF impact mechanical oscillator are fixed as follows: $m = 1\,\text{kg}$, $k = 1\,\text{N/m}$, $c = 0\,N/(\text{m/s})$, $d = 0.3\,\text{m}$, $l = -0.1\,\text{m}$, $r = 0.8$, and $w = 0.8\,\text{rad}\cdot\text{s}^{-1}$. The numerical results of the optimization problem in Theorem 2 are given in Table 1 for different values of the parameter ε. In this table we provide the maximum bound p of the disturbance v and the corresponding controller gain $\mathscr{K}$. Notice that the symbol (!) in Table 1 means that optimization problem in Theorem 2 under LMIs (24a)–(24c) is unfeasible. Actually, it was found to be unfeasible for all $\varepsilon \leq 0.09$.

The first interesting and attractive observation that can be explored from Table 1 is that the size of the matrix gain $\mathscr{K}$ is very small. In addition, the second attractive result is that

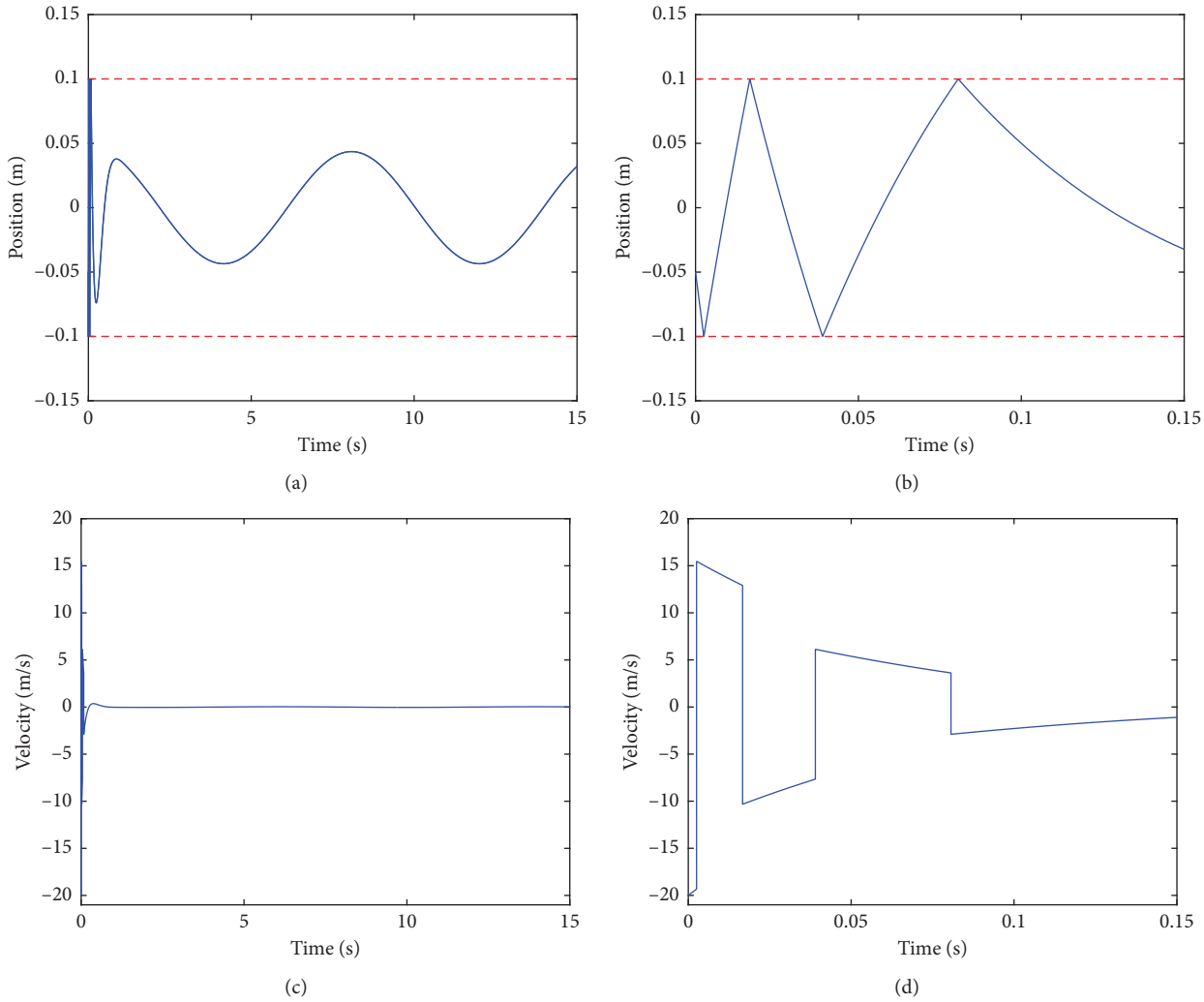

Figure 6: Simulation results of the two-sided asymmetric 1-DoF impact mechanical oscillator with $d = 0.1$.

for all fixed values of the parameter ε we obtained almost the same maximum bound p of the disturbance signal $v(t)$, say about 2.78.

Figure 5 show the simulation results for the impact oscillator using the values of p and $\mathscr{K}$ obtained in Table 1 for $\varepsilon = 0.091$. The initial condition adopted for the simulation is $[0.2 \;\; 1]^T$. Figure 5(a) reveals the temporal evolution of the position of the oscillator. Figure 5(b) shows it velocity. Figure 5(c) illustrates the applied controller u. In Figure 5(d), we transposed the control signal u and the disturbance v. It is obvious that the mass's position of the impact oscillator will converge progressively in time to the zero-equilibrium point, around which the oscillator oscillates with a sinusoidal signal of a small amplitude 0.0247. In addition, the velocity oscillates around the zero state between ± 0.0198. According to this behavior, the controller will oscillate with a sinusoidal form of amplitude 2.774. Following this result and from Figure 5(d), we stress that the controller u becomes opposite to the disturbance signal. Hence, this demonstrates that the controller u has rejected approximately the persistent disturbance v.

Notice that for the adopted initial condition, the oscillator does not experience impacts with the left and the right end-stops. In order to observe the impacts with the two end-stops, we modified the value of d to be $d = 0.1$ and we adopted another initial condition $[-0.05 \;\; -20]^T$. For this new value of the parameter d and for $\varepsilon = 0.091$, we obtained $p = 2.58$ and $\mathscr{K} = [-57.9597 \;\; -12.9790]$. The simulation results are given in Figures 6 and 7. In Figure 6(a), we plot the temporal evolution of the mass position of the impact oscillator. Figure 6(b) is an enlargement of Figure 6(a) for a simulation time between 0 and 0.15 s. Figures 6(c) and 6(d) show the variation of the velocity of the oscillator. Figure 7(a) reveals the temporal variation of the controller u. Figure 7(b) is a blow-up view of Figure 7(a). Figures 7(c) and 7(d) demonstrate the temporal evolution of the Lyapunov function $\mathscr{V}(\mathbf{z})$ defined by expression (15).

It is obvious from these simulation results that the mass of the oscillator experiences in the present case impacts with the two end-stops before its stabilization around the zero-equilibrium point. The amplitude of the position oscillation is almost 0.043, whereas that of the velocity is about 0.035. As

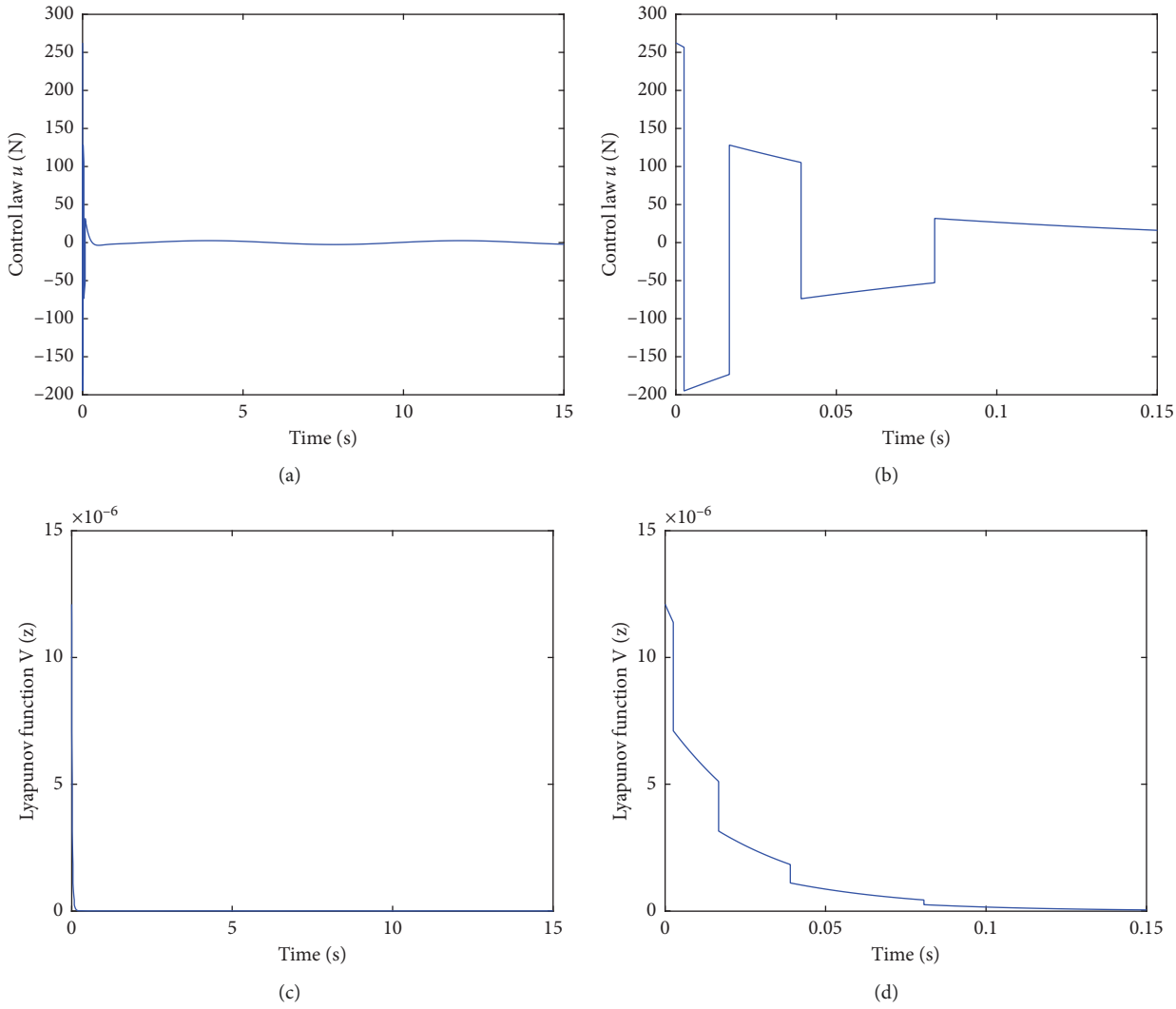

Figure 7: Simulation results for the case $d = 0.1$ showing the temporal variation of the controller u and the Lyapunov function $\mathscr{V}(\mathbf{z})$.

seen in Figure 6(d), at the impact with an end-stop, the velocity of the impact mechanical oscillator undergoes an instantaneous transition according to the restitution rule $\dot{\mathbf{x}}^+ = -r\dot{\mathbf{x}}^-$. When an impact occurs, the Lyapunov function decreases instantaneously, as shown in Figure 7(c). This behavior reveals that the energy of the mechanical oscillator decreases at the impact events.

Remark 5. In the previous simulations, we considered a chaotic motion of the 1-DoF impact mechanical oscillator to be controlled. We can choose a regular motion of the uncontrolled mechanical system, and we will obtain the same results, that is, the robust control of the impact oscillator to the zero-equilibrium point despite the presence of the impacts with the two end-stops and also despite the presence of the external persistent disturbing torque. The choice of a chaotic behavior to be controlled can be explained by the fact that a chaotic motion is very sensitive to initial conditions and then its control is more "difficult" than a regular motion.

7. Conclusion and Future Works

In this paper, a robust control of the position of a two-sided 1-DoF impact mechanical oscillator under an unknown external disturbing torque by means of a state-feedback controller is proposed. Thus, the control problem of such an impact oscillator was formulated as a stabilization problem of an impulsive hybrid dynamics subject to state constraints. Our approach for the design of the stability conditions was based mainly on the use of the S-procedure lemma and also the Finsler lemma to transform the stability conditions under constraints into BMI conditions. We used the Schur complement lemma and the matrix inversion lemma to convert these BMIs into LMIs allowing the computation of the feedback gain and also the maximum bound of the disturbance. The simulation results show that the impact mechanical oscillator is robustly stabilized around the zero-equilibrium point.

Our future direction is to consider uncertainties in all the parameters of the impact oscillator. Thus, our objective is to design a robust controller for the impulsive hybrid dynamics

under parametric uncertainties and disturbances. In addition, in this paper, we assumed that the position and the velocity of the oscillator are available for measurement. When this is not the case, we will consider the design of a static output feedback controller or an observer-based feedback controller to solve this problem. Another future work is to consider the problem of the impacting trajectory tracking, which is more difficult than that solved in the present paper.

Data Availability

The data used to support the findings of this study are available from the corresponding author upon request.

Conflicts of Interest

The authors declare that there are no conflicts of interest regarding the publication of this paper.

References

[1] R. A. Ibrahim, "Vibro-impact dynamics: modeling, mapping and applications," *Lecture Notes in Applied and Computational Mechanics*, Vol. 43, Springer-Verlag Berlin Heidelberg, Berlin, Germany, 1st Edition, 2009.

[2] Q. Tian, P. Flores, and H. M. Lankarani, "A comprehensive survey of the analytical, numerical and experimental methodologies for dynamics of multibody mechanical systems with clearance or imperfect joints," *Mechanism and Machine Theory*, vol. 122, pp. 1–57, 2018.

[3] P. Perlikowski, K.-C. Woo, S. Lenci, and T. Kapitaniak, "Special issue: dynamics of systems with impacts," *Journal of Computational and Nonlinear Dynamics*, vol. 16, no. 6, Article ID 060301, 2017.

[4] M. di Bernardo, C. Budd, A. R. Champneys, and P. Kowalczyk, "Piecewise-smooth dynamical systems: theory and applications," in *Applied Mathematical Sciences*, Vol. 163, Springer Science & Business Media, New Work, NY, USA, 2008.

[5] D. J. Wagg and S. R. Bishop, "Chatter, sticking and chaotic impacting motion in a two-degree of freedom impact oscillator," *International Journal of Bifurcation and Chaos*, vol. 11, no. 1, pp. 57–71, 2001.

[6] L. S. Yousuf and D. B. Marghitu, "Experimental and simulation results of a cam and flat-faced follower mechanism," *Journal of Computational and Nonlinear Dynamics*, vol. 12, no. 6, Article ID 061001, 2017.

[7] M. Kapitaniak, V. Vaziri, J. Paez Chavez, and M. Wiercigroch, "Numerical study of forward and backward whirling of drill-string," *Journal of Computational and Nonlinear Dynamics*, vol. 12, no. 6, Article ID 061009, 2017.

[8] U. Andreaus, P. Baragatti, M. De Angelis, and S. Perno, "A preliminary experimental study about two-sided impacting SDOF oscillator under harmonic excitation," *Journal of Computational and Nonlinear Dynamics*, vol. 12, no. 6, Article ID 061010, 2017.

[9] U. Andreaus, P. Baragatti, M. De Angelis, and S. Perno, "Shaking table tests and numerical investigation of two-sided damping constraint for end-stop impact protection," *Nonlinear Dynamics*, vol. 90, no. 4, pp. 2387–2421, 2017.

[10] L. Guofang, W. Ding, and S. Wu, "Global behavior of vibroimpact system with multiple non-smooth mechanical factors," *Journal of Computational and Nonlinear Dynamics*, vol. 12, no. 6, Article ID 061004, 2017.

[11] Y. Yan, Y. Liu, and M. Liao, "A comparative study of the vibro-impact capsule systems with one-sided and two-sided constraints," *Nonlinear Dynamics*, vol. 89, no. 2, pp. 1063–1087, 2017.

[12] U. Andreaus and M. De Angelis, "Nonlinear dynamic response of a base-excited SDOF oscillator with double-side unilateral constraints," *Nonlinear Dynamics*, vol. 84, no. 3, pp. 1447–1467, 2016.

[13] H. Gritli and S. Belghith, "Diversity in the nonlinear dynamic behavior of a one-degree-of-freedom impact mechanical oscillator under OGY-based state-feedback control law: order, chaos and exhibition of the border-collision bifurcation," *Mechanism and Machine Theory*, vol. 124, pp. 1–41, 2018.

[14] U. Andreaus and M. De Angelis, "Experimental and numerical dynamic response of a SDOF vibro-impact system with double gaps and bumpers under harmonic excitation," *International Journal of Dynamics and Control*, vol. 7, no. 4, pp. 1278–1292, 2019.

[15] U. Andreaus and P. Casini, "Friction oscillator excited by moving base and colliding with a rigid or deformable obstacle," *International Journal of Non-linear Mechanics*, vol. 37, no. 1, pp. 117–133, 2002.

[16] K. Witkowski, G. Kudra, G. Wasilewski, and J. Awrejcewicz, "Modelling and experimental validation of 1-degree-of-freedom impacting oscillator," *Proceedings of the Institution of Mechanical Engineers, Part I: Journal of Systems and Control Engineering*, vol. 233, no. 4, pp. 418–430, 2019.

[17] S. Skurativskyi, G. Kudra, G. Wasilewski, and J. Awrejcewicz, "Properties of impact events in the model of forced impacting oscillator: experimental and numerical investigations," *International Journal of Non-linear Mechanics*, vol. 113, pp. 55–61, 2019.

[18] F. Casas and C. Grebogi, "Control of chaotic impacts," *International Journal of Bifurcation and Chaos*, vol. 7, no. 4, pp. 951–955, 1997.

[19] S. R. Bishop, D. J. Wagg, and D. Xu, "Use of control to maintain period-1 motions during wind-up or wind-down operations of an impacting driven beam," *Chaos, Solitons & Fractals*, vol. 9, no. 1-2, pp. 261–269, 1998.

[20] S. L. T. de Souza and I. L. Caldas, "Controlling chaotic orbits in mechanical systems with impacts," *Chaos, Solitons & Fractals*, vol. 19, no. 1, pp. 171–178, 2004.

[21] H. Gritli, S. Belghith, and N. Khraief, "Chaos control of an impact mechanical oscillator based on the OGY method," in *Handbook of Research on Advanced Intelligent Control Engineering and Automation, Ch. 9*, A. T. Azar and S. Vaidyanathan, Eds., pp. 259–278, IGI Global, Hershey, PA, USA, 2015.

[22] C. J. Begley and L. N. Virgin, "On the ogy control of an impact-friction oscillator," *Journal of Vibration and Control*, vol. 7, no. 6, pp. 923–931, 2001.

[23] J. Awrejcewicz, K. Tomczak, and C.-H. Lamarque, "Controlling systems with impacts," *International Journal of Bifurcation and Chaos*, vol. 9, no. 3, pp. 547–553, 1999.

[24] G. W. Luo and X. H. Lv, "Controlling bifurcation and chaos of a plastic impact oscillator," *Nonlinear Analysis: Real World Applications*, vol. 10, no. 4, pp. 2047–2061, 2009.

[25] S. L. T. de Souza, I. L. Caldas, and R. L. Viana, "Damping control law for a chaotic impact oscillator," *Chaos, Solitons & Fractals*, vol. 32, no. 2, pp. 745–750, 2007.

[26] E. Gutiérrez and D. K. Arrowsmith, "Control of a double impacting mechanical oscillator using displacement

feedback," *International Journal of Bifurcation and Chaos*, vol. 14, no. 9, pp. 3095–3113, 2004.

[27] H. Xu, S. Yin, G. Wen, S. Zhang, and Z. Lv, "Discrete-in-time feedback control of near-grazing dynamics in the two-degree-of-freedom vibro-impact system with a clearance," *Nonlinear Dynamics*, vol. 87, no. 2, pp. 1127–1137, 2017.

[28] J.-Y. Lee and J.-J. Yan, "Position control of double-side impact oscillator," *Mechanical Systems and Signal Processing*, vol. 21, no. 2, pp. 1076–1083, 2007.

[29] H. Gritli and S. Belghith, "Master-slave controlled synchronization to control chaos in an impact mechanical oscillator," in *Proceedings of the 12th International Multi-Conference on Systems, Signals Devices (SSD)*, pp. 1–6, Mahdia, Tunisia, March 2015.

[30] F. Turki, H. Gritli, and S. Belghith, "A linear matrix inequality approach for the position control of a double-side impact mechanical oscillator via a state feedback law," in *Proceedings of the 2018 International Conference on Advanced Systems and Electric Technologies (IC_ASET)*, pp. 118–124, Hammamet, Tunisia, March 2018.

[31] H. Gritli, F. Turki, and S. Belghith, "State-feedback control via LMI approach of a 1-DoF disturbed impacting mechanical oscillator under double-side rigid constraints," in *Proceedings of the 2018 International Conference on Advanced Systems and Electric Technologies (IC_ASET)*, pp. 441–448, Hammamet, Tunisia, March 2018.

[32] F. Turki, H. Gritli, and S. Belghith, "Robust feedback control of a mechanical system under double-side constraints using LMIs and ellipsoidal sets," in *Proceedings of the 2018 IEEE 15th International Multi-Conference on Systems, Signals Devices (SSD15)*, pp. 1308–1314, Hammamet, Tunisia, March 2018.

[33] H. Gritli and S. Belghith, "Robust feedback control of the underactuated Inertia Wheel Inverted Pendulum under parametric uncertainties and subject to external disturbances: LMI formulation," *Journal of The Franklin Institute*, vol. 355, no. 18, pp. 9150–9191, 2018.

[34] H. Gritli, N. Khraief, A. Chemori, and S. Belghith, "Self-generated limit cycle tracking of the underactuated inertia wheel inverted pendulum under IDA-PBC," *Nonlinear Dynamics*, vol. 89, no. 3, pp. 2195–2226, 2017.

[35] S. L. T. de Souza and I. L. Caldas, "Calculation of Lyapunov exponents in systems with impacts," *Chaos, Solitons & Fractals*, vol. 19, no. 3, pp. 569–579, 2004.

[36] K. Czolczynski, A. Okolewski, and B. Blazejczyk-Okolewska, "Lyapunov exponents in discrete modelling of a cantilever beam impacting on a moving base," *International Journal of Non-linear Mechanics*, vol. 88, no. Supplement C, pp. 74–84, 2017.

[37] W. Serweta, A. Okolewski, B. Blazejczyk-Okolewska, K. Czolczynski, and T. Kapitaniak, "Lyapunov exponents of impact oscillators with Hertz's and Newton's contact models," *International Journal of Mechanical Sciences*, vol. 89, pp. 194–206, 2014.

[38] W. Serweta, A. Okolewski, B. Blazejczyk-Okolewska, K. Czolczynski, and T. Kapitaniak, "Mirror hysteresis and Lyapunov exponents of impact oscillator with symmetrical soft stops," *International Journal of Mechanical Sciences*, vol. 101-102, pp. 89–98, 2015.

[39] P. C. Müller, "Calculation of lyapunov exponents for dynamic systems with discontinuities," *Chaos, Solitons & Fractals*, vol. 5, no. 9, pp. 1671–1681, 1995.

[40] H. Gritli and S. Belghith, "Computation of the Lyapunov exponents in the compass-gait model under OGY control via a hybrid Poincaré map," *Chaos, Solitons & Fractals*, vol. 81, pp. 172–183, 2015.

[41] H. Gritli and S. Belghith, "Bifurcations and chaos in the semi-passive bipedal dynamic walking model under a modified OGY-based control approach," *Nonlinear Dynamics*, vol. 83, no. 4, pp. 1955–1973, 2016.

[42] S. Boyd, L. El-Ghaoui, E. Feron, and V. Balakrishnan, "Linear matrix inequalities in system and control theory," in *Studies in Applied and Numerical Mathematics*, vol. 15, SIAM, Philadelphia, PA, USA, 1st edition, 1994.

[43] P. Kohan-Sedgh, A. Khayatian, and M. H. Asemani, "Conservatism reduction in simultaneous output feedback stabilisation of linear systems," *IET Control Theory & Applications*, vol. 10, no. 17, pp. 2243–2250, 2016.

Hindawi
Complexity
Volume 2019, Article ID 1410278, 15 pages
https://doi.org/10.1155/2019/1410278

Research Article

Adaptive Neural Network Control of a Class of Fractional Order Uncertain Nonlinear MIMO Systems with Input Constraints

Changhui Wang, Mei Liang, and Yongsheng Chai

School of Electromechanical and Automotive Engineering, Yantai University, 32 Qingquan Road, Laishan District, Yantai, China

Correspondence should be addressed to Mei Liang; mmglm@163.com and Yongsheng Chai; chaiysh@163.com

Received 31 August 2019; Revised 23 October 2019; Accepted 14 November 2019; Published 28 November 2019

Guest Editor: John Cortés-Romero

An adaptive backstepping control scheme for a class of incommensurate fractional order uncertain nonlinear multiple-input multiple-output (MIMO) systems subjected to constraints is discussed in this paper, which ensures the convergence of tracking errors even with dead-zone and saturation nonlinearities in the controller input. Combined with backstepping and adaptive technique, the unknown nonlinear uncertainties are approximated by the radial basis function neural network (RBF NN) in each step of the backstepping procedure. Frequency distributed model of a fractional integrator and Lyapunov stability theory are used for ensuring asymptotic stability of the overall closed-loop system under input dead-zone and saturation. Moreover, the parameter update laws with incommensurate fractional order are used in the controller to compensate unknown nonlinearities. Two simulation results are presented at the end to ensure the efficacy of the proposed scheme.

1. Introduction

Due to the unique advantages in describing the hereditary and memory properties of multifarious materials and processes, fractional calculus as a research hotspot has recently attracted more and more attentions and interests in viscoelastic systems, control theory, engineering, and some interdisciplinary fields although it is considered as a branch of mathematics that has few applications for a long time [1–4]. As a powerful tool used to model many real-world behaviors, fractional order systems can provide more practical value and accurate results in many practical system applications [5–18], such as fractional oscillators, fractional damping, quenching phenomenon, and some biological systems. Sequentially, many researchers have paid close attention to the applications of fractional order differential equations in both engineering and theory and have drawn some wonderful and meaningful results in the literatures [19–24].

It is known that a precise physical model of the engineering plant is difficult to build because of the uncertainties and noises. Thus, most studies have concentrated on the controller design of the fractional order nonlinear system with uncertainties [25–28]. Due to the inherent approximation capability, neural networks (NNs) or fuzzy logic systems are usually used to approximate the system uncertainties in the integer order system. The scholars in [24] have designed an adaptive fuzzy control scheme for a class of fractional order systems with parametric uncertainty and input constraint. In [29], an adaptive backstepping controller is designed for a class of fractional order systems with unknown parameters based on the indirect Lyapunov method, in which the control problem of fractional order is converted to the integer order one. Using the fractional order extension of the Lyapunov direct method, an adaptive backstepping control method for a class of fractional order nonlinear systems with unknown nonlinearity is developed in [30]. In [31, 32], an output feedback control scheme for a class of triangular fractional order nonlinear systems is given. For a class of a fractional order rotational mechanical system with disturbances and uncertainties, a robust adaptive NN control is presented in [33]. Based on dual radial basis function (RBF) NNs, an adaptive fractional sliding mode controller is proposed to enhance the performance of the system in [34]. In [35], an adaptive NN

control scheme is given for a class of fractional order systems with nonlinearities and backlash-like hysteresis. For a class of uncertain fractional order nonlinear systems with external disturbance and input saturation, an adaptive NN backstepping control method based on the indirect Lyapunov method is designed in [36]. In [37], an adaptive fuzzy control scheme for a category of uncertain nonstrict-feedback systems with constraints is designed. The authors of [38] design an observer-based adaptive fuzzy controller for a class of single-input single-output nonlinear systems with unknown dynamics.

There are many fractional order nonlinear multiple-input multiple-output (MIMO) systems in practice, and it is important to develop control approaches for fractional order nonlinear MIMO systems. In comparison with plenty of research studies on fractional order SISO nonlinear systems, there are few research studies on the fractional order nonlinear MIMO systems due to existing uncertainties in the coupling matrices and unknown nonlinear functions in the nonlinear MIMO, where they are very challenging issues. For a class of incommensurate fractional order nonlinear MIMO systems with external disturbance, a fractional adaptive RBF NN backstepping control scheme is designed in [39], which is constructed using the backstepping technology. In [40], the consensus problem of fractional order MIMO systems with linear models is researched via the observer-based protocols. In [41], a discontinuous distributed controller is proposed for a class of fractional order MIMO systems. In [42], an adaptive output feedback controller is designed for a class of nonlinear fractional order MIMO systems with input nonlinearities. For a class of fractional order uncertain nonlinear MIMO dynamic systems with dead-zone input and external disturbances, a fractional adaptive type-2 fuzzy backstepping control scheme is presented in [43], which is constructed using the backstepping dynamic surface control and fractional adaptive type-2 fuzzy technique.

In many industrial processes, actuators usually possess the input saturation and dead-zone which are the most important nonsmooth nonlinearities and severely limit the system performance. However, as far as we know, although many previous works have been proposed to control fractional order nonlinear MIMO systems, no works have studied the tracking problem of incommensurate fractional order nonlinear MIMO systems with unknown nonlinearities, input dead-zone, and saturation.

Motivated by the above observations, a new adaptive NN backstepping control method is proposed for a class of incommensurate fractional order nonlinear MIMO systems with unknown nonlinearities, input dead-zone, and saturation. In summary, our contributions mainly include the following three aspects. Firstly, our proposed adaptive incommensurate fractional order NN controller can apply to both commensurate and incommensurate fractional order nonlinear MIMO systems with unknown nonlinearities, input dead-zone, and saturation, which is more broadly applicable. Secondly, the structure of adaptation laws with incommensurate fractional order closer to the characteristics of the system itself and the orders of the parameters adaptation laws cannot be consistent with the fractional order system binging more degree of freedom.

The paper is organized as follows. Section 2 gives the basic preliminary results on fractional order systems, and RBF NN are presented. Section 3 presents the adaptive fractional order controller design. Section 4 gives the simulation results to verify the proposed controller. Section 5 draws the conclusions.

2. Preliminary

The αth Caputo fractional derivative is defined as follows [44]:

$$t_0 D_t^{\alpha} f(t) = \frac{1}{\Gamma(n-\alpha)} \int_{t_0}^{t} \frac{f^{(n)}(t)}{(t-\tau)^{\alpha+1-n}} \mathrm{d}\tau, \tag{1}$$

where $\Gamma(\alpha) = \int_0^{\infty} e^{-t} t^{\alpha-1} \mathrm{d}t$, $n-1 < \alpha < n, n \in \mathbb{Z}^+$, and $t_0 D_t^{\alpha}$ is the classical αth order derivative operator. When $t_0 = 0$, $t_0 D_t^{\alpha}$ can be abbreviated as D^{α}.

Remark 1. The fractional order derivative is an extension of the conventional integer order derivative, and the main difference is that the fractional order derivative has interesting properties and potential applications. However, under the Caputo fractional derivative, the fractional order derivative of constant is 0, which is the same as the integer one.

Lemma 1 (see [45]). *Consider a nonlinear fractional-order system:*

$$D^{\alpha} x(t) = f(x(t)), \quad \alpha \in (0,1), x(t) \in \mathbb{R}^n. \tag{2}$$

The system is exactly equivalent to the continuous frequency distributed model described by

$$\begin{cases} \dfrac{\partial z(\omega,t)}{\partial t} = -\omega z(\omega,t) + f(x(t)), \\ x(t) = \displaystyle\int_0^{\infty} \mu_{\alpha}(\omega) z(\omega,t) \mathrm{d}\omega, \end{cases} \tag{3}$$

where $\mu_{\alpha}(\omega) = \sin(\alpha\pi)/\omega^{\alpha}\pi$. $z(\omega,t)$ is the infinite dimension distributed state variable.

In the developed control design procedure, the RBF NN will be used to approximate any continuous function $f(X)$ on a compact set Ω.

Lemma 2 (see [46]). *For a given desired level of accuracy $\varepsilon > 0$, any smooth function $f(X)$ can be approximated by the RBF NN $\theta^{*T}\vartheta(X)$ as*

$$f(x) = \theta^{*\mathrm{T}}\vartheta(x) + \varsigma(x), \quad |\varsigma(x)| \le \varepsilon, \tag{4}$$

where

$$\theta^* = \arg\min_{\theta} \left[\sup_X \left| f(X) - \theta^{\mathrm{T}}\vartheta(X) \right| \right], \tag{5}$$

$l > 1$ is the neural network node number, $X \in \Omega$ is the input vector, and $\theta = [\,\theta_1 \;\; \theta_2 \;\; \cdots \;\; \theta_l\,]^T \in \mathbb{R}^l$ is the weight vector;

$\vartheta(X) = [\vartheta_1(X), \vartheta_2(X), \ldots, \vartheta_l(X)]^T$, *and* $\vartheta_i(X)$ *can be selected as*

$$\vartheta_i(X) = \exp\left(\frac{-(X-\mu_i)^{\mathrm{T}}(X-\mu_i)}{\delta^2}\right), \quad i = 1, 2, \ldots, l, \tag{6}$$

where δ *is the width of the Gaussian function and* $\mu_i = (\mu_{i1}, \mu_{i2}, \ldots, \mu_{in})^T$ *is the center of the respective field.*

3. Adaptive Neural Network Backstepping Controller

In this paper, we consider a class of incommensurate fractional order nonlinear MIMO systems with unknown nonlinearities presented as follows:

$$\begin{cases} D^{\alpha_{i,1}} x_{i,1} = d_{i,1} x_{i,2} + f_{i,1}\left(\overline{x}_{i,1}\right) + g_{i,1}\left(\overline{x}_{i,1}\right), \\ D^{\alpha_{i,2}} x_{i,2} = d_{i,2} x_{i,3} + f_{i,2}\left(\overline{x}_{i,2}\right) + g_{i,2}\left(\overline{x}_{i,2}\right), \\ \vdots \\ D^{\alpha_{i,n_i-1}} x_{i,n_i-1} = d_{i,n_i-1} x_{i,n_i} + f_{i,n_i-1}\left(\overline{x}_{i,n_i-1}\right) + g_{i,n_i-1}\left(\overline{x}_{i,n_i-1}\right), \\ D^{\alpha_{i,n_i}} x_{i,n_i} = d_{i,n_i} u_i + f_{i,n_i}(x) + g_{i,n_i}(x), \\ y_i = x_{i,1}, \end{cases} \tag{7}$$

where $\alpha_{i,j_i} \in (0,1)$ is the system incommensurate fractional order, $\overline{x}_{i,j_i} = \left(x_{1,j_i}\, x_{2,j_i} \cdots x_{i,j_i}\right)^{\mathrm{T}} \in \mathbb{R}^{j_i}$ and $x = \left(x_{1,n_i}^{\mathrm{T}}\ x_{2,n_i}^{\mathrm{T}} \cdots x_{n,n_i}^{\mathrm{T}}\right)^{\mathrm{T}}$ are the state vectors, $y_i \in \mathbb{R}$ is the system output, $d_{i,j_i} \in \mathbb{R}$ is the known constant, $f_{i,j_i}(\cdot) \in \mathbb{R}$ is an unknown continuous nonlinear function, $g_{i,j_i}(\cdot) \in \mathbb{R}$ is an known continuous nonlinear function, $j_i = 1, 2, \ldots, n_i$, and $i = 1, 2, \ldots, n$.

$u_i(t) \in \mathbb{R}$ is the control input suffering from saturation and dead-zone. The dead-zone is in the following form:

$$u_i = D(\lambda_i) = \begin{cases} a_{i,r}\left(\lambda_i - b_{i,r}\right), & \lambda_i \geq b_{i,r}, \\ 0, & \lambda_i \in \left(-b_{i,l}, b_{i,r}\right), \\ a_{i,l}\left(\lambda_i + b_{i,l}\right), & \lambda_i \leq -b_{i,l}, \end{cases} \tag{8}$$

where $b_{i,r} > 0$ and $b_{i,l} > 0$ are unknown parameters of the dead-zone and $a_{i,r}$ and $a_{i,l}$ are slope of the dead-zone, and they are positive constants; the saturation nonlinearity is defined as follows:

$$\lambda_i = \mathrm{sat}(\xi_i) = \begin{cases} \xi_{i,\max}, & \xi_i \geq \xi_{i,\max}, \\ \xi_i, & \xi_i \in \left(\xi_{i,\min}, \xi_{i,\max}\right), \\ \xi_{i,\min}, & \xi_i \leq \xi_{i,\min}, \end{cases} \tag{9}$$

where $\xi_{i,\max} > 0$ and $\xi_{i,\min} < 0$ are the saturation limits.

Define the right inverse D^+ of D as

$$\xi_i = D^+(\nu_i) = \begin{cases} \dfrac{\nu_i}{a_{i,r} + b_{i,r}}, & \nu_i > 0, \\ 0, & \nu_i = 0, \\ \dfrac{\nu_i}{a_{i,l} - b_{i,l}}, & \nu_i < 0. \end{cases} \tag{10}$$

According to [16], the nonsymmetric saturation and dead-zone control input can be rewritten as follows:

$$\begin{aligned} u_i &= D\left(\mathrm{sat}\left(D^+(\nu_i)\right)\right) \\ &= \begin{cases} a_{i,r}\left(\xi_{i,\max} - b_{i,r}\right), & \nu_i \geq a_{i,r}\left(\xi_{i,\max} - b_{i,r}\right), \\ \nu_i, & \lambda_i \in \Big(-a_{i,l}\left(\xi_{i,\min} - b_{i,l}\right), \\ & \quad a_{i,r}\left(\xi_{i,\max} - b_{i,r}\right)\Big), \\ -a_{i,l}\left(\xi_{i,\min} - b_{i,l}\right), & \lambda_i \leq -a_{i,l}\left(\xi_{i,\min} - b_{i,l}\right). \end{cases} \end{aligned} \tag{11}$$

It is clear that the input saturation and dead-zone problem can be transformed by an input saturation (11), in which ν_i is the control law to be designed.

Our target is to design the input ν_i such that the system output y_i can follow the desired signal $y_{i,d}$. Some following assumptions for the controller design are given.

Assumption 1. It is supposed that the reference signals $y_{i,d}$ and the n_ith order derivatives $D^{n_i} y_{i,d}$ are continuous and bounded.

Assumption 2. For input constraints (11), there exist $\zeta_i^* > 0$ such that $|\Delta_i| \leq \zeta_i^*$, where $\Delta_i = u_i(\nu_i) - \nu_i$, $i = 1, 2, \ldots, n$.

In the following parts, the output feedback neural network fractional adaptive control based on backstepping and stability procedure will be developed. The recursive design algorithm has (i, n_i) steps according to the backstepping design method. In step (i, j_i), a virtual control function v_{i,j_i} is developed, and the true control law ν_i is designed at the final step. The virtual controllers and the real control functions will be developed according to the following steps.

The recursive backstepping algorithm can be presented as the follows.

Step $(i, 1)$: based on Lemma 1, a RBF NN can be used to approximate the unknown function $f_{i,1}(\overline{x}_{i,1})$ from (7) by a RBF NN as follows:

$$\widehat{f}_{i,1}\left(\overline{x}_{i,1}, \theta_{i,1}\right) = \theta_{i,1}^{\mathrm{T}} \vartheta_{i,1}\left(\overline{x}_{i,1}\right), \tag{12}$$

where $\theta_{i,1} \in \mathbb{R}^{m_{i,1}}$ is parameter estimation. The ideal parameter $\theta_{i,1}^*$ is described by

$$\theta_{i,1}^* = \arg\min_{\theta_{i,1}} \left[\sup_{x_{i,1}} \left| f_{i,1}\left(\overline{x}_{i,1}\right) - \widehat{f}_{i,1}\left(\overline{x}_{i,1}, \theta_{i,1}\right) \right| \right]. \quad (13)$$

Let

$$\begin{aligned} \widetilde{\theta}_{i,1} &= \theta_{i,1}^* - \theta_{i,1}, \\ \varepsilon_{i,1}\left(\overline{x}_{i,1}\right) &= \widehat{f}_{i,1}\left(\overline{x}_{i,1}, \theta_{i,1}^*\right) - \widehat{f}_{i,1}\left(\overline{x}_{i,1}\right). \end{aligned} \quad (14)$$

According to [47], the optimal approximation error $\varepsilon_{i,1}(\overline{x}_{i,1})$ is bounded, i.e., $|\varepsilon_{i,1}(\overline{x}_{i,1})| \le \overline{\varepsilon}_{i,1}$, and $\overline{\varepsilon}_{i,1} > 0$ is unknown.

Therefore, one can obtain

$$\begin{aligned} & f_{i,1}\left(\overline{x}_{i,1}, \theta_{i,1}\right) - \widehat{f}_{i,1}\left(\overline{x}_{i,1}\right) \\ &= \widehat{f}_{i,1}\left(\overline{x}_{i,1}, \theta_{i,1}\right) - \widehat{f}_{i,1}\left(x_{i,1}, \theta_{i,1}^*\right) + \widehat{f}_{i,1}\left(x_{i,1}, \theta_{i,1}^*\right) \\ &\quad - f_{i,1}\left(x_{i,1}\right) \\ &= \theta_{i,1}^{\mathrm{T}} \vartheta_{i,1}\left(\overline{x}_{i,1}\right) - \theta_{i,1}^{*\mathrm{T}} \vartheta_{i,1}\left(\overline{x}_{i,1}\right) + \varepsilon_{i,1}\left(\overline{x}_{i,1}\right) \\ &= -\widetilde{\theta}_{i,1}^{\mathrm{T}} \vartheta_{i,1}\left(\overline{x}_{i,1}\right) + \varepsilon_{i,1}\left(\overline{x}_{i,1}\right). \end{aligned} \quad (15)$$

Due to (1) and the estimated error $\widetilde{\theta}_{i,1} = \theta_{i,1}^* - \theta_{i,1}$ from (14), the following equation can be given:

$$D^{\beta_{i,1}} \widetilde{\theta}_{i,1} = D^{\beta_{i,1}} \theta_{i,1}^* - D^{\beta_{i,1}} \theta_{i,1} = -D^{\beta_{i,1}} \theta_{i,1}, \quad (16)$$

where $\beta_{i,1} \in (0,1)$. According to Lemma 1 and (16), the following frequency distributed model can be obtained:

$$\begin{cases} \dfrac{\partial z_{\theta_{i,1}}(\omega,t)}{\partial t} = -\omega z_{\theta_{i,1}}(\omega,t) - D^{\beta_{i,1}} \theta_{i,1}, \\ \widetilde{\theta}_{i,1} = \displaystyle\int_0^\infty \mu_{\beta_{i,1}}(\omega) z_{\theta_{i,1}}(\omega,t) \mathrm{d}\omega, \end{cases} \quad (17)$$

where $z_{\theta_{i,1}}(\omega,t) \in \mathbb{R}^{m_{i,1}}$ and $\mu_{\beta_{i,1}}(\omega) = \sin(\beta_{i,1}\pi)/\omega^{\beta_{i,1}}\pi$. Denoting $e_{i,1} = y_i - y_{i,d}$, it follows from (7) and (15) that

$$\begin{aligned} D^{\alpha_{i,1}} e_{i,1} &= D^{\alpha_{i,1}} y_i - D^{\alpha_{i,1}} y_{i,d} \\ &= d_{i,2} x_{i,2} + f_{i,1}\left(\overline{x}_{i,1}\right) + g_{i,1}\left(\overline{x}_{i,1}\right) - D^{\alpha_{i,1}} y_{i,d} \\ &= d_{i,2} x_{i,2} + \widetilde{\theta}_{i,1}^{\mathrm{T}} \vartheta_{i,1}\left(\overline{x}_{i,1}\right) - \varepsilon_{i,1}\left(\overline{x}_{i,1}\right) \\ &\quad + \theta_{i,1}^{\mathrm{T}} \vartheta_{i,1}\left(\overline{x}_{i,1}\right) + g_{i,1}\left(\overline{x}_{i,1}\right) - D^{\alpha_{i,1}} y_{i,d}. \end{aligned} \quad (18)$$

Let a virtual control input $v_{i,1}(e_{i,1}, x_{i,1}, y_{i,d}) = v_{i,1}$ be

$$\begin{aligned} v_{i,1} = & -\theta_{i,1}^{\mathrm{T}} \vartheta_{i,1}\left(\overline{x}_{i,1}\right) - k_{i,1} e_{i,1} - l_{i,1} \mathrm{sign}\left(e_{i,1}\right) - g_{i,1}\left(\overline{x}_{i,1}\right) \\ & + D^{\alpha_{i,1}} y_{i,d}, \end{aligned} \quad (19)$$

where $k_{i,1}$ and $l_{i,1}$ are the design parameters. Let

$$e_{i,2} = d_{i,2} x_{i,2} - v_{i,1}. \quad (20)$$

Substituting (19) and (20) into (18) gives

$$\begin{aligned} D^{\alpha_{i,1}} e_{i,1} = & e_{i,2} - k_{i,1} e_{i,1} - l_{i,1} \mathrm{sign}\left(e_{i,1}\right) \\ & + \widetilde{\theta}_{i,1}^{\mathrm{T}} \vartheta_{i,1}\left(\overline{x}_{i,1}\right) - \varepsilon_{i,1}\left(\overline{x}_{i,1}\right). \end{aligned} \quad (21)$$

According to Lemma 1, equation (21) will be

$$\begin{cases} \dfrac{\partial z_{i,1}(\omega,t)}{\partial t} = -\omega z_{i,1}(\omega,t) + e_{i,2} - k_{i,1} e_{i,1} - l_{i,1} \mathrm{sign}\left(e_{i,1}\right) \\ \quad + \widetilde{\theta}_{i,1}^{\mathrm{T}} \vartheta_{i,1}\left(\overline{x}_{i,1}\right) - \varepsilon_{i,1}\left(\overline{x}_{i,1}\right), \\ e_{i,1} = \displaystyle\int_0^\infty \mu_{\alpha_{i,1}}(\omega) z_{i,1}(\omega,t) \mathrm{d}\omega, \end{cases} \quad (22)$$

where $\mu_{\alpha_{i,1}}(\omega) = \sin(\alpha_{i,1}\pi)/\omega^{\alpha_{i,1}}\pi$.

Selecting the Lyapunov function $V_{i,1}$ as

$$\begin{aligned} V_{i,1} = & \frac{1}{2\sigma_{i,1}} \int_0^\infty \mu_{\beta_{i,1}}(\omega) z_{\theta_{i,1}}^T(\omega,t) \Lambda_{i,1}^{-1} z_{\theta_{i,1}}(\omega,t) \mathrm{d}\omega \\ & + \frac{1}{2} \int_0^\infty \mu_{\alpha_{i,1}}(\omega) z_{i,1}^2(\omega,t) \mathrm{d}\omega, \end{aligned} \quad (23)$$

where $\sigma_{i,1} > 0$. Based on frequency distributed model (17) and (22), the derivative of $V_{i,1}$ is expressed as

$$\begin{aligned}\dot{V}_{i,1}(t) &= \frac{1}{\sigma_{i,1}}\int_0^\infty \mu_{\beta_{i,1}}(\omega) z_{\theta_{i,1}}^{\mathrm{T}}(\omega,t)\Lambda_{i,1}^{-1}\dot{z}_{\theta_{i,1}}(\omega,t)\mathrm{d}\omega + \int_0^\infty \mu_{\alpha_{i,1}}(\omega) z_{i,1}(\omega,t)\dot{z}_{i,1}(\omega,t)\mathrm{d}\omega \\ &\le -\frac{1}{\sigma_{i,1}}\int_0^\infty \mu_{\beta_{i,1}}(\omega)\omega z_{\theta_{i,1}}^{\mathrm{T}}(\omega,t)\Lambda_{i,1}^{-1} z_{\theta_{i,1}}(\omega,t)\mathrm{d}\omega - \frac{1}{\sigma_{i,1}}\int_0^\infty \mu_{\beta_{i,1}}(\omega) z_{\theta_{i,1}}^{\mathrm{T}}(\omega,t)\mathrm{d}\omega\Lambda_{i,1}^{-1} D^{\beta_{i,1}}\theta_{i,1} \\ &\quad - \int_0^\infty \omega\mu_{\alpha_{i,1}}(\omega) z_{i,1}(\omega,t) z_{i,1}(\omega,t)\mathrm{d}\omega + e_{i,1}\left(e_{i,2} - k_{i,1}e_{i,1} - l_{i,1}\mathrm{sign}\left(e_{i,1}\right) - \varepsilon_{i,1}\left(\overline{x}_{i,1}\right)\right) \\ &= -\frac{1}{\sigma_{i,1}}\int_0^\infty \mu_{\beta_{i,1}}(\omega)\omega z_{\theta_{i,1}}^{\mathrm{T}}(\omega,t)\Lambda_{i,1}^{-1} z_{\theta_{i,1}}(\omega,t)\mathrm{d}\omega - \int_0^\infty \omega\mu_{\alpha_{i,1}}(\omega) z_{i,1}^2(\omega,t)\mathrm{d}\omega - \widetilde{\theta}_{i,1}^{\mathrm{T}}\left(\frac{1}{\sigma_{i,1}}\Lambda_{i,1}^{-1}D^{\beta_{i,1}}\theta_{i,1} + e_{i,1}\vartheta_{i,1}\left(\overline{x}_{i,1}\right)\right) \\ &\quad + e_{i,1}\left(e_{i,2} - k_{i,1}e_{i,1} - l_{i,1}\mathrm{sign}\left(e_{i,1}\right) - \varepsilon_{i,1}\left(\overline{x}_{i,1}\right)\right) \\ &\le -\frac{1}{\sigma_{i,1}}\int_0^\infty \mu_{\beta_{i,1}}(\omega)\omega z_{\theta_{i,1}}^{\mathrm{T}}(\omega,t)\Lambda_{i,1}^{-1} z_{\theta_{i,1}}(\omega,t)\mathrm{d}\omega - \int_0^\infty \omega\mu_{\alpha_{i,1}}(\omega) z_{i,1}^2(\omega,t)\mathrm{d}\omega - \widetilde{\theta}_{i,1}^{\mathrm{T}}\left(\frac{1}{\sigma_{i,1}}\Lambda_{i,1}^{-1}D^{\beta_{i,1}}\theta_{i,1} + e_{i,1}\vartheta_{i,1}\left(\overline{x}_{i,1}\right)\right) \\ &\quad + e_{i,1}e_{i,2} - k_{i,1}e_{i,1}^2 - l_{i,1}\left|e_{i,1}\right| + \left|e_{i,1}\right|\left|\varepsilon_{i,1}\left(\overline{x}_{i,1}\right)\right| \\ &\le -\frac{1}{\sigma_{i,1}}\int_0^\infty \mu_{\beta_{i,1}}(\omega)\omega z_{\theta_{i,1}}^{\mathrm{T}}(\omega,t)\Lambda_{i,1}^{-1} z_{\theta_{i,1}}(\omega,t)\mathrm{d}\omega - \int_0^\infty \omega\mu_{\alpha_{i,1}}(\omega) z_{i,1}^2(\omega,t)\mathrm{d}\omega - \widetilde{\theta}_{i,1}^{\mathrm{T}}\left(\frac{1}{\sigma_{i,1}}\Lambda_{i,1}^{-1}D^{\beta_{i,1}}\theta_{i,1} + e_{i,1}\vartheta_{i,1}\left(\overline{x}_{i,1}\right)\right) \\ &\quad + e_{i,1}e_{i,2} - k_{i,1}e_{i,1}^2 - \left(l_{i,1} - \overline{\varepsilon}_{i,1}\right)\left|e_{i,1}\right|. \end{aligned} \tag{24}$$

Based on LaSalle invariance principle [48] and equation (24), if $e_{i,2} = 0$, $k_{i,1} > 0$, $l_{i,1} > \overline{\varepsilon}_{i,1}$, and the fractional order adaptation laws are designed as

$$D^{\beta_{i,1}}\theta_{i,1} = \sigma_{i,1}\Lambda_{i,1}\vartheta_{i,1}\left(\overline{x}_{i,1}\right)e_{i,1}, \tag{25}$$

one can obtain $\dot{V}_{i,1} < 0$.

Step $(i,2)$: it follows from (7) and (20) that

$$\begin{aligned} D^{\alpha_{i,2}}e_{i,2} &= D^{\alpha_{i,2}}x_{i,2} - D^{\alpha_{i,2}}v_{i,1} \\ &= d_{i,3}x_{i,3} + f_{i,2}\left(\overline{x}_{i,2}\right) + g_{i,2}\left(\overline{x}_{i,2}\right) - D^{\alpha_{i,2}}v_{i,1} \\ &= d_{i,3}x_{i,3} + g_{i,2}\left(\overline{x}_{i,2}\right) + f_{i,2}\left(\overline{x}_{i,2}\right) - D^{\alpha_{i,2}}v_{i,1} \\ &= d_{i,3}x_{i,3} + g_{i,2}\left(\overline{x}_{i,2}\right) + F_{i,2}\left(\overline{x}_{i,2}\right), \end{aligned} \tag{26}$$

where $F_{i,2}(\overline{x}_{i,2}) = f_{i,2}(\overline{x}_{i,2}) - D^{\alpha_{i,2}}v_{i,1}$ is the unknown function. According to the procedures in step $(i,1)$, a RBF NN is used to approximate $F_{i,2}(\overline{x}_{i,2})$ as follows:

$$\widehat{F}_{i,2}\left(\overline{x}_{i,2},\theta_2\right) = \theta_{i,2}^{\mathrm{T}}\vartheta_{i,2}\left(\overline{x}_{i,2}\right), \tag{27}$$

where $\theta_{i,2} \in \mathbb{R}^{m_{i,2}}$ is the parameter estimation.

With the estimated error $\widetilde{\theta}_{i,2} = \theta_{i,2}^* - \theta_{i,2}$ and (1), the following equation can be obtained:

$$D^{\beta_{i,2}}\widetilde{\theta}_{i,2} = D^{\beta_{i,2}}\theta_{i,2}^* - D^{\beta_{i,2}}\theta_{i,2} = -D^{\beta_{i,2}}\theta_{i,2}, \tag{28}$$

where $0 < \beta_{i,2} < 1$.

According to Lemma 1 and (28), the following frequency distributed model can be obtained:

$$\begin{cases} \dfrac{\partial z_{\theta_{i,2}}(\omega,t)}{\partial t} = -\omega z_{\theta_{i,2}}(\omega,t) - D^{\beta_{i,2}}\theta_{i,2}, \\ \\ \widetilde{\theta}_{i,2} = \displaystyle\int_0^\infty \mu_{\beta_{i,2}}(\omega) z_{\theta_{i,2}}(\omega,t)\mathrm{d}\omega, \end{cases} \tag{29}$$

where $z_{\theta_{i,2}}(\omega,t) \in \mathbb{R}^{m_{i,2}}$ and $\mu_{\beta_{i,2}}(\omega) = \sin(\beta_{i,2}\pi)/\omega^{\beta_{i,2}}\pi$.

Rewrite (26) as

$$D^{\alpha_{i,2}}e_{i,2} = d_{i,3}x_{i,3} + g_{i,2}\left(\overline{x}_{i,2}\right) + \widetilde{\theta}_{i,2}^{\mathrm{T}}\vartheta_{i,2}\left(\overline{x}_{i,2}\right) - \varepsilon_{i,2}\left(\overline{x}_{i,2}\right) + \theta_{i,2}^{\mathrm{T}}\vartheta_{i,2}\left(\overline{x}_{i,2}\right), \tag{30}$$

where $\varepsilon_{i,2}(\overline{x}_{i,2}) = \widehat{F}_{i,2}(\overline{x}_{i,2}, \theta_{i,2}^{*}) - F_{i,2}(\overline{x}_{i,2})$, satisfying $|\varepsilon_{i,2}(\overline{x}_{i,2})| \le \overline{\varepsilon}_{i,2}$, and $\overline{\varepsilon}_2 > 0$ is the unknown positive constant.

A virtual control input is designed as

$$v_{i,2} = -\theta_{i,2}^{\mathrm{T}}\vartheta_{i,2}\left(\overline{x}_{i,2}\right) - k_{i,2}e_{i,2} - l_{i,2}\mathrm{sign}\left(e_{i,2}\right) - g_{i,2}\left(\overline{x}_{i,2}\right) - e_{i,1}, \tag{31}$$

where $k_{i,2}$ and $l_{i,2}$ are the design parameters.

Let

$$e_{i,3} = d_{i,3}x_{i,3} - v_{i,2}. \tag{32}$$

Substituting (31) and (32) into (30) gives

$$D^{\alpha_{i,2}}e_{i,2} = e_{i,3} - k_{i,2}e_{i,2} - l_{i,2}\mathrm{sign}\left(e_{i,2}\right) - e_{i,1} + \widetilde{\theta}_{i,2}^{\mathrm{T}}\vartheta_{i,2}\left(\overline{x}_{i,2}\right) - \varepsilon_{i,2}\left(\overline{x}_{i,2}\right). \tag{33}$$

Its frequency distributed model corresponds to

$$\begin{cases} \dfrac{\partial z_{i,2}(\omega,t)}{\partial t} = -\omega z_{i,2}(\omega,t) + e_{i,3} - k_{i,2}e_{i,2} - l_{i,2}\mathrm{sign}\left(e_{i,2}\right) \\ \quad -e_{i,1} + \widetilde{\theta}_{i,2}^{\mathrm{T}}\vartheta_{i,2}\left(\overline{x}_{i,2}\right), \\ e_{i,2} = \displaystyle\int_0^{\infty} \mu_{\alpha_{i,2}}(\omega) z_{i,2}(\omega,t)\mathrm{d}\omega, \end{cases} \tag{34}$$

where $\mu_{\alpha_{i,2}}(\omega) = \sin(\alpha_{i,2}\pi)/\omega^{\alpha_{i,2}}\pi$.

Selecting the Lyapunov function $V_{i,2}$ as

$$V_{i,2} = V_{i,1} + \frac{1}{2\sigma_{i,2}}\int_0^{\infty} \mu_{\beta_{i,2}}(\omega) z_{\theta_{i,2}}^{\mathrm{T}}(\omega,t)\Lambda_{i,2}^{-1} z_{\theta_{i,2}}(\omega,t)\mathrm{d}\omega + \frac{1}{2}\int_0^{\infty} \mu_{\alpha_{i,2}}(\omega) z_{i,2}^{2}(\omega,t)\mathrm{d}\omega, \tag{35}$$

where $\sigma_{i,2} > 0$. According to frequency distributed model (30) and (34), the derivative of (35) is

$$\begin{aligned} \dot{V}_{i,2}(t) &= \dot{V}_{i,1}(t) + \frac{1}{\sigma_{i,2}}\int_0^{\infty} \mu_{\beta_{i,2}}(\omega) z_{\theta_{i,2}}^{\mathrm{T}}(\omega,t)\Lambda_{i,2}^{-1}\dot{z}_{\theta_2}(\omega,t)\mathrm{d}\omega \\ &\quad + \int_0^{\infty} \mu_{\alpha_{i,2}}(\omega) z_{i,2}(\omega,t)\dot{z}_{i,2}(\omega,t)\mathrm{d}\omega \\ &= \dot{V}_{i,1}(t) - \frac{1}{\sigma_{i,2}}\int_0^{\infty} \omega\mu_{\beta_{i,2}}(\omega) z_{\theta_{i,2}}^{\mathrm{T}}(\omega,t)\Lambda_{i,2}^{-1} z_{\theta_{i,2}}(\omega,t)\mathrm{d}\omega \\ &\quad - \frac{1}{\sigma_{i,2}}\widetilde{\theta}_{i,2}^{\mathrm{T}}\Lambda_{i,2}^{-1}D^{\beta_{i,2}}\theta_{i,2} - \int_0^{\infty} \omega\mu_{\alpha_{i,2}}(\omega) z_{i,2}^{2}(\omega,t)\mathrm{d}\omega \\ &\quad + e_{i,2}e_{i,3} - k_{i,2}e_{i,2}^{2} - l_{i,2}e_{i,2}\mathrm{sign}\left(e_{i,2}\right) - e_{i,1}e_{i,2} + \widetilde{\theta}_{i,2}^{\mathrm{T}}\vartheta_{i,2} \\ &\quad \cdot \left(\overline{x}_{i,2}\right)e_{i,2} - \varepsilon_{i,2}\left(\overline{x}_{i,2}\right)e_{i,2} \\ &\le \dot{V}_{i,1}(t) - \frac{1}{\sigma_{i,2}}\int_0^{\infty} \omega\mu_{\beta_{i,2}}(\omega) z_{\theta_{i,2}}^{\mathrm{T}}(\omega,t)\Lambda_{i,2}^{-1} z_{\theta_{i,2}}(\omega,t)\mathrm{d}\omega \\ &\quad - \int_0^{\infty} \omega\mu_{\alpha_{i,2}}(\omega) z_{i,2}^{2}(\omega,t)\mathrm{d}\omega - \widetilde{\theta}_{i,2}^{\mathrm{T}} \\ &\quad \cdot \left(\frac{1}{\sigma_{i,2}}\Lambda_{i,2}^{-1}D^{\beta_{i,2}}\theta_{i,2} - \vartheta_{i,2}\left(\overline{x}_{i,2}\right)e_{i,2}\right) + e_{i,2}e_{i,3} - e_{i,1}e_{i,2} \\ &\quad - k_{i,2}e_{i,2}^{2} - \left(l_{i,2} - \overline{\varepsilon}_{i,2}\right)|e_{i,2}| \\ &\le -\frac{1}{\sigma_{i,1}}\int_0^{\infty} \mu_{\beta_{i,1}}(\omega)\omega z_{\theta_{i,1}}^{\mathrm{T}}(\omega,t)\Lambda_{i,1}^{-1} z_{\theta_{i,1}}(\omega,t)\mathrm{d}\omega \\ &\quad - \int_0^{\infty} \omega\mu_{\alpha_{i,1}}(\omega) z_{i,1}^{2}(\omega,t)\mathrm{d}\omega - \frac{1}{\sigma_{i,2}}\int_0^{\infty} \omega\mu_{\beta_{i,2}}(\omega) z_{\theta_{i,2}}^{\mathrm{T}} \\ &\quad \cdot (\omega,t)\Lambda_{i,2}^{-1} z_{\theta_{i,2}}(\omega,t)\mathrm{d}\omega - \int_0^{\infty} \omega\mu_{\alpha_{i,2}}(\omega) z_{i,2}^{2}(\omega,t)\mathrm{d}\omega \\ &\quad - \widetilde{\theta}_{i,1}^{\mathrm{T}}\left(\frac{1}{\sigma_{i,1}}\Lambda_{i,1}^{-1}D^{\beta_{i,1}}\theta_{i,1} + e_{i,1}\vartheta_{i,1}\left(\overline{x}_{i,1}\right)\right) \\ &\quad - \widetilde{\theta}_{i,2}^{\mathrm{T}}\left(\frac{1}{\sigma_{i,2}}\Lambda_{i,2}^{-1}D^{\beta_{i,2}}\theta_{i,2} - \vartheta_{i,2}\left(\overline{x}_{i,2}\right)e_{i,2}\right) + e_{i,1}e_{i,2} \\ &\quad - k_{i,1}e_{i,1}^{2} - \left(l_{i,1} - \overline{\varepsilon}_{i,1}\right)|e_{i,1}| + e_{i,2}e_{i,3} - e_{i,1}e_{i,2} - k_{i,2}e_{i,2}^{2} \\ &\quad - \left(l_{i,2} - \overline{\varepsilon}_{i,2}\right)|e_{i,2}| \\ &\le -\frac{1}{\sigma_{i,1}}\int_0^{\infty} \mu_{\beta_{i,1}}(\omega)\omega z_{\theta_{i,1}}^{\mathrm{T}}(\omega,t)\Lambda_{i,1}^{-1} z_{\theta_{i,1}}(\omega,t)\mathrm{d}\omega \\ &\quad - \int_0^{\infty} \omega\mu_{\alpha_{i,1}}(\omega) z_{i,1}^{2}(\omega,t)\mathrm{d}\omega - \frac{1}{\sigma_{i,2}}\int_0^{\infty} \omega\mu_{\beta_{i,2}}(\omega) z_{\theta_{i,2}}^{\mathrm{T}} \\ &\quad \cdot (\omega,t)\Lambda_{i,2}^{-1} z_{\theta_{i,2}}(\omega,t)\mathrm{d}\omega \\ &\quad - \int_0^{\infty} \omega\mu_{\alpha_{i,2}}(\omega) z_{i,2}^{2}(\omega,t)\mathrm{d}\omega - \widetilde{\theta}_{i,1}^{\mathrm{T}} \\ &\quad \cdot \left(\frac{1}{\sigma_{i,1}}\Lambda_{i,1}^{-1}D^{\beta_{i,1}}\theta_{i,1} + e_{i,1}\vartheta_{i,1}\left(\overline{x}_{i,1}\right)\right) \\ &\quad - \widetilde{\theta}_{i,2}^{\mathrm{T}}\left(\frac{1}{\sigma_{i,2}}\Lambda_{i,2}^{-1}D^{\beta_{i,2}}\theta_{i,2} - \vartheta_{i,2}\left(\overline{x}_{i,2}\right)e_{i,2}\right) + e_{i,2}e_{i,3} \\ &\quad - k_{i,1}e_{i,1}^{2} - \left(l_{i,1} - \overline{\varepsilon}_{i,1}\right)|e_{i,1}| - k_{i,2}e_{i,2}^{2} - \left(l_{i,2} - \overline{\varepsilon}_{i,2}\right)|e_{i,2}|. \end{aligned} \tag{36}$$

Based on LaSalle invariance principle and equation (36), if $e_{i,3} = 0$, $k_{i,2} > 0$, $l_{i,2} > \bar{\varepsilon}_{i,2}$, and the fractional order adaptation laws are designed as

$$D^{\beta_{i,2}}\theta_{i,2} = -\sigma_{i,2}\Lambda_{i,2}\vartheta_{i,2}\left(\overline{x}_{i,2}\right)e_{i,2}, \tag{37}$$

one can get $\dot{V}_{i,2} < 0$.

Step $(i, j_i), 3 \le j_i \le n_i - 1$: define

$$e_{i,j_i} = d_{i,j_i}x_{i,j_i} - v_{i-1,j_i}, \tag{38}$$

where v_{i-1,j_i} is the virtual control input. Just like the procedures in step $(i,1)$ and $(i,2)$, one has

$$\begin{aligned} D^{\alpha_{i,j_i}}e_{i,j_i} &= D^{\alpha_{i,j_i}}x_{i,j_i} - D^{\alpha_{i,j_i}}v_{i-1,j_i} \\ &= d_{i,j_i+1}x_{i,j_i+1} + f_{i,j_i}\left(\overline{x}_{i,j_i}\right) + g_{i,j_i}\left(\overline{x}_{i,j_i}\right) - D^{\alpha_{i,j_i}}v_{i-1,j_i} \\ &= d_{i,j_i+1}x_{i,j_i+1} + g_{i,j_i}\left(\overline{x}_{i,j_i}\right) + F_{i,j_i}\left(\overline{x}_{i,j_i}\right), \end{aligned} \tag{39}$$

where $F_{i,j_i}(\overline{x}_{i,j_i}) = f_{i,j_i}(\overline{x}_{i,j_i}) - D^{\alpha_{i,j_i}}v_{i-1,j_i}$ is the unknown function. According to Lemma 2, let

$$\widehat{F}_{i,j_i}\left(\overline{x}_{i,j_i}, \theta_{i,j_i}\right) = \theta_{i,j_i}^{\mathrm{T}}(t)\vartheta_{i,j_i}\left(\overline{x}_{i,j_i}\right), \tag{40}$$

where $\theta_i \in \mathbb{R}^{m_i}$ is the parameter estimation.

With the estimated error defined as $\widetilde{\theta}_{i,j_i} = \theta^*_{i,j_i} - \theta_{i,j_i}$ and (1), the following equation can be obtained:

$$D^{\beta_{i,j_i}}\widetilde{\theta}_{i,j_i} = D^{\beta_{i,j_i}}\theta^*_{i,j_i} - D^{\beta_{i,j_i}}\theta_{i,j_i} = -D^{\beta_{i,j_i}}\theta_{i,j_i}, \tag{41}$$

where $\beta_{i,j_i} \in (0,1)$.

According to Lemma 1, (41) can be written described as

$$\begin{cases} \dfrac{\partial z_{\theta_{i,j_i}}(\omega,t)}{\partial t} = -\omega z_{\theta_{i,j_i}}(\omega,t) - D^{\beta_{i,j_i}}\theta_{i,j_i}, \\ \widetilde{\theta}_{i,j_i} = \displaystyle\int_0^\infty \mu_{\beta_{i,j_i}}(\omega)z_{\theta_{i,j_i}}(\omega,t)\mathrm{d}\omega, \end{cases} \tag{42}$$

where $z_{\theta_{i,j_i}}(\omega,t) \in \mathbb{R}^{m_{i,j_i}}$ and $\mu_{\beta_{i,j_i}}(\omega) = \sin(\beta_{i,j_i}\pi)/\omega^{\beta_{i,j_i}}\pi$.

From (40), (39) can be rewritten as follows:

$$\begin{aligned} D^{\alpha_{i,j_i}}e_{i,j_i} = d_{i,j_i+1}x_{i,j_i+1} &+ \widetilde{\theta}_{i,j_i}^{\mathrm{T}}\vartheta_{i,j_i}\left(\overline{x}_{i,j_i}\right) + g_{i,j_i}\left(\overline{x}_{i,j_i}\right) \\ &- \varepsilon_{i,j_i}\left(\overline{x}_{i,j_i}\right) + \theta_{i,j_i}^{\mathrm{T}}\vartheta_{i,j_i}\left(\overline{x}_{i,j_i}\right), \end{aligned} \tag{43}$$

where $\varepsilon_{i,j_i}(\overline{x}_{i,j_i}) = \widehat{F}_{i,j_i}(\overline{x}_{i,j_i}, \theta^*_{i,j_i}) - F_{i,j_i}(\overline{x}_{i,j_i})$, satisfying $|\varepsilon_{i,j_i}(\overline{x}_{i,j_i})| \le \bar{\varepsilon}_{i,j_i}$, $\bar{\varepsilon}_{i,j_i} > 0$.

Design a virtual control input as

$$v_{i,j_i} = -\theta_{i,j_i}^{\mathrm{T}}\vartheta_{i,j_i}\left(\overline{x}_{i,j_i}\right) - k_{i,j_i}e_{i,j_i} - l_{i,j_i}\mathrm{sign}\left(e_{i,j_i}\right) - e_{i,j_i-1}, \tag{44}$$

where $k_{i,j_i} > 0$ and $l_{i,j_i} > 0$ are the design parameters.

Substituting (38) and (44) into (43) gives

$$\begin{aligned} D^{\alpha_{i,j_i}}e_{i,j_i} = e_{i,j_i+1} &- k_{i,j_i}e_{i,j_i} - l_{i,j_i}\mathrm{sign}\left(e_{i,j_i}\right) - e_{i,j_i-1} \\ &+ \widetilde{\theta}_{i,j_i}^{\mathrm{T}}\vartheta_{i,j_i}\left(\overline{x}_{i,j_i}\right) - \varepsilon_{i,j_i}\left(\overline{x}_{i,j_i}\right). \end{aligned} \tag{45}$$

Its frequency distributed model corresponds to

$$\begin{cases} \dfrac{\partial z_{i,j_i}(\omega,t)}{\partial t} = -\omega z_{i,j_i}(\omega,t) + e_{i,j_i+1} - k_{i,j_i}e_{i,j_i} - l_{i,j_i}\mathrm{sign}\left(e_{i,j_i}\right) \\ \quad -e_{i,j_i+1} + \widetilde{\theta}_{i,j_i}^{\mathrm{T}}\vartheta_{i,j_i}\left(\overline{x}_{i,j_i}\right) - \varepsilon_{i,j_i}\left(\overline{x}_{i,j_i}\right), \\ e_{i,j_i} = \displaystyle\int_0^\infty \mu_{\alpha_{i,j_i}}(\omega)z_{i,j_i}(\omega,t)\mathrm{d}\omega, \end{cases} \tag{46}$$

where $\mu_{\alpha_{i,j_i}}(\omega) = \sin(\alpha_{i,j_i}\pi)/\omega^{\alpha_{i,j_i}}\pi$.

Selecting the Lyapunov function V_{i,j_i} as

$$V_{i,j_i} = V_{i,j_i-1} + \frac{1}{2\sigma_{i,j_i}}\int_0^\infty \mu_{\beta_{i,j_i}}(\omega)z_{\theta_{i,j_i}}^{\mathrm{T}}(\omega,t)\Lambda_{i,j_i}^{-1}z_{\theta_{i,j_i}}(\omega,t)\mathrm{d}\omega + \frac{1}{2}\int_0^\infty \mu_{\alpha_{i,j_i}}(\omega)z_{i,j_i}^2(\omega,t)\mathrm{d}\omega, \tag{47}$$

where $\sigma_{i,j_i} > 0$. Then, its derivative on the basis of frequency distributed model (42) and (46) is expressed as

$$\dot{V}_{i,j_i} = \dot{V}_{i,j_i-1} + \frac{1}{\sigma_{i,j_i}} \int_0^\infty \mu_{\beta_{i,j_i}}(\omega) z_{\theta_{i,j_i}}^{\mathrm{T}}(\omega,t) \Lambda_{i,j_i}^{-1} \dot{z}_{\theta_i}(\omega,t)\mathrm{d}\omega + \int_0^\infty \mu_{\alpha_{i,j_i}}(\omega) z_{i,j_i}(\omega,t) \dot{z}_{i,j_i}(\omega,t)\mathrm{d}\omega$$

$$= \dot{V}_{i,j_i-1} - \frac{1}{\sigma_{i,j_i}} \int_0^\infty \omega\mu_{\beta_{i,j_i}}(\omega) z_{\theta_{i,j_i}}^{\mathrm{T}}(\omega,t) \Lambda_{i,j_i}^{-1} z_{\theta_{i,j_i}}(\omega,t)\mathrm{d}\omega - \int_0^\infty \omega\mu_{\alpha_{i,j_i}}(\omega) z_{i,j_i}(\omega,t) z_{i,j_i}(\omega,t)\mathrm{d}\omega - \frac{1}{\sigma_{i,j_i}} \widetilde{\theta}_{i,j_i}^{\mathrm{T}} \Lambda_{i,j_i}^{-1} D^{\beta_{i,j_i}} \theta_{i,j_i} + e_{i,j_i}$$

$$\cdot \left(e_{i,j_i+1} - k_{i,j_i} e_{i,j_i}\right) + e_{i,j_i}\left(-l_{i,j_i}\mathrm{sign}\left(e_{i,j_i}\right) - e_{i,j_i-1} + \widetilde{\theta}_{i,j_i}^{\mathrm{T}} \vartheta_{i,j_i}\left(\overline{x}_{i,j_i}\right) - \varepsilon_{i,j_i}\left(\overline{x}_{i,j_i}\right)\right)$$

$$= \dot{V}_{i,j_i-1} - \frac{1}{\sigma_{i,j_i}} \int_0^\infty \omega\mu_{\beta_{i,j_i}}(\omega) z_{\theta_{i,j_i}}^{\mathrm{T}}(\omega,t) \Lambda_{i,j_i}^{-1} z_{\theta_{i,j_i}}(\omega,t)\mathrm{d}\omega - \int_0^\infty \omega\mu_{\alpha_{i,j_i}}(\omega) z_{i,j_i}(\omega,t) z_{i,j_i}(\omega,t)\mathrm{d}\omega$$

$$- \widetilde{\theta}_{i,j_i}^{\mathrm{T}}\left(\frac{1}{\sigma_{i,j_i}} \Lambda_{i,j_i}^{-1} D^{\beta_{i,j_i}} \theta_{i,j_i} - \vartheta_{i,j_i}\left(\overline{x}_{i,j_i}\right) e_{i,j_i}\right) + e_{i,j_i} e_{i,j_i+1} - k_{i,j_i} e_{i,j_i}^2 - l_{i,j_i} e_{i,j_i} \mathrm{sign}\left(e_{i,j_i}\right) - e_{i,j_i-1} e_{i,j_i} - \varepsilon_{i,j_i}\left(\overline{x}_{i,j_i}\right) e_{i,j_i}$$

$$\le \dot{V}_{i,j_i-1} - \frac{1}{\sigma_{i,j_i}} \int_0^\infty \omega\mu_{\beta_{i,j_i}}(\omega) z_{\theta_{i,j_i}}^{\mathrm{T}}(\omega,t) \Lambda_{i,j_i}^{-1} z_{\theta_{i,j_i}}(\omega,t)\mathrm{d}\omega - \int_0^\infty \omega\mu_{\alpha_{i,j_i}}(\omega) z_{i,j_i}(\omega,t) z_{i,j_i}(\omega,t)\mathrm{d}\omega$$

$$- \widetilde{\theta}_{i,j_i}^{\mathrm{T}}\left(\frac{1}{\sigma_{i,j_i}} \Lambda_{i,j_i}^{-1} D^{\beta_{i,j_i}} \theta_{i,j_i} - \vartheta_{i,j_i}\left(\overline{x}_{i,j_i}\right) e_{i,j_i}\right) + e_{i,j_i} e_{i,j_i+1} - k_{i,j_i} e_{i,j_i}^2 - e_{i,j_i-1} e_{i,j_i} - \left(l_{i,j_i} - \overline{\varepsilon}_{i,j_i}\right)\left|e_{i,j_i}\right|$$

$$\le -\sum_{m=1}^{j_i-1}\left(\frac{1}{\sigma_{i,m}} \int_0^\infty \omega\mu_{\beta_{i,m}}(\omega) z_{\theta_{i,m}}^{\mathrm{T}}(\omega,t) \Lambda_{i,m}^{-1} z_{\theta_{i,m}}(\omega,t)\mathrm{d}\omega\right) - \sum_{m=1}^{j_i-1}\left(\int_0^\infty \omega\mu_{\alpha_{i,m}}(\omega) z_{i,m}^2(\omega,t)\mathrm{d}\omega\right)$$

$$- \sum_{m=1}^{j_i-1}\left(\widetilde{\theta}_{i,m}^{\mathrm{T}}\left(\frac{1}{\sigma_{i,m}} \Lambda_{i,m}^{-1} D^{\beta_{i,m}} \theta_{i,m} + \vartheta_{i,m}\left(\overline{x}_{i,m}\right) e_{i,m}\right)\right)$$

$$- \sum_{m=1}^{j_i-1}\left(k_{i,m} e_{i,m}^2 + \left(l_{i,m} - \overline{\varepsilon}_{i,m}\right)\left|e_{i,m}\right|\right) + e_{i,j_i-1} e_{i,j_i} - \frac{1}{\sigma_{i,j_i}} \int_0^\infty \omega\mu_{\beta_{i,j_i}}(\omega) z_{\theta_{i,j_i}}^{\mathrm{T}}(\omega,t) \Lambda_{i,j_i}^{-1} z_{\theta_{i,j_i}}(\omega,t)\mathrm{d}\omega$$

$$- \int_0^\infty \omega\mu_{\alpha_{i,j_i}}(\omega) z_{i,j_i}(\omega,t) z_{i,j_i}(\omega,t)\mathrm{d}\omega - \widetilde{\theta}_{i,j_i}^{\mathrm{T}}\left(\frac{1}{\sigma_{i,j_i i,j_i}}^{\mathrm{T}} \Lambda_{i,j_i}^{-1} D^{\beta_{i,j_i}} \theta_{i,j_i} - \vartheta_{i,j_i}\left(\overline{x}_{i,j_i}\right) e_{i,j_i}\right) + e_{i,j_i} e_{i,j_i+1} - k_{i,j_i} e_{i,j_i}^2 - e_{i,j_i-1} e_{i,j_i}$$

$$- \left(l_{i,j_i} - \overline{\varepsilon}_{i,j_i}\right)\left|e_{i,j_i}\right|$$

$$\le -\sum_{m=1}^{j_i}\left(\frac{1}{\sigma_{i,m}} \int_0^\infty \omega\mu_{\beta_{i,m}}(\omega) z_{\theta_{i,m}}^{\mathrm{T}}(\omega,t) \Lambda_{i,m}^{-1} z_{\theta_{i,m}}(\omega,t)\mathrm{d}\omega\right) - \sum_{m=1}^{j_i}\left(\int_0^\infty \omega\mu_{\alpha_{i,m}}(\omega) z_{i,m}^2(\omega,t)\mathrm{d}\omega\right)$$

$$- \sum_{m=1}^{j_i}\left(\widetilde{\theta}_{i,m}^{\mathrm{T}}\left(\frac{1}{\sigma_{i,m}} \Lambda_{i,m}^{-1} D^{\beta_{i,m}} \theta_{i,m} + \vartheta_{i,m}\left(\overline{x}_{i,m}\right) e_{i,m}\right)\right) - \sum_{m=1}^{j_i}\left(k_{i,m} e_{i,m}^2 + \left(l_{i,m} - \overline{\varepsilon}_{i,m}\right)\left|e_{i,m}\right|\right) + e_{i,j_i} e_{i,j_i+1}. \tag{48}$$

According to LaSalle invariance principle and equation (48), if $e_{i,j_i+1} = 0$, $k_{i,j_i} > 0$, $l_{i,j_i} > \overline{\varepsilon}_{i,j_i}$, and the fractional order adaptation laws are designed as

$$D^{\beta_{i,j_i}} \theta_{i,j_i} = -\sigma_{i,j_i} \Lambda_{i,j_i} \vartheta_{i,j_i}\left(\overline{x}_{i,j_i}\right) e_{i,j_i}, \tag{49}$$

one can get $\dot{V}_{i,j_i} < 0$.

Step (i, n_i): define

$$e_{i,n_i} = x_{i,n_i} - v_{i,n_i-1}, \tag{50}$$

where v_{i,n_i-1} is a virtual control input.

From Assumption 2 and (50), one has

$$\begin{aligned} D^{\alpha_{i,n_i}} e_{i,n_i} &= D^{\alpha_{i,n_i}} x_{i,n_i} - D^{\alpha_{i,n_i}} v_{i,n_i-1} \\ &= d_{i,n_i} u_i(\nu_i) + f_{i,n_i}(x) + g_{i,n_i}(x) - D^{\alpha_{i,n_i}} v_{i,n_i-1} \\ &= d_{i,n_i} \nu_i + d_{i,n_i} \Delta_i + f_{i,n_i}(x) + g_{i,n_i}(x) - D^{\alpha_{i,n_i}} v_{i,n_i-1} \\ &= d_{i,n_i} \nu_i + d_{i,n_i} \Delta_i + g_{i,n_i}(x) + F_{i,n_i}(x), \end{aligned} \tag{51}$$

where $F_{i,n_i}(x) = f_{i,n_i}(x) - D^{\alpha_{i,n_i}} v_{i,n_i-1}$ is an unknown function.

Let

$$\widehat{F}_{i,n_i}\left(x, \theta_{i,n_i}\right) = \theta_{i,n_i}^{\mathrm{T}} \vartheta_{i,n_i}(x), \tag{52}$$

where $\theta_{i,n_i} \in \mathbb{R}^{m_{i,n_i}}$ is parameter estimation.

Define the estimated error $\widetilde{\theta}_{i,n_i} = \theta_{i,n_i}^{*} - \theta_{i,n_i}$, and then the following equation can be obtained:

$$D^{\beta_{i,n_i}} \widetilde{\theta}_{i,n_i} = D^{\beta_{i,n_i}} \theta_{i,n_i}^{*} - D^{\beta_{i,n_i}} \theta_{i,n_i} = -D^{\beta_n} \theta_{i,n_i}, \tag{53}$$

where $\beta_{i,n_i} \in (0,1)$. Due to Lemma 1, (53) will be

$$\begin{cases} \dfrac{\partial z_{\theta_{i,n_i}}(\omega,t)}{\partial t} = -\omega z_{\theta_{i,n_i}}(\omega,t) - D^{\beta_{i,n_i}} \theta_{i,n_i}, \\ \widetilde{\theta}_{i,n_i} = \displaystyle\int_0^{\infty} \mu_{\beta_{i,n_i}}(\omega) z_{\theta_{i,n_i}}(\omega,t) \mathrm{d}\omega, \end{cases} \tag{54}$$

where $z_{\theta_{i,n_i}}(\omega,t) \in \mathbb{R}^{m_{i,n_i}}$ and $\mu_{\beta_{i,n_i}}(\omega) = \sin(\beta_{i,n_i}\pi)/\omega^{\beta_{i,n_i}}\pi$.

From (52), (51) can be rewritten as

$$\begin{aligned} D^{\alpha_{i,n_i}} e_{i,n_i} = {} & d_{i,n_i} \nu_i + d_{i,n_i} \Delta_i + \widetilde{\theta}_{i,n_i}^{\mathrm{T}} \vartheta_{i,n_i}(x) - \varepsilon_{i,n_i}(x) \\ & + \theta_{i,n_i}^{\mathrm{T}} \vartheta_{i,n_i}(x), \end{aligned} \tag{55}$$

where $\varepsilon_{i,n_i}(x) = \widehat{F}_{i,n_i}(x, \theta_{i,n_i}^{*}) - F_{i,n_i}(x)$, $|\varepsilon_{i,n_i}(\overline{x}_{i,n_i})| \le \overline{\varepsilon}_{i,n_i}$, and $\overline{\varepsilon}_{i,n_i} > 0$.

Design the controller ν_i as

$$\begin{aligned} \nu_i = \frac{1}{d_{i,n_i}} \Big(& -\theta_{i,n_i}^{\mathrm{T}} \vartheta_{i,n_i}(x) - k_{i,n_i} e_{i,n_i} - e_{i,n_i-1} \\ & - \left(l_{i,n_i} + \left| d_{i,n_i} \right| \zeta_i \right) \mathrm{sign}\left(e_{i,n_i} \right) \Big), \end{aligned} \tag{56}$$

where k_{i,n_i} and l_{i,n_i} are design parameters and ζ_i is the estimation of the unknown constant ζ_i^{*}.

Define $\widetilde{\zeta}_i = \zeta_i^{*} - \zeta_i$, and then the following equation is obtained:

$$D^{\chi_i} \widetilde{\zeta}_i = D^{\chi_i} \zeta_i^{*} - D^{\chi_i} \zeta_i = -D^{\chi_i} \zeta_i, \tag{57}$$

where $0 < \chi_i < 1$.

Due to Lemma 1, (57) will be

$$\begin{cases} \dfrac{\partial z_{\zeta_i}(\omega,t)}{\partial t} = -\omega z_{\overline{d}_i}(\omega,t) - D^{\chi_i} \zeta_i, \\ \widetilde{\zeta}_i = \displaystyle\int_0^{\infty} \mu_{\chi_i}(\omega) z_{\zeta_i}(\omega,t) \mathrm{d}\omega, \end{cases} \tag{58}$$

where $\mu_{\chi_i}(\omega) = \sin(\chi_i\pi)/\omega^{\chi_i}\pi$.

Substituting (50) and (56) into (55) gives

$$\begin{aligned} D^{\alpha_{i,n_i}} e_{i,n_i} = {} & -k_{i,n_i} e_{i,n_i} - \left(l_{i,n_i} + \left| d_{i,n_i} \right| \zeta_i \right) \mathrm{sign}\left(e_n \right) - e_{i,n_i-1} \\ & - \widetilde{\theta}_{i,n_i}^{\mathrm{T}} \vartheta_{i,n_i}(x) - \varepsilon_{i,n_i}(x) + d_{i,n_i} \Delta_i, \end{aligned} \tag{59}$$

then the following frequency distributed model is obtained:

$$\begin{cases} \dfrac{\partial z_{i,n_i}(\omega,t)}{\partial t} = -\omega z_{i,n_i}(\omega,t) - k_{i,n_i} e_{i,n_i} - \left(l_{i,n_i} + \left| d_{i,n_i} \right| \zeta_i \right) \mathrm{sign} \\ \quad \left(e_{i,n_i} \right) - e_{i,n_i-1} - \theta_{i,n_i}^{\mathrm{T}} \vartheta_{i,n_i}(x) - \varepsilon_{i,n_i}(x) + d_{i,n_i} \Delta_i, \\ e_{i,n_i} = \displaystyle\int_0^{\infty} \mu_{\alpha_{i,n_i}}(\omega) z_{i,n_i}(\omega,t) \mathrm{d}\omega, \end{cases} \tag{60}$$

where $\mu_{\alpha_{i,n_i}}(\omega) = \sin(\alpha_{i,n_i}\pi)/\omega^{\alpha_{i,n_i}}\pi$.

Selecting the Lyapunov function V_{i,n_i} as

$$\begin{aligned} V_{i,n_i} = {} & V_{i,n_i-1} + \frac{1}{2\sigma_{i,n_i}} \int_0^{\infty} \mu_{\beta_{i,n_i}}(\omega) z_{\theta_{i,n_i}}^{\mathrm{T}}(\omega,t) \Lambda_{i,n_i}^{-1} z_{\theta_{i,n_i}}(\omega,t) \mathrm{d}\omega \\ & + \frac{1}{2} \int_0^{\infty} \mu_{\alpha_{i,n_i}}(\omega) z_{i,n_i}^2(\omega,t) \mathrm{d}\omega \\ & + \frac{1}{2\rho_i} \int_0^{\infty} \mu_{\chi_i}(\omega) z_{\zeta_i}^2(\omega,t) \mathrm{d}\omega, \end{aligned} \tag{61}$$

where $\sigma_{i,n_i}, \rho_i > 0$.

Based on the procedures in step $(i, j_i), 3 \le j_i \le n_i - 1$, the derivative of V_{i,n_i} on the basis of frequency distributed model (54), (58), and (60) is

$$\begin{aligned}
\dot{V}_{i,n_i} &= \dot{V}_{i,n_i-1} - \frac{1}{\sigma_{i,n_i}}\int_0^\infty \omega\mu_{\beta_{i,n_i}}(\omega) z_{\theta_{i,n_i}}^{\mathrm{T}}(\omega,t)\Lambda_{i,n_i}^{-1} z_{\theta_{i,n_i}}(\omega,t)\mathrm{d}\omega - \int_0^\infty \omega\mu_{\alpha_{i,n_i}}(\omega) z_{i,n_i}^2(\omega,t)\mathrm{d}\omega - \frac{1}{\rho_i}\int_0^\infty \omega\mu_{\chi_i}(\omega) z_{\zeta_i}^2(\omega,t)\mathrm{d}\omega \\
&\quad - \widetilde{\theta}_{i,n_i}^{\mathrm{T}}\left(\frac{1}{\sigma_{i,n_i}}\Lambda_{i,n_i}^{-1} D^{\beta_{i,n_i}}\theta_{i,n_i} - \vartheta_{i,n_i}(x)e_{i,n_i}\right) - k_{i,n_i}e_{i,n_i}^2 - \left(l_{i,n_i} + \left|d_{i,n_i}\right|\zeta_i\right)\left|e_{i,n_i}\right| - e_{i,n_i-1}e_{i,n_i} - e_{i,n_i}\varepsilon_{i,n_i}(x) + d_{i,n_i}e_{i,n_i}\Delta_i - \frac{1}{\rho_i}\widetilde{\zeta}_i D^{\chi_i}\zeta_i \\
&\le -\sum_{m=1}^{n_i-1}\left(\frac{1}{\sigma_{i,m}}\int_0^\infty \omega\mu_{\beta_{i,m}}(\omega) z_{\theta_{i,m}}^{\mathrm{T}}(\omega,t)\Lambda_{i,m}^{-1} z_{\theta_{i,m}}(\omega,t)\mathrm{d}\omega\right) - \sum_{m=1}^{n_i-1}\left(\int_0^\infty \omega\mu_{\alpha_{i,m}}(\omega) z_{i,m}^2(\omega,t)\mathrm{d}\omega\right) \\
&\quad - \sum_{m=1}^{n_i-1}\left(\widetilde{\theta}_{i,m}^{\mathrm{T}}\left(\frac{1}{\sigma_{i,m}}\Lambda_{i,m}^{-1} D^{\beta_{i,m}}\theta_{i,m} + \vartheta_{i,m}\left(\overline{x}_{i,m}\right)e_{i,m}\right)\right) \\
&\quad - \sum_{m=1}^{n_i-1}\left(k_{i,m}e_{i,m}^2 + \left(l_{i,m} - \overline{\varepsilon}_{i,m}\right)\left|e_{i,m}\right|\right) + e_{i,j_i}e_{i,j_i+1} - \frac{1}{\sigma_{i,n_i}}\int_0^\infty \omega\mu_{\beta_{i,n_i}}(\omega) z_{\theta_{i,n_i}}^{\mathrm{T}}(\omega,t)\Lambda_{i,n_i}^{-1} z_{\theta_{i,n_i}}(\omega,t)\mathrm{d}\omega - \int_0^\infty \omega\mu_{\alpha_{i,n_i}}(\omega) z_{i,n_i}^2(\omega,t)\mathrm{d}\omega \\
&\quad - \frac{1}{\rho_i}\int_0^\infty \omega\mu_{\chi_i}(\omega) z_{\zeta_i}^2(\omega,t)\mathrm{d}\omega - \widetilde{\theta}_{i,n_i}^{\mathrm{T}}\left(\frac{1}{\sigma_{i,n_i}}\Lambda_{i,n_i}^{-1} D^{\beta_{i,n_i}}\theta_{i,n_i} - \vartheta_{i,n_i}(x)e_{i,n_i}\right) - k_{i,n_i}e_{i,n_i}^2 - \left(l_{i,n_i} + \left|d_{i,n_i}\right|\zeta_i\right)\left|e_{i,n_i}\right| - e_{i,n_i-1}e_{i,n_i} + \left|e_{i,n_i}\right|\overline{\varepsilon}_{i,n_i} \\
&\quad + \left|d_{i,n_i}\right|\left|e_{i,n_i}\right|\zeta_i^* - \frac{1}{\rho_i}\widetilde{\zeta}_i D^{\chi_i}\zeta_i \\
&\le -\sum_{m=1}^{n_i}\left(\frac{1}{\sigma_{i,m}}\int_0^\infty \omega\mu_{\beta_{i,m}}(\omega) z_{\theta_{i,m}}^{\mathrm{T}}(\omega,t)\Lambda_{i,m}^{-1} z_{\theta_{i,m}}(\omega,t)\mathrm{d}\omega\right) - \sum_{m=1}^{n_i}\left(\int_0^\infty \omega\mu_{\alpha_{i,m}}(\omega) z_{i,m}^2(\omega,t)\mathrm{d}\omega\right) \\
&\quad - \sum_{m=1}^{n_i}\left(\widetilde{\theta}_{i,m}^{\mathrm{T}}\left(\frac{1}{\sigma_{i,m}}\Lambda_{i,m}^{-1} D^{\beta_{i,m}}\theta_{i,m} + \vartheta_{i,m}\left(\overline{x}_{i,m}\right)e_{i,m}\right)\right) - \sum_{m=1}^{n_i}\left(k_{i,m}e_{i,m}^2 + \left(l_{i,m} - \overline{\varepsilon}_{i,m}\right)\left|e_{i,m}\right|\right) - \widetilde{\zeta}_i\left(\frac{1}{\rho_i}D^{\chi_i}\zeta_i - \left|d_{i,n_i}\right|\left|e_{i,n_i}\right|\right).
\end{aligned} \tag{62}$$

To update θ_{i,n_i} and ζ_i, design the fractional order adaptation laws as follows:

$$D^{\beta_{i,n_i}}\theta_{i,n_i} = -\sigma_{i,n_i}\Lambda_{i,n_i}\vartheta_{i,n_i}(x)e_{i,n_i}, \tag{63}$$

$$D^{\chi_i}\zeta_i = \rho_i\left|d_{i,n_i}\right|\left|e_{i,n_i}\right|. \tag{64}$$

According to (62)–(64), and LaSalle invariance principle, if $k_{i,n_i} > 0$ and $l_{i,n_i} > \overline{\varepsilon}_{i,n_i}$, one can get $\dot{V}_{i,n_i} < 0$.

The following Theorem 1 gives the stability result of the closed-loop system.

Theorem 1. *Consider the incommensurate fractional order nonlinear MIMO system (7) with unknown nonlinearities and external disturbance; if the control input is chosen as (56) with (19), (31), and (44) and the adaptation laws are designed as (25), (37), (49), (63), and (64), then all the signals in the closed-loop system are globally uniformly bounded with the proper design parameters $k_{i,j_i}, l_{i,j_i}, \Lambda_{i,j_i}, \sigma_{i,j_i}, \beta_{i,j_i}, \rho_i$, and χ_i, $j_i = 1, 2, \ldots, n_i$, $i = 1, 2, \ldots, n$, and the tracking error $e_{i,1} = y_i - y_{i,d}$ tends to zero asymptotically when $t \longrightarrow \infty$.*

Proof. According to step $(i,1)$, $(i,2)$, (i,j_i), (i,n_i), $3 \le j_i \le n_i - 1$, if the control input is chosen as (56) with (19), (31), and (44), and the adaptation laws are designed as (25), (37), (49), (63), and (64), then with a proper choice of the design parameters $k_{i,j_i}, l_{i,j_i}, \Lambda_{i,j_i}, \sigma_{i,j_i}, \beta_{i,j_i}, \rho_i$, and χ_i, one can get $\dot{V}_{i,j_i} < 0$, $j_i = 1, 2, \ldots, n_i$, $i = 1, 2, \ldots, n$. Due to the LaSalle invariant principle, $z_{i,j_i}(\omega,t)$, $z_{\theta_{i,j_i}}(\omega,t)$, and $z_{\zeta_i}(\omega,t)$ can be close to the set of all points. When $\dot{V}_{i,j_i} = 0$, $z_{i,j_i}(\omega,t) = 0$, $z_{\theta_{i,j_i}}(\omega,t) = 0$, and $z_{\zeta_i}(\omega,t) = 0$ can be obtained, which is the only equilibrium point. That is the error variables $e_{i,1}$, $\widetilde{\theta}_{i,j_i}$, and $\widetilde{\zeta}_i$ convergent to zero asymptotically. Therefore, the tracking error $e_{i,1}$ tends to zero asymptotically and all the signals are uniformly bounded. □

Remark 2. The orders of the parameter estimation laws β_{i,j_i} and χ_i are not fixed to the system order α_{i,j_i}. This brings more degree of freedom in our design and we can achieve better control performance by adjusting β_{i,j_i} and χ_i. In addition, if $\alpha_{i,j_i} = \alpha$, the result will be commensurate fractional order system with input constraints. Our design scheme is still applicable.

Remark 3. It can be found that the tracking errors can be made smaller by increasing the parameters k_{i,j_i}, when the

parameters $l_{i,j_i}, \Lambda_{i,j_i}, \sigma_{i,j_i}, \beta_{i,j_i}, \rho_i$, and χ_i are fixed. Meanwhile, when the control gain k_{i,j_i} is too big, the parameters may be drifting. In order to balance the system performance and control action in applications, the design parameters must be carefully chosen.

Remark 4. In fact, the tracking error may get into a smaller range of zero due to the sign function used in controller (56) with (19), (31), and (44), which may result the chattering phenomenon. Meanwhile, the sign function can be replaced by the continuous function $\arctan(10\cdot)$ to alleviate the chattering phenomenon.

4. Simulation

Two examples are presented in this simulation section to show the effectiveness of the proposed method.

4.1. Example 1. The following incommensurate fractional order nonlinear MIMO system is considered

$$\begin{cases} D^{0.5}x_{1,1} = 0.8x_{1,2} - 0.095x_{1,1}^2 + 0.25x_{1,1}^3, \\ D^{0.6}x_{1,2} = 0.95u_1 + \dfrac{x_{1,2} - 0.5x_{1,1}^2}{1 + 0.8x_{1,1}^3} - 0.15\sin\left(x_{1,1}^2 x_{1,2}\right), \\ y_1 = x_{1,1}, \\ D^{0.65}x_{2,1} = 0.45x_{2,2} - 0.1x_{2,1}^3 + 0.5\sin\left(x_{2,1}\right), \\ D^{0.8}x_{2,2} = 0.6u_2 + 0.3x_{1,2}x_{2,2} - 0.6x_{2,1}^2 + 0.1\cos\left(x_{1,2}x_{2,1}\right), \\ y_2 = x_{2,1}, \end{cases} \tag{65}$$

where $f_{1,1}(\overline{x}_{1,1}) = -0.06x_{1,1}^2$, $f_{1,2}(x) = x_{1,2} - 0.5x_{1,1}^2/1 + 0.8x_{1,1}^3$, $f_{2,1}(\overline{x}_{2,1}) = -0.1x_{2,1}^3$, and $f_{2,2}(x) = 0.3x_{1,2}x_{2,2} - 0.6x_{2,1}^2$ are the unknown functions. $g_{1,1}(\overline{x}_{1,1}) = 0.25x_{1,1}^3$, $g_{1,2}(x) = -0.15\sin(x_{1,1}^2 x_{1,2})$, $g_{2,1}(\overline{x}_{2,1}) = 0.5\sin(x_{2,1})$, and $g_{2,2}(x) = 0.1\cos(x_{1,2}x_{2,1})$ are the known continuous nonlinear functions.

The slop parameters of dead-zone are $a_{1,r} = a_{1,l} = a_{2,r} = a_{2,l} = 1$. The dead-zone ranges are considered as $b_{1,r} = b_{1,l} = 11$ and $b_{2,r} = b_{2,l} = 5$. The saturation levels are $\xi_{1,\max} = 16$, $\xi_{1,\min} = 15$, $\xi_{2,\max} = 13$, and $\xi_{2,\min} = 8$.

The reference signal for the system output are chosen as $y_{1,d} = 0.8\sin(t + 0.5)$ and $y_{2,d} = 0.6\cos(t + 0.15)$.

The following membership functions to deal with the unknown nonlinear terms are designed as

$$\begin{aligned} \vartheta_{1,1}\left(\overline{x}_{1,1}\right) &= \exp\left(-\frac{\left(x_{1,1} - x_{s_1}\right)^2}{\delta_1^2}\right), \\ \vartheta_{1,2}\left(\overline{x}_{1,2}\right) &= \exp\left(-\frac{\left(x_{1,1} - x_{s_1}\right)^2}{\delta_1^2} - \frac{\left(x_{1,2} - x_{s_2}\right)^2}{\delta_2^2}\right), \\ \vartheta_{2,1}\left(\overline{x}_{2,1}\right) &= \exp\left(-\frac{\left(x_{1,1} - x_{s_1}\right)^2}{\delta_1^2}\right), \\ \vartheta_{2,2}\left(\overline{x}_{2,2}\right) &= \exp\left(-\frac{\left(x_{1,2} - x_{s_1}\right)^2}{\delta_1^2} - \frac{\left(x_{2,1} - x_{s_2}\right)^2}{\delta_2^2} - \frac{\left(x_{2,2} - x_{s_3}\right)^2}{\delta_3^2}\right), \\ \delta_1 &= \delta_2 = \delta_3 = 0.5, \\ x_{s_1} &\in \left\{0.5s_1 - 2 \,\middle|\, s_1 = 1, 2, \ldots, 6\right\}, \\ x_{s_2} &\in \left\{s_2 - 2 \,\middle|\, s_2 = 1, 2, 3\right\}, \\ x_{s_3} &\in \left\{0.5s_3 - 1.5 \,\middle|\, s_3 = 1, 2, \ldots, 5\right\}. \end{aligned} \tag{66}$$

The design parameters are chosen as $k_{1,1} = 45, k_{1,2} = 35, k_{2,1} = 115, k_{2,2} = 29$, $l_{1,1} = l_{1,2} = l_{2,1} = l_{2,2} = 0.01$, $\sigma_{1,1} = \sigma_{1,2} = \sigma_{2,1} = \sigma_{2,2} = 0.01$, $\Lambda_{1,1} = I_6, \Lambda_{1,2} = I_{18}, \Lambda_{2,1} = I_6, \Lambda_{2,2} = I_{90}$, $\rho_1 = \rho_2 = 0.01$, $\beta_{1,1} = \beta_{1,2} = \beta_{2,1} = \beta_{2,2} = 0.6$, and $\chi_1 = \chi_2 = 0.6$. The initial condition are $x_{1,1}(0) = x_{1,2}(0) = x_{2,1}(0) = x_{2,2}(0) = 0$, $\theta_{1,1}(0) = 0_{6\times1}, \theta_{1,2}(0) = 0_{18\times1}$, $\theta_{2,1}(0) = 0_{6\times1}, \theta_{2,2}(0) = 0_{90\times1}$, and $\zeta_1(0) = \zeta_2(0) = 0$.

The trajectories of system output, reference signal, and tracking error are presented in Figure 1 to show the tracking performance of the control system. It demonstrates that the reference signals could be tracked well by the output signals subject to the unknown nonlinear terms and uncertain disturbances. Figure 2 displays the trajectories of the system states $x_{1,2}$ and $x_{2,2}$. The estimation of ζ_1 and ζ_2 are displayed in Figure 3, and system control input u_1 and u_2 are presented in Figure 4. It is clear that all the signals in the closed loop adaptive control system are bounded.

4.2. Example 2. To show more results of the proposed method, the following incommensurate fractional order nonlinear MIMO system is considered:

$$\begin{cases} D^{0.9}x_{1,1} = 0.3x_{1,2} - 0.8\sin\left(x_{1,1}\right) + 0.6x_{1,1}^3\cos\left(x_{1,1}\right), \\ D^{0.8}x_{1,2} = 0.8u_1 + 0.13\cos\left(x_{1,1}^3 x_{1,2}^2\right) - 0.5\cos\left(x_{1,1}^2 x_{1,2}^3\right), \\ y_1 = x_{1,1}, \\ D^{0.85}x_{2,1} = 0.5x_{2,2} - 0.8\sin\left(x_{2,1}\right) + 0.5x_{2,1}\sin\left(x_{2,1}\right), \\ D^{0.6}x_{2,2} = 0.6u_2 + \sin\left(x_{1,1}x_{1,2}^2x_{2,1}\right) + 0.3\cos\left(x_{1,1}x_{1,2}x_{2,1}\right), \\ y_2 = x_{2,1}, \end{cases} \tag{67}$$

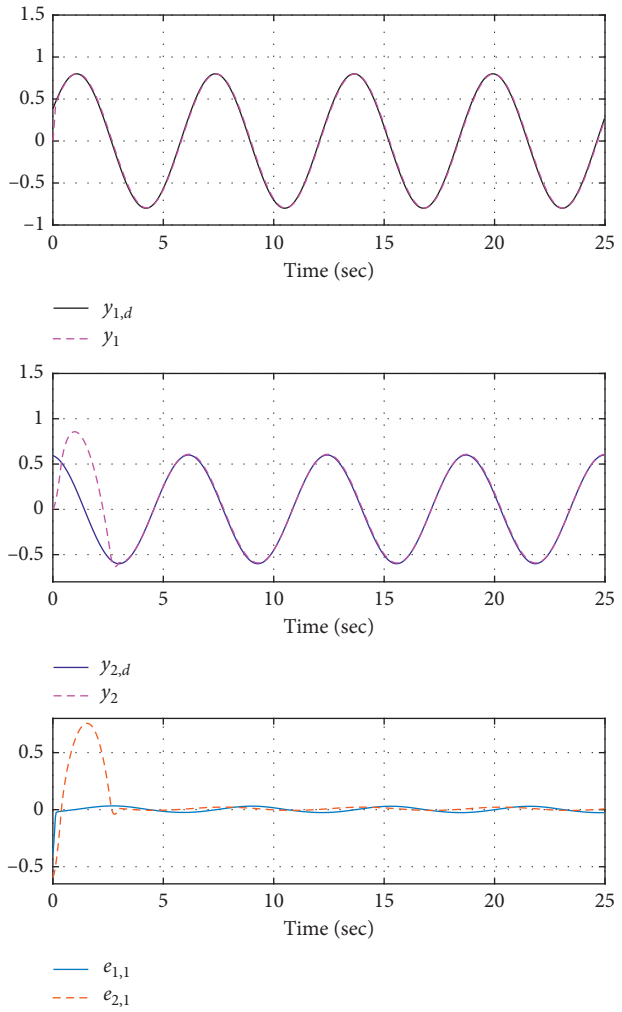

FIGURE 1: Evolution of $y_1.y_2$, $y_{1,d}$, $y_{2,d}$ and tracking errors $e_{1,1}$ and $e_{2,1}$.

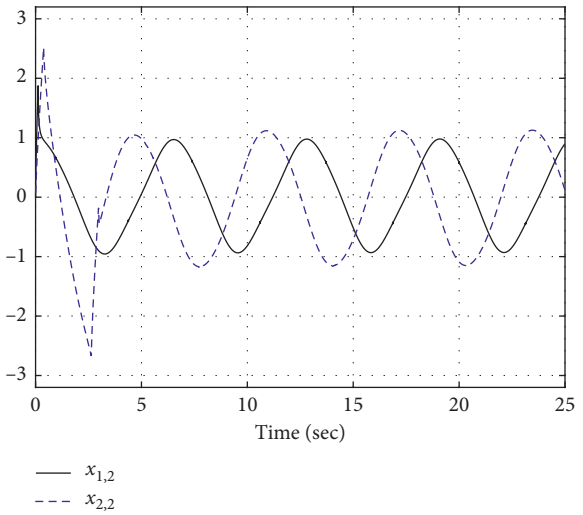

FIGURE 2: Evolution of states $x_{1,2}$ and $x_{2,2}$.

where $f_{1,1}(\overline{x}_{1,1}) = -0.8\sin(x_{1,1})$, $f_{1,2}(x) = 0.13\cos(x_{1,1}^3 x_{1,2}^2)$, $f_{2,1}(\overline{x}_{2,1}) = -0.8\sin(x_{2,1})$, and $f_{2,2}(x) = \sin(x_{1,1}x_{1,2}^2 x_{2,1})$ are the unknown functions. $g_{1,1}(\overline{x}_{1,1}) = 0.6x_{1,1}^3\cos(x_{1,1})$, $g_{1,2}(x) = -0.5\cos(x_{1,1}^2 x_{1,2}^3)$, $g_{2,1}(\overline{x}_{2,1}) = 0.5x_{2,1}\sin(x_{2,1})$, and $g_{2,2}(x) = 0.3\cos(x_{1,1}x_{1,2}x_{2,1})$ are the known continuous nonlinear functions.

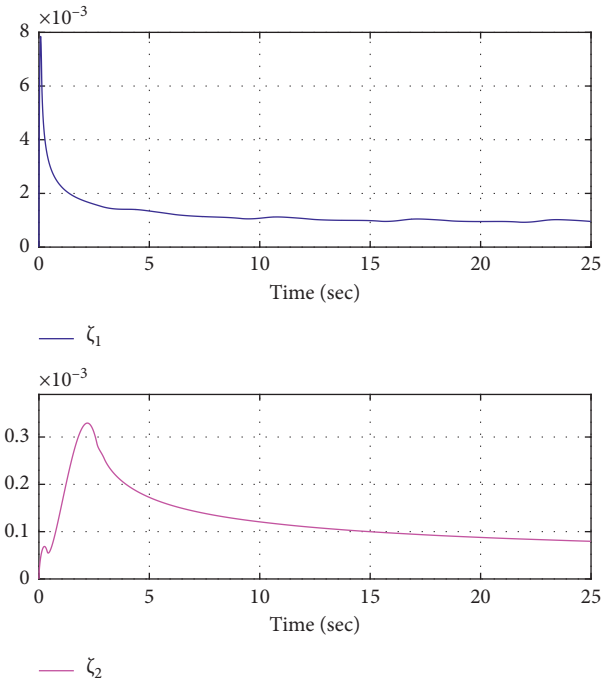

FIGURE 3: Evolution of the estimation of the ζ_1 and ζ_2.

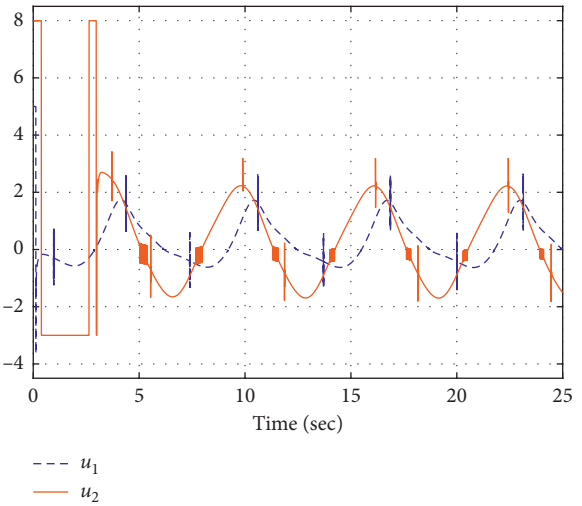

FIGURE 4: Evolution of the control inputs u_1 and u_2.

The slop parameters of dead-zone are $a_{1,r} = a_{1,l} = a_{2,r} = a_{2,l} = 1$. The dead-zone ranges are considered as $b_{1,r} = b_{1,l} = 8$ and $b_{2,r} = b_{2,l} = 6$. The saturation levels are $\xi_{1,\max} = 18$, $\xi_{1,\min} = 16$, $\xi_{2,\max} = 25$, and $\xi_{2,\min} = 23$.

The reference signal for the system output are chosen as $y_{1,d} = 0.95\sin(0.8t + 0.1)$ and $y_{2,d} = 0.8\sin(t + 3)$.

The following membership functions to deal with the unknown nonlinear terms are designed as

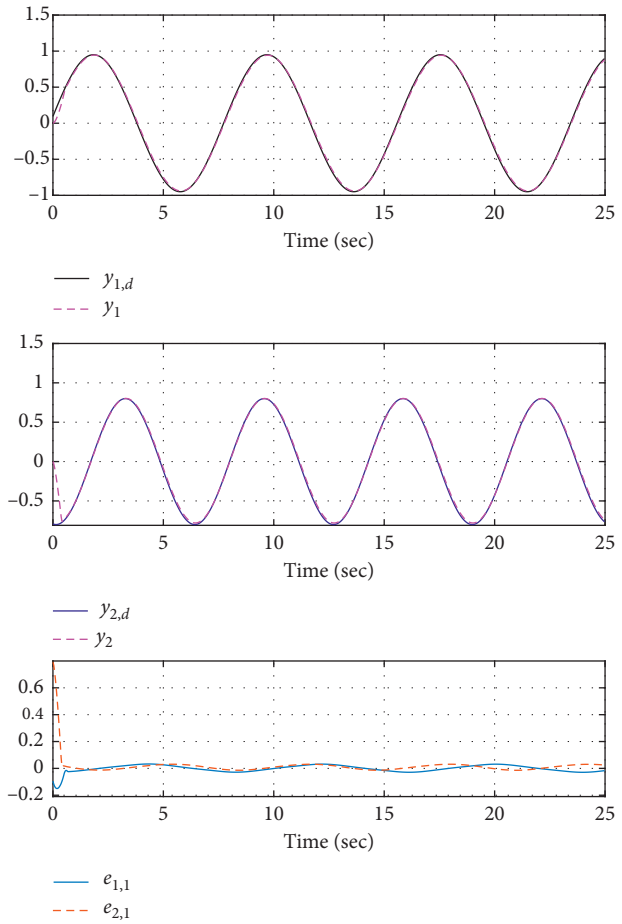

FIGURE 5: Evolution of $y_1.y_2$, $y_{1,d}$, $y_{2,d}$, and tracking errors $e_{1,1}$ and $e_{2,1}$.

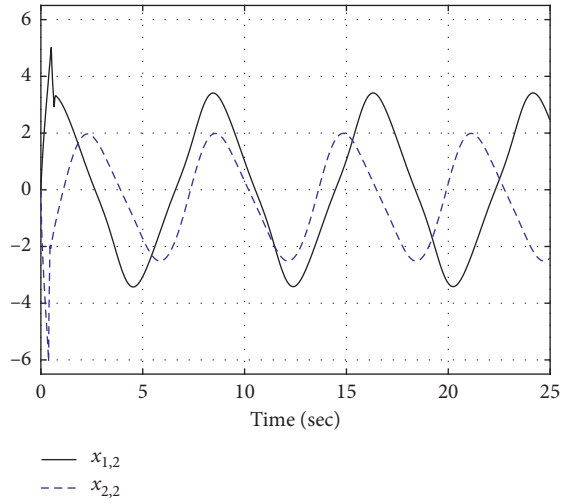

FIGURE 6: Evolution of states $x_{1,2}$ and $x_{2,2}$.

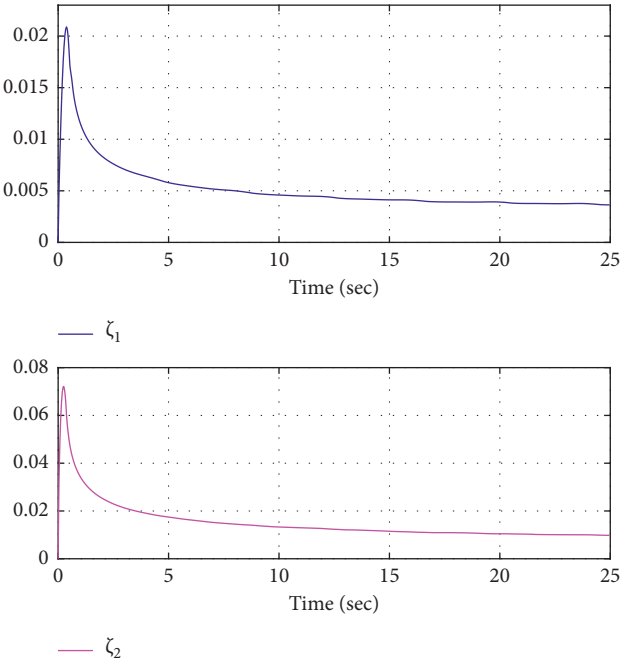

FIGURE 7: Evolution of the estimation of the ζ_1 and ζ_2.

$$\vartheta_{1,1}(\overline{x}_{1,1}) = \exp\left(-\frac{(x_{1,1}-x_{s_1})^2}{\delta_1^2}\right),$$

$$\vartheta_{1,2}(\overline{x}_{1,2}) = \exp\left(-\frac{(x_{1,1}-x_{s_1})^2}{\delta_1^2} - \frac{(x_{1,2}-x_{s_2})^2}{\delta_2^2}\right),$$

$$\vartheta_{2,1}(\overline{x}_{2,1}) = \exp\left(-\frac{(x_{1,1}-x_{s_1})^2}{\delta_1^2}\right),$$

$$\vartheta_{2,2}(\overline{x}_{2,2}) = \exp\left(-\frac{(x_{1,2}-x_{s_1})^2}{\delta_1^2} - \frac{(x_{2,1}-x_{s_2})^2}{\delta_2^2} - \frac{(x_{2,2}-x_{s_3})^2}{\delta_3^2}\right),$$

$$\delta_1 = \delta_2 = \delta_3 = 0.5,$$

$$x_{s_1} \in \{0.5s_1 - 2 \mid s_1 = 1, 2, \ldots, 6\},$$

$$x_{s_2} \in \{s_2 - 2 \mid s_2 = 1, 2, 3\},$$

$$x_{s_3} \in \{0.5s_3 - 1.5 \mid s_3 = 1, 2, \ldots, 5\}. \tag{68}$$

The design parameters are chosen as $k_{1,1} = 125, k_{1,2} = 45, k_{2,1} = 115$, and $k_{2,2} = 25$, $l_{1,1} = l_{1,2} = l_{2,1} = l_{2,2} = 0.01$, $\sigma_{1,1} = \sigma_{1,2} = \sigma_{2,1} = \sigma_{2,2} = 0.03$, $\Lambda_{1,1} = I_6, \Lambda_{1,2} = I_{18}, \Lambda_{2,1} =$

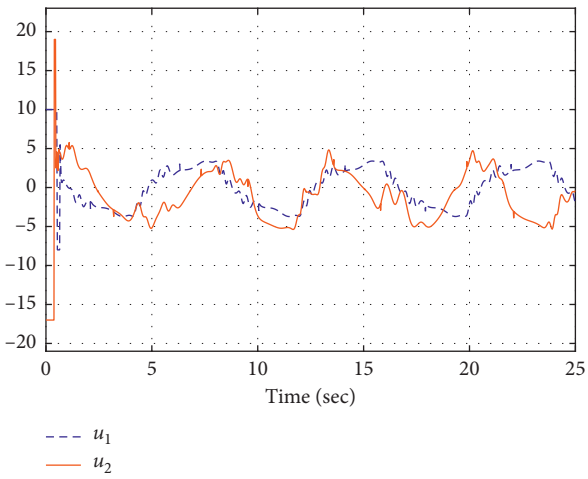

Figure 8: Evolution of the control inputs u_1 and u_2.

I_6, and $\Lambda_{2,2} = I_{90}$, $\rho_1 = \rho_2 = 0.01$, $\beta_{1,1} = \beta_{1,2} = \beta_{2,1} = \beta_{2,2} = 0.7$, and $\chi_1 = \chi_2 = 0.6$. The initial conditions are $x_{1,1}(0) = x_{1,2}(0) = x_{2,1}(0) = x_{2,2}(0) = 0$, $\theta_{1,1}(0) = 0_{6\times1}$, $\theta_{1,2}(0) = 0_{18\times1}$, $\theta_{2,1}(0) = 0_{6\times1}$, $\theta_{2,2}(0) = 0_{90\times1}$, and $\zeta_1(0) = \zeta_2(0) = 0$.

Figure 5 represents the tracking performance, and the tracking errors $e_{1,1}$ and $e_{2,1}$ converge to a smaller range of zero. Figure 6 shows the trajectories of the system states $x_{1,2}$ and $x_{2,2}$. Figure 7 depicts the estimation of the ζ_1 and ζ_2. The control inputs u_1 and u_2 are depicted in Figure 8. It is clear that the signals in the closed loop system are bounded.

The abovementioned simulation results demonstrate that although there are unknown nonlinearities and input constraints, the proposed adaptive NN controller can guarantee the good tracking performance, and all the closed-loop signals are bounded.

5. Conclusion

An adaptive NN backstepping control scheme for a class of incommensurate uncertain fractional order nonlinear MIMO systems subjected to with dead-zone and saturation is proposed in this paper. The RBF NN is used to approximate an unknown nonlinear terms in each step of the backstepping procedure. The adaptive NN controller is constructed by the backstepping and adaptive technique. The adaptation laws with incommensurate fractional order for parameters estimation are designed to compensate unknown nonlinearities in the controller. Through the simulation results, it is verified that the tracking errors of the closed-loop system can reach a small neighborhood of zero even in the presence of dead-zone and saturation simultaneously. This ensures the efficacy of the proposed approach. In the future, the selection of the orders of the parameter estimation laws will be considered for the control adjustment.

Data Availability

The data used to support the findings of this study are included within the article, which are available for researchers.

Conflicts of Interest

The authors declare that they have no conflicts of interest.

Acknowledgments

This paper was supported in part by the Doctoral Program of Shandong Provincial Natural Science Foundation of China (ZR2019BF048), Key R&D Program of Shandong Province in 2019 (Public Welfare Science and Technology Tackling Category) (2019GGX104071), Shandong Scientific Research Projects of Colleges and Universities (J18KA062), and Foundation of State Key Laboratory of Automotive Simulation and Control (20171105).

References

[1] T. J. Freeborn, B. Maundy, and A. S. Elwakil, "Fractional-order models of supercapacitors, batteries and fuel cells: a survey," *Materials for Renewable and Sustainable Energy*, vol. 4, no. 3, p. 9, 2015.

[2] Z. Gao, "Robust stabilization criterion of fractional-order controllers for interval fractional-order plants," *Automatica*, vol. 61, pp. 9–17, 2015.

[3] Y. Luo, Y. Chen, and Y. Pi, "Experimental study of fractional order proportional derivative controller synthesis for fractional order systems," *Mechatronics*, vol. 21, no. 1, pp. 204–214, 2011.

[4] I. Petráš and R. L. Magin, "Simulation of drug uptake in a two compartmental fractional model for a biological system," *Communications in Nonlinear Science and Numerical Simulation*, vol. 16, no. 12, pp. 4588–4595, 2011.

[5] I. Podlubny, *Fractional Differential Equations*, Academic Press, Cambridge, MA, USA, 1999.

[6] J. Shen and J. Lam, "Non-existence of finite-time stable equilibria in fractional-order nonlinear systems," *Automatica*, vol. 50, no. 2, pp. 547–551, 2014.

[7] M. A. Duarte-Mermoud, N. Aguila-Camacho, J. A. Gallegos, and R. Castro-Linares, "Using general quadratic lyapunov functions to prove lyapunov uniform stability for fractional order systems," *Communications in Nonlinear Science and Numerical Simulation*, vol. 22, no. 1–3, pp. 650–659, 2015.

[8] H.-B. Bao and J.-D. Cao, "Projective synchronization of fractional-order memristor-based neural networks," *Neural Networks*, vol. 63, pp. 1–9, 2015.

[9] C. A. Monje, Y. Chen, B. M. Vinagre, D. Xue, and V. Feliu-Batlle, *Fractional-order Systems and Controls: Fundamentals and Applications*, Springer Science & Business Media, Berlin, Germany, 2010.

[10] I. Pan and S. Das, *Intelligent fractional order systems and control: an introduction*, Springer, Berlin, Germany, 2012.

[11] D. Baleanu, J. A. T. Machado, and A. C. Luo, *Fractional Dynamics and Control*, Springer Science & Business Media, Berlin, Germany, 2011.

[12] Y. Xu, Y. Li, and D. Liu, "A method to stochastic dynamical systems with strong nonlinearity and fractional damping," *Nonlinear Dynamics*, vol. 83, no. 4, pp. 2311–2321, 2016.

[13] Y. Xu and Z. Zheng, "Quenching phenomenon of a time-fractional diffusion equation with singular source term," *Mathematical Methods in the Applied Sciences*, vol. 40, no. 16, pp. 5750–5759, 2017.

[14] Y. Xu, Y. Li, and D. Liu, "Response of fractional oscillators with viscoelastic term under random excitation," *Journal of*

Computational and Nonlinear Dynamics, vol. 9, no. 3, Article ID 031015, 2014.

[15] Y. Xu, "Quenching phenomenon in a fractional diffusion equation and its numerical simulation," *International Journal of Computer Mathematics*, vol. 95, no. 1, pp. 98–113, 2018.

[16] Y. Guo, C. Lin, B. Chen, and Q. Wang, "Necessary and sufficient conditions for the dynamic output feedback stabilization of fractional-order systems with order $0 < \alpha < 1$," *Science China Information Sciences*, vol. 62, no. 9, Article ID 199201, 2019.

[17] K. Khettab, S. Ladaci, and Y. Bensafia, "Fuzzy adaptive control of fractional order chaotic systems with unknown control gain sign using a fractional order nussbaum gain," *IEEE/CAA Journal of Automatica Sinica*, vol. 6, no. 3, pp. 816–823, 2019.

[18] B. Bourouba and S. Ladaci, "Robust fuzzy adaptive sliding mode stabilization for fractional-order chaos," *Algorithms*, vol. 11, no. 7, p. 101, 2018.

[19] R. Sakthivel, C. K. Ahn, and M. Joby, "Fault-tolerant resilient control for fuzzy fractional order systems," *IEEE Transactions on Systems, Man, and Cybernetics: Systems*, vol. 49, no. 9, pp. 1797–1805, 2019.

[20] A. T. Azar, A. G. Radwan, and S. Vaidyanathan, *Mathematical Techniques of Fractional Order Systems*, Elsevier, Amsterdam, Netherlands, 2018.

[21] X. Zhang and Y. Chen, "Admissibility and robust stabilization of continuous linear singular fractional order systems with the fractional order α: the $0 < \alpha < 1$ case," *ISA Transactions*, vol. 82, pp. 42–50, 2018.

[22] J. Fei and C. Lu, "Adaptive fractional order sliding mode controller with neural estimator," *Journal of the Franklin Institute*, vol. 355, no. 5, pp. 2369–2391, 2018.

[23] Y. Wei, Y. Chen, T. Liu, and Y. Wang, "Lyapunov functions for nabla discrete fractional order systems," *ISA Transactions*, vol. 88, pp. 82–90, 2019.

[24] S. Mirzajani, M. P. Aghababa, and A. Heydari, "Adaptive T-S fuzzy control design for fractional-order systems with parametric uncertainty and input constraint," *Fuzzy Sets and Systems*, vol. 365, pp. 22–39, 2019.

[25] S. Ladaci and A. Charef, "On fractional adaptive control," *Nonlinear Dynamics*, vol. 43, no. 4, pp. 365–378, 2006.

[26] B. Shi, J. Yuan, and C. Dong, "On fractional model reference adaptive control," *The Scientific World Journal*, vol. 2014, Article ID 521625, 8 pages, 2014.

[27] D. Sheng, Y. Wei, S. Cheng, and J. Shuai, "Adaptive backstepping control for fractional order systems with input saturation," *Journal of the Franklin Institute*, vol. 354, no. 5, pp. 2245–2268, 2017.

[28] M. Chen, C. Jiang, and Q. Wu, "Backstepping control for a class of uncertain nonlinear systems with neural network," *International Journal of Nonlinear Science*, vol. 3, no. 2, pp. 137–143, 2007.

[29] Y. Wei, Y. Chen, S. Liang, and Y. Wang, "A novel algorithm on adaptive backstepping control of fractional order systems," *Neurocomputing*, vol. 165, pp. 395–402, 2015.

[30] Q. Wang, J. Zhang, D. Ding, and D. Qi, "Adaptive mittag-leffler stabilization of a class of fractional order uncertain nonlinear systems," *Asian Journal of Control*, vol. 18, no. 6, pp. 2343–2351, 2016.

[31] Y. Wei, P. W. Tse, Z. Yao, and Y. Wang, "Adaptive backstepping output feedback control for a class of nonlinear fractional order systems," *Nonlinear Dynamics*, vol. 86, no. 2, pp. 1047–1056, 2016.

[32] C. Hua, J. Ning, G. Zhao, and Y. Li, "Output feedback nn tracking control for fractional-order nonlinear systems with time-delay and input quantization," *Neurocomputing*, vol. 290, pp. 229–237, 2018.

[33] S. Shao, M. Chen, S. Chen, and Q. Wu, "Adaptive neural control for an uncertain fractional-order rotational mechanical system using disturbance observer," *IET Control Theory and Applications*, vol. 10, no. 16, pp. 1972–1980, 2016.

[34] N. Liu and J. Fei, "Adaptive fractional sliding mode control of active power filter based on dual rbf neural networks," *IEEE Access*, vol. 5, pp. 27590–27598, 2017.

[35] Y. Wu and H. Lv, "Adaptive neural network backstepping control for a class of uncertain fractional-order chaotic systems with unknown backlash-like hysteresis," *Aip Advances*, vol. 6, no. 8, Article ID 085121, 2016.

[36] C. Wang and M. Liang, "Adaptive nn tracking control for nonlinear fractional order systems with uncertainty and input saturation," *IEEE Access*, vol. 6, pp. 70035–70044, 2018.

[37] Q. Zhou, L. Wang, C. Wu, H. Li, and H. Du, "Adaptive fuzzy control for nonstrict-feedback systems with input saturation and output constraint," *IEEE Transactions on Systems, Man, and Cybernetics: Systems*, vol. 47, no. 1, pp. 1–12, 2016.

[38] M. R. Askari, M. Shahrokhi, and M. Khajeh Talkhoncheh, "Observer-based adaptive fuzzy controller for nonlinear systems with unknown control directions and input saturation," *Fuzzy Sets and Systems*, vol. 314, pp. 24–45, 2017.

[39] C. Wang and M. Liang, "Adaptive backstepping control of a class of incommensurate fractional order nonlinear mimo systems with unknown disturbance," *IEEE Access*, vol. 7, pp. 150949–150959, 2019.

[40] W. Zhu, W. Li, P. Zhou, and C. Yang, "Consensus of fractional-order multi-agent systems with linear models via observer-type protocol," *Neurocomputing*, vol. 230, pp. 60–65, 2017.

[41] P. Gong, "Distributed tracking of heterogeneous nonlinear fractional-order multi-agent systems with an unknown leader," *Journal of the Franklin Institute*, vol. 354, no. 5, pp. 2226–2244, 2017.

[42] Z. Yang, S. Zheng, F. Liu, and Y. Xie, "Adaptive output feedback control for fractional-order multi-agent systems," *ISA Transactions*, 2019, In press.

[43] A. A. Jafari, S. M. A. Mohammadi, M. M. Farsangi, and M. H. Naseriyeh, "Observer-based fractional-order adaptive type-2 fuzzy backstepping control of uncertain nonlinear mimo systems with unknown dead-zone," *Nonlinear Dynamics*, vol. 95, no. 4, pp. 3249–3274, 2019.

[44] S. Das, *Functional Fractional Calculus for System Identification and Controls*, Springer, Berlin, Germany, 2008.

[45] J. C. Trigeassou, N. Maamri, and A. Oustaloup, "The infinite state approach: origin and necessity," *Computers & Mathematics with Applications*, vol. 66, no. 5, pp. 892–907, 2013.

[46] R. M. Sanner and J.-J. E. Slotine, "Gaussian networks for direct adaptive control," *IEEE Transactions on Neural Networks*, vol. 3, no. 6, pp. 837–863, 1992.

[47] S. Tong and Y. Li, "Adaptive fuzzy output feedback control of mimo nonlinear systems with unknown dead-zone inputs," *IEEE Transactions on Fuzzy Systems*, vol. 21, no. 1, pp. 134–146, 2013.

[48] T. Basar, *An Invariance Principle in the Theory of Stability*, Wiley-IEEE Press, Hoboken, NJ, USA, 2001.

Hindawi
Complexity
Volume 2019, Article ID 5453184, 10 pages
https://doi.org/10.1155/2019/5453184

Research Article

Risk Analysis of Emergency Based on Fuzzy Evidential Reasoning

Xiaojiao Qiao[1] **and Dan Shi**[2]

[1]*School of Management, Tianjin University of Technology, Tianjin, China*
[2]*School of Business, Dalian University of Technology, Panjin, LiaoNing Province, China*

Correspondence should be addressed to Dan Shi; shidan56@dlut.edu.cn

Received 26 July 2019; Revised 12 October 2019; Accepted 1 November 2019; Published 22 November 2019

Guest Editor: Baltazar Aguirre-Hernandez

Risk analysis of emergency is vital to effective emergency management. However, conventional analysis is challenged by the emerging problems as risk of emergency appearing increasingly complicated. The risk attributes of emergency originate in complicated sources, and their information is always incomplete. To ensure the efficiency and stability of emergency risk analysis, we proposed an elaborative approach composed of structural description framework and fuzzy evidential reasoning. Firstly, the risk attributes are identified by structural description framework. The information as evidence is obtained and normalized for further analysis. Secondly, risk analysis model with fuzzy evidential reasoning is constructed, and risk grade is evaluated. Finally, a certain railway project accident is taken as an example to test the model and some managerial insights are demonstrated. An approach combining structural description framework and fuzzy evidential reasoning model is feasible and effective; furthermore, it provides stable support for emergency risk analysis.

1. Introduction

Over the past decades, research on emergency management has gained enormous attention in both academia and practice [1–4]. Due to the complexity of emergency and its severity consequence, it is vital to investigate deeply on the emergency management involving risk analysis, development control, and evolution management [5]. There are various types of emergency, and they make emergency management even more complicated. In China, according to the overall state emergency plan, emergency mainly contains four categories: natural disasters, social security, public health, and technical accidents. Taking earthquakes, a typical natural disaster, as an example, it performs complex on its consequence [6]. The consequence usually appears as a complex disaster chain including casualties, economic loss, fires, landslides, floods, plague, and social panic. Another example is railway project accident [7], which is even harder to cope with for the reason that such accident combines industrial technology and natural situation with social environment factors together. So, many works are carried on by the lens of complexity science [8–10], and a series of positive progress is made [11–13]. Considering the complexity of the emergency and its consequence, it will benefit to emergency management if the decision maker could react as early as possible [14]. Therefore, the risk analysis of emergency is of great significance.

As a critical part of emergency management, risk analysis of emergency is actually a complicated work [15]. Accurate and stable analysis of emergency risk means great on many aspects [16], such as to reduce frequency of occurrence [17], lower the initial loss [18], and control the evolution process effectively [19]. Therefore, it is necessary to propose advanced approach to better solve problems of risk analysis. Taking China emergency management as an example, risk management with characteristics of all-phase, all-stakeholder, and all-type was not informed until 2003. Therefore, to make further progress on risk analysis research, especially on coping with the increasingly complicated risk circumstance, it is suggested to develop more flexible and adaptable analysis approach.

Some researchers notice that emergency risk usually performs poor due to the imperfect information either inadequate or loss [20, 21]. To deal with such decision

scenarios, evidential theory and evidential reasoning method are introduced [22]. In a basic evidential model, it focuses on solving problem with the characteristic of proposition uncertainty to set uncertainty [23]. This could be realized by contrasting the propositions and sets one by one. Take $\Theta = \{G_1, G_2, \ldots, G_n\}$ as a set, in which the elements are mutually exclusive and exhaustive. The set is so called identification framework. Besides, the mass (m) describes the belief of the framework, which satisfies $m(\varnothing) = 0$, and $\sum_{A\subseteq\Theta} m(A) = 1$, wherein $\varnothing$ signifies empty set and A stands for any subset of Θ. As it develops to evidential reasoning, its advantage of dealing with decision scenarios without complete information is increasingly obvious [24–29]. Therefore, a common knowledge for decision makers as well as researchers is formed that evidential reasoning could solve problems with characteristics of multiattributes.

Recent relevant works on evidential reasoning approach concentrate on the update of evidential reason rule, the implementation of this method in practice, and the integration with other methods. Among the extensive research dedicated to the evidential reasoning, the following works are very representative. Wang and Elhag [30] model the bridge risk by artificial neural network, evidential reasoning, and multiple regression analysis. After a comparison of their modelling mechanisms, they argue the remarkable advantage of evidential reasoning is its ability of modelling quantitative and qualitative data using the distributed modelling framework. Some works focus on updating the evidential rule. Yang and Xu [31] improve the evidential reasoning approach by a new rule considering evidence weights and reliabilities. Liu et al. [32] concern the hesitant fuzzy information and highlight the importance of information processing in emergency management. Some works focus on how to use evidential reasoning to solve the problems. Kong et al. [33] develop the belief rule-based inference methodology using the evidential reasoning approach and help the decision maker to predict trauma outcome. Xu et al. [34] investigate a purely data-driven work and propose a classification method using evidential reasoning. Zhang et al. [35] consider a fuzzy rule and conduct a navigational risk assessment. Some works establish novel analysis framework by integrating evidential reasoning with other approaches. Wang et al. [36] incorporate the analytic hierarchy process with evidential reasoning, by which they help contractors to select appropriate subcontractor. Evidential reasoning in this work contributes to rank the alternative subcontractors. Ng [37] takes evidential reasoning-based approach as a fast-track and objective tool and uses it to rank the available design alternatives. Working with the combination of multiattribute decision and non-life cycle assessment, it is proved that evidential reasoning benefits the evaluation of design alternatives' environmental performances. Kong et al. [38] make a combination of the principal component analysis and the evidential reasoning approach and provide a new framework to assess patient satisfaction.

To sum up, two streams of research are closely related to our work: emergency management, especially risk analysis, and approach that may contribute to risk analysis, especially evidential reasoning. The existing studies have made significant contributions to risk analysis and evidential reasoning. However, it is worth mentioning that little attention was paid to risk analysis of technical accident such as railway project accident. It may be induced by the lack of understanding for the risk analysis of such emergency. Considering the information in emergency is always uncertain and incomplete, we adopt the fuzzy evidential reasoning. Further, to better understand risk attributes, we introduce structural description framework to the fuzzy evidential reasoning. Therefore, we propose an analysis approach by incorporating the structural description framework in fuzzy evidential reasoning. To prove the validity of the model we proposed, we run a case study on railway project accident. Railway project accident is a complex system which may contain transportation accidents, public facility accidents, equipment destruction, environmental pollution, industrial hazard, and economic loss [39]. Furthermore, it is a typical technical accident and is seldom analyzed in emergency research. Therefore, our work is different from previous studies. We propose a novel approach for risk analysis by combining structural description framework with fuzzy evidential reasoning, especially when the information is imperfect either uncertain or incomplete. We firstly establish accident structural description framework, identification framework, and it helps to identify risk attributes rapidly and accurately. Secondly, we construct fuzzy belief structural model and normalize all the information we collected as evidence. Thirdly, the fuzzy evidential reasoning model is used to further processing of risk attributes. Finally, we obtain the risk analysis results, so as to provide solution for risk analysis of emergency.

The remainder of this paper is organized as follows. Section 2 establishes structural description framework for identification of risk attributes. Section 3 illustrates the model, and Section 4 takes certain railway project accident as an example to test the validity of our work. Finally, Section 5 concludes our work and offers directions for the future research.

2. Analysis of Risk Attributes

The accurate identification of emergency risk attributes is the premise of risk analysis. The core object is to identify the general attribute and basic attribute [40]. As there is no universal or uniform model for different emergencies [41], we propose a reasonable analysis framework. We determine the basic risk sources followed by their possible outcome and set them as the evidence. After that, we assign the reasoning rules and transform all the evidence to the general attribute. Till then, we accomplish emergency risk attributes analysis and lay foundation for the construction of fuzzy evidential reasoning model.

2.1. Identification of Emergency Risk Attributes. With regarding to the complicated characteristics of emergency, may be high uncertainty and severity consequence, we ought to consider both internal and external risk attributes of such complex system. To systematically illustrate

emergency, it adopts a set form to establish structural description framework as Emergency = {{Emergency Type}, {Key Attribute}, {Secondary Attribute}, {Environmental Attribute}, {Hazard Attribute}} [40]. This framework significantly helps to understand the emergency and its severity as well. Looking back to the framework, it provides a simple way to identify risk attributes, covering the risk source, pattern, trend, and consequence. Therefore, this framework could also be applied to emergency risk attribute identification and correspondingly simplified as Emergency = {{Key Attribute}, {Secondary Attribute}, {Environmental Attribute}}. Among which, key attribute is the risk factor inside the emergency. To some extent, the risk grade (risk value) directly determines the severity of the initial consequences once the event occurs. The secondary attribute also stems from the inside of emergency and usually affects emergency indirectly. The environmental attribute exists outside of emergency, affects the emergency observably and measurably, but not necessarily controllably. For the convenience of further analysis, these three attributes are collectively referred as general attributes. Besides, to illustrate specific emergency risk, each general attribute could be subdivided to basic attribute. That is, the general attributes are extracted to describe the common characters, while the basic attributes are used to highlight the specific status. Then, the identification framework for emergency risk attribute is established as shown in Figure 1.

Considering the relationship among general attributes, basic attributes, and emergency risk grade, we obtain the reasoning rules as follows. If no basic attribute of certain general attribute belongs to certain risk grade, then the general attribute does not belong to this risk grade either. If all the basic attributes of certain general attribute belong to a certain risk grade, then the general attribute also belongs to this risk grade. If the basic attribute of the general attribute belongs to multiple grades, then the general attribute should be allocated to different grades under specific rules. Using the framework shown in Figure 1, we can identify the risk attributes, find the sources for risk, evaluate the occurrence probability, and predict the possible consequences. Once the risk attribute analysis framework is set up, it would support the subsequent modelling research on risk analysis of emergency.

2.2. Fuzzy Belief Model of Emergency. Considering the complicated characteristics of risk attribute, it is necessary to normalize all the risk attributes for further analysis. Usually, it takes grade to describe emergency risk. The grade should contain several standards to assess risk. The standards may cover severity of the emergency, frequency of emergency occurrence, and emergency consequence. Taking CRH brake system failure risk as an example, the risk grade is defined by grade I to grade IV. As to natural disaster risk, it is subdivided to five grades. There are also some emergency risk grades described by the qualitative method. For example, fault mode severity can be classified to insignificant, marginal, critical, and catastrophic; incident frequency can be described as seldom, little, average, usually, and always. Additionally, there are also some quantitative description methods, such as the risk value. The evidence for risk attribute is so diverse that the evidence ought to be normalized before further analysis. Combining the fuzzy set theory and the belief structure model, we establish fuzzy belief structure.

Assume emergency has N fuzzy risk grades and the adjacent two grades may intersect. Given membership functions, we symbol fuzzy numbers for each grade as FG_n and further describe them with triangular fuzzy number or trapezoidal fuzzy number. The intersection between FG_n and FG_{n+1} is denoted as $\mathrm{FG}_{n,\,n+1}$, as is shown in Figure 2. Then, the emergency fuzzy risk can be illustrated by $\mathrm{FG} = \{\mathrm{FG}_1, \mathrm{FG}_2, \ldots, \mathrm{FG}_n, \ldots, \mathrm{FG}_N\}$. Together with the belief model, we obtain the fuzzy belief model as follows:

$$\mathrm{FBS}(\mathrm{E}) = \{(\mathrm{FG}_n, \beta_n), \quad n = 1, 2, \ldots, N\}, \tag{1}$$

wherein FG_n represents fuzzy risk grade, N depicts the total number of grades, and β_n denotes the belief of emergency risk grade falling on grade FG_n. Moreover, we have $\beta_n \geq 0, 0 \leq \sum_{n=1}^{N} \beta_n \leq 1$. Specifically, $\sum_{n=1}^{N} \beta_n = 1$ indicates that the risk attribute information is completely known, while $\sum_{n=1}^{N} \beta_n = 0$ indicates that people know nothing about risk attribute at all.

3. Model

Based on the aforementioned analysis, the evidential reasoning model would be proposed. The model would be ultimately established through the following four steps. Firstly, risk attributes are identified. By the structural description framework for emergency, we could obtain the general attribute and further get the basic attribute through experience on emergency management. Secondly, information of risk attributes is normalized. We collect the information of all the risk attributes and take them as evidence for further reasoning. Then, we set the normalization rules for evidence both qualitative and quantitative. Thirdly, the general attributes contributing to risk are calculated. The major work in this step is mainly composed of calculation on mass value and correspondingly belief for all the general attributes, as well as allocation of the intersection reliability. Finally, the emergency risk analysis results are obtained. The framework of evidential reasoning model is shown in Figure 3. As the first step has been prepared by risk attribute analysis, we would pursue the model construction from the second step.

3.1. Conversion of Fuzzy Belief Structure. Evidence of risk attribute has the characteristics of multifeature, multistandard, and multilength, which increases the complexity of risk analysis. Therefore, it is necessary to normalize the evidence of risk attributes before subsequent analysis. To solve this problem, we adopt fuzzy belief structure model. Given fuzzy risk grades $\mathrm{FG} = \{\mathrm{FG}_n, n = 1, 2, \ldots, N\}$, fuzzy belief structure is $\mathrm{FBS}(\mathrm{E}) = \{(\mathrm{FG}_n, \beta_n), n = 1, 2, \ldots, N\}$. Assuming that risk attribute R has evidence with length l, its

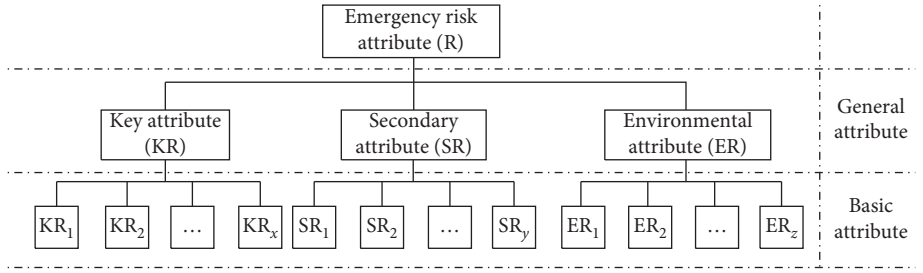

Figure 1: Emergency risk attribute identification framework.

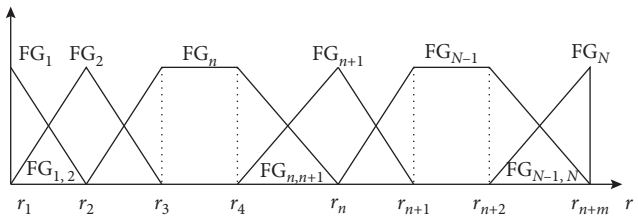

Figure 2: Fuzzy risk grade.

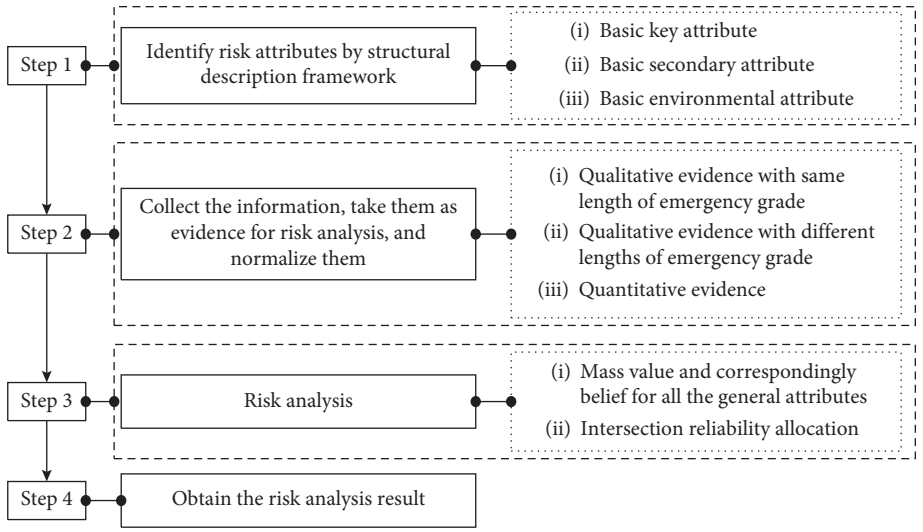

Figure 3: Framework of fuzzy evidential reasoning model.

risk grade is $\mathrm{FG}^{Rl} = \{\mathrm{FG}_{nl}, n = 1, 2, \ldots, N\}$ and its fuzzy belief structure could be labeled as $\mathrm{FBS}(Rl) = \{(\mathrm{FG}_{nl}, \alpha_n), n = 1, 2, \ldots, N\}$. Regarding that evidence could be illustrated either qualitatively or quantitatively (even with different lengths), we set the processing rules as follows.

If the risk attribute has qualitative evidence with the same length comparing to emergency fuzzy risk grade, i.e., $N_l = N$, then the evidence could be converted directly by

$$\left(\mathrm{FG}_{n2}^{Rl}, \alpha_{n2}\right) \Longleftrightarrow \left(\mathrm{FG}_{n1}, \beta_{n1}\right), \quad n_1 = n_2, n_1 \in N, n_2 \in N_l. \tag{2}$$

If the evidence is qualitative with different lengths comparing to fuzzy risk grade, i.e., $N \neq N_l$, then we could convert it to FG_{n1} by belief $\gamma_{n1,n2}(n_1 \in N, n_2 \in N_l)$. Therefore,

$$\left(\mathrm{FG}_{n2}^{Rl}, \alpha_{n2}\right) \Longleftrightarrow \left(\mathrm{FG}_{n1}, \gamma_{n1,n2}\right), \quad n_1 \in N, n_2 \in N_l, \tag{3}$$

wherein $0 \leq \gamma_{n1,n2} \leq 1$ and $\sum_{n1=1}^{N} \gamma_{n1,n2} = 1$.

If the risk attribute has quantitative evidence and its risk value belongs to fuzzy risk grade FG_n and FG_{n+1} with membership $\mu\mathrm{FG}_n$ and $\mu\mathrm{FG}_{n+1}$ separately, then it converts as

$$\left(\mathrm{FG}_{n2}^{Rl}, \alpha_{n2}\right) \Longleftrightarrow \left(\mathrm{FG}_{n1}, \frac{\mu_{\mathrm{FG}n}}{\mu_{\mathrm{FG}n} + \mu_{\mathrm{FG}n+1}}\right), \left(\mathrm{FG}_{n+1}, \frac{\mu_{\mathrm{FG}n+1}}{\mu_{\mathrm{FG}n} + \mu_{\mathrm{FG}n+1}}\right), \quad n_1 \in N, n_2 \in N_l. \tag{4}$$

By (2)–(4), the basic risk attribute evidence is normalized.

3.2. Fuzzy Evidential Reasoning Model. As aforementioned, we establish a structural description framework consisting of key attributes, secondary attributes, and environmental attributes; we could use this framework, i.e., $R = \{\{\text{KR}\}, \{\text{SR}\}, \{\text{ER}\}\}$ to describe emergency risk attributes. Each general attribute could be subdivided into some certain basic attributes. From then on, we take KR as an example to construct model. Assume the number of KR's basic attributes is X and get $\text{FBS}_x^{\text{KR}} = \{(\text{FG}_n, \beta_n^x)\}, n = 1, 2, \ldots, N, x = 1, 2, \ldots, X$ after fuzzy belief structure converting. Setting the corresponding weight of KR_xas ω_x, and $\sum_{x=1}^{X} \omega_x = 1$, the mass value of each basic risk attributes could be obtained by

$$m_n^x = \omega_x \beta_n^x, \quad n = 1, 2, \ldots, N, x = 1, 2, \ldots, X. \tag{5}$$

Additionally, there also exists some risk which could not be ascertained due to incomplete or even totally unknown information in practice, which is measured by

$$m_G^x = 1 - \sum_{n=1}^{N} m_n^x = 1 - \sum_{n=1}^{N} \omega_x \beta_n^x, \quad n = 1, 2, \ldots, N, x = 1, 2, \ldots, X. \tag{6}$$

By normalization weights ω_x to ω', we can further process the evidence of KR. The risk evaluation result of KR is $\text{FBS}(\text{KR}) = \left\{(\text{FG}_n, \beta_n^{\text{KR}})\right\}, n = 1, 2, \ldots, N, x = 1, 2, \ldots, X$. Therefore, we obtain the mass value of KR by using the following equation:

$$m_n^{\text{KR}} = \omega' \left\{ \prod_{x=1}^{X} \left[m_n^x + m_G^x \right] - \prod_{x=1}^{X} m_G^x \right\}, \quad n = 1, 2, \ldots, N. \tag{7}$$

The mass value of the intersection between two adjacent risk grades is

$$m_{n,n+1}^{\text{KR}} = \omega' \mu_{\text{FG}n,n+1}^{\max} \left\{ \prod_{x=1}^{X} \left(m_n^x + m_{n+1}^x + m_G^x \right) - \prod_{x=1}^{X} \left(m_n^x + m_G^x \right) - \prod_{x=1}^{X} \left(m_{n+1}^x + m_G^x \right) + \prod_{x=1}^{X} m_G^x \right\}, \quad n = 1, 2, \ldots, N-1. \tag{8}$$

The mass value of uncertain risk grades due to imperfect information is

$$m_G^{\text{KR}} = \omega' \left\{ \prod_{x=1}^{X} m_G^x \right\}. \tag{9}$$

Specially, ω' is determined by $\sum_{n=1}^{N} m(G_n) + \sum_{n=1}^{N-1} G_{n,n+1} = 1$.

Belief for each mass value is

$$\beta_n^{\text{KR}} = \frac{m_n^{\text{KR}}}{1 - \overline{m}_G^{\text{KR}}}, \quad n = 1, 2, \ldots, N, \tag{10}$$

$$\beta_{n,n+1}^{\text{KR}} = \frac{m_{n,n+1}^{\text{KR}}}{1 - \overline{m}_G^{\text{KR}}}, \quad n = 1, 2, \ldots, N-1. \tag{11}$$

We obtain the primary analysis result by $\{(\text{FG}_n^{\text{KR}}, \beta_n^{\text{KR}}), (\text{FG}_{n,n+1}^{\text{KR}}, \beta_{n,n+1}^{\text{KR}}), (\text{FG}_G^{\text{KR}}, \beta_G^{\text{KR}})\}$. However, the intersection between two grades does not exist in reality. Therefore, it still needs further analysis on $(\text{FG}_{n,n+1}^{\text{KR}}, \beta_{n,n+1}^{\text{KR}})$.

3.3. Allocation of Fuzzy Intersection Belief. Considering the risk grade is regulated clear in reality, it is necessary to process the intersection between adjacent risk grades. To insure the analysis is reasonable, we set the reasoning rules as follows. If the intersection $\text{FG}_{n,n+1}$ totally belongs to FG_n or FG_{n+1}, then its belief also belongs to FG_n or FG_{n+1}. If the intersection $\text{FG}_{n,n+1}$ varies from FG_n to FG_{n+1}, as shown in Figure 4, and the endpoints are set by FG_n and FG_{n+1}, then we allocate $(m_{n,n+1}^{\text{KA}}, \beta_{n,n+1}^{\text{KA}})$ within this interval.

As it is shown in Figure 4, the proportion of grade FG_n in $S_{n,n+1}$ is $\delta_n^{\text{KR}'}$, while the proportion of grade FG_{n+1} is $\delta_{n+1}^{\text{KR}'}$. $\delta_n^{\text{KR}'} + \delta_{n+1}^{\text{KR}'} = 1$, and they are determined by (12) and (13) separately:

$$\delta_n^{\text{KR}'} = \frac{1}{2} \left[\left(1 - \frac{d_n}{d_n + d_{n+1}} \right) + \frac{S_n}{S_n + S_{n+1}} \right], \tag{12}$$

$$\delta_{n+1}^{\text{KR}'} = \frac{1}{2} \left[\left(1 - \frac{d_{n+1}}{d_n + d_{n+1}} \right) + \frac{S_{n+1}}{S_n + S_{n+1}} \right]. \tag{13}$$

Therefore, the belief allocated to grade FG_n is

$$\beta_n^{\text{KR}'} = \frac{S_n + \delta_n^{\text{KR}'} S_{n,n+1}}{S_n + S_{n,n+1} + S_{n+1}}. \tag{14}$$

However, the belief allocated to grade FG_{n+1} is

$$\beta_{n+1}^{\text{KR}'} = \frac{S_{n+1} + \delta_{n+1}^{\text{KR}'} S_{n,n+1}}{S_n + S_{n,n+1} + S_{n+1}}. \tag{15}$$

Then, combining with $\left\{(m_n^{\text{KR}}, \beta_n^{\text{KR}}), (m_{n,n+1}^{\text{KR}}, \beta_{n,n+1}^{\text{KR}}), (m_G^{\text{KR}}, \beta_G^{\text{KR}})\right\}$, we get the initial risk analysis result of accident as

$$\left\{ \left(m_n^{\text{KA}}, \beta_n^{\text{KA}} + \beta_n^{\text{KA}'} \right), \left(m_G^{\text{KA}}, \beta_G^{\text{KA}} \right) \right\}. \tag{16}$$

Since the key attribute, secondary attribute, and environmental attribute have been differentiated when we identify general risk attribute, it is not necessary to rank the risk attributes like risk analysis paradigm in general.

3.4. Analysis of Fuzzy Evidential Reasoning Results. To understand the risk grade more intuitively, we take a further analysis. It also benefits emergency management, such as release warning signals and formulate emergency response in different stages of the emergency. To solve this problem, we use the expected risk value. As the risk grade and its belief could be obtained by (16), we determine the grade risk values as follows. Assuming the risk value of the highest grade to 1 and the lowest grade to 0, the $n-2$ grades among them could be determined by specific accident. The analysis result would be finally obtained by the summation of all the risk values:

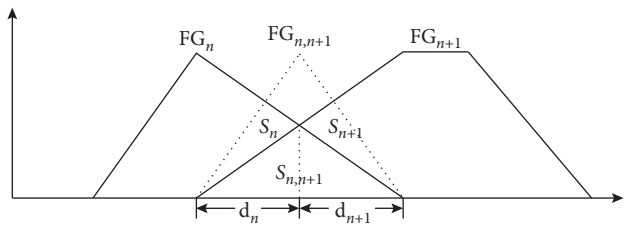

Figure 4: Fuzzy intersection reliability allocation.

$$U^{\mathrm{KA}} = \sum_{n=1}^{N} \beta_n r_n. \tag{17}$$

Based on the analysis of the key attribute, we can analyze the risk of the secondary attribute and environmental attribute as the same way proposed by (1)–(17). With regarding to the expected risk value of KR, SR, and ER, it would exactly help to analyze accident risk. That is, given the information of risk attributes, the fuzzy evidential reasoning model would make sense on estimating to what extent the accident would happen. Besides, this approach also helps to evaluate the severity of the accident consequence.

4. Model Analysis on Case Study

Here, we take railway project accident as an example. Railway project accident is a typical technical accident and seldom researched in previous works. We determine the information and evidence of risk attribute mainly from the following two documents: *Technical Code for Risk Management of Railway Construction Engineering* (issued by China Railway in 2014), *Statistics of Construction Risk* (a series of documents declared by certain railway project in 2018).

4.1. Model Solution

4.1.1. Step 1. Using the emergency risk attribute identification framework, we determine the general attributes and their basic attributes. Then, calculate the risk grade, weight, and value of all attributes. Finally, we obtain 21 basic attributes, and their information is summarized as shown in Table 1.

4.1.2. Step 2. Considering the specific condition of railway project in China, we measure the risk grade of railway project accident by {Catastrophic, critical, general, Marginal, insignificant}, which simplifies as FG = {FG$_1$, FG$_2$, FG$_3$, FG$_4$, FG$_5$}. With regard to Figure 2, finally, we determine the fuzzy risk grade for railway project accident as in Figure 5.

4.1.3. Step 3. We take further process of basic risk attributes. To simplify but without loss of generality, we omit the process of getting the ultimate evidence from multi-information. Calculation starts from *cut slope height*, whose risk value is 2; triangular fuzzy number for FG$_1$ is (0, 0, 4) and for FG$_2$ is (0, 4, 8). Then, we obtain fuzzy belief of *cut slope height* as {(FG$_1$, 0.5), (FG$_2$, 0.5), (FG$_3$, 0), (FG$_4$, 0), (FG$_5$, 0)}, take (0.5, 0.5, 0, 0, 0) for short. All the basic attribute analysis results are demonstrated in the third column in Table 2. Then, we get the mass value by (5)–(7), and the result is shown in the fourth column in Table 2. Based on equations (8)–(11), we get the primary result on railway project accident risk analysis and it is shown in the fifth column in Table 2. Note that there is still an intersection between the adjacent grades; therefore, we pursue to allocate the intersection by the following steps.

4.1.4. Step 4. By equation (12)–(16), we allocate the intersection belief to the two adjacent grades and get the result on risk evaluation considering risk grade and its belief. As mentioned before, we further calculate the expected risk value for each basic attribute by using equation (17). Finally, we conclude the results of this step and list them in Table 3.

4.2. Results Analysis. We could draw some managerial insight out of the above results. One interesting point is that the risk value of the key attribute is not significantly high comparing with the traditional recognition. We explain this counterintuitive result from the perspective of practice. In reality, people tend to spend enormous money and high effort on this aspect, and it leads to technology progress and effective regulation. Therefore, although the key attribute is vital to railway project accident, the failure rate and risk value is low. It is in line with the development status of China railway project.

Secondary attribute performs relatively average in risk grade and belief, which is basically consistent with the actual situation. Unexpectedly, the belief allocated for the environmental attribute is relatively high. It may be due to the geological condition which is important to railway project and its operation. As it is shown in the statistics data of railway project accident, major economic losses and casualties are usually caused by environmental attribute.

To some extent, these findings will push managers to rethink the role of traditional experience recognition and related training. Moreover, we also provide reference for risk prevention, early warning, and response of railway project accident. Especially, it would obviously benefit to the railway company with capital constraints.

Table 1: Railway project accident risk analysis and evident definition.

General attribute	Basic attribute	Risk consequence	Risk grade	Risk weight	Risk value
Key attribute	Cut slope height	Slide slump, blocks peeling off, roadbed deformation	FG_1	0.2	2
	Bank slope height	Embankment settlement, slope collapse	FG_3	0.1	9
	Special construction conditions	Casualty, economic loss, postproject risks	FG_2	0.2	6
	Special construction technologies	Project failure, economic loss, derivative project failure, postproject risks	FG_1	0.2	1
	Deep foundation pit	Structural design failure, settlement deformation, unexpected accidents	FG_2	0.2	7
	Existing railway effects	Technological bottleneck, roadbed deterioration, schedule delay	FG_4	0.1	16
Secondary attribute	Project schedule	Go over budget, alleviate function, interface project delay	FG_4	0.1	15
	Function loss	Below the market demand	FG_3	0.05	9
	Project investment	Project abandon, poor quality, social conflicts	FG_4	0.1	11
	Environment protect	Destroy environment like cultural relics and natural habitats. Social conflict and welfare	FG_1	0.15	1
	Social status along the project	Social conflict, go over budget, schedule delay	FG_5	0.05	17
	Locomotive depot configuration	Operational risk, social investigation	FG_4	0.05	14
	Vehicle configuration	Operational risk	FG_5	0.05	18
	Terminal location	Project abandon, infrastructure settlement	FG_3	0.05	14
	Project interface	Project isolation, project failure	FG_3	0.2	9
	Infrastructure relocation	Go over budget, schedule delay, group conflict	FG_2	0.15	6
	Residual risk	Unexpected loss	FG_3	0.05	—
Environmental attribute	Weather condition	Project duration, operational risk	FG_3	0.15	9
	Underground water	Settlement, roadbed deformation, water pollution	FG_5	0.25	18
	Geological condition	Roadbed risk, social conflict, project abandon, karst water and mud inrush disaster, bombing	FG_3	0.25	7
	Stuff quality	Casualty, operational risk, project failure	FG_2	0.35	3

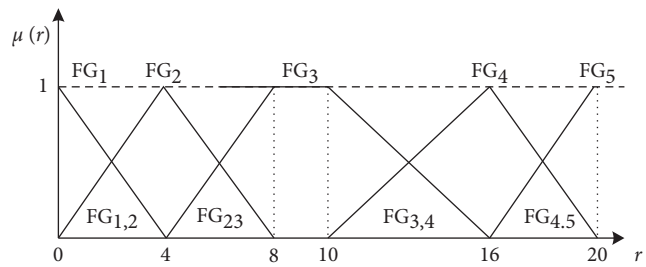

Figure 5: Fuzzy risk grade of railway project accident.

Table 2: Analysis results of risk attributes (I).

General attribute	Basic attribute	Belief	Mass	Primary result
Key attribute	Cut slope height	(0.5, 0.5, 0, 0, 0)	(0.1, 0.1, 0, 0, 0)	{(FG_1, 0.0241), ($FG_{1,2}$, 0.0136), (FG_2, 0.1906), ($FG_{2,3}$, 0.1742), (FG_3, 0.1814), ($FG_{3,4}$, 0.0258), (FG_4, 0.048), ($FG_{4,5}$, 0.0127), (FG_5, 0)}
	Bank slope height	(0, 0, 1, 0, 0)	(0, 0, 0.1, 0, 0)	
	Special construction conditions	(0, 0.5, 0.5, 0, 0)	(0, 0.1, 0.1, 0, 0)	
	Special construction technologies	(0.3333, 0.6667, 0, 0, 0)	(0.0666, 0.1333, 0, 0, 0)	
	Deep foundation pit	(0.875, 0.125, 0, 0, 0)	(0.1750, 0.025, 0, 0, 0)	
	Existing railway effects	(0.0, 0, 1, 0)	(0.0, 0, 0.1, 0)	

Table 2: Continued.

General attribute	Basic attribute	Belief	Mass	Primary result
Secondary attribute	Project schedule	(0, 0, 0, 0.625, 0.375)	(0, 0, 0, 0.0625, 0.0375)	{(FG_1, 0.1002), ($FG_{1,2}$, 0.0106), (FG_2, 0.1057), ($FG_{2,3}$, 0.059), (FG_3, 0.1067), ($FG_{3,4}$, 0.0871), (FG_4, 0.1323), ($FG_{4,5}$, 0.0144), (FG_5, 0.1632)}
	Function loss	(0, 0, 1, 0, 0)	(0, 0, 0.05, 0, 0)	
	Project investment	(0, 0, 0.1667, 0.8333, 0)	(0, 0, 0.0167, 0.0833, 0)	
	Environment protect	(0.5, 0.5, 0, 0, 0)	(0.075, 0.075, 0, 0, 0)	
	Social status along the project	(0, 0, 0, 0.875, 0.125)	(0, 0, 0, 0.0438, 0.0625)	
	Locomotive depot configuration	(0.0, 0, 0.6667, 0.3333)	(0, 0, 0, 0.0333, 0.0167)	
	Vehicle configuration	(0.0, 0, 0.8889, 0.1111)	(0, 0, 0, 0.0444, 0.0056)	
	Terminal location	(0, 0, 0.4286, 0.5714, 0)	(0, 0, 0, 0.0214, 0.0286)	
	Project interface	(0, 0, 1, 0, 0)	(0, 0, 0.2, 0, 0)	
	Infrastructure relocation	(0, 0.8571, 0.1429, 0, 0, 0)	(0, 0.1286, 0.0214, 0, 0)	
	Residual risk	(0, 0, 0, 0, 0)	(0, 0, 0, 0, 0)	
Environmental attribute	Weather condition	(0, 0, 1, 0, 0)	(0, 0, 0.15, 0, 0)	{(FG_1, 0.1123), ($FG_{1,2}$, 0.0344), (FG_2, 0.1031), ($FG_{2,3}$, 0.0357), (FG_3, 0.1708), ($FG_{3,4}$, 0.0258), (FG_4, 0.0746), ($FG_{4,5}$, 0.0322), (FG_5, 0.0096)}
	Underground water	(0, 0, 0, 0.3333, 0.6667)	(0, 0, 0, 0.0833, 0.1667)	
	Geological condition	(0, 0.25, 0.75, 0, 0)	(0, 0.0625, 0.1875, 0, 0)	
	Staff quality	(0.8571, 0.1429, 0, 0, 0)	(0.3, 0.05, 0, 0, 0)	

Table 3: Analysis results of risk attributes (II).

	FG_1	FG_2	FG_3	FG_4	FG_5	Expected risk value
Key attribute	0.0319	0.2805	0.2764	0.0672	0.0064	0.5742
Secondary attribute	0.1057	0.1395	0.1787	0.1831	0.1704	0.5649
Environmental attribute	0.1295	0.1392	0.2015	0.1036	0.0257	0.4151

5. Conclusions

Emergency risk analysis is vital to emergency management; especially, it plays an important role on learning emergency operational mechanism. Aiming at providing a stable approach to analyze emergency risk, this paper proposes an analytical approach incorporating structural description framework and fuzzy evidential reasoning. It starts from the establishment of risk attribute identification, which is taking emergency structural description framework as the foundation. Then, we assess the risk grade of risk attributes by evidential reasoning. By a case study on railway project accident, it is proved that the approach outperforms comparing to current risk management. It could provide theoretical support for the risk prevention and decision-making involving in each stage.

To conclude, our study proposes a novel approach for accident risk analysis by combining structural description framework and fuzzy evidential reasoning, especially when the information is imperfect either uncertain or incomplete. We firstly establish accident structural description framework, identification framework; it helps to recognize risk attributes rapidly and accurately. Secondly, we construct fuzzy belief structural model and normalize all the information. Thirdly, the fuzzy evidential reasoning model is used to combine basic attributes. Finally, we obtain the analysis results, so as to assist the decision-making of emergency risk prevention or response.

The limitations of our work are also obvious due to the model construction. Firstly, the evidential reasoning rule we used here is very basic. It is in premise of the implicit assumption that the fuzzy risk grade is defined clearly. However, the grade may be obscure in reality, and it may induce the fact that the evidence belongs to three or more different grades. Secondly, the basic attributes of our case study are relatively small. We obtain such attributes from deep analysis of daily records of specific railway project and statistics of construction risk, and they are undoubtedly helpful to make risk analysis. Considering the analysis result, especially the analysis of key attribute, it still needs more detailed works on the basic attributes to highlight the critical of the key attribute. Finally, our work merely focuses on the occurrence risk of emergency, indeed risk is always developing. So, we have to further alleviate the difficulty of evidential reasoning application or do the risk analysis taking emergency development or evolution under consideration.

Regarding above limitations and the fact that risk management is the basic of emergency development management and evolution research, it needs further study. As to future work, the research could enrich the evidential reasoning rule by new tools of data mining and expand the attributes' scope from occurrence risk to development risk and evolution risk. Further, the research could enrich the works on risk prevention and early warning. In addition, future work may introduce various constraints to close the reality, especially the resource constraints. After that, it could finally provide great references for relevant managers and help to make scientific and efficient decisions.

Data Availability

All the data generated or analyzed during this study are included in this paper.

Conflicts of Interest

The authors declare that there are no conflicts of interest regarding the publication of this paper.

Acknowledgments

The first author acknowledges support from the Humanities and Social Science Foundation of Ministry of Education of China (grant no. 17YJC630113) and NSFC (grant nos. 71572115 and 91646117). The second author acknowledges support from NSFC (grant nos. 71702021 and 71802143) and the Fundamental Research Funds for the Central Universities (DUT18RC(4)021).

References

[1] N. Altay and W. G. Green, "OR/MS research in disaster operations management," *European Journal of Operational Research*, vol. 175, no. 1, pp. 475–493, 2006.

[2] G. Green and R. Batta, "Review of recent developments in OR/MS research in disaster operations management," *European Journal of Operational Research*, vol. 230, no. 2, pp. 201–211, 2013.

[3] L. Zhou, X. Wu, Z. Xu, and H. Fujita, "Emergency decision making for natural disasters: an overview," *International Journal of Disaster Risk Reduction*, vol. 27, pp. 567–576, 2018.

[4] N. Argyris and S. French, "Nuclear emergency decision support: a behavioural OR perspective," *European Journal of Operational Research*, vol. 262, no. 1, pp. 180–193, 2017.

[5] S. Thorvaldsdóttir and R. Sigbjörnsson, "Disaster-function management: basic principles," *Natural Hazards Review*, vol. 15, no. 1, pp. 48–57, 2014.

[6] Y. Zhang, W. G. Weng, and Z. L. Huang, "A scenario-based model for earthquake emergency management effectiveness evaluation," *Technological Forecasting and Social Change*, vol. 128, pp. 197–207, 2018.

[7] C. W. Yang, Z. H. Li, X. Y. Guo, W. Y. Yu, J. Jin, and L. Zhu, "Application of BP neural network model in risk evaluation of railway construction," *Complexity*, vol. 2019, Article ID 2946158, 12 pages, 2019.

[8] M.-S. Chang, Y.-L. Tseng, and J.-W. Chen, "A scenario planning approach for the flood emergency logistics preparation problem under uncertainty," *Transportation Research Part E: Logistics and Transportation Review*, vol. 43, no. 6, pp. 737–754, 2007.

[9] J. Ren, Y. Yusuf, and N. Burns, "A decision-support framework for agile enterprise partnering," *The International Journal of Advanced Manufacturing Technology*, vol. 41, no. 1-2, pp. 180–192, 2009.

[10] V. A. Bañuls, M. Turoff, and S. R. Hiltz, "Collaborative scenario modeling in emergency management through cross-impact," *Technological Forecasting and Social Change*, vol. 80, no. 9, pp. 1756–1774, 2013.

[11] S. Luna and M. J. Pennock, "Social media applications and emergency management: a literature review and research agenda," *International Journal of Disaster Risk Reduction*, vol. 28, pp. 565–577, 2018.

[12] T. B. Vu and I. Noy, "Regional effects of natural disasters in China: investing in post-disaster recovery," *Natural Hazards*, vol. 75, no. S2, pp. 111–126, 2015.

[13] M. Kumasaki, M. King, M. Arai, and L. Yang, "Anatomy of cascading natural disasters in Japan: main modes and linkages," *Natural Hazards*, vol. 80, no. 3, pp. 1425–1441, 2016.

[14] Z. Y. Wang, X. D. Liu, and S. T. Zhang, "A new decision method for public opinion crisis with the intervention of risk perception of the public," *Complexity*, vol. 2019, Article ID 9527218, 14 pages, 2019.

[15] S. D. Guikema, "Natural disaster risk analysis for critical infrastructure systems: an approach based on statistical learning theory," *Reliability Engineering & System Safety*, vol. 94, no. 4, pp. 855–860, 2009.

[16] T. Christensen, O. Andreas Danielsen, P. Laegreid, and L. H. Rykkja, "Comparing coordination structures for crisis management in six countries," *Public Administration*, vol. 94, no. 2, pp. 316–332, 2016.

[17] X. Lu and L. Xue, "Managing the unexpected: sense-making in the Chinese emergency management system," *Public Administration*, vol. 94, no. 2, pp. 414–429, 2016.

[18] M. A. Cole, R. J. R. Elliott, T. Okubo, and E. Strobl, "Pre-disaster planning and post-disaster aid: examining the impact of the great East Japan earthquake," *International Journal of Disaster Risk Reduction*, vol. 21, pp. 291–302, 2017.

[19] P. J. Ren, Z. S. Xu, and J. Gu, "Assessments of the effectiveness of an earthquake emergency plan implementation with hesitant analytic hierarchy process," *International Journal of Information Technology & Decision Making*, vol. 15, no. 6, pp. 1367–1389, 2016.

[20] S. Gupta, M. K. Starr, R. Z. Farahani, and N. Matinrad, "Disaster management from a POM perspective: mapping a new domain," *Production and Operations Management*, vol. 25, no. 10, pp. 1611–1637, 2016.

[21] M. Setbon, J. Raude, C. Fischler, and A. Flahault, "Risk perception of the "mad cow disease" in France: determinants and consequences," *Risk Analysis*, vol. 25, no. 4, pp. 813–826, 2005.

[22] J.-B. Yang, "Rule and utility based evidential reasoning approach for multiattribute decision analysis under uncertainties," *European Journal of Operational Research*, vol. 131, no. 1, pp. 31–61, 2001.

[23] J. B. Yang and D. L. Xu, "On the evidential reasoning algorithm for multiple attribute decision analysis under uncertainty," *IEEE Transactions on Systems, Man, and Cybernetics—Part A: Systems and Humans*, vol. 32, no. 3, pp. 289–304, 2002.

[24] J. B. Yang, Y. M. Wang, D. L. Xu, and K. S. Chin, "The evidential reasoning approach for MADA under both probabilistic and fuzzy uncertainties," *European Journal of Operational Research*, vol. 171, no. 1, pp. 309–343, 2006.

[25] D.-L. Xu, "An introduction and survey of the evidential reasoning approach for multiple criteria decision analysis," *Annals of Operations Research*, vol. 195, no. 1, pp. 163–187, 2012.

[26] M. Sonmez, J. B. Yang, and G. D. Holt, "Addressing the contractor selection problem using an evidential reasoning approach," *Engineering Construction and Architectural Management*, vol. 8, no. 3, pp. 198–210, 2001.

[27] Y.-M. Wang, J.-B. Yang, and D.-L. Xu, "Environmental impact assessment using the evidential reasoning approach," *European Journal of Operational Research*, vol. 174, no. 3, pp. 1885–1913, 2006.

[28] M. Zhou, X.-B. Liu, J.-B. Yang, and C. Fang, "Group evidential reasoning approach for MADA under fuzziness and uncertainties," *International Journal of Computational Intelligence Systems*, vol. 6, no. 3, pp. 423–441, 2013.

[29] A. Akhoundi and S. Nazif, "Sustainability assessment of wastewater reuse alternatives using the evidential reasoning approach," *Journal of Cleaner Production*, vol. 195, no. 10, pp. 1350–1376, 2018.

[30] Y. M. Wang and T. Elhag, "A comparison of neural network, evidential reasoning and multiple regression analysis in modelling bridge risks," *Expert Systems with Applications*, vol. 32, no. 3, pp. 336–348, 2007.

[31] J.-B. Yang and D.-L. Xu, "Evidential reasoning rule for evidence combination," *Artificial Intelligence*, vol. 205, pp. 1–29, 2013.

[32] X. Liu, Z. Wang, and S. Zhang, "A new methodology for hesitant fuzzy emergency decision making with unknown weight information," *Complexity*, vol. 2018, Article ID 5145348, 12 pages, 2018.

[33] G. Kong, D. L. Xu, J. B. Yang et al., "Belief rule-based inference for predicting trauma outcome," *Knowledge-Based Systems*, vol. 95, pp. 35–44, 2016.

[34] X. Xu, J. Zheng, J. B. Yang, D. L. Xu, and Y. W. Chen, "Data classification using evidence reasoning rule," *Knowledge-Based Systems*, vol. 116, pp. 144–151, 2017.

[35] D. Zhang, X. Yan, J. Zhang, Z. Yang, and J. Wang, "Use of fuzzy rule-based evidential reasoning approach in the navigational risk assessment of inland waterway transportation systems," *Safety Science*, vol. 82, pp. 352–360, 2016.

[36] G. Wang, F. Cetindere, A. Damci, and B. N. Bingol, "Smart home subcontractor selection using the integration of AHP and evidential reasoning approaches," *Procedia Engineering*, vol. 164, pp. 347–353, 2016.

[37] C. Y. Ng, "Evidential reasoning-based Fuzzy AHP approach for the evaluation of design alternatives' environmental performances," *Applied Soft Computing*, vol. 46, pp. 381–397, 2016.

[38] G. L. Kong, L. L. Jiang, X. F. Yin et al., "Combining principal component analysis and the evidential reasoning approach for healthcare quality assessment," *Annals of Operations Research*, vol. 271, no. 2, pp. 679–699, 2018.

[39] Y. Lei, C. Huang, and Y. Wu, "Operational risk assessment for international transport corridor: a case study of China-Pakistan economic corridor," *Discrete Dynamics in Nature and Society*, vol. 2019, Article ID 5730746, 7 pages, 2019.

[40] Y. J. Li, X. J. Qiao, and X. C. Sun, "Study on emergency structural description framework," *Journal of University of Electronic Science and Technology of China (Social Sciences Edition)*, vol. 5, no. 1, pp. 28–33, 2013.

[41] X. Xu, X. Yin, and X. Chen, "A large-group emergency risk decision method based on data mining of public attribute preferences," *Knowledge-Based Systems*, vol. 163, pp. 495–509, 2019.

Hindawi
Complexity
Volume 2019, Article ID 9428087, 13 pages
https://doi.org/10.1155/2019/9428087

Research Article

Ground Attack Strategy of Cooperative UAVs for Multitargets

Qirui Zhang and Ruixuan Wei

Air Force Engineering University, Xi'an City, Shaanxi Province 710038, China

Correspondence should be addressed to Qirui Zhang; xianyangrui@126.com

Received 14 July 2019; Revised 11 September 2019; Accepted 30 October 2019; Published 20 November 2019

Guest Editor: Baltazar Aguirre-Hernandez

Humans have a fundamental ability, that is, to share vision among each other to fulfill common goals, which cooperative UAVs do not have. The difficulties mainly lie in the homologous mathematical description of humans and elusive experimental practice. This paper proposed a parallel multiview splicing on clouds, which first review both theory and practice studies in UAVs. These terms are then reconsidered from humans' vision sharing. Next, a conceptual model of parallel multiview splicing on clouds is proposed and the mathematical deduction if fulfilled. Furthermore, an experimental cooperative UAVs platform is built to practically implement the algorithms. Both the simulated and practiced results have validated the feasibility of our method. Finally, a general discussion and proposals for addressing future issues are given.

1. Introduction

The unmanned aerial vehicle (UAV) combat system plays an important role in acquiring information superiority, implementing precise strike, and completing fast combat tasks in current rapid combat and information war [1]. Especially the intelligent UAV, which integrates artificial intelligence to perceiving environment, making attack strategy and assessing task, etc., can lead to the initiative and victory in the war [2].

However, the task accomplishment of single UAV is often unsatisfactory. When a single UAV invades an enemy-occupied area, it often fails to complete effective attack due to its own load limitation, enemy interference, and interception attack. Therefore, it needs cooperation among multiple UAVs to guarantee the task completion [3, 4].

With the development of technology and equipment, the air confrontation between big powers will be in a state of high intensity. The traditional methods consider manned vehicles as the main body of future aerial combat, until the significance of cooperative UAVs (Co-UAVs) is discovered. The cooperative UAVs show a new type of combat effectiveness [5], which has the following advantages.

(a) Intelligence advantage: Co-UAVs have distributed sensors, which can cooperate with each other to achieve precise targets positioning. The networked operations can share information among UAVs, achieving "Any one knows, everyone knows" in the swarm. The intelligence sharing lays foundation for the realization of cooperative attack.

(b) Speed advantage: Co-UAVs can automatically decompose tasks online according to battlefield situation and give the subtasks to corresponding vehicles. The assigned UAVs can react quickly and coordinate with other operations such as interference suppression, fire strike, and damage assessment, which shortens the "perception-decision-action" cycle and speeds up the combat process.

(c) Cooperation advantage: the cooperation between UAVs can cooperate autonomously and adaptively, which makes the swarm act as single one. As a result, the uniform intensive attack and dense defense can be achieved.

(d) Quantity advantage: Co-UAVs usually use low-cost unmanned platform, which is small in size and large in quantity. It can maintain the high-pressure situation and continuous attack towards the enemy, paralyzing the defense system of opposition rapidly and achieving the operational purpose in the shortest time.

As a subversive modern attack strategy against the enemy, cooperative UAVs have been regarded as the core to triumph. Especially, the swarm intelligence (SI) of Co-UAVs

is widely applied as the key technology to win the future combat [6].

In theory, Suresh and Ghose [7] proposed a self-adapting ground attack strategy for UAVs by establishing a path function within the detection range. They combine reconnaissance, interference, and autonomous attack to build an adaptive ground attack strategy for Co-UAVs. Luo et al. [8] propose an online-offline integrated cooperation strategy of UAVs, which uses offline expert decision-making to analyze battlefield environment so as to establish the environmental impact map; it uses online robust decision-making model to evaluate the scenarios faced by each UAV so as to adopt the best robust attack action. Wang et al. [9] tries to find the best strategy of Co-UAVs by using the Radial Basis Function Neural Network (RBF-NN) and to evaluate the performance of cooperation. Also, an alterable neural network is introduced to search the precise candidate feasible solution set, which improves the efficiency of the RBF-NN. In [10], an interval consistency model based on an auction algorithm is proposed, purposing on solving the consistency problem of Co-UAVs, making UAVs reach the target at the same time.

In practice, as the Research Laboratory of the United States Air Force (USAF) showed in 2002, the key to success in future complex battlefield is to use multi-UAVs, which includes searching and attacking, investigation and suppression, psychological warfare, and tactical restraint [11]. Co-UAVs are the breakthrough point of future unmanned warfare. In the subsequent research of USAF, hundreds of simulation experiments were conducted to simulate the interception of Co-UAVs' attacks to Aegis air defense system [12]. The results show that the defense system is difficult to intercept all UAVs and the defense system has been repeatedly broken through, which indicates the superior attack performance of Co-UAVs. In 2015, the Defense Advanced Research Projects Agency (DARPA) published the "Gremilins" project, which plans to develop partially recoverable Co-UAVs for reconnaissance and electronic warfare [13]. The Gremilins can defeat the enemy by suppressing missile defense system, cutting off communication, and attacking the enemy's data network based on a large amount of UAVs. In 2016, China Electronics Technology Corporation (CETC) firstly established Co-UAVs test prototype in China and verified the cooperative principle of 67 UAVs. In 2017, 119 fixed-wing UAVs' flight test was completed by CETC [14].

Both the theoretical and practical research studies indicate that the Co-UAVs have become the winning force of battlefield, which has the ability to change the game rules in the future [15]. However, the former research mainly focuses on the preplanned strategies, which means the ground attack strategy is preestablished before the UAVs arrive in the battlefield. It is very hard to preplan all the scenarios exhaustively, for the battlefield is unknown (or partially unknown) in advance.

Here, a human cooperation inspired approach of Co-UAVs is presented. We first take an explanation to goal-oriented cooperation of humans, especially the strategy making based on vision sharing. Then, a human-like model called parallel multiview splicing on clouds (PMVSC) which incorporates these biobehavioral-science insights in a structured cooperative system of UAVs. In addition to the development of PMVSC, we applied the model to a variety of ground attack tasks for multitargets that required mutual cooperation of UAVs. Finally, PMVSC is experimented in a real scenario (in which there are two distinct kinds objects to test the precise processing performance of Co-UAVs for multitargets) based on the experimental multi-UAVs platform.

2. Goal-Oriented Cooperation of Humans Based on Vision Sharing

The cooperation of humans (CoH) has been illustrated by social psychologist Lewin et al. [16, 17]. He pointed out that humans' cooperation is a complex group behavior (**B**) which is affected by internal individuals (**I**) and external environment (**E**):

$$\mathbf{B} = f(\mathbf{I}, \mathbf{E}), \tag{1}$$

where $\mathbf{B} = [B_1, B_2, \ldots, B_n]^{\mathrm{T}}$ represents the behavior set of individuals and n is the total amount of individuals in group. $\mathbf{I} = [I_1, I_2, \ldots, I_n]^T$ is the internal conditions and characteristics of individuals, which consists of various physiological and psychological factors, such as physiological needs, physiological characteristics, ability, and personality. $\mathbf{E} = [E_1, E_2, \ldots, E_n]^T$ is the external environment around every individual.

The Lewin CoH model reveals the general principles of human behavior to some extent. However, it is a passive cooperation model with no clear goals. Goal-oriented behavior is the process of seeking to achieve general goals of group. In a cooperative mission, every individual has his own task; they work independently as well as parallel to fulfill the general goal. So, equation (1) can be revised as follows:

$$\mathbf{B} = f(\mathbf{I}, \mathbf{E}, \mathbf{G}), \tag{2}$$

where $\mathbf{G} = [G_1, G_2, \ldots, G_n]^T$ represents the group goals, which is composed with each individual goal.

Take a typical scenario, as shown in Figure 1, for example. The general goal is to find all the objects (the red circle in Figure 1) in the environment, but there are obstacles blocking the sight. Each individual can only see local objects and environment (the translucent vision). They share their visions to get the overall environment so as to consult together to get a proper objects assignment.

3. Goal-Oriented Cooperation Mechanism Based on Vision Sharing

3.1. Outline of Parallel Multiview Splicing on Clouds. A graphical representation of our proposed architecture is given in Figure 2, which proposes that perceiving, cognizing, and assigning targets upon UAVs' cooperation system in environment is like in the case of goal-oriented cooperation of humans based on vision sharing, and each individual is responsible for specific target, together to fulfill the overall goal.

In PMVSC, the targets (including the true and the false) are firstly perceived by UAVs and each UAV can only know the targets in its own field of vision (FoV). There are several

Figure 1: A typical scenario of humans' cooperation.

UAVs over the target environment, detecting the targets by onboard cameras. Though an UAV can get local information through the perceive module, it cannot remove repeated targets in group. Each UAV uploads its perceived information in FoV to clouds through the vision sharing module. The vision sharing module preprocesses the detected environment information of respective UAVs, and then the separated FoV are combined to make a full and detailed environment in a single map. Next, the entire map is transferred to the cognize module to distinguish whether the targets are true or false. The valuable and true targets are necessary to be attacked, while disguised and false targets not. Finally, the information of true targets is delivered to the next module, which is responsible for task assignment and path planning.

For the PMVSC architecture, to achieve such complicate processes, a number of components are required to explicate, which are described in the following sections together with mathematical algorithms derivation.

3.2. The Components and Algorithms of PMVSC. Supposing there are N UAVs to perform the attack task. For the kth UAV in group, the image perceived by the camera is $I_k(x, y)$, where (x, y) is the position in direction of x- and y-axis in the perceived image. In the perceived module, the colorful image should be preprocessed to make it more convenient for subsequent processing.

The original image I_k from camera is in the red, green, and blue model (RGB-model); each color appears in the primary spectral components of red, green, and blue color. The model is based on the Cartesian coordinate system. The RGB-model has advantages in observation and application. However, as pointed out by Ali et al. [18], the RGB-model has two inferiors compared to the hue, saturation, and illumination model (HSI-model): (a) the three components are used to describe the image together, resulting in a lot of unnecessary information among the components which will increase the calculation. (b) The change of Euclidean distance between point and point in RGB space is not proportionate to the change of actual color. When color separation is carried out, it is easy to make false separation, omit useful information, or mix useless information with useful information.

Figure 3 shows the HSI cylindrical color space model, where f_{h}, f_{s}, and f_{i} represent the value of hue, saturation, and illumination, respectively:

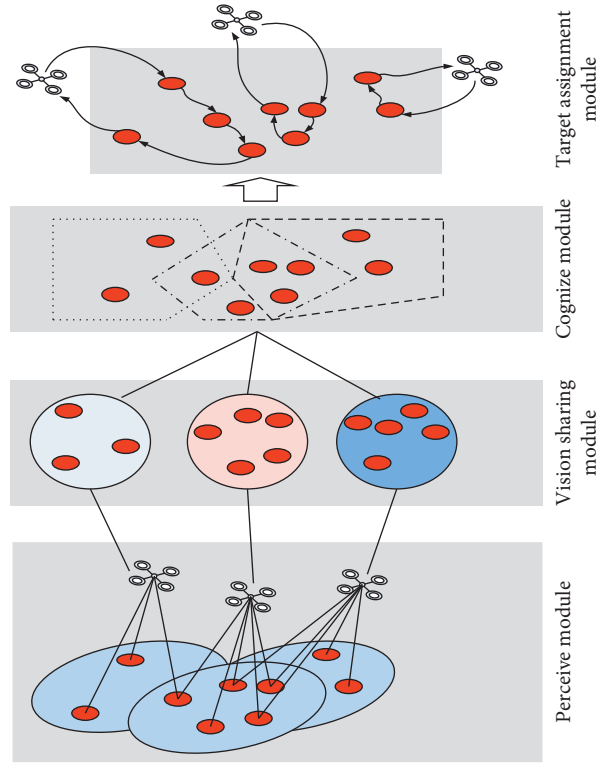

Figure 2: Outline of parallel multiview splicing on clouds.

$$f_{\mathrm{h}} = \arccos\left\{\frac{1/2\left[\left(f_{\mathrm{r}} - f_{\mathrm{g}}\right) + \left(f_{\mathrm{r}} - f_{\mathrm{b}}\right)\right]}{\left[\left(f_{\mathrm{r}} - f_{\mathrm{g}}\right)^2 + \left(f_{\mathrm{r}} - f_{\mathrm{g}}\right)\left(f_{\mathrm{g}} - f_{\mathrm{b}}\right)\right]^{1/2}}\right\},$$

$$f_{\mathrm{s}} = 1 - \frac{3}{f_{\mathrm{r}} + f_{\mathrm{g}} + f_{\mathrm{b}}}\left[\min\left(f_{\mathrm{r}}, f_{\mathrm{g}}, f_{\mathrm{b}}\right)\right],$$

$$f_i = \frac{1}{3}\left(f_{\mathrm{r}} + f_{\mathrm{g}} + f_{\mathrm{b}}\right), \tag{3}$$

where f_{r}, f_{g}, and f_{b} represent the normalized value of red, green, and blue color in the image.

The perceive module functions on converting RGB to HSI. In HSI-model, the image features are obvious in its space. After converting RGB space to HSI space, the connection of each information structure is more compact, each component is more independent of each other, and the loss of color information is less, which lays a good foundation for segmentation and target recognition.

After transfer RGB to HSI, the information of I_k should be uploaded to the vision sharing module, which purposes on information normalization and image invariance, which is shown in Figure 4.

In image processing, the moment invariant feature can reflect shape information of the image, and it has the ability of translation invariance and scalability invariance [19]. For an obtained image $I_k(x, y)$, define its $(\mathrm{p} + \mathrm{q})$-order origin moment as follows:

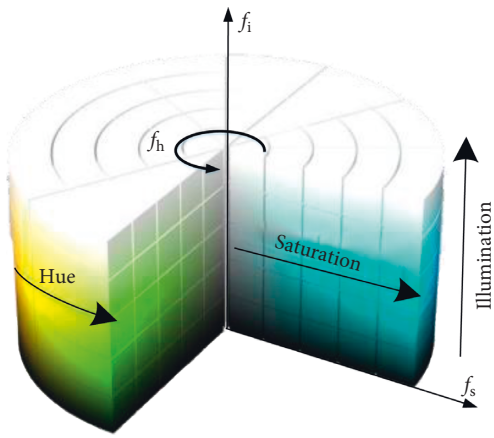

Figure 3: HSI cylindrical color space model.

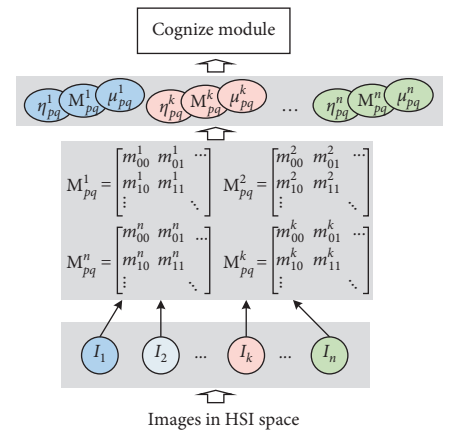

Figure 4: Schematic of the vision sharing module.

$$m_{pq}^{k} = \sum_{y=1}^{M_k} \sum_{x=1}^{N_k} x^p y^q I_k(x, y), \tag{4}$$

where M_k and N_k represents the maximum row and column scale of image $I_k(x, y)$ and (x, y) is the position in direction of x- and y-axis in $I_k(x, y)$, $p, q \in \{0, 1, 2, \ldots\}$.

However, the origin moment m_{pq}^{k} responds to changes in $I_k(x, y)$. To achieve the invariance of translation and scalability, the m_{pq}^{k} is improved to $(p+q)$-order central moment:

$$\mu_{pq}^{k} = \sum_{\text{row}=1}^{M_k} \sum_{\text{col}=1}^{N_k} (x - \overline{x})^p (y - \overline{y})^q I_k(x, y), \tag{5}$$

where $\overline{x}$ and $\overline{y}$ represent the centroid position of the image, and they can be calculated by the following equation:

$$\begin{aligned} \overline{x} &= \frac{\sum_x \sum_y x I_k(x, y)}{\sum_x \sum_y I_k(x, y)}, \\ \overline{y} &= \frac{\sum_x \sum_y y I_k(x, y)}{\sum_x \sum_y I_k(x, y)}. \end{aligned} \tag{6}$$

Because the μ_{pq}^{k} can only keep the translation invariance, so normalized central moment η_{pq}^{k} is defined to obtain the ability of scalability invariance:

$$\eta_{pq}^{k} = \frac{\mu_{pq}}{\mu_{00}^{(p+q)/2}} = \frac{\sum_{\text{row}=1}^{M_k} \sum_{\text{col}=1}^{N_k} (x - \overline{x})^p (y - \overline{y})^q I_k(x, y)}{\left[\sum_{\text{row}=1}^{M_k} \sum_{\text{col}=1}^{N_k} I_k(x, y)\right]^{(p+q)/2}}. \tag{7}$$

In a cognize module, as shown in Figure 5 , the main functions are rotation invariance, image mosaic, and targets classification.

From [20], we can infer that the rotation invariance can be obtained by the set of equations (8) based on normalized central distance:

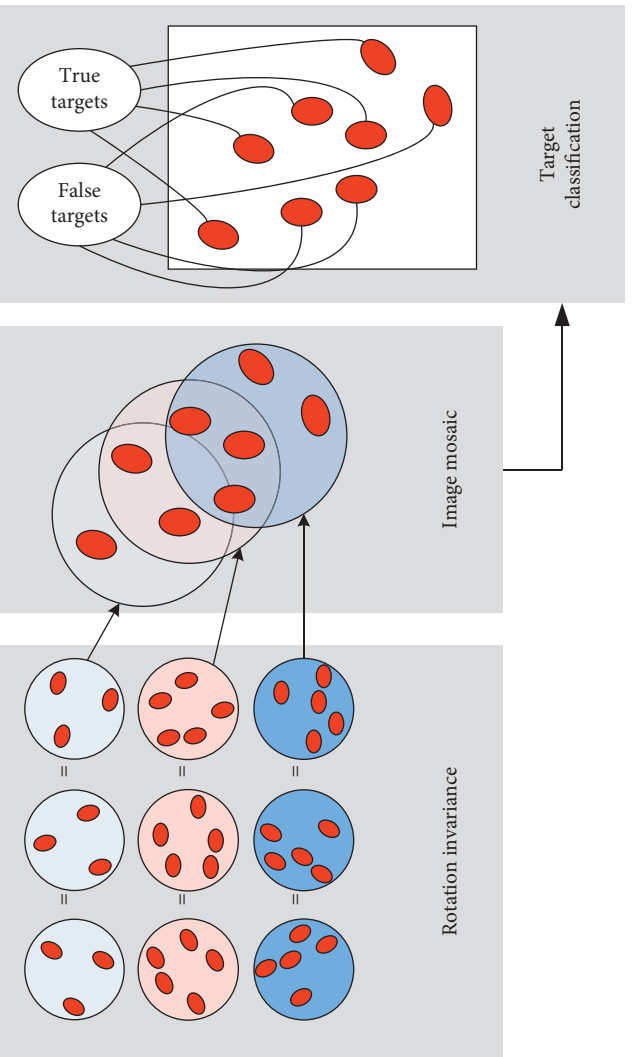

Figure 5: Schematic of the cognize module.

$$\begin{cases} \varphi_1 = \eta_{20} - \eta_{02}, \\ \varphi_2 = (\eta_{20} - \eta_{02})^2 + 4\eta_{11}^2, \\ \varphi_3 = (\eta_{30} - 3\eta_{12})^2 + (3\eta_{21} - \eta_{03})^2, \\ \varphi_4 = (\eta_{30} + \eta_{12})^2 + (\eta_{21} + \eta_{03})^2, \\ \varphi_5 = (\eta_{30} - 3\eta_{12})(\eta_{30} + \eta_{12})\left[(\eta_{30} + \eta_{12})^2 - 3(\eta_{21} + \eta_{03})^2\right] + 3(\eta_{21} - \eta_{03})(\eta_{21} + \eta_{03})\left[3(\eta_{30} + \eta_{12})^2 - (\eta_{21} + \eta_{03})^2\right], \\ \varphi_6 = (\eta_{20} - \eta_{02})\left[(\eta_{30} + \eta_{12})^2 - (\eta_{21} + \eta_{03})^2\right] + 4\eta_{11}(\eta_{30} + \eta_{12})(\eta_{21} + \eta_{03}), \\ \varphi_7 = (3\eta_{21} - \eta_{03})\left[(\eta_{30} + \eta_{12})(\eta_{30} + \eta_{12})^2 - 3(\eta_{21} + \eta_{03})^2\right] - (\eta_{30} - 3\eta_{12})(\eta_{21} + \eta_{03})\left[3(\eta_{30} + \eta_{12})^2 - (\eta_{21} + \eta_{03})^2\right]. \end{cases} \tag{8}$$

To the images $I_k(x, y)$ and $I_l(x, y)$, as shown in Figure 6, the crucial procedure of image mosaic is to find the most similar region in both and to montage the two images based on the common region. Supposing the test region is a square with length L_{tr}, the similarity between two images is defined as $\text{sim}[(I_k I_l), L_{\text{tr}}]$. Then, the image mosaic can be fulfilled by calculating the minimum value:

$$\begin{aligned} \text{Sim}[(I_k, I_l), L_{\text{tr}}] &= \sum_{i=1}^{L_{\text{tr}}} \sum_{j=1}^{L_{\text{tr}}} \Big\| \Big[f\big(I_k(x_{a+i}, y_{b+j}), L_{\text{tr}}\big) \\ &\quad - f\big(I_k(x_{c+i}, y_{d+j}), L_{\text{tr}}\big)\Big] \Big\| \\ &= \Bigg\| \sum_{i=1}^{L_{\text{tr}}} \sum_{j=1}^{L_{\text{tr}}} \Big[\big(I_k(x_{a+i}, y_{b+j})\big) - I_k(x_{c+i}, y_{d+j})\Big] \\ &\quad - \sum_{i=1}^{L_{\text{tr}}} \sum_{j=1}^{L_{\text{tr}}} \frac{\big[\big(I_k(x_{a+i}, y_{b+j})\big) - I_k(x_{c+i}, y_{d+j})\big]^2}{L_{\text{tr}}} \Bigg\|. \end{aligned} \tag{9}$$

Once the image is mosaicked ready, all the detected targets are combined in a whole image $\text{WI}(x, y)$. Then, the targets should be classified to find out the true targets to attack. For the accurate recognition of multitargets, feature extraction and feature classification are the key issues. True and false targets are very similar, and even the distortion of real targets in the process of recognition will lead to recognition errors. A cognitive-based intelligent recognition method is used in this paper to classify target features with similarity constraints to achieve high accuracy of recognition.

Assume there are N targets in $\text{WI}(x, y)$. For the ith and jth targets $\text{TG}_i(x_i, y_i)$ and $\text{TG}_j(x_j, y_j)$, a matrix feature space $S_{\text{V}} \in \mathbb{R}^{N \times N}$ can be introduced to express the similarity between TG_i and TG_j:

$$S_{\text{v}}^{ij} = \begin{cases} \dfrac{\text{TG}_i^T \text{TG}_j}{\|\text{TG}_i\| \|\text{TG}_j a\|}, & \text{if } \text{TG}_i \text{ is similar to } \text{TG}_j, \\ 0, & \text{else.} \end{cases} \tag{10}$$

Then, the problem of feature classification and recognition for true and false targets can be transformed into the problem of similarity constraints on feature vector $\mathbf{TG} = \{\text{TG}_1, \text{TG}_2, \ldots, \text{TG}_N\} \subset \text{WI}$. To classify the targets with similar features, that is to minimize the similarity of the same kind of targets equation (11) shows

$$\min_{\text{TG}} \left\| S_{\text{V}} - \text{TG}^T \text{TG} \right\|_F. \tag{11}$$

Since equation (11) is an optimization problem of matrices, it is necessary to transform it into a singular value matrix in order to obtain the optimal solution. Let the singular values of matrix S_{V} be

$$S_{\text{V}} = P \sum P^T, \tag{12}$$

where P is the transformation matrix and $\sum$ is the singular value matrix of $N \times N$.

Assuming that $\sum_k$ is a diagonal matrix composed of the first $\sum_k$ singular values of matrix K and S_{V} is a left singular value vector corresponding to $P_{\bullet k}$, there is a definite solution of $\min_{\text{TG}} \|S_{\text{V}} - \text{TG}^T \text{TG}\|_F$:

$$\mathbf{U}_k = \sum_k^{1/2} P_{\bullet k}^T. \tag{13}$$

For any orthogonal matrix $\mathbf{T}$, to verify that $I_k = \mathbf{U}_k \cdot \mathbf{T}$ is still the solution of $\min_{\text{TG}} \|S_{\text{V}} - \text{TG}^T \text{TG}\|_F$ problem. Therefore, the problem of the original objective function can be rewritten as follows:

$$\begin{cases} \min\limits_{\mathbf{TG}, T} \left\| \mathbf{U}_k \mathbf{T}^T - \mathbf{TG} \right\|_F, \\ \text{s.t.} \quad \mathbf{T}^T \mathbf{T} = I. \end{cases} \tag{14}$$

If $\mathbf{U}_k$ is used as the input layer and $\mathbf{TG}$ as the output layer of the network, the problem can be used as the deep confidence network model to solve, which is similar to the energy function of deep confidence networks [21]. Take the $u_i \in \mathbf{U}_k$ of each network input layer as a visible variable and $\text{TG}_I \in \mathbf{TG}$ as a hidden variable, and the energy function can be defined by using the Gauss-constrained Boltzmann machine model as equation (15) in order to classify the feature data reasonably:

$$E(u, TG; \theta) = \sum_{i=1}^{D} \frac{(u_i - d_i)}{2\sigma_i^2} - \sum_{i=1}^{D} \sum_{j=1}^{M} T_{ij} \text{TG}_j \frac{u_i}{\sigma_i} - \sum_{j=1}^{M} c_j \text{TG}_j, \tag{15}$$

where $\theta = \{T, d, c, \sigma\}$ are the model parameters and D and M represent the number of visible and hidden units in the network, respectively.

By defining the range of value for model similarity constraint parameter σ, the similarity of data eigenvalue classification can be changed. That is to say, it achieves the cognitive recognition characteristics of similar targets, and

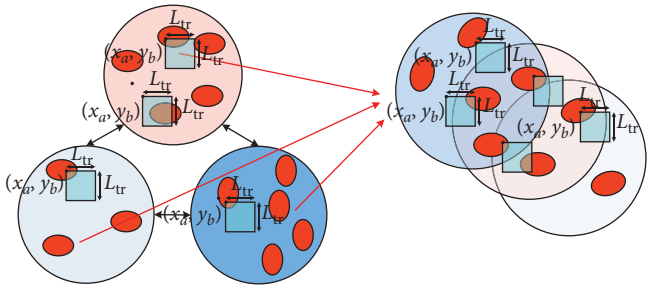

Figure 6: Schematic of optimal image mosaic.

finally it can distinguish true targets $\mathbf{TG}^F$ and false targets $\mathbf{TG}^F$ from $\mathrm{WI}(x, y)$, which is shown in Figure 7. For a target $\mathbf{TG}_j$, the feature point is S_v^j. Supposing the feature points of samples are $\mathbf{S}_F$ and $\mathbf{S}_T$. From equation (12), if $QS_v^jQ^T = P\mathbf{S}_FP^T$, TG_j belongs to the false target, or it is true target.

In the last process, the true target assignment of Co-UAVs is studied. Although many intelligent methods have been used to study multiagent cooperative problems [22–26], especially for the unpredictable results of each UAV's behavior in target assignment, it will affect the implementation of all strategies of subsequent UAVs. However, these methods are too subjective, and they are highly coupled with real-time tasks allocation process. It is necessary to introduce some more objective and dynamic methods for targets assignment. In this paper, the Bayesian network is introduced into UAV target assignment task modeling to solve the dynamic adjustment and real-time strategy in target assignment.

The Bayesian network is a directed acyclic graph with probability annotations, which can be used to reveal learning and statistical inference functions for prediction, causal analysis, etc. For multiple UAVs' target assignment task in this paper, its Bayesian network can be expressed as follows:

$$B = \langle G, P \rangle, \tag{16}$$

where $G = \langle U, S, A \rangle$ is a directed acyclic graph, $U = \{u_1, u_2, u_3, \ldots, u_N\}$ is a member of Co-UAVs participating in the mission, S is a set of arcs of graph G, and P is a probability annotation of graph G, which is shown in Figure 8.

For any UAV member u_k, each element in P represents the conditional probability density of the target node. The rule of probability density is as follows:

$$\begin{aligned} P(S) &= P\left(S_{T1}, S_{T2}, S_{T3}, \ldots, S_{Tm}\right) \\ &= \prod_{i=1}^{m} P\left(S_{Tm} \mid S_{T1}, S_{T2}, \ldots, S_{Tm-1}\right), \end{aligned} \tag{17}$$

where the calculation of probabilistic $P(s)$ needs 2^{m-1} probabilistic values, and the amount of calculation is very huge.

Therefore, the introduction of variable independence hypothesis in Bayesian networks can greatly reduce the prior probability of the definition of Bayesian networks. For the probability density rule constructed in this paper, we can find a minimum subset $S_u \subseteq \{S_{T1}, S_{T2}, S_{T3}, \ldots, S_{Tm-1}\}$, for

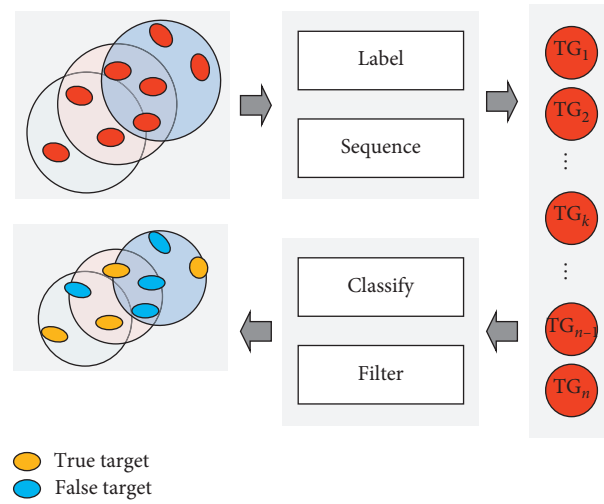

Figure 7: Schematic of targets classification.

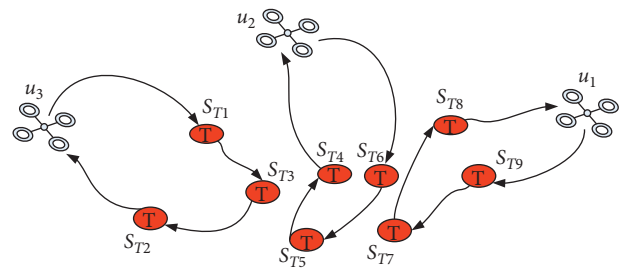

Figure 8: Schematic of targets assignment based on the Bayesian network.

any target task node S_{Tm} in the network structure, which is not independent of S_{Tm} condition:

$$P\left(S_{Tm} \mid S_{T1}, S_{T2}, \ldots, S_{Tm-1}\right) = P\left(S_{Tm} \mid S_u\right), \tag{18}$$

where S_u is the parent node set of S_{Tm} in graph $G = \langle U, S, A \rangle$. In this way, the probability distribution of mission node S_{Tm} allocated to UAV u_k can be determined uniquely:

$$P_{u_k}(S_{Tm}) = \prod_{i=1}^{m} p\left(S_{Tm} \mid S_u\right). \tag{19}$$

Finally, the else true targets can be assigned by the other Co-UAVs, such as UAV member u_l:

$$P_{u_l}(S_{Tn}) = \prod_{i=1}^{m} p\left(S_{Tn} \mid S_u\right), \quad S_{Tn} \neq S_{Tm}. \tag{20}$$

4. Experiments

4.1. The Experimental Platform of UAVs. The experiments have been conducted on the Co-UAVs with adaptive camera, flight controller, algorithmic solver, and data transmitter. Figure 9 shows a single UAV platform, which perceives outside environment from its onboard adaptive resolution camera embedded on the 3-DOF pan-tilt platform, inside real-time flight status from inner sensors

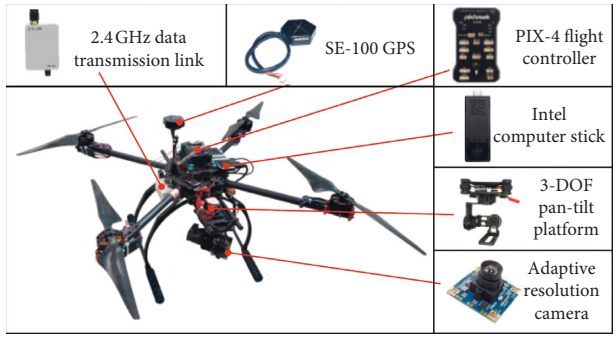

Figure 9: A single UAV experimental platform.

Figure 10: Co-UAVs' experimental platform.

integrated in the PIX-4 flight controller. Then, the information of outside environment and inside status are transmitted to airborne Intel computer stick, which functions on algorithm computing, target recognizing, and instruction generating. Finally, the generated instructions are converted to motor commands via the PIX-4 controller.

The Co-UAVs' experimental platform is shown in Figure 10. The mobile screen can read all data from onboard Intel computer stick and change the algorithm parameters. The ground station functions on obtaining real-time information from flying UAVs, including image features, flight status, and cooperative information. After calculation, the ground station sends control commands to each UAV.

4.2. Image Mosaic. Figures 11(a)–11(d) show 4 images captured by cameras onboard by Co-UAVs, which are transferred to clouds (ground station).

The combined image of the whole environment can be obtained by applying the image mosaic algorithm proposed in this paper. Define the test region is a square with length $L_{tr} = 80$ pixels and the threshold value of image mosaic $\text{sim}[(I_k, I_i), L_{tr}]$ is 0.85. The result of WI is shown in Figure 12.

In Figure 12, the four images are montaged together. Also, the information of the whole environment can be obtained through the image mosaic. Result shows the proposed method can find similar region between images, and montage the four images based on the common region, indicating the superiority and feasibility of PMVSC.

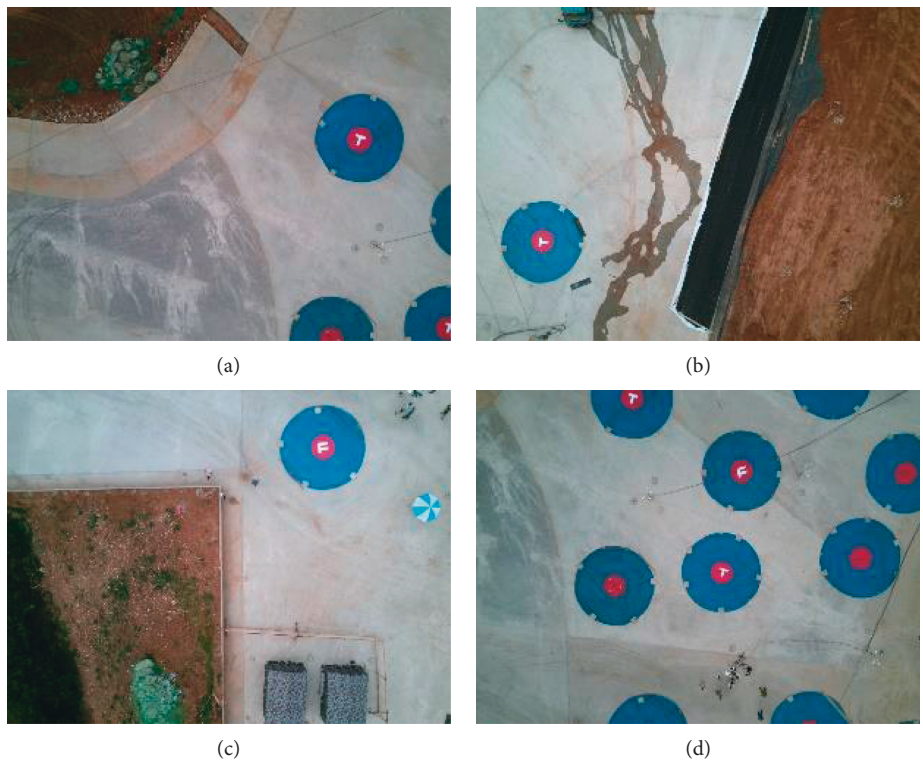

(a) (b) (c) (d)

Figure 11: The 4 images captured by cameras onboard by Co-UAVs. (a) Image 1. (b) Image 2. (c) Image 3. (d) Image 4.

Figure 12: Image mosaic of four images from Co-UAVs.

4.3. Targets' Recognition. Setting $S = S_r \cup S_F = \{S_{T1}, S_{T2}, S_{T3}, S_{F1}, S_{F2}, S_{F3}\}$ and $U = \{u1, u2, u3\}$, that is, there are three true targets and three false targets in the targets' area and three UAVs are involved in the search and attack mission. Set model parameters $T = I_{N\times N}$ as unit matrix and $d = 0.2$, $c = 0.4$, and $\sigma = 0.15$ as related constraints for feature constraints of targets.

The standard true and false targets used for training are shown in Figure 13, and the test results of each UAV in actual flight are shown in Figure 14. Even if the target has a large distortion (such as dust cover, edge deformation, and random influence of the direction of true or false identification), the proposed method can extract feature points to calculate similarity and classify them and recognize them accurately.

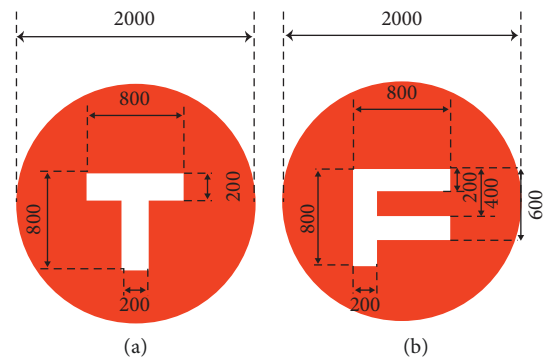

(a) (b)

Figure 13: Standard true and false targets for training (unit: mm).

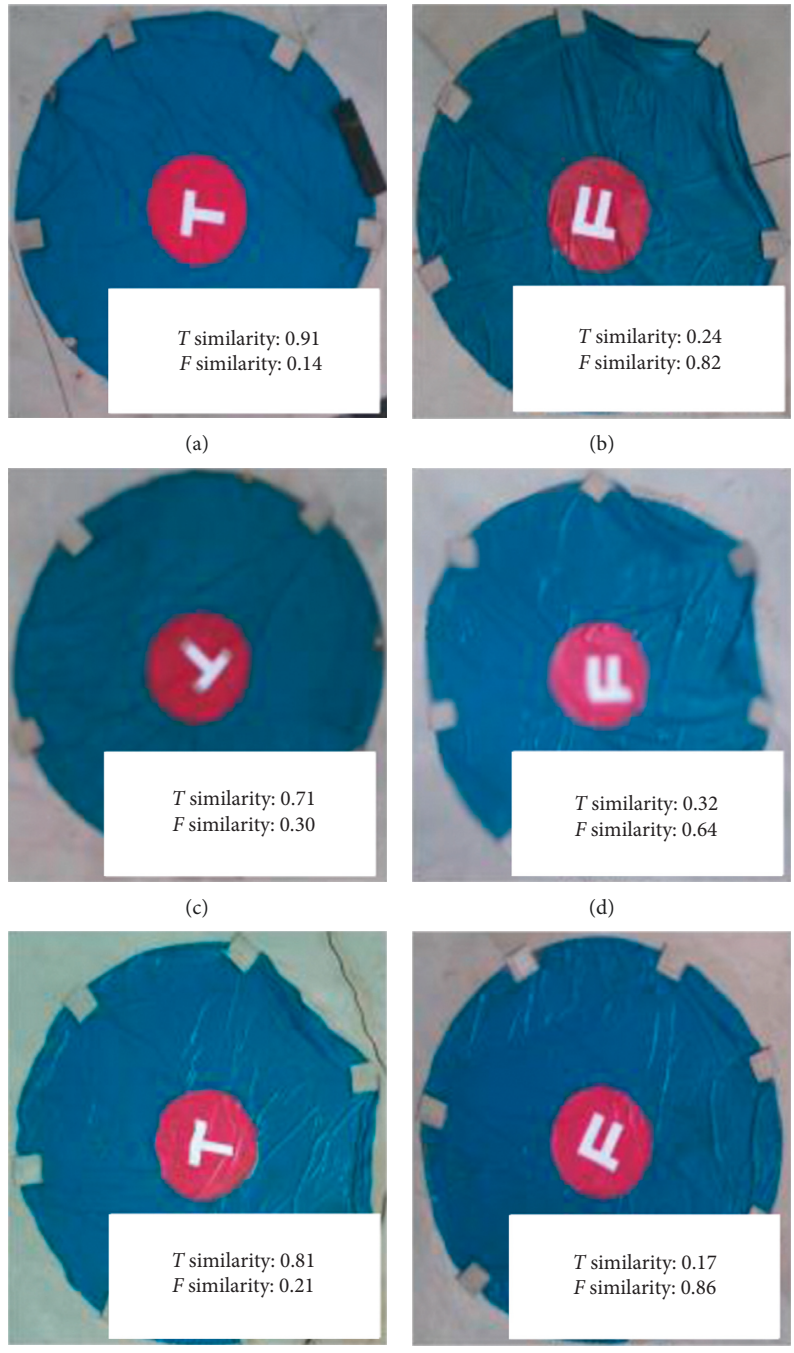

Figure 14: Accurate recognition of multiple targets.

In order to describe the target recognition process of this algorithm, a real target (Figure 14(a)) and a false target (Figure 14(f)) are selected to elaborate, and the pictures in the process of processing are presented as shown in Figures 15 and 16, respectively.

The airborne computer first transforms the acquired image into HSI color space, which can be recognized by the machine. After eliminating the useless information, it extracts the eigenvalues of the transformed image. However, in the original eigenvalue space, the eigenvalues are almost full of the whole eigenvalue space, so it is impossible to classify the features to distinguish the target type. Therefore, according to the algorithm constructed in this paper, the feature space is transformed. In the transformed feature space, the eigenvalues have obvious distribution characteristics and can be directly classified. Figures 15(d) and 16(d) are identified as different types of target categories, where Figure 15(d) belongs to *T* target

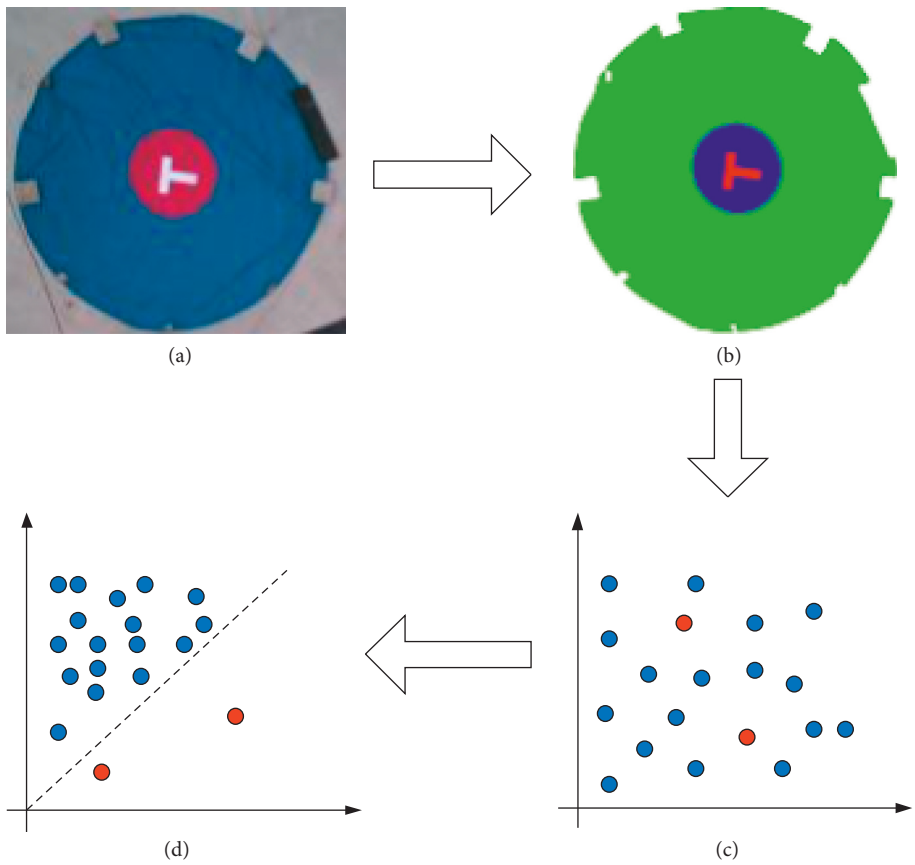

Figure 15: The true target process.

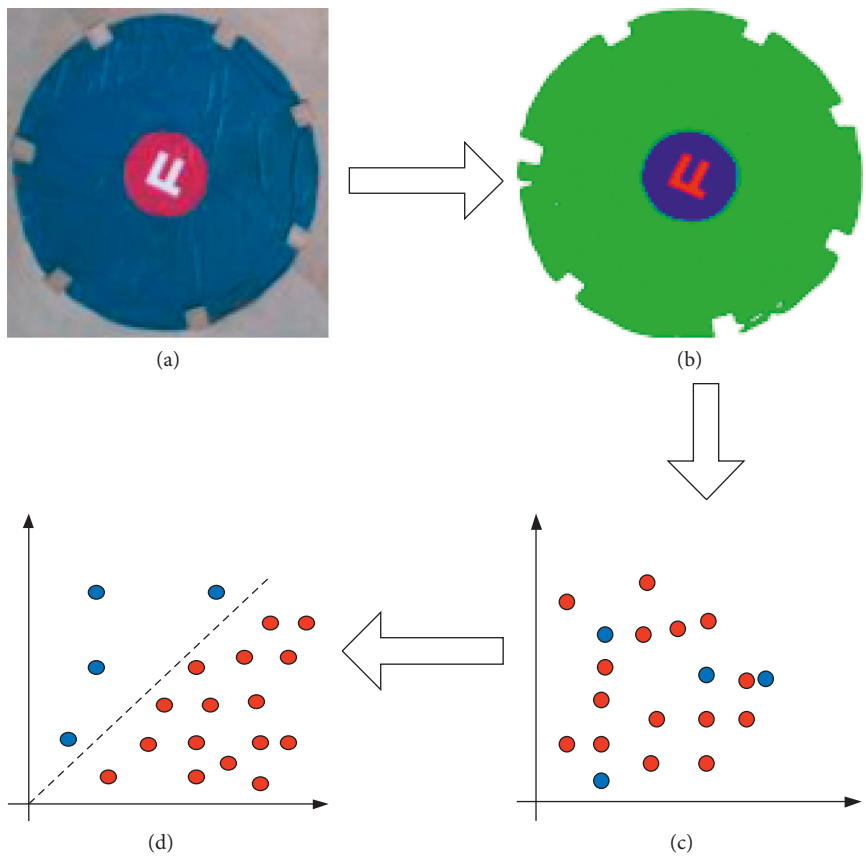

Figure 16: The false target process.

and Figure 15(d) belongs to F target. Finally, the true and false targets are identified in the new feature space and the task of accurate multitarget group recognition is completed.

4.4. Targets' Assignment. Assuming the UAV has detected all the true targets, it is necessary to assign the task of each UAV so that the Co-UAVs can cooperate to fulfill the task with the minimum cost. For the lth member of Co-UAVs $u1$, the probability of attacking the true target S_{Ti} is

$$P(S_{Ti}) = \prod_{i=1}^{3} p\left(S_{Ti} \mid \{S_T - S_{Ti}\}\right). \tag{21}$$

Figure 17 is a picture of cooperative attack of multiple UAVs over the targets. Three UAVs will attack its corresponding targets, and their attack probability to respective targets is 0.83, 0.82, and 0.86. All $P(S_{Ti})$ are labelled in Figure 11, and the optimal task allocation decision among all UAVs can be obtained by choosing the maximal probability value. Based on the UAV experimental platform, the relevant target assignment algorithms in this paper are tested. Not limited to the derivation of theoretical simulation, this paper applies the algorithm to practice and completely reproduces the feasibility of the algorithm from the actual Co-UAVs' platform.

4.5. Experimental Results on Co-UAVs. In order to verify the effectiveness and feasibility of the proposed mechanism, PMVSC is tested in a real environment. In the experiment, 3 Co-UAVs were used to cluster, search, identify, and locate the true and false targets (circular target, diameter 7 m, and target recognition area 2 m) in the target area and then attack the target. The area is about 1000 m × 250 m, and the flight area includes the take-off and landing area (the rectangular area of the take-off and landing area is 100 m × 50 m) and the target area (the rectangular area of 200 m × 300 m). Six targets were set in the target area. During each attach task, three targets are randomly selected and placed a white sign "T" in the target center to represent the true target. Similarly, the other three targets use "F" sign to represent the false target.

The schematic illustration of the actual experimental environment is shown in Figure 18 (the experimental area is the irregular area shown in the figure due to the limitation of the actual environment), which contains hidden targets (grey), real targets, and false targets (red).

Figure 19 shows a practical area of three Co-UAVs in the aerial above targets' environment. There are multiple targets needing recognition. Each UAV can perceive outside world from onboard camera, and the perceived information is transferred to clouds (which is shown in Figure 18, the green area) to merge independent and partial images to a whole image and to distinguish the true targets. Finally, the true

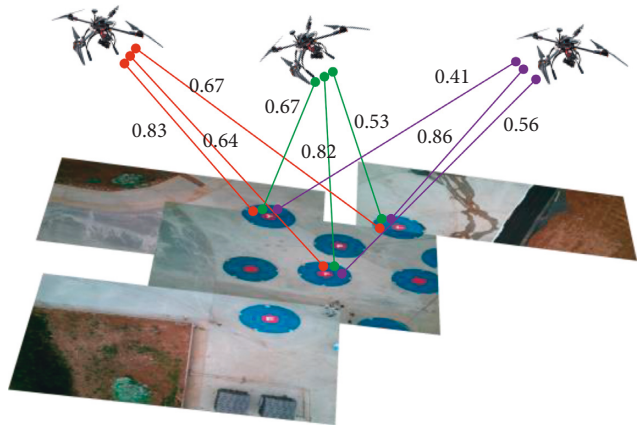

Figure 17: Cooperative attack of multiple UAVs over the targets.

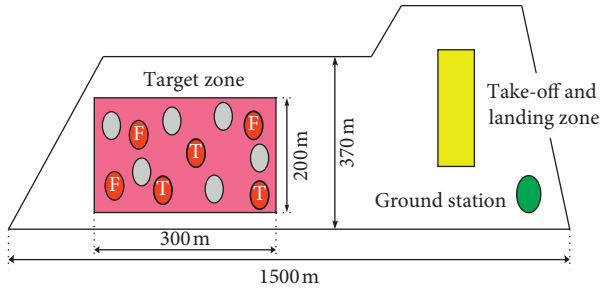

Figure 18: Schematic illustration of the actual experimental environment.

Figure 19: Three Co-UAVs' flight experiment.

targets are assigned to respective UAVs to attack, which is shown in Figures 20(a) and 20(b). In Figure 20(a), the armed UAV (which carries a white sandbag as ammunition) gets attack command, and then flies to the assigned target. Also, Figure 20(b) is the result after attack, from which we can see the target is attacked precisely, indicating the feasibility and validity of the proposed method based on Co-UAVs.

(a) (b)

Figure 20: Three Co-UAVs' flight experiment.

5. Conclusions

Aiming at the problem of attacking multitargets, this paper proposes a strategy of multi-UAVs' precise target recognition, attack, and task assignment based on PMVSC. Following are some concluding remarks.

(a) A humanoid mechanism and algorithm is built referring to humans' vision sharing model. The proposed PMVSC not only performs well in simulations but also in experimental practices.

(b) A UAV platform is built, which consists of onboard camera, 3-DOF pan-tilt, PIX flight controller, and computer stick. The Co-UAVs are based on multiple UAVs and ground station. All the proposed algorithms (including vision sharing, target recognition, and target assignment) are tested on Co-UAVs to confirm the proposed method is practically feasible.

(c) The proposed constructive mechanism is expected to shed new insight on our understanding of human vision sharing, which can directly reflect in the design of human-like algorithms.

Still, there are several issues in need of further study.

(a) The cooperation among dozens of UAVs: though the cooperation and formation of UAVs have been studied, the proposed method is applied in only three UAVs; thus, how to make it general and be possible implemented in more UAVs is an important work.

(b) Moving targets attack: in this paper, the targets are placed on ground, which means they are static. Compared with moving targets, static targets are much harder to attack. Research on dynamic targets needs further study.

Data Availability

All data generated or analyzed during this study are included within the manuscript. Besides, all data included in this study are available upon request by contacting the corresponding author.

Conflicts of Interest

The authors declare that they have no conflicts of interest.

Acknowledgments

This work was supported in part by the National Natural Science Foundation of China under Grant 61573373.

References

[1] Y. Gao and D. Li, "UAV swarm cooperative situation perception consensus evaluation method based on three-parameter interval number and heronian mean operator," *IEEE Access*, vol. 6, pp. 73328–73340, 2018.

[2] S. Shim, T. Kim, and S. Hyun, "Control integrated query processing system for coordination of multiple UAVs," in *Proceedings of the 2017 14th IEEE Annual Consumer Communications & Networking Conference (CCNC)*, pp. 528–533, Las Vegas, NV, USA, January 2017.

[3] Z. Shi, X. Huang, Y. Hua, and D. Xu, "Statistical physics method for multi-base multi-UAV cooperative reconnaissance mission planning," in *Proceedings of the 2015*

IEEE Advanced Information Technology, Electronic and Automation Control Conference (IAEAC), pp. 64–68, IEEE, Chongqing, China, December 2015.

[4] J. Yang, J. Xi, C. Wang, and X. Xie, "Multi-base multi-UAV cooperative patrol route planning novel method," in *Proceedings of the 2018 33rd Youth Academic Annual Conference of Chinese Association of Automation (YAC)*, pp. 688–693, IEEE, Nanjing, China, May 2018.

[5] P. Li and H. Duan, "A potential game approach to multiple UAV cooperative search and surveillance," *Aerospace Science and Technology*, vol. 68, pp. 403–415, 2017.

[6] W. Geng, F. Kong, and D. Ma, "Study on tactical decision of UAV medium-range air combat," in *Proceedings of the 26th Chinese Control and Decision Conference (2014 CCDC)*, pp. 135–139, Changsha, China, May-June 2014.

[7] M. Suresh and D. Ghose, "UAV grouping and coordination tactics for ground attack missions," *IEEE Transactions on Aerospace and Electronic Systems*, vol. 48, no. 1, pp. 673–692, 2012.

[8] H. Luo, G. Wang, X. Hu, and W. Xia, "Task allocation model for multi UAVs based on agents," *Fire Control & Command Control*, vol. 7, no. 39, pp. 22–27, 2014.

[9] N. Wang, X. Gu, J. Chen, L. Shen, and M. Ren, "A hybrid neural network method for UAV attack route integrated planning," in *Advances in Neural Networks—ISNN 2009*, pp. 226–235, Springer, Berlin, Germany, 2009.

[10] M. Zhao, B. Li, and M. Wang, "Auction algorithm based multi-UAV arriving simultaneously to attack multiple targets with uncertain information," *Electronics Optics and Control*, vol. 22, no. 2, pp. 89–94, 2015.

[11] G. Jia and Z. Hou, "The analysis and enlightenment about the UAV swarming project of the United States Military," *National Defense Science & Technology*, vol. 38, no. 4, pp. 53–57, 2017.

[12] E. J. Walsh, "Integrated combat systems," *Sea Power*, vol. 1, no. 44, p. 152, 2001.

[13] C. Yuan, "The gremilins project of defense advanced research projects agency," *Ordnance Knowledge*, vol. 1, no. 9, pp. 37–39, 2016.

[14] J. Yu, "When UAVs have swarm intelligence," *People's Daily*, vol. 7, no. 7, p. 1, 2017.

[15] W. Grimm and K. H. Well, *Modelling Air Combat as Differential Game Recent Approaches and Future Requirements*, Springer, Berlin, Germany, 1991.

[16] K. Lewin, R. Lippitt, and R. K. White, "Patterns of aggressive behavior in experimentally created "social climates"," *The Journal of Social Psychology*, vol. 10, no. 2, pp. 269–299, 1939.

[17] K. Lewin and P. Grabbe, "Conduct, knowledge, and acceptance of new values," *Journal of Social Issues*, vol. 1, no. 3, pp. 53–64, 1945.

[18] N. M. Ali, N. Khair, A. M. Rashid, and Y. M. Mustafah, "Performance comparison between RGB and HSV color segmentations for road signs detection," *Applied Mechanics and Materials*, vol. 393, no. 1, pp. 550–555, 2013.

[19] M. El Mallahi, A. Mesbah, H. Karmouni, A. El Affar, A. Tahiri, and H. Qjidaa, "Radial Charlier moment invariants for 2D object/image recognition," in *Proceedings of the 2016 5th International Conference on Multimedia Computing and Systems (ICMCS)*, pp. 41–45, IEEE, Marrakech, Morocco, September-October 2016.

[20] J. Zhao and X. Wang, "Vehicle-logo recognition based on modified HU invariant moments and SVM," *Multimedia Tools and Applications*, vol. 78, no. 1, pp. 75–97, 2019.

[21] B. Zhang, Y. Kou, M. Wu, and J. Zuo, "Close-range air combat situation assessment using deep belief network," *Journal of Beijing University of Aeronautics and Astronautics*, vol. 43, no. 7, pp. 1450–1459, 2017.

[22] Q. Chen and U. Dayal, *Multi-Agent Cooperative Transactions for E-Commerce*, pp. 311–322, Springer, Berlin, Germany, 2000.

[23] J. Hu, L. Xie, J. Xu, and Z. Xu, "Multi-agent cooperative target search," *Sensors*, vol. 6, no. 14, pp. 8428–9408, 2014.

[24] J. Xi, C. Wang, H. Liu, and L. Wang, "Completely distributed guaranteed-performance consensualization for high-order multiagent systems with switching topologies," *IEEE Transactions on Systems, Man, and Cybernetics: Systems*, vol. 49, no. 7, pp. 1338–1348, 2019.

[25] J. Xi, M. He, H. Liu, and J. Zhang, "Admissible output consensualization control for singular multi-agent systems with time delays," *Journal of the Franklin Institute*, vol. 353, no. 16, pp. 4074–4090, 2016.

[26] Q. Zhang and R. Wei, "Unmanned aerial vehicle perception system following visual cognition invariance mechanism," *IEEE Access*, vol. 7, pp. 45951–45960, 2019.

Hindawi
Complexity
Volume 2019, Article ID 7672068, 16 pages
https://doi.org/10.1155/2019/7672068

WILEY | Hindawi

Research Article

Global Robust Exponential Synchronization of Multiple Uncertain Neural Networks Subject to Event-Triggered Strategy

Jin-E Zhang and Huan Liu

Hubei Normal University, Hubei 435002, China

Correspondence should be addressed to Jin-E Zhang; zhang86021205@163.com

Received 13 July 2019; Accepted 18 September 2019; Published 3 November 2019

Guest Editor: Raúl Villafuerte-Segura

This paper proposes the event-triggered strategy (ETS) for multiple neural networks (NNs) with parameter uncertainty and time delay. By establishing event-triggered mechanism and using matrix inequality techniques, several sufficient criteria are obtained to ensure global robust exponential synchronization of coupling NNs. In particular, the coupling matrix need not be the Laplace matrix in this paper. In addition, the lower bounds of sampling time intervals are also found by the established event-triggered mechanism. Eventually, three numerical examples are offered to illustrate the obtained results.

1. Introduction

Multisystem network is a complex dynamical network, which has received great attraction due to its many applications in various fields, such as secure communications and biological systems. The dynamical characteristics of multisystem networks have been paid more and more attention in the fields of science and engineering (see [1–4]). As we know, synchronization of a coupling system means that its all subsystems produce common behavior under different initial values. The coupling scheme describing the interaction rules between subsystems plays an important role in ensuring the synchronization. In particular, the synchronization of multisystem networks has become a hotpot of nonlinear scientific research because the synchronization of multisystem networks can better describe many observed natural phenomena and can create ordered multisystem networks. As a kind of control, coupling is the key to ensure the synchronization of complex dynamical networks; hence, several coupling schemes are proposed to realize the synchronization. However, most of the existing works require that the coupling matrix is always the Laplace matrix; that is, the row sums of the coupling matrix all are zero and the nondiagonal elements are nonnegative, which greatly restrict us to design a good performance coupling controller. In fact, we notice that there are some non-Laplacian coupling in complex dynamical networks, so we can try to achieve the synchronization of multisystem networks by constructing non-Laplacian coupling matrix. In addition, in recent decades, NNs have become a hot research topic because of its rich content and wide application; therefore, there are many results in the research of NNs, such as in [1, 5–12]. The authors in [1] proposed a new ETS to achieve the synchronization of multiple NNs (MNNs). The dynamical characteristics of nonautonomous fractional-order delay NNs were studied in [5]. Wu and Zeng [9] derived two anti-synchronization algorithms to realize exponential anti-synchronization of memristive recurrent NNs. In [10], some results were established to ensure the Lagrange stability of NNs with memristive synapses. Wu and Zeng [11] discussed a class of memristive NNs, and several sufficient criteria were established for exponential stabilization by using matrix inequality techniques. Wu et al. [12] proposed a novel and efficacious method to study the periodic NNs, and some new results for the periodic NNs were obtained. Therefore, it is an interesting and far-reaching research topic to study the synchronization of MNNs by constructing a proper non-Laplacian coupling matrix.

Parametric uncertainty arises from a partial understanding of mathematical models, for instance, empirical

quantities and constitutive laws (see [13–22]). The uncertainty of parameters must be considered in actual system because the parameters of the model in the process of industrial control are often uncertain. It is fortunate that uncertain parameters have been considered in many models in order to describe practical problems more accurately. In [13], the dynamical characteristics of stochastic nonlinear systems with parametric uncertainty were concerned. Maharajan et al. [14] investigated the problem of enhanced results on robust finite-time passivity for uncertain discrete-time Markovian jumping BAM delayed NNs. The authors in [17] provided several novel delay-dependent stability criteria to ensure robust stability of uncertain stochastic systems. Huang et al. [20] investigated robust state estimation of uncertain neural networks by designing robust state estimator and using new bounding technique. Zhu et al. [22] discussed the stability of uncertain neutral systems, and some new criteria were provided to guarantee the stability of the model. Moreover, fractional-order system is a charming research field, which describes the real world more accurately than integer-order system. Recently, Zhang [21] studied uncertain fractional-order system and its application. The uncertain parameters of the above models are required to be norm-bounded; it is a common way to deal with these uncertain parameters by using inequality techniques. With the mature of the technology, some problems in MNNs have been well solved; however, it is still a great challenge to design a feedback controller with good performance when we analyze multisystem networks. There are many papers about the topic of parametric uncertainty, but the issue about trusted control in the MNNs with uncertain parameters still has a long way to go and much further work is worth studying. In addition, time delay is often inevitable in practical systems, which may lead to instability of the system; in other words, time delay is the important reason for instability of the model. Although parameter uncertainty and time delay bring difficulties to the theoretical analysis of dynamical characteristics of system, in practical application, the analysis of model is often unreasonable without considering uncertain parameter and time delay. Hence, theoretical knowledge and practical experience urge us to study the dynamics problems of MNNs with parameter uncertainty and time delay.

Event-triggered mechanism is a very important sampling mechanism, that is, the emergence of certain events rely on the state of the system and this is also the difference between event-triggered feedback control and the traditional sampling mechanism. Because continuous-time control requires the continuous information, it is expensive and unrealistic in the real world. Unlike continuous-time control, event-triggered mechanism is a discontinuous-time control, which only requires the local communication data. Considering the sampling period, the sampling data control scheme usually adopts zero-order hold to keep the last sampling system state and control signal which is sent to the next event. In event-triggered mechanism, the sampling will not start and the controller will not be updated, unless its size reaches the specified threshold; therefore, the greatest advantage of event-triggered mechanism is to reduce communication data. Furthermore, event-triggered mechanism has been widely studied due to its effectiveness in practical systems, for example, [23–26] and references therein. Dolk and Heemels [23] investigated a networked control system subject to event-triggered control and its application to packet losses. In [24], a new decentralized event-triggered item for distributed networked systems was proposed to reduce the waste of network resources. The event-triggered rule was proposed to solve the problem of excessive use of communication resources in [25]. The authors in [26] studied neural networks by the proposed event-triggered rule, and the rule effectively solved a large number of computational problems. It is not difficult to find that event-triggered mechanism is very useful and meaningful sampling mechanism because many practical problems can be solved via ETS, but there are few research results on the combination of event-triggered mechanism and MNNs.

Based on the above discussion, the synchronization of MNNs with parameter uncertainty and time delay is studied and emphasized. By establishing the event-triggered mechanism, this paper derives several sufficient criteria to guarantee the synchronization of the systems; it shows that these results are different from the previous ones. Furthermore, the lower bounds of sampling time intervals are also obtained; that is, if the triggering time t_k is known, we can predict the next triggering time t_{k+1}. Roughly speaking, this paper has three highlights: (1) Most existing works on multisystem networks require that the coupling matrix is always the Laplace matrix, in which row sums of coupling matrix all are zero and nondiagonal elements are nonnegative. Because of the particularity of Laplacian matrix, the design of coupling controller is greatly limited. In fact, we have found some non-Laplacian coupling in coupled dynamic networks. In this paper, the coupling matrix need not be the Laplace matrix; that is to say, row sums of coupling matrix can be nonzero constant and nondiagonal elements are arbitrary. (2) Some criteria are proposed to ensure the synchronization of MNNs with parameter uncertainty and time delay by establishing event-triggered mechanism and using matrix inequality techniques. Compared with the most of the existing papers, the results obtained are more simple and convenient in this paper. (3) We can find the lower bounds of the sampling time intervals by the established event-triggered mechanism, and then, we can know that the Zeno behavior will not happen.

The remaining part of this paper is designed as follows. Section 2 introduces the model of MNNs with parameter uncertainty and time delay and some preliminary knowledge. Section 3 gives several sufficient criteria to achieve the global robust exponential synchronization, and the lower bounds of the sampling time intervals are also found. Section 4 provides three numerical examples to demonstrate the obtained results. In the end, Section 5 summarizes the paper's relevant conclusion.

2. Preliminaries and Problem Formulation

Throughout the paper, R^n represents the n-dimensional Euclidean space. I stands for an identity matrix with proper dimensionality. Let $C_\tau := C([-\tau, 0], R^n)$ be a Banach space that composed of all the continuous functions $\varphi : [-\tau, 0]$ to

R^n. $\|\cdot\|_2$ and $\|\cdot\|_{\inf}$ stand for 2-norm and inf-norm, respectively, and let us write $\|\cdot\|_2$ in terms of $\|\cdot\|$ for the sake of simplicity. For a matrix $A = (a_{ij})_{n\times n}$, $a_{\max} = \max\{|a_{ij}|\}$, and $a_{\min} = \min\{|a_{ij}|\}$; furthermore, A^T stands for its transpositive, and $A > 0$, $A < 0$, $A \geq 0$, and $A \leq 0$ mean that A are positive definite, negative definite, positive semidefinite, and negative semidefinite, respectively. diag$\{\cdot\}$ is representative of diagonal matrix. ϕ refers to empty set. If no otherwise specified, matrices are supposed to have compatible dimensions.

Consider a group of r NNs with parameter uncertainty and time delay, and the model of kth NNs with parameter uncertainty and time delay is given as follows:

$$\begin{aligned}\frac{\mathrm{d}z_k(t)}{\mathrm{d}t} &= -(D+\Delta D)z_k(t) + (B+\Delta B)f(z_k(t)) \\ &\quad + (C+\Delta C)g(z_k(t-\tau)) + J(t) + u_k(t),\end{aligned} \tag{1}$$

where $k \in \mathcal{J} = \{1, 2, \ldots, r\}$; $t \geq 0$; $z_k(t) = (z_{k1}(t), z_{k2}(t), \ldots, z_{kn}(t))^T \in R^n$ refers to the state vector; $D = \mathrm{diag}\{d_1, d_2, \ldots, d_n\}$ is the real diagonal positive-definite matrix standing for the neuron self-inhibitions; $J(t) \in R^n$ is the input or bias; $\tau > 0$ represents the transmission delay; $f(z_k(t)) = (f_1(z_{k1}(t)), f_2(z_{k2}(t)), \ldots, f_n(z_{kn}(t)))^T$ and $g(z_k(t-\tau)) = (g_1(z_{k1}(t-\tau)), g_2(z_{k2}(t-\tau)), \ldots, g_n(z_{kn}(t-\tau)))^T$ are the neuron activation functions; $B = (b_{km})_{n\times n}$ is the weight matrix and $C = (c_{km})_{n\times n}$ is the delay weight matrix; ΔB, ΔC, and ΔD are the norm-bounded uncertainty terms; and $u_k(t) \in R^n$ denotes the control input.

The distributed event-triggered controller is given below:

$$u_k(t) = \lambda \sum_{m=1}^{r} y_{km} z_m(t_{ms}), \quad t \in [t_{ks}, t_{k(s+1)}), \tag{2}$$

for $k \in \mathcal{J}$ and $s \geq 1$, where $\{t_{ks}\}$ refers to the sampling time sequence, $\lambda > 0$ represents coupling gain, and $K = (y_{km})_{r\times r}$ stands for the coupling matrix such that

$$\sum_{m=1}^{r} y_{km} = \varrho \in R. \tag{3}$$

Next, we define the following distributed event-triggered function:

$$H_{ks}(t) = \|z_k(t) - z_k(t_{ks})\| - \alpha_k \sum_{m\in\mathcal{J}_k} \|z_k(t_{ms}) - z_k(t_{ks})\|, \tag{4}$$

and the sampling time sequence $\{t_{ks}\}$ satisfies ETS:

$$t_{k(s+1)} = \inf\{t > t_{ks}, H_{ks} > 0\}, \tag{5}$$

for $k \in \mathcal{J}$ and $s \geq 1$, where $\alpha_k > 0$ refers to the control parameter and $\mathcal{J}_k \subseteq \mathcal{J}$ with $\mathcal{J}_k = \{m, m \neq k, y_{km} \neq 0\}$.

Remark 1. Let $\Phi_{km} = \alpha_k \sum_{m\in\mathcal{J}_k} \|z_k(t_{ms}) - z_k(t_{ks})\|$ be the sth threshold on the kth neuron. It is not difficult to find that Φ_{km} determines sampling time of the kth neuron, and Φ_{km} is closely related to the control parameter α_k and subset $\mathcal{J}_k$. In particular, if $\alpha_k = 0$ or $\mathcal{J}_k = \phi$, the kth neuron will have sampling time at any $t \geq t_0$; that is to say, the Zeno behavior does happen when $\alpha_k = 0$ or $\mathcal{J}_k = \phi$. It should be noted that the transmission event is triggered and the controller is updated when the measurement error $\|z_k(t) - z_k(t_{ks})\|$ exceeds the threshold Φ_{km} in the event-triggered controller; unlike the event-triggered controller, the impulse controller samples on the determined impulse time sequence $\{t_{ks}\}$. Thus, we can know that the sampling time sequence $\{t_{ks}\}$ satisfies $t_{k(s+1)} = \inf\{t > t_{ks}, H_{ks} > 0\}$ in the event-triggered controller, and the sampling time sequence $\{t_{ks}\}$ is known in the impulse controller.

Then, we can rewritte model (1) as follows:

$$\begin{aligned}\frac{\mathrm{d}z_k(t)}{\mathrm{d}t} &= -(D+\Delta D)z_k(t) + (B+\Delta B)f(z_k(t)) \\ &\quad + (C+\Delta C)g(z_k(t-\tau)) + J(t) \\ &\quad + \lambda \sum_{m=1}^{r} y_{km} z_m(t_{ms}), \quad t \in [t_{ks}, t_{k(s+1)}).\end{aligned} \tag{6}$$

The initial conditions of model (6) are assumed to be

$$z_k(t_0 + \vartheta) = \varphi_k(\vartheta), \tag{7}$$

where $\varphi_k \in C_\tau$, $\vartheta \in [-\tau, 0]$, and $k = 1, 2, \ldots, n$.

Let $z(t, t_0, \varphi)$ stands for the solution of model (6); in order to avoid this paper being too long, we assume that there exists a unique solution of system (6).

System (6) is called to be globally robustly exponentially synchronized, namely, each subsystem in (6) can achieve global robust exponential synchronization if there are constants $M \geq 1$ and $h > 0$ satisfying

$$\|z_k(t) - z_m(t)\| \leq M \max_{i,j\in\mathcal{J}} \|\varphi_i - \varphi_j\| e^{-h(t-t_0)}, \tag{8}$$

for any $t \geq 0$ and $k, m \in \mathcal{J}$, where h stands for convergence rate.

For the sake of discussion, we give two basic assumptions.

Assumption 1

$$\begin{aligned}\Delta D &= M_1 R_1(t) N_1, \\ \Delta B &= M_2 R_2(t) N_2, \\ \Delta C &= M_3 R_3(t) N_3,\end{aligned} \tag{9}$$

where M_i and N_i $(i = 1, 2, 3)$ are constant matrices with proper dimensionality and $R_i(t)$ are the unknown matrix with $R_i^T(t)R_i(t) \leq I$ $(i = 1, 2, 3)$.

Assumption 2. For any $u, v \in R$ and $k \in \mathcal{J}$, the activation functions $f_k(u)$ and $g_k(u)$ are all continuous in R and satisfy

$$\begin{aligned}0 < \frac{f_k(u) - f_k(v)}{u - v} \leq p_k, \\ 0 < \frac{g_k(u) - g_k(v)}{u - v} \leq q_k,\end{aligned} \tag{10}$$

where $p_k > 0$ and $q_k > 0$ represent Lipschitz constants. Let $P = \mathrm{diag}\{p_1^2, p_2^2, \ldots, p_n^2\}$ and $Q = \mathrm{diag}\{q_1^2, q_2^2, \ldots, q_n^2\}$.

Remark 2. Assumption 1 guarantees the boundedness of ΔB, ΔC, and ΔD. Assumption 2 ensures the speciality of the activation functions $f_k(u)$ and $g_k(u)$. The Lipschitz constants $p_k > 0$ and $q_k > 0$ are dependent on the activation functions $f_k(u)$ and $g_k(u)$ rather than fixed. Lipschitz continuity is a smoother condition than uniform continuity; intuitively, Lipschitz continuity restricts the speed of function change. Furthermore, the slope of the function satisfying Lipschitz condition must be less than a real number called Lipschitz constant. In differential equation theory, Lipschitz condition is a core condition in the existence and uniqueness theorem of solutions under initial conditions.

Next, two important lemmas are introduced as follows.

Lemma 1 (see [19]). *Let F, G, and $S(t)$ be real matrices and $\eta > 0$ is a constant; if $S^T(t)S(t) \le I$, then*

$$F^T S^T(t) G^T + GS(t)F \le \frac{1}{\eta} F^T F + \eta G G^T. \tag{11}$$

Lemma 2 (see [18]). *Let F, G, P, and $Q(t)$ be real matrices; if $P > 0$ and $Q^T(t)Q(t) \le I$, then*

(1) For scalar $\xi > 0$ and vectors z_1 and z_2 of proper dimensionality

$$2 z_1^T F^T Q(t) G z_2 \le \frac{1}{\xi} z_1^T F^T F z_1 + \xi z_2^T G^T G z_2. \tag{12}$$

(2) For matrix $P > 0$ of suitable dimensions:

$$2 z_1^T z_2 \le z_1^T P^{-1} z_1 + z_2^T P z_2. \tag{13}$$

3. Main Results

Let $\varepsilon_{km}(t) = z_k(t) - z_m(t)$ be the synchronization error and $\mu_k(t) = z_k(t) - z_k(t_{ks})$ be the measurement error for $t \in [t_{ks}, t_{k(s+1)})$. Then, by establishing event-triggered mechanism and using matrix inequality techniques, we obtain several novel conditions to achieve global robust exponential synchronization of system (6), and the lower bounds of sampling time interval are also found.

Theorem 1. *Under ETS (5), for model (6), if Assumptions 1 and 2 hold, $\eta > 0$ and $\xi_i > 0$ ($i = 1, 2, \ldots, 5$) are constants, $\alpha_k > 0$, and $\mathcal{F}_k \ne \phi$ for $k \in \mathcal{F}$, then $\inf_{s \ge 1}\{t_{k(s+1)} - t_{ks}\} > 0$ for any $s \ge 1$.*

Proof. From $\mu_k(t) = z_k(t) - z_k(t_{ks})$, we have

$$\begin{aligned}\frac{\mathrm{d}\mu_k(t)}{\mathrm{d}t} &= -(D + \Delta D) z_k(t) + (B + \Delta B) f(z_k(t)) \\ &\quad + (C + \Delta C) g(z_k(t - \tau)) + u_k(t), \quad t \in [t_{ks}, t_{k(s+1)}),\end{aligned} \tag{14}$$

then

$$\begin{aligned}\frac{\mathrm{d}\|\mu_k(t)\|^2}{\mathrm{d}t} &= 2\mu_k^T(t)[-(D + \Delta D) z_k(t) + (B + \Delta B) f(z_k(t)) \\ &\quad + (C + \Delta C) g(z_k(t - \tau)) + u_k(t)] \\ &= 2\mu_k^T(t)(D + \Delta D) z_k(t_{ks}) - 2\mu_k^T(t)(D + \Delta D)\mu_k(t) \\ &\quad + 2\mu_k^T(t)(B + \Delta B)[f(z_k(t)) - f(z_k(t_{ks}))] \\ &\quad + 2\mu_k^T(t)(C + \Delta C)[g(z_k(t - \tau)) - g(z_k(t_{k\bar{s}}))] \\ &\quad + 2\mu_k^T(t) u_k(t) + 2\mu_k^T(t)(B + \Delta B) f(z_k(t_{ks})) \\ &\quad + 2\mu_k^T(t)(C + \Delta C) g(z_k(t_{k\bar{s}})).\end{aligned} \tag{15}$$

For each $t \in [t_{ks}, t_{k(s+1)})$, there exists a $\tilde{s} \in [0, s]$ satisfying $t - \tau \in [t_{k\tilde{s}}, t_{k(\tilde{s}+1)}]$; according to the event-triggered function, for any $t \in [t_{ks}, t_{k(s+1)})$, there exists a $\bar{s} \in [0, s]$ satisfying

$$\|\mu_k(t - \tau)\| \le \alpha_k \sum_{m \in \mathcal{F}_k} \|z_m(t_{m\bar{s}}) - z_k(t_{k\bar{s}})\|. \tag{16}$$

According to Lemmas 1 and 2, we get

$$\begin{aligned}2\mu_k^T(t)\Delta D z_k(t_{ks}) &= 2\mu_k^T(t) M_1 R_1(t) N_1 z_k(t_{ks}) \\ &\le \frac{1}{\xi_1}\mu_k^T(t) M_1 M_1^T \mu_k(t) \\ &\quad + \xi_1 z_k^T(t_{ks}) N_1^T N_1 z_k(t_{ks}),\end{aligned} \tag{17}$$

$$\begin{aligned}-2\mu_k^T(t)\Delta D \mu_k(t) \le \mu_k^T(t)&\left(\eta M_1 M_1^T + \frac{1}{\eta} N_1^T N_1\right) \\ &\cdot \mu_k(t),\end{aligned} \tag{18}$$

$$\begin{aligned}&2\mu_k^T(t)\Delta B[f(z_k(t)) - f(z_k(t_{ks}))] \\ &= 2\mu_k^T(t) M_2 R_2(t) N_2[f(z_k(t)) - f(z_k(t_{ks}))] \\ &\le \frac{1}{\xi_2}\mu_k^T(t) M_2 M_2^T \mu_k(t) + \xi_2[f(z_k(t)) \\ &\quad - f(z_k(t_{ks}))]^T N_2^T N_2[f(z_k(t)) - f(z_k(t_{ks}))],\end{aligned} \tag{19}$$

$$\begin{aligned}&2\mu_k^T(t)\Delta C[g(z_k(t - \tau)) - g(z_k(t_{k\bar{s}}))] \\ &= 2\mu_k^T(t) M_3 R_3(t) N_3[g(z_k(t - \tau)) - g(z_k(t_{k\bar{s}}))] \\ &\le \frac{1}{\xi_3}\mu_k^T(t) M_3 M_3^T \mu_k(t) + \xi_3[g(z_k(t - \tau)) - g(z_k(t_{k\bar{s}}))]^T \\ &\quad \cdot N_3^T N_3[g(z_k(t - \tau)) - g(z_k(t_{k\bar{s}}))],\end{aligned} \tag{20}$$

$$\begin{aligned}2\mu_k^T(t)\Delta B f(z_k(t_{ks})) &= 2\mu_k^T(t) M_2 R_2(t) N_2 f(z_k(t_{ks})) \\ &\le \frac{1}{\xi_4}\mu_k^T(t) M_2 M_2^T \mu_k(t) + \xi_4 f^T(z_k(t_{ks})) \\ &\quad \cdot N_2^T N_2 f(z_k(t_{ks})),\end{aligned} \tag{21}$$

$$2\mu_k^T(t)\Delta C g\left(z_k\left(t_{k\bar{s}}\right)\right) = 2\mu_k^T(t)M_3R_3(t)N_3 g\left(z_k\left(t_{k\bar{s}}\right)\right) \le \frac{1}{\xi_5}\mu_k^T(t)M_3M_3^T\mu_k(t) + \xi_5 g^T\left(z_k\left(t_{k\bar{s}}\right)\right) \cdot N_3^T N_3 g\left(z_k\left(t_{k\bar{s}}\right)\right). \tag{22}$$

Combining (15)–(22), we obtain

$$\begin{aligned}\frac{\left\|\mathrm{d}\mu_k(t)\right\|^2}{\mathrm{d}t} &\le 2\mu_k^T(t)Dz_k\left(t_{ks}\right) + \frac{1}{\xi_1}\mu_k^T(t)M_1M_1^T\mu_k(t) + \xi_1 z_k^T\left(t_{ks}\right)N_1^TN_1z_k\left(t_{ks}\right) - 2\mu_k^T(t)D\mu_k(t) + \mu_k^T(t)\left[\eta M_1M_1^T + \frac{1}{\eta}N_1^TN_1\right]\mu_k^T(t)\\ &+ 2\mu_k^T(t)B\left[f\left(z_k(t)\right) - f\left(z_k\left(t_{ks}\right)\right)\right] + \frac{1}{\xi_2}\mu_k^T(t)M_2M_2^T\mu_k(t) + \xi_2\left[f\left(z_k(t)\right) - f\left(z_k\left(t_{ks}\right)\right)\right]^T N_2^TN_2\left[f\left(z_k(t)\right) - f\left(z_k\left(t_{ks}\right)\right)\right]\\ &+ 2\mu_k^T(t)C\left[g\left(z_k(t-\tau)\right) - g\left(z_k\left(t_{k\bar{s}}\right)\right)\right] + \frac{1}{\xi_3}\mu_k^T(t)M_3M_3^T\mu_k(t) + \xi_3\left[g\left(z_k(t-\tau)\right) - g\left(z_k\left(t_{k\bar{s}}\right)\right)\right]^T N_3^TN_3\\ &\cdot \left[g\left(z_k(t-\tau)\right) - g\left(z_k\left(t_{k\bar{s}}\right)\right)\right] + 2\mu_k^T(t)u_k(t) + 2\mu_k^T(t)Bf\left(z_k\left(t_{ks}\right)\right) + 2\mu_k^T(t)Cg\left(z_k\left(t_{k\bar{s}}\right)\right) + \frac{1}{\xi_4}\mu_k^T(t)M_2M_2^T\mu_k(t)\\ &+ \xi_4 f^T\left(z_k\left(t_{ks}\right)\right)N_2^TN_2f\left(z_k\left(t_{ks}\right)\right) + \frac{1}{\xi_5}\mu_k^T(t)M_3\cdot M_3^T\mu_k(t) + \xi_5 g^T\left(z_k\left(t_{k\bar{s}}\right)\right)N_3^TN_3g\left(z_k\left(t_{k\bar{s}}\right)\right)\\ &\le \left[\|D\| + \frac{1}{\xi_1}\left\|M_1M_1^T\right\| - 2\|D\| + \eta\left\|M_1M_1^T\right\| + \frac{1}{\eta}\left\|N_1^TN_1\right\| + \|B\| + \frac{1}{\xi_2}\left\|M_2M_2^T\right\| + \|C\| + \frac{1}{\xi_3}\left\|M_3M_3^T\right\| + \|B\| + \frac{1}{\xi_4}\left\|M_2M_2^T\right\|\right.\\ &\left. + \|C\| + \frac{1}{\xi_5}\left\|M_3M_3^T\right\| + 1\right]\left\|\mu_k(t)\right\|^2 + \left[\|D\| + \xi_1\left\|N_1^TN_1\right\|\right]\left\|z_k\left(t_{ks}\right)\right\|^2 + \left[\|B\| + \xi_2\left\|N_2^TN_2\right\|\right]\left\|f\left(z_k(t)\right) - f\left(z_k\left(t_{ks}\right)\right)\right\|^2\\ &+ \left[\|C\| + \xi_3\left\|N_3^TN_3\right\|\right]\left\|g\left(z_k(t-\tau)\right) - g\left(z_k\left(t_{k\bar{s}}\right)\right)\right\|^2 + \left[\|B\| + \xi_4\left\|N_2^TN_2\right\|\right]\left\|f\left(z_k\left(t_{ks}\right)\right)\right\|^2 + \left[\|C\| + \xi_5\left\|N_3^TN_3\right\|\right]\left\|g\left(z_k\left(t_{k\bar{s}}\right)\right)\right\|^2\\ &+ \left\|\mu_k(t)\right\|^2\\ &\le \left[-\|D\| + 2\|B\| + 2\|C\| + \left(\frac{1}{\xi_1} + \eta\right)\left\|M_1M_1^T\right\| + \frac{1}{\eta}\left\|N_1^TN_1\right\| + \left(\frac{1}{\xi_2} + \frac{1}{\xi_4}\right)\left\|M_2M_2^T\right\| + \left(\frac{1}{\xi_3} + \frac{1}{\xi_5}\right)\left\|M_3M_3^T\right\|\right.\\ &\left. + \|B\|\|P\| + \xi_2\left\|N_2^TN_2\right\|\|P\| + 1\right]\left\|\mu_k(t)\right\|^2 + \left[\|C\|\|Q\| + \xi_3\left\|N_3^TN_3\right\|\|Q\|\right]\cdot\left\|\mu_k(t-\tau)\right\|^2 + \left[\|D\| + \xi_1\left\|N_1^TN_1\right\|\right]\left\|z_k\left(t_{ks}\right)\right\|^2\\ &+ \left[\|B\| + \xi_4\left\|N_2^TN_2\right\|\right]\left\|f\left(z_k\left(t_{ks}\right)\right)\right\|^2 + \left[\|C\| + \xi_5\left\|N_3^TN_3\right\|\right]\left\|g\left(z_k\left(t_{k\bar{s}}\right)\right)\right\|^2 + \left\|u_k(t)\right\|^2.\end{aligned} \tag{23}$$

Thus,

$$\frac{\mathrm{d}\left\|\mu_k(t)\right\|^2}{\mathrm{d}t} \le \Lambda\left\|\mu_k(t)\right\|^2 + \Omega_{ks}, \tag{24}$$

where

$$\begin{aligned}\Omega_{ks} &= \left[\|C\|\|Q\| + \xi_3\left\|N_3^TN_3\right\|\|Q\|\right]\left(\alpha_k\sum_{m\in\mathcal{F}_k}\left\|z_m\left(t_{m\bar{s}}\right) - z_k\left(t_{k\bar{s}}\right)\right\|\right)^2\\ &+ \left[\|D\| + \xi_1\left\|N_1^TN_1\right\|\right]\left\|z_k\left(t_{ks}\right)\right\|^2\left\|M_2M_2^T\right\| + \left[\|B\| + \xi_4\left\|N_2^TN_2\right\|\right]\\ &\cdot\left\|f\left(z_k\left(t_{ks}\right)\right)\right\|^2 + \left[\|C\| + \xi_5\left\|N_3^TN_3\right\|\right]\left\|g\left(z_k\left(t_{k\bar{s}}\right)\right)\right\|^2\\ &+ \left\|\lambda\sum_{m=1}^{r}y_{km}z_m\left(t_{ms}\right)\right\|^2,\end{aligned} \tag{25}$$

and $\Lambda > 0$ such that

$$\begin{aligned}\Lambda \ge\ & -\|D\| + 2\|B\| + 2\|C\| + \left(\frac{1}{\xi_1} + \eta\right)\left\|M_1M_1^T\right\| + \frac{1}{\eta}\left\|N_1^TN_1\right\|\\ &+ \left(\frac{1}{\xi_2} + \frac{1}{\xi_4}\right)\left\|M_2M_2^T\right\| + \left(\frac{1}{\xi_3} + \frac{1}{\xi_5}\right)\left\|M_3M_3^T\right\|\\ &+ \|B\|\|P\| + \xi_2\left\|N_2^TN_2\right\|\|P\| + 1.\end{aligned} \tag{26}$$

Since $\mu_k\left(t_{ks}\right) = 0$, according to (24), we have

$$\left\|\mu_k\left(t_{k(s+1)}\right)\right\|^2 + \frac{\Omega_{ks}}{\Lambda} \le \frac{\Omega_{ks}}{\Lambda}e^{\Lambda\left(t_{k(s+1)} - t_{ks}\right)}. \tag{27}$$

From ETS (5), we get

$$e^{\Lambda\left(t_{k(s+1)} - t_{ks}\right)} \ge 1 + \frac{\Lambda\left(\alpha_k\sum_{m\in\mathcal{F}_k}\left\|z_m\left(t_{m\bar{s}}\right) - z_k\left(t_{k\bar{s}}\right)\right\|\right)^2}{\Omega_{ks}}, \tag{28}$$

then

$$t_{k(s+1)} - t_{ks} \geq \frac{1}{\Lambda} \ln \left[1 + \frac{\Lambda \left(\alpha_k \sum_{m \in \mathcal{F}_k} \left\| z_m \left(t_{m\bar{s}} \right) - z_k \left(t_{k\bar{s}} \right) \right\| \right)^2}{\Omega_{ks}} \right]; \quad (29)$$

hence, we can know $\inf_{s \geq 1} \left\{ t_{k(s+1)} - t_{ks} \right\} > 0$ when $\mathcal{F}_k \neq \phi$. The proof is finished. □

Remark 3. By Theorem 1, we can know $\alpha_k > 0$ and $\mathcal{F}_k \neq \phi$ implying that the Zeno behavior does not happen for sampling time sequence $\{t_{ks}\}$. In addition, if $\alpha_k > 0$ and $\mathcal{F}_k \neq \phi$, there is no Zeno behavior for model (6) under ETS (5).

Theorem 2. *Let condition (5), Assumption 1, and Assumption 2 hold; there is $l \in \mathcal{F}$ satisfying $\alpha_k > 0$ and $\mathcal{F}_k \neq \phi$ $(k \in \mathcal{F} \backslash \{l\})$. Then, model (6) is globally robustly exponentially synchronized under ETS (5) if there exist $r - 1$ constants $\zeta_k > 0$ $(k \in \mathcal{F} \backslash \{l\})$ and a constant $\nu > 0$ satisfying*

$$\frac{\Psi K_l + K_l^T \Psi}{2} + \nu I \leq 0, \quad (30)$$

and there is $0 < \alpha_{\max} < 1/(r + r_{\max} - 1)$ and three constants $\eta > 0$, $\xi_6 > 0$, and $\xi_7 > 0$ satisfying

$$\begin{aligned} &-2d_{\min} - 2\lambda \left(\frac{\nu}{\zeta_{\max}} - \frac{\alpha_{\max}(r-1)(r + r_{\max} - 1)\zeta_{\max} y_{l\max}}{(1 - \alpha_{\max}(r + r_{\max} - 1))\zeta_{\min}} \right) \\ &+ \|B\| + \|C\| + \|B\|\|P\| + \eta \left\| M_1 M_1^T \right\| + \frac{1}{\eta} \left\| N_1^T N_1 \right\| \\ &+ \frac{1}{\xi_6} \left\| M_2 M_2^T \right\| + \xi_6 \left\| N_2^T N_2 \right\| \|P\| + \frac{1}{\xi_7} \left\| M_3 M_3^T \right\| \\ &+ \|C\|\|Q\| + \xi_7 \left\| N_3^T N_3 \right\| \|Q\| < 0, \end{aligned} \quad (31)$$

where $d_{\min} = \min_{1 \leq k \leq n} \{d_k\}$, $K_l = (y_{km} - y_{lm})_{k,m \in \mathcal{F} \backslash \{l\}}$, $\Psi = \operatorname{diag}\left\{ \zeta_{l_1}, \zeta_{l_2}, \ldots, \zeta_{l_{r-1}} \right\}$, $\{l_1, l_2, \ldots, l_{r-1}\}$ *denotes for rearrangement of* $\mathcal{F} \backslash \{l\}$ *with* $l_1 < l_2 < \cdots < l_{r-1}$, $y_{l\max} = \max_{k,m \in \mathcal{F} \backslash \{l\}} \{|y_{km} - y_{lm}|\}$, r_k *stands for the number of elements in* $\mathcal{F}_k$, *and* $r_{\max} = \max_{1 \leq k \leq r} \{r_k\}$.

Proof. By Theorem 1, for any $k \in \mathcal{F} \backslash \{l\}$, $t_{ks} \longrightarrow \infty$ as $s \longrightarrow \infty$, then, there exists a $s \geq 1$ satisfying $t \in [t_{ks}, t_{k(s+1)})$:

$$\begin{aligned} \frac{d\varepsilon_{kl}(t)}{dt} &= \frac{dz_k(t)}{dt} - \frac{dz_l(t)}{dt} \\ &= -(D + \Delta D)(z_k(t) - z_l(t)) + (B + \Delta B)[f(z_k(t)) \\ &\quad - f(z_l(t))] + (C + \Delta C)[g(z_k(t - \tau)) \\ &\quad - g(z_l(t - \tau))] + u_k(t) - u_l(t), \end{aligned} \quad (32)$$

where

$$u_k(t) - u_l(t) = \lambda \sum_{m=1, m \neq l}^{r} (y_{km} - y_{lm})(z_m(t_{ms}) - z_l(t)), \quad (33)$$

since

$$\begin{aligned} u_k(t) &= \lambda \varrho z_l(t) + \lambda \sum_{m=1, m \neq l}^{r} y_{km}(z_m(t_{ms}) - z_l(t)), \\ u_l(t) &= \lambda \varrho z_l(t) + \lambda \sum_{m=1, m \neq l}^{r} y_{lm}(z_m(t_{ms}) - z_l(t)). \end{aligned} \quad (34)$$

Let $W_k(t) = \varepsilon_{kl}^T(t)\varepsilon_{kl}(t)$ and $W(t) = \sum_{k \in \mathcal{F} \backslash \{l\}} \zeta_k W_k(t)$, then

$$\begin{aligned} \frac{dW_k(t)}{dt} &= 2\varepsilon_{kl}^T(t) \frac{d\varepsilon_{kl}(t)}{dt} \\ &\leq -2\varepsilon_{kl}^T(t)(D + \Delta D)\varepsilon_{kl}^T(t) + 2\varepsilon_{kl}^T(t)(B + \Delta B) \\ &\quad \cdot [f(z_k(t)) - f(z_l(t))] + 2\varepsilon_{kl}^T(t)(C + \Delta C) \\ &\quad \cdot [g(z_k(t - \tau)) - g(z_l(t - \tau))] \\ &\quad + 2\varepsilon_{kl}^T(t)(u_k(t) - u_l(t)). \end{aligned} \quad (35)$$

By Lemma 2, we have

$$\begin{aligned} &2\varepsilon_{kl}^T(t)\Delta B[f(z_k(t)) - f(z_l(t))] \\ &\leq \frac{1}{\xi_6} \varepsilon_{kl}^T(t) M_2 M_2^T \varepsilon_{kl}(t) + \xi_6 [f(z_k(t)) - f(z_l(t))]^T N_2^T N_2 \\ &\quad \cdot [f(z_k(t)) - f(z_l(t))], \end{aligned} \quad (36)$$

$$\begin{aligned} &2\varepsilon_{kl}^T(t)\Delta C[g(z_k(t - \tau)) - g(z_l(t - \tau))] \\ &\leq \frac{1}{\xi_7} \varepsilon_{kl}^T(t) M_3 M_3^T \varepsilon_{kl}(t) + \xi_7 [g(z_k(t - \tau)) - g(z_l(t - \tau))]^T \\ &\quad \cdot N_3^T N_3 [g(z_k(t - \tau)) - g(z_l(t - \tau))]. \end{aligned} \quad (37)$$

Substituting (36) and (37) into (35), we get

$$\begin{aligned} \frac{dW(t)}{dt} \leq \Bigg[&-2d_{\min} + \eta \left\| M_1 M_1^T \right\| + \frac{1}{\eta} \left\| N_1^T N_1 \right\| + \|B\| \\ &+ \|B\|\|P\| + \frac{1}{\xi_6} \left\| M_2 M_2^T \right\| + \xi_6 \left\| N_2^T N_2 \right\| \|P\| + \|C\| \\ &+ \frac{1}{\xi_7} \left\| M_3 M_3^T \right\| \Bigg] W(t) + \left[\|C\|\|Q\| + \xi_7 \left\| N_3^T N_3 \right\| \|Q\| \right] W(t - \tau) \\ &+ 2\zeta_k \varepsilon_{kl}^T(t)(u_k(t) - u_l(t)). \end{aligned} \quad (38)$$

According to (2) and (5), we obtain

$$\begin{aligned}\varepsilon_{kl}^{T}(t)\left(u_k(t)-u_l(t)\right) &= \varepsilon_{kl}^{T}(t)\lambda\sum_{m=1,m\neq l}^{r}\left(y_{km}-y_{lm}\right)\\ &\quad\cdot\left(z_m\left(t_{ms}\right)-z_l(t)\right)\\ &= \varepsilon_{kl}^{T}(t)\lambda\sum_{m=1,m\neq l}^{r}\left(y_{km}-y_{lm}\right)\\ &\quad\cdot\left(\varepsilon_{ml}(t)-\mu_m(t)\right)\\ &= \lambda\sum_{m=1,m\neq l}^{r}\left(y_{km}-y_{lm}\right)\varepsilon_{kl}^{T}(t)\varepsilon_{ml}(t)\\ &\quad-\lambda\varepsilon_{kl}^{T}(t)\sum_{m=1,m\neq l}^{r}\left(y_{km}-y_{lm}\right)\mu_m(t).\end{aligned} \tag{39}$$

From ETS (5), one has

$$\begin{aligned}\left\|\mu_k(t)\right\| &\le \alpha_k\sum_{m\in\mathcal{F}_k}\left\|z_m\left(t_{ms}\right)-z_k\left(t_{ks}\right)\right\|\\ &\le \alpha_k\sum_{m\in\mathcal{F}_k}\left\|\mu_k(t)-\mu_m(t)+\varepsilon_{ml}(t)-\varepsilon_{kl}(t)\right\|\\ &\le \alpha_{\max}\Bigg[r_k\left\|\mu_k(t)\right\|+\sum_{m\in\mathcal{F}_k}\left\|\mu_m(t)\right\|+\sum_{m\in\mathcal{F}_k}\left\|\varepsilon_{ml}(t)\right\|\\ &\quad+r_k\left\|\varepsilon_{kl}(t)\right\|\Bigg]\\ &\le \alpha_{\max}\left[r_{\max}\left\|\mu_k(t)\right\|+(r-1)\left\|\mu_m(t)\right\|\right.\\ &\quad\left.+(r-1)\left\|\varepsilon_{ml}(t)\right\|+r_{\max}\left\|\varepsilon_{kl}(t)\right\|\right],\end{aligned} \tag{40}$$

then

$$\sum_{m\in\mathcal{F}_k}^{r}\left\|\mu_m(t)\right\|\le G_l\sum_{m\in\mathcal{F}_k}^{r}\left\|\varepsilon_{ml}(t)\right\|,\quad k\in\mathcal{F}, \tag{41}$$

where

$$G_l=\frac{\alpha_{\max}\left(r+r_{\max}-1\right)}{1-\alpha_{\max}\left(r+r_{\max}-1\right)}. \tag{42}$$

By (41), we have

$$\begin{aligned}&\left|\sum_{k,m\in\mathcal{F}\setminus\{l\}}\zeta_k\left(y_{km}-y_{lm}\right)\varepsilon_{kl}(t)\mu_m(t)\right|\\ &\quad\le\zeta_{\max}y_{l\max}\sum_{k,m\in\mathcal{F}\setminus\{l\}}\left\|\varepsilon_{kl}(t)\right\|\left\|\mu_m(t)\right\|\\ &\quad\le G_l\zeta_{\max}y_{l\max}\sum_{k,m\in\mathcal{F}\setminus\{l\}}\left\|\varepsilon_{kl}(t)\right\|\left\|\varepsilon_{ml}(t)\right\|\\ &\quad\le G_l\zeta_{\max}y_{l\max}(r-1)\sum_{k,m\in\mathcal{F}\setminus\{l\}}\left\|\varepsilon_{kl}(t)\right\|^2\\ &\quad\le\frac{G_l(r-1)\zeta_{\max}y_{l\max}}{\zeta_{\min}}W(t).\end{aligned} \tag{43}$$

According to (18), one gets

$$\begin{aligned}\sum_{k,m\in\mathcal{F}\setminus\{l\}}\zeta_k\left(y_{km}-y_{lm}\right)\varepsilon_{kl}^{T}(t)\varepsilon_{ml}(t) &= \sum_{k,m\in\mathcal{F}\setminus\{l\}}\frac{1}{2}\left[y_{km}\zeta_k+y_{mk}\zeta_m\right.\\ &\quad\left.-y_{lm}\zeta_k-y_{lk}\zeta_m\right]\varepsilon_{kl}^{T}(t)\varepsilon_{ml}(t)\\ &\le-\nu\sum_{k\in\mathcal{F}\setminus\{l\}}\varepsilon_{kl}^{T}(t)\varepsilon_{kl}(t)\\ &\le-\frac{\nu}{\zeta_{\max}}W(t).\end{aligned} \tag{44}$$

Combining (39), (43), and (44), we obtain

$$\begin{aligned}&\sum_{k,m\in\mathcal{F}\setminus\{l\}}\zeta_k\varepsilon_{kl}^{T}(t)\left(u_k(t)-u_l(t)\right)\\ &\quad\le\lambda\left[-\frac{\nu}{\zeta_{\max}}+\frac{G_l(r-1)\zeta_{\max}y_{l\max}}{\zeta_{\min}}\right]W(t).\end{aligned} \tag{45}$$

From the definition of $W(t)$, one has

$$\begin{aligned}\frac{\mathrm{d}W(t)}{\mathrm{d}t} &\le -2d_{\min}-2\lambda\left(\frac{\nu}{\zeta_{\max}}-\frac{G_l(r-1)\zeta_{\max}y_{l\max}}{\zeta_{\min}}\right)\\ &\quad+\|B\|+\|C\|+\|B\|\|P\|+\eta\left\|M_1M_1^{T}\right\|+\frac{1}{\eta}\left\|N_1^{T}N_1\right\|\\ &\quad+\frac{1}{\xi_6}\left\|M_2M_2^{T}\right\|+\xi_6\left\|N_2^{T}N_2\right\|\|P\|+\frac{1}{\xi_7}\left\|M_3M_3^{T}\right\|W(t)\\ &\quad+\left[\|C\|\|Q\|+\xi_7\left\|N_3^{T}N_3\right\|\|Q\|\right]W(t-\tau).\end{aligned} \tag{46}$$

By (31), there is a constant $h>0$ such that

$$\begin{aligned}&2h-2d_{\min}-2\lambda\left(\frac{\nu}{\zeta_{\max}}-\frac{G_l(r-1)\zeta_{\max}y_{l\max}}{\zeta_{\min}}\right)\\ &\quad+\|B\|+\|C\|+\|B\|\|P\|+\eta\left\|M_1M_1^{T}\right\|+\frac{1}{\eta}\left\|N_1^{T}N_1\right\|\\ &\quad+\frac{1}{\xi_6}\left\|M_2M_2^{T}\right\|+\xi_6\left\|N_2^{T}N_2\right\|\|P\|+\frac{1}{\xi_7}\left\|M_3M_3^{T}\right\|\\ &\quad+\left(1+e^{2h\tau}\right)\left(\|C\|\|Q\|+\xi_7\left\|N_3^{T}N_3\right\|\|Q\|\right)\le 0.\end{aligned} \tag{47}$$

Let $V(t)=e^{2h(t-t_0)}W(t)$, then

$$\begin{aligned}\frac{dV(t)}{dt} &\le \left[2h - 2d_{\min} - 2\lambda\left(\frac{\nu}{\zeta_{\max}} - \frac{G_l(r-1)\zeta_{\max}y_{l\max}}{\zeta_{\min}}\right)\right.\\ &\quad + \|B\| + \|C\| + \|B\|\|P\| + \eta\left\|M_1M_1^T\right\| + \frac{1}{\eta}\left\|N_1^TN_1\right\|\\ &\quad \left.+ \frac{1}{\xi_6}\left\|M_2M_2^T\right\| + \xi_6\left\|N_2^TN_2\right\|\|P\| + \frac{1}{\xi_7}\left\|M_3M_3^T\right\|\right]V(t)\\ &\quad + e^{2h\tau}\left[\|C\|\|Q\| + \xi_7\left\|N_3^TN_3\right\|\|Q\|\right]V(t-\tau)\\ &\le [2h - 2d_{\min} - 2\lambda\left(\frac{\nu}{\zeta_{\max}} - \frac{G_l(r-1)\zeta_{\max}y_{l\max}}{\zeta_{\min}}\right)\\ &\quad + \|B\| + \|C\| + \|B\|\|P\| + \eta\left\|M_1M_1^T\right\| + \frac{1}{\eta}\left\|N_1^TN_1\right\|\\ &\quad + \frac{1}{\xi_6}\left\|M_2M_2^T\right\| + \xi_6\left\|N_2^TN_2\right\|\|P\| + \frac{1}{\xi_7}\left\|M_3M_3^T\right\|\\ &\quad \left.+\left(1 + e^{2h\tau}\right)\left(\|C\|\|Q\| + \xi_7\left\|N_3^TN_3\right\|\|Q\|\right)\right]V(t) \le 0,\end{aligned} \tag{48}$$

when $V(t+\vartheta) \le V(t)$ for any $\vartheta \in [-\tau, 0]$.

Let

$$\begin{aligned}\widetilde{V}(t) &= \sup_{\vartheta\in[-\tau,0]} V(t+\vartheta),\\ \widetilde{W}(t) &= \sup_{\vartheta\in[-\tau,0]} W(t+\vartheta),\end{aligned} \tag{49}$$

then, we have

$$\frac{d\widetilde{V}(t)}{dt} \le 0, \quad \forall t \ge t_0; \tag{50}$$

hence,

$$W(t) \le \sum_{m\in\mathcal{F}\setminus\{l\}} \zeta_m\left\|\widetilde{\varepsilon}_{lm}(t_0)\right\|^2 e^{-2h(t-t_0)}, \tag{51}$$

which implies

$$\left\|\varepsilon_{kl}(t)\right\| \le \sqrt{\frac{\zeta_{\max}}{\zeta_{\min}}}\left\|\widetilde{\varepsilon}_l(t_0)\right\|e^{-h(t-t_0)}, \tag{52}$$

for all $k \in \mathcal{F}\setminus\{l\}$, where $\varepsilon_l(t) = (\varepsilon_{l_1l}^T(t), \varepsilon_{l_2l}^T(t), \ldots, \varepsilon_{l_{r-1}l}^T(t))$ and

$$\begin{aligned}\left\|\widetilde{\varepsilon}_{kl}(t)\right\| &= \sup_{\vartheta\in[-\tau,0]}\left\|\varepsilon_{kl}(t+\vartheta)\right\|,\\ \left\|\widetilde{\varepsilon}_l(t)\right\| &= \sup_{\vartheta\in[-\tau,0]}\left\|\varepsilon_l(t+\vartheta)\right\|.\end{aligned} \tag{53}$$

Then, for any $k, m \in \mathcal{F}$ and $t \ge t_0$, we obtain

$$\left\|\varepsilon_{km}(t)\right\| \le \left\|\varepsilon_{kl}(t)\right\| + \left\|\varepsilon_{ml}(t)\right\| \le 2\sqrt{\frac{\zeta_{\max}}{\zeta_{\min}}}\left\|\widetilde{\varepsilon}_l(t_0)\right\|e^{-h(t-t_0)}. \tag{54}$$

Thus, model (6) is globally robustly exponentially synchronized with convergence rate h. The proof is finished. □

Theorem 3. *Let condition (5), Assumption 1, and Assumption 2 hold; there is $l \in \mathcal{F}$ satisfying $\alpha_k > 0$ and $\mathcal{F}_k \ne \phi$ $(k \in \mathcal{F}\setminus\{l\})$. Moreover, if there exist $r-1$ constants $\zeta_k > 0$ satisfying*

$$\beta_k = -[y_{kk} - y_{lk}] - \frac{1}{\zeta_k}\sum_{m=1,m\ne k,l}^{r}\zeta_m|y_{km} - y_{lm}| > 0, \tag{55}$$

and there is $0 < \alpha_{\max} < 1/(2r_{\max})$ and three constants $\eta > 0$, $\xi_6 > 0$, and $\xi_7 > 0$ satisfying

$$\begin{aligned}&-2d_{\min} - 2\lambda\left(\beta_{\min} - \frac{2\alpha_{\max}r_{\max}\zeta_{\max}\left\|K_l\right\|_{\inf}}{(1-2\alpha_{\max}r_{\max})\zeta_{\min}}\right) + \|B\| + \|C\|\\ &\quad + \|B\|\|P\| + \eta\left\|M_1M_1^T\right\| + \frac{1}{\eta}\left\|N_1^TN_1\right\| + \frac{1}{\xi_6}\left\|M_2M_2^T\right\|\\ &\quad + \xi_6\left\|N_2^TN_2\right\|\|P\| + \frac{1}{\xi_7}\left\|M_3M_3^T\right\| + \|C\|\|Q\|\\ &\quad + \xi_7\left\|N_3^TN_3\right\|\|Q\| < 0,\end{aligned} \tag{56}$$

then model (6) is globally robustly exponentially synchronized under ETS (5).

Proof. Let $\overline{W}(t) = \max_{k\in\mathcal{F}\setminus\{l\}}\left\{(1/\zeta_k)\|\varepsilon_{kl}(t)\|^2\right\}$, and fixing $k \in \mathcal{F}\setminus\{l\}$ satisfying

$$\overline{W}(t) = \frac{1}{\zeta_k}\left\|\varepsilon_{kl}(t)\right\|^2, \tag{57}$$

then

$$\begin{aligned}\frac{d\overline{W}(t)}{dt} &= \frac{2}{\zeta_k}\left\|\varepsilon_{kl}(t)\right\|\frac{d\left\|\varepsilon_{kl}(t)\right\|}{dt}\\ &= \frac{2}{\zeta_k}\left\|\varepsilon_{kl}(t)\right\|\mathrm{sign}\left(\varepsilon_{kl}(t)\right)^T\frac{d\varepsilon_{kl}(t)}{dt}\\ &\le \left[-2d_{\min} + \eta\left\|M_1M_1^T\right\| + \frac{1}{\eta}\left\|N_1^TN_1\right\|\right.\\ &\quad + \|B\| + \|B\|\|P\| + \frac{1}{\xi_6}\left\|M_2M_2^T\right\|\\ &\quad \left.+ \xi_6\left\|N_2^TN_2\right\|\|P\| + \|C\| + \frac{1}{\xi_7}\left\|M_3M_3^T\right\|\right]\overline{W}(t)\\ &\quad + \left[\|C\|\|Q\| + \xi_7\left\|N_3^TN_3\right\|\|Q\|\right]\overline{W}(t-\tau)\\ &\quad + \frac{2}{\zeta_k}\left\|\varepsilon_{kl}(t)\right\|\mathrm{sign}\left(\varepsilon_{kl}(t)\right)^T\left(u_k(t) - u_l(t)\right),\end{aligned} \tag{58}$$

where

$$u_k(t) - u_l(t) = \lambda \sum_{m\in\mathcal{F}\setminus\{l\}} (y_{km} - y_{lm})(z_m(t_{ms}) - z_l(t)). \tag{59}$$

Then, one gets

$$\begin{aligned}\operatorname{sign}(\varepsilon_{kl}(t))^T (u_k(t) - u_l(t)) &= \lambda \operatorname{sign}(\varepsilon_{kl}(t))^T \\ &\quad \cdot \sum_{m\in\mathcal{F}\setminus\{l\}} (y_{km} - y_{lm})(\varepsilon_{ml}(t) - \mu_m(t)) \\ &\le \lambda (y_{kk} - y_{lk}) \|\varepsilon_{kl}(t)\| \\ &\quad + \lambda \sum_{m\in\mathcal{F}\setminus\{l,k\}} |y_{km} - y_{lm}| \|\varepsilon_{ml}(t)\| \\ &\quad + \lambda \sum_{m\in\mathcal{F}\setminus\{l\}} |y_{km} - y_{lm}| \|\mu_m(t)\|.\end{aligned} \tag{60}$$

By Theorem 1, we obtain

$$||\mu(t)||_{\max} \le \widetilde{G}_l ||\varepsilon_l(t)||_{\max}, \tag{61}$$

where $\widetilde{G}_l = (2\alpha_{\max} r_{\max})/(1 - 2\alpha_{\max} r_{\max})$, $\|\mu(t)\|_{\max} = \max_{k\in\mathcal{F}\setminus\{l\}}\{\|\mu_k(t)\|\}$, and $\|\varepsilon_l(t)\|_{\max} = \max_{m\in\mathcal{F}\setminus\{l\}}\{\|\varepsilon_{kl}(t)\|\}$.

By (60) and (61), we have

$$\begin{aligned}&\frac{1}{\zeta_k}\|\varepsilon_{kl}(t)\| \operatorname{sign}(\varepsilon_{kl}(t))^T (u_k(t) - u_l(t)) \\ &\le \lambda \left[y_{kk} - y_{lk} + \frac{1}{\zeta_k} \sum_{m\in\mathcal{F}\setminus\{l,k\}}^{r} \zeta_m |y_{km} - y_{lm}| \right] \overline{W}(t) \\ &\quad + \frac{1}{\zeta_k} \|\varepsilon_{kl}(t)\| \lambda \sum_{m\in\mathcal{F}\setminus\{l\}}^{r} |y_{km} - y_{lm}| \|\mu(t)\|_{\max} \\ &\le -\lambda \beta_k \overline{W}(t) + \lambda \widetilde{G}_l \frac{\zeta_{\max} \|K_l\|_{\inf}}{\zeta_{\min}} \overline{W}(t);\end{aligned} \tag{62}$$

thus, one has

$$\begin{aligned}\frac{d\overline{W}(t)}{dt} &\le \left[-2d_{\min} - 2\lambda \left(\beta_{\min} - \widetilde{G}_l \frac{\zeta_{\max} \|K_l\|_{\inf}}{\zeta_{\min}} \right) \right. \\ &\quad + \eta \|M_1 M_1^T\| + \frac{1}{\eta} \|N_1^T N_1\| + \|B\| + \|B\| \|P\| \\ &\quad \left. + \frac{1}{\xi_6} \|M_2 M_2^T\| + \xi_6 \|N_2^T N_2\| \|P\| + \|C\| \right. \\ &\quad \left. + \frac{1}{\xi_7} \|M_3 M_3^T\| \right] \overline{W}(t) \\ &\quad + \left[\|C\| \|Q\| + \xi_7 \|N_3^T N_3\| \|Q\| \right] \overline{W}(t - \tau).\end{aligned} \tag{63}$$

From (56), we can know that there is a $h > 0$ such that

$$\begin{aligned}&2h - 2d_{\min} - 2\lambda \left(\beta_{\min} - \frac{2\alpha_{\max} r_{\max} \zeta_{\max} \|K\|_{\inf}}{(1 - 2\alpha_{\max} r_{\max}) \zeta_{\min}} \right) \\ &\quad + \|B\| + \|C\| + \|B\| \|P\| + \eta \|M_1 M_1^T\| + \frac{1}{\eta} \|N_1^T N_1\| \\ &\quad + \frac{1}{\xi_6} \|M_2 M_2^T\| + \xi_6 \|N_2^T N_2\| \|P\| + \frac{1}{\xi_7} \|M_3 M_3^T\| \\ &\quad + \left(1 + e^{2h\tau}\right) \left(\|C\| \|Q\| + \xi_7 \|N_3^T N_3\| \|Q\| \right) \le 0.\end{aligned} \tag{64}$$

Similar to Theorem 2, by (63), we get

$$\overline{W}(t) \le \frac{1}{\zeta_{\min}} \|\widetilde{\varepsilon}_l(t_0)\|^2 e^{-2h(t - t_0)}, \tag{65}$$

then

$$\|\varepsilon_{kl}(t)\| \le \sqrt{\frac{\zeta_{\max}}{\zeta_{\min}}} \|\widetilde{\varepsilon}_l(t_0)\| e^{-h(t - t_0)}, \quad k \in \mathcal{F}\setminus\{l\}. \tag{66}$$

Thus, model (6) is globally robustly exponentially synchronized with convergence rate h under ETS (5). The proof is finished. □

Remark 4. Comparing Theorem 2 to Theorem 3, it is not hard to see that when r is large enough and $r_{\max}$ is relatively small, condition (30) is better than condition (55), but condition (31) is not as good as condition (56).

Theorem 4. *Let condition (4), Assumption 1, and Assumption 2 hold; $\alpha_k > 0$ and $\mathcal{F}_k \neq \phi$. Then model (6) is globally robustly exponentially synchronized under ETS (5) if there exist r constants $\zeta_k > 0$ ($k \in \mathcal{F}$) and a constant $\nu > 0$ satisfying*

$$\frac{\overline{\Psi}K + K^T\overline{\Psi}}{2} + \nu I \le 0, \tag{67}$$

and there is $0 < \alpha_{\max} < 1/(r + r_{\max})$ and three constants $\eta > 0$, $\xi_8 > 0$, and $\xi_9 > 0$ satisfying

$$\begin{aligned}&-2d_{\min} - 2\lambda \left(\frac{\nu}{\zeta_{\max}} - \frac{\alpha_{\max}(r + r_{\max}) r \zeta_{\max} y_{\max}}{(1 - \alpha_{\max}(r + r_{\max}))\zeta_{\min}} \right) + \|B\| + \|C\| \\ &\quad + \|B\| \|P\| + \eta \|M_1 M_1^T\| + \frac{1}{\eta} \|N_1^T N_1\| + \frac{1}{\xi_8} \|M_2 M_2^T\| \\ &\quad + \xi_8 \|N_2^T N_2\| \|P\| + \frac{1}{\xi_9} \|M_3 M_3^T\| + \|C\| \|Q\| \\ &\quad + \xi_9 \|N_3^T N_3\| \|Q\| < 0,\end{aligned} \tag{68}$$

where $d_{\min} = \min_{1\le k\le n}\{d_k\}$, $K = (y_{km})_{k,m\in\mathcal{F}}$, $\overline{\Psi} = \operatorname{diag}\{\zeta_1, \zeta_2, \ldots, \zeta_r\}$, *and* $y_{\max} = \max_{k,m\in\mathcal{F}}\{|y_{km}|\}$.

Proof. A reference system is given by

$$\begin{aligned}\frac{dz_0(t)}{dt} &= -(D + \Delta D) z_0(t) + (B + \Delta B) f(z_0(t)) + (C + \Delta C) \\ &\quad \cdot g(z_0(t - \tau)) + J(t) + \gamma \rho z_0(t), \quad t \ge t_0,\end{aligned} \tag{69}$$

where $u_0 = \lambda\varrho z_0(t)$, and there exists a $s \geq 1$ satisfying $t \in [t_{ks}, t_{k(s+1)})$.

According to (6) and (69), we have

$$\begin{aligned}\frac{d\varepsilon_{k0}(t)}{dt} &= \frac{dz_k(t)}{dt} - \frac{dz_0(t)}{dt}\\ &= -(D+\Delta D)\left(z_k(t)-z_0(t)\right) + (B+\Delta B)\\ &\quad \left[f\left(z_k(t)\right) - f\left(z_0(t)\right)\right] + (C+\Delta C)\\ &\quad \left[g\left(z_k(t-\tau)\right) - g\left(z_0(t-\tau)\right)\right] + u_k(t) - u_0(t),\end{aligned} \tag{70}$$

where

$$u_k(t) - u_0(t) = \lambda \sum_{m=1, m\neq l}^{r} y_{km}\left(z_m(t_{ms}) - z_0(t)\right). \tag{71}$$

Let $\hat{W}_k(t) = \varepsilon_{k0}^T(t)\varepsilon_{k0}(t)$ and $\hat{W}(t) = \sum_{k\in\mathcal{F}} \zeta_k \hat{W}_k(t)$, then

$$\begin{aligned}\frac{d\hat{W}_k(t)}{dt} &= 2\varepsilon_{k0}^T(t)\frac{d\varepsilon_{k0}(t)}{dt}\\ &\leq -2\varepsilon_{k0}^T(t)(D+\Delta D)\varepsilon_{k0}^T(t) + 2\varepsilon_{k0}^T(t)(B+\Delta B)\\ &\quad \cdot \left[f\left(z_k(t)\right) - f\left(z_0(t)\right)\right] + 2\varepsilon_{k0}^T(t)(C+\Delta C)\\ &\quad \cdot \left[g\left(z_k(t-\tau)\right) - g\left(z_0(t-\tau)\right)\right]\\ &\quad + 2\varepsilon_{k0}^T(t)\left(u_k(t) - u_0(t)\right).\end{aligned} \tag{72}$$

By Lemma 2, we have

$$\begin{aligned}&2\varepsilon_{k0}^T(t)\Delta B\left[f\left(z_k(t)\right) - f\left(z_0(t)\right)\right]\\ &\leq \frac{1}{\xi_8}\varepsilon_{k0}^T(t)M_2M_2^T\varepsilon_{k0}(t)\\ &\quad + \xi_8\left[f\left(z_k(t)\right) - f\left(z_0(t)\right)\right]^T N_2^T N_2\\ &\quad \cdot \left[f\left(z_k(t)\right) - f\left(z_0(t)\right)\right],\end{aligned} \tag{73}$$

$$\begin{aligned}&2\varepsilon_{k0}^T(t)\Delta C\left[g\left(z_k(t-\tau)\right) - g\left(z_0(t-\tau)\right)\right]\\ &\leq \frac{1}{\xi_9}\varepsilon_{k0}^T(t)M_3M_3^T\varepsilon_{k0}(t)\\ &\quad + \xi_9\left[g\left(z_k(t-\tau)\right) - g\left(z_0(t-\tau)\right)\right]^T\\ &\quad \cdot N_3^T N_3\left[g\left(z_k(t-\tau)\right) - g\left(z_0(t-\tau)\right)\right].\end{aligned} \tag{74}$$

Substituting (73) and (74) into (72), we get

$$\begin{aligned}\frac{d\hat{W}(t)}{dt} \leq &\left[-2d_{\min} + \eta\left\|M_1M_1^T\right\| + \frac{1}{\eta}\left\|N_1^TN_1\right\|\right.\\ &+\|B\| + \|B\|\|P\| + \frac{1}{\xi_8}\left\|M_2M_2^T\right\|\\ &\left.+\xi_8\left\|N_2^TN_2\right\|\|P\| + \|C\| + \frac{1}{\xi_9}\left\|M_3M_3^T\right\|\right]\hat{W}(t)\\ &+\left[\|C\|\|Q\| + \frac{1}{\xi_9}\left\|N_3^TN_3\right\|\|Q\|\right]\\ &\cdot \hat{W}(t-\tau) + 2\zeta_k\varepsilon_{k0}^T(t)\left(u_k(t) - u_0(t)\right).\end{aligned} \tag{75}$$

Similar to Theorem 2, we obtain

$$\left\|\varepsilon_{k0}(t)\right\| \leq \sqrt{\frac{\zeta_{\max}}{\zeta_{\min}}}\left\|\tilde{\varepsilon}_0(t_0)\right\|e^{-h(t-t_0)}, \tag{76}$$

for all $k \in \mathcal{F}$, where $\varepsilon_0(t) = (\varepsilon_{10}^T, \ldots, \varepsilon_{r0}^T)^T$, $\|\tilde{\varepsilon}_0(t_0)\| = \sup_{\vartheta\in[-\tau,0]}\|\varepsilon_0(t+\vartheta)\|$, and h is a position constant such that

$$\begin{aligned}&2h - 2d_{\min} - 2\lambda\left(\frac{\nu}{\zeta_{\max}} - \frac{\alpha_{\max}(r+r_{\max})r\zeta_{\max}y_{\max}}{(1-\alpha_{\max}(r+r_{\max}))\zeta_{\min}}\right)\\ &+\|B\| + \|C\| + \|B\|\|P\| + \eta\left\|M_1M_1^T\right\| + \frac{1}{\eta}\left\|N_1^TN_1\right\|\\ &+\frac{1}{\xi_8}\left\|M_2M_2^T\right\| + \xi_8\left\|N_2^TN_2\right\|\|P\| + \frac{1}{\xi_9}\left\|M_3M_3^T\right\|\\ &+\left(1+e^{2h\tau}\right)\left(\|C\|\|Q\| + \xi_9\left\|N_3^TN_3\right\|\|Q\|\right) \leq 0.\end{aligned} \tag{77}$$

Then, for any $k, m \in \mathcal{F}$ and $t \geq t_0$, we get

$$\left\|\varepsilon_{km}(t)\right\| \leq \left\|\varepsilon_{k0}(t)\right\| + \left\|\varepsilon_{m0}(t)\right\| \leq 2\sqrt{\frac{\zeta_{\max}}{\zeta_{\min}}}\left\|\tilde{\varepsilon}_0(t_0)\right\|e^{-h(t-t_0)}. \tag{78}$$

Thus, the proof is finished. □

Theorem 5. *Let condition (4), Assumption 1, and Assumption 2 hold; $\alpha_k > 0$ and $\mathcal{F}_k \neq \phi$ $(k \in \mathcal{F})$, and if there exist r constants $\zeta_k > 0$ $(k \in \mathcal{F})$ satisfying*

$$\beta_k = -y_{kk} - \frac{1}{\zeta_k}\sum_{m=1}^{r}\zeta_m|y_{km}| > 0, \tag{79}$$

and there is $0 < \alpha_{\max} < 1/(2r_{\max})$ and three constants $\eta > 0$, $\xi_8 > 0$, and $\xi_9 > 0$ satisfying

$$\begin{aligned}&-2d_{\min} - 2\lambda\left(\beta_{\min} - \frac{2\alpha_{\max}r_{\max}\zeta_{\max}\|K\|_{\inf}}{(1-2\alpha_{\max}r_{\max})\zeta_{\min}}\right)\\ &+\|B\| + \|C\| + \|B\|\|P\| + \eta\left\|M_1M_1^T\right\|\\ &+\frac{1}{\eta}\left\|N_1^TN_1\right\| + \frac{1}{\xi_8}\left\|M_2M_2^T\right\| + \xi_8\left\|N_2^TN_2\right\|\|P\|\\ &+\frac{1}{\xi_9}\left\|M_3M_3^T\right\| + \|C\|\|Q\| + \xi_9\left\|N_3^TN_3\right\|\|Q\| < 0,\end{aligned} \tag{80}$$

then model (6) is globally robustly exponentially synchronized under ETS (5).

Remark 5. From Theorems 2–5, it is easy to find that they are closely related. In Theorems 2 and 3, the coupling matrix can be unstable. However, in Theorems 4 and 5, the coupling matrix must be stable. Theorems 4 and 5 can be derived from Theorems 2 and 3, respectively, when the coupling matrix is stable, but Theorems 3 and 4 are more simpler and convenient than Theorems 2 and 3.

Remark 6. Most existing works on multisystem networks (see [2–4]) require that the coupling matrix is always the Laplace matrix, in which row sums of coupling matrix all are zero and nondiagonal elements are nonnegative. In this paper, the coupling matrix need not be the Laplace matrix; that is to say, row sums of coupling matrix can be nonzero constant and nondiagonal elements are arbitrary. Compared with the previous works, the advantage of this paper is that the coupling matrix need not be the Laplace matrix, and the criteria obtained are more simple and convenient.

Remark 7. Actually, if we consider MNNs with non-Laplace coupling matrix and norm-unbounded uncertainty terms in this paper, we can get Theorem 1 by changing (17)–(22) and get Theorems 2 and 3 by changing (36) and (37). Similarly, we also get Theorems 4 and 5 by changing (72) and (74). In addition, if we consider time-varying delay instead of constant delay into system (6), when the time-varying delay $\tau_{ks}(t)$ is bounded, namely, there exists a constant σ satisfying $0 < \tau_{ks}(t) < \sigma$, and several similar conclusions can be obtained.

4. Three Numerical Examples

We consider model (1) with $n = 2$, where activation function $f(z) = g(z)$ and $f(z) = (f_1(z_1), f_2(z_2))^T$ such that

$$f_m(z_m) = \frac{\left(|z_m + 1| - |z_m - 1|\right)}{2}, \quad m = 1, 2, \tag{81}$$

the weight matrices

$$\begin{aligned} D &= \begin{bmatrix} 4 & 0 \\ 0 & 4 \end{bmatrix}, \\ B &= \begin{bmatrix} 0.2 & 0.1 \\ 0.1 & 0.2 \end{bmatrix}, \\ C &= \begin{bmatrix} -0.2 & 0.1 \\ 0.1 & -0.2 \end{bmatrix}, \\ \Delta D &= \sin\begin{bmatrix} 1 & 0 \\ 0 & 1 \end{bmatrix}, \\ \Delta B &= \cos\begin{bmatrix} 1 & 1 \\ 1 & 1 \end{bmatrix}, \\ \Delta C &= \sin\begin{bmatrix} 1 & 1 \\ 1 & 1 \end{bmatrix}. \end{aligned} \tag{82}$$

Example 1. Consider system (6) with $r = 4$. Let $\tau = 0.001$, $\eta = 0.5$, $\xi_6 = 0.5$, $\xi_7 = 0.5$, and coupling matrix

$$K = \begin{bmatrix} -1.19 & 0 & 0.4 & 0.8 \\ 0 & -1.19 & 0.2 & 1 \\ 0 & 0.2 & -1.19 & 1 \\ 1 & 0.2 & 0 & -1.19 \end{bmatrix}, \tag{83}$$

we know that $\varrho = 0.01$ and K has a positive eigenvalue 0.01. Choosing $l = 1$, then

$$K_1 = \begin{bmatrix} -1.19 & -0.2 & 0.2 \\ 0.2 & -1.59 & 0.2 \\ 0.2 & -0.4 & -1.99 \end{bmatrix}. \tag{84}$$

Let $\nu = 1.0546$, then

$$\frac{K_1 + K_1^T}{2} + \nu I \le 0, \tag{85}$$

which implies that condition (30) holds, where $\zeta_i = 1\,(2 \le i \le 4)$; let $\lambda = 10$ and $\alpha_k = 0.012$, then

$$\begin{aligned} &-2d_{\min} - 2\lambda\left(\nu - \frac{\alpha_{\max}(r-1)(r + r_{\max} - 1)g_{l\max}}{1 - \alpha_{\max}(r + r_{\max} - 1)}\right) \\ &+ \|B\| + \|C\| + \|B\|\|P\| + \eta\left\|M_1 M_1^T\right\| + \frac{1}{\eta}\left\|N_1^T N_1\right\| \\ &+ \frac{1}{\xi_6}\left\|M_2 M_2^T\right\| + \xi_6\left\|N_2^T N_2\right\|\|P\| + \frac{1}{\xi_7}\left\|M_3 M_3^T\right\| \\ &+ \|C\|\|Q\| + \xi_7\left\|N_3^T N_3\right\|\|Q\| = -0.8420 < 0; \end{aligned} \tag{86}$$

hence, condition (31) holds; furthermore, we choose the initial states $z_1(\vartheta) = (0.6, 0.5)^T$, $z_2(\vartheta) = (-1, 0.8)^T$, $z_3(\vartheta) = (0.7, -1)^T$, and $z_4(\vartheta) = (-1.2, 0.2)^T$ for $\vartheta \in [-0.001, 0]$. Figure 1 describes the evolutions of the event-triggered controller and synchronization errors. Figure 2 depicts the threshold and the evolutions of measurement errors. By Theorem 2, we can know that system (6) is globally robustly exponentially synchronized under ETS (5).

Example 2. Let $\tau = 0.001$, $\eta = 0.5$, $\xi_8 = 0.5$, $\xi_9 = 0.5$, and coupling matrix

$$K = \begin{bmatrix} -1.06 & 0 & 0.02 & 0.04 \\ 0 & -1.03 & -0.02 & 0.06 \\ -0.02 & 0 & -1.08 & 0.01 \\ 0.02 & 0 & 0.04 & -1.06 \end{bmatrix}, \tag{87}$$

we know that $\varrho = -1$ and K is a stable matrix. Let $\nu = 1.25$, then

$$\frac{K + K^T}{2} + \nu I \le 0; \tag{88}$$

hence, condition (67) holds, where $\zeta_i = 1\,(1 \le i \le 4)$; choosing $\lambda = 10$ and $\alpha_k = 0.021$, then

$$\begin{aligned} &-2d_{\min} - 2\lambda\left(\nu - \frac{\alpha_{\max}(r + r_{\max})r y_{\max}}{1 - \alpha_{\max}(r + r_{\max})}\right) \\ &+ \|B\| + \|C\| + \|B\|\|P\| + \eta\left\|M_1 M_1^T\right\| + \frac{1}{\eta}\left\|N_1^T N_1\right\| \\ &+ \frac{1}{\xi_8}\left\|M_2 M_2^T\right\| + \xi_8\left\|N_2^T N_2\right\|\|P\| + \frac{1}{\xi_9}\left\|M_3 M_3^T\right\| \\ &+ \|C\|\|Q\| + \xi_9\left\|N_3^T N_3\right\|\|Q\| \\ &= -0.64 < 0, \end{aligned} \tag{89}$$

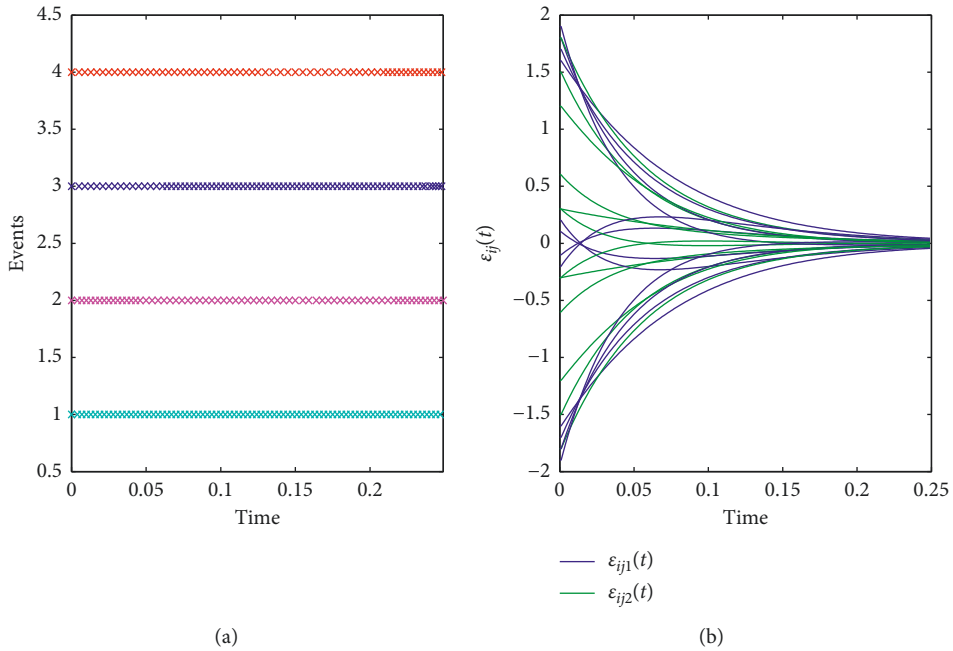

Figure 1: Time evolutions of the event-triggered controller and the synchronization errors in Example 1.

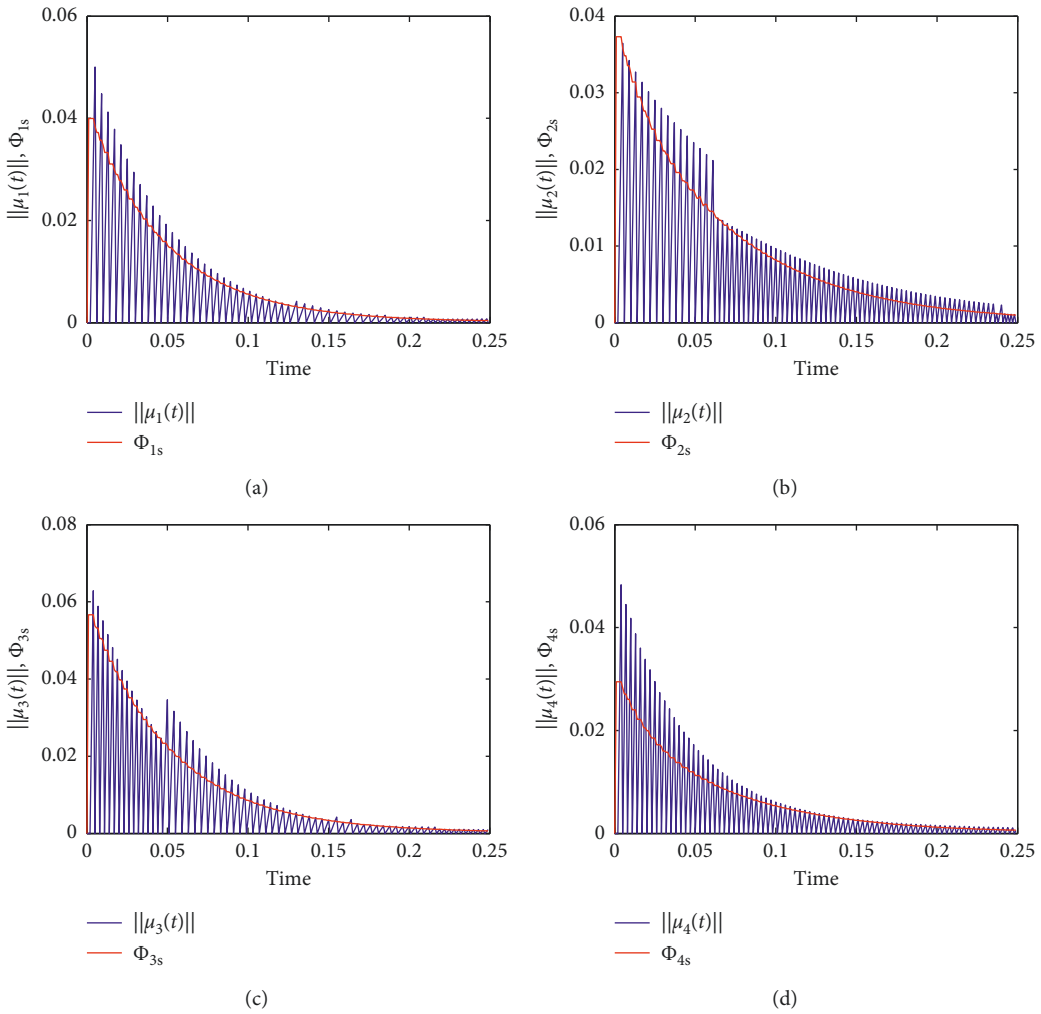

Figure 2: Time evolutions of measurement errors $\mu_k(t)$ and the thresholds Φ_{ks} $(k = 1, 2, 3, 4)$ in Example 1.

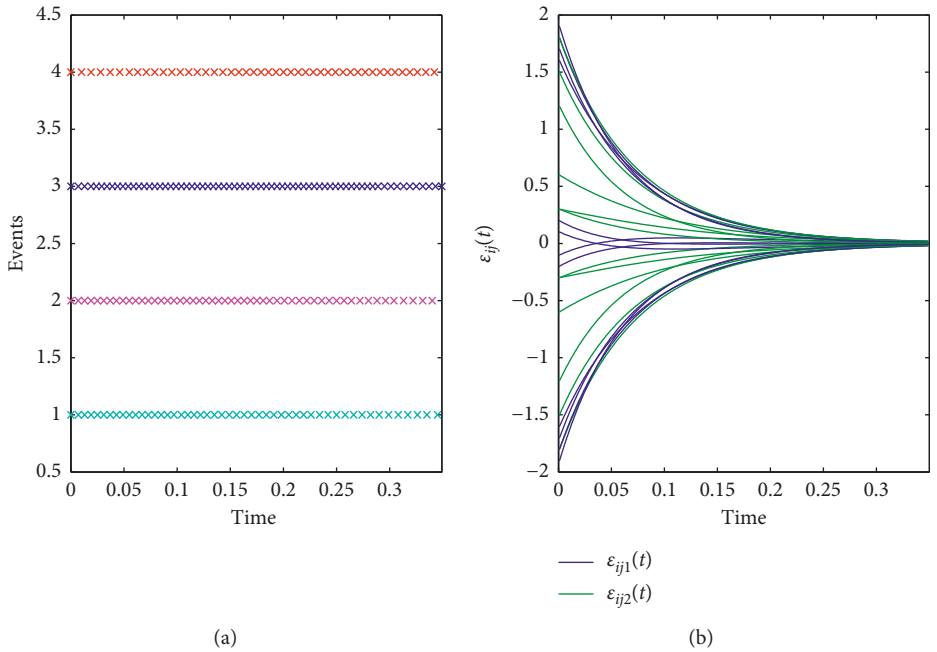

Figure 3: Time evolutions of the event-triggered controller and the synchronization errors in Example 2.

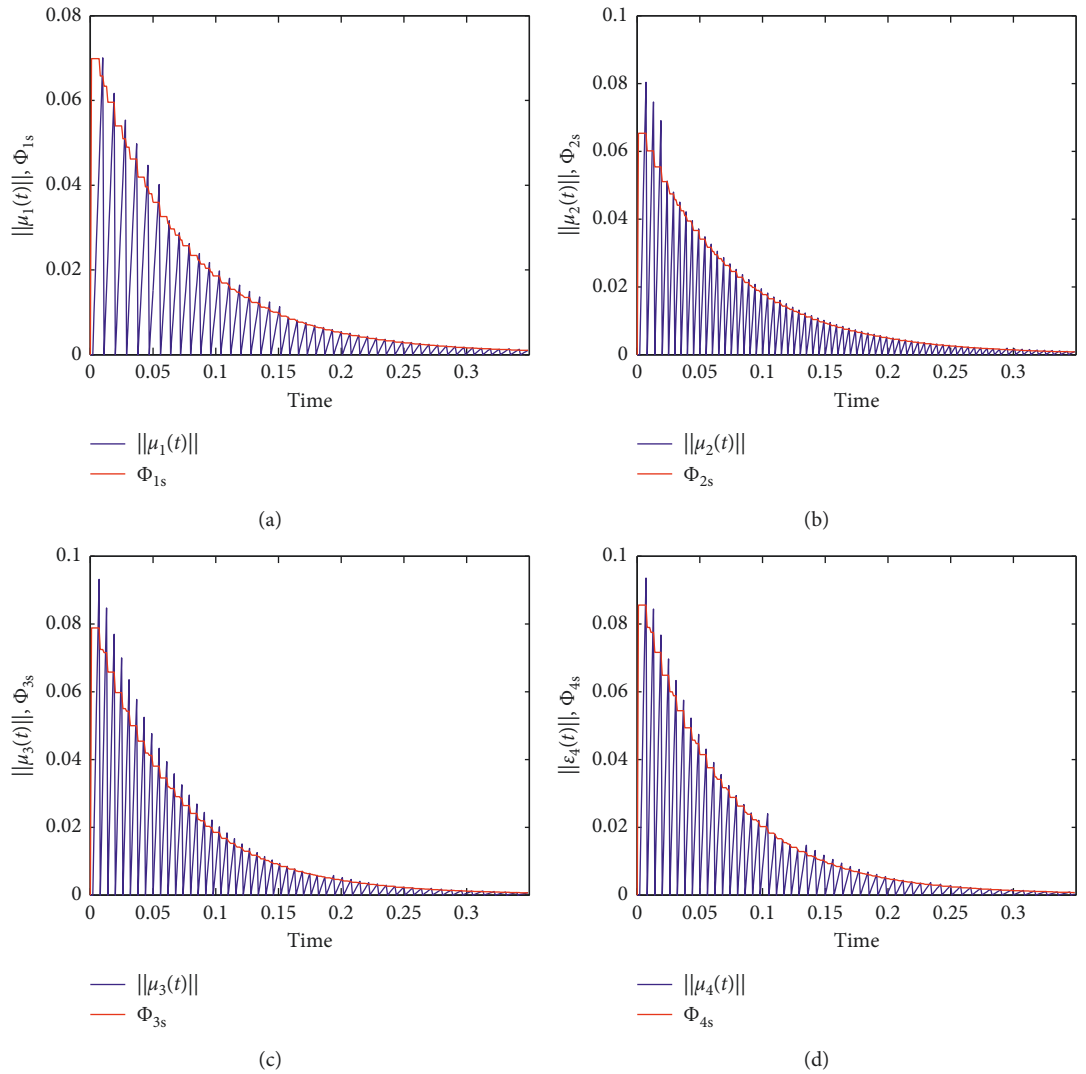

Figure 4: Time evolutions of measurement errors $\mu_k(t)$ and the thresholds Φ_{ks} $(k = 1, 2, 3, 4)$ in Example 2.

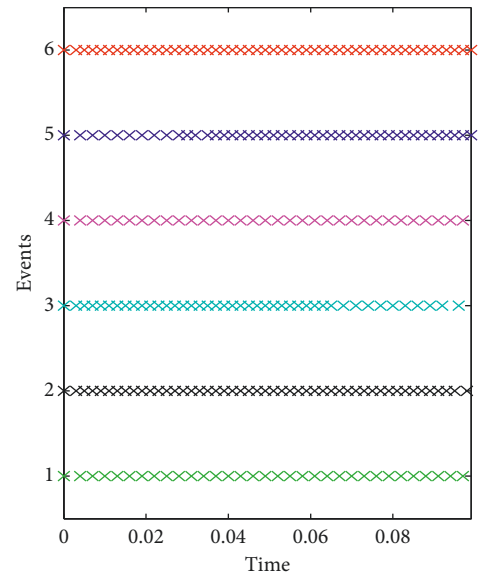

(a)

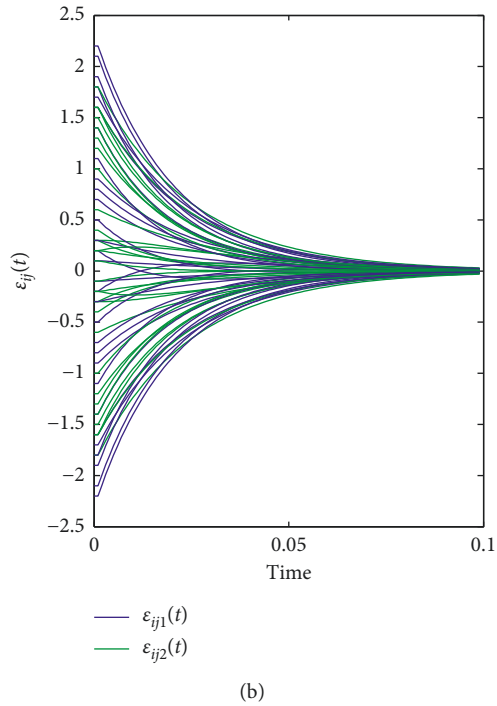

(b)

FIGURE 5: Time evolutions of the event-triggered controller and the synchronization errors in Example 3.

thus, condition (68) holds; furthermore, we choose the initial states $z_1(\vartheta) = (0.6, 0.5)^T$, $z_2(\vartheta) = (-1, 0.8)^T$, $z_3(\vartheta) = (0.7, -1)^T$, and $z_4(\vartheta) = (-1.2, 0.2)^T$ for $\vartheta \in [-0.001, 0]$. Figure 3 describes the evolutions of the event-triggered controller and synchronization errors. Figure 4 depicts the threshold and the evolutions of measurement errors. By Theorem 4, we can know that system (6) is globally robustly exponentially synchronized under ETS (5).

Example 3. Let $\tau = 0.001$, $\eta = 0.5$, $\xi_8 = 0.5$, $\xi_9 = 0.5$, and coupling matrix

$$K = \begin{bmatrix} -2.6 & 0 & 0.2 & 0 & 0 & 0.4 \\ 0 & -2.3 & -0.3 & 0 & 0 & 0.6 \\ 0 & -0.2 & -2.3 & 0 & 0 & 0.5 \\ 0 & -0.3 & 0 & -2.7 & 0 & 1 \\ 0 & 0 & 0.1 & 0 & -2.6 & 0.5 \\ 0.4 & 0 & 0 & 0 & 0.2 & -2.6 \end{bmatrix}, \tag{90}$$

we know that $\varrho = -2$ and K is a stable matrix. Let $\nu = 0.99$, then

$$\beta_k = -y_{kk} - \frac{1}{\zeta_k} \sum_{m=1}^{6} \zeta_m |y_{km}| \geq 0.4; \tag{91}$$

hence, condition (79) holds, where $\zeta_i = 1\,(1 \leq i \leq 6)$, choosing $\lambda = 18$ and $\alpha_k = 0.015$, then

$$\begin{aligned} &-2d_{\min} - 2\lambda\left(\beta_{\min} - \frac{2\alpha_{\max} r_{\max} \|K\|_{\inf}}{1 - 2\alpha_{\max} r_{\max}}\right) \\ &+ \|B\| + \|C\| + \|B\|\|P\| + \eta\left\|M_1 M_1^T\right\| \\ &+ \frac{1}{\eta}\left\|N_1^T N_1\right\| + \frac{1}{\xi_8}\left\|M_2 M_2^T\right\| \\ &+ \xi_8\left\|N_2^T N_2\right\|\|P\| + \frac{1}{\xi_9}\left\|M_3 M_3^T\right\| + \|C\|\|Q\| \\ &+ \xi_9\left\|N_3^T N_3\right\|\|Q\| = -0.2636 < 0, \end{aligned} \tag{92}$$

thus, condition (80) holds; in addition, we choose the initial states $z_1(\vartheta) = (0.6, 0.5)^T$, $z_2(\vartheta) = (-1, 0.8)^T$, $z_3(\vartheta) = (0.7, -1)^T$, $z_4(\vartheta) = (-1.2, 0.2)^T$, $z_5(\vartheta) = (-1.5, -0.8)^T$, and $z_6(\theta) = (-0.1, 0.6)^T$ for $\vartheta \in [-0.01, 0]$. Figure 5 describes the evolutions of the event-triggered controller and synchronization errors. Figure 6 depicts the threshold and the evolutions of measurement errors. By Theorem 5, we can know that system (6) is globally robustly exponentially synchronized under ETS (5).

Remark 8. It can be seen that the row sums of coupling matrices in Examples 1, 2, and 3 all are 0.01, −1, and −2, respectively, and there are nondiagonal elements in Examples 2 and 3. Thus, our coupling matrices all are non-Laplacian.

5. Concluding Remarks

This paper has introduced a novel ETS for MNNs with parameter uncertainty and time delay. By using matrix inequality techniques and establishing the event-triggered mechanism, some sufficient criteria are derived for judging global robust exponential synchronization of the system; in addition, the lower bounds of the sampling time intervals are also obtained. In particular, the most existing papers on multisystem networks require that the coupling matrix is Laplace matrix, in which row sums of coupling matrix all are zero and nondiagonal elements are nonnegative. However, the coupling matrix need not be the Laplace matrix in this paper; that is to say, row sums of coupling matrix can be nonzero constant and nondiagonal elements are arbitrary. In

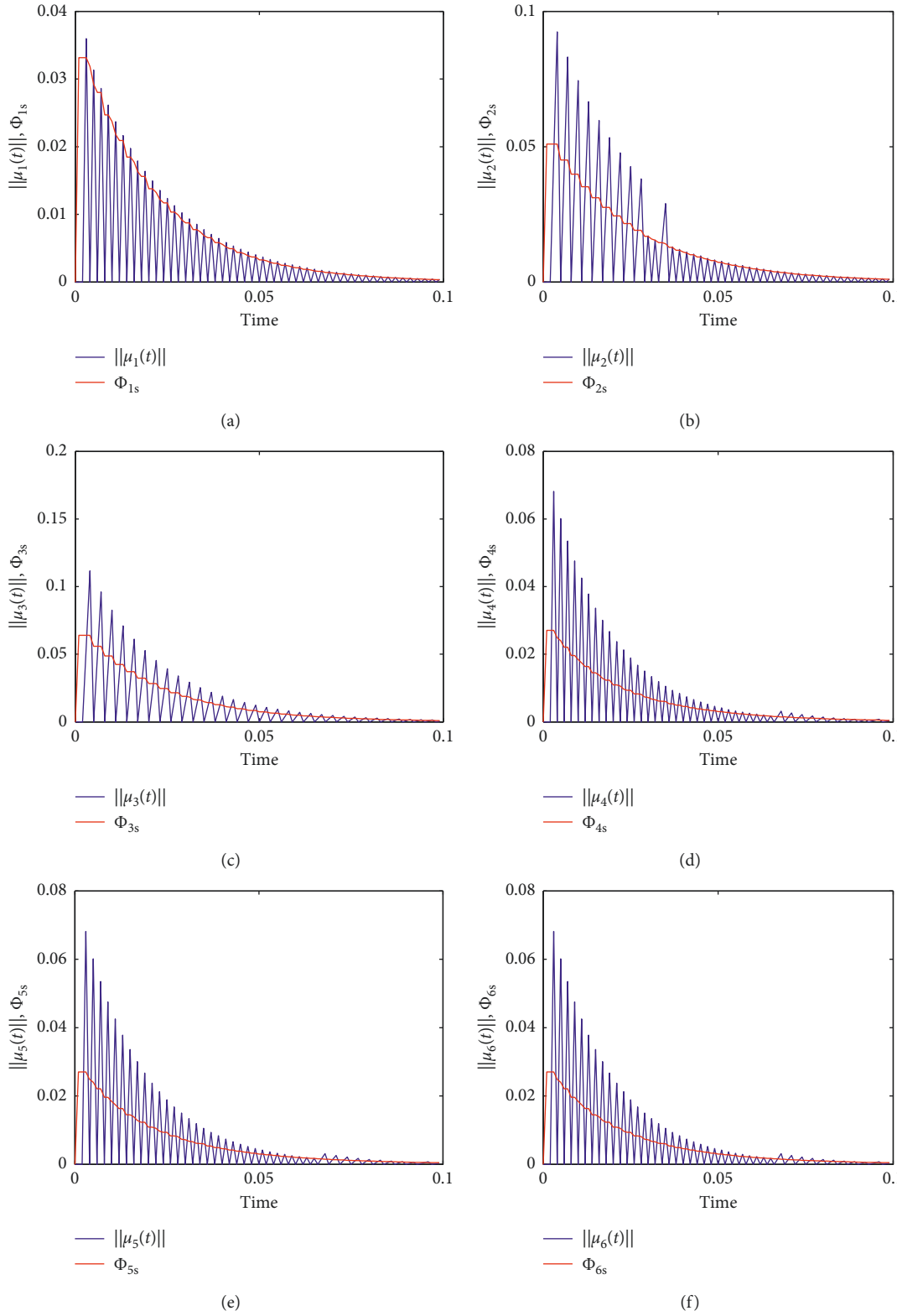

FIGURE 6: Time evolutions of measurement errors $\mu_k(t)$ and the thresholds Φ_{ks} $(k = 1, 2, 3, 4, 5, 6)$ in Example 3.

the future, we can do the following works: (1) MNNs will be extended to fractional-order MNNs. (2) It is meaningful to study MNNs with parameter uncertainty and time delay via centralized and decentralized data-sampling approaches. (3) MNNs with parameter uncertainty and time-varying delay may be valuable research topic. (4) It is a challenge to study MNNs with non-Laplace coupling matrix and norm-unbounded uncertainty terms.

Data Availability

No data were used to support this study.

Conflicts of Interest

The authors declare that there are no conflicts of interest regarding the publication of this paper.

Acknowledgments

This work was supported by the Research Project of Hubei Provincial Department of Education of China under Grant B2019129.

References

[1] J. Chen, B. Chen, Z. Zeng, and P. Jiang, "Event-triggered synchronization strategy for multiple neural networks with time delay," *IEEE Transactions on Cybernetics*, 2019.

[2] T. Chen, X. Liu, and W. Lu, "Pinning complex networks by a single controller," *IEEE Transactions on Circuits and Systems I: Regular Papers*, vol. 54, no. 6, pp. 1317–1326, 2007.

[3] X. Liu and T. Chen, "Cluster synchronization in directed networks via intermittent pinning control," *IEEE Transactions on Neural Networks*, vol. 22, no. 7, pp. 1009–1020, 2011.

[4] X. Yang and J. Lu, "Finite-time synchronization of coupled networks with Markovian topology and impulsive effects," *IEEE Transactions on Automatic Control*, vol. 61, no. 8, pp. 2256–2261, 2016.

[5] B. Chen and J. Chen, "Global $o(t^{-\alpha})$ stability and global asymptotical periodicity for a non-autonomous fractional-order neural networks with time-varying delays," *Neural Networks*, vol. 73, pp. 47–57, 2016.

[6] A. Pratap, R. Raja, J. Cao, G. Rajchakit, and F. E. Alsaadi, "Further synchronization in finite time analysis for time-varying delayed fractional order memristive competitive neural networks with leakage delay," *Neurocomputing*, vol. 317, pp. 110–126, 2018.

[7] A. Pratap, R. Raja, J. Cao, G. Rajchakit, and H. M. Fardoun, "Stability and synchronization criteria for fractional order competitive neural networks with time delays: an asymptotic expansion of Mittag Leffler function," *Journal of the Franklin Institute*, vol. 356, no. 4, pp. 2212–2239, 2019.

[8] A. Pratap, R. Raja, C. Sowmiya, O. Bagdasar, J. Cao, and G. Rajchakit, "Robust generalized Mittag-Leffler synchronization of fractional order neural networks with discontinuous activation and impulses," *Neural Networks*, vol. 103, pp. 128–141, 2018.

[9] A. Wu and Z. Zeng, "Anti-synchronization control of a class of memristive recurrent neural networks," *Communications in Nonlinear Science and Numerical Simulation*, vol. 18, no. 2, pp. 373–385, 2013.

[10] A. Wu and Z. Zeng, "Lagrange stability of neural networks with memristive synapses and multiple delays," *Information Sciences*, vol. 280, pp. 135–151, 2014.

[11] A. L. Wu and Z. G. Zeng, "Exponential stabilization of memristive neural networks with time delays," *IEEE Transactions on Neural Networks and Learning Systems*, vol. 23, no. 12, pp. 1919–1929, 2012.

[12] A. Wu, Z. Zeng, and J. Zhang, "Global exponential convergence of periodic neural networks with time-varying delays," *Neurocomputing*, vol. 78, no. 1, pp. 149–154, 2012.

[13] X. Miao and L. Li, "New stability criteria for uncertain nonlinear stochastic time-delay systems," *Circuits, Systems, and Signal Processing*, vol. 34, no. 8, pp. 2441–2456, 2015.

[14] C. Maharajan, R. Raja, J. D. Cao, G. Ravi, and G. Rajchakit, "Global exponential stability of Markovian jumping stochastic impulsive uncertain BAM neural networks with leakage, mixed time delays, and α-inverse Holder activation function," *Advances in Difference Equations*, vol. 1, p. 113, 2018.

[15] R. Raja, U. Karthik Raja, R. Samidurai, and A. Leelamani, "Improved stochastic dissipativity of uncertain discrete-time neural networks with multiple delays and impulses," *International Journal of Machine Learning and Cybernetics*, vol. 6, no. 2, pp. 289–305, 2015.

[16] R. Raja and R. Samidurai, "New delay dependent robust asymptotic stability for uncertain stochastic recurrent neural networks with multiple time varying delays," *Journal of the Franklin Institute*, vol. 349, no. 6, pp. 2108–2123, 2012.

[17] J. Yu, K. Zhang, and S. Fei, "Further results on mean square exponential stability of uncertain stochastic delayed neural networks," *Communications in Nonlinear Science and Numerical Simulation*, vol. 14, no. 4, pp. 1582–1589, 2009.

[18] B. Y. Zhang, S. Y. Xu, G. D. Zong, and Y. Zou, "Delay-dependent exponential stability for uncertain stochastic Hopfield neural networks with time-varying delays," *IEEE Transactions on Circuits and Systems I: Regular Papers*, vol. 56, no. 6, pp. 1241–1247, 2009.

[19] Y. Wang, L. Xie, and C. E. de Souza, "Robust control of a class of uncertain nonlinear systems," *Systems & Control Letters*, vol. 19, no. 2, pp. 139–149, 1992.

[20] H. Huang, G. Feng, and J. Cao, "Robust state estimation for uncertain neural networks with time-varying delay," *IEEE Transactions on Neural Networks*, vol. 19, no. 8, pp. 1329–1339, 2008.

[21] J.-E. Zhang, "Stabilization of uncertain fractional-order complex switched networks via impulsive control and its application to blind source separation," *IEEE Access*, vol. 6, pp. 32780–32789, 2018.

[22] Q. Zhu, S. Senthilraj, R. Raja, and R. Samidurai, "Stability analysis of uncertain neutral systems with discrete and distributed delays via the delay partition approach," *International Journal of Control, Automation and Systems*, vol. 15, no. 5, pp. 2149–2160, 2017.

[23] V. Dolk and M. Heemels, "Event-triggered control systems under packet losses," *Automatica*, vol. 80, pp. 143–155, 2017.

[24] Q.-Y. Fan and G.-H. Yang, "Sampled-data output feedback control based on a new event-triggered control scheme," *Information Sciences*, vol. 414, pp. 306–318, 2017.

[25] D. Liu and F. Hao, "Decentralized event-triggered control strategy in distributed networked systems with delays," *International Journal of Control, Automation and Systems*, vol. 11, no. 1, pp. 33–40, 2013.

[26] R. Zhang, X. Yi, W. Lu, and T. Chen, "Stability of analytic neural networks with event-triggered synaptic feedbacks," *IEEE Transactions on Neural Networks and Learning Systems*, vol. 27, no. 2, pp. 483–494, 2016.

Hindawi
Complexity
Volume 2019, Article ID 8698294, 6 pages
https://doi.org/10.1155/2019/8698294

Research Article

Reachable Set Bounding for Homogeneous Nonlinear Systems with Delay and Disturbance

Xingao Zhu[1] **and Yuangong Sun**[1,2,3]

[1]*School of Mathematical Sciences, University of Jinan, Jinan 250022, China*
[2]*School of Mathematical Sciences, Qufu Normal University, Qufu 273165, China*
[3]*College of Mathematics and Systems Science, Shandong University of Science and Technology, Qingdao 266590, China*

Correspondence should be addressed to Yuangong Sun; sunyuangong@163.com

Received 18 April 2019; Accepted 13 June 2019; Published 1 July 2019

Guest Editor: Raúl Villafuerte-Segura

Reachable set bounding for homogeneous nonlinear systems with delay and disturbance is studied. By the usage of a new method for stability analysis of positive systems, an explicit necessary and sufficient condition is first derived to guarantee that all the states of positive homogeneous time-delay systems with degree $p > 1$ converge asymptotically within a specific ball. Furthermore, the main result is extended to a class of nonlinear time variant systems. A numerical example is given to demonstrate the effectiveness of the obtained results.

1. Introduction

Recent years have witnessed a rapid development of reachable set bounding for linear systems in [1–11], to name a few. In most of existing references, the traditional Lyapunov-Krasovskii function method is most commonly used. However, such a method is usually difficult to derive explicit conditions for reachable set estimation of nonlinear systems with delay and disturbance.

Due to the ubiquitous existence of time delay in practical engineering and its adverse effect on stability [12–15] and oscillation [16–19], it has attracted wide attention in recent years. So far, less attention has been paid to reachable set bounding for nonlinear time-delay systems. Such a problem was discussed in [20, 21] for certain nonlinear perturbed systems with delay, where the involved nonlinear terms satisfy a linear growth condition. Reachable set bounding for continuous-time and discrete-time homogeneous time-delay positive systems of degree one was studied in [22]. The decay rates of homogeneous positive systems of any degree with time-varying delays were given in [23]. Recently, the same problem was considered in [24] for homogeneous positive systems of degree $p > 1$, while time delay was not taken into consideration. The problem of reachable set estimation of switched positive systems with discrete and distributed delays subject to bounded disturbances was investigated in [25].

Positive systems are dynamical systems whose states remain nonnegative whenever the initial states are nonnegative ([26, 27]). In view of the special structure of positive systems, a special method was commonly used for stability analysis of positive systems in [28–33], which is different from the traditional Lyapunov-Krasovskii function method.

Motivated by the work in [23, 24], we study in this paper reachable set bounding for homogeneous nonlinear time-delay systems with bounded disturbance. By developing the methods used in [23, 24], we first establish a necessary and sufficient condition such that all the solutions of positive homogeneous time-delay systems with degree $p > 1$ converge asymptotically within a specific ball, which contains those results in [23, 24] in special cases. The main result is also applied to certain nonlinear time variant systems with delay and disturbance.

Throughout this paper, $\mathbb{R}^n$ is the set of n-dimensional real vectors. Denote by x_i the ith coordinate of $x \in \mathbb{R}^n$ for $i \in \langle n \rangle = \{1, 2, \ldots, n\}$. Given $x, y \in \mathbb{R}^n$, say $x \succ y$ (or $y \prec x$) if $x_i > y_i$, $x \succeq y$ (or $y \preceq x$) if $x_i \geq y_i$, $i \in \langle n \rangle$. Denote $\mathbb{R}^n_+ = \{x \in \mathbb{R}^n : x \succeq 0\}$. For $x = (x_i) \in \mathbb{R}^n$,

denote $|x| = (|x_i|) \in \mathbb{R}_+^n$ and $\|x\|_\infty = \max_{i\in\langle n\rangle}|x_i|$. Let $\mathscr{B}(\varepsilon)=\{x \in \mathbb{R}^n | \|x\|_\infty \le \varepsilon\}$, where $\varepsilon > 0$ is a constant. For given $r > 0$, denote $\mathbb{BF}_r([0,\infty],\mathbb{R}^n) = \{\omega : [0,\infty] \longrightarrow \mathbb{R}^n | \|\omega(t)\|_\infty \le r, \forall t \ge 0\}$. An $n \times n$-dimensional matrix A is called Metzler if all its off-diagonal entries are nonnegative.

2. Preliminaries

In this paper, nonlinear time-delay systems of the form

$$\begin{aligned} \dot{x}(t) &= f(x(t)) + g((x(t-\tau(t)))) + \omega(t), \quad t \ge 0 \\ x(t) &= \varphi(t), \quad t \in [-h, 0], \end{aligned} \tag{1}$$

are investigated, where $x(t) \in \mathbb{R}^n$ is the state vector, $f, g : \mathbb{R}^n \longrightarrow \mathbb{R}^n$ are continuous vector functions satisfying $f(0) = g(0) = 0$, $\tau(t)$ is a time delay satisfying $0 \le \tau(t) \le h$, $h > 0$ is a constant, $\omega(t) \in \mathbb{BF}_r([0,\infty],\mathbb{R}^n)$ is the disturbance, and the initial state $\varphi(t) : [-h, 0] \longrightarrow \mathbb{R}^n$ is continuous. Note that when $\tau(t) \equiv 0$, system (1) takes the form of the system considered in [24].

The following definitions and lemma in [34] will be required.

Definition 1. Assume that $f : \mathbb{R}^n \longrightarrow \mathbb{R}^n$ is continuous on $\mathbb{R}^n$ and continuously differentiable on $\mathbb{R}^n \setminus \{0\}$. The vector function f is called cooperative if the Jacobian matrix $(\partial f/\partial x)(x)$, $x \in \mathbb{R}^n \setminus \{0\}$, is Metzler.

Definition 2. A vector function $f : \mathbb{R}^n \longrightarrow \mathbb{R}^n$ is called homogeneous of degree $p > 0$ if $f(\lambda x) = \lambda^p f(x)$, $x \in \mathbb{R}^n$, $\lambda > 0$.

Definition 3. A vector function $g : \mathbb{R}^n \longrightarrow \mathbb{R}^n$ is called order-preserving on $\mathbb{R}_+^n$ provided that $g(x) \succeq g(y)$, where $x, y \in \mathbb{R}_+^n$, $x \succeq y$.

Lemma 4. *A cooperative vector function f satisfies $f_i(u) \ge f_i(v)$, where $u, v \in \mathbb{R}^n \setminus \{0\}$, $u \succeq v$, $u_i = v_i$, $i \in \langle n\rangle$.*

In this paper, we need the following assumptions:

(H1) f and g are continuously differentiable on $\mathbb{R}^n\setminus\{0\}$ and homogeneous of degree $p > 1$;

(H2) f is cooperative and g is order-preserving on $\mathbb{R}_+^n$;

(H3) $\omega(t) \succeq 0$ for $t \ge 0$.

Following the proof given in [22], we can easily obtain the following lemma.

Lemma 5. *System (1) is positive under assumptions (H2) and (H3).*

3. Main Results

Theorem 6. *Suppose that (H1)-(H3) are valid. Then, we have the following equivalent statements:*

(i) *There is an n-dimensional vector $v \succ 0$ satisfying $f(v)+g(v) \prec 0$.*

(ii) *The solution $x(t)$ of system (1) satisfies*

$$\|x(t)\|_\infty \le \alpha + (\beta + \gamma t)^{-1/(p-1)} \tag{2}$$

for any $t \ge 0$, any initial state $\varphi(t) \in \mathscr{C}([-h, 0], \mathbb{R}_+^n)$, any disturbance $\omega(t) \in \mathbb{BF}_r([0,\infty],\mathbb{R}_+^n)$, and any bounded delay $\tau(t)$, where α, β, and γ are appropriate nonnegative constants dependent on r, h, and the initial state φ, and $\alpha = 0$ if $r = 0$.

In addition, if condition (i) holds, α, β, and γ can be chosen as follows:

$$\begin{aligned} \alpha &= \theta\rho, \\ \beta &= (K\rho)^{1-p}, \\ \gamma &= (p-1)\eta\rho^{1-p}, \end{aligned} \tag{3}$$

where $\rho = \max_{i\in\langle n\rangle} v_i$,

$$\begin{aligned} \theta &= \left(\frac{r}{-\max_{i\in\langle n\rangle}[f_i(v) + g_i(v)]}\right)^{1/p}, \\ K &= \begin{cases} 0, & \|\varphi\|_v \le \theta, \\ \left[(\|\varphi\|_v)^p - \theta^p\right]^{1/p}, & \|\varphi\|_v > \theta, \end{cases} \end{aligned} \tag{4}$$

$\|\varphi\|_v = \max_{i\in\langle n\rangle, t\in[-h,0]}(|\varphi_i(t)|/v_i)$, η satisfies $0 < \eta < \min_{i\in\langle n\rangle}\eta_i$, and η_i satisfies the following equation:

$$\frac{f_i(v)}{v_i} + \frac{g_i(v)}{v_i}\left[1 + (p-1)K^{p-1}\eta_i h\right]^{p/(p-1)} + \eta_i = 0, \quad i \in \langle n\rangle. \tag{5}$$

Proof. (i)$\Longrightarrow$(ii) Given the initial state $\varphi \in \mathscr{C}([-h, 0], \mathbb{R}_+^n)$, from Lemma 5 we have $x(t) \succeq 0$, $t \ge 0$. Based on definitions of K and $\|\varphi\|_v$, we have

$$\frac{x_i(t)}{v_i} \le (\theta^p + K^p)^{1/p}, \quad t \in [-h, 0], \ i \in \langle n\rangle. \tag{6}$$

Set

$$z_i(t) = \begin{cases} \dfrac{x_i(t)}{v_i} - \left\{\theta^p + \left[K^{1-p} + (p-1)\eta t\right]^{-p/(p-1)}\right\}^{1/p}, & t \ge 0, \ i \in \langle n\rangle, \\ \dfrac{x_i(t)}{v_i} - (\theta^p + K^p)^{1/p}, & t \in [-h, 0], \ i \in \langle n\rangle. \end{cases} \tag{7}$$

Then (6) and (7) yield $z_i(t) \le 0$, $t \in [-h, 0]$, $i \in \langle n\rangle$. Next, we show that $z_i(t) \le 0$ for $i \in \langle n\rangle$ and $t \ge 0$. If it is not true, there is a constant $t_* \ge 0$ and an index $k \in \langle n\rangle$ guaranteeing $z_i(t) \le 0$ for $i \in \langle n\rangle$, $t \in [0, t_*]$, and $z_k(t_*) = 0$. Therefore,

$$\dot{z}_k(t_*) \ge 0, \tag{8}$$

$$\frac{x_i(t)}{v_i} \le \left\{\theta^p + \left[K^{1-p} + (p-1)\eta t\right]^{-p/(p-1)}\right\}^{1/p}, \quad t \in [0, t_*],\ i \in \langle n\rangle. \tag{9}$$

$$\frac{x_k(t_*)}{v_k} = \left\{\theta^p + \left[K^{1-p} + (p-1)\eta t_*\right]^{-p/(p-1)}\right\}^{1/p}. \tag{10}$$

Using Lemma 4 and the homogeneity of f, we get from (9) and (10) that

$$\begin{aligned} &f_k(x(t_*)) \\ &\le f_k\left(\left\{\theta^p + \left[K^{1-p} + (p-1)\eta t_*\right]^{-p/(p-1)}\right\}^{1/p} v\right) \\ &= \left\{\theta^p + \left[K^{1-p} + (p-1)\eta t_*\right]^{-p/(p-1)}\right\} f_k(v) \\ &= \theta^p f_k(v) + \left[K^{1-p} + (p-1)\eta t_*\right]^{-p/(p-1)} f_k(v). \end{aligned} \tag{11}$$

For the case when $\tau(t_*) \le t_*$, it holds that

$$\frac{x_i(t_* - \tau(t_*))}{v_i} \le \left\{\theta^p + \left[K^{1-p} + (p-1)\eta(t_* - \tau(t_*))\right]^{-p/(p-1)}\right\}^{1/p}, \quad i \in \langle n\rangle. \tag{12}$$

Considering g is homogeneous and order-preserving, we conclude

$$\begin{aligned} g_k(x(t_* - \tau(t_*))) &\le g_k\left(\left\{\theta^p + \left[K^{1-p} + (p-1)\eta(t_* - \tau(t_*))\right]^{-p/(p-1)}\right\}^{1/p} v\right) \\ &= \left\{\theta^p + \left[K^{1-p} + (p-1)\eta(t_* - \tau(t_*))\right]^{-p/(p-1)}\right\} \\ &\cdot g_k(v) = \theta^p g_k(v) + \left[K^{1-p} + (p-1)\eta(t_* - \tau(t_*))\right]^{-p/(p-1)} g_k(v). \end{aligned} \tag{13}$$

Note that

$$\begin{aligned} &\left[K^{1-p} + (p-1)\eta(t_* - \tau(t_*))\right]^{-p/(p-1)} \\ &= \left[K^{1-p} + (p-1)\eta t_*\right]^{-p/(p-1)} \\ &\quad \times \left[\frac{\eta(p-1)\tau(t_*)}{K^{1-p} + \eta(p-1)(t_* - \tau(t_*))} + 1\right]^{p/(p-1)} \\ &\le \left[K^{1-p} + (p-1)\eta t_*\right]^{-p/(p-1)} \\ &\quad \times \left[1 + (p-1)K^{p-1}\eta h\right]^{p/(p-1)}. \end{aligned} \tag{14}$$

We further get from (13) and (14) that

$$\begin{aligned} g_k(x(t_* - \tau(t_*))) &\le \theta^p g_k(v) \\ &+ \left[K^{1-p} + \eta(p-1)t_*\right]^{-p/(p-1)} \\ &\cdot \left[1 + (p-1)K^{p-1}\eta h\right]^{p/(p-1)} g_k(v). \end{aligned} \tag{15}$$

For the case when $\tau(t_*) > t_*$, it holds that $z_i(t_* - \tau(t_*)) \le 0$; i.e.,

$$\frac{x_i(t_* - \tau(t_*))}{v_i} \le \left(\theta^p + K^p\right)^{1/p}, \quad i \in \langle n\rangle. \tag{16}$$

It thus follows that

$$\begin{aligned} g_k(x(t_* - \tau(t_*))) &\le \left(\theta^p + K^p\right) g_k(v) = \theta^p g_k(v) \\ &+ \left[K^{1-p} + (p-1)\eta t_*\right]^{-p/(p-1)} \\ &\cdot K^p \left[K^{1-p} + (p-1)\eta t_*\right]^{p/(p-1)} g_k(v) \le \theta^p g_k(v) \\ &+ \left[K^{1-p} + (p-1)\eta t_*\right]^{-p/(p-1)} \\ &\cdot \left[1 + (p-1)K^{p-1}\eta h\right]^{p/(p-1)} g_k(v). \end{aligned} \tag{17}$$

Next, we can conclude from (1) and (7) that

$$\begin{aligned} \dot{z}_k(t_*) &= \frac{f_k(x(t_*)) + g_k(x(t_* - \tau(t_*))) + w_k(t_*)}{v_k} \\ &+ \eta\left\{\theta^p + \left[K^{1-p} + (p-1)\eta t_*\right]^{-p/(p-1)}\right\}^{(1-p)/p} \\ &\cdot \left[K^{1-p} + (p-1)\eta t_*\right]^{(1-2p)/(p-1)} \\ &\le \frac{f_k(x(t_*)) + g_k(x(t_* - \tau(t_*))) + w_k(t_*)}{v_k} \\ &+ \eta\left[K^{1-p} + (p-1)\eta t_*\right]^{-p/(p-1)}. \end{aligned} \tag{18}$$

Consequently, (11), (15), (17), and (18) imply that

$$\dot{z}_k(t_*) \le \frac{\theta^p[f_k(v)+g_k(v)]+r}{v_k} + \Big[K^{1-p} + (p-1)\eta t_*\Big]^{-p/(p-1)} \times \left\{\frac{f_k(v)}{v_k} + \frac{g_k(v)}{v_k}\Big[1+(p-1)K^{p-1}\eta h\Big]^{p/(p-1)} + \eta\right\}. \tag{19}$$

On the other hand, the definitions of θ and η yield that

$$\theta^p[f_k(v)+g_k(v)]+r \le \theta^p \max_{i\in\langle n\rangle}[f_i(v)+g_i(v)]+r = 0, \tag{20}$$

and

$$\frac{f_k(v)}{v_k} + \frac{g_k(v)}{v_k}\Big[1+(p-1)K^{p-1}\eta h\Big]^{p/(p-1)} + \eta < 0. \tag{21}$$

Combining this with (19), we have $\dot{z}_k(t_*) < 0$, which contradicts (8). Therefore, $z_i(t) \le 0$, $t \ge 0$, $i \in \langle n\rangle$; i.e.,

$$\frac{x_i(t)}{v_i} \le \left\{\theta^p + \Big[K^{1-p} + (p-1)\eta t\Big]^{-p/(p-1)}\right\}^{1/p}, \quad t \ge 0,\ i \in \langle n\rangle. \tag{22}$$

From the well-known inequality $(a+b)^q \le a^q + b^q$ for $a, b \ge 0$ and $0 < q < 1$, we further get

$$\frac{x_i(t)}{v_i} \le \theta + \Big[K^{1-p} + (p-1)\eta t\Big]^{-1/(p-1)}, \quad t \ge 0,\ i \in \langle n\rangle. \tag{23}$$

It implies (2).

(ii)$\Longrightarrow$(i) For the particular case when $r = 0$ and $h = 0$, system (1) reduces to

$$\dot{x}(t) = f(x(t)) + g(x(t)), \quad t \ge 0. \tag{24}$$

Given the initial condition $x(0) \succeq 0$, each solution of system (24) satisfies

$$\|x(t)\|_\infty \le (\beta + \gamma t)^{-1/(p-1)}. \tag{25}$$

That is, system (24) is asymptotically stable. Based on Proposition 4.1 in [35], there is a vector $v \succ 0$ such that $f(v)+g(v) \prec 0$. The proof is complete. □

Remark 7. It can be seen from Theorem 6 that the bound of the reachable set is determined by the bound of disturbances, the choice of v, and the value of p. When the bound of disturbances and the value of p are given, an appropriate vector v can be chosen to guarantee a minimal bound of the reachable set by solving the following nonlinear optimization problem: $\min_{v\succ 0}\theta$ subject to $f(v) + g(v) \prec 0$, where θ is defined as in Theorem 6.

Remark 8. If $\omega(t) = 0$ for $t \ge 0$, then Theorem 6 reduces to the main result given in [23]. If $g(x) = 0$ for $x \in \mathbb{R}^n$, then Theorem 6 reduces to the main result given in [24].

Finally, consider the following nonlinear time-varying system

$$\dot{x}(t) = \widetilde{f}(t, x(t)) + \widetilde{g}(t, (x(t-\tau(t))) + \omega(t), \quad t \ge 0$$
$$x(t) = \varphi(t), \quad t \in [-h, 0], \tag{26}$$

where $x(t), \tau(t), \omega(t)$, and $\varphi(t)$ are the same as in (1), and $\widetilde{f}, \widetilde{g} : [0,\infty)\times\mathbb{R}^n \longrightarrow \mathbb{R}^n$ are vector functions satisfying $\widetilde{f}(t,0) = \widetilde{g}(t,0) = 0$.

Suppose that $\widetilde{f}$ and $\widetilde{g}$ satisfy the following assumption:

(H4) $\widetilde{f}$ and $\widetilde{g}$ are continuous on $[0,\infty)\times\mathbb{R}^n$, continuously differentiable with respect to x on $\mathbb{R}^n\backslash\{0\}$, and there are vector functions f and g satisfying (H1) and (H2), and for $x_i \ne 0$,

$$\widetilde{f}_i(t,x)\operatorname{sign} x_i \le f_i(|x|), \quad |\widetilde{g}_i(t,x)| \le g_i(|x|), \quad t \ge 0,\ i \in \langle n\rangle. \tag{27}$$

Without the restriction on the disturbance that $\omega(t) \succeq 0$ for $t \ge 0$, we can get the following reachable set bounding criterion for system (26).

Theorem 9. *Suppose that (H4) is valid. If there is an n-dimensional vector $v \succ 0$ such that $f(v) + g(v) \prec 0$, the solution of system (26) satisfies (2), where constants α, β, and γ are defined by (3).*

Proof. Set

$$y_i(t) = \begin{cases} \dfrac{|x_i(t)|}{v_i} - \left\{\theta^p + \Big[K^{1-p} + (p-1)\eta t\Big]^{-p/(p-1)}\right\}^{1/p}, & t \ge 0,\ i \in \langle n\rangle, \\ \dfrac{|x_i(t)|}{v_i} - (\theta^p + K^p)^{1/p}, & t \in [-h, 0],\ i \in \langle n\rangle. \end{cases} \tag{28}$$

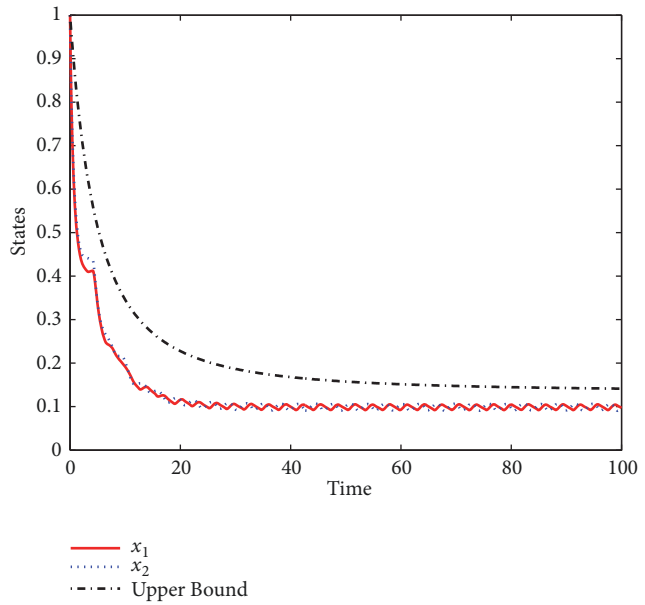

FIGURE 1: The states of system (1).

Based on definitions of K and $\|\varphi\|_v$, it holds that $y_i(t) \le 0$, $t \in [-h, 0]$, $i \in \langle n \rangle$. For the case when $x_i(t) \ne 0$, $t \ge 0$, notice that

$$\begin{aligned} \dot{y}_i(t) &= D_- \left|x_i(t)\right| = \dot{x}_i(t) \operatorname{sign} x_i(t) \\ &\le f_i(|x(t)|) + g_i(|x(t-\tau(t))|) + \left|w_i(t)\right|, \\ &\qquad i \in \langle n \rangle. \end{aligned} \tag{29}$$

Here D_- denotes the left derivative. Similar to the analysis in Theorem 6, it is not difficult to conclude that $y_i(t) \le 0$, $t \ge 0$, $i \in \langle n \rangle$. Consequently, (2) holds. The proof is complete. □

4. Numerical Example

Consider system (1) with

$$\begin{aligned} f(x_1, x_2) &= \begin{pmatrix} -3 & 6 \\ 2 & -2 \end{pmatrix} \begin{pmatrix} x_1^{3/2} \\ x_2^{3/2} \end{pmatrix} - \sqrt{x_1^3 + x_2^3} \begin{pmatrix} 3 \\ 1 \end{pmatrix}, \\ g(x_1, x_2) &= \begin{pmatrix} 0.2x_2^{3/2} \\ 0.4x_1^{3/2} \end{pmatrix}, \\ \omega(t) &= \begin{pmatrix} 0.05\,|\sin t| \\ 0.04\,|\cos t| \end{pmatrix}, \\ \tau(t) &= 5 + \sin t, \quad t \ge 0. \end{aligned} \tag{30}$$

It is easy to verify that assumptions (H1)-(H2) hold. Let $v = (1, 1)^T$. Then $f(v) + g(v) \prec 0$. By a direct calculation, it yields $h = 6$, $r = 0.05$, $\alpha \approx 0.1345$, and $\gamma \approx 0.11$.

We conclude from Theorem 6 that there is a ball $\mathcal{B}(0.1345)$ such that all the states of system (1) converge asymptotically within it. Given the initial state $\varphi(t) = (1, 1)^T$, $t \in [-6, 0]$, noting that $\|\varphi\|_v = 1$ and $\beta \approx 1.0749$, solution (1) satisfies

$$\|x(t)\|_\infty \le 0.1345 + (1.0749 + 0.11t)^{-2}, \quad t \ge 0. \tag{31}$$

Figure 1 presents the simulation.

5. Conclusion

This paper has been concerned with reachable set bounding for homogeneous nonlinear time-delay systems with disturbance. We not only derive explicit reachable set bounding criterion independent of delay, but also estimate the decay rate. It will be interesting to extend our work to the case of unbounded delays and discrete-time systems.

Data Availability

The data used to support the findings of this study are included within the article.

Conflicts of Interest

We declare that there are no conflicts of interest regarding this paper.

Acknowledgments

This work is supported by the National Natural Science Foundation of China under grant 61873110.

References

[1] E. Fridman and U. Shaked, "On reachable sets for linear systems with delay and bounded peak inputs," *Automatica*, vol. 39, no. 11, pp. 2005–2010, 2003.

[2] J.-H. Kim, "Improved ellipsoidal bound of reachable sets for time-delayed linear systems with disturbances," *Automatica*, vol. 44, no. 11, pp. 2940–2943, 2008.

[3] Z. Q. Zuo, D. W. C. Ho, and Y. J. Wang, "Reachable set bounding for delayed systems with polytopic uncertainties: the maximal Lyapunov-Krasovskii functional approach," *Automatica*, vol. 46, no. 5, pp. 949–952, 2010.

[4] O. M. Kwon, S. M. Lee, and J. H. Park, "On the reachable set bounding of uncertain dynamic systems with time-varying delays and disturbances," *Information Sciences*, vol. 181, no. 17, pp. 3735–3748, 2011.

[5] P. T. Nam and P. N. Pathirana, "Further result on reachable set bounding for linear uncertain polytopic systems with interval time-varying delays," *Automatica*, vol. 47, no. 8, pp. 1838–1841, 2011.

[6] P. T. Nam, P. N. Pathirana, and H. Trinh, "Exponential convergence of time-delay systems in the presence of bounded disturbances," *Journal of Optimization Theory and Applications*, vol. 157, no. 3, pp. 843–852, 2013.

[7] N. D. That, P. T. Nam, and Q. P. Ha, "Reachable set bounding for linear discrete-time systems with delays and bounded disturbances," *Journal of Optimization Theory and Applications*, vol. 157, no. 1, pp. 96–107, 2013.

[8] Z. Zuo, Y. Chen, Y. Wang, D. W. Ho, M. Z. Chen, and H. Li, "A note on reachable set bounding for delayed systems with polytopic uncertainties," *Journal of The Franklin Institute*, vol. 350, no. 7, pp. 1827–1835, 2013.

[9] J. Lam, B. Zhang, Y. Chen, and S. Xu, "Reachable set estimation for discrete-time linear systems with time delays," *International Journal of Robust and Nonlinear Control*, 2013.

[10] B. Zhang, J. Lam, and S. Xu, "Reachable set estimation and controller design for distributed delay systems with bounded disturbances," *Journal of The Franklin Institute*, vol. 351, no. 6, pp. 3068–3088, 2014.

[11] L. V. Hien and H. M. Trinh, "A new approach to state bounding for linear time-varying systems with delay and bounded disturbances," *Automatica*, vol. 50, no. 6, pp. 1735–1738, 2014.

[12] J. Qi and Y. Sun, "Global exponential stability of certain switched systems with time-varying delays," *Applied Mathematics Letters*, vol. 26, no. 7, pp. 760–765, 2013.

[13] G. Zong, H. Ren, and L. Hou, "Finite-time stability of interconnected impulsive switched systems," *IET Control Theory & Applications*, vol. 10, no. 6, pp. 648–654, 2016.

[14] Y. Li, Y. Sun, and F. Meng, "New criteria for exponential stability of switched time-varying systems with delays and nonlinear disturbances," *Nonlinear Analysis: Hybrid Systems*, vol. 26, pp. 284–291, 2017.

[15] Y. Li, Y. Sun, F. Meng, and Y. Tian, "Exponential stabilization of switched time-varying systems with delays and disturbances," *Applied Mathematics and Computation*, vol. 324, pp. 131–140, 2018.

[16] H. Liu, F. Meng, and P. Liu, "Oscillation and asymptotic analysis on a new generalized Emden-Fowler equation," *Applied Mathematics and Computation*, vol. 219, no. 5, pp. 2739–2748, 2012.

[17] J. Shao, Z. Zheng, and F. Meng, "Oscillation criteria for fractional differential equations with mixed nonlinearities," *Advances in Difference Equations*, p. 323, 2013.

[18] J. Shao, F. Meng, and Z. Zheng, "Oscillation theorems for linear matrix Hamiltonian systems," *Applied Mathematics and Computation*, vol. 253, pp. 402–409, 2015.

[19] H. Liu and F. Meng, "Interval oscillation criteria for second-order nonlinear forced differential equations involving variable exponent," *Advances in Difference Equations*, Paper No. 291, 14 pages, 2016.

[20] P. T. Nam, P. N. Pathirana, and H. Trinh, "Reachable set bounding for nonlinear perturbed time-delay systems: the smallest bound," *Applied Mathematics Letters*, vol. 43, pp. 68–71, 2015.

[21] X. Zhu, Y. Sun, and X.-J. Xie, "State bounding for nonlinear time-varying systems with delay and disturbance," *Journal of The Franklin Institute*, vol. 355, no. 16, pp. 8213–8224, 2018.

[22] N. Zhang, Y. Sun, and P. Zhao, "State bounding for homogeneous positive systems of degree one with time-varying delay and exogenous input," *Journal of The Franklin Institute*, vol. 354, no. 7, pp. 2893–2904, 2017.

[23] J. G. Dong, "On the decay rates of homogeneous positive systems of any degree with time-varying delays," *Institute of Electrical and Electronics Engineers Transactions on Automatic Control*, vol. 60, no. 11, pp. 2983–2988, 2015.

[24] Yuangong Sun and Fanwei Meng, "Reachable Set Estimation for a Class of Nonlinear Time-Varying Systems," *Complexity*, vol. 2017, Article ID 5876371, 6 pages, 2017.

[25] D. Tian, S. Liu, Y. Sun, and J. Xia, "Reachable set estimation for switched positive systems with mixed time-varying delays and bounded disturbances," *IET Control Theory & Applications*, vol. 12, no. 15, pp. 2003–2009, 2018.

[26] L. Farina and S. Rinaldi, *Positive Linear Systems: Theory and Applications*, Wiley, New York, NY, USA, 2000.

[27] T. Kaczorek, *Positive 1D and 2D Systems*, Springer-Verlag, New York, NY, USA, 2002.

[28] X. Liu, W. Yu, and L. Wang, "Stability analysis of positive systems with bounded time-varying delays," *IEEE Transactions on Circuits and Systems II: Express Briefs*, vol. 56, no. 7, pp. 600–604, 2009.

[29] X. Liu, W. Yu, and L. Wang, "Stability analysis for continuous-time positive systems with time-varying delays," *IEEE Transactions on Automatic Control*, vol. 55, no. 4, pp. 1024–1028, 2010.

[30] H. R. Feyzmahdavian, T. Charalambous, and M. Johansson, "Exponential stability of homogeneous positive systems of degree one with time-varying delays," *IEEE Transactions on Automatic Control*, vol. 59, no. 6, pp. 1594–1599, 2014.

[31] Y. Sun, Y. Tian, and X.-J. Xie, "Stabilization of positive switched linear systems and its application in consensus of multiagent systems," *IEEE Transactions on Automatic Control*, vol. 62, no. 12, pp. 6608–6613, 2017.

[32] Yuangong Sun, Zhaorong Wu, and Fanwei Meng, "Common Weak Linear Copositive Lyapunov Functions for Positive Switched Linear Systems," *Complexity*, vol. 2018, Article ID 1365960, 7 pages, 2018.

[33] N. Zhang, Y. Sun, and F. Meng, "State bounding for switched homogeneous positive nonlinear systems with exogenous input," *Nonlinear Analysis: Hybrid Systems*, vol. 29, pp. 363–372, 2018.

[34] H. L. Smith, *Monotone dynamical systems: an introduction to the theory of competitive and cooperative systems, ameircan mathematical society*, 1995.

[35] V. S. Bokharaie, O. Mason, and F. Wirth, "Stability and positivity of equilibria for subhomogeneous cooperative systems," *Nonlinear Analysis. Theory, Methods & Applications*, vol. 74, no. 17, pp. 6416–6426, 2011.

Hindawi
Complexity
Volume 2019, Article ID 2538206, 12 pages
https://doi.org/10.1155/2019/2538206

Research Article

A PI-Type Sliding Mode Controller Design for PMSG-Based Wind Turbine

Jun Liu, Feihang Zhou, Chencong Zhao, and Zhuoran Wang

College of Automation, Xi'an University of Technology, China

Correspondence should be addressed to Feihang Zhou; qq987102679@126.com

Received 2 April 2019; Revised 10 May 2019; Accepted 28 May 2019; Published 19 June 2019

Guest Editor: Baltazar Aguirre-Hernandez

Because the PMSG (permanent magnet synchronous generator)-based WECS (wind energy conversion system) has some uncertainties, the conventional control strategy with poor robustness is sometimes difficult to meet the performance requirements of control. In order to ensure efficient and stability of the system, this paper proposed a novel PI (proportional-integral)-type SMC (sliding mode control) strategy for PMSG-based WECS uncertainties and presented the detailed analysis and design process. Compared with the conventional control method, the PI-type SMC proposed in this paper not only can make the closed-loop system globally stable, but also has a better robustness and slightly reduced the current ripple and distortion. Finally, the simulation results verify the correctness and effectiveness of this algorithm.

1. Introduction

Environment problems such air pollution and global warming caused by fossil fuels have drawn the world's attention to exploration and utilization of renewable energy sources, in recent years [1–5]. At present, wind energy is the fastest growing renewable energy source and is most prevalent in coastal regions spanning temperate and boreal climates [6–8]. There is great potential for wind power development in China, USA, Denmark, and other countries, due to their high average wind velocities [9]. Therefore, the research on wind power generation technology has a significant value nowadays. Compared with the constant-speed constant-frequency wind turbine, the variable-speed constant-frequency wind turbines can obtain the maximum energy conversion due to its rotational speed could vary with wind speed to ensure that the system has the OTSR (optimal tip speed ratio) and maximum wind energy utilization coefficient. The variable-speed constant-frequency wind energy conversion system (WECS) consists of DFIG (doubly fed induction generator)-based WECS and PMSG (permanent magnet synchronous generator)-based WECS. The PMSG-based WECS was selected to study in this paper, due to the fact that PMSG has many superior characteristics such as wider speed control range, higher reliability, and more efficient performance compared with DIFG [10].

In fact, the practical systems have many uncertainties. The uncertainties of PMSG or PMSM (permanent magnet synchronous motor) consist of the unmodeled converter dynamics and the parameters perturbations [11–14]. A robust control scheme for PMSM uncertainties based on an adaptive DOB (disturbance observer) was introduced in [11]. The results indicated that the controller obtained a good control performance. Reference [12] proposed a robust nonlinear predictive control strategy for PMSM uncertainties. The control system obtained a high speed tracking precision. In [13], a PFC (predictive functional control) + ESO (extended state observer) method was studied. After that, the effectiveness of this new method was verified. Reference [14] proposed a novel decoupled PI current control method for the PMSG-based WECS. This method can successfully achieve improved the transient performances and the nominal performance recovery under the model uncertainty.

SMC (sliding mode control) first proposed in the early 1950s has a good robustness and powerful ability to reject the plant uncertainties and disturbances [15, 16]. References [15, 16] summarized the development of SMC and examined key technical research issues and future perspectives. Although

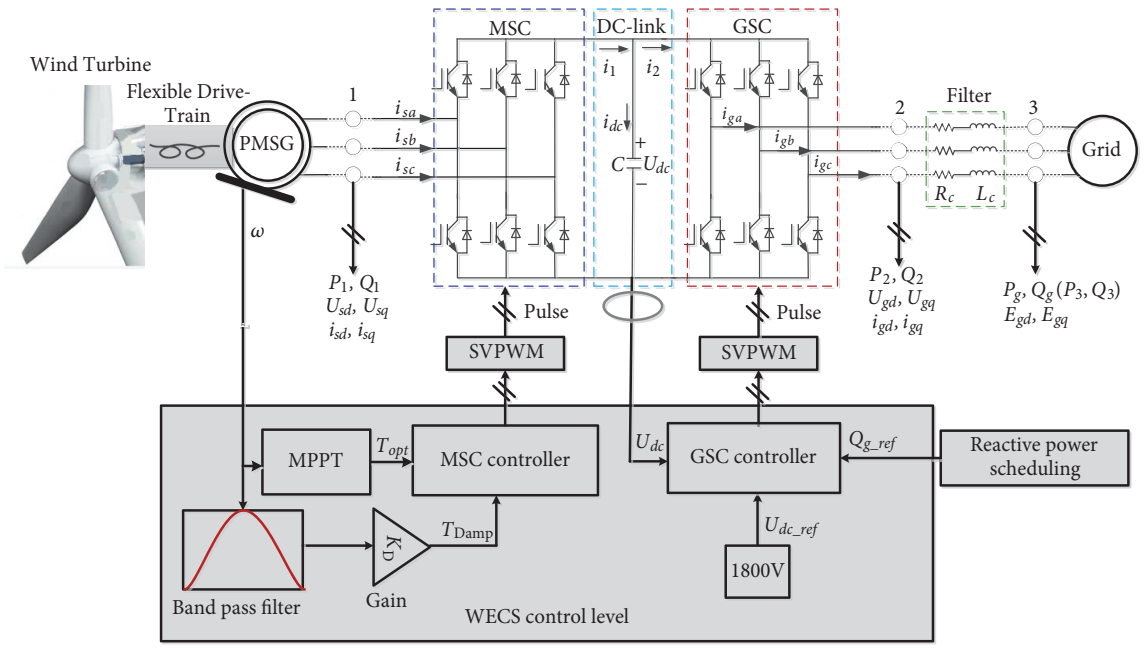

Figure 1: A WECS configuration.

the SMC has been widely and extensively employed in some industrial applications for a long term, it is still the researching focus for scholars and worth studying in depth. A DPC (direct power control) based on SMC for the grid-connected WECS was presented in [17]. When the grid voltage is unbalanced, the controller also can regulate the instantaneous active and reactive powers directly in stator stationary reference frame. Reference [18] enhanced the exponential reaching law to improve the control efficiency and performance of SMC used in PMSG-based WECS.

An adaptive second-order SMC strategy was explored in [19]. This method can effectively deals with the presence of model uncertainties, intrinsic nonlinear behavior of WECS, and random wind. A SMC method for mismatched uncertainties via a nonlinear DOB was developed in [20]. Meanwhile, the I-SMC (integral sliding-model control) with a good steady-state precision was mentioned in [20, 21]. The PI-type SMC is derived by the I-SMC and FBL (feedback linearization) approach and has been widely used in renewable energy conversion systems and the electric motor drives [21–23]. Furthermore, compared with the I-SMC, the proportional and integral parameters of the PI-type SMC are able to be adjusted to better meet the control performance indexes such as the celerity and accuracy.

Based on the above background, this paper presents a novel PI-type SMC for the PMSG-based WECS. Although the inspiration for this paper comes from literature [20–23], the whole designing thought and procedure of the proposed controller are completely different from the methods in [20–23]. Furthermore, [20, 23] just only referred to the control of PMSG without the consideration of grid-connected control. And the study subjects in [22, 23] and this paper are different. At the same time, the suppression of flexible drive-train torsional vibration also has been regarded as a control target in this paper. Then, we set up a detailed 2 MW WECS simulation test platform based on MATLAB/SIMULINK/SimPowerSysterms to verify the effectiveness and correctness of the proposed method. A large number of existing packaging modules in SimPowerSysterms are used in the simulation test platform that is relatively close to the real physical system. Finally, the simulation results indicate the proposed strategy has good control performance.

2. PMSG-Based WECS Model

The simplified PMSG-based WECS mainly consists of a wind turbine, a flexible drive-train, a PMSG, fully rated converters, and its control level shown in Figure 1. In order to capture the maximum wind energy, the maximum power point tracking (MPPT) strategy is adopted to control the machine-side converter (MSC). In the loop control level, the grid-side converter (GSC) control is to regulate the reactive power and keep DC-link voltage U_{dc} stable at 1800V. Meanwhile, in order to suppress the torsional vibration of flexible drive-train, the damping compensation torque T_{Damp} was introduced.

2.1. PMSG and MSC Dynamic Model. The PMSG and MSC mathematical model is [5, 20–27]

$$\begin{aligned}\frac{\mathrm{d}i_{sd}}{\mathrm{d}t} &= -\frac{R_s}{L_{sd}}i_{sd} + \frac{L_{sq}}{L_{sd}}n_p\omega i_{sq} + \frac{1}{L_{sd}}U_{sd} - \frac{1}{L_{sd}}\varepsilon_{sd}\\ \frac{\mathrm{d}i_{sq}}{\mathrm{d}t} &= -\frac{R_s}{L_{sq}}i_{sq} - \frac{L_{sd}}{L_{sq}}n_p\omega i_{sd} - \frac{n_p\omega\psi}{L_{sq}} + \frac{1}{L_{sq}}U_{sq}\\ &\quad - \frac{1}{L_{sq}}\varepsilon_{sq}\end{aligned} \tag{1}$$

where U_{sd} and U_{sq} are the d-axis and q-axis stator armature voltages. i_{sd} and i_{sq} are the d-axis and q-axis components of stator currents. L_{sd} and L_{sq} are the d-axis and q-axis stator inductances. ω is the rotor speed. n_{p} represents magnetic pole logarithms. R_{s} is the stator resistance. ψ represents the permanent magnet chain. And the disturbance vector ε_{sd} and ε_{sq} represent model uncertainties including the external disturbances and the PWM offset. ε_{sd} and ε_{sq} were generally assumed to be bounded by D_{sd} and D_{sd}.

$$\begin{aligned} \left|\varepsilon_{sd}\right| &\le D_{sd}; \\ \left|\varepsilon_{sd}\right| &\le D_{sq} \end{aligned} \tag{2}$$

where D_{sd} and D_{sq} are the boundaries of ε_{sd} and ε_{sq}.

The PMSG torque is given by

$$T_g = 1.5 n_p \left[\left(L_{sd} - L_{sq}\right) i_{sd} i_{sq} + \psi i_{sq}\right] \tag{3}$$

2.2. GSC Dynamic Model. The GSC dynamic model is given by

$$\begin{aligned} \frac{\mathrm{d}i_{gd}}{\mathrm{d}t} &= -\frac{R_c}{L_c} i_{gd} + \omega_g i_{gq} + \frac{1}{L_c} E_{gd} - \frac{1}{L_c} U_{gd} - \frac{1}{L_c} \varepsilon_{gd} \\ \frac{\mathrm{d}i_{gq}}{\mathrm{d}t} &= -\frac{R_c}{L_c} i_{gq} - \omega_g i_{gd} + \frac{1}{L_c} E_{gq} - \frac{1}{L_c} U_{gq} - \frac{1}{L_c} \varepsilon_{gq} \end{aligned} \tag{4}$$

where U_{gd} and U_{gq} are the control voltages. i_{gd} and i_{gq} are the components of grid-side currents. ω_g is the power grid frequency. L_c and R_c are the filter inductance and resistance. E_{gd} and E_{gq} express the d-axis and q-axis power grid potential components (usually, $E_{gq} = 0$). The ω_g and E_{gd} can be gotten by the voltage phase-locked loop. ε_{gd} and ε_{gq} are also the uncertainties and meet

$$\begin{aligned} \left|\varepsilon_{gd}\right| &\le D_{gd}; \\ \left|\varepsilon_{gd}\right| &\le D_{gq} \end{aligned} \tag{5}$$

D_{gd} and D_{gq} are the boundaries of ε_{gd} and ε_{gq}.

3. PI-Type Sliding Mode Controller Design

3.1. Control Objectives. If the state vector $\boldsymbol{x}$ and the reference state vector $\boldsymbol{x}_{\_ref}$ are

$$\boldsymbol{x} = \left[i_{sd} \;\; i_{sq} \;\; i_{gd} \;\; i_{gq}\right]^{\mathrm{T}} \tag{6}$$

$$\boldsymbol{x}_{ref} = \left[i_{sd\_ref} \;\; i_{sq\_ref} \;\; i_{gd\_ref} \;\; i_{gq\_ref}\right]^{\mathrm{T}} \tag{7}$$

the control objectives of WECS can be expressed as

$$\lim_{t \longrightarrow +\infty} \boldsymbol{e} = \lim_{t \longrightarrow +\infty} \boldsymbol{x}_{ref} - \boldsymbol{x} = \boldsymbol{0} \tag{8}$$

where $\boldsymbol{e}$ is the error vector. In the above formula, usually we have

$$\begin{aligned} i_{sd\_ref} &= 0 \\ i_{sq\_ref} &= \frac{2T_{g\_ref}}{3n_p\psi} = \frac{2\left(T_{opt} + T_{Damp}\right)}{3n_p\psi} \\ i_{gd\_ref} &= \left(K_P + \frac{K_I}{s}\right)\left(U_{dc\_ref} - U_{dc}\right) \\ i_{gq\_ref} &= \frac{Q_{g\_ref}}{E_{gd}} \end{aligned} \tag{9}$$

where K_P and K_I are the PI (proportional-integral) parameters. The optimal torque T_{opt} in (9) meets [1, 26–29]

$$T_{opt} = K_{opt}\omega^2 \quad \text{with } K_{opt} = \frac{\pi\rho R^5 C_{P\_\max}}{2\lambda_{opt}^3} \tag{10}$$

where R is the wind wheel radius, ρ is the air density, $C_{P\_\max}$ is defined as the maximum wind energy conversion coefficient, λ_{opt} is the OTSR (optimal tip speed ratio), and the damping compensation torque T_{Damp} is given by [29–38]

$$T_{Damp} = K_D H(s)\,\omega \tag{11}$$

where $K_D \in R^+$ and $H(s)$ is the transfer function of bandpass filter shown in [29–38].

3.2. Design of Proportional-Integral (PI)-Type Sliding Mode Controller. The PI-type sliding surface $\boldsymbol{S}$ can be defined as

$$\boldsymbol{S} = \left(\boldsymbol{K} + \frac{1}{s}\boldsymbol{I}\right)\boldsymbol{e} \tag{12}$$

where

$$\boldsymbol{S} = \left[S_1 \;\; S_2 \;\; S_3 \;\; S_4\right]^{\mathrm{T}} \tag{13}$$

$$\boldsymbol{K} = \mathrm{diag}\left\langle K_1, K_2, K_3, K_4\right\rangle \tag{14}$$

$$\boldsymbol{I} = \mathrm{diag}\left\langle I_1, I_2, I_3, I_4\right\rangle \tag{15}$$

s is Laplace variable. $K_i \in R^+$ and $I_i \in R^+$ (i=1,2,3,4). Obviously, we also can get

$$\begin{aligned} S_1\varepsilon_{sd} &\le \left|S_1\varepsilon_{sd}\right| = D_{sd}S_1\,\mathrm{sgn}\left(S_1\right) \\ S_2\varepsilon_{sq} &\le \left|S_2\varepsilon_{sq}\right| = D_{sq}S_2\,\mathrm{sgn}\left(S_2\right) \\ S_4\varepsilon_{gd} &\le \left|S_4\varepsilon_{gd}\right| = D_{gd}S_4\,\mathrm{sgn}\left(S_4\right) \\ S_5\varepsilon_{gq} &\le \left|S_5\varepsilon_{gq}\right| = D_{gq}S_5\,\mathrm{sgn}\left(S_5\right) \end{aligned} \tag{16}$$

if the Lyapunov function is defined as

$$V = \frac{1}{2}\boldsymbol{S}^{\mathrm{T}}\boldsymbol{S} = \sum_{i=1}^{4} V_i \tag{17}$$

where

$$V_i = \frac{1}{2}S_i^2 \tag{18}$$

Equations (19)-(22) can be gotten by taking the derivative of (17).

$$\begin{aligned}\dot{V}_1 &= S_1\dot{S}_1 = S_1\left(K_1\dot{e}_{sd} + I_1e_{sd}\right)\\ &= S_1\left\{K_1\left(\begin{array}{c}\dot{i}_{sd\_ref} + \frac{R_s}{L_{sd}}i_{sd} - \frac{L_{sq}}{L_{sd}}n_p\omega i_{sq}\\ -\frac{1}{L_{sd}}U_{sd} + \frac{1}{L_{sd}}\varepsilon_{sd}\end{array}\right)\right.\\ &\quad\left. + I_1e_{sd}\right\}\\ &\le S_1\left\{K_1\left(\begin{array}{c}\dot{i}_{sd\_ref} + \frac{R_s}{L_{sd}}i_{sd} - \frac{L_{sq}}{L_{sd}}n_p\omega i_{sq}\\ -\frac{1}{L_{sd}}U_{sd} + \frac{1}{L_{sd}}D_{sd}\,\mathrm{sgn}\left(S_1\right)\end{array}\right)\right.\\ &\quad\left. + I_1e_{sd}\right\}\end{aligned} \tag{19}$$

$$\begin{aligned}\dot{V}_2 &= S_2\dot{S}_2 = S_2\left(K_2\dot{e}_{sq} + I_2e_{sq}\right)\\ &= S_2\left\{K_2\left(\begin{array}{c}\dot{i}_{sq\_ref} + \frac{R_s}{L_{sq}}i_{sq} + \frac{L_{sd}}{L_{sq}}n_p\omega i_{sq}\\ +\frac{n_p\omega\psi}{L_{sq}} - \frac{1}{L_{sq}}U_{sq} + \frac{1}{L_{sq}}\varepsilon_{sq}\end{array}\right)\right.\\ &\quad\left. + I_2e_{sq}\right\}\\ &\le S_2\left\{K_2\left(\begin{array}{c}\dot{i}_{sq\_ref} + \frac{R_s}{L_{sq}}i_{sq} + \frac{L_{sd}}{L_{sq}}n_p\omega i_{sq} + \frac{n_p\omega\psi}{L_{sq}}\\ -\frac{1}{L_{sq}}U_{sq} + \frac{1}{L_{sq}}D_{sq}\,\mathrm{sgn}\left(S_2\right)\end{array}\right)\right.\\ &\quad\left. + I_2e_{sq}\right\}\end{aligned} \tag{20}$$

$$\begin{aligned}\dot{V}_3 &= S_3\dot{S}_3 = S_3\left(K_3\dot{e}_{gd} + I_3e_{gd}\right)\\ &= S_3\left\{K_3\left(\begin{array}{c}\dot{i}_{gd\_ref} + \frac{R_c}{L_c}i_{gd} - \omega_g i_{gq} -\\ \frac{1}{L_c}E_{gd} + \frac{1}{L_c}U_{gd} + \frac{1}{L_c}\varepsilon_{gd}\end{array}\right)\right.\\ &\quad\left. + I_3e_{gd}\right\}\\ &\le S_3\left\{K_3\left(\begin{array}{c}\dot{i}_{gd\_ref} + \frac{R_c}{L_c}i_{gd} - \omega_g i_{gq} -\\ \frac{1}{L_c}E_{gd} + \frac{1}{L_c}U_{gd} + \frac{1}{L_c}D_{gd}\,\mathrm{sgn}\left(S_4\right)\end{array}\right)\right.\\ &\quad\left. + I_3e_{gd}\right\}\end{aligned} \tag{21}$$

$$\begin{aligned}\dot{V}_4 &= S_4\dot{S}_4 = S_4\left(K_4\dot{e}_{gq} + I_4e_{gq}\right)\\ &= S_4\left\{K_4\left(\begin{array}{c}\dot{i}_{gq\_ref} + \frac{R_c}{L_c}i_{gq} + \omega_g i_{gd} -\\ \frac{1}{L_c}E_{gq} + \frac{1}{L_c}U_{gq} + \frac{1}{L_c}\varepsilon_{gq}\end{array}\right)\right.\\ &\quad\left. + I_4e_{gq}\right\}\\ &\le S_4\left\{K_4\left(\begin{array}{c}\dot{i}_{gq\_ref} + \frac{R_c}{L_c}i_{gq} + \omega_g i_{gd} - \frac{1}{L_c}E_{gq}\\ +\frac{1}{L_c}U_{gq} + \frac{1}{L_c}D_{gq}\,\mathrm{sgn}\left(S_3\right)\end{array}\right)\right.\\ &\quad\left. + I_4e_{gq}\right\}\end{aligned} \tag{22}$$

Let

$$\begin{aligned}&K_1\left(\dot{i}_{sd\_ref} + \frac{R_s}{L_{sd}}i_{sd} - \frac{L_{sq}}{L_{sd}}n_p\omega i_{sq} - \frac{1}{L_{sd}}U_{sd}\right.\\ &\left. + \frac{1}{L_{sd}}D_{sd}\,\mathrm{sgn}\left(S_1\right)\right) + I_1e_{sd} = -\gamma_1S_1\end{aligned} \tag{23}$$

$$K_2\left(\dot{i}_{sq\_ref}+\frac{R_s}{L_{sq}}i_{sq}+\frac{L_{sd}}{L_{sq}}n_p\omega i_{sq}+\frac{n_p\omega\psi}{L_{sq}}-\frac{1}{L_{sq}}U_{sq}+\frac{1}{L_{sq}}D_{sq}\operatorname{sgn}(S_2)\right)+I_2e_{sq}=-\gamma_2S_2 \tag{24}$$

$$K_3\left(\dot{i}_{gd\_ref}+\frac{R_c}{L_c}i_{gd}-\omega_g i_{gq}-\frac{1}{L_c}E_{gd}+\frac{1}{L_c}U_{gd}+\frac{1}{L_c}D_{gd}\operatorname{sgn}(S_4)\right)+I_3e_{gd}=-\gamma_3S_3 \tag{25}$$

$$K_4\left(\dot{i}_{gq\_ref}+\frac{R_c}{L_c}i_{gq}+\omega_g i_{gd}-\frac{1}{L_c}E_{gq}+\frac{1}{L_c}U_{gq}+\frac{1}{L_c}D_{gq}\operatorname{sgn}(S_4)\right)+I_4e_{gq}=-\gamma_4S_4 \tag{26}$$

Equation (27) can be gotten.

$$\dot{V}\le-\sum_{i=1}^{4}\gamma_iS_i^2\le 0 \tag{27}$$

where $\gamma_i > 0$. Therefore, the control laws are given by (28) -(31) and the control structure diagram is shown in Figure 2.

$$U_{sd}=\frac{L_{sd}}{K_1}(\gamma_1S_1+I_1e_{sd})+L_{sd}\dot{i}_{sd\_ref}+R_si_{sd}-L_{sq}n_p\omega i_{sq}+D_{sd}\operatorname{sgn}(S_1) \tag{28}$$

$$U_{sq}=\frac{L_{sq}}{K_2}(\gamma_2S_2+I_2e_{sq})+L_{sq}\dot{i}_{sq\_ref}+R_si_{sd}+L_{sd}n_p\omega i_{sd}+n_p\omega\psi+D_{sq}\operatorname{sgn}(S_2) \tag{29}$$

$$U_{gd}=-\frac{L_c}{K_3}(\gamma_3S_3+I_3e_{gd})-L_c\dot{i}_{gd\_ref}-R_ci_{gd}+L_c\omega_gi_{gq}+E_{gd}-D_{gd}\operatorname{sgn}(S_3) \tag{30}$$

$$U_{gq}=-\frac{L_c}{K_4}(\gamma_4S_4+I_4e_{gq})-L_c\dot{i}_{gq\_ref}-R_ci_{gq}-L_c\omega_gi_{gd}+E_{gq}-D_{gq}\operatorname{sgn}(S_4) \tag{31}$$

From (17) and (27), it is clear that the Lyapunov energy function V is greater than or equal to 0 and the derivative of V is less than or equal to 0. Hence, the whole system is asymptotically stable based on Lyapunov stability theorem.

3.3. Tracking Accuracy Analysis. In order to analyze the tracking accuracy, we need to introduce Theorem 1 here.

Theorem 1. *For any dynamic system with state vector* $X=[x_1\ x_2\ \dots\ x_n]^T$ *and assuming* $L=f(X)\ge 0$ *is a Lyapunov function of system, if* $\dot{L}\le-\sum_{i=1}^{n}k_ix_i^2$ *or* $\dot{L}\le-\sum_{i=1}^{n}k_i|x_i|$ *where* $k_i\in R^+$, *then* $\lim_{t\longrightarrow\infty}x_i=0$.

Table 1: WECS parameters.

Parameters	Value
Wind turbine inertia moment J_{tur} [kg·m^2]	2×10^4
Air density ρ [kg/m^3]	1.225
Blade length R [m]	31
Maximum utilization coefficient of wind energy C_{P_max}	0.476
Rated wind speed v_{rate} [m/s]	14
Rated power P_{rate} [MW]	2
Rated torque T_{rate} [kN·m]	4×10^2
Rate rotor speed ω_{rate} [rad/s]	5
Generator pole logarithm n_p	102
Permanent flux φ [Wb]	1.25
Stator-resistance R_S [Ω]	0.001
stator-reluctance L [mH]	8.35
DC-Link voltage [V]	1800
DC-Link capacitor C [F]	0.22
System resistance R_c [Ω]	0.001
System inductor L_c [mH]	6
Power grid potential E_{gd} [V]	380
Generator inertia moment J_{gen} [kg·m^2]	700

Proof. There are three cases.

① If $L\equiv$ constant ≥ 0, then $0\equiv\dot{L}\le-\sum_{i=1}^{n}k_ix_i^2\le 0$, and further $k_ix_i^2=0$. Due to $k_i\neq 0$, thus $x_i=0$. This means that there are not continuous and stable equilibrium points $f(X)\equiv$ constant >0 such as stable limit cycle in this system.

② Assuming $L(0)=$ constant, due to $\dot{L}\le-\sum_{i=1}^{n}k_ix_i^2$, then

$$L(0)-L(+\infty)\ge\int_0^{+\infty}k_ix_i^2\mathrm{d}t\ge 0. \tag{32}$$

$\forall x_i$, if $\lim_{t\longrightarrow\infty}x_i\neq 0$, then $\int_0^{+\infty}k_ix_i^2\mathrm{d}t\longrightarrow+\infty$, and furthermore $L(+\infty)\longrightarrow-\infty$. Obviously, this is in contradiction with $L\ge 0$. Thus $\lim_{t\longrightarrow\infty}x_i=0$.

③ Given $L(0)\longrightarrow+\infty$, according to Lyapunov stability criterion, the system is stable. So, there must be t_1 meeting $L(t_1)=$ constant. Otherwise $L(+\infty)\longrightarrow+\infty$. This is clearly in contradiction with system stability. If we redefined t_1 as 0, we can get $\lim_{t\longrightarrow\infty}x_i=0$ by ②.

When $\dot{L}\le-\sum_{i=1}^{n}k_i|x_i|$, we have the same conclusion in the same way.

Based on Theorem 1, we have

$$\lim_{t\longrightarrow+\infty}\boldsymbol{S}=[0\ \ 0\ \ 0\ \ 0]^{\mathrm{T}} \tag{33}$$

From (12) and (33), we can get

$$\lim_{t\longrightarrow+\infty}\boldsymbol{e}=\lim_{s\longrightarrow0}s^2(\boldsymbol{K}s+\boldsymbol{I})^{-1}\boldsymbol{S}=[0\ \ 0\ \ 0\ \ 0]^{\mathrm{T}} \tag{34}$$

The above formula shows that the steady-state error of the system is always 0 regardless of the input. Therefore, the proposed strategy can obtain a good tracking accuracy. □

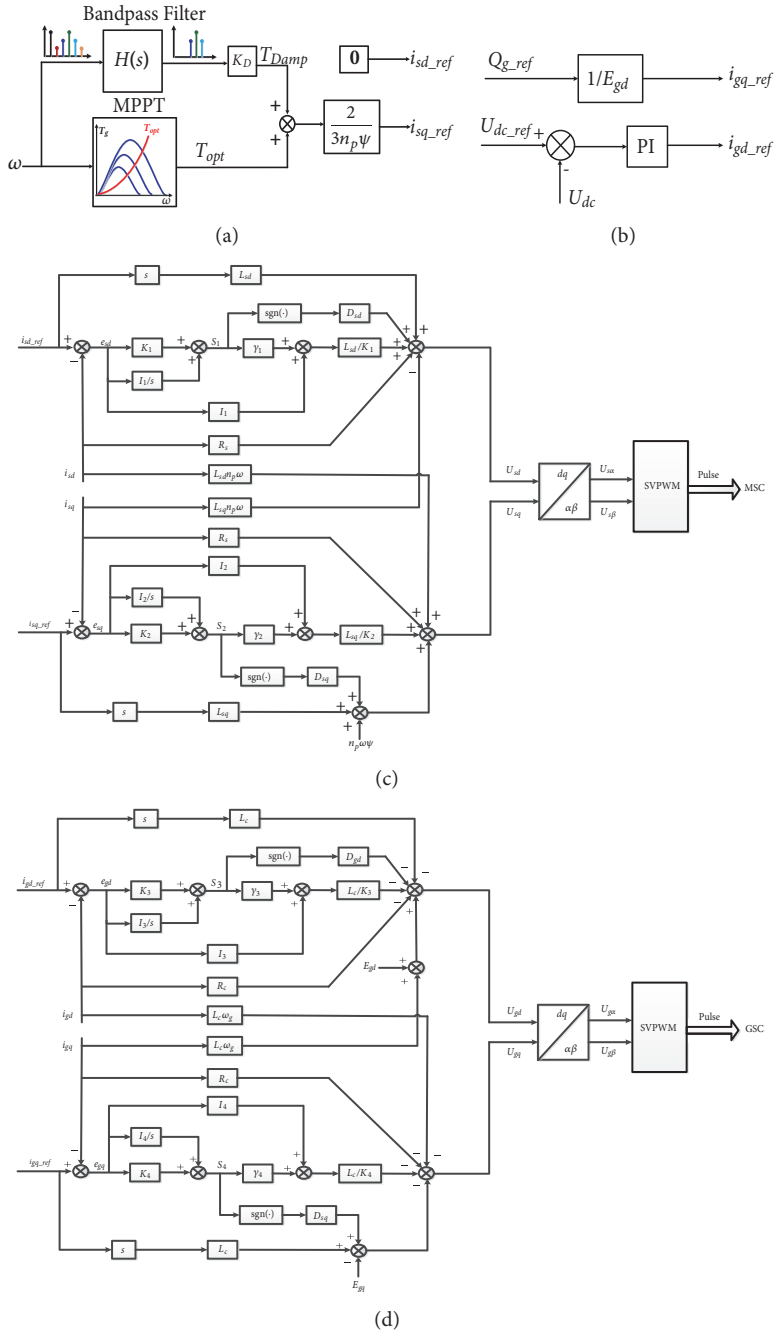

Figure 2: Control structure diagram of WECS.

4. Algorithm Analysis and Verification

In this section, a detailed simulation test platform is constructed to verify the correctness and effectiveness of the new algorithm, shown in Figure 3. The simulation test platform is based on the MATLAB/Simulink environment and the packaged modules in SimPowerSysterms are used in this simulation test platform, including the wind turbine, PMSG, and VSCs. Meanwhile, the two mass block spring damping model mentioned in [21–31] is adopted to describe the dynamics of flexible drive chain. Therefore, the simulation test platform is relatively close to the actual physical system, due to the adoption of many packaged modules. The controller of WECS consists of MSC controller and GSC controller which are mentioned in Figure 3. The system parameters are shown in Table 1. In general, the actual wind speed is time-varying and random; however we also believe the wind speed is constant for a short period of time. Hence, we assume that the

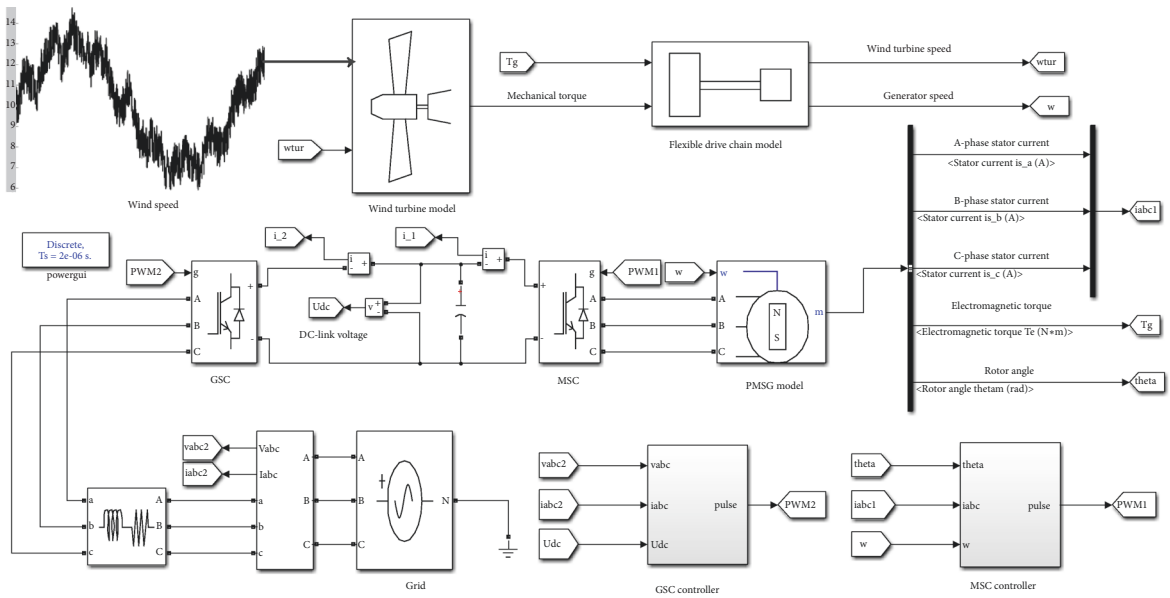

Figure 3: Simulation test platform.

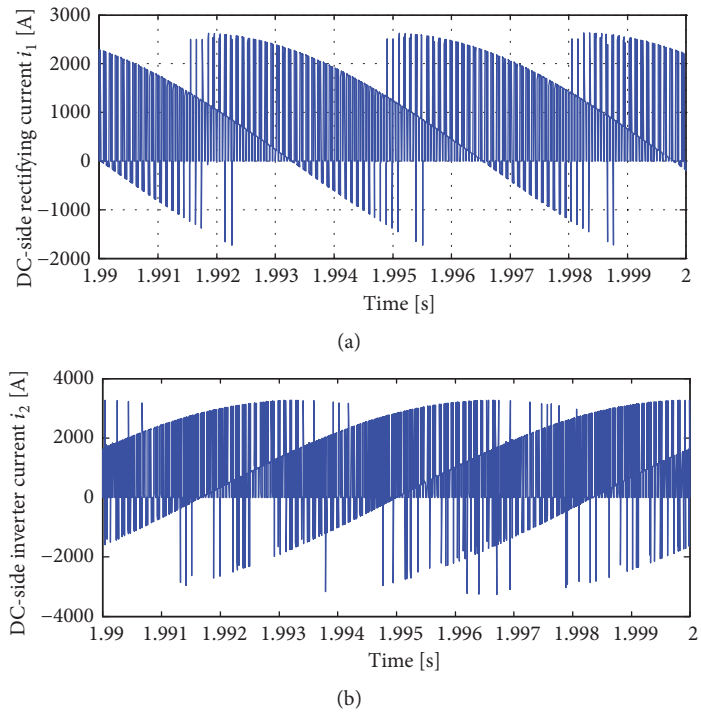

Figure 4: DC-link currents.

wind speed meets $v = 12 + 0.4 \times \text{rand}(t)$. The DC-link currents i_1 and i_2 are shown in Figure 4 and the other response curves of WECS are shown in Figure 5.

From Figure 4, we know that the DC-link currents i_1 and i_2 are bidirectional. This means that the MSC or GSC is able to switch between rectifier and inverter state. However, because of the mean values of i_1 and i_2 are positive, therefore the MSC is basically working as a rectifier and the GSC is mostly in the state of inverter. This is in accordance with the actual accident situation and can verify the accuracy of the model in a sense.

Figure 5 shows the response curves of wind energy utilization coefficient C_P, DC-link voltage U_{dc}, d-axis, and q-axis components of stator current and grid current. The disturbance component of the wind speed is the main causes of C_P, U_{dc}, current, and power fluctuations. Figure 5(a) depicts the wind energy utilization coefficient C_P is always

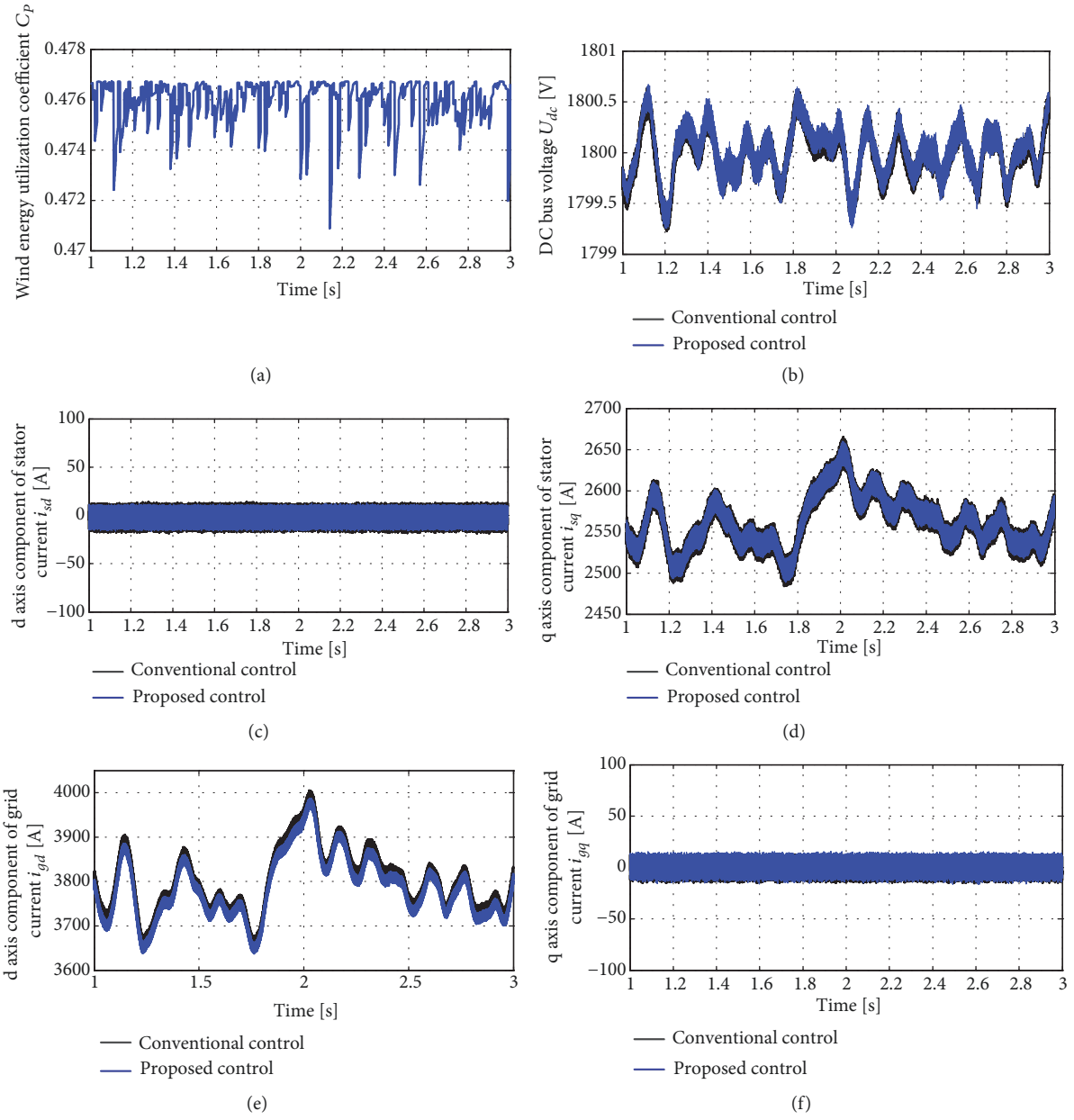

Figure 5: Response curves of WECS.

in the vicinity of the maximum value C_{P_max} (or 0.4763) under the proposed control strategy. This implies the WECS is operating in MPPT mode to capture the maximum wind energy under the rated wind speed. It is clear that the DC-link voltage U_{dc} is very close to its reference U_{dc_ref} (or 1800V) and the deviation does not exceed 0.8V by Figure 5(b). Figures 5(b)–5(f) show that the proposed control can reduce the current ripple of stator currents and grid currents compared with the conventional control, because the uncertainty of the unmodeled dynamics is taken into account in the design of the proposed controller. In one word, the proposed control strategy has a better robustness than the conventional control strategy.

The electromagnetic torque and sliding mode surfaces curves are shown in Figures 6 and 7. It is clear that the electromagnetic torque fluctuation under the proposed control method is smaller, compared with the conventional control method. Meanwhile, Figure 7 shows all steady-state values of sliding mode surfaces are tend to zero. Thus, the correctness of the analysis in Section 3.3 is verified by Figure 7. Furthermore, the proposed scheme was further verified for the suppression of current harmonics. Here, we take the A-phase stator current of generator as an example. The A-phase stator current waveform is shown in Figure 8. Obviously, the proposed method also can reduce the current distortion.

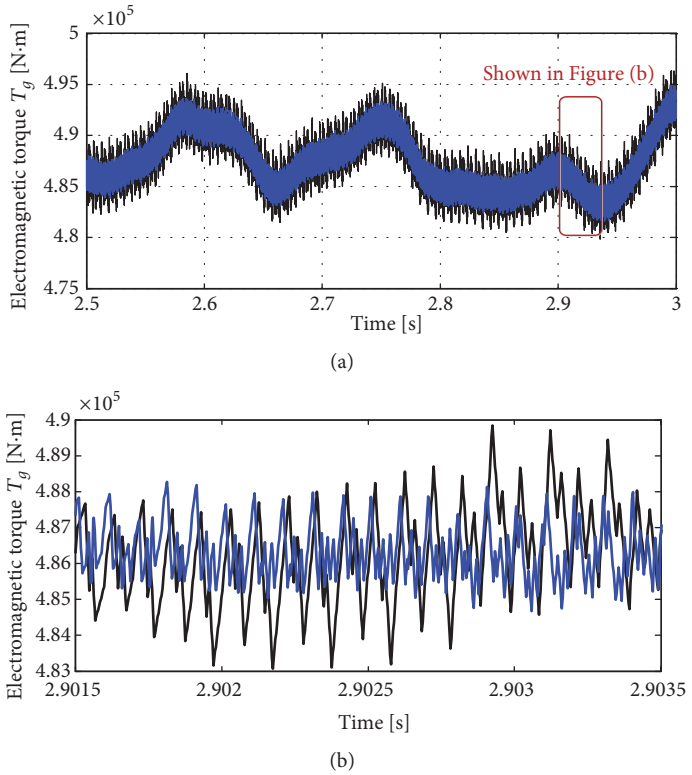

Figure 6: Electromagnetic torque curve.

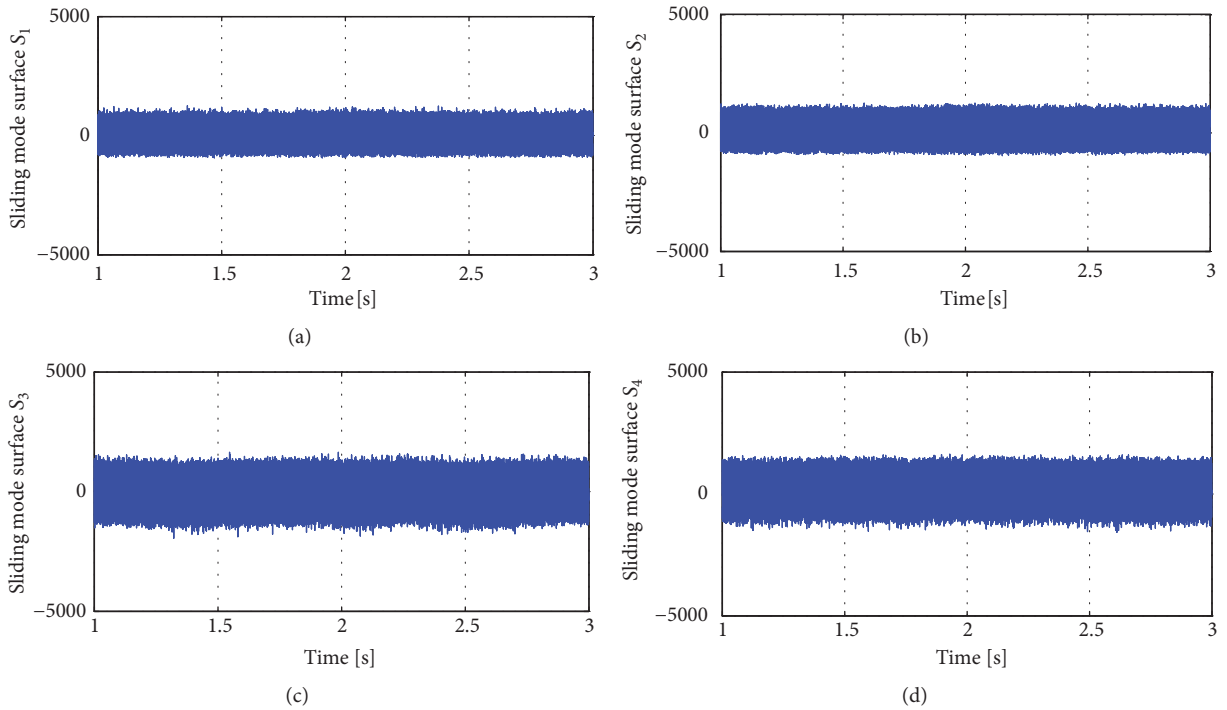

Figure 7: Sliding mode surface curve.

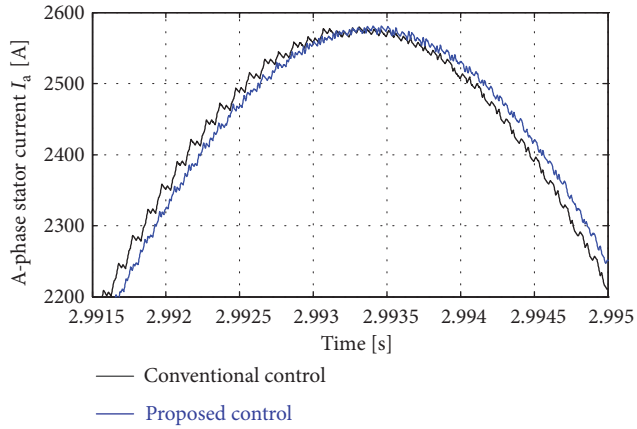

Figure 8: A-phase stator current waveform.

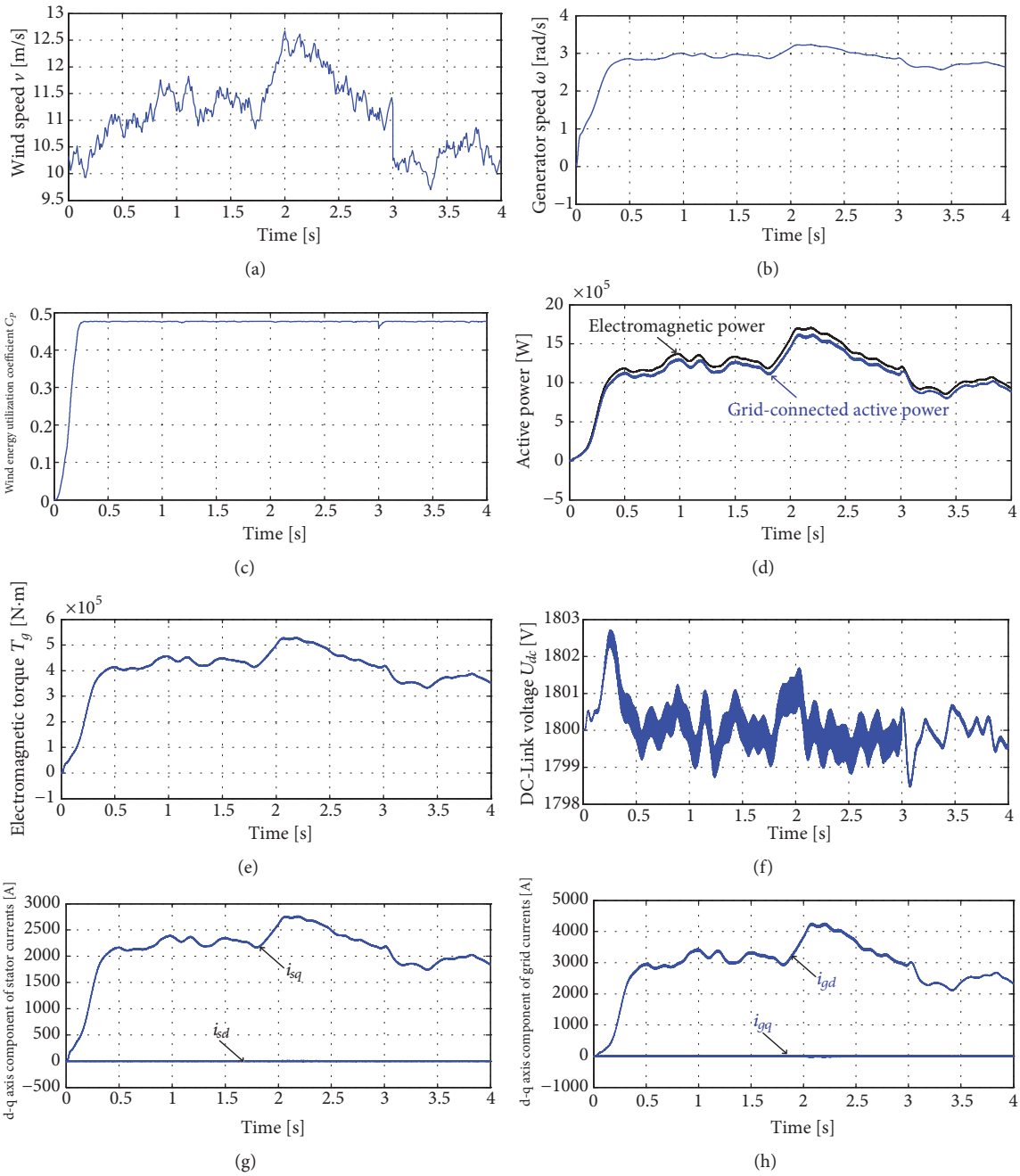

Figure 9: Variable wind speed and system responses.

To further verify the effectiveness of the proposed method, the system responses under variable wind speed must be observed and analyzed. As Figure 9(a) shows, the wind speed varied from 10 m/s to 12.5m/s. At this time, the system response curves under the variable wind speed are shown in Figures 9(b)–9(h). It is clear that the results demonstrated the correctness and effectiveness of the proposed approach again. Figures 9(c) and 9(f) show that the wind energy utilization coefficient C_P is always maintained at its maximum value C_{P_max} (0.476) and the DC-link voltage U_{dc} always fluctuates around U_{dc_ref} (1800V), whether the wind speed changes. From Figure 9(d), the grid-connected active power is always less than the electromagnetic power due to the copper loss.

5. Conclusion

A novel PI-type SMC was proposed to ensure efficient and stability of PMSG-based WECS, in this paper. The presented strategy with a strong robustness for the uncertainties and disturbances of the system can make the closed-loop system globally stable and more performant, compared with the conventional control method. Finally, a 2MW WECS simulation test platform which is based on the MATLAB/MATLAB/SIMULINK/SimPowerSysterms environment was built to verify the maturity and effectiveness of this presented control algorithm. The simulation results indicated that the new method is able to reduce the current distortion and torque fluctuation, which has important actual significance for the control of practical wind turbine.

Data Availability

The data used to support the findings of this study are available from the corresponding author upon request.

Conflicts of Interest

The authors declare that there are no conflicts of interest regarding the publication of this paper.

Acknowledgments

The research was supported by Key R&D projects in Shaanxi (Grant no. 2017GY-061).

References

[1] J. Liu, H. Meng, Y. Hu, Z. Lin, and W. Wang, "A novel MPPT method for enhancing energy conversion efficiency taking power smoothing into account," *Energy Conversion and Management*, vol. 101, pp. 738–748, 2015.

[2] D. Song, J. Yang, X. Fan et al., "Maximum power extraction for wind turbines through a novel yaw control solution using predicted wind directions," *Energy Conversion and Management*, vol. 157, pp. 587–599, 2018.

[3] F. Zhou and J. Liu, "Pitch controller design of wind turbine based on nonlinear PI/PD control," *Shock and Vibration*, vol. 2018, Article ID 7859510, 14 pages, 2018.

[4] D. Song, X. Fan, J. Yang, A. Liu, S. Chen, and Y. H. Joo, "Power extraction efficiency optimization of horizontal-axis wind turbines through optimizing control parameters of yaw control systems using an intelligent method," *Applied Energy*, vol. 224, pp. 267–279, 2018.

[5] F. Zhou and J. Liu, "A robust control strategy research on PMSG-based WECS considering the uncertainties," *IEEE Access*, vol. 6, pp. 51951–51963, 2018.

[6] S. Li, T. A. Haskew, R. P. Swatloski, and W. Gathings, "Optimal and direct-current vector control of direct-driven PMSG wind turbines," *IEEE Transactions on Power Electronics*, vol. 27, no. 5, pp. 2335–2337, 2012.

[7] P. Li, R.-X. Li, Y. Cao, D.-Y. Li, and G. Xie, "Multi-objective sizing optimization for island microgrids using triangular aggregation model and levy-harmony algorithm," *IEEE Transactions on Industrial Informatics*, p. 99, 2017.

[8] P. Li, R. Dargaville, Y. Cao, D. Li, and J. Xia, "Storage aided system property enhancing and hybrid robust smoothing for large-scale pv systems," *IEEE Transactions on Smart Grid*, vol. 8, no. 6, pp. 2871–2879, 2017.

[9] M. Little and K. Pope, "Performance modelling for wind turbines operating in harsh conditions," *International Journal of Energy Research*, vol. 41, no. 3, pp. 417–428, 2017.

[10] J. Yan, H. Lin, Y. Feng, X. Guo, Y. Huang, and Z. Q. Zhu, "Improved sliding mode model reference adaptive system speed observer for fuzzy control of direct-drive permanent magnet synchronous generator wind power generation system," *IET Renewable Power Generation*, vol. 7, no. 1, pp. 28–35, 2013.

[11] Y. A.-R. I. Mohamed, "Design and implementation of a robust current-control scheme for a PMSM vector drive with a simple adaptive disturbance observer," *IEEE Transactions on Industrial Electronics*, vol. 54, no. 4, pp. 1981–1988, 2007.

[12] R. Errouissi, M. Ouhrouche, W.-H. Chen, and A. M. Trzynadlowski, "Robust nonlinear predictive controller for permanent-magnet synchronous motors with an optimized cost function," *IEEE Transactions on Industrial Electronics*, vol. 59, no. 7, pp. 2849–2858, 2012.

[13] H. Liu and S. Li, "Speed control for PMSM servo system using predictive functional control and extended state observer," *IEEE Transactions on Industrial Electronics*, vol. 59, no. 2, pp. 1171–1183, 2012.

[14] R. Errouissi, A. Al-Durra, and M. Debouza, "A novel design of PI current controller for PMSG-based wind turbine considering transient performance specifications and control saturation," *IEEE Transactions on Industrial Electronics*, vol. 65, no. 11, pp. 8624–8634, 2018.

[15] X. H. Yu and O. Kaynak, "Sliding-mode control with soft computing: a survey," *IEEE Transactions on Industrial Electronics*, vol. 56, no. 9, pp. 3275–3285, 2009.

[16] O. Kaynak, K. Erbatur, and M. Ertugrul, "The fusion of computationally intelligent methodologies and sliding-mode control—a survey," *IEEE Transactions on Industrial Electronics*, vol. 48, no. 1, pp. 4–17, 2001.

[17] L. Shang and J. Hu, "Sliding-mode-based direct power control of grid-connected wind-turbine-driven doubly fed induction generators under unbalanced grid voltage conditions," *IEEE Transactions on Energy Conversion*, vol. 27, no. 2, pp. 362–373, 2012.

[18] S. M. Mozayan, M. Saad, H. Vahedi, H. Fortin-Blanchette, and M. Soltani, "Sliding mode control of PMSG wind turbine based on enhanced exponential reaching law," *IEEE Transactions on Industrial Electronics*, vol. 63, no. 10, pp. 6148–6159, 2016.

[19] C. Evangelista, P. Puleston, F. Valenciaga, and L. M. Fridman, "Lyapunov-designed super-twisting sliding mode control for wind energy conversion optimization," *IEEE Transactions on Industrial Electronics*, vol. 60, no. 2, pp. 538–545, 2013.

[20] J. Yang, S. Li, and X. Yu, "Sliding-mode control for systems with mismatched uncertainties via a disturbance observer," *IEEE Transactions on Industrial Electronics*, vol. 60, no. 1, pp. 160–169, 2013.

[21] R. Errouissi and A. Al-Durra, "A novel PI-type sliding surface for PMSG-based wind turbine with improved transient performance," *IEEE Transactions on Energy Conversion*, vol. 33, no. 2, pp. 834–844, 2018.

[22] C. Xia, G. Jiang, W. Chen, and T. Shi, "Switching-gain adaptation current control for brushless DC motors," *IEEE Transactions on Industrial Electronics*, vol. 63, no. 4, pp. 2044–2052, 2016.

[23] J. Hu, H. Nian, B. Hu, Y. He, and Z. Q. Zhu, "Direct active and reactive power regulation of DFIG using sliding-mode control approach," *IEEE Transactions on Energy Conversion*, vol. 25, no. 4, pp. 1028–1039, 2010.

[24] B. Beltran, T. Ahmed-Ali, and M. El Hachemi Benbouzid, "Sliding mode power control of variable-speed wind energy conversion systems," *IEEE Transactions on Energy Conversion*, vol. 23, no. 2, pp. 551–558, 2008.

[25] C. J. Smith, C. J. Crabtree, and P. C. Matthews, "Impact of wind conditions on thermal loading of PMSG wind turbine power converters," in *Proceedings of the 8th IET International Conference on Power Electronics, Machines and Drives, PEMD 2016*, UK, April 2016.

[26] J. Lu, Y. Hu, X. Zhang, Z. Wang, J. Liu, and C. Gan, "High frequency voltage injection sensorless control technique for ipmsms fed by a three-phase four-switch inverter with a single current sensor," *IEEE/ASME Transactions on Mechatronics*, vol. 99, no. 1, p. 1, 2018.

[27] J. Lu, X. Zhang, Y. Hu, J. Liu, C. Gan, and Z. Wang, "Independent phase current reconstruction strategy for ipmsm sensorless control without using null switching states," *IEEE Transactions on Industrial Electronics*, vol. 99, p. 1, 2017.

[28] F. Fateh, W. N. White, and D. Gruenbacher, "Torsional vibrations mitigation in the drivetrain of DFIG-based grid-connected wind turbine," *IEEE Transactions on Industry Applications*, vol. 53, no. 6, pp. 5760–5767, 2017.

[29] I. P. Girsang, J. S. Dhupia, E. Muljadi, M. Singh, and J. Jonkman, "Modeling and control to mitigate resonant load in variable-speed wind turbine drivetrain," *IEEE Journal of Emerging and Selected Topics in Power Electronics*, vol. 1, no. 4, pp. 277–286, 2013.

[30] E. A. Bossanyi, "The design of closed loop controllers for wind turbines," *Wind Energy*, vol. 3, no. 3, pp. 149–163, 2000.

[31] E. A. Bossanyi, "Wind turbine control for load reduction," *Wind Energy*, vol. 6, no. 3, pp. 229–244, 2003.

[32] Bossanyi, Ervin, and D. Witcher, "Controller for 5MW reference turbine," Project UpWind, Bristol, England, 2009.

[33] F. Zhang, W. E. Leithead, and O. Anaya-Lara, "A combined controller design of power system stabilizer and wind turbine drivetrain damping filter," in *Proceedings of the International Conference on Sustainable Power Generation and Supply, SUPERGEN 2012*, p. 41, September 2012.

[34] J. Licari, C. E. Ugalde-Loo, J. B. Ekanayake, and N. Jenkins, "Damping of torsional vibrations in a variable-speed wind turbine," *IEEE Transactions on Energy Conversion*, vol. 28, no. 1, pp. 172–180, 2013.

[35] D. H. Anca and G. Michalke, "Modelling and control of variable-speed multi-pole permanent magnet synchronous generator wind turbine," *Wind Energy*, vol. 11, pp. 537–554, 2008.

[36] T. Orlowska-Kowalska and K. Szabat, "Damping of torsional vibrations in two-mass system using adaptive sliding neuro-fuzzy approach," *IEEE Transactions on Industrial Informatics*, vol. 4, no. 1, pp. 47–57, 2008.

[37] R. Muszynski and J. Deskur, "Damping of torsional vibrations in high-dynamic industrial drives," *IEEE Transactions on Industrial Electronics*, vol. 57, no. 2, pp. 544–552, 2010.

[38] A. Lorenzo-Bonache, A. Honrubia-Escribano, F. Jiménez-Buendía, Á. Molina-García, and E. Gómez-Lázaro, "Generic type 3 wind turbine model based on IEC 61400-27-1: Parameter analysis and transient response under voltage dips," *Energies*, vol. 10, no. 9, 2017.